

NASA Ames Research Center

1991

Research
&
Technology

On the cover:

The use of color graphics is a powerful and flexible visualization tool. The photograph on the cover shows annual carbon dioxide emissions from soils as modeled from global data bases. Without color, the information in photographs such as this would not be conveyed. (See page 220)

(NASA-TM-103924) 1991 RESEARCH AND
TECHNOLOGY Technical Memorandum,
Fiscal Year 1991 (NASA) ~~2097~~

N93-16652

Unclas

485970

332p

G3/99 0139618

ORIGINAL PAGE
COLOR PHOTOGRAPH

NASA Ames Research Center

1991

Research & Technology


National Aeronautics and Space Administration

Foreword

Each year, brief summaries of selected achievements at both the Ames-Moffett and Ames-Dryden sites of Ames Research Center are compiled as a NASA Technical Memorandum.

This year's report, Research and Technology 1991, presents some of the challenging work recently accomplished in the areas of Aerospace Systems, Aerophysics, Space Research, and Flight Research. Here, you can sample the scope and diversity of the research that is now being conducted and obtain a view of the stimulating research challenges of the future.

If you would like further information on any of the Ames research and technology programs, please call the contact person(s) at the end of each article.

A handwritten signature in black ink, reading "Dale L. Compton". The signature is stylized, with the first name "Dale" circled and the last name "Compton" written in a cursive script.

DALE L. COMPTON
Director

Aerospace Systems Directorate

Aircraft Technology Division

Page

Infrared Flow Visualization and Computational Fluid Dynamics Code Validation	1
<i>Larry Birckelbaw</i>	
Hypersonic Vehicle Design-Synthesis Methodology	2
<i>Jeff V. Bowles, Mark Ardema, Tom Whittaker, Loc C. Huynh</i>	
Hypersonic Waverider Aerothermodynamic Vehicle Optimization	4
<i>Jeff V. Bowles, Tom Whittaker, Loc. C. Huynh</i>	
Single-Stage-to-Orbit Vehicle Comparison	5
<i>Jeff V. Bowles, Tom Whittaker</i>	
Tiltwing Simulation Study	7
<i>Lloyd Corliss</i>	
High-Speed Rotorcraft Design Synthesis	8
<i>Thomas Galloway, Jim Phillips</i>	
Oblique All-Wing Supersonic Transport Aircraft	9
<i>Tom Galloway, Paul Gelhausen, Mark Waters</i>	
Aircraft Synthesis Program Institute	10
<i>Paul Gelhausen</i>	
Design Synthesis of High-Speed Transport Aircraft	11
<i>Paul Gelhausen, Mark Moore</i>	
Electroexpulsive Deicing System/High-Frequency Ship Antenna Interference Test	13
<i>L. Haslim</i>	
Lightweight Telescoping Rescue Boom for Helicopters	14
<i>L. Haslim</i>	
Passive Chlorophyll Detector for Agricultural Use	15
<i>L. Haslim</i>	
Rotor Airloads Correlation using Computational Fluid Dynamics/Lifting-Line Methods	17
<i>Francisco Hernandez</i>	
High-Altitude Aircraft Studies	18
<i>George H. Kidwell</i>	
Rotor-Mounted, High-Speed Data Acquisition System	20
<i>Robert M. Kufeld</i>	
XV-15/Advanced Technology Blades: Dynamic Loads	21
<i>M. Maisei, B. Wellman</i>	
High-Speed Tiltrotor and High-Speed Tiltwing Feasibility Study	22
<i>David R. Schleicher, Thomas L. Galloway</i>	
Second-Generation Comprehensive Analysis System for Tiltrotors	23
<i>Karen S. Studebaker</i>	
High-Speed Rotorcraft Studies	24
<i>Peter Talbot</i>	

Aerospace Systems Directorate (continued)

Page

Information Sciences Division (continued)

Evolutionary Tree Reconstruction	66
<i>Peter Cheeseman, Megan Eskey</i>	
Principal Investigator in a Box	67
<i>Silvano Colombano, Irving Statler, Michael Compton</i>	
Integrated Planning, Scheduling, and Control	68
<i>Mark Drummond</i>	
Large-Space-Structure Damage Identification	70
<i>B. J. Glass, A. Macalou</i>	
SETI Hardware Diagnostic and Control Systems	71
<i>B. J. Glass, R. Swab</i>	
Space Station Freedom Thermal-Control-System Automation Testbed	72
<i>B.J. Glass</i>	
Networked Processor Performance Prediction	73
<i>Terry Grant</i>	
The Effects of Video Compression on Acceptability of Images for Monitoring Life Sciences Experiments	74
<i>Richard F. Haines, Sherry L. Chuang</i>	
Robotic Vision Using an Optical Correlator	75
<i>Butler P. Hine, Max B. Reid, John D. Downie</i>	
Intelligent-Knowledge-Base Refinement	77
<i>Smadar Kedar</i>	
Scientists' Intelligent Graphical Modeling Assistant	78
<i>Richard Keller</i>	
Mission Controller Assistant Project	79
<i>Deepak Kulkarni</i>	
Efficient Learning Algorithms Project	80
<i>Philip Laird</i>	
ICARUS: An Integrated Cognitive Architecture	81
<i>Pat Langley, Wayne Iba</i>	
Microprocessor for the Space Station Freedom Data Management System	82
<i>Y. K. Liu</i>	
Real-Time Operating System for the Space Station Freedom Data Management System	82
<i>Y. K. Liu, J. Gibson</i>	
Efficient Scheduling Algorithms	83
<i>Steve Minton</i>	
Advanced Architectures and Software Engineering	84
<i>Daniel L. Ostermiller, Andre Goforth</i>	
Modeling Techniques for Fault-Tolerant Computing Systems	85
<i>F. Ann Patterson-Hine</i>	
Superfluid Helium On-Orbit Transfer	86
<i>Eric Raymond</i>	

Aerospace Systems Directorate (continued)**Page****Information Sciences Division (continued)**

Photonics and Optical Processing	87
<i>Max B. Reid</i>	
Parallel Systems Research	88
<i>Cathy Schulbach</i>	

Aerospace Human Factors Research Division

Automatic Calibration for Sensor Images	89
<i>Albert J. Ahumada, Jr., Jeffrey B. Mulligan</i>	
Electronic Chart Display Development	90
<i>Vernol Battiste</i>	
3-D Auditory Displays in Aeronautical Applications	92
<i>Durand R. Begault</i>	
Extravehicular Activity Self-Rescue in Virtual Environments	93
<i>Adam R. Brody, Stephen R. Ellis</i>	
Control Delegation in the Automated Cockpit	94
<i>Stephen Casner</i>	
Design of Visual Information Displays	95
<i>Stephen Casner</i>	
Dynamic Anthropometric Modeling	95
<i>Kevin M. Corker</i>	
Enroute Flight Planning	96
<i>Kevin Corker, Everett Palmer</i>	
Flight Management System Human Factors	97
<i>Kevin Corker, Everett Palmer</i>	
Symbolic Operator Model	98
<i>Kevin M. Corker, E. James Hartzell</i>	
Human Performance in Virtual Environments	99
<i>Stephen R. Ellis, Kenneth E. Nemire</i>	
Telerobotic Planning and Operational Interfaces	100
<i>Stephen R. Ellis</i>	
Distance Estimation with Night-Vision Devices	102
<i>David C. Foyle, Mary K. Kaiser</i>	
Flight Displays Using Superimposed Symbolology	103
<i>David C. Foyle, Robert S. McCann</i>	
Army–NASA Aircrew/Aircraft Integration Program	105
<i>E. James Hartzell</i>	
Context, Computation, and Complexity: Applications to Aviation Display Design	106
<i>E. James Hartzell</i>	
Enhancing Air Traffic Control Displays	107
<i>James C. Johnston, Krista Horlitz, Robert Edmiston</i>	

Aerospace Systems Directorate (continued)

Page

Aerospace Human Factors Research Division (continued)

Visual Augmentation for Night Flight	108
<i>Mary K. Kaiser, Walter W. Johnson, Lyn Mowafy</i>	
Visual Cues for Temporal Range Estimation	110
<i>Mary K. Kaiser, Lyn Mowafy</i>	
Team Performance in Space-Analogous Environments	111
<i>Barbara G. Kanki, Judith Orasanu</i>	
Social/Organizational Influences on Team Performance	112
<i>Barbara G. Kanki, Judith Orasanu</i>	
Visibility Modeling Tool	113
<i>James O. Larimer</i>	
Display/Viewer System Models for Display Design	114
<i>James O. Larimer</i>	
Data Link Human Factors Research	115
<i>Sandra Lozito, Alison McGann, Kevin Corker</i>	
Virtual Planetary Exploration	116
<i>Michael W. McGreevy, Lewis Hitchner</i>	
Vision-Based Halftoning	117
<i>Jeffrey B. Mulligan, Albert J. Ahumada</i>	
Automation and Crew Coordination	118
<i>Judith Orasanu, Barbara G. Kanki, Everett Palmer</i>	
Crew Factors in Aircrew Performance	119
<i>Judith Orasanu, Barbara G. Kanki</i>	
Distributed Cognition	120
<i>Everett Palmer</i>	
Electronic Checklists	121
<i>Everett Palmer, Asaf Degani</i>	
Human Self-Motion Perception	122
<i>John Perrone, Leland S. Stone</i>	
Intelligent Integrated Displays for Launch-Control Operators	123
<i>Roger Remington</i>	
Crew Fatigue Factors in Flight Operations	124
<i>Mark R. Rosekind, Philippa Gander</i>	
Fatigue Countermeasures in Flight Operations	125
<i>Mark R. Rosekind, Philippa Gander</i>	
The Astronaut Science Advisor	126
<i>Irving C. Statler</i>	
Perceptual Compression of Digital Video	127
<i>Andrew B. Watson</i>	

Aerospace Systems Directorate (continued)**Page****Aerospace Human Factors Research Division (continued)**

Listening with Someone Else's Ears	128
<i>Elizabeth M. Wenzel</i>	
Simulating Complex Virtual Acoustic Environments	130
<i>Elizabeth M. Wenzel</i>	

Flight Systems and Simulation Research Division

Neural Network Algorithms for Passive Ranging	132
<i>Yair Barniv</i>	
Automated Nap-of-the-Earth Guidance and Control	133
<i>V. H. L. Cheng</i>	
Helicopter Flight Simulation	134
<i>V. H. L. Cheng, T. Lam</i>	
Evaluation of Automated Nap-of-the-Earth Guidance	136
<i>R. Coppenbarger, V. H. L. Cheng</i>	
RASCAL Flight Facility	137
<i>Michelle M. Eshow</i>	
Four-Dimensional Aircraft/Air Traffic Control Integration Study	138
<i>Steven Green, Wim den Braven</i>	
Field Evaluation of CTAS	139
<i>A. David Jones</i>	
The Traffic Management Advisory Station	140
<i>Frank Neuman</i>	
Attitude Control with Linear Error Dynamics	141
<i>Russell Paielli, Ralph Bach</i>	
Passive Range Map Refinement Using Texture and Segmentation	142
<i>Banavar Sridhar</i>	
Vision-Based Techniques for Rotorcraft Low-Altitude Flight	144
<i>Banavar Sridhar, Raymond Suorsa</i>	

Aerophysics Directorate

Page

Aerodynamics Division

Flow Through Boundary-Layer Bleed Holes	147
<i>Wei J. Chyu</i>	
High-Speed Civil Transport Design and Analysis	148
<i>Susan E. Cliff-Hovey, Michael D. Madson</i>	
Aircraft Optimization	149
<i>John W. Gallman</i>	
Supersonic Transport Wing Design	151
<i>Raymond M. Hicks, James J. Reuther</i>	
Supersonic Aerodynamics of a Highly Swept Oblique Wing	152
<i>Robert A. Kennelly, Jr., Stephen C. Smith, James M. Strong</i>	
Business Jet Design Modifications Using TRANAIR	153
<i>Michael D. Madson, Robert A. Kennelly, Jr.</i>	
Design and Analysis of Low-Sonic-Boom Configurations	154
<i>Michael D. Madson, Susan E. Cliff-Hovey</i>	
Unstructured Cartesian-Grid-Based Euler Solutions	155
<i>John E. Melton</i>	
Experimental Sonic Boom	156
<i>Joel P. Mendoza</i>	
Cruise Missile Turboprop Installation Interactions Test	157
<i>Ronald C. Smith</i>	

Fluid Dynamics Division

Simulation of the SOFIA Flow Field	158
<i>Christopher A. Atwood, William R. Van Dalsem</i>	
Simulation of High-Speed Impulsive Rotor Noise	159
<i>James Douglas Baeder</i>	
A New Wing-Design Code for High-Speed Civil Transports	161
<i>I. Chang, F. Torres</i>	
Direct Numerical Simulation of Turbulent Flow over Riblets	163
<i>Haecheon Choi, Parviz Moin, John Kim</i>	
Modeling Compressed Turbulence	164
<i>Gary N. Coleman, Nagi N. Mansour</i>	
Supersonic Laminar Flow Control	165
<i>Jolen Flores, Eugene Tu, Lyndell King</i>	
Three-Dimensional Simulations of Multistage Compressor Flows	166
<i>Karen L. Gundy-Burlet, Man Mohan Rai</i>	
Hypersonic Shock-Wave/Boundary-Layer Interaction Flows	167
<i>C. C. Horstman, M. I. Kussoy</i>	
Hypersonic Forebody Analysis	167
<i>Scott L. Lawrence</i>	

Aerophysics Directorate (continued)**Page****Fluid Dynamics Division (continued)**

S3D—An Interactive Surface-Grid-Generation Tool	169
<i>Raymond C. Luh, Larry Pierce, David Yip</i>	
Pressure-Sensitive Paint in the Supersonic High-Sweep Oblique Wing Test	171
<i>B. G. McLachlan, J. H. Bell, R. A. Kennelly</i>	
Surface Representation with a Scanning 3-D Laser Digitizer	172
<i>Marshal L. Merriam, Timothy J. Barth</i>	
Dynamic Subgrid Scale Model for Large-Eddy Simulation of Turbulence	173
<i>Parviz Moin</i>	
Low-Aspect-Ratio Wing Experiment	174
<i>M. Olsen, H. L. Seegmiller</i>	
Direct Simulation of Transition on a Flat Plate	176
<i>Man Mohan Rai, Parviz Moin</i>	
An Experimental/Computational Study of Heat Transfer in Sharp-Fin-Induced Turbulent Interactions	177
<i>P. E. Rodi</i>	
The Evolution of a Turbulent Mixing Layer	178
<i>Michael M. Rogers, Robert D. Moser</i>	
Flow over Multielement Airfoils	179
<i>Stuart E. Rogers, N. Lyn Wiltberger, Dochan Kwak</i>	
Boundary-Layer Measurements in the Ames 80- by 120-Foot Wind Tunnel	181
<i>S. G. Saddoughi, S. V. Veeravalli</i>	
YAV-8B V/STOL Research Aircraft Flow Simulation	182
<i>Merritt H. Smith, Kalpana Chawla, William R. Van Dalsem</i>	
Canard-Wing Aerodynamic Interaction	183
<i>Eugene L. Tu</i>	
Comparison of Compressibility Corrections for Turbulence Models Applied to High-Speed Shear Layers	185
<i>J. Viegas</i>	
Simulation of Turbulent Flow on a Highly Parallel Computer	186
<i>Alan A. Wray</i>	
Initial Rollup of a Wingtip Vortex	187
<i>Greg G. Zilliac, Jim S. Chow, Peter Bradshaw</i>	

Numerical Aerodynamic Simulation Systems Division

The NAS Parallel Benchmarks	189
<i>D. H. Bailey, H. D. Simon, T. A. Lasinski, J. T. Barton</i>	

Aerophysics Directorate (continued)

Page

Thermosciences Division

Modeling of the Fabrication of Ceramic Coatings and Composites	191
<i>Domenick E. Cagliostro</i>	
MESUR Heat Shield Computations	192
<i>William D. Henline</i>	
Composite Flexible Blanket Insulation	193
<i>Demetrius A. Kourtides</i>	
Advanced Toughened Uni-Piece Fibrous Insulation (TUFI-MT)	194
<i>Daniel B. Leiser</i>	
TOPHAT Thermal Protection System Performance	195
<i>Salvatore R. Riccitiello</i>	
TABI Aeroacoustic Performance	197
<i>Paul M. Sawko</i>	
Computerized Film Reading	198
<i>Leslie A. Yates</i>	
Constructed Images from Computed Flow Fields	199
<i>Leslie A. Yates</i>	
Trim-Angle Measurements	200
<i>Leslie A. Yates, Ethiraj Venkatapathy</i>	

Space Research Directorate

Page

Advanced Life Support Division

Lunar Outpost Life-Support-System Analysis	201
<i>Mark G. Ballin, William C. Likens, Vincent J. Bilardo, Jr.</i>	
Adsorption Research for Life-Support Systems	203
<i>John E. Finn, Sanford S. Davis</i>	
The CELSS Test Facility: A Foundation for Crop Research in Space	204
<i>C. L. Straight, R. D. MacElroy</i>	
Advanced Life-Support System Design	205
<i>Rebecca C. Williamson, Peter J. Sharer, Bruce W. Webbon</i>	

Space Projects Division

Resonant Infrared Photoconductor	207
<i>Jam Farhoomand, Robert E. McMurray</i>	
Mars Environmental Survey (MESUR)—Feasibility of a Low-Cost Global Approach	208
<i>G. Scott Hubbard, Paul F. Wercinski, George L. Sarver, Robert P. Hanel, Ruben Ramos</i>	
An Si(Li) Gamma-Ray Detector Stack for Future Mars Missions	209
<i>G. Scott Hubbard, Robert E. McMurray, Jr., Robert G. Keller, Paul F. Wercinski, John T. Walton, Kari Vierinen</i>	
Superfluid-Helium-Gap Heat Switch	212
<i>Ali Kashani, Ben Helvensteijn, Randall Wilcox</i>	
Advanced Low-Temperature Readouts	213
<i>Robert E. McMurray, Jr., Mark E. McKelvey, Craig R. McCreight</i>	
He-3–He-4 Dilution Refrigerator	214
<i>Pat Roach, Ben Helvensteijn</i>	

Earth System Science Division

Oakland Hills Fire Storm: Remote Sensing and Emergency Management	216
<i>James A. Brass</i>	
Ozone-Depletion Research	217
<i>Guy V. Ferry</i>	
Detection of Changes in Migratory Waterfowl Habitats in California	217
<i>Liane S. Guild, Laurence L. Strong</i>	
Meteorological Satellite Downlink and Display System	218
<i>Steve Hipkind</i>	
ERS-1 Investigations of High-Latitude Wetlands	219
<i>Leslie A. Morrissey</i>	
Terrestrial Ecosystem Trace-Gas Fluxes: Application of a Global Model	220
<i>Christopher S. Potter, Pamela A. Matson, Steven A. Klooster</i>	

Space Research Directorate (continued)

Page

Earth System Science Division (continued)

Measurement of Graphitic Carbon (Soot) in the Stratosphere	221
<i>Rudolf F. Pueschel</i>	
Evolution of Carbon Fixation	221
<i>Lynn J. Rothschild</i>	
Earth Science Advanced Aircraft	222
<i>Philip B. Russell, Jennifer Baer-Riedhart, Steven S. Wegener</i>	
Biospheric Monitoring and Disease Prediction	223
<i>Michael Spanner, Byron Wood, Louisa Beck, Sheri Whitney, Rick Ross, Liane Guild</i>	
Radiative Effects of Aerosols and Clouds	224
<i>Francisco P. J. Valero</i>	
Studies of Stratospheric Trace Gases	225
<i>James F. Vedder</i>	
Cloud and Radiation Parameterizations for Use in Weather and Climate Models	226
<i>Douglas L. Westphal</i>	
Airborne Tracking Sun Photometer	227
<i>Robert C. Wrigley</i>	

Search for Extraterrestrial Intelligence Office

The Search for Extraterrestrial Intelligence (SETI)	228
<i>Peter R. Backus</i>	

Life Science Division

Biochemistry of Bone Mineral Deficits in Space	229
<i>Sara B. Arnaud</i>	
Intramuscular Pressure to Optimize Space Exercise	230
<i>Richard E. Ballard, Michael Aratow, Donald E. Watenpaugh</i>	
Acute Blood-Volume Redistribution with Posture	231
<i>Gregory A. Breit, Donald E. Watenpaugh, Alan R. Hargens</i>	
Behavioral and Neural Adaptation to Altered Gravity	233
<i>Nancy G. Daunton, Merylee Cocoran, Muriel Ross</i>	
Effects of Glucose Solutions on Thermoregulation	234
<i>John E. Greenleaf, Alan S. Dearborn, Andrew C. Ertl</i>	
Role of Muscle Function and Growth Hormones in the Prevention of Muscle Atrophy	235
<i>Richard E. Grindeland</i>	
Cellular Growth and Aging Phenomena	237
<i>Rosalind A. Grymes, Joan Vernikos</i>	
Circulatory Changes during Simulated Microgravity	238
<i>Yasuaki Kawai, M. Shannon Stout, Gita Murthy</i>	

Space Research Directorate (continued)

Page

Life Science Division (continued)

Increased Intracranial Pressure during Simulated Microgravity	239
<i>Gita Murthy, Donald E. Watenpaugh, Alan R. Hargens</i>	
Macular Bioaccelerometer Plasticity in Novel Gravitational Environments	240
<i>Muriel D. Ross</i>	
Dynamic Inter-Limb Resistance Exercise Device	242
<i>Douglas F. Schwandt, Alan R. Hargens, Scott E. Parazynski</i>	
A 4-Day Head-Down Bed-Rest Analog for Quick Screening of 0-G Countermeasure Effectiveness	243
<i>Joan Vernikos</i>	
Atrial Natriuretic Peptide Reduces Leg Capillary Filtration	245
<i>Donald E. Watenpaugh, Alan R. Hargens</i>	
Influence of Loading History on Muscle Fiber Cross-Sectional Area	246
<i>Robert T. Whalen</i>	

Space Science Division

The Nanophase Iron Mineral(s) in Mars Soil	248
<i>Amos Banin, Talia Ben-Shlomo, Leon Margulies, David F. Blake, Andreas U. Gehring</i>	
The Satellites of Mars	248
<i>Jeffrey F. Bell, Fraser Fanale, Dale P. Cruikshank</i>	
Low-Temperature Phase Changes in Cometary Ice Analogs	249
<i>David Blake, Lou Allamandola</i>	
Planetary Lightning	250
<i>William J. Borucki, John W. Dyer, Julio A. Magalhaes, H. Sarma Lakkaraju, Chris P. McKay</i>	
Search for Lightning on Neptune	251
<i>William J. Borucki, Phan Pham</i>	
Two-Dimensional Infrared Array Cameras	252
<i>Jesse D. Bregman, David M. Rank</i>	
Research on the Origins of Chondrule Dust Rims	253
<i>Ted Bunch</i>	
Molecule Formation in Star-Forming Regions	254
<i>Steven B. Charnley, Alexander G. G. M. Tielens</i>	
Solid Cyanide-Bearing Material on Outer-Solar-System Bodies	256
<i>Dale P. Cruikshank, William K. Hartmann, David J. Tholen, Louis J. Allamandola, Clifford N. Matthews</i>	
Particle-gas Dynamics in the Protoplanetary Nebula	256
<i>Jeff Cuzzi</i>	
Planetary Ring Dynamics and Morphology	257
<i>Jeff Cuzzi</i>	
Hydrocarbons Produced in the Hydrothermal Aquifers of Yellowstone National Park	258
<i>David J. Des Marais</i>	

Space Research Directorate (continued)

Page

Space Science Division (continued)

Planetary Protection and the Mars Environmental Survey Mission	259
<i>Donald L. DeVincenzi</i>	
Airborne Astronomy	260
<i>Edward W. Dunham, Edwin F. Erickson, Jacqueline A. Davidson</i>	
Asteroid 951 Gaspra	261
<i>Jeffrey D. Goldader, David J. Tholen, Dale P. Cruikshank, William K. Hartmann</i>	
Solving a Coupled Schrödinger Equation for the X ² Π State of OH	262
<i>David Goorvitch, David C. Galant</i>	
Water on Mars	263
<i>Robert M. Haberle</i>	
On the Origin of the Nitrate Reductase from Halobacterium Denitrificans	264
<i>Lawrence I. Hochstein, Frank Lang</i>	
The Relationship of Halobacterial ATPases to ATP Synthases and Vacuolar ATPases	264
<i>Lawrence I. Hochstein, Helga Stan-Lotter</i>	
Center for Star Formation	265
<i>David Hollenbach, Patrick Cassen</i>	
Prokaryotic Membrane Evolution	266
<i>Linda L. Jahnke, Helga Stan-Lotter, Lawrence I. Hochstein</i>	
Modulated-Voltage Microvolume Metastable Ionization Detector for Gas Chromatography	267
<i>Daniel R. Kojiro, Norishige Takeuchi, Donald E. Humphry</i>	
Space Shuttle Glovebox Experiment for Testing Particle-Dispersion Methods	268
<i>J. R. Marshall</i>	
Object 2201 Oljato: Asteroid or Comet?	269
<i>L. A. McFadden, A. L. Cochran, E. S. Barker, D. P. Cruikshank, W. K. Hartmann, S. J. Ostro</i>	
History of Water on Mars: A Biological Perspective	269
<i>Christopher P. McKay, E. Imre Friedmann, Robert A. Wharton, Wanda L. Davis</i>	
Titan's Greenhouse and Anti-Greenhouse Effects	270
<i>Christopher P. McKay, James B. Pollack, Regis Courtin</i>	
The Diffuse Interstellar Dust Absorption Feature Near 3.4 Micrometers in the Near Infrared	271
<i>Yvonne J. Pendleton, Lou Allamandola, Farid Salama, Scott Sandford, Xander Tielens</i>	
Simulation of Titan's Aerosols	272
<i>Shelly K. Pope</i>	
An Infrared Camera for Operation at 10 and 20 Micrometers	273
<i>Thomas L. Roellig, Mark E. McKelvey, Lynne K. Deutsch, Yvonne J. Pendleton, Fred C. Witteborn, Craig R. McCreight</i>	
Oxygen Evolution and Life on Mars	274
<i>Lynn J. Rothschild</i>	
Carbonates on Mars? Some Old Information	275
<i>Ted L. Roush, John P. Monteverdi, Glenn C. Carle, James B. Pollack</i>	

Space Research Directorate (continued)**Page****Space Science Division (continued)**

Diode Laser Spectroscopy of Stable Isotopes	276
<i>T. B. Sauke, J. F. Becker</i>	
Experiments to Identify Mineral Biomarkers	277
<i>D. E. Schwartz, R. L. Mancinelli, M. R. White</i>	
A Novel Method for Preparing PLOT Columns	278
<i>Thomas C. Shen</i>	
Telepresence for Planetary Exploration	279
<i>Carol R. Stoker, Owen Gwynne</i>	
New 120-Detector Infrared Spectrometer	281
<i>Fred C. Witteborn, Jesse D. Bregman, Thomas P. Greene</i>	
Gravity Waves in the Atmosphere of Venus	282
<i>Richard E. Young, Howard Houben</i>	
Airbursts and Craters on Venus	283
<i>Kevin Zahnle</i>	

Dryden Flight Research Facility Directorate

Page

Research Engineering Division

X-29 High-Angle-of-Attack Control Improvements	285
<i>Jeffrey E. Bauer, Robert Clarke</i>	
A Real-Time Flight-Control Clearance Test Technique for Hypersonic Vehicles	286
<i>John T. Bosworth</i>	
Determination of Thrust-Vectoring Effectiveness on Jet Aircraft by Infrared Photography	287
<i>Albion H. Bowers, Larry D. Birckelbaw</i>	
Flight-Determined Stability Margins for Multiloop Control Systems	288
<i>John J. Burken</i>	
Automated Flight Qualification	290
<i>Vince Chacon</i>	
X-29 Aerodynamic Characterization	291
<i>David F. Fisher, John H. Del Frate</i>	
Supersonic Flight-Test Verification of Phase Reversal	293
<i>Robert J. Geenen, Bianca T. Anderson</i>	
Performance-Seeking Control Flight Results	295
<i>Glenn Gilyard</i>	
Airborne Instrumentation Computer System	297
<i>Paul Harney</i>	
Systems-Research Testbed Aircraft	298
<i>Dave McBride</i>	
Thrust-Vectoring Research	299
<i>Joseph W. Pahle</i>	
In-Flight Structural Excitation	300
<i>Lura E. Vernon</i>	
Flight-Simulator Electric Control Stick	302
<i>Charles A. Wagner, Michael D. Najera</i>	

Appendix

Color Plates	305
--------------------	-----

Infrared Flow Visualization and Computational Fluid Dynamics Code Validation

Larry Birckelbaw

A nonintrusive measurement technique using a high-resolution, dual-wavelength infrared imaging system has been employed to gather data on various jet-induced flow fields. The digital infrared images are then postprocessed using computational fluid dynamics (CFD) image-enhancement tools to provide detailed flow visualization. For validation of CFD codes, a computational technique is under development that will permit direct quantitative comparison of the measured infrared data with CFD-predicted values. This technique involves the construction of a two-dimensional (2-D) infrared image from the corresponding three-dimensional CFD-predicted flow field.

A number of detailed jet-flow-visualization studies have been done which dramatically demonstrate the technique. These include infrared imaging of the F-18 High Angle of Attack Research Vehicle (HARV) Hot Loads Tests at Dryden to measure the plume deflection angles and turning vane temperatures, and imaging of the static lift augmentation tests of the E-7 short takeoff and vertical landing (STOVL) research model in the Ames Outdoor Aerodynamic Research Facility. A series of dedicated infrared flight tests using the NASA YAV-8B research aircraft have also been conducted to obtain infrared flow-field and surface-heating data at a variety of flight conditions. An example of the infrared images obtained for a slow, low-level approach is shown in the figure. The figure demonstrates that infrared-flow-visualization provides an effective means of examining the complex nature of the multiple-jet-induced flow field. In addition to the infrared flow visualization research, a proof-of-concept computational method for constructing a 2-D infrared image from the predicted flow field has been demonstrated.

The use of infrared imaging as a noninvasive flow-field visualization and measurement technique has provided valuable CFD validation data from full-



Fig. 1. Infrared flow visualization of YAV-8B Harrier aircraft. (See color plate 1 in Appendix)

scale aircraft such as the YAV-8B and has greatly improved our understanding of the complex jet-induced flow fields about those aircraft. Predictions from the validated CFD methods will provide insight into the mechanisms responsible for phenomena such as jet-induced lift loss and hot gas ingestion.

Plans are to continue use of the infrared imaging system to examine the complex flow fields about various aircraft and components and to accelerate development of the CFD validation technique. Additional imaging will be obtained on the Vertical/Short Takeoff and Landing Systems Research Aircraft, the F-18 HARV, and on a number of small-scale tests planned for the Ames Jet Calibration and Hover Test Facility. Development of a CFD validation technique will continue with the results from the small-scale tests used to further refine and validate the computational 2-D infrared-image-generation technique.

**Ames-Moffett contact: L. Birckelbaw
(415) 604-4468**

Headquarters program office: OAST

Hypersonic Vehicle Design-Synthesis Methodology

Jeff V. Bowles, Mark Ardema, Tom Whittaker, Loc C. Huynh

In support of the National Aerospace Plane (NASP) program and more generic hypersonic aircraft studies, the Systems Analysis Branch of the Aircraft Technology Division has continued the enhancement and refinement of conceptual design methodologies to analyze and evaluate hypersonic vehicle concepts. Because of the highly synergistic nature of hypersonic vehicles, the focus of this effort is on the integration of the various disciplinary technology models to capture the inherent design tradeoffs. These analysis models are generally of a simplified nature, but are highly coupled within the synthesis code. Recently completed models include a simplified nose-to-tail propulsion-analysis tool for predicting ramjet and scramjet engine performance, and an optimal-trajectory model for dual-mode-propulsion, hypersonic launch vehicles.

The simplified nose-to-tail propulsion model consists of a planar, inviscid, two-dimensional (2-D), real-gas, weak-wave flow code coupled to a one-dimensional (1-D) subsonic/supersonic combustor analysis code to predict nose-to-tail flow path characteristics. The weak-wave code solves the inviscid inlet flow field as a function of vehicle forebody/ramp geometry, including cowl position, angle of attack, and free-stream Mach number. Equivalent 1-D flow properties are then computed at the inlet throat, and the 1-D combustor mass, momentum, and energy equations with wall skin friction and heat transfer are solved stepwise through the burner. The nozzle flow field is then computed from the combustor exit solution using the real-gas, weak-wave 2-D code, including nozzle and cowl flap geometry. First-order estimates of axial and normal forces and pitching moment are computed as a function of vehicle geometry and flight condition. Overall propulsion-system heat loads are then used to determine fuel-inlet temperature or to compute required engine cooling equivalence ratio.

The simplified nose-to-tail propulsion analysis code has been developed and run at a range of Mach numbers from 4 to 24 at various combinations of flight dynamic pressures, angles of attack, and cowl positions. Computed flow-field properties for the inlet, combustor, and nozzle agree well with those determined by other methods or equivalent codes. Reasonable conservation of mass, momentum, and energy are also demonstrated. Propulsion-system performance with various fuels, including hydrogen, hydrocarbons, and mixtures of fuels, has been computed. The first figure presents the Mach number and pressure flow-field results for a Mach number of 8.0 and an angle of attack of 5.0 degrees. Airframe and cowl are shown as white regions. The combustor geometry shown in the figure has been idealized; the computed engine performance was for a 3.0-area-ratio combustor.

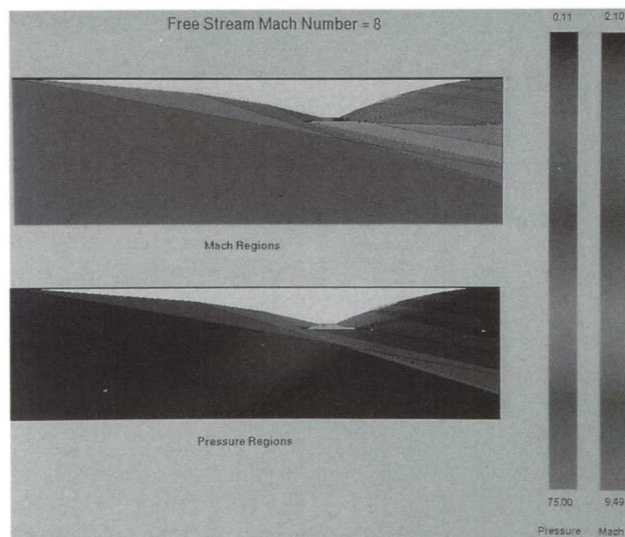


Fig. 1. Mach and pressure flow field nose to tail. (See color plate 2 in Appendix)

The simplified trajectory model involved the development of a near-optimal guidance law for the ascent trajectory from Earth surface to Earth orbit of a hypersonic, dual-mode-propulsion, lifting vehicle. The guidance law is suitable for use in the trajectory subroutine of the hypersonic vehicle design-synthesis program; it computes the aircraft flightpath as well as an algorithm for throttle control of the two propulsion modes.

Beginning with the equations of motion of a point-mass aircraft that is moving relative to a rotating, spherical Earth, the assumptions of small angle of attack and small flightpath angle are invoked to arrive at the energy-state approximation. The independent control variables are vehicle velocity and the throttle settings of the airbreathing and rocket propulsion systems (Π_a and Π_r , respectively). Because hydrogen-fueled hypersonic aircraft are sensitive to volume as well as to mass, a weighted sum (with weighting factor K) of fuel mass and volume is used for parametric optimization (multiple synthesis runs). The constraints on Π_a are complicated, because of (1) the variable geometry of the engine, (2) the transition from ramjet to scramjet, and (3) the need for liquid hydrogen for structural cooling. The constraints on vehicle velocity include maximum dynamic pressure, minimum dynamic pressure, maximum airframe heating, and maximum engine duct pressure.

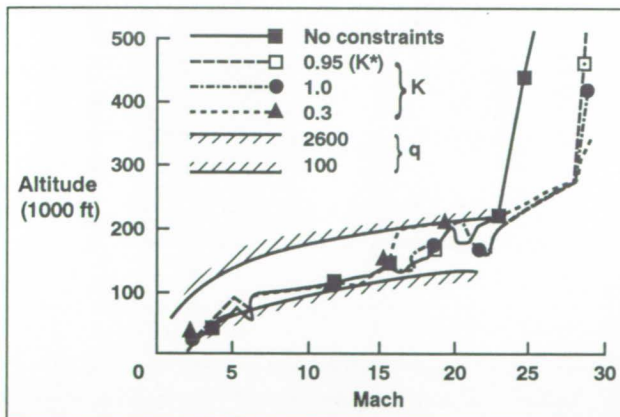


Fig. 2. Optimal trajectory for hypersonic vehicles.

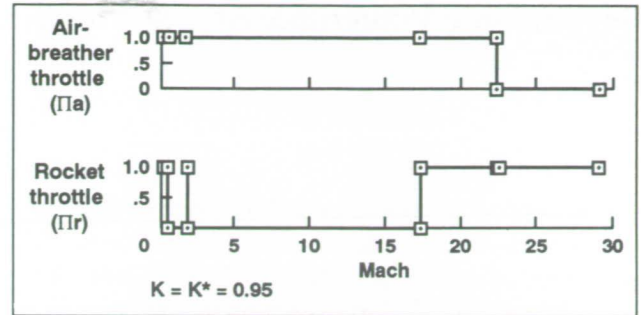


Fig. 3. Engine throttle schedule for hypersonic vehicles.

The second and third figures show the resulting optimal trajectory and the associated optimal throttle controls in which the airbreather starts at full throttle and continues to some hypersonic Mach number, at which point it is turned completely off. For $K = 0.95$, this point is Mach 22, and for $K = 0.30$, it is Mach 17. The rocket comes on full before the airbreather is turned off, so that there is a period when both are on, and at the end of the trajectory only the rocket is on; the rocket is turned on at Mach 17 for $K = 0.95$ and at Mach 13 for $K = 0.30$. For the minimum-gross-weight vehicle, $K = 0.95$. For the case $K = 0.30$, fuel volume is weighted relatively high and therefore the rocket is used relatively more and the airbreather less. In all cases, the rocket was throttled to full briefly at takeoff and through transonic drag rise. The constraints on throttle control are shown in the figure. The flightpaths shown include a constant-energy dive in the transonic region, typical of energy-state optimum paths. They then briefly ride the duct pressure limit before entering a long unconstrained phase. When the airbreather is turned off, they all transition to a high altitude; this is especially true for the $K = 0.30$ case, whose trajectory follows the minimum dynamic pressure boundary after Mach 17. A case with the constraints removed was also run.

Ames-Moffett contact: J. Bowles
(415) 604-6651

Headquarters program office: OAST

Hypersonic Waverider Aerothermodynamic Vehicle Optimization

Jeff V. Bowles, Tom Whittaker, Loc C. Huynh

In support of generic hypersonic aircraft studies, the Systems Analysis Branch has developed an integrated analysis tool for the design and optimization of hypersonic waverider configurations. Waverider configurations are vehicles that derive favorable aerodynamic interference effects to enhance lift at supersonic or hypersonic speeds, and hence offer the potential for improved lift-to-drag ratios. Included in the optimization process are several design constraints on the vehicle configuration.

The geometric definition of a hypersonic waverider configuration is computed by solving the differential equation for the streamlines for a real-gas axisymmetric flow field. The generating surface can be specified either as a free-stream surface (i.e., the upper vehicle surface), or the lower vehicle surface at an arbitrary longitudinal location. A sixth-order polynomial is used to describe the surface geometry. Solution of the real-gas Taylor-Macoll equations gives the inviscid flow properties on the lower surface. A simplified compressible-boundary-layer reference enthalpy method is used to compute the local skin-friction coefficient, which is used in turn to compute both skin-friction drag and equilibrium radiation surface temperatures. Leading-edge temperatures are computed using a swept-cylinder model. Pressure lift and drag are computed by integration of the pressure coefficient over the surface of the vehicle. Base drag is computed using a 70% vacuum pressure coefficient in the vehicle base region. The waverider aerothermal analysis code is coupled with a numerical optimizer (by the method of feasible directions) to optimize the configuration for best viscous lift-to-drag ratio. Other vehicle performance characteristics (e.g., overall drag) may also be selected for the objective function. Design constraints are imposed for vehicle volume, leading-edge surface radiation temperatures, length-to-span ratio, and wing structural thickness.

A 15-foot waverider-configured vehicle flying at an altitude of 92,500 feet was optimized for maximum lift-to-drag ratio for a Mach-8 design point with a 12-degree generating shock. The figure shows the vehicle's geometric design, along with upper- and lower-surface temperature distributions. The constraints are (1) a volume of 1.5% of body length cubed, (2) a leading-edge temperature of 3200 degrees Rankine, (3) a span-to-length ratio of 0.75, and (4) a wing-tip included angle of 5 degrees. The total vehicle lift-to-drag ratio is slightly over 5. Optimal vehicles for other combinations of design constraints have also been generated. Caret-wing configurations can also be generated by the analysis code, and they are typically the optimal designs for

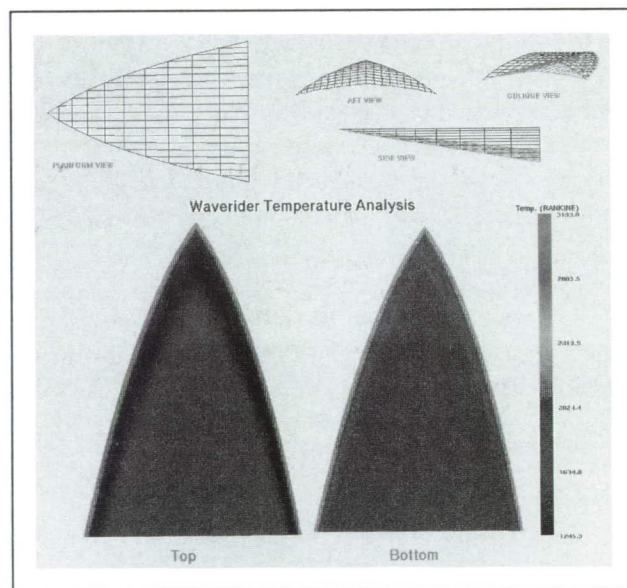


Fig. 1. Optimized Mach 8 Waverider general configuration and surface temperature distribution. (See color plate 3 in Appendix)

low vehicle-volume and leading-edge-temperature constraints.

The waverider aerothermal analysis code forms the basis for optimization of waverider configurations with realistic design constraints imposed on the overall vehicle design. Viscous drag effects and aerothermodynamic impacts are included in the design optimization process, with vehicle volume and structural aspects also considered.

Propulsion-system integration, structural analysis, and internal vehicle layout will be addressed next. A

mission analysis model will then be added and the optimal vehicle design will be determined, including maximum-trimmed-specific-impulse and minimum-gross-weight configurations. Finally, off-design performance of the waverider will be included in an overall vehicle design optimization using the Branch's hypersonic vehicle synthesis code.

**Ames-Moffett contact: J. Bowles
(415) 604-6651**

Headquarters program office: OAST

Single-Stage-to-Orbit Vehicle Comparison

Jeff V. Bowles, Tom Whittaker

As part of the generic hypersonics research program, the Systems Analysis Branch has completed a comparative mission performance analysis of an all-rocket configuration and an air-breather/rocket-assist hybrid vehicle, both sized for single-stage-to-orbit (SSTO) capability. Relative performance, including vehicle empty weight, mission fuel fraction, gross weight, reentry cross range, and overall program costs, was computed.

Mission requirements for both concepts included SSTO to a 120-nautical-mile polar orbit, carrying the same payload weight and volume. Technology levels for structural concept and material selection were compatible with the designs' respective "initial operational capability" date. The all-rocket design is a vertical-takeoff/vertical-landing (VTVL) concept consisting of a blunted-cone configuration with an axisymmetric plug-nozzle base. A lifting-body shape was selected for the air-breather/rocket hybrid design, which has horizontal-takeoff/horizontal-landing (HTHL) capability. The Ames hypersonic vehicle conceptual design code HAVOC was used to compute aerodynamic and propulsion-system performance, and structural/weight characteristics were used to size each vehicle. The all-rocket vehicle flew a low-dynamic-pressure (≤ 200 pounds per square foot) trajectory, and the ascent trajectory for the air-breather/rocket hybrid was optimized for dual-mode-propulsion-system performance. Both vehicles use

maximum lift-to-drag ratio descent trajectories to maximize the reentry cross range.

Aerodynamic analysis showed superior performance for the all-body shape of the air-breather/rocket hybrid design, which has approximately one-third the zero-lift flat-plate drag area that the all-rocket configuration has. The optimized ascent trajectory for the air-breather hybrid resulted in an order-of-magnitude increase in flight dynamic pressure over that of the rocket. The higher aerodynamic loads and aerothermodynamic heating doubled the unit structural weight for the air-breather hybrid. As well as having greater surface area and propulsion-system weight, the hybrid has an empty weight approximately 2.5 times that of the all-rocket (see figure). The significantly better propulsion-system performance of the hybrid requires about 60% of the mission propellant weight that the rocket requires, and the propellant mass fraction of the air-breather hybrid is around 70%, versus 90% for the all-rocket. The design gross weight of the air-breather/rocket hybrid is roughly two-thirds that of the all-rocket concept. With almost twice the lift-to-drag ratio, the all-body hybrid has a reentry cross range near 3000 nautical miles, compared to 1100 nautical miles for the rocket vehicle. Sensitivity studies show that aerodynamic-drag and empty-weight variations have a somewhat higher impact on the air-breather hybrid's performance than they do on the all-rocket vehicle's performance,

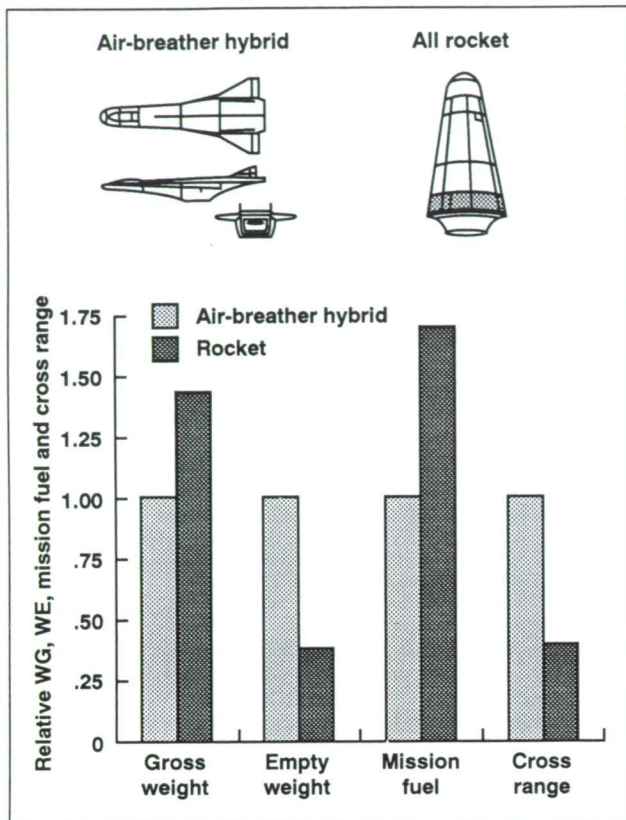


Fig. 1. Relative gross weight, empty weight, mission fuel, and reentry-cross-range capability for hybrid air-breather/rocket versus all-rocket design.

whereas the propulsion-system specific impulse sensitivity of the hybrid is only half that of the rocket design.

Several alternative all-rocket configurations (e.g., HTHL and vertical-takeoff/horizontal-landing wing-body designs) were also studied. The VTVL configuration had the lowest gross weight of all of the all-rocket designs, with the lowest structural and landing-gear weight. However, significant operational, propulsion-system performance, and stability and control issues exist for the VTVL all-rocket configuration that must be resolved.

All-rocket and air-breather/rocket hybrid concepts both represent viable candidates for the SSTD mission, with empty-weight characteristics balanced against mission fuel requirements. The air-breather/rocket hybrid design has gross weight and cross range advantages, but with research-and-development and acquisition costs closely related to empty weight, the all-rocket is approximately half as expensive overall.

Ames-Moffett contact: J. Bowles
(415) 604-6651

Headquarters program office: OAST

Tiltwing Simulation Study

Lloyd Corliss

There is continued interest in the tiltwing concept for vertical/short takeoff and landing (VSTOL) operations both for civil transport and for military special operations. Two initial simulation studies have been conducted on the NASA Ames Vertical Motion Simulator (VMS), in September 1990 and October 1991. These simulations compared two wing-tilting control schemes in a variety of tasks involving conversion and reconversion between hover and forward flight. The inherent handling qualities of the schemes were studied as well as their effects on piloting techniques. The first of the two control schemes is a conventional programmed-flap approach in which the wing tilt is controlled directly by the pilot and the flap is scheduled (programmed) relative to the wing incidence angle. The second control scheme is a novel geared-flap approach in which the flap acts as a servo for positioning the wing relative to the fuselage. This approach involves a free-pivoting wing, with which the pilot's input results primarily in a flap deflection. The math model was sized for an 87,000-pound, four-propeller configuration with an auxiliary tail thruster for low-speed pitch control (see figure).

The first simulation showed that, whereas the two wing-tilting schemes had different response characteristics, the Cooper-Harper handling-qualities ratings were comparable. A second simulation was conducted to explore piloting techniques and control-system refinements. This simulation included a refined math model, the addition of aircraft pitch stabilization, and a further tailoring of the geared-flap control

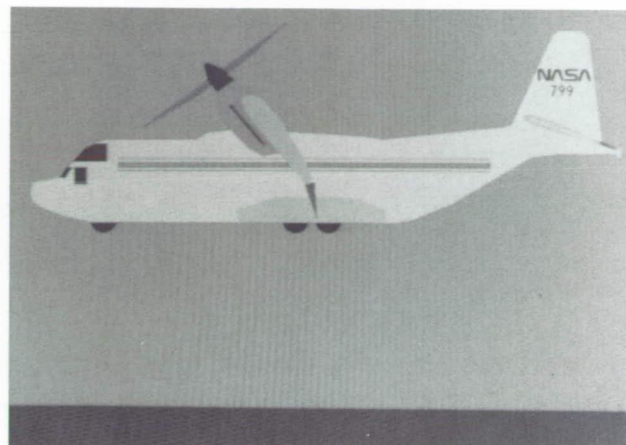


Fig. 1. Transport configuration for tiltwing control system simulation.

system. A significant improvement in handling qualities was observed when pitch attitude stabilization was added to both the programmed and geared-flap control schemes. Tailoring the damping about the wing pivot of the geared flap greatly reduced the misleading longitudinal motion cues noted in the first simulation. Additional studies of the damping and wing pivot location and of the effects of the tail thruster on control power requirements are warranted.

Ames-Moffett contact: L. Corliss

(415) 604-6269

Headquarters program office: OAST

High-Speed Rotorcraft Design Synthesis

Thomas Galloway, Jim Phillips

Tiltwing and stopped-rotor aircraft are attractive rotorcraft concepts for providing efficient hover performance and high-speed forward flight capability. The Systems Analysis Branch has enhanced the vertical/short takeoff and landing (V/STOL) aircraft sizing and performance computer program (VASCOMP) so that the performance and sizing requirements of these high-speed rotorcraft concepts can be estimated and critical design and technology factors identified.

Tiltwing concepts are supported by the propeller during hover operations, such as takeoffs and landings, and by the wing during high-speed cruise flight. The conversion from forward cruise flight to hover is the most critical sequence because of the possibility of wing stall as forward flight speed is reduced. In this condition, the propeller normal force acts far aft and additional propeller thrust is required to balance the normal force. This additional thrust increases the propeller slipstream momentum, which decreases the local wing angle of attack and therefore delays the onset of wing stall. These effects were included in VASCOMP, using a first-order model of this characteristic to ensure the proper sizing of tiltwing aircraft. The figure shows a comparison of wing stall for two wing-chord-to-propeller-diameter ratios (C/D), with and without propeller normal force modeled. Without the normal force modeled (black symbols), the tiltwing with the lower C/D stalls during reconversion, thus the concept is limited to higher C/D s and a heavier aircraft. When the normal force is included in the model (open symbols), the wing is unstalled at lower C/D s, thus a smaller wing with a lower cruise drag is needed, which results in a lighter-weight aircraft at the same cruise speed.

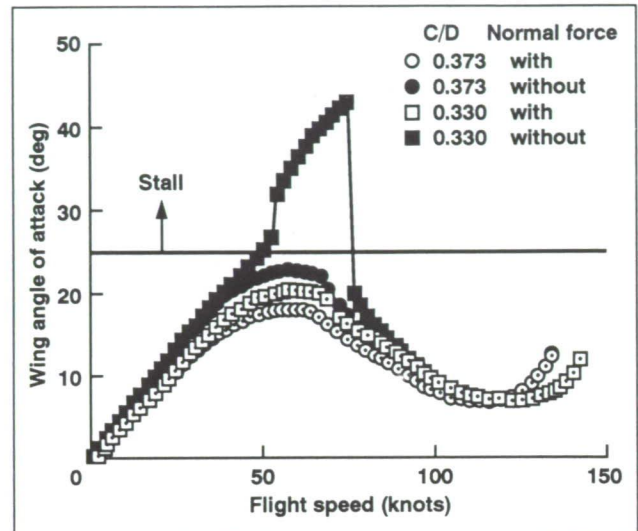


Fig. 1. Tiltwing reconversion.

Current stopped-rotor concepts that are being evaluated use turbine engines in conjunction with tip-jet or circulation-control rotors. A method was developed to model the integration of the engine performance, duct sizing, and tip-jet or circulation-control performance requirements for sizing these components of a stopped-rotor design. The Georgia Institute of Technology is incorporating this methodology into the VASCOMP synthesis program.

Ames-Moffett contact: T. Galloway

(415) 604-6181

Headquarters program office: OAST

Oblique All-Wing Supersonic Transport Aircraft

Tom Galloway, Paul Gelhausen, Mark Waters

The variable-geometry oblique wing is an aircraft concept pioneered by R. T. Jones at Ames Research Center in the late 1950s. Jones predicted that a straight wing swept fore and aft, as shown in the first figure, would minimize induced and wave drag in supersonic flight. Wind tunnel tests and flight tests have been conducted over the past 25 years which verify that Jones' theories for the oblique wing are correct.

The wing-body design has been studied most extensively, but recent work, again initiated by Jones, has concentrated on an oblique all-wing (OAW) aircraft, shown conceptually in the second figure. The Systems Analysis Branch is involved in a detailed evaluation of the OAW aircraft as a supersonic transport that will cruise at a flight Mach number between 1.6 and 2.0. Mach 2 is likely an upper limit for an acceptable OAW aircraft design, established by the constraint of a maximum sweep angle of no more than 70 degrees.

The advantage of the OAW stems from improved aerodynamics and from the potential of reduced structural weight. Excellent aerodynamic performance is achieved over the full Mach-number range because the wing sweep angle can be varied. This is particularly important at takeoff. The engines are sized at cruise, and, with the aircraft's excellent low-speed performance, takeoff is easily achieved at partial power. The result is an estimated sideline noise just below the Federal Air Regulations Part 36 requirement.

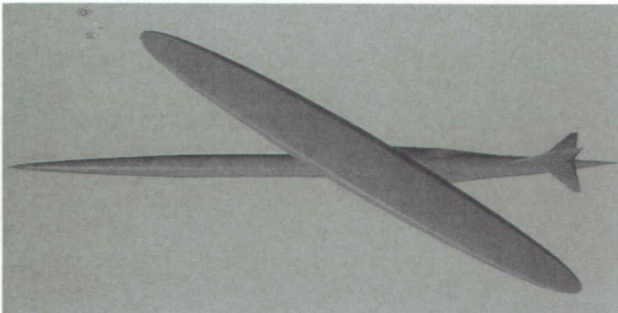


Fig. 1. Oblique wing-body (OWB).

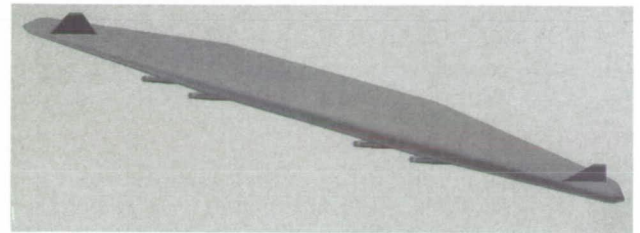


Fig. 2. Oblique all-wing (OAW).

The potential for reduced structural weight for the OAW aircraft is a result of the aircraft's having been designed as a "spanloader." The weight of the aircraft—payload, fuel, and systems—is distributed along the span of the wing, thereby reducing the bending moments that result from a difference in weight and lift at any spanwise location on the wing. An important objective of the current study is to derive efficient interior designs that maximize this spanloading effect.

Preliminary design synthesis of a 500-passenger OAW transport for a range of 5500 nautical miles has defined an aircraft that has the nominal takeoff weight of the current Boeing 747. The estimated direct operating cost is slightly less than that for the Boeing 747, and the block time is reduced by approximately 40%. If these results prove to be accurate, the OAW aircraft will be a logical candidate for development. However, there are design constraints which must be evaluated more carefully. First, the wing must be quite thick—the required interior headroom will result in a wing at least 8 feet thick. Also, the chordwise center of gravity should be at approximately 32% of the wing chord. This gives maximum chord lengths of about 55–60 feet. Wing aspect ratio for good performance is nominally 10, and therefore the wingspan is approximately 400–430 feet. Thus the OAW aircraft is large, and the aircraft may be incompatible with present airport ground operations.

Another factor that must be evaluated more carefully is the orientation of passengers with respect to the direction of flight. The OAW aircraft is at a sweep angle of nominally 30 degrees at takeoff, and current plans are to orient the cabin seating so that passengers face the direction of flight at this sweep angle. This orientation has a significant effect on the size of the passenger cabin and thus on the total wing planform.

Ongoing studies are evaluating the geometric constraints of the OAW more carefully to determine their effect on the gross weight and economic perfor-

mance of the aircraft. It is likely that the economic performance may be lower than that indicated above. However, if the OAW aircraft can be shown to have economic performance and noise characteristics comparable to modern subsonic aircraft, and give a 40% savings in trans-Pacific block time, it will be a serious candidate for future development.

Ames-Moffett contact: T. Galloway

(415) 604-6181

Headquarters program office: OAST

Aircraft Synthesis Program Institute

Paul Gelhausen

The Aircraft Synthesis Program (ACSYNT) Institute brings together NASA, manufacturers of airframes and engines, Virginia Polytechnic Institute (VPI), and other academic institutions to work in direct collaboration on the further development of aircraft synthesis methods. Under this jointly sponsored research agreement, ACSYNT, a computer program originally developed at Ames Research Center, is continually updated and expanded to broaden the types of aircraft and increase the number of technical and economic parameters addressed during the conceptual design analysis. The institute provides a cooperative environment for communication and enhances the utilization of resources to achieve common goals. Members of the institute pay an annual fee that is used to fund further research. New members are Boeing Commercial Airplane Company, Cessna, Defense Group, Inc., and the Naval Technical Intelligence Center.

This project uses the FORTRAN, C, PHIGS, and UNIX programming standards to develop a code that is machine and graphics-device independent and thus executable on a wide range of current UNIX workstations. The program is currently running on Apollo, Silicon Graphics, IBM, and Sun workstations, all of which are using the same graphics calls.

Recent research has improved the interface to higher-order aerodynamic methods, which are used to validate ACSYNT's semiempirical methods. The figure shows an aircraft model that has been generated by applying an automatic wing-fuselage blending algorithm that creates a second-order continuous fillet. A model like this can be used to quickly study

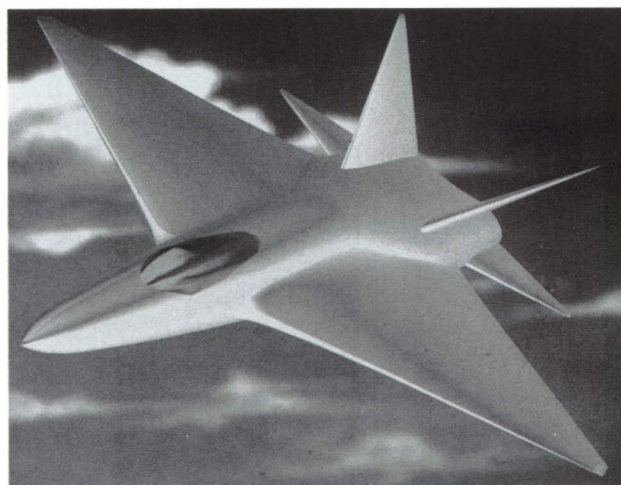


Fig. 1. Blended wing-body configuration from automatic filleting methodology.

the volume and surface area distributions of conceptual configurations, and can be used as initial input to higher-order methods. The user interface has been greatly enhanced by streamlining the original menu structure and using a spreadsheet input with on-line help for the parametric variables. These capabilities are combined with existing multidisciplinary synthesis and optimization techniques to create a powerful, integrated design tool.

The institute has established the following near-term goals:

1. Restructure the geometric and aerodynamic data to allow more general aircraft geometry.
2. Fully implement B-spline surfaces to utilize all of the tools that have been developed for geometric analysis of the conceptual design.

3. Integrate the Navy-NASA Engine Program (NNEP) with ACSYNT to provide a substantial improvement of the propulsion modeling and design capability available to users.

4. Incorporate a library containing geometric, aerodynamic, and weight information on aircraft components.

**Ames-Moffett contact: P. Gelhausen
(415) 604-5701**

Headquarters program office: OAST

Design Synthesis of High-Speed Transport Aircraft

Paul Gelhausen, Mark Moore

The High-Speed Research Program is addressing technology development and risk reduction for economically viable and environmentally acceptable high-speed civil transports (HSCT). Through the use of the ACSYNT aircraft design synthesis program, concepts can be geometrically modeled; sized for a specific mission using aerodynamic, propulsion, and weight estimations; and then further analyzed for the economic, sonic boom, and takeoff noise characteristics. Concepts can be investigated through sensitivity analysis or optimized with certain size, performance, cost, or sonic boom constraints. Subsonic aircraft correlation models have also been developed for comparison with HSCT configurations to ensure a balanced assessment of results. There have been three key developments to ACSYNT in support of HSCT design studies: (1) ability to model arbitrary wing planform geometry, (2) use of higher-order aerodynamic analysis in the early stages of design, and (3) economic-analysis enhancements.

The ability to analyze arbitrary wing planform geometry is an important consideration since many of the possible configurations of HSCT include cranked delta wings with leading- or trailing-edge extensions.

Improvements have been made that permit complex wings to be geometrically modeled, using multiple-wing-section panels, and then analyzed.

In order to verify the aerodynamic estimation procedures used in ACSYNT, the same geometric computer models are used for higher-order aerodynamic analysis. Two examples of this procedure can be seen in the determination of supersonic wave drag and induced drag, which are critical to the HSCT. Complex surface geometries such as that depicted in the first figure can be analyzed using the Harris wave drag program and the Vorlax vortex lattice method



Fig. 1. Geometry model of a high-speed civil transport.

program. Visualization tools permit previewing and modification of the paneling schemes, and graphical analysis of the results, such as cross-sectional area distribution and pressure distribution using color coding, as shown in the second figure. These results are also important for verification of takeoff-and-landing aerodynamics that can size the aircraft.

The economic analysis has been greatly enhanced, permitting the estimation of return on investment for both manufacturing and operations. Research-and-development and manufacturing costs are determined through the use of first-unit cost estimations based on item weight. Complexity factors are used to account for item comparative complexity as well as differences in material cost and complexity. Operational costs are determined as direct expenses, with a breakdown into crew, fuel, financing, and maintenance costs, and indirect expenses, with a breakdown into system and local maintenance, passenger and traffic services, and administrative

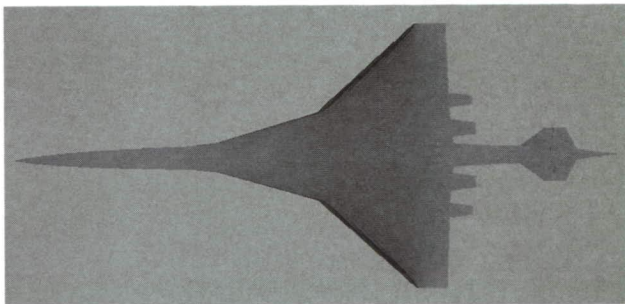


Fig. 2. Pressure distribution predicted using VORLAX. (See color plate 4 in Appendix)

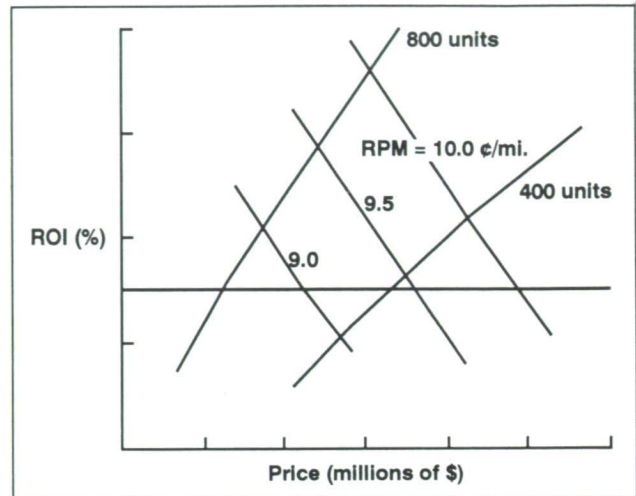


Fig. 3. Predicted return on investment as a function of aircraft price.

costs. The third figure shows the predicted return-on-investment (ROI) results for a transport aircraft based on the potential revenue per passenger mile (RPM) and the number of aircraft manufactured. Aircraft economics can now be used as optimization objectives or constraints. This capability will ensure that the most economically viable concepts are pursued.

**Ames-Moffett contact: P. Gelhausen
(415) 604-5701**

Headquarters program office: OAST

Electroexpulsive Deicing System/High-Frequency Ship Antenna Interference Test

L. Haslim

High-frequency (HF) communications is the prime mode in naval vessels. However, atmospheric-ice thicknesses of several inches can attenuate the ship communications range. This attenuation occurs when ice bridges the active antenna area across the antenna base insulator to ship ground. Bridging by saltwater-spray ice can also completely short out the antenna.

An Ames version of the electroexpulsive deicing system (EEDS) was designed, built, and evaluation tested by simulated deicing of the active HF mast region from the insulator base. This program was undertaken cooperatively with the Naval Ocean Systems Center (NOSC). The evaluation was per-

formed at NOSC's antenna test lab using 35-foot HF ship mast antennas (see figure). The test evaluated the impact of both the inactive and the energized EEDS on the antenna's transmission and reception characteristics in a nonicing environment. The EEDS was found to have no adverse effect on the HF antenna's transmission or reception over the entire range of operating frequencies (2–30 megahertz). The EEDS system was also shielded so that it could function satisfactorily under all operating conditions. The shielding, which did not inhibit the deicing boot performance, was achieved by wrapping the boot with a thin sandwich of Faraday cage material.

1. EEDS deicing boot
2. EEDS pulse power cable
(Power supply is beneath in tunnel, near transmitter)
3. Antenna lead
4. Antenna impedance matching coil
5. 35-foot HF antenna mast

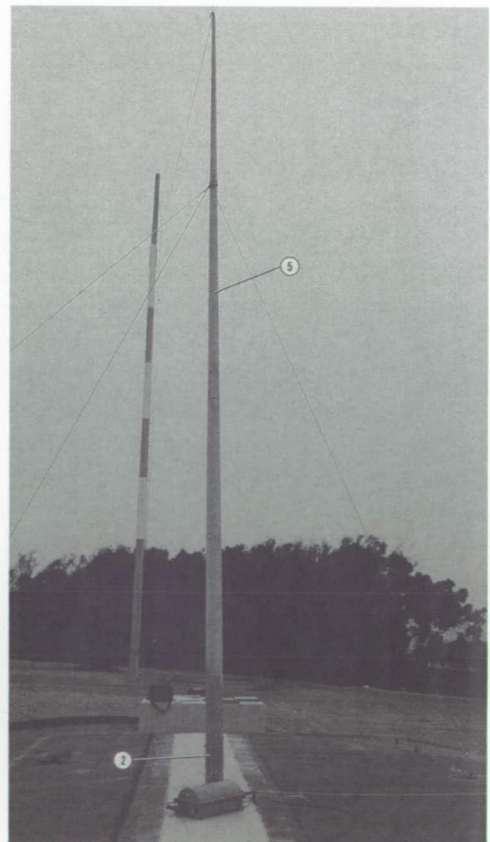
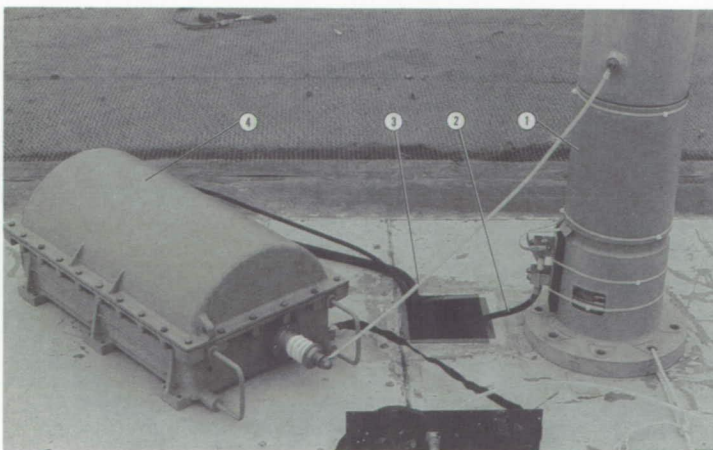


Fig 1. EEDS applied to insulator base of Navy HF Communications antenna at NOSC antenna facility for radio frequency compatibility tests.

These tests have advanced EEDS in the following ways.

1. With the Ames shielding, EEDS will operate efficiently in a high-electromagnetic-field environment, such as the high-power-density environment that resulted from operating it in close proximity to 1000 watts of transmitted power.

2. EEDS will not interfere with transmission, reception, or functioning of operating HF ship mast antennas from minimum to maximum transmitting power of 1000 watts.

3. The electromagnetic interference and radio-frequency interference of the EEDS are well understood.

4. The EEDS is ready for sea-trial demonstration on HF masts.

Ames-Moffett contact: L. Haslim

(415) 604-6575

Headquarters program office: NAVSEA

Lightweight Telescoping Rescue Boom for Helicopters

L. Haslim

The goal of this project was to devise a method to accurately place a rescue line from a helicopter directly over a rescuee and allow a full expanded view of the operation by the helicopter pilot. A retractable boom, for which a U.S. Government Patent (No. 5,020,742) was issued on June 4, 1991, has been designed to project from the location of the existing rescue hoist to the front of the helicopter where it will be within the pilot's view and beyond the downwash from the main rotor (see first figure). Another feature of this design is a novel lightweight device (second figure) enabling extension and retraction of the telescoping rescue boom. This device effectively yields a stiff, nonkinking, push-pull rod capable of extending or retracting the rescue boom without a large weight penalty. In rescue operations, no load is borne by the boom. Rather, as weight is placed on the rescue line, the line progressively unsnaps from eyelets that carry it beneath the boom, and finally connects only to the standard, existing lift hoist located on the aircraft. A design study by Kaman Aerospace (makers of the Navy's SH-2 helicopter) has indicated that the concept and design are feasible. A preliminary study estimates that the total weight of the telescoping boom will be less than 60 pounds, and that the boom can be easily accommodated on the helicopter's existing "hardpoint," which can carry 600 pounds.



Fig. 1. Lightweight, telescoping rescue boom in use.

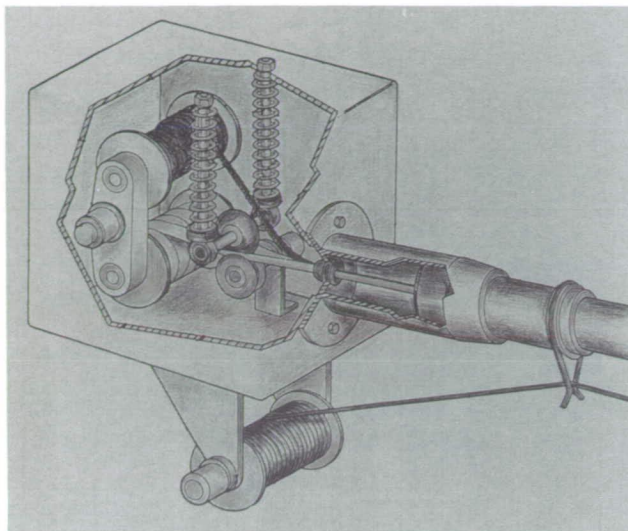


Fig. 2. Device for extension and retraction of the telescoping rescue boom.

The development of the Ames lightweight rescue boom for helicopters creates the potential for greatly enhancing the utility of rotorcraft for rescue operations. The concept provides a potential helicopter system that can be positioned in the line of vision of the pilot, reduces exposure of the rescue victim to downwash created by the main rotor, and permits the relatively easy positioning of the rescue line between obstacles such as masts and superstructures during shipboard rescues. The potential light-weight extension and retraction mechanism may have many spin-off applications, including the in situ erection of telescopic structures in space.

Ames-Moffett contact: L. Haslim

(415) 604-6575

Headquarters program office: OAST

Passive Chlorophyll Detector for Agricultural Use

L. Haslim

Plants die unnecessarily in forests and on farms around the world because the human eye cannot detect an unhealthy plant's early warning signs. An optical filter developed at the Ames Research Center enhances these signs, and has the potential to alert scientists and farmers before conditions become irreversible.

The passive chlorophyll detector (PCD) uses a dyed optical filter to discriminate the reflectance spectra of chlorophyll-bearing vegetation and trees. The filter conveys plant stress caused by such factors as insufficient water or minerals by exaggerating the visual effects of incipient chlorosis. Examples of the reflectance spectra for corn leaves with various levels of water content is shown in the first figure. Observing vegetation through special PCD goggles makes unhealthy, yellowed plants appear more yellow, and green plants seem more green, for a striking contrast (second figure). Thus an untrained observer can potentially see what formerly only an experienced farmer could detect.

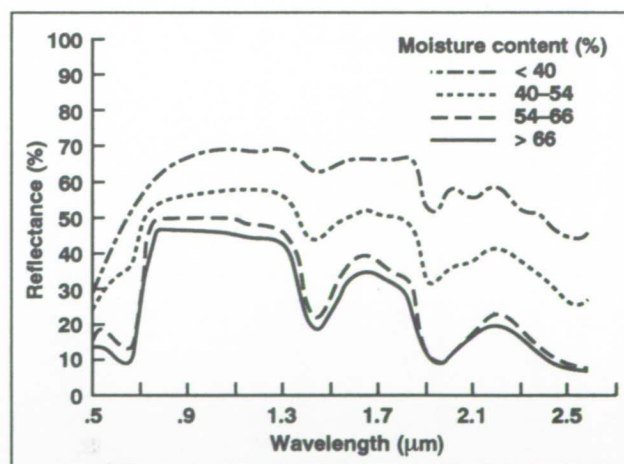


Fig. 1. Reflectance spectra of corn leaves with various levels of water content.

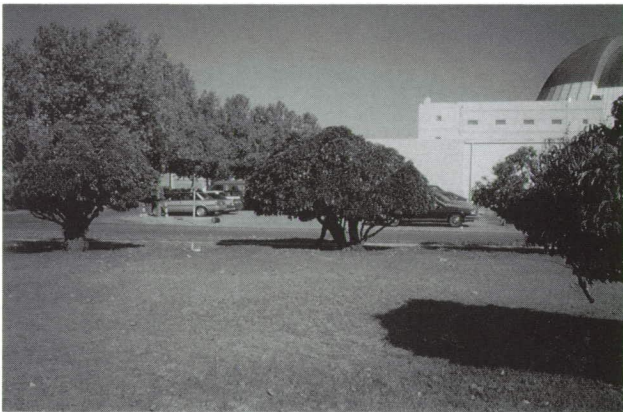
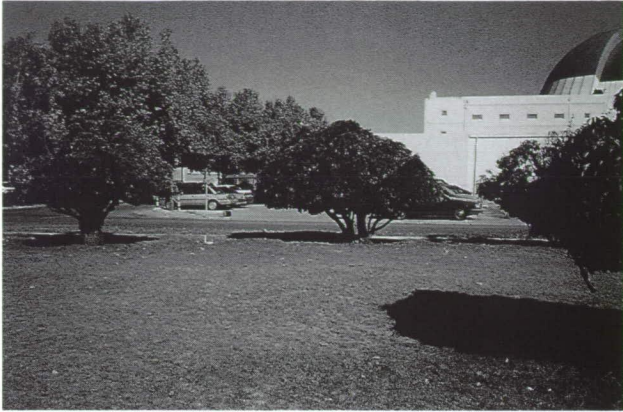


Fig. 2. Viewing foliage with the unassisted human eye (top) fails to reveal areas of plant stress that are highlighted (in red) when the passive chlorophyll detector is used. (See color plate 5 in Appendix)

The ability to economically and easily discriminate, evaluate, and record the spectral reflectance of vegetation allows immediate real-time information to be obtained on the condition or health of the plants. An advantage of this system is that processing of infrared film or sensor information is not required.

The low-cost PCD filters can be tailored for various types of foliage and used by farmers to determine when to nurse or replant unhealthy fields, thereby increasing crop yields. The PCD would allow environmental scientists to monitor the health of forests and wetlands exposed to acid rain or contaminated groundwater. Large areas could be evaluated rapidly by flying over and filming them using a camera with a PCD film over the lens. Such cameras could even be used on routine inspection flights in remote-piloted aircraft to provide real-time imaging.

Ames-Moffett contact: L. Haslim

(415) 604-6575

Headquarters program office: OAST

ORIGINAL PAGE
BLACK AND WHITE PHOTOGRAPH

Rotor Airloads Correlation using Computational Fluid Dynamics/Lifting-Line Methods

Francisco Hernandez

The objective of this work is to assess the predictive capability of current state-of-the-art rotorcraft aerodynamic codes for modern rotors by comparing results with existing flight-test data. The comprehensive rotorcraft code CAMRAD/JA is used to model the aerodynamics and dynamics of the complete rotorcraft configuration. To obtain the detailed blade airloads, the Full-Potential Rotor Code (FPR) is coupled with CAMRAD/JA in an iterative loop. The final solutions are the predicted airloads on the rotor system, which are then compared with flight measurements at different operating conditions.

To evaluate the effectiveness of CAMRAD/JA coupled with FPR, a detailed airloads correlation effort on an AH-1G Cobra helicopter has been completed. This computational method was used to

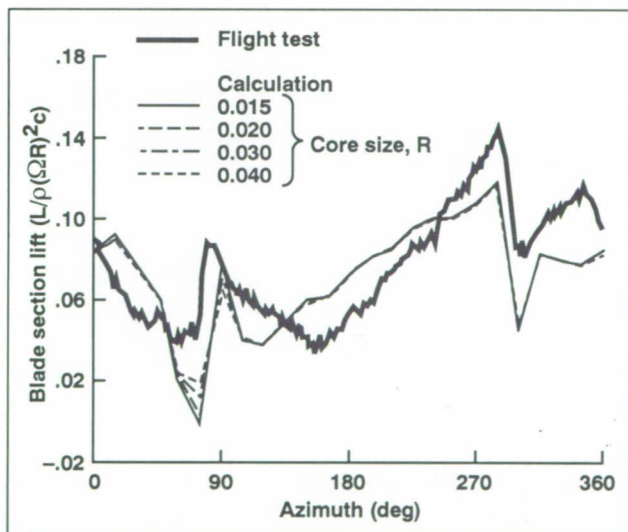


Fig. 1. Blade-vortex-interaction loading calculations, AH-1G Cobra ($V = 82$ knots, $r/R = 0.97$).

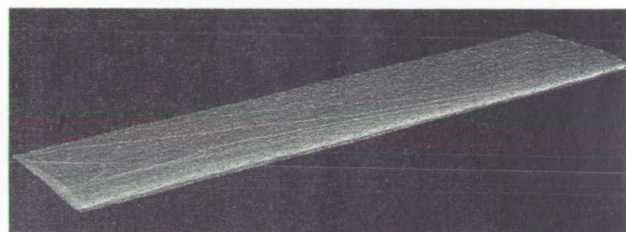


Fig. 2. Calculated Mach contours for AH-1G blade for high-speed flight conditions where compressibility is encountered. (See color plate 6 in Appendix)

calculate the blade airloads and give insight into the nature of blade-vortex-interaction loads at low advance ratios. The first figure shows the correlation between calculated and measured blade-section lift in a flight condition appropriate for blade-vortex interactions. In the figure, blade-vortex encounters are readily apparent at azimuth angles around 90 degrees and 280 degrees. The calculated values use various vortex core sizes to show their effect on the lift loading. For this case, the effect of vortex core size was minimal.

At high advance ratios, the same approach was used to predict the transonic compressibility effects present on the advancing side of the rotor disk. The use of CAMRAD/JA coupled with FPR allowed both a quantitative and a qualitative analysis of the flow phenomena in a very efficient manner. The second figure shows predicted Mach contours at a high advance ratio where transonic flow is present. The results of this correlation work were presented at an AHS Specialist meeting in October 1991.

CAMRAD/JA coupled with FPR and other computational methods has been used to predict the rotor airloads on the UH-60 Blackhawk and to compare them with existing experimental data from the Duits-Nederlandse Windtunnel (DNW) in the Netherlands. The CAMRAD/JA-FPR model has been developed in preparation for Phase II of the UH-60 Airloads Program, currently under way at Ames.

The accurate prediction of rotor airloads is one of the biggest challenges in the field of theoretical aerodynamics and one that remains to be solved. Current rotorcraft aerodynamic codes make use of many approximations and assumptions that ultimately must be replaced by more accurate methods. In order to determine the validity of such methods and

improve upon them, correlation work with experimental data is needed. Such improved codes will help in the design of better rotor systems.

Computational methods are being used to model the UH-60 Blackhawk rotor system from hover to high advance ratios. Preliminary results have been compared with model wind tunnel data at different flight conditions. These methods will help in the prediction of rotor airloads during Phase II of the UH-60 Airloads Program.

**Ames-Moffett contact: F. Hernandez
(415) 604-1322**

Headquarters program office: OAST

High-Altitude Aircraft Studies

George H. Kidwell

NASA and other government agencies, in conjunction with universities, require uncrewed research aircraft in which to perform atmospheric, Earth remote sensing, and even astronomy missions. Measurements and sampling within the upper stratosphere are of particular importance in developing or refining ozone depletion models. The stratospheric missions that have been conducted at the poles have utilized NASA's three ER-2 aircraft, which have an altitude ceiling of approximately 70,000 feet. However, atmospheric scientists have identified requirements for sustained in-situ data collection at altitudes of 100,000 feet or greater, which will require aircraft with large payloads and long range. This is far beyond the capabilities of any existing aircraft. There are additional applications, such as long-duration remote sensing, that vie for space in advanced-capability research aircraft.

The Systems Analysis Branch has been studying alternative aircraft configurations, technologies, and missions in order to evaluate the state of the art for very-high-altitude aircraft and to estimate the scope and cost of a program to achieve various scientific objectives. One direction of these studies is to assess design options such as the airframe layout or the type of powerplant, to determine the leading candidates in terms of their potential and the technical risk. This information will be used to develop an appropriate research program if current technology is not adequate to meet requirements.

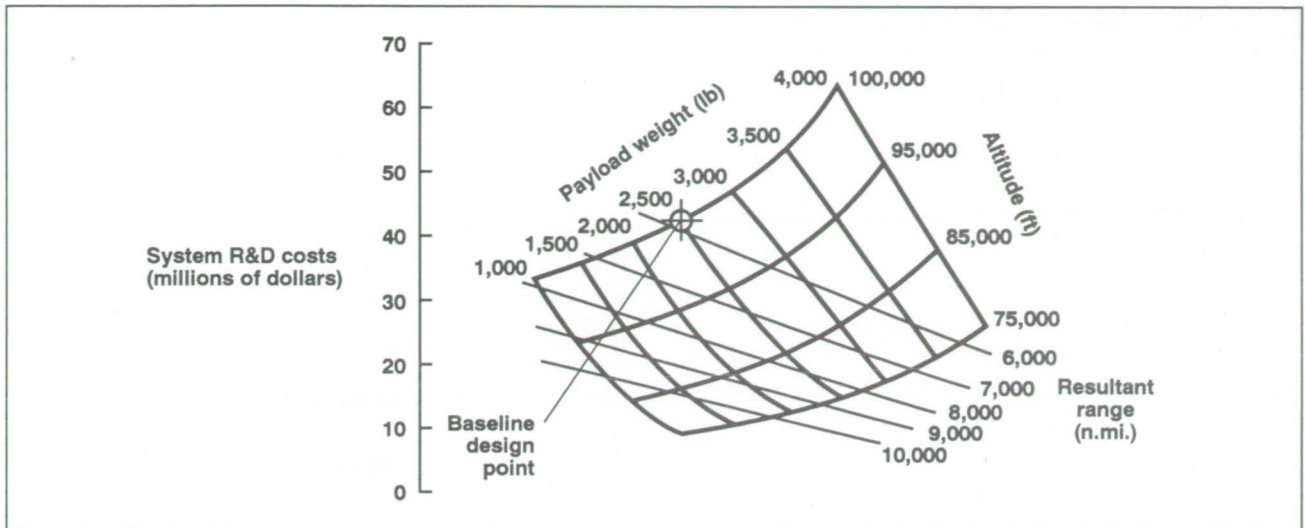


Fig. 1. Research-and-development cost as a function of mission parameters.

The figure shows how estimates of research and development costs vary with altitude, range, and payload weight for one research aircraft concept. The design mission was to carry a payload of 2,500 pounds for a total range of 6,000 nautical miles at a cruise altitude of 100,000 feet. It can be seen that for higher values of these parameters, the cost increases much more quickly than at the lower values; that is, the rate of change (sensitivity) increases. Note that the gross weight of the aircraft has been held

constant, so that range is a dependent parameter. This means that a decrease in payload weight for constant cruise altitude allows more fuel to be carried, resulting in longer range.

Ames-Moffett contact: G. Kidwell

(415) 604-5886

Headquarters program office: OAST

Rotor-Mounted, High-Speed Data Acquisition System

Robert M. Kufeld

A high-speed, airborne data acquisition system has been developed for rotorcraft research flight testing. The data acquisition system will collect the airfoil pressure distribution, blade stresses, control loads, and blade motion for various helicopter research programs. This system is capable of collecting up to 350 data parameters at a rate of over 2000 data samples per second. The total bit rate of the system will be over 7.5 megabits per second. The high sample rate is required to capture changes within the pressure distribution in less than one-degree increments of rotor azimuthal travel. In addition, all data will be synchronized for analysis.

Ten identical pulse-code-modulator (PCM) encoders are joined together to meet the high-speed data collection requirements. The 10 data systems are controlled by a common synchronization pulse which initiates data collection through sample-and-hold amplifiers. The data passes through filters to the analog-to-digital PCM encoders, then flows as a digital stream through a slip ring into the helicopter's cabin. Each PCM system's data set includes time data and rotor position data to confirm synchronization.

The data system is mounted in a circular container and attached to the top of the main rotor hub as



Fig. 1. Data system mounted on main rotor hub.

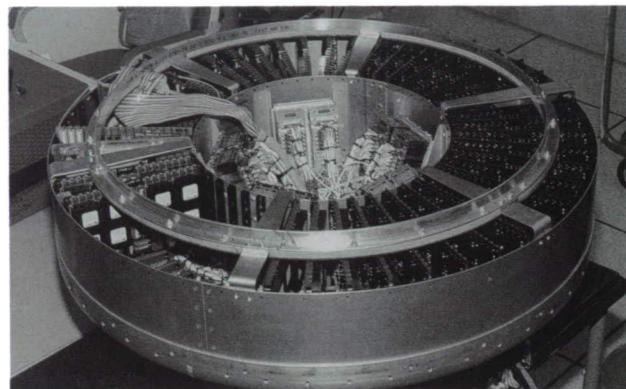


Fig. 2. Internal configuration of data system.

shown in the first figure. The second figure shows the PCM encoders and signal-conditioning modules arranged inside the container.

Inside the cabin, the PCM data streams are multiplexed into one 7.5-megabit-per-second data stream for recording and processing. The multiplexor unit also monitors and displays error in the data stream for efficient testing.

The high-speed data acquisition is required for the UH-60 Helicopter Airloads Research Project. This project is the most ambitious airloads project to date in terms of quantity of data. The data acquired by this system will greatly increase the body of knowledge and understanding of rotorcraft aerodynamics and dynamics, and will enable development of accurate computer codes for engineering analysis and aircraft design.

Ames-Moffett contact: R. Kufeld
(415) 604-5664

Headquarters program office: OAST

ORIGINAL PAGE
BLACK AND WHITE PHOTOGRAPH

XV-15/Advanced Technology Blades: Dynamic Loads

M. Maisel, B. Wellman

The overall objectives of this program are to determine the impact of the advanced technology blades (ATB) on the performance, dynamics, loads, and aeroelastic stability of the XV-15 Tiltrotor Research Aircraft. The data obtained provide a configuration perturbation for the development and validation of analytical prediction codes.

Advanced aerodynamics and mixed-matrix composite materials are combined in the design of the ATB. The highly twisted blades are configured with a compound planform, thin tips, and an increased solidity, to improve hover lift capability without degrading performance at high speeds in airplane mode. Flight tests of the ATB will support the development of a wide range of analytical methodologies. The figure shows the ATB on the XV-15 in airplane-mode flight.

Initial flight testing revealed unanticipated high oscillatory loads in the XV-15 rotor control system. Subsequent analyses identified potential control-system and blade modifications to reduce loads and improve structural dynamic stability. To validate the analyses, variations in tip twist, blade chordwise center of gravity, control stiffness, and blade sweep have been examined in flight. These flight investigations, which provided ATB performance and loads data in all operational modes, have been completed. Also, improvements in the stability and control augmentation system have been installed for flight evaluations.

The measured XV-15/ATB control-loads flight investigation revealed limitations and deficiencies in current analytical methods. The flight data provides an important configuration perturbation (from the original XV-15 blades) to develop and validate predictive codes.



Fig. 1. XV-15 in airplane-mode flight with ATB.

A vibration survey will be conducted immediately after the flight activity to document the airframe resonant frequencies in support of the dynamics and load analyses. Control-system and blade modifications to increase stability and reduce loads will be performed during a time-scheduled major transmission inspection and overhaul. A full spectrum of tiltrotor experiments in support of advanced tiltrotor-transport technology will commence in late FY92 after the inspection/overhaul and subsequent run-in effort is completed.

**Ames-Moffett contact: M. Maisel
(415) 604-6472**

Headquarters program office: OAST

ORIGINAL PAGE
BLACK AND WHITE PHOTOGRAPH

High-Speed Tiltrotor and High-Speed Tiltwing Feasibility Study

David R. Schleicher, Thomas L. Galloway

NASA's high-speed-rotorcraft technology research has the objective of enabling good hover performance with a forward flight speed as high as 450 knots. In pursuit of this objective, several vehicle concepts are being investigated. A feasibility study was conducted by the Systems Analysis Branch assessing the technology needs for a tiltrotor and a tiltwing aircraft to achieve these goals.

Baseline models, incorporating 1990 technology and using XV-15, V-22, CL-84, and XC-142A parameter values and performance trends, were developed for a high-speed tiltrotor (HSTR) and a high-speed

tiltwing (HSTW). Using the VASCOMP design-synthesis program, the two concepts were sized for a civil transport mission with a 450-knot, 600-nautical-mile cruise capability, carrying a payload of 30 passengers and baggage. These current-technology models were then optimized for minimum gross weight and designated as the current-technology baseline concepts. Advances in six technical disciplines were then applied separately to and combined in the baseline HSTR and HSTW. The combined and individual effects of each technology on the HSTR and HSTW gross weights are compared in the figure.

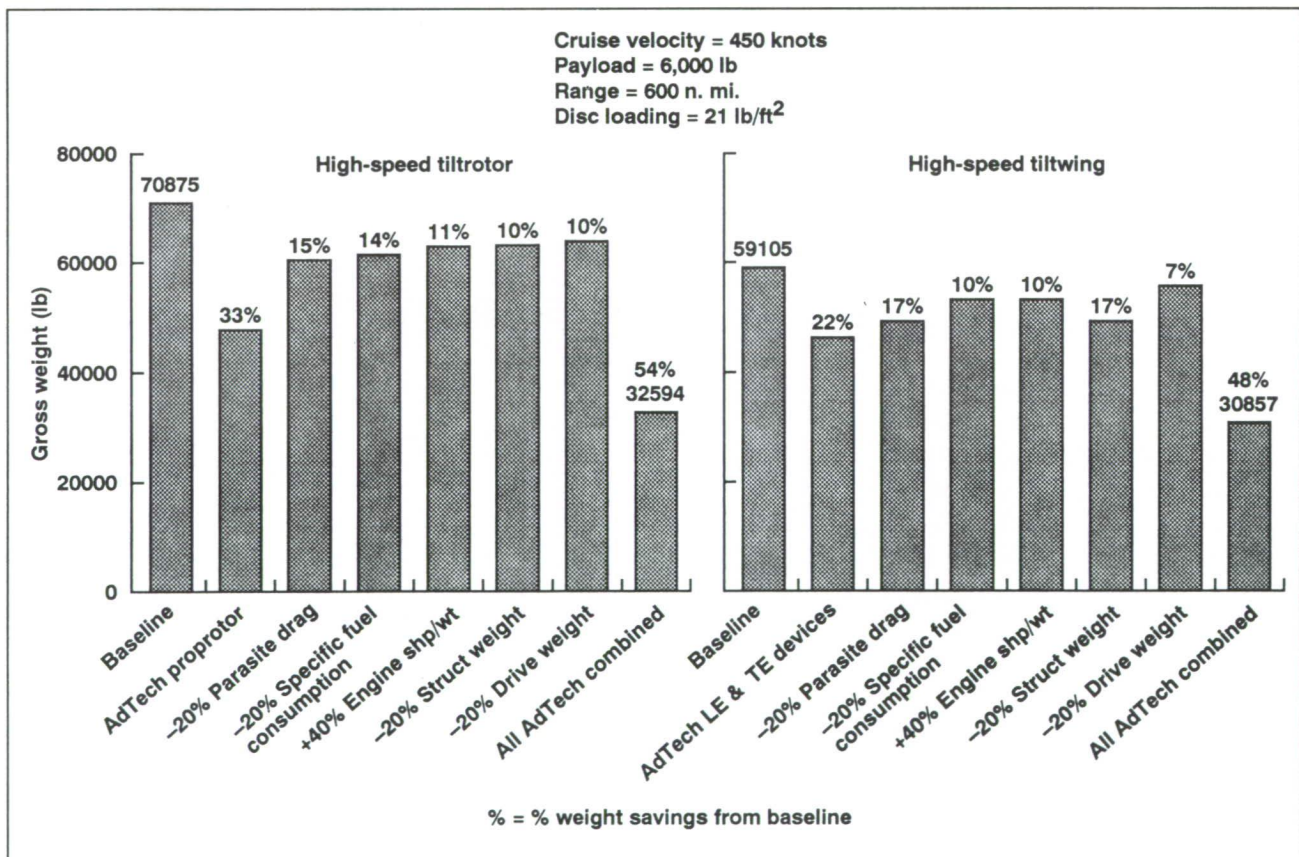


Fig. 1. Advanced-technology impact on the high-speed tiltrotor and the high-speed tiltwing.

This initial study determined that the most significant technologies for reducing gross weight are the advanced proprotor for the HSTR, and wing leading- and trailing-edge devices for the HSTW. The advanced proprotor achieved an increase in drag-divergence Mach number from 0.63 to 0.72 over that for the proprotor. The advanced leading-edge and trailing-edge devices achieved an increase of 1.0 in wing C_{Lmax} and a 10-degree increase in the wing maximum angle of attack. The other technology advances, when applied individually to the HSTR, resulted in smaller gross-weight savings of 10% to 15%. For the HSTW, drag reduction and structural-

weight-savings technology each offered significant weight savings of 17%. On the other hand, achieving the size required for a viable HSTR or HSTW cruising at 450 knots may require the weight savings obtained by a combination of all the available technologies.

Future NASA high-speed rotorcraft research will focus on specific technologies that reduce the size and cost of these vehicles to economically viable levels.

**Ames-Moffett contact: D. Schleicher
(415) 604-5789**

Headquarters program office: OAST

Second-Generation Comprehensive Analysis System for Tiltrotors

Karen S. Studebaker

The Second-Generation Comprehensive Analysis System for Tiltrotors (2GCHAS) is a newly released, comprehensive, interdisciplinary rotorcraft code developed by the Army to analyze advanced tiltrotor concepts such as highly swept blades and variable-diameter rotors. This code will be used to study potential performance benefits and stability characteristics at high speeds (approximately 400 knots).

An analytical model of the XV-15 advanced technology blade (ATB) is used to study the effect of blade sweep on rotor stability. First, a 2GCHAS model of the unswept ATBs was made. Then this model was compared to an existing CAMRAD/JA model of the rotor to verify the 2GCHAS code. Next, sweep was added to the blade, as shown in the first figure.

Good correlation with the XV-15 CAMRAD/JA model (see second figure) was achieved for the basic case of a rotating XV-15 blade without aerodynamics. The addition of collective pitch, coning, and aerodynamics is in process. This is the first actual application of the newly released code, which has been in development for 10 years.

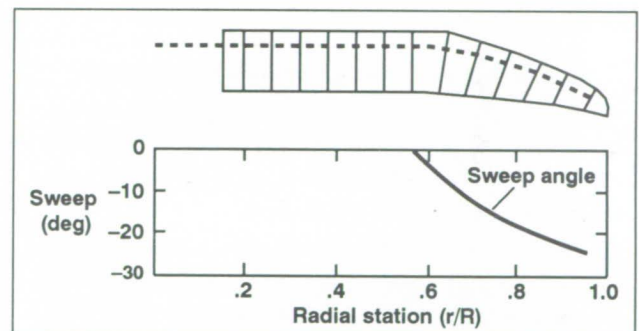


Fig. 1. Potential sweep distribution to be used in 2GCHAS for high-speed tiltrotor modeling.

One of the limiting factors of operating a tiltrotor at high speeds (400 knots) is the drag divergence Mach number (M_{dd}) reached at high tip speeds. A highly swept blade has a higher M_{dd} ; therefore, higher speeds should be obtainable. Very little analysis has been done in this area because of

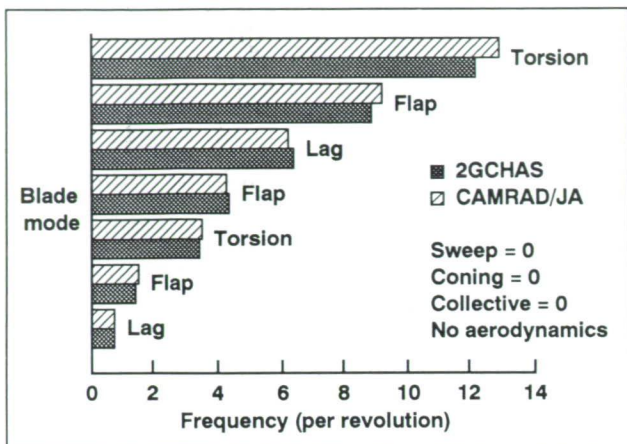


Fig. 2. Baseline XV-15 advanced technology blade comparison between CAMRAD/JA and 2GCHAS.

limitations of rotorcraft codes in modeling sweep. The unique flexibility of 2GCHAS makes it a perfect tool for studying large amounts of blade sweep.

Our plan is to complete the study of highly swept rotors and assess their performance and stability. In addition, a model of a variable-diameter tiltrotor is planned. The variable-diameter tiltrotor is another example of a rotor system that cannot be modeled with existing codes.

Ames-Moffett contact: K. Studebaker
(415) 604-4682
Headquarters program office: OAST

High-Speed Rotorcraft Studies

Peter Talbot

The objective of these high-speed rotorcraft studies was to define rotorcraft configurations with low-disk-loading and high-cruise-speed capabilities (to 450 knots) and to identify critical technology needs and attributes of the designs.

Four contracts of approximately \$250,000 were awarded for three tasks: (1) concept selection, (2) mission analysis of concept-mission combinations, and (3) identification of critical technologies associated with the concept. In addition, parallel in-house studies were done.

Four contractor reports were produced, in which eight concepts were examined in detail. Included were tiltrotor, folding tiltrotor, variable-diameter tiltrotor, tiltwing, and stopped-rotor concepts. Three of the concepts are illustrated in the figures. The tiltrotor was the first choice of three of the four contractors.

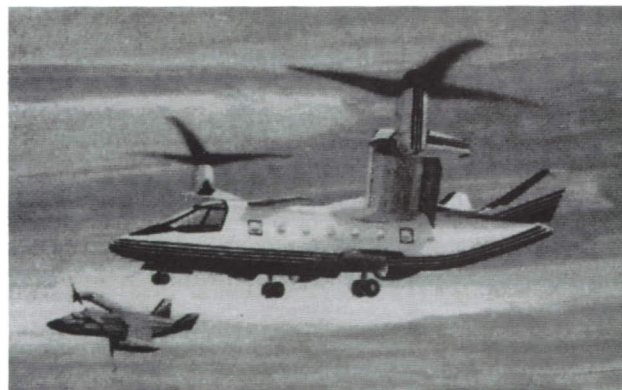


Fig. 1. High-speed civil tiltrotor (Boeing Helicopter and Bell Helicopter).

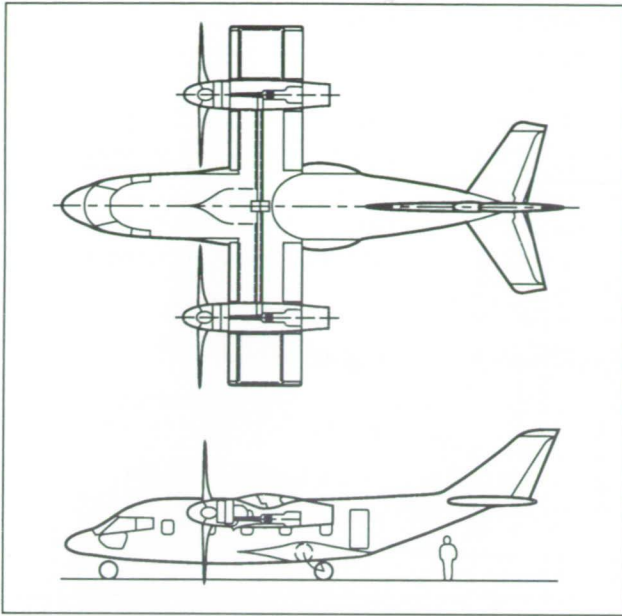


Fig. 2. High-speed military tiltwing transport (Sikorsky Aircraft and MDHC).

For each concept, detailed estimates of weights and performance were made. Each contractor identified critical technologies and made quantitative estimates of the benefits of these technologies. Based on these evaluations, technical plans for advancing the technologies were made.

The studies provided an estimate of the feasibility, sizing, and technical problems associated with high-speed, low-disk-loading vertical takeoffs and landings, and provided guidelines for development of technical plans for the NASA Advanced Tiltrotor Transport Technology Program. The study results will be used as guidance for further development of technology for the next generation of rotorcraft.

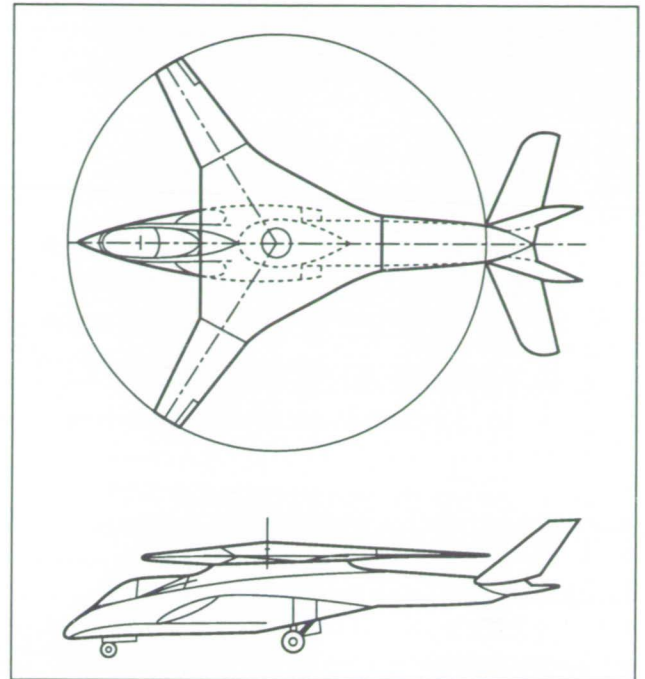


Fig. 3. Stopped-rotor attack aircraft (MDHC).

More detailed studies of tiltrotors and of aeromechanical concerns such as proprotors will be undertaken. A Request for Proposal has been issued for a cost/benefit/risk-assessment study and for a NASA Research Announcement to investigate specific technologies applicable to tiltrotors and other advanced configurations.

Ames-Moffett contact: P. Talbot
(415) 604-5108

Headquarters program office: OAST

Desktop Propeller-Design Code

Peter Talbot

The objective of this study was to create a preliminary design code for determining propeller or rotor thrust and power when geometry, tip speed, blade pitch, and Mach number for axial flight conditions are given.

Using classical blade-element-momentum theory and generalized section characteristics, a working code for hover and axial flight, PDP 4.1, was created and then modified during the course of a large number of correlations with propeller and rotor experimental data. Empirical modifications to section data were incorporated to force agreement with experiment (especially at high thrust coefficient and low advance ratio).

Excellent correlation was achieved with a variety of rotors and propellers. The code was modified to include compressibility, tip loss, and Reynolds-number effects, and shows these effects in a realistic manner. The code was used successfully in determining power and thrust for a coaxial-propeller-interaction investigation and is contemplated for use as the rotor module in the VASCOMP design-synthesis program. The code has proved useful for approximate estimates of power and thrust for new designs that are

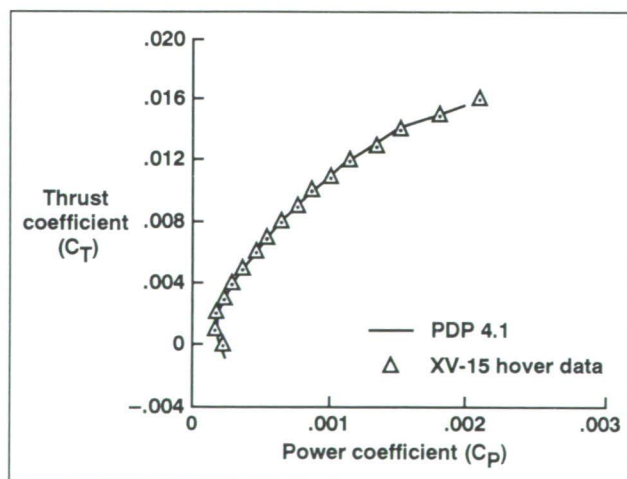


Fig. 1. Correlation with XV-15 hover data.

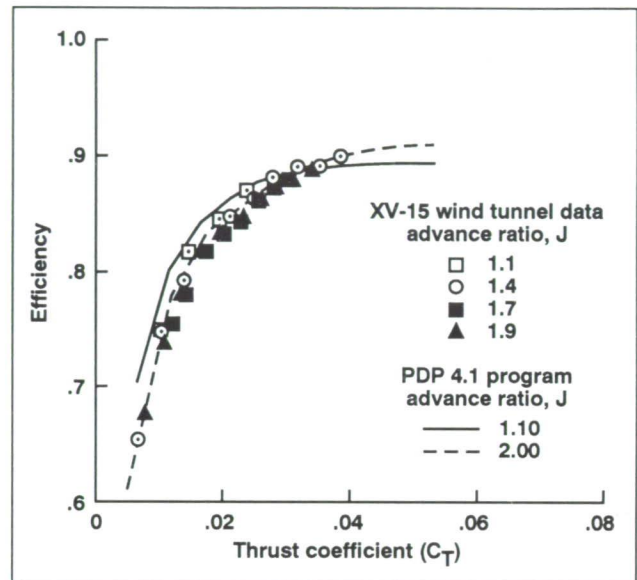


Fig. 2. Comparison of calculated versus measured propeller efficiency.

minor modifications of existing propellers. Correlations of the program with hover and forward-flight data for the XV-15 rotors are shown in the figures.

Propeller performance data usually are available only through charts or tables, and this form is not flexible enough for rapid yet accurate estimates of propeller characteristics. Novel designs not in the charts can be examined using this code. More advanced codes (e.g., lifting line) are usually too complex for incorporating into preliminary design codes. This program is a blend of small size and reasonable engineering accuracy.

We are currently attempting to modify the code to investigate eight-bladed propfans and swept propfans.

Ames-Moffett contact: P. Talbot
(415) 604-5108

Headquarters program office: OAST

Analysis of Rotorcraft Phenomena Using CAMRAD/JA

Joseph Totah, John Madden III

The objectives of this study were to evaluate the accuracies of the state-of-the-art comprehensive rotorcraft analysis codes, such as CAMRAD/JA (Comprehensive Analytical Model of Rotorcraft Aerodynamics and Dynamics/Johnson Aeronautics), in the prediction of rotor system performance, loads, and stability, and to identify and address sources of inaccuracy in order to enhance the analysis and design of advanced rotor systems. Limitations of the codes are being identified through extensive correlation efforts. Improvements in the codes are judged by respective improvements in correlation. Advanced high-speed-tiltrotor blade optimization efforts have also been initiated using a rigorous two-point optimization of the XV-15/advanced technology blades (XV-15/ATB) rotor system. The validity of the results of the optimization effort will be strengthened by improvements in correlation of the current comprehensive codes.

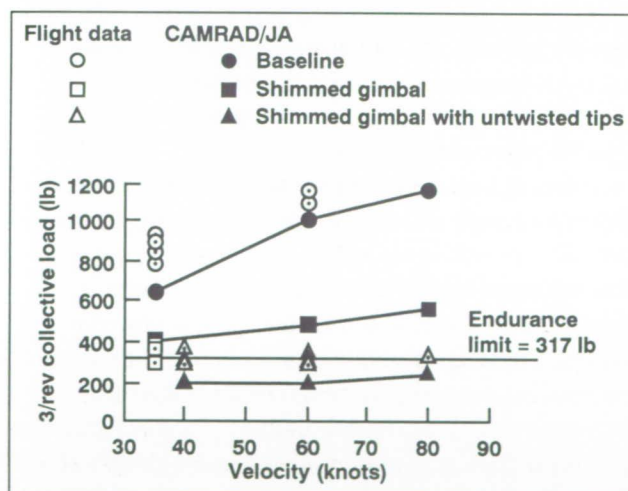


Fig. 1. XV-15/ATB collective-actuator-loads correlation using a modified version of CAMRAD/JA; helicopter mode (35 to 80 knots).

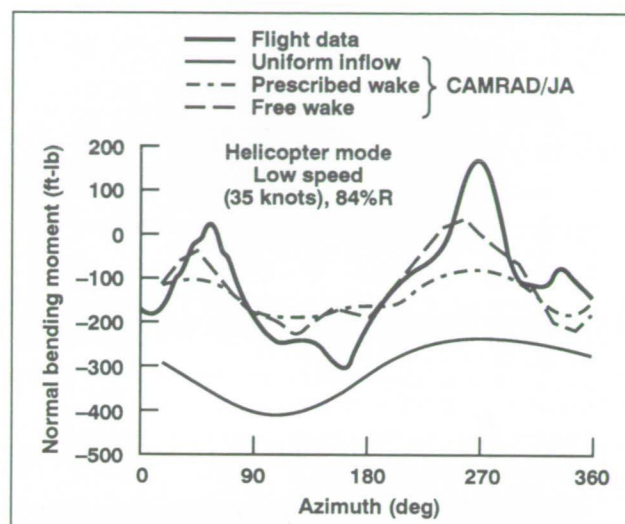


Fig. 2. XV-15/ATB normal bending-moment correlation using a modified version of CAMRAD/JA showing variation in correlation for different wake models; helicopter mode, mean sea level, 35 knots.

Extensive correlation efforts have been performed and reported using predictions generated from a modified version of CAMRAD/JA and an XV-15/ATB rotor correlated with control-system-loads flight data, as shown in the first figure. This effort identified the importance of accounting for control-system flexibility. The modified version of CAMRAD/JA reflected this flexibility, and this resulted in improved correlation (second figure). The modified version is currently being used to generate results for the advanced high-speed-tiltrotor blade optimization effort. The predicted gains in performance and stability resulting from this effort will reflect the improved accuracy obtained with the modified version of CAMRAD/JA.

Extensive correlation results have been obtained using CAMRAD to predict airloads for the AH-1G and correlating them with AH-1G airload measurements. A major effort was also undertaken to upgrade the UH-60 CAMRAD model through improved input and improved input source documentation. Sikorsky has completed the draft documentation and furnished it to Ames.

Further aeroelastic stability and airloads correlation efforts are planned for the XV-15/ATBs, the

AH-1G Cobra, and the UH-60 Phase II program in order to ensure that sources of inaccuracies are identified and comprehensive rotorcraft analysis codes are improved and reflected in the advanced high-speed-tiltrotor blade optimization effort.

**Ames-Moffett contact: J. Totah
(415) 604-4126**

Headquarters program office: OAST

Investigations of Jet-Induced Flows in Hover

Douglas A. Wardwell, Craig E. Hange

The overall purpose of these investigations is to gain a better understanding of jet-induced effects in hover for short-takeoff-and-vertical-landing (STOVL) aircraft configurations; these effects include suckdown, hot-gas ingestion, and fountain effects. Small-scale experiments are necessary to identify and evaluate such phenomena and to provide results that can be extrapolated with confidence to full-scale, high-speed fighter aircraft designs.

Ames Research Center is developing a small-scale Jet Calibration and Hover Test (JCAHT) Facility for investigation of aerodynamic forces and hot-gas flow fields during hover. The JCAHT Facility consists of

two parts. The Jet Calibration Rig (JCR) has the capability to perform nozzle calibrations and jet flow surveys. The Hover Test Rig (HTR) has a variable-height ground plane for aircraft model tests. The model does not touch the nozzle/thrust system. This setup permits measurement of the aerodynamic forces without the thrust force being detected by the internal strain gage balance. Other measurements that are taken include nozzle pressures and temperatures, some flow-field pressures and temperatures, and ground plane height.

Recent tests conducted at the JCAHT Facility were a San Jose State University (SJSU) study and a parametric planform study sponsored by the Air Force. The objective of the SJSU study was to identify the flow field on the model surfaces. This information will be used to properly instrument the model with thermocouples for future tests studying hot-gas ingestion characteristics for various planform and inlet locations. Testing was conducted with cold dry-air jet flows. During the test, water condensed out of the entrained air around the jet flow, providing some flow visualization as shown in the first figure. Notice the flow halfway between the nozzles: this is part of the fountain flow. The fountain flow is generated when

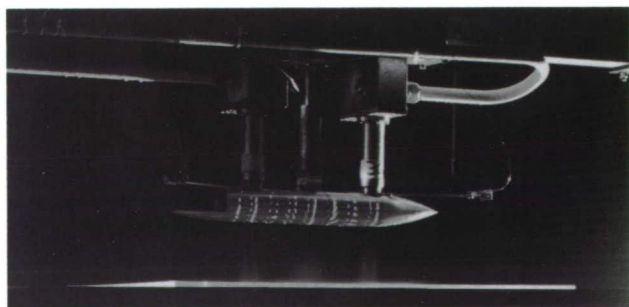


Fig. 1. San Jose State University model on the Hover Test Rig showing the jet flow.

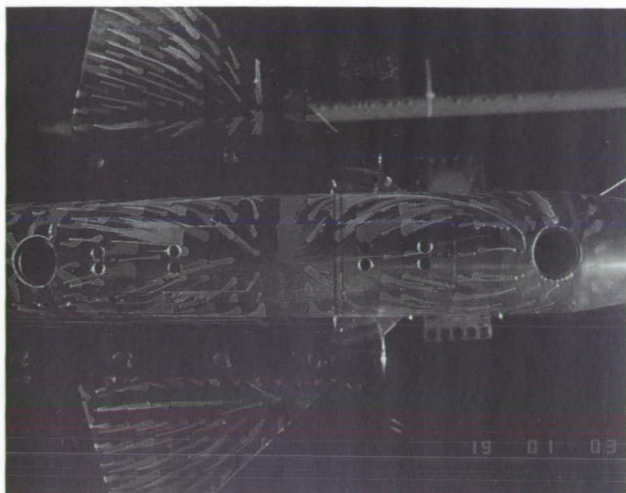


Fig. 2. San Jose State University model showing an oil flow pattern for a high-wing configuration with nozzle pressure ratio 3.48, height 4.5 inches. (See color plate 7 in Appendix)

the radial jet flow along the ground from the two nozzles collides, forming an upflow, or fountain. The second figure is a photo taken looking up through a Plexiglas cover on the groundplane. It shows the bottom view of the flow streamlines (from fluorescent oil) for a high-wing configuration with inlets under the wing. The conditions were nozzle pressure ratios (NPR) of 3.48, and a model height of 4.5 inches above the ground plane. The fountain flow can be identified halfway between the jets.

The main objective of the Air Force study was to expand the current STOVL data base on jet-induced interactions in and out of ground effect. Previous

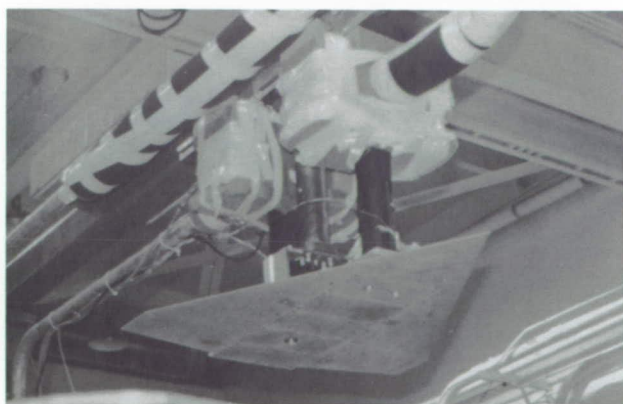


Fig. 3. Air Force delta-wing model mounted on the Hover Test Rig.

studies concentrated on the forces and moments induced in ground effect, but little was learned about the distribution of pressures that generated these forces and moments. This series of tests included many pressure taps on the model lower surface as well as a balance to measure the model forces and moments induced on 32 different flat-plate planform/nozzle configurations. Both the JCR and the HTR were used for these tests. The third figure shows one of the Air Force model configurations on the HTR. Nozzle pressure ratios of 2.0, 4.0, and 6.0 were investigated at ground heights from 60 inches to as low as 2 inches from the nozzle exit. The fourth figure shows a plot of C_p versus model station for a two-post delta-wing configuration with an NPR of 4.0, a height of 6 inches, and a jet spacing of 16 inches. The red and yellow sections indicate positive pressures from the fountain flow, and the blue sections indicate negative pressures. The strong negative pressures are caused by a set of vortices between the jets and the fountain flow. These vortices dominate the flow field at low heights, whereas the fountain can, but does not necessarily, dominate at intermediate heights. Further tests incorporating forward velocity were conducted at Langley Research Center.

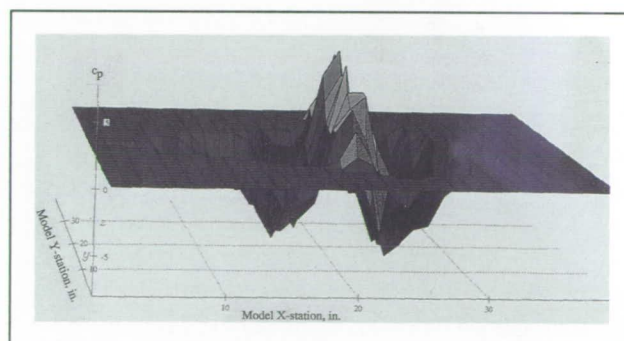


Fig. 4. Plot of pressure top location versus C_p for a two-post delta-wing configuration with nozzle pressure ratio 4.0, a height of 6 inches, and a jet spacing of 16 inches. (See color plate 8 in Appendix)

These tests greatly expand the data base for jet-induced ground effects for STOVL jet configurations. The data will be used to develop and enhance prediction techniques, to develop CFD analysis methods, and to understand and identify the effects of model and test-facility parameters when testing for the effects of jet-induced flow.

It is intended that an improved empirical prediction method for jet-induced lift and pitching moments of STOVL aircraft in ground effect can be developed with data from these tests.

All future tests at the JCAHT Facility will be done with air heaters that will provide nozzle air temperatures ranging from ambient to 800 °F. Follow-on tests with fully instrumented models will be needed to

provide data for modifying and/or improving a hot-gas-ingestion prediction routine for STOVL aircraft in and out of ground effect.

**Ames-Moffett contact: D. Wardwell
(415) 604-6566**

Headquarters program office: OAST

Acoustic Laboratory Data Acquisition/Analysis System

Michael E. Watts

A low-cost, portable, easy-to-use rotorcraft acoustics data-acquisition-and-analysis system for ground and in-flight acoustics data has been developed. The Acoustic Laboratory Data Acquisition/Analysis System (ALDAS) uses an Apple Macintosh computer. Digitizing boards that acquire data on four channels simultaneously were installed in a Macintosh IIx computer. A program was developed to control the analog-to-digital conversion boards and to perform the data analysis.

The ALDAS has been used extensively for processing and analysis of BV-360 rotor whirl tower, BO-105/YO-3A IRAP, and XV-15 onboard microphone test data. The use of the system for evaluation of experimental and theoretical data is shown in the first figure. The second figure shows spectral analysis results analyzed by the program. Recent upgrades to enhance the system and meet specific user requirements have been incorporated. These upgrades include the following.

1. Improved amplitude spectrum analysis, with the ability to perform window sweeping with linear and power spectral averaging.
2. Third-octave analysis using linear and dBA weightings.
3. Four types of digital filtering (low pass, high pass, band pass, and band stop) using one of six filter windows.
4. Autoscaling or user selectable scale now included in plotting options.
5. A four-channel digital-oscilloscope feature with selectable time base and window resolution dependent on number of channels showing.
6. Improved plot labeling to show history of analysis performed on data.
7. Sample rate can be controllable from an external signal. This allows truly variable sample rates to be used.
8. Many improved minor features to make the program more usable and to facilitate the upcoming IRAP investigations.

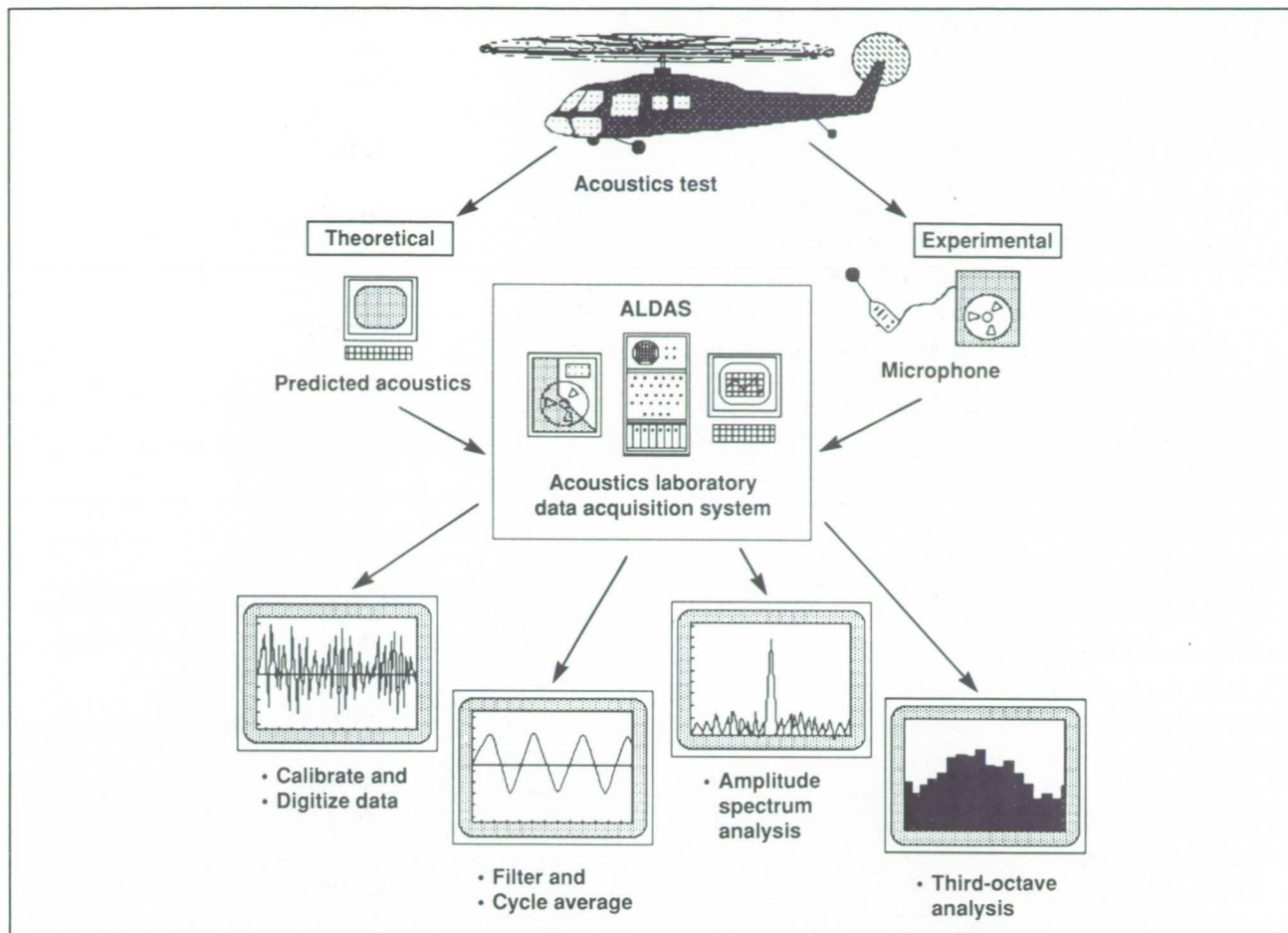


Fig. 1. Use of ALDAS for experimental and theoretical acoustic data analysis.

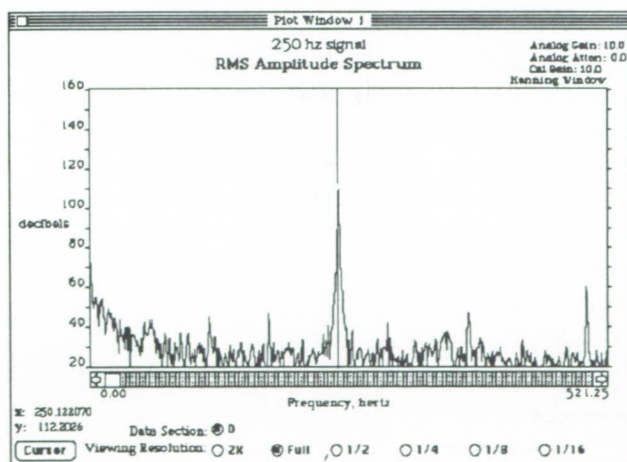


Fig. 2. Sample spectral analysis from ALDAS.

The availability of the ALDAS makes the processing and analysis of high-frequency data convenient and portable at a relatively low cost. New analysis options can be rapidly incorporated as requirements are identified. No longer does high-frequency data processing require a major investment.

Ames-Moffett contact: M. Watts
(415) 604-6574
Headquarters program office: OAST

Data Management and Analysis Package

Michael E. Watts, James Chase

To provide a means of managing and analyzing high-frequency time history data obtained from pressure-instrumented rotor blade tests, an existing code, the Data Management and Analysis Package (DATAMAP), has been upgraded. DATAMAP was written in the late 1970s by Bell Helicopter Textron under an Army contract. Ames took the leadership for this program in the mid-1980s and has been maintaining and improving it since then. To bring the code up to modern programming standards, three primary steps have been implemented.

1. The code has been broken into individual routines linked by common blocks. This has improved logic tracking and code maintenance.

2. A new data storage format (DAT-TH) has been implemented which allows better data management and quicker access times. The new format uses the advanced keyed access FORTRAN feature.

3. DATAMAP has been integrated with the TRENDS data analysis package.

In the past year, much of the accomplishment has been in eliminating some of the more insidious bugs that have been resident in DATAMAP since it was created. A plan for improving the internal command structure has been two-thirds implemented. DATAMAP version 4.5 was delivered to Kaman Aerospace and has been requested by Simula Corporation. The use of DATAMAP for a rotor airloads investigation for the UH-60 is illustrated in the first figure.

Two additional steps are required to make DATAMAP a more modern and viable research tool:

1. Improvement of the internal command structure. Currently, the program uses a block data structure to control the defaults and the logic path for implementation of the commands issued. This layered-type programming style was necessary for implementation

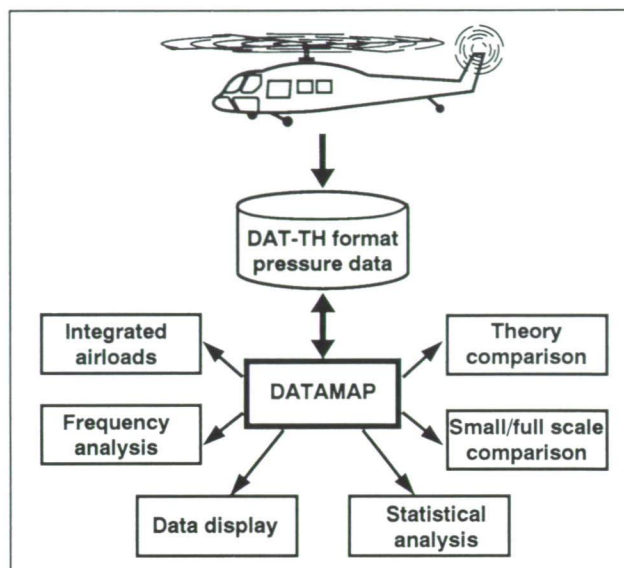


Fig. 1. Illustration of use of DATAMAP for the UH-60 airloads program.

of a program the size of DATAMAP on an IBM in the 1970s. However, it makes the modification of default values, new command additions, or subfields within a command difficult because of the necessary cross-referencing into the block data structures.

2. Replacement of the Textronics Plot10 plotting package with more advanced graphics, including color and three-dimensional plotting. The improvement in the internal command structure is on schedule, and replacement of the graphics package will begin in January 1992.

Ames-Moffett contact: M. Watts
(415) 604-6574

Headquarters program office: OAST

XV-15/Advanced Technology Blades: Acoustics

Brent Wellman

The overall objectives of this program are to determine the external far-field noise signature of the XV-15 Tiltrotor Research Aircraft fitted with advanced technology blades (ATB). These blades were designed using state-of-the-art airfoil sections, current performance codes, and advanced materials to yield a highly twisted, complex planform design with thin tips for reduced noise and greater hover capability without degrading high-speed performance. Comparison with the data gathered for the XV-15 with conventional metal blades will illuminate the net gains in rotor quietness achieved by the unique features of the ATB.

During late 1990, acoustic flight tests of the XV-15/ATB were conducted in collaboration with the Applied Acoustics Branch of Langley Research Center. The aircraft was flown in hover over the center of a semicircular array of microphones. The hover altitude was varied so that noise propagation at various angles with respect to the tip path plane could be measured. Correcting the measured noise levels for distance gives a picture of their intensity over the surface of a hemisphere centered on the aircraft. This data was plotted graphically and is shown in the figure. The test also led to the discovery of an area to the rear and below the aircraft where impulsive noise, characteristic of blade-vortex interaction, is prominent.

Because of the high thrust capability of the ATB, they could be operated at slow speeds to test the effect on noise generation. Tip speeds tested ranged from the XV-15 design value of 771 feet per second down to 645 feet per second. As expected, the lower-tip-speed condition coupled with the thin-tip cross sections resulted in a significantly lower acoustic signature.

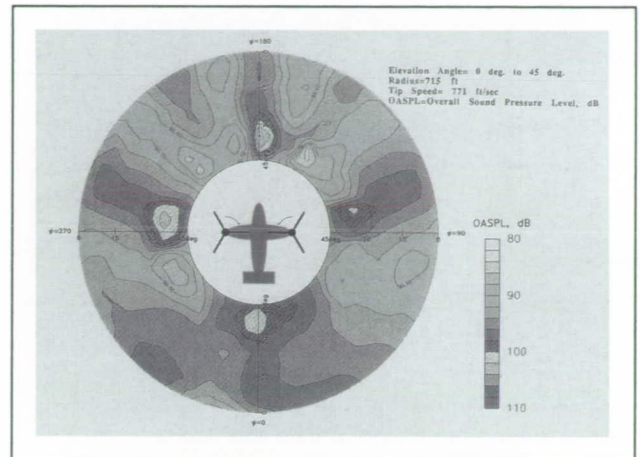


Fig. 1. Acoustic intensity over the surface of a hemisphere centered on the XV-15 aircraft. (See color plate 9 in Appendix)

This work was continued and expanded in 1991 to include acoustic measurements for flyover and approach-to-landing configurations. In a second joint operation with Langley Research Center, the XV-15/ATB was flown over a rectangular microphone array. Noise signature data will be compared for various airspeeds, glide slopes, and rotor speeds with the nacelles at various angles. These configurations are important to the development of a civil tiltrotor aircraft that can meet or exceed reasonable noise criteria.

Ames-Moffett contact: B. Wellman

(415) 604-6573

Headquarters program office: OAST

Impact of Future Technology and Mission Requirements on Multirole Tactical Aircraft

Samuel B. Wilson III, Jeffrey J. Samuels,
Andrew S. Hahn, David R. Schleicher, Kevin B. Carbajal

The objective of this study was to assess the effects of future technology levels and mission requirements on multimission tactical aircraft. Study of the vehicle weight trends will support the U.S. Navy's Future Carrier Study.

Three multirole aircraft models were developed: (1) an Air Force version designed to land on existing airstrips, (2) a Navy version capable of landing on a carrier deck using conventional arresting techniques, and (3) a short-takeoff-and-vertical-landing (STOVL) version designed to land vertically on modern carriers. These aircraft designs used a consistent set of aircraft subsystems, engine data as installed, and weapons and weapons carriage. Using the ACSYNT design synthesis code, the three aircraft were sized for an 800-nautical mile, multirole mission that included supersonic high-altitude and subsonic high- and low-altitude cruise segments. The three aircraft were designed for two timeframes (1990 and 1995), taking into account changing technology and mission requirements. For example, 1990 aircraft used an afterburner for supercruise, whereas 1995 aircraft were required to have dry supercruise capability. The effects of these differences on gross weight were compared.

The results shown in the figure reflect the effects of the weight penalties associated with carrier landing requirements, STOVL capability, and the dry supercruise requirement for 1995. In addition, for 1990, the effect of adding hover thrust augmentation to the STOVL aircraft is shown. In the 1990 timeframe, the Navy airplane weighs 21% more than the Air Force airplane, and the unaugmented STOVL aircraft weighs 25% more than the Navy airplane. The augmented-landing STOVL aircraft weighs about the same as the Navy airplane. As a result of advances in technology and the dry supercruise requirement, the 1995 Navy airplane is 19% heavier than the Air Force airplane, and the unaugmented STOVL aircraft is 6% lighter than the Navy airplane.

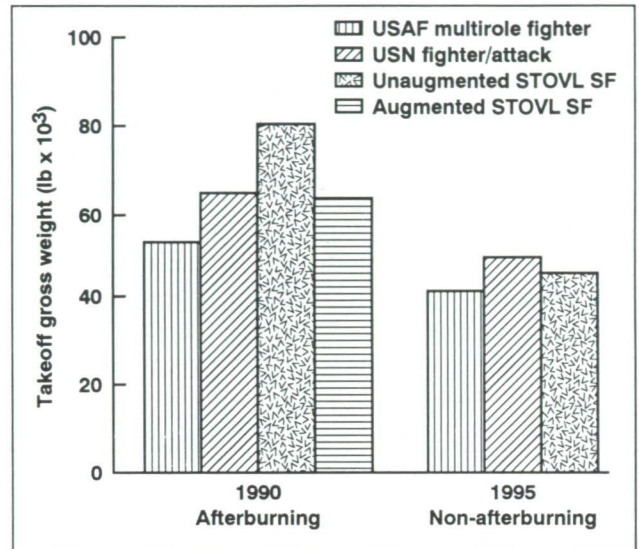


Fig. 1. Multimission aircraft size as a function of technology level and dry supercruise requirements.

This study highlights the effects of changing technology and mission requirements on the so-called STOVL and navalization penalties. STOVL has less of a penalty compared to 1995 technology Navy aircraft capable of dry supercruise.

Ames-Moffett contact: S. Wilson III
(415) 604-5903
Headquarters program office: OAST

FAA/NASA Helicopter Simulator Workshop

John Zuk

Advanced visual and motion system technologies have enabled fixed-wing-aircraft simulators to be fully qualified for the training of flightcrews. However, there has been limited use of these technologies in helicopter simulators. In addition, the Federal Aviation Regulations have not yet addressed crewmember certification in helicopter simulators. Accordingly, the Federal Aviation Administration (FAA) has recognized the need to seek assistance from informed industry and government sources in defining existing helicopter-simulation technology levels and identifying the technological advances needed for state-of-the-art helicopter simulation. NASA is supporting the FAA in this endeavor through an Interagency Agreement. The FAA and NASA co-sponsored a Helicopter Training Simulator Workshop in April 1991, in Santa Clara, California, which attracted simulator manufacturers, training organizations, users, military representatives, government regulators and researchers, and representatives from five countries. Twenty invited presentations were given, and five working-group panels addressed the following subjects: Using Simulators for Training; Fidelity and Training Transfer; Cost Effective Training; Visual Scenes and Pilot Performance; and Motion and Visual System Engineering Performance. In addition, a first public hearing was held for comments on the Draft Advisory Circular.

The workshop identified technical issues, and determined the following: (1) Helicopter simulators are deficient in hover and low-speed capability. Model fidelity, transport delay time, required field of view, visual-scene texturing, and amount of motion were the major information requirements for proper simulation at hover and low speed. (2) The amount of simulation fidelity required for transfer of training is a basic question in the training. Another question is, with computational and visual-scene advances, when and what motion cues can be substituted for

actual motion and still maintain sufficient fidelity? (3) Simulator design must enable a positive transfer of piloting skills from simulator to helicopter, and enable simulators to affect human behavior and judgment. Representatives of industry and the Department of Defense stated their desire to join NASA and the FAA in addressing the issue of transfer of training. They would consider using their facilities and aircrews to evaluate transfer-of-training measures that address simulator specifications affecting aircrew training and training effectiveness. (4) Industry needs to evaluate use of frequency-response measures to qualify the engineering fidelity of simulators.

The workshop highlighted the need to finalize and implement the FAA regulations in Title 14 CFR Part 142 (Certified Training School Requirements) and the Helicopter Simulator Qualification Advisory Circular (AC120-XX). The FAA National Simulator Program Manager was able to enlist the support of 30 experts in finalizing this advisory circular. Via special exemption, an FAA-issued Helicopter Simulator Qualification Advisory Circular will allow industry to develop simulators rapidly compared to the very long process today.

The helicopter simulator will allow economical training that is essential for safe helicopter operation. Today, simulator training credit is only allowed for re-currency and still requires flight checking. But future, affordable Level-D simulators will enable full-spectrum training, re-currency, and rating checks with positive transfer of training to the helicopter. The need will be even greater when future commuter rotorcraft, such as the civil tiltrotor, go into operation.

Ames-Moffett contact: J. Zuk

(415) 604-6568

Headquarters program office: OAST

Large-Scale Tiltrotor Test Rig

Mike Derby

The Rotorcraft Aeromechanics Branch has made considerable progress in developing a large-scale tiltrotor test rig (LTTR) for use in conducting rotor-performance and aeroacoustic wind tunnel tests of tiltrotor aircraft proprotors. This new test rig will be used to acquire data encompassing the entire flight regime of tiltrotor aircraft from hover through transition and into high-speed forward flight. Studies of both isolated proprotor and rotor/wing interactional aerodynamics will be possible using this new test rig. The LTTR will be used in several of the National Full-scale Aerodynamics Complex facilities, including the Outdoor Aerodynamic Research Facility, the 40- by 80-Foot Subsonic Wind Tunnel and the 80- by 120-Foot Subsonic Wind tunnel. The LTTR will play a critical roll in meeting NASA's goal of developing enabling technology for civil tiltrotor aircraft. Concurrently with the LTTR development, the Rotorcraft Aeromechanics Branch is planning several long-term research programs aimed at developing tiltrotor aircraft technology. Large-scale testing will provide the data necessary for developing aeroacoustic prediction methodologies and for demonstrating advanced tiltrotor technology.

The LTTR will accommodate proprotors from 20 to 25 feet in diameter, and can provide up to 3000 horsepower at a maximum rpm of 725. Initially the LTTR will be configured for a three-bladed proprotor, but the test-rig rotor control system will incorporate features that will enable testing of proprotors with different numbers of blades. The test rig will include a six-component rotor balance and an instrumented flex-coupling to measure rotor torque. The LTTR also features a removable, pressure-instrumented (steady and dynamic), semispan wing which can be installed for rotor/wing interaction investigations or removed for isolated rotor studies. The tunnel mounting arrangement will ensure minimal aerodynamic interference on the proprotor/wing from the test-rig support structure (see figure).

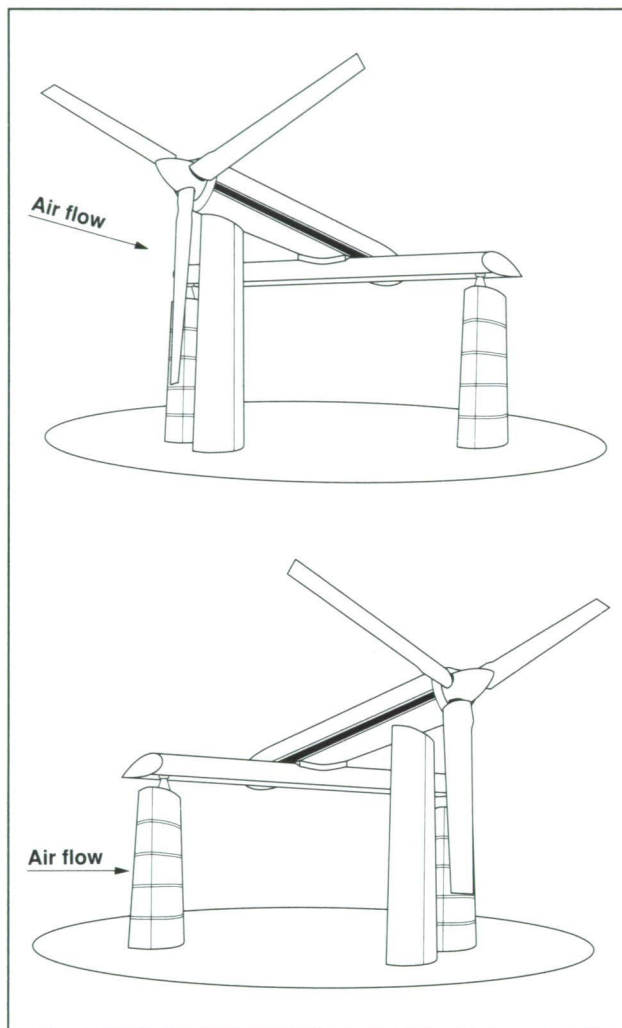


Fig. 1. Test rig in (a) airplane mode; (b) helicopter mode.

Current plans call for the LTTR to be first used for testing full-scale XV-15 metal rotor blades and the XV-15 advanced technology blades in the 80- by 120-foot wind tunnel. This test will focus on aeroacoustic measurements of propellers while simulating transition during terminal-area operations. The large test section will allow a complete mapping of the rotor transition matrix with minimal wall effects. A specially developed acoustic microphone traverse for the 80- by 120-foot wind tunnel will be

used to acquire a comprehensive acoustic survey. The acoustic data acquired will be compared to flight-test data from the XV-15 aircraft for both rotors. Late calendar year 1993 is targeted for the initial LTTR testing.

Ames-Moffett contact: M. Derby
(415) 604-6856

Headquarters program office: OAST

A New Analysis for Static Aeroelasticity

Fort Felker

An important problem in aeronautics is the computation of the steady transonic flow about a flexible body. The flow about the body depends on the shape of the body, but the shape of the body is also affected by the flow. Problems in which there is strong coupling between steady aerodynamics and steady structural deformations are generally referred to as static aeroelasticity problems.

A new analysis has been developed for transonic static aeroelasticity problems. In this analysis, the discretized governing equations for the structural and fluid dynamic systems are regarded as a single set of coupled, nonlinear algebraic equations. The solution of the system, which defines the steady-state body shape and fluid flow, is directly found using Newton's method. Newton's method converges to the equilibrium solution rapidly, and usually only five to ten iterations are required.

To demonstrate the method, the flow in a two-dimensional, transonic, convergent-divergent nozzle with flexible walls was computed. The Navier-Stokes equations were used as the governing equations for the fluid flow, and a finite-element method was used to represent the flexible walls. The figure shows the ratio of wall pressure to total pressure as a function of the streamwise coordinate, x . Results obtained for rigid and flexible walls are shown, and it can be seen that wall flexibility has a significant effect on the pressure distribution.

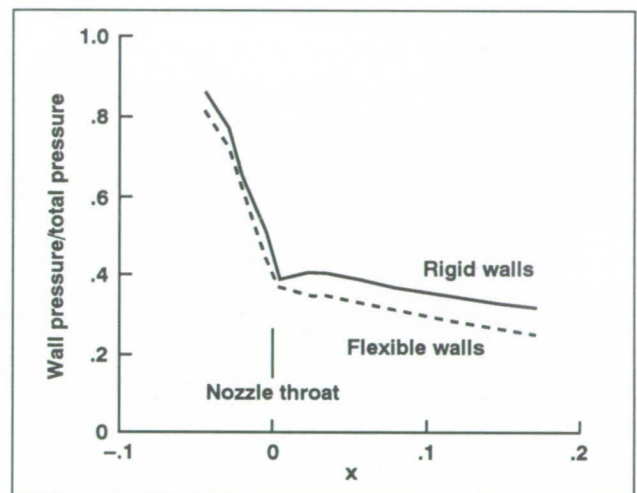


Fig. 1. Comparison of wall pressure ratios with and without wall flexibility in a two-dimensional, transonic, convergent-divergent nozzle.

Ames-Moffett contact: F. Felker
(415) 604-6096

Headquarters program office: OAST

Full-Scale Higher Harmonic Control at High Airspeeds and Moderate Thrust in the Ames 40- by 80-Foot Wind Tunnel

Sesi Kottapalli, Jane Leyland

The Rotorcraft Aeromechanics Branch is planning to conduct an open-loop higher harmonic control (HHC) test in the Ames 40- by 80-Foot Wind Tunnel up to airspeeds of 200 knots with the four-bladed Sikorsky S-76 articulated rotor operating at 10,000 pounds thrust. The recently modified and enhanced Ames Rotor Test Apparatus will provide support during the test.

All HHC pretest activities have been specified. Test objectives and approach, run conditions, data

acquisition, and post-test data processing requirements have been specified and documented. A series of checkout tests intended to verify the proper and safe functioning of the HHC system down to the individual actuator level has been developed.

Analytical results from the HHC pretest aeroelastic analysis show that, as expected, HHC reduces the hub loads. It was found that this reduction in hub loads is maintained at high airspeeds and moderate thrust, as the figure shows. The HHC test is based on these and other analytical results. Briefly, the test procedure will be as follows. First, baseline (without HHC) experimental and analytical trends in hub loads will be compared in order to validate the analysis. After that, the effect of open-loop HHC (individual 3-, 4-, or 5-per-rev input) on full-scale hub loads will be demonstrated at airspeeds up to 200 knots at a thrust level of 10,000 pounds.

Ames-Moffett contact: S. Kottapalli

(415) 604-3092

Headquarters program office: OAST

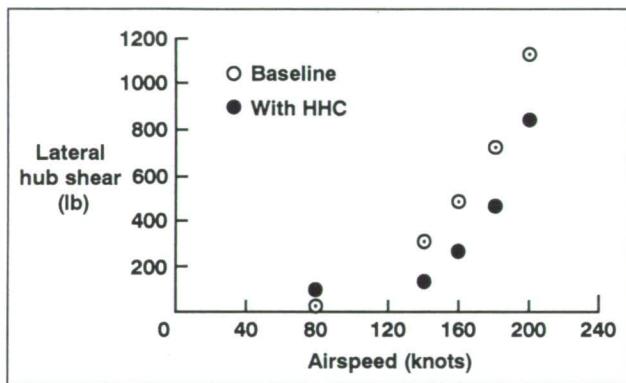


Fig. 1. Effect of 3-per-rev HHC input (amplitude of 1 degree) on lateral hub shear, S-76, 10,000 pounds.

Correlation Study of the Lynx Helicopter

Benton Lau

The correlation study of the Lynx helicopter is a joint research program with Westland Helicopter, Ltd. The program objectives are to (1) reduce and document the flight test data, (2) correlate the flight test results with CAMRAD/JA (Comprehensive Analytical Model of Rotorcraft Aerodynamics and Dynamics, Johnson Aeronautics) and Westland's R150 analysis, and (3) assess the modeling requirements to predict rotor performance, rotor structural loads, control loads, and retreating blade stall. The flight test data were reduced and the results are being documented.

The flight boundary predicted by CAMRAD/JA showed good correlation with experimental results, as shown in the figure. This boundary was defined by the limit of the oscillatory control loads. The aircraft pitch and the blade feathering angle were well predicted by CAMRAD/JA. The waveform prediction of the oscillatory lag bending loads was good at the inboard sections, but poor to fair at the outboard sections. For the flap bending loads, the waveform prediction was poor at the inboard sections, but fair to good at the outboard stations. The poor prediction can be attributed to the inaccurate description of aerodynamic characteristics of the blade airfoil. Because the aerodynamic characteristics at high angles of attack and at high Mach numbers were not available, airfoil characteristics of NACA 0012 were substituted.

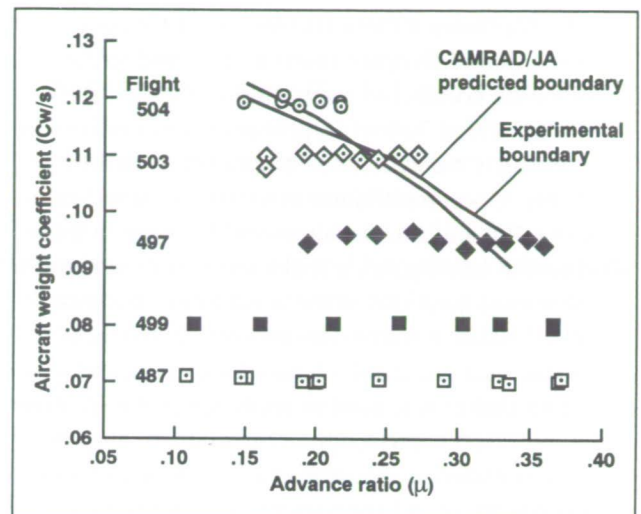


Fig. 1. Summary of Lynx flight conditions.

Ames-Moffett contact: B. Lau
(415) 604-6714

Headquarters program office: OAST

was made an option in the stand-alone program. It appears that this procedure will be the preferred method for use in the early trials.

There appear to be some mathematical conditioning problems associated with the direct optimization of the weighting coefficients of the conventional controller. This most likely occurs when the "solution" has zero components which have associated weighting coefficients that approach infinity. Solutions were obtained to the trial problem by manually restarting the algorithm whenever an overflow occurred.

An example of an early comparison of controllers for an S-76 in forward flight with a (6×6) T-matrix and third, fourth, and fifth harmonic magnitude upper limits of 2 degrees on the control vector illustrated the power of optimization: specifically,

1. Manual optimization of the weighting coefficients of the conventional controller, where the individual coefficients were assumed to have the same value (the usual approach), yielded a vibration metric of 17.865.

2. Optimization of the individual weighting coefficients of the conventional controller (i.e., the opti-

mized conventional controller) yielded a vibration metric of 2.162.

3. Direct optimization of the control subject to constraints in accordance with optimization theory (i.e., the optimal controller) yielded a vibration metric of 0.503.

The analysis plan calls for providing a general $(N \times M)$ T-matrix capability in the stand-alone program, computation of T-matrices and associated previous-step control and measurement vectors for the S-76 and BO-105 rotor systems for various flight conditions using the Comprehensive Analytical Model of Rotorcraft Aerodynamics and Dynamics, Johnson Aeronautics (CAMRAD/JA) analysis code, and comparison of the optimal controller with the conventional controller and the optimized conventional controller.

**Ames-Moffett contact: J. Leyland
(415) 604-3092**

Headquarters program office: OAST

0.658-Scale V-22 Rotor Forward-Flight Performance Test

Jeffrey S. Light, Michael Derby

A test of a 0.658-scale V-22 rotor was conducted in the Ames 40- by 80-Foot Wind Tunnel to examine forward-flight performance (first figure). The Ames Prop Test Rig was used to power the rotor and to measure performance and loads. Test conditions included tip Mach numbers of 0.575 and 0.625, and tunnel speeds up to 230 knots. Dynamic data obtained during testing include hub and rotor balance data. Overall rotor performance during testing is shown in the second figure. This figure shows the high efficiency of the V-22 rotor in forward flight. Except for the lowest value, advance ratio has no significant effect on rotor performance.



Fig. 1. Isolated V-22 rotor in the 40- by 80-Foot Wind Tunnel.

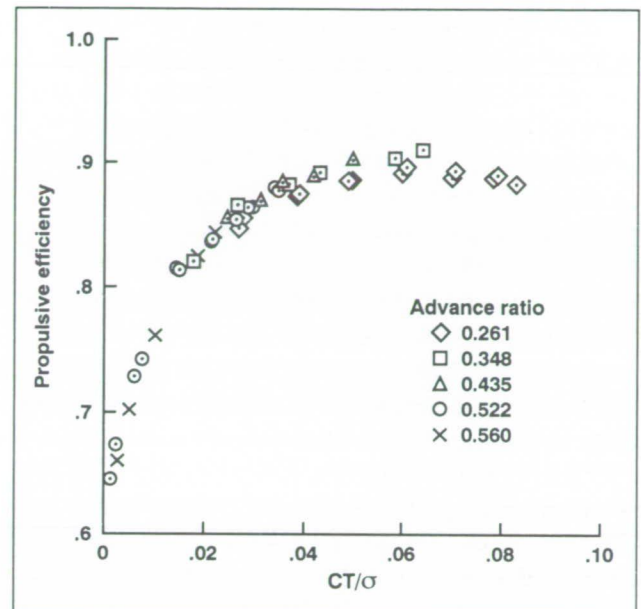


Fig. 2. Measured V-22 forward-flight performance.

The data in the second figure have not been corrected for spinner drag, so comparison with isolated rotor predictions is not yet possible. This limitation is especially critical for low-thrust/high-advance-ratio cases where the spinner drag is very high compared to rotor thrust.

Ames-Moffett contact: J. Light

(415) 604-4881

Headquarters program office: OAST

Forward-Flight Shadowgraph Flow Visualization of Helicopter Rotor Wakes

Jeffrey S. Light, Alexandra Swanson, Thomas R. Norman

Under a grant from the University of Maryland, extensive studies on rotor wake visualization were conducted using the wide-field shadowgraph technique. The wide-field shadowgraph technique is an important tool for visualizing and quantifying the wake vortex structure generated by rotors in forward flight. This work included both hover and forward-flight testing of a small-scale rotor. The experiments were performed with an isolated rotor and with a body representing a helicopter fuselage. Particular attention was paid to quantifying the isolated-rotor wake geometry, blade-vortex interaction phenomena near the rotor disk, and the distortion of the wake due to the presence of the body. The wide-field shadowgraph method provided quantitative measurements of the vortex trajectories as a function of wake age, as well as estimates of the tip-vortex core radius. The test results have yielded many rotor-wake structure measurements that are useful for validating rotor-wake and rotor/body interactional models for forward flight.

The rotor wake geometry was quantified through careful application of the wide-field shadowgraph technique. The first figure shows an example of the tip-vortex trajectories near the leading edge of the

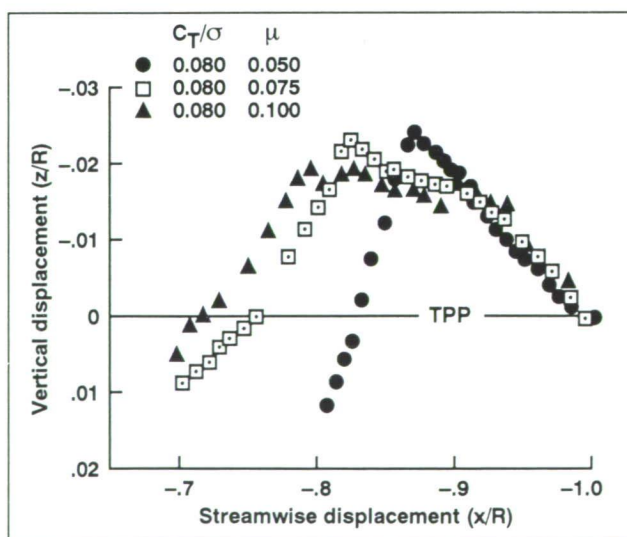


Fig. 1. Measurements of tip-vortex trajectories near the leading edge of the rotor.

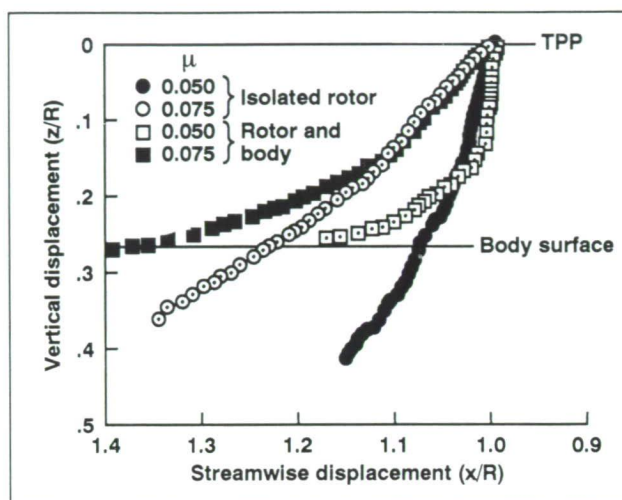


Fig. 2. Wake displacements versus wake age at rear of disk for rotor/body configuration.

rotor. In this figure, the leading edge of the rotor is to the right, and the airflow is from right to left. At the front of the rotor disk, the wake vortices are convected above the rotor plane. After the first blade passage, the vortices are convected downward through the disk, and blade-vortex interactions result. This behavior is consistent with past observations of rotor wakes. The presence of the fuselage did not significantly affect the vortex trajectories at the front of the rotor disk.

The presence of the fuselage does, however, significantly alter the wake geometry at the rear of the disk, as shown in the second figure. As the tip vortices come close to the body, their vertical displacements are progressively retarded and the vortices follow trajectories that are almost parallel to the body surface. Increasing advance ratio also significantly alters the wake geometry by shifting the tip-vortex trajectories downstream.

Ames-Moffett contact: J. Light
(415) 604-4881

Headquarters program office: OAST

Navier-Stokes Tiltrotor Download Research

Jeffrey S. Light, Johnson Lee

Through a grant with Stanford University, computational fluid dynamics is being applied to the tiltrotor wing download problem. A method has been developed to study rotor/wing interactions for a simplified tiltrotor configuration. This method incorporates an actuator disk model of the rotor with the solution of the thin-layer Navier-Stokes equations for the wing. Previous work with the analysis has shown the ability to capture many of the complex, three-dimensional flow features of the tiltrotor wake/wing interaction including the fountain effect, leading- and trailing-edge separation, and the unsteady wake beneath the wing. The wing model has recently been modified to include a tangential blowing jet on the wing leading edge. This blowing jet is similar to the type that has been shown experimentally to reduce wing download.

Predictions were made for rotor conditions corresponding to a tip Mach number of 0.72 and a thrust coefficient of 0.0117. The jet exit was positioned at the wing leading edge and ran the length of the wingspan, and the flow was directed toward the wing lower surface. Comparisons between cases with and without blowing show that the blowing jet caused entrainment of the flow outside the jet. The jet also caused the separation point to be shifted slightly farther aft of the leading edge on the lower surface. However, moving the location of the separation point aft did not cause a decrease in the download. The actual decrease in download can be attributed to the fact that static pressure reduction in the jet is felt upstream. This static pressure reduction causes a flow acceleration (and corresponding pressure drop) even before the jet is reached. The figure shows the computed wing surface pressures at 70% of the wingspan.

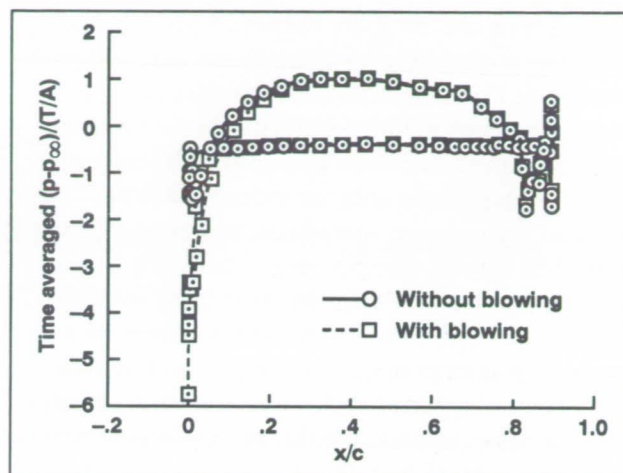


Fig. 1. Computed wing surface pressures at 70% of the wingspan with and without blowing.

On the lower surface near the leading edge, blowing is seen to reduce the static pressure, and therefore actually contributes to the download. However, the reduction of pressure is greater on the upper surface than on the lower surface, which results in a net reduction in download. These results agree well with earlier experimental observations.

Ames-Moffett contact: J. Light
(415) 604-4881

Headquarters program office: OAST

Evaluation of the Unsteady Aerodynamics Capability of the PMARC Code

Daniel Martin

The computer program PMARC (Panel Method Ames Research Center) was developed in recent years to compute inviscid, incompressible flows around streamlined bodies. It is steadily gaining acceptance in the aerospace community as a versatile research tool. This panel code also has the capability to calculate the unsteady loading on bodies undergoing prescribed motion. The purpose of this study is to evaluate the accuracy with which PMARC computes unsteady aerodynamic loading and to determine the appropriate settings of key parameters to obtain the best results. The code will be used to investigate the dynamic behavior and unsteady aerodynamics of free-pitching tips on wings and helicopter rotor blades for future applications to improve performance.

In the present study, a two-dimensional (2-D) theoretical model developed by Theodorsen is used for comparison of unsteady lift and pitching moment. These closed-form potential flow solutions are widely accepted and have been used extensively to predict aerodynamic loading of wings for flutter calculations. To achieve near-2-D flow conditions, a wing of aspect ratio 100 was modeled with PMARC and the sectional properties at the midspan section were compared to results predicted by Theodorsen's equations. Sinusoidal pitching motion at amplitudes of 5 and 10 degrees was prescribed for the wing. Sectional lift and pitching moment correlations have been obtained for reduced frequencies of between 0.1 and 0.5 for two cycles of motion.

A number of PMARC input parameters were varied to determine the combinations that yield the best results as compared to the theoretical predictions. For example, the figure shows the impact of the streamwise position of the row of doublets closest to the trailing edge (C_1 is the fraction of the total distance traveled by the doublet if convected by the free-stream velocity). Variation of this key parameter compensates for the lack of a continuous wake vorticity model in calculating transient unsteady loads, and introduces both amplitude and phase errors on the midspan sectional lift coefficient.

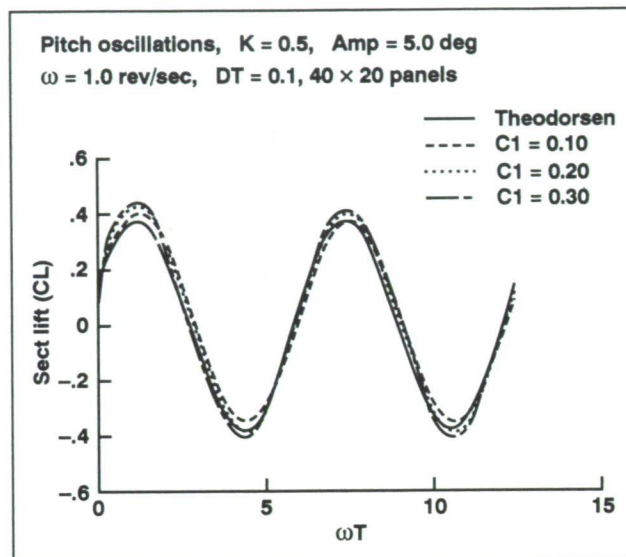


Fig. 1. Effect of doublets closest to the trailing edge on section lift time history.

The effect of time-step size, chordwise panel density, and amplitude of motion on lift and pitching moment have also been studied. Correlation data were obtained for a few cases of the wing in heaving motion and in combined pitching and heaving motion. The acceleration of a wing of aspect ratio 6 from rest to a finite speed has also been modeled and the results compared to data produced by another panel method code. Overall, the results show that midspan sectional lift and moment coefficients correlate extremely well with the theory as long as the key parameters listed above are properly selected.

Ames-Moffett contact: D. Martin

(415) 604-4566

Headquarters program office: OAST

Enhanced Free-Wake Efficiency Using Adaptive Resolution and Code Vectorization

Wayne O. Miller

A new free-wake model has been developed that is up to two orders of magnitude faster than existing models of comparable accuracy. This increased speed was achieved by improving both the analytical and the computational aspects of the problem. Many flow fields, such as the wakes of rotorcraft and airplanes, are characterized by concentrated regions of vorticity embedded in otherwise irrotational flow. Free-wake methods, which model only the fluid vorticity, are inherently efficient for this type of problem. The vortical wake is discretized into vortex elements, which are convected and distorted as material elements of the fluid under their own induced velocity. Despite their concise description of the fluid, free-wake methods can still pose a serious computational challenge. Computing the instantaneous velocity field for a wake discretized into N elements presents an order- N^2 task, and converged solutions often are order N^3 in effort. Thus the time required to find a solution rapidly reaches unacceptable proportions as N is increased to improve resolution or to add realistic complexity.

Adaptive resolution is based on the observation that the velocity field induced by a vortex element is strong near the element, but rapidly decays with distance. This requires that a wake model be highly accurate in the near field, though it need not be so accurate in the far field where its induced velocity is relatively weak. Furthermore, note that increasing the resolution will improve the near-field accuracy, but will have little effect on the far-field accuracy. Improved near-field accuracy may thus come at great cost since the far-field calculations make up the bulk of the N^2 problem. Adaptive resolution addresses this issue by treating each element as a hierarchy of subelements as suggested in the figure. In the far field, an element is modeled by one large subelement (part (b) of the figure), so that the expensive far-field calculations are done with an optimum resolution.

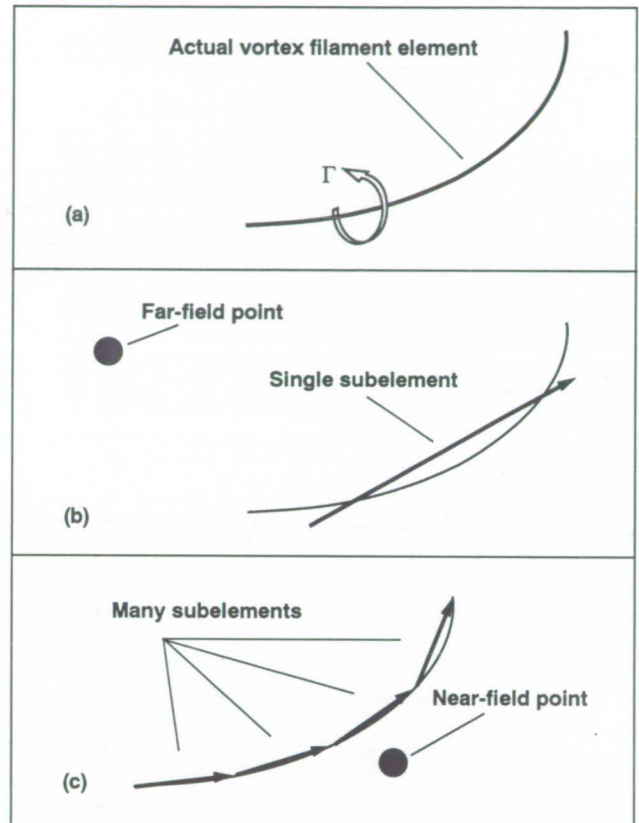


Fig. 1. Schematic of adaptive resolution. (a) Actual vortex-filament element of circulation strength Γ , (b) Far-field evaluations, (c) Near-field evaluations.

In the near field, smaller and more numerous subelements are used as needed to maintain accuracy (part (c) of the figure). This approach, also known as the subvortex method in two dimensions, is essentially a numerical quadrature scheme where the number of intervals is adjusted to match the integrand behavior. Comparison with other contemporary models shows that the adaptive resolution model is three to ten times faster for a given level of accuracy.

Code vectorization is a mature approach for improving the execution speed of a program by using special vector and pipeline CPU architectures to perform many similar operations concurrently. The present free-wake code was written specifically to vectorize efficiently for a Cray Y-MP. Results show that the vectorized code runs a full order of magnitude faster than the baseline scalar code. Combining vectorization and adaptive resolution results in a

free-wake model that can reduce execution time by two orders of magnitude over that required for contemporary free-wake models, while maintaining high accuracy.

Ames-Moffett contact: W. Miller
(415) 604-6719

Headquarters program office: OAST

Reduction of Noise in Helicopter Blade–Vortex Interactions

Marianne Mosher

When a rotor blade passes near or through a tip vortex produced by another blade, it generates impulsive sound that can be loud and annoying. All helicopters produce this type of noise when landing, often inducing community objections to heliports.

The figure shows pressure contours from a blade–vortex interaction with an unmodified airfoil. This research investigates the possibility of reducing the noise caused by blade–vortex interaction by modifying the airfoil. In particular, the addition of blowing near the leading edge of the airfoil is being investigated. The blowing produces a jet of air around the leading edge of the airfoil. This jet causes the vortex to interact with the airfoil as if the airfoil had a compliant surface instead of a rigid surface, thereby reducing the amplitude of pressure fluctuations on and around the airfoil.

A two-dimensional computational model of blade–vortex interaction produced by researchers at Ames is being used for this investigation. The program is modified to include blowing.

Ames-Moffett contact: M. Mosher
(415) 604-4560
Headquarters program office: OAST

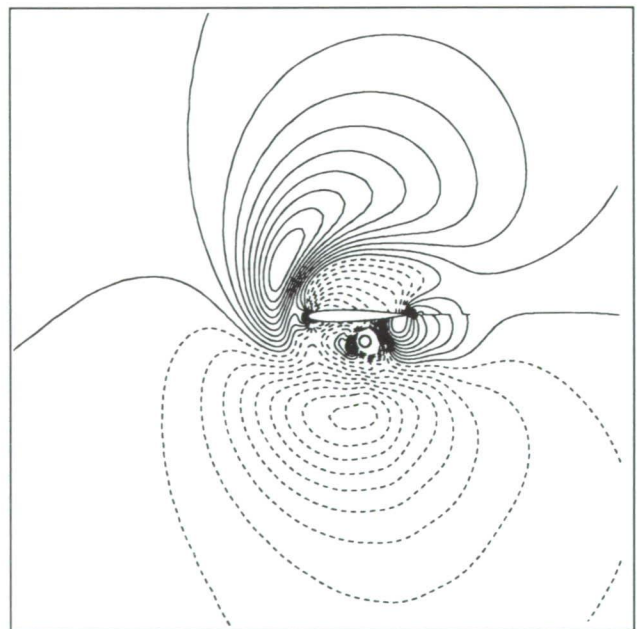


Fig. 1. Acoustic pressure perturbation from blade–vortex interaction.

Full-Scale Aerodynamic Interaction Program

Tom Norman, Gloria Yamauchi

Data from a full-scale test of a Bell 412 rotor system with a simple axisymmetric fuselage were reduced and analyzed. Results from the wind tunnel test revealed that the magnitude of the aerodynamic interactions on the simple fuselage were small. The importance of rotor shaft and hub interactions was also shown. Hub effects on the fuselage aerodynamic coefficients are shown in the first figure. In addition, comparisons between full- and small-scale results demonstrated the importance of model configuration and installation differences. The second figure shows a comparison of the rotor effect on the upper-surface pressures for full- and small-scale data; $(\Delta C_p)_R$ represents the difference in pressure coefficient caused by the rotor. The large differences between the full-scale and 1/6-scale results are attributed mainly to the lack of a rotor mast in the 1/6-scale test. The reason for the offset between the full-scale and 0.15-scale data is unclear, although potential causes include the

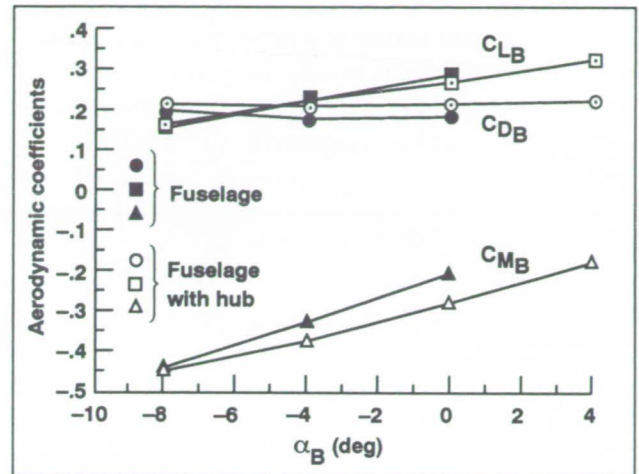


Fig. 1. Effect of hub on fuselage aerodynamic coefficients. Velocity = 120 knots, dynamic pressure = 47.5 lb/ft².

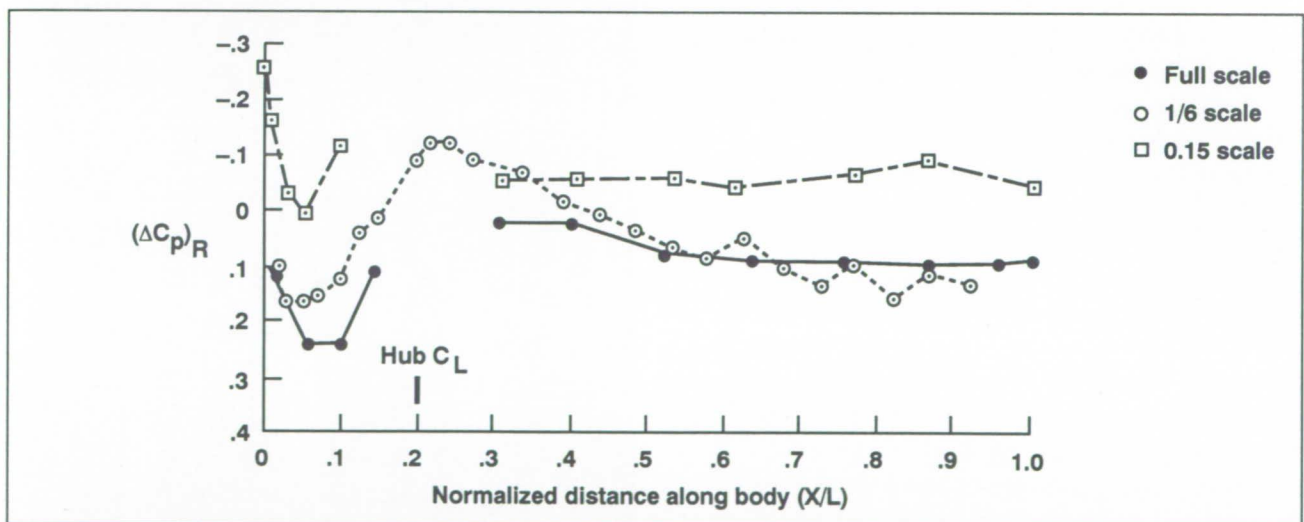


Fig. 2. Effect of rotor on upper-surface pressures. Thrust coefficient = 0.0055 (nominal), advance ratio = 0.20, body angle = 0 degrees (shaft angle = -4 degrees).

unscaled hub and the significantly different model mounting system used in the 0.15-scale test. Additional small-scale data are needed for lower speeds, where rotor/fuselage interactions are larger.

The rotor and rotor wake caused large, unsteady pressure fluctuations on the top of the fuselage which were similar in character to small-scale results. This result supports the idea that the basic phenomena which cause unsteady loading on a full-scale fuselage can be studied, at least qualitatively, in small scale.

The magnitude of this unsteady loading was dependent on the loading source. Pressure fluctuations caused by blade passage were dependent on rotor thrust, whereas fluctuations caused by close wake interaction were dependent on advance ratio.

Ames-Moffett contact: T. Norman

(415) 604-6653

Headquarters program office: OAST

Full-Scale Test of an F/A-18 at High Angles of Attack

James C. Ross

The objective of this test was to examine the high-angle-of-attack aerodynamics of fighter aircraft. Particular emphasis was placed on understanding the leading-edge-extension-vortex-induced tail buffet and on developing a pneumatic forebody flow control concept for lateral control at high angle of attack. The test has also provided important data for computational fluid dynamics (CFD) validation, and for resolution of scaling issues that have become apparent in comparing small-scale wind tunnel data with flight results.

A retired Navy F/A-18A was converted to a wind tunnel model for testing in the Ames 80- by 120-Foot Wind Tunnel, as shown in the figure. The model is heavily instrumented to measure time-averaged forebody pressure distributions and the unsteady pressure distribution on one of the vertical tails. In addition, the nose of the aircraft was modified by the addition of jet-type and slot-type blowing for flow control at very high angles of attack.

Data from the high-angle-of-attack wind tunnel tests correlated well with flight data for the overall forces and moments as well as for the radome and forebody pressure distributions. The unsteady vertical tail pressure data will be used to address wind tunnel scaling issues, to identify flow structures and dominant frequencies in the burst vortex, and to validate CFD analyses. Preliminary analysis of these data

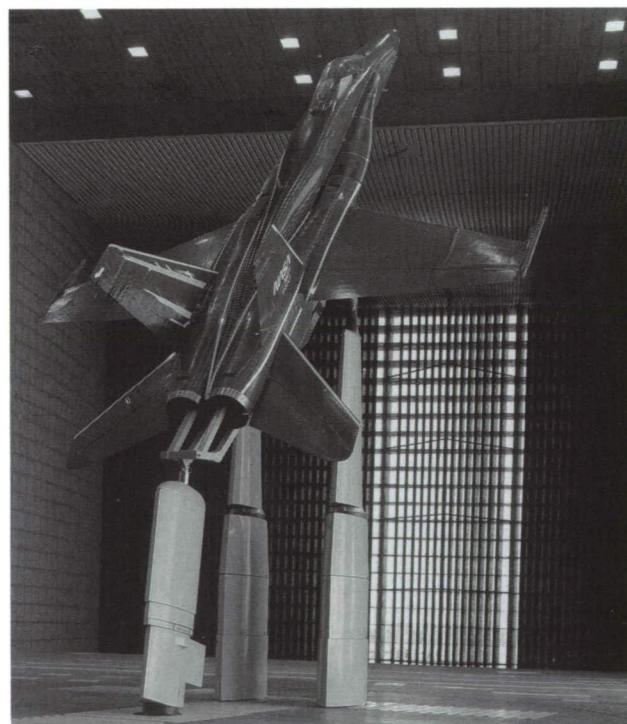


Fig. 1. F/A-18 aircraft in the Ames 80- by 120-Foot Wind Tunnel.

indicates that the nondimensionalized frequency content of the fin pressure measured in the full-scale wind tunnel test is similar to that observed in several small-scale experiments. Unsteady pressure measurements are not yet available from the flight experiment.

The pneumatic forebody flow control was shown to be effective for practical blowing slot lengths and blowing rates. At an angle of attack of 50 degrees, the pneumatic system can provide more yawing moment than a full rudder deflection does at low angles of attack.

Tests of the forebody strake control system were also performed. These results will be used in designing the flight control system for the flight tests planned on the F-18 High Alpha Research Vehicle.

The pressure distributions measured on the full-scale model will provide a rich source of CFD valida-

tion data which will help to improve the accuracy of three-dimensional Navier-Stokes computations. CFD efforts are currently under way to compute the unsteady burst-vortex-induced pressures on the F-18 tail. These wind tunnel measurements are an important part of the validation of CFD for unsteady flows.

It has been demonstrated that pneumatic forebody flow control can generate control yawing moments of sufficient magnitude to provide directional control at extreme angles of attack where rudder control is no longer effective.

Ames-Moffett contact: J. Ross

(415) 604-6722

Headquarters program office: OAST

High-Speed Research: High-Lift Systems

James C. Ross

The objective of this element of the High-Speed Research program is to develop advanced high-lift systems that will help reduce the community noise impact and contribute to the economic success of new high-speed civil-transport (HSCT) aircraft.

A combined computational and experimental program is being followed. After small-scale testing, theoretical and computational analyses, and a literature search on suitable high-lift devices, the trapped vortex and miniature split flap were selected as promising technologies.

Potential-flow analyses have demonstrated the stability conditions required for trapping a vortex on a wing. The need for two fences to trap a vortex with very little suction at the vortex core was a significant discovery. Preliminary water-channel and wind-tunnel tests showed the effectiveness of the two-fence configuration for simple geometries. These results also validated the computational work. Additional Navier-

Stokes analyses showed that the vortex trapping process is not sensitive to Reynolds number.

Cooperative wind-tunnel tests were performed with the Boeing Commercial Airplane Company at the University of Washington Aeronautical Laboratory. These tests showed that for a representative HSCT model, a double-fence configuration generated a tighter vortex than did a single fence.

Subsequent tests at NASA Ames examined vortex trapping on a variable-sweep rectangular wing, shown in the figure, and on the Boeing low-speed model. The results of the tests were mixed. A significant lift increase was generated by the trapped vortex on the simple swept wing. Trapping a vortex on the wing of the HSCT model, however, was only 20% as effective as on the simple wing. This performance difference is being examined to determine what geometric parameters are important for effective vortex trapping.

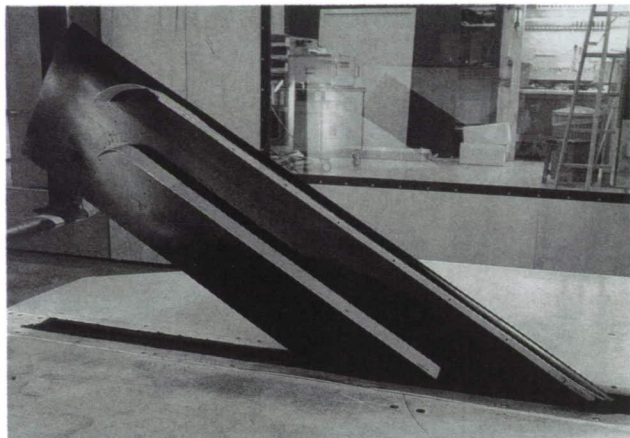


Fig. 1. Variable-sweep rectangular wing.

The miniature split flaps proved to be very effective in increasing the lift at a given angle of attack without generating large drag increments. The flaps are approximately 1.5% of the local wing chord and are deflected 90 degrees downward. The drag penalty is relatively small as a result of the small size of the flaps. In fact, at moderate lift coefficients (representative of flight climb conditions) the lift-to-drag ratio for a given lift coefficient can be greater with the flaps deflected than for the clean wing.

Ames-Moffett contact: J. Ross
(415) 604-6722

Headquarters program office: OAST

Atmospheric Turbulence and Measured Tail Rotor Acoustics

A full-scale Lynx tail rotor was tested in hover at the Ames Outdoor Aerodynamic Research Facility. The investigation was designed to provide an understanding of the acoustics of an isolated tail rotor, without the effects of the main rotor wake or other helicopter components, hovering out of ground effect in atmospheric turbulence. In addition to rotor noise and performance measurements, near-field and far-field turbulence measurements were made. The investigation included a study of the effects of atmospheric turbulence on rotor noise and the effects of the rotor on atmospheric eddy lengths and root-mean-squared (rms) turbulence velocities.

The Lynx tail rotor consists of four constant-chord, untwisted blades. The rotor hub has conventional flapping and feathering hinges. The rotor inflow was measured with two single hot-film anemometers ("hot-films") and a pitot-static probe, shown in the figure. The hot-films and the pitot-static probe were mounted on a tower with a traversing mechanism. One hot-film and the pitot-static probe remained fixed, while the other hot-film was moved with the traversing mechanism. Prior to data acquisition, the two probes were placed as close together as possible. During the run, the movable probe was passed

upward and away from the fixed probe. Data were acquired at several discrete probe-separation distances during the run. A turbulence grid was installed upstream from the rotor for several runs. The purpose of the grid was to change the character of the turbulence by introducing small-scale turbulence.

A second pair of hot-films was mounted on a tower located upstream and to the side of the tail rotor (shown in the figure). These probes were used to measure the atmospheric turbulence in the far field. As with the near-field tower, one hot-film remained fixed while the other hot-film was moved away from the fixed probe. Atmospheric windspeed and wind direction were measured using a cup anemometer and a weather vane located on a third tower roughly 150 feet upstream from the rotor, 180 feet from the rotor axis, and 33 feet above the ground.

Eight microphones were used to acquire acoustic data. The microphones were placed in an array around the rotor at distances of 2.5, 4.5, and 10 rotor radii away from the hub. All but one of the microphones were at the same height as the rotor. Acoustic foam was used to substantially reduce the rotor noise reflected from the ground, the near-field tower, and the Tail Rotor Test Rig.

David B. Signor, Gloria K. Yamauchi,
Marianne Mosher, Martin Hagen, Albert George

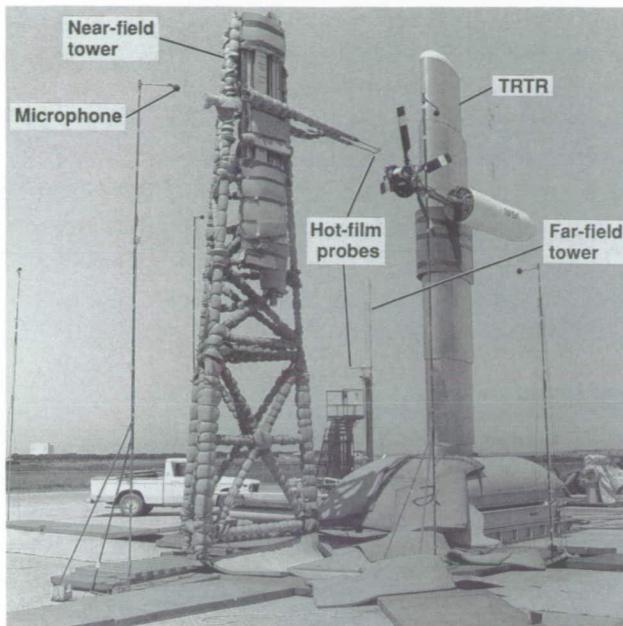


Fig. 1. Experimental setup.

Acoustic data were acquired with varying windspeed, wind direction, eddy lengths, and rms turbulence velocities, as found in the atmosphere. Measurements were made with two tip Mach numbers and five collectives. Background noise levels were typically at least 20 decibels below the acoustic levels with the rotor in operation.

Performance data from this investigation were published in NASA TM-101057. Acoustic and atmospheric turbulence data will be presented at the 1992 American Helicopter Society Annual Forum.

Ames-Moffett contact: D. Signor

(415) 604-4562

Headquarters program office: OAST

In-Flight Rotorcraft Acoustics Program

The program objectives are to obtain in-flight rotor acoustics measurements that are directly comparable to acoustic measurements made in the Ames 40- by 80- and 80- by 120-Foot Wind Tunnels. The acoustics measured in flight will be used to validate and substantiate the wind-tunnel data for investigating important noise mechanisms such as blade-vortex interaction. Another objective is the development of new in-flight test techniques for studying main-rotor and tail-rotor noise mechanisms.

To meet these objectives, the Ames YO-3A aircraft is flown in close formation with a test helicopter. The YO-3A is a low-noise aircraft equipped with instrumentation for acquiring acoustic data. It is positioned relative to the test helicopter so that the tail-mounted microphone corresponds to microphone locations during wind-tunnel data acquisition. (The helicopters are commercially leased aircraft or NASA research aircraft.) The methodology for this type of in-flight testing was developed by the U.S. Army. The

David B. Signor, Gloria K. Yamauchi, Marianne Mosher

helicopter rotors of interest are the MBB BO-105, Sikorsky S-76, Bell 412, and Sikorsky UH-60.

The first flight test of the In-Flight Rotorcraft Acoustics Program was completed in 1991. The BO-105 in formation flight with the YO-3A is shown in the figure. The acoustic data from the BO-105 helicopter flight test are preliminary and indicate the need for an accurate measurement of the rotor-to-microphone distance. After completion of the first flight test, procurement of accurate air-to-air distance-measuring equipment was initiated.

Accurate stationkeeping is critical for correlating in-flight acoustics with wind-tunnel acoustics. The distance between the helicopter rotor and the microphones mounted on the YO-3A must be known as a function of time. A system that can display and record the aircraft separation distance with an accuracy of ± 1 foot for a 30-second acoustic data record is required. Stationkeeping with this accuracy is difficult



Fig. 1. BO-105 helicopter in formation flight with the Ames YO-3A.

and has not been achieved in the past. The flight test with the BO-105 provided insights for developing a more accurate and robust system.

The YO-3A acoustic-data-acquisition system was exercised for the first time in several years. Subsequent analysis of the data taken with the BO-105 has revealed that some instruments need refurbishment and/or replacement. The necessary upgrades will be completed prior to further data acquisition.

The S-76 rotor system flight test is scheduled for June 1992. The remaining rotor systems will be flight tested subsequently.

Ames-Moffett contact: D. Signor
(415) 604-4562

Headquarters program office: OAST

Quiet Sensors and Struts for Wind-Tunnel Studies

Paul T. Soderman

An Ames 40- by 80-Foot Wind Tunnel test of special acoustic sensors developed by a defense contractor for flight has been completed. Results show that advanced-technology microphones shaped like pitot probes with the sensor openings several probe diameters downstream from the nose shoulder generate 6 to 10 decibels less wind noise than do the commercial microphones with nose cones that are currently used in wind-tunnel research. The figure shows the new and reference microphones mounted on struts in the 40- by 80-foot test section. Part of the reduction of turbulence-induced noise was achieved by summing the signals from two sensors in the same probe or by summing signals from two sensors in adjacent probes. Uncorrelated sound was thereby canceled.

Noise induced by wind over microphone struts is also being studied, in the Ames 7- by 10-Foot Wind Tunnel. Airfoil shapes and probe holders have been found that minimize aerodynamic noise. The effect of probe misalignment on microphone wind noise has been quantified. Tones from a flow-survey apparatus in the test section have been identified and eliminated.

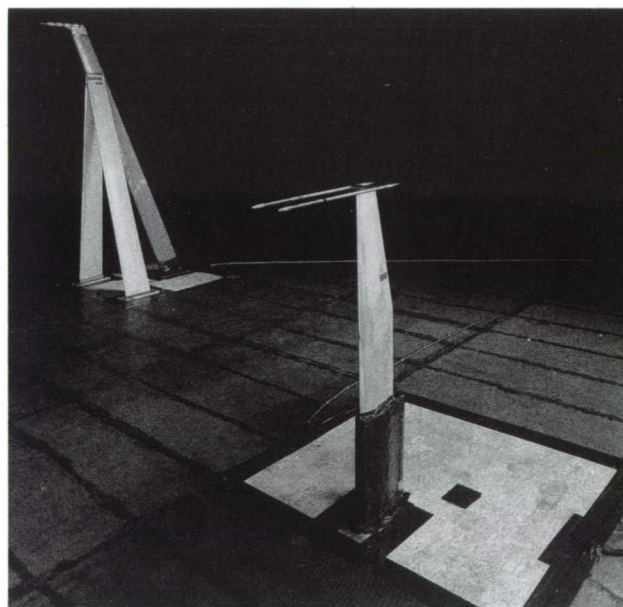


Fig. 1. Advanced technology microphones (foreground) and reference microphone (background) in the Ames 40- by 80-Foot Wind Tunnel.

Subsequent low levels of flow noise have led to the discovery of resonance tones induced in commercial nose cones. Previously, these tones had been attributed to the wind tunnel. Accelerometers in the struts are used to separate microphonics from airborne sound.

Improved acoustic sensors and support struts will result in significantly lower background noise in closed-return wind tunnels without any modification

to the facility as long as wind is the dominant noise source, which is commonly the case. The quality of acoustic data acquired from low-noise advanced ducted propellers, jet noise suppressors, and similar devices will be significantly improved.

Ames-Moffett contact: P. Soderman
(415) 604-6675
Headquarters program office:

A Zonal Flow Analysis Method—3-D Flow

Paul M. Stremel

The flow field surrounding a rotorcraft is complex and difficult to model, therefore a three-dimensional (3-D) analysis is needed to provide sufficiently accurate results for predicting rotorcraft performance. An enormous amount of computer memory and computational effort is required for this type of analysis. A zonal method has been developed to provide a computationally efficient procedure. The method has been developed for two-dimensional (2-D) flow analysis and is currently being tested for 3-D flow.

The flow about a rectangular wing with a NACA 0012 airfoil section has been calculated in order to verify the zonal method for 3-D analysis. A comparison of the results using ARC3D with those predicted by the zonal method (ZAP3D) are presented in the figure. The contour plots represent the vertical velocity component at the plane of symmetry of the wing. The flow about the wing is calculated for a Mach number of 0.12 and an incidence angle of 8 degrees. The results predicted by ARC3D, shown in part (a) of the figure, clearly demonstrate the trajectory and expansion of the wing wake downstream from the wing. In comparison, a similar plot for the vertical velocity component predicted by ZAP3D demonstrates the interaction of the wing wake with the outer viscous boundary. The outer viscous boundary is located at 1.2 chordlengths. ZAP3D is being modified to eliminate this interaction and provide an outer boundary that will allow for the expansion of the wing wake.

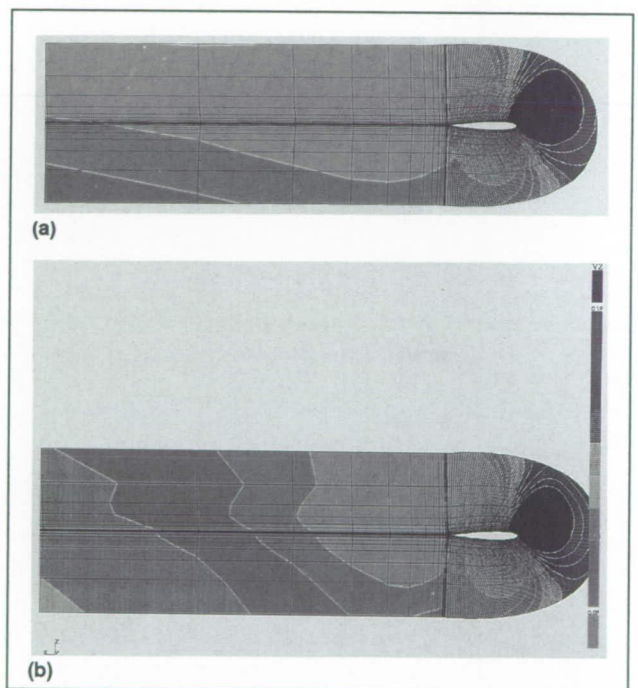


Fig. 1. Comparison of computed vertical velocity contours at wing plane of symmetry. (a) ARC3D, far-field boundary at 17 airfoil chords, (b) ZAP3D, far-field boundary at 1.2 airfoil chords. (See color plate 10 in Appendix)

Ames-Moffett contact: P. Stremel
(415) 604-4563
Headquarters program office: OAST

Two-Dimensional Tiltrotor Download

Paul M. Stremel

The accurate prediction of download is essential in the design of efficient tiltrotor aircraft. Download is the force on a tiltrotor aircraft in hover resulting from the wake of the rotors. Obviously, in order to optimize payload, download must be minimized. The application of existing computational methods to tiltrotor download has resulted in limited success. This is true not only for three-dimensional flow but for two-dimensional (2-D) download (the flow about airfoils at -90 degrees to the free stream). When compared with experimental results for 2-D download, existing methods have proved incapable of accurately predicting the airfoil surface pressure.

To accurately predict tiltrotor download, a new method has been developed to calculate the viscous flow about airfoils at -90 degrees incidence. This unique method provides for the direct solution of the

incompressible Navier–Stokes equations by means of a fully coupled implicit technique. The solution is calculated on a body-fitted computational mesh incorporating a staggered-grid methodology. In the staggered-grid method, the vorticity is defined at the node points and the velocity components are defined at the mesh cell sides. The staggered-grid orientation provides for the accurate representation of the vorticity at the node points and the conservation of mass at the mesh cell centers. The method provides for the direct solution of the flow-field equations and satisfies the conservation of mass to machine zero at each time step. In addition, the boundary conditions for the vorticity at the airfoil surface and at the far-field boundary are solved for implicitly as part of the solution, which provides for the accurate time-dependent flow around the airfoil.

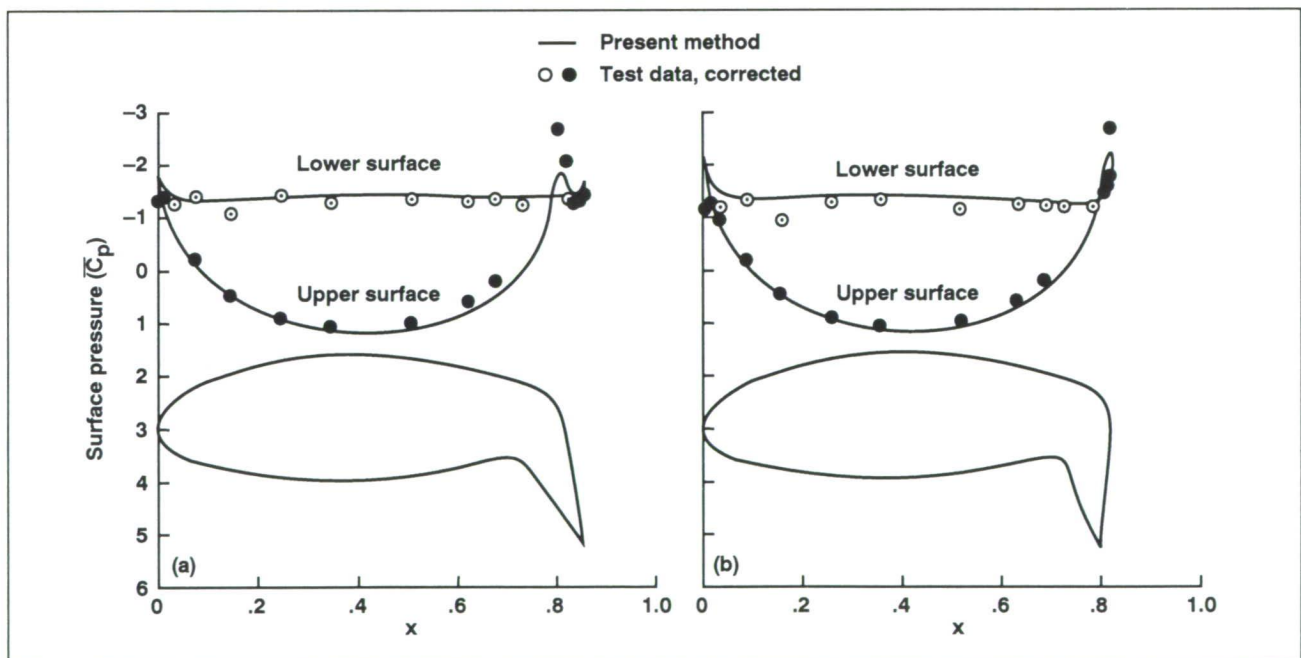


Fig. 1. Average surface-pressure comparison for an XV-15 airfoil at -90 degrees incidence. (a) $\delta_f = 60$ degrees, (b) $\delta_f = 75$ degrees.

Comparisons with experimental data have been made in order to evaluate the ability of this new method to predict 2-D download. Comparisons were made of the predicted and measured average surface pressure on an airfoil that is representative of the wing of an XV-15 tiltrotor aircraft. Shown in the figure are the surface-pressure comparisons for flap deflections (δ_f) of 60 and 75 degrees. The predicted results were calculated for a Reynolds number of 200, whereas the experimental results were measured at a Reynolds number of one million. Comparisons of the measured pressure distributions and those predicted by the present method for the XV-15 airfoil show excellent agreement. The lower-surface pressure is accurately predicted. The negative pressure peak on the upper

surface caused by flap deflection is accurately predicted in location at $\delta_f = 60$ degrees, as is the pressure distribution on the flap at $\delta_f = 75$ degrees. Differences in the comparisons near the leading edge of the airfoil are felt to be the result of Reynolds-number effects between the calculated and the measured values. In general, however, the predicted results are shown to be in excellent agreement with those measured in experiment.

Ames-Moffett contact: P. Stremel

(415) 604-4563

Headquarters program office: OAST

Shadowgraphs of S-76 Wake Interactions

Alexandra Swanson

Preparations are under way for a shadowgraph test to be conducted in the Ames 80- by 120-Foot Wind Tunnel. This will be the first time the wide-field shadowgraph technique will be used to visualize rotor wakes of a full-scale rotor system. Because of the magnitude of such an effort, the flow visualization will be limited to a few regions of the wake. Specific objectives include investigating the outer 50% of the blade for parallel blade-vortex interactions on the advancing side of the rotor system. Data will be obtained for blade azimuths of 45 to 135 degrees at advance ratios of 0.10 to 0.20. Tip-vortex-core size and blade-vortex spacing will also be examined. The information obtained will be correlated with data from acoustic research activities and will be used to validate prediction analyses.

A specially configured video imaging system was developed for real-time acquisition and storage of data on high-resolution flow-field structures. The system is capable of asynchronous image capture for various rpm conditions. It includes a camera control unit which sends an external trigger from a phototachometer to two strobes and two video cameras simultaneously. The video cameras are each capable of capturing 11 consecutive image frames at the same instant. These images are captured by two frame-grabber boards and can be saved as tagged image file format files. Modifications to the image-processing software are planned to resolve three-dimensional rotor wake measurements from simultaneously acquired image pairs.

Ames-Moffett contact: A. Swanson

(415) 604-6856

Headquarters program office: OAST

Shadowgraphs of Tiltrotor Wakes

Alexandra Swanson, Jeffrey Light

Results from a recent small-scale V-22 tiltrotor test provide a better understanding of the wake geometry of tiltrotors. Measurements were made of the wake geometry of the isolated tiltrotor and the tiltrotor in the presence of a semispan wing and image plane. Specific areas that were examined include (1) changes in the wake geometry boundaries of the isolated tiltrotor as it varies with thrust, (2) the tiltrotor wake in the presence of the wing and image plane, and (3) a detailed study of the relationship between tip-vortex-core size as it varies with thrust and wake age.

Shadowgraph flow-visualization measurements of the visible outer core region of the tip vortex were acquired. The first figure is a representative shadowgraph showing details of the tip-vortex-core structure. Although no velocimetry was conducted, measurements from this test strongly indicate that the vortex core is sensitive to thrust and wake age. The second

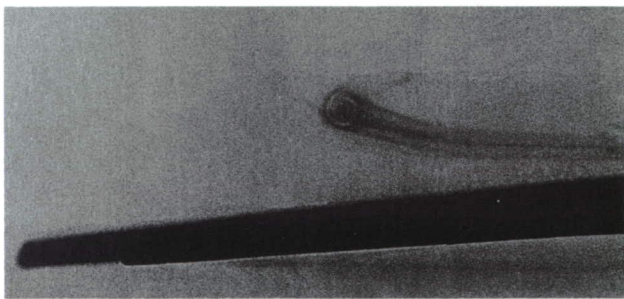


Fig. 1. Wide-field shadowgraph close-up of tip-vortex core.

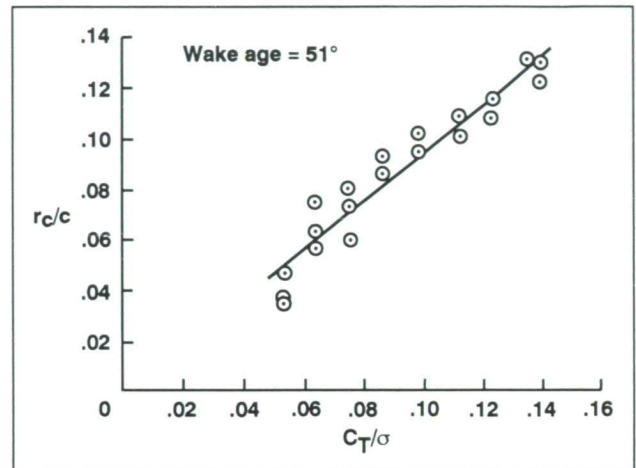


Fig. 2. Tip-vortex-core radius versus thrust coefficient.

figure shows the relative effect of thrust on the core measurements for one wake age. These results show a linear relationship between the core measurement and the thrust condition. In the third figure, results show that the core measurement increased with wake age. The shadowgraph core measurements of the tiltrotor appear to be in agreement with the tip-vortex-core radius typically used for helicopter analyses.

Analysis and review of the wake geometry data yielded the following conclusions. The radial tip-vortex position for the isolated tiltrotor is unsteady at high thrust coefficients after the first blade passage (wake age = 120 degrees). A wake expansion for the

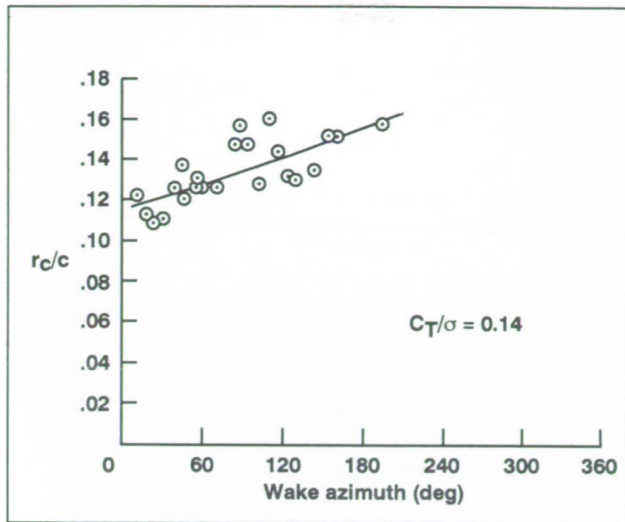


Fig. 3. Tip-vortex-core radius versus wake azimuth.

isolated rotor occurs after three blade passages, a finding that conflicts with the classical assumption of a continuously contracting wake. Similar results were found in the Lynx tail rotor test conducted at Ames in 1986, in which the radial wake boundary contracted and expanded after one complete revolution. Results also verify that the presence of the wing and image plane contribute significantly to the radial expansion of the wake. Finally, the core size is greatly affected by thrust condition and wake age. It is believed that this empirical data will enable improvements in prescribed and free-wake models of tiltrotors.

Ames-Moffett contact: A. Swanson
(415) 604-6856

Headquarters program office: OAST

NASA/McDonnell Douglas Canard Rotor/Wing Test

Stephen Swanson, Steve Christensen

NASA Ames Research Center and McDonnell Douglas Helicopter Company have entered into a joint program to evaluate the aerodynamic characteristics of a new high-speed rotorcraft concept called the canard rotor/wing (CRW). The CRW is a stoppable-rotor aircraft that can hover and fly at low speeds like a conventional helicopter but also, in its stopped-rotor mode, can fly at high speeds comparable to those of current commercial aircraft. For helicopter-mode flight, the CRW uses a two-bladed, teetering rotor which is driven by reaction jets located at the tips of the blades. These reaction jets provide the required rotor power to generate lift, without the weight of a transmission or the addition of a tail rotor to counteract rotor torque. The rotor airfoil cross sections are symmetric elliptical sections that are not augmented by mechanical flaps or circulation control. Conventional turbofan engines are used for aircraft propulsion as well as to supply high-pressure air to the rotor reaction jets. As the forward flight speed of the CRW increases, the aircraft lift is transferred from the rotor

to a canard and a horizontal tail. At the conversion speed, the lift has been completely transferred from the rotor. The rotor rotation can then be stopped and the rotor locked into a fixed-wing configuration for high-speed flight. In principle, transferring the lift away from the rotor minimizes (a) the stresses placed on the rotor, (b) the control requirements of the rotor, and (c) the aircraft vibrations produced while the rotor rotation is being stopped, thereby helping to reduce the design challenge of developing the stoppable-rotor system.

Although stoppable-rotor-type concepts have been studied in the past, the CRW represents a different approach to the idea. As a start in determining the feasibility of the CRW, a low-speed, fixed-wing test is being completed in the Ames 40- by 80-Foot Wind Tunnel. This test will identify the aerodynamic characteristics of the CRW during conversion (with the rotor stopped) and at higher speeds approaching cruise. The accompanying

photograph shows the test model mounted in the wind tunnel in its cruise configuration. The major objectives of the test are to

1. Assess the aerodynamic performance of the CRW in its conversion and cruise configurations.

2. Improve the control-surface effectiveness of the tail and the canard in the conversion and cruise configurations.

3. Determine the longitudinal-stability characteristics of the CRW at the estimated conversion speed, comparing static stability of two candidate tail designs, an H tail and a T tail.

4. Determine the effects of rotor azimuth positions on the low-speed aerodynamics.

Key to the success of the CRW is the aircraft's lift-to-drag ratio in cruise configuration. NASA is studying the impact of low-drag rotor hub and pylon fairings on the lift-to-drag ratio of the CRW. Previous work completed at Ames helped to identify rotor hub and pylon fairings that reduced the overall drag of a conventional helicopter airframe. Similar success is hoped for in making the CRW an efficient high-speed rotorcraft.

Ames-Moffett contact: S. Swanson

(415) 604-4565

Headquarters program office: OAST

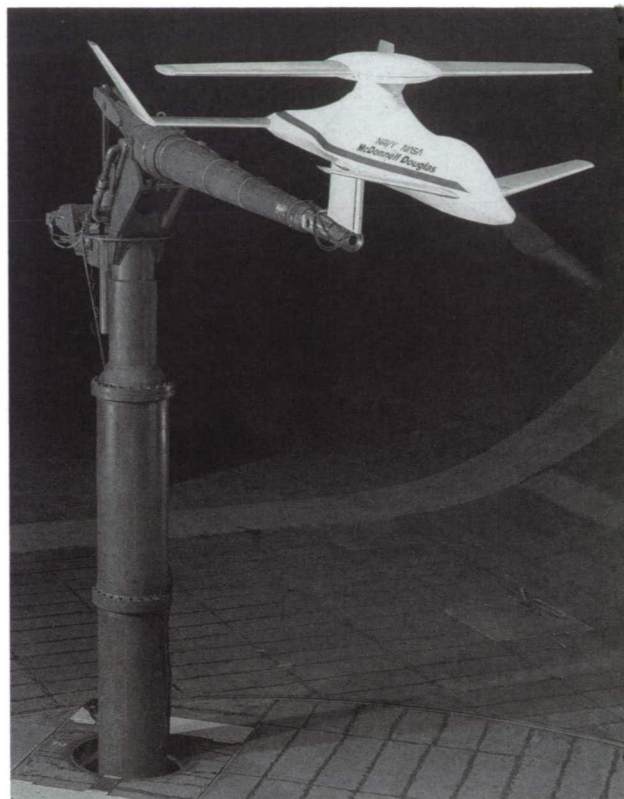


Fig. 1. Canard rotor/wing model in the Ames 40- by 80-Foot Wind Tunnel.

The Design Reuse Assistant

Catherine Baudin, Jody Gevins

The goal of the Design Reuse Assistant (Dedal) project is to facilitate the capture and reuse of previous design experience by monitoring design modifications in response to requirement changes. Design adaptation is a complex task because it requires an understanding of how design features relate to design requirements. For complex artifacts these relationships can be difficult to trace, and text-based documents make it difficult to retrieve such dependency links.

Dedal is a multimedia environment and is the result of a collaboration between NASA and the Stanford Center for Design Research (CDR). To capture traces of design activity during the design process, CDR investigated the use of an Electronic Design Notebook (EDN) to record the designer's notes and design-meeting reports, and the use of videotaped records. The EDN helps to retrieve text and graphic design material; Dedal organizes this information for reuse.

A design record in Dedal includes text and graphics documents as well as "machine intelligible" models of the structure, function, and behavior of an artifact. The system uses these models for different purposes: (1) to point out the parts of the device that relate to a given requirement or to predict the impact of a design change. The system is coupled with a constraint-based CAD tool which manages the relations among equations, computational procedures, and design constraints; and (2) to act as expert librarians that help the user locate relevant segments of design information. An inference mechanism exploits dependency relations among the design elements to help match the questions to the indices. If the information is available, Dedal retrieves previously considered alternative designs.

Based on cognitive studies conducted at the CDR and at Ames, we developed a language to describe the content and form of design documents. We use this language to index design information such as engineering-notebook pages or transcripts of conversations among designers. Our approach is a compromise between domain-independent, argumentation-based systems and pure, model-based approaches which assume a complete formalization of all design documents.

In 1991 we experimented with Dedal to organize technical documentation for a class of small electro-mechanical devices. We tested the approach to retrieve design records for the continuously variable damper, which is a new variety of shock absorber. We entered models of the damper requirements, structure, and behavior, as well as some alternative decisions considered and disregarded, and indexed on-line documents and videotaped material associated with the shock absorber design. To test the first version of our system we conducted an experiment in which a mechanical engineer designed a new shock absorber by modifying the variable-damper design using Dedal. We focused on how a mechanical engineer formulates questions to the system and on the quality of the answers provided.

**Ames-Moffett contact: C. Baudin
(415) 604-4745**

Headquarters program office: OAST

Generalized Approximate Reasoning in Intelligent Control

Hamid Berenji

The goal of this research is to develop a set of techniques and architectures for knowledge-based control systems. This research examines the roles of approximate reasoning and artificial neural networks in the control of dynamic systems. We are developing methods for combining the strength of these techniques in knowledge representation and in learning from experience.

The previous reinforcement-learning models for learning control do not use existing knowledge of a physical system's behavior, but rather train a neural network from scratch. The learning process is usually lengthy, and even after the learning is completed, the resulting control strategy cannot be easily explained. On the other hand, controllers that are based on approximate reasoning provide a clear understanding of control strategy but cannot learn from experience. We have introduced a new method for learning to

refine the control rules of controllers that are based on approximate reasoning. Our generalized approximate-reasoning-based intelligent control (GARIC) architecture, shown in the figure, can accept the rules that human operators use in the control of a physical system and then later refine these rules by automatic learning from experience. GARIC's learning method resembles human learning in the sense that it can start with some approximate (imprecise) rules and calibrate them by repeated trials. A reinforcement-learning technique is used in conjunction with a multilayer neural network model of an approximate-reasoning-based controller. The model learns by updating its prediction of the physical system's behavior. Unlike previous models, GARIC can use the control knowledge of an experienced operator and fine-tune it through the process of learning.

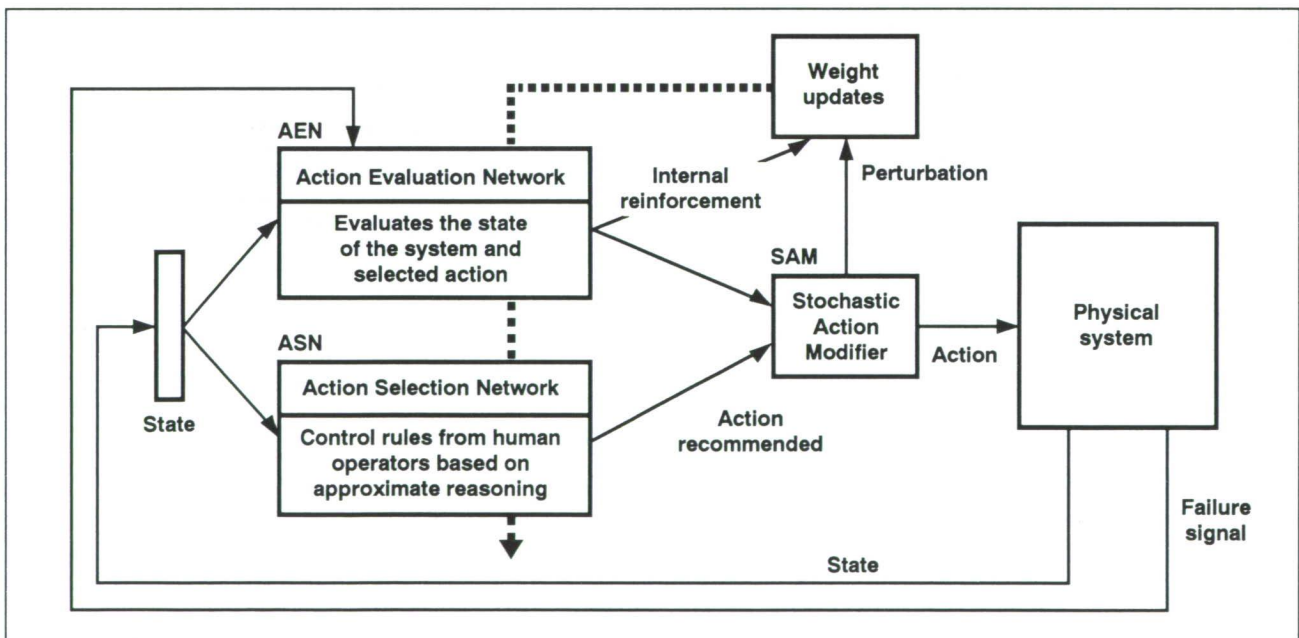


Fig. 1. The GARIC architecture.

In 1991, we demonstrated the application of the new approach to the small but challenging real-world control problem of cart-pole balancing. The GARIC architecture has demonstrated that (1) it is possible to develop controllers using approximate reasoning even if no analytical model of the dynamic system is available, (2) it is possible to refine approximate reasoning-based controllers by using reinforcement learning, and (3) controllers developed according to the GARIC architecture can be less susceptible to changes in the environment. In empirical testing on the cart-pole-balancing problem, GARIC showed a learning speed that was orders of magnitude greater than that of previous controllers.

Currently we are, in collaboration with the Information Systems Directorate at Johnson Space Center, applying GARIC to the simulation of the space shuttle rendezvous and docking control. GARIC will also be applied to a larger set of benchmark control problems to study its performance further. The current user-interface system of GARIC will be extended to provide on-line control-rule modification and flexibility in selection of the decision-making logic used in control.

**Ames-Moffett contact: H. Berenji/P. Friedland
(415) 604-6070/4277
Headquarters program office: OAST**

Model-Based Learning

Wray Buntine

This project involves developing tools for analyzing data. The tools build classifiers or regressions, which are prescriptions for predicting values of target variables in a domain. The tasks are sometimes referred to as supervised learning, discrimination or induction, and regression, and are studied in the fields of artificial intelligence (AI), pattern recognition, statistics, and neural networks. The tools are used for learning from historical cases collected in a data base.

The tools are being developed for the case in which the amount of data is too small to easily determine which classifier or regression to choose. When there is a large amount of data, the best classifier can be chosen as the one with the best "fit" to the data; with smaller amounts, a more intelligent choice than "best fit" is required because there will be several quite different classifiers that are a "reasonable fit" to the data and none will be a clear best fit. In this case, Bayesian statistics and decision theory are appropriate to use in designing the learning algorithms. This is the only theoretical method from AI, statistics, pattern recognition, or neural networks that is specifically aimed at the smaller-sample case. This

theoretical guide is important because empirical, ad hoc development of algorithms in the past has been time consuming and is often plagued by unexplained problems. Empirical validation of the algorithms is also important for checking approximations made in interpreting the Bayesian theory. We do this empirical validation by applying the algorithms to a battery of recognized learning problems taken from the literature, or to manufactured problems.

In 1991, a decision-tree software package called the IND package was distributed in beta-test form, and is being prepared for release through COSMIC, NASA's software distribution center. A decision tree built from data using the software is used to sequentially test variables in order to make a decision. The package includes the classical statistical and AI methods for decision-tree learning, as well as methods that incorporate the Bayesian principles described above. The package is currently in beta testing at several universities and at some industrial laboratories, including AT&T, Boeing, and British Petroleum. The package has been compared with existing AI and

statistical tools and has been shown to be significantly superior in its prediction capabilities.

Algorithms have been designed for doing regression and logistic regression, which are prediction methods related to feed-forward neural networks, using the principles described above. These have been described at conferences and in journal articles,

and their incorporation into the IND package is planned for 1992.

**Ames-Moffett contact: W. Buntine/P. Friedland
(415) 604-3389/4277**

Headquarters program office: OAST

Bayesian Learning Group

The Bayesian learning group is involved in a number of projects that use Bayesian statistical methods to solve complex inference problems involving noisy data. Such problems frequently arise in NASA applications. Our current projects are as follows.

1. Automatic Classification. For several years we have been developing probabilistic techniques for the automatic classification of data. Automatic classification is a useful technique for exploratory data analysis. This research has been implemented and tested in our AutoClass program. AutoClass accepts as input a set of independent data cases, each described by the same set of attributes. Then, using appropriate prior expectations and a likelihood model describing possible attribute relationships, AutoClass seeks the most probable classification of the given data. It does not need to be told how many classes are present—it infers this from the data.

Recent AutoClass developments include models for full and partial correlation, hierarchical interclass relationships, and angular data. Copies of this experimental AutoClass version have been distributed to a number of researchers, and a semiproduction version is being prepared for distribution by NASA's COSMIC software-distribution center. A massively parallel version is being prepared for operation on the NAS Connection Machine. Previous work leads us to expect near-linear speedup of the core computations.

Peter Cheeseman, John Stutz, Bob Kanefsky

Much of our recent effort was devoted to applying AutoClass to LandSat-image data. This entailed special programs for displaying and manipulating the large (million-pixel) data files, and modifying AutoClass to generate its classification of the image data from a subsample and then to classify the entire data set. These large data sets also require the parallel version. We found that AutoClass gives reasonable-looking classifications and that some classes have obvious interpretations. We prepared a report describing AutoClass and a classification of an intensively studied area in Kansas (the first ISILCP field experiment), and are seeking collaborators familiar with the area.

A related Bayesian learning project has developed software for automatically inferring decision trees from data. A decision tree allows the user to predict specific values of a particular variable, given other information about that variable. This prediction is based on the statistical similarity of the new case to previous cases. The Bayesian approach has been shown to give superior performance to other decision-tree algorithms for a large number of data bases. This decision-tree code is also being prepared for general distribution through COSMIC.

2. Remote-Sensing Image Analysis. Whereas AutoClass generates useful classifications of remotely

sensed images, it assumes the independence of each datum (pixel). This assumption arises because AutoClass is a general-purpose classification system and so does not "know" anything about properties of images, such as spatial correlations. But much of the information in image data lies in the adjacency of pixels and in the continuity of features that extend over many pixels. We are now developing probability models to account for such adjacency and continuity. Our long-term goal is to model a remote object's shape and surface cover, using data from multiple images and accounting for multiple illumination and viewing angles, seasonal variations, surface and atmospheric scattering, and camera and spacecraft characteristics. We are currently addressing all of these issues except atmospheric and seasonal effects. We will be testing our ideas on Viking Orbiter images of Mars, thus atmospheric and seasonal effects will be minimal. We have obtained the Viking Imaging CD-ROM data base and are developing software to access and display this data on our systems.

3. Identifying Hard Nondeterministic Polynomial Problems. We are working on continuous-variable and probabilistic methods for constraint satisfaction as an alternative to the standard discrete search techniques in a potentially wide range of problem domains. The resulting algorithms were tested in the simple domain of graph colorability, against the best

standard methods, on randomly generated graphs. We found that most graphs are quite easily colored even by the standard exhaustive algorithm, even though the graph colorability has been formally proved to be intractable. Investigating further, we discovered that problem difficulty in this and other intractable domains can be predicted as a function of how tightly constrained the problem is. Tightly constrained problems, as well as loosely constrained ones, can easily be solved or proved unsolvable. These two broad problem regions are separated by a narrow transition region that contains all of the difficult problem instances that require near exhaustive search, and thus are intractable. This is a significant advance over the standard computer-science analysis which simply classifies problems as tractable or intractable on a worst-case basis. Our analysis points the way toward general methods for characterizing the relative difficulty of intractable-problem instances. Such methods will make it easy to identify and solve apparently intractable problems.

Ames-Moffett contact: P. Cheeseman
(415) 604-4946
Headquarters program office: OAST

Evolutionary Tree Reconstruction

Peter Cheeseman, Megan Eskey

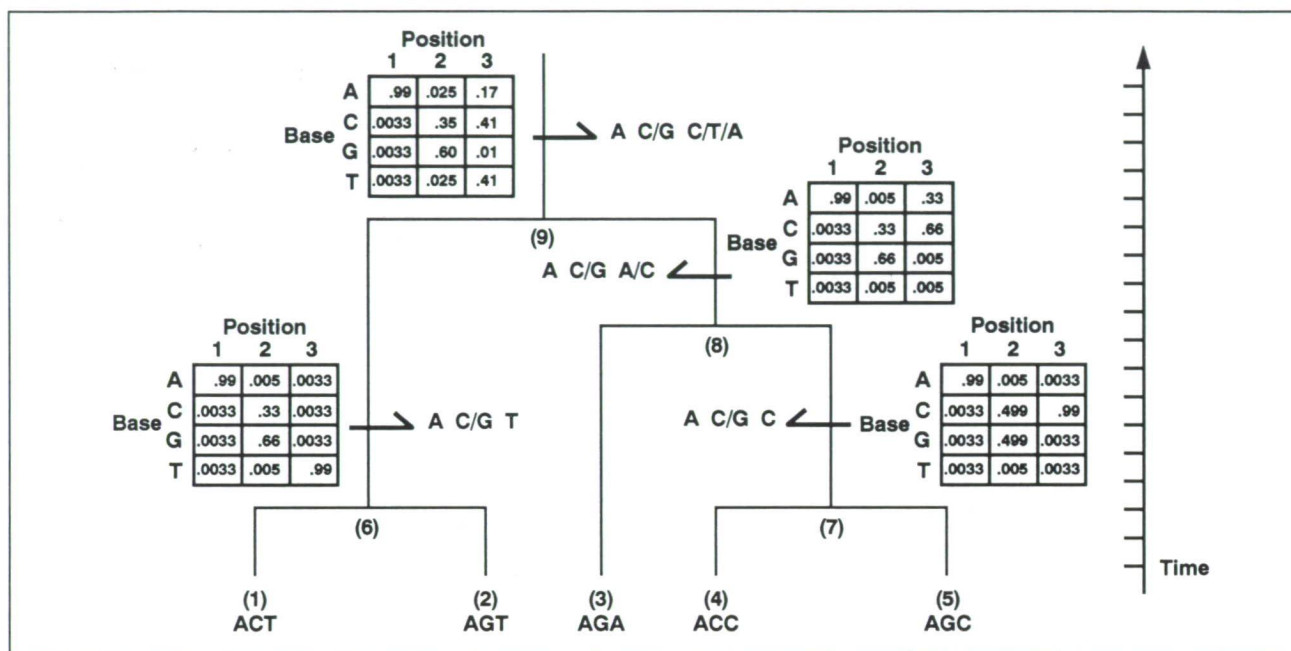


Fig. 1. A simple evolutionary tree.

We have developed a general theory for reconstructing paths of evolution from molecular-sequence data (sequences of DNA and amino acids), and have begun the preliminary design and implementation of a system called GenesYs. GenesYs uses a Bayesian version of minimal-message-length (MML) encoding (MML/Bayes) to reconstruct a set of highly probable evolutionary trees. The goal of our research is to improve current computer-based methodologies for phylogenetic reconstruction. One advantage to our approach is that MML/Bayes provides a mechanism for the necessary tradeoff between the complexity of a given model of evolutionary processes and the model's fit to the data. We intend to test our system on a range of data types, including data that has been

well studied, such as that for cytochrome C, and hypervariable data, such as the noncoding region of human mitochondrial DNA. Ultimately, we will apply the system to RNA-sequence data in the hope that it will provide insight into the evolutionary events leading to the accretion of complex genomes. A simple tree is shown in the figure. Nodes (1) through (5) are input data, and nodes (6) through (9) are the probabilistic ancestors generated by the system. Branch lengths are proportional to time.

**Ames-Moffett contact: P. Cheeseman/P. Friedland
(415) 604-4946/4277**

Headquarters program office: OAST

Principal Investigator in a Box

Silvano Colombano, Irving Statler, Michael Compton

The goal of the Principal-Investigator-in-a-Box project is to improve the scientific return on experiments performed in space by providing astronaut experimenters with an "intelligent assistant" that encapsulates much of the domain- and experiment-related knowledge commanded by the principal investigator (PI) on the ground. By using expert-systems technology and flight-qualified personal computers, it is possible to encode the requisite knowledge and make it available to astronauts as they perform experiments in space. The system performs four major functions: diagnosis and troubleshooting of experimental apparatus, data collection, protocol management, and detection of "interesting" data.

The experiment used for development of the PI-in-a-Box system measures adaptation of the human

neurovestibular system to weightlessness. The so-called "Rotating Dome" experiment (devised by Laurence Young of MIT) was flown on the recent Spacelab Life Sciences One (SLS-1) mission in June 1991. Experimental data was downlinked from the orbiter, and the PI-in-a-Box system then captured the data and analyzed it in real time (see figure). The system kept track of the time being used by the experiment, recognized noteworthy data, summarized data statistically, and generated new protocols that could be used to optimize the experiment. The data collected during the mission is now being used to evaluate the system's advice and to fine-tune its performance in preparation for in-flight use on SLS-2 in 1993.

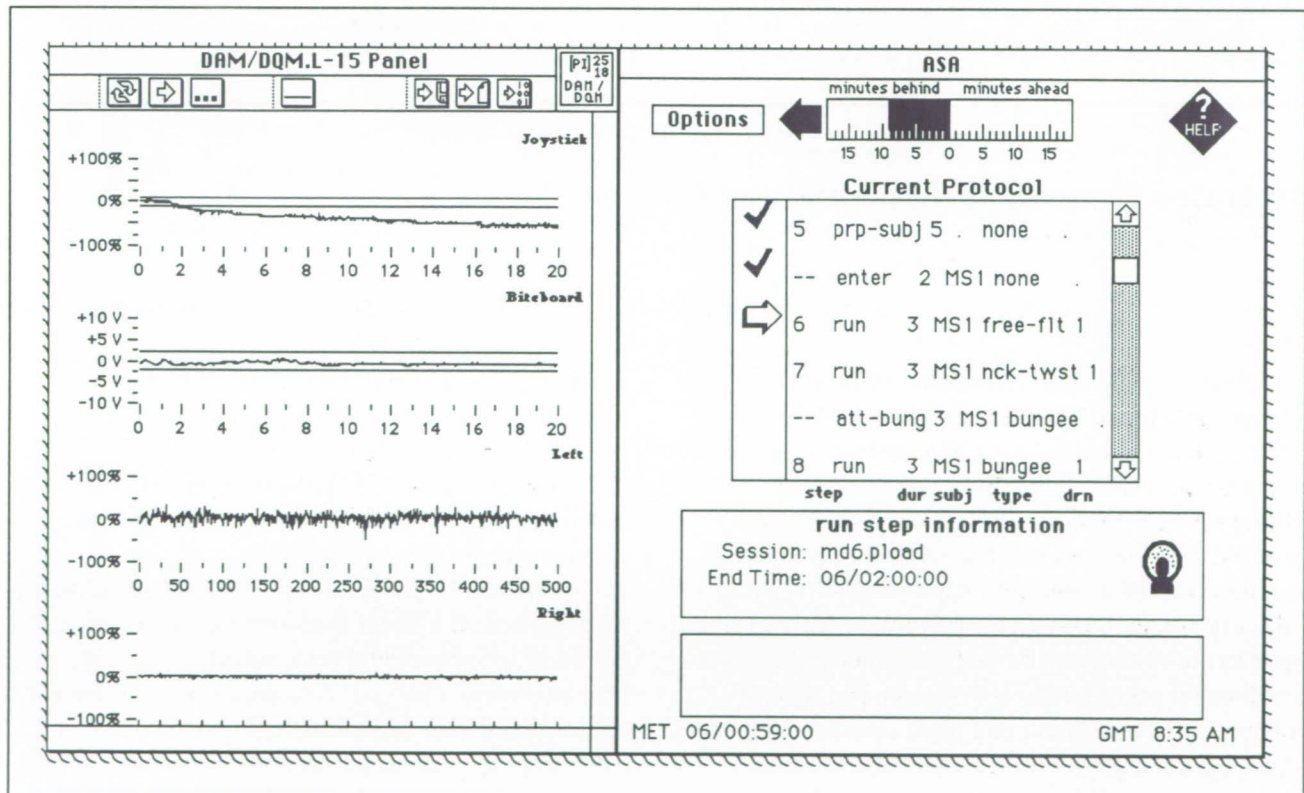


Fig. 1. The user interface for the PI-in-a-Box system. The left panel shows the raw data collected from the Rotating Dome experiment. The right panel shows the current experimental protocol, experiment run step information, and a "time bar" showing that the experiment is running nine minutes behind schedule.

The PI-in-a-Box system was used in support of the Rotating Dome experiment during three major phases of the SLS-1 mission: preflight baseline data collection at Johnson Space Center (JSC), collection of down-linked data during flight, and postflight data collection at Ames-Dryden.

The Rotating Dome experiment was carried out on mission days 5 and 6. During these experiment sessions, the system was used on the ground near the Science Monitoring Area (SMA) at JSC. The system was connected to the same stream of raw data that was downlinked from the Spacelab and monitored by the principal investigators inside the SMA.

During SLS-1 it was proved that the system works under realistic conditions:

1. The data-collection and quality-monitoring modules correctly acquired and interpreted the data, and were able to keep up with the real-time data stream.
2. The data-analysis routines correctly interpreted the data and provided meaningful quick-look analyses and statistical summaries of the experimental data that were printed out and taken to the PIs in the SMA, who generally agreed with the analyses.

3. The system generated new protocols which included steps to pursue the "interesting" data and which would make optimal use of the time remaining for the experiment. These new protocols were also printed out and taken into the SMA, where they were used by the PI team to plan for the possibility of subsequent experiment sessions.

Next year, the project team will focus primarily on preparing for the planned flight of the system on board SLS-2. The software will be reinstalled on flight-qualified portable Macintosh computers, and preparations will be made for training the SLS-2 crew on operation of the system. The team is investigating issues involved in generalization of the system and looking at other potential applications of PI-in-a-Box to spaceborne science. The system will also be used during pre- and post-flight data-collection sessions for the SLS-2 flight in May 1993.

**Ames-Moffett contact: S. Colombano/P. Friedland
(415) 604-4380/4277**

Headquarters program office: OAST

Integrated Planning, Scheduling, and Control

Mark Drummond

Scheduling has been studied for many years, and it is now possible to buy an "off-the-shelf" scheduling system suitable for many sorts of problems. However, there are two shortcomings built into almost all existing scheduling systems. First, the user must define his or her requirements in terms of a set of actions. This means that the user must explicitly define each and every action to be taken—it is not possible to give a goal to the system and have it determine the best set of actions for accomplishing that goal. The second problem is that the output of a traditional scheduler is simply a printed schedule. A traditional scheduler provides no help with the execution of a schedule. When a schedule "breaks," as a result of an unforeseen event or an unavailable resource, the scheduling process must be started from scratch, and another complete schedule produced.

The Entropy Reduction Engine (ERE) project is a focus for research on planning and scheduling in the context of actual plan execution. The eventual goal of the ERE project is a set of software tools for designing and deploying integrated planning and scheduling systems that are able to effectively control their environments. To produce such software tools, we are working toward a better theoretical understanding of planning and scheduling with regard to closed-loop plan execution. Our goal is to design and implement an integrated planning and scheduling system that overcomes the two difficulties mentioned above. Our system is able to accept a statement of the goals that should be achieved, as well as the actions that should be taken; this capability represents a significant functional improvement over traditional scheduling

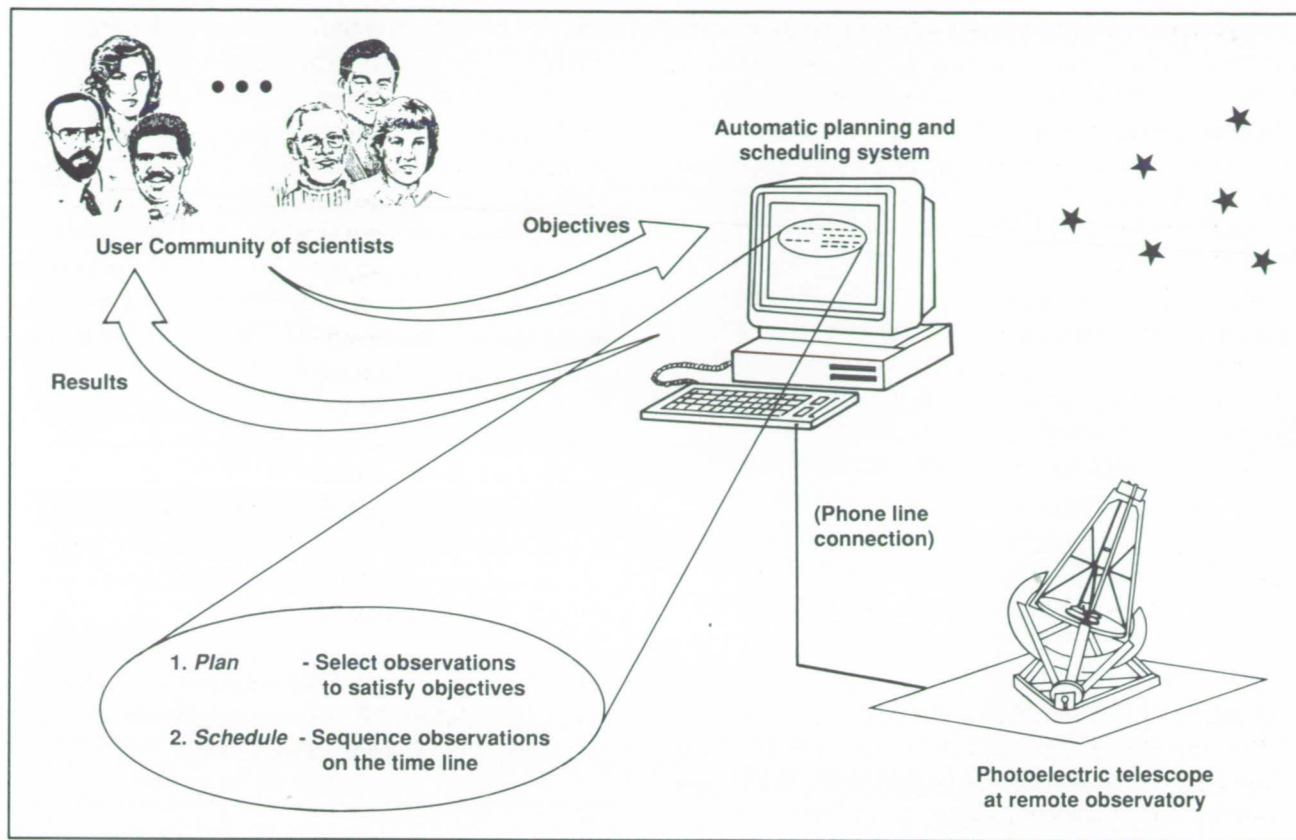


Fig. 1. Automatic planning and scheduling system for existing photoelectric telescopes.

systems. Also, our system helps a user to actually execute a schedule, and feedback from the environment is used to incrementally guide the selection of further actions. In the past year, the ERE project has been used to study the tradeoff between reaction and deliberation. The results of this study show that the probability of achieving a goal changes as a system uses increasingly more deliberation in its reasoning.

This work is being demonstrated on the problem of planning and scheduling automatic photoelectric telescope (APT) observations. The APT is a currently available technology that allows astronomers to make observations of stellar phenomena without actually visiting the telescope site. Whereas the current technology does provide for remote access, it does not help astronomers to plan their individual observation schedules, nor does it help with the scheduling of observations for the community as a whole. Our

project is building a system that addresses both of these aspects of the task. The figure shows how a community of scientists can send their scientific objectives to an automatic planning and scheduling system. This system translates the scientists' objectives into commands that make sense to the remote telescope, schedules those commands according to defined objective criteria, and monitors the execution of the commands on the telescope. In the past year we have developed a prototype of this application which has been reviewed favorably by astronomers, and we are actively extending its functionality.

**Ames-Moffett contact: M. Drummond/P. Friedland
(415) 604-4710/4277**

Headquarters program office: OAST

Large-Space-Structure Damage Identification

B. J. Glass, A. Macalou

The desire to extend the life-span, improve the vibration damping, and increase the robustness of the control of flexible aerospace structures has recently stimulated considerable interest in “smart structures” technologies. Smart structures can be typified as those that have embedded sensors and actuators, and whose signals are interpreted using pattern-matching or artificial-intelligence techniques. Structural model changes resulting from inaccurate a priori parameters, faulty assembly, or accumulated damage can be identified by changes in the frequency-domain response. Increased model accuracy can then be used to refine the controller design, thereby improving stability margins and robustness.

If structural characteristics change slowly, conventional numeric adaptive techniques can be used. Most smart-structures work in vibration control has assumed a slowly changing dynamic structure. However, for a common class of aerospace structures, changes can occur discontinuously over time. These time-varying flexible structures might be damaged in battle, or large space structures might be altered during construction, payload movement, or collision with space debris. Changes to these structures could include altered system order, new boundary conditions, or large deviations in parameter values.

Rather than assuming an invariant model form, our approach assumes a set of possible models and chooses among them according to current dynamic response and modal analysis. Frames and inheritance are used to represent this set of models as a taxonomy, as shown in the figure. Such an organization of model space is analogous to fault trees used in industrial process control and in some expert systems. A modified best-first search algorithm is used to find the model that has the closest match to current structural characteristics. Once a model is identified, it becomes the new a priori model for parameter identification and control redesign. When models that

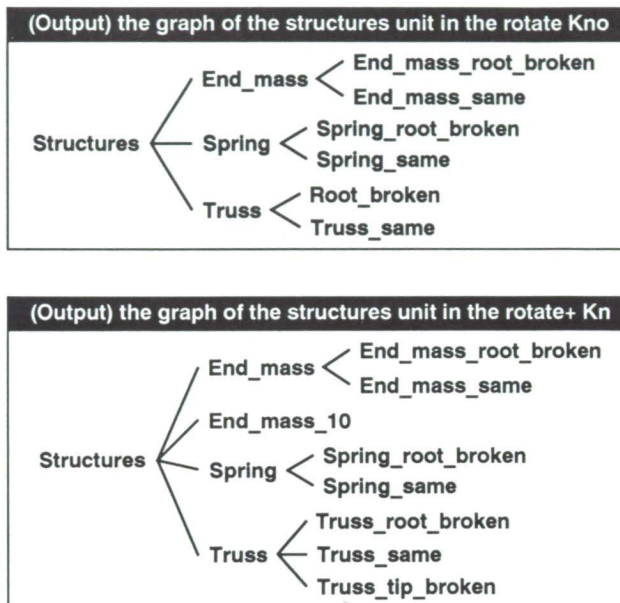


Fig. 1. Two taxonomic representations of a set of damage models generated from a flexible pivoting truss example, showing the addition of two newly encountered cases.

exhibit failures and nonlinearities are included in the search tree, it becomes possible to incorporate these features into the process of controller synthesis. This controller model replacement constitutes a new and different kind of “smartness” for smart structures.

Another advantage of the model-identification procedure is its capability to adapt to new or unanticipated structural states—to learn—by the systematic addition of newly encountered models as new leaves and branches on the search tree.

Ames-Moffett contact: B. Glass

(415) 604-3379

Headquarters program office: not sponsored

SETI Hardware Diagnostic and Control Systems

B. J. Glass, R. Swab

The Search for Extraterrestrial Intelligence (SETI) Microwave Observing Project Targeted Search is a ground-based project to search systematically for evidence of microwave transmissions from intelligent extraterrestrial life. The search phase of the project will require approximately seven years to complete. Current scientific thought strongly supports the premise that extraterrestrial intelligent life is possible. The consensus of the scientific community is contained in the 1982 Field Committee report. The SETI Microwave Observing Project has been designed to meet their recommendations.

The SETI project requires a high degree of automation in a system that will be operating for days or weeks with minimal supervision. Over the next two years, fault detection, isolation, and recovery will be partly manual. After that, the process will need to be handled remotely, or automatically. The current approach to treating faults emphasizes early detection and quick repair (saving the hardware at all times),

with a secondary emphasis on avoidance of false failure reports. The end result of a diagnostic process should be the determination of which line-replaceable unit can be replaced or reconfigured by the equipment operator in order to be able to continue observations to satisfy mission goals.

Using the hardware and software design and implementation deemed appropriate, this work is presently configuring and specifying sensors, tests, and diagnostics that will lead to a high degree of automation in fault detection and recovery in the SETI Targeted Search System (TSS) observation equipment. The figure shows a top-level block diagram of this process. Qualitative and quantitative causal modeling, in conjunction with analog and digital control theory, are being used to provide an appropriate basis for characterization and analysis of SETI equipment. The use of prototyping in an object-oriented environment is well suited to those aspects of the SETI system that are in themselves experimental.

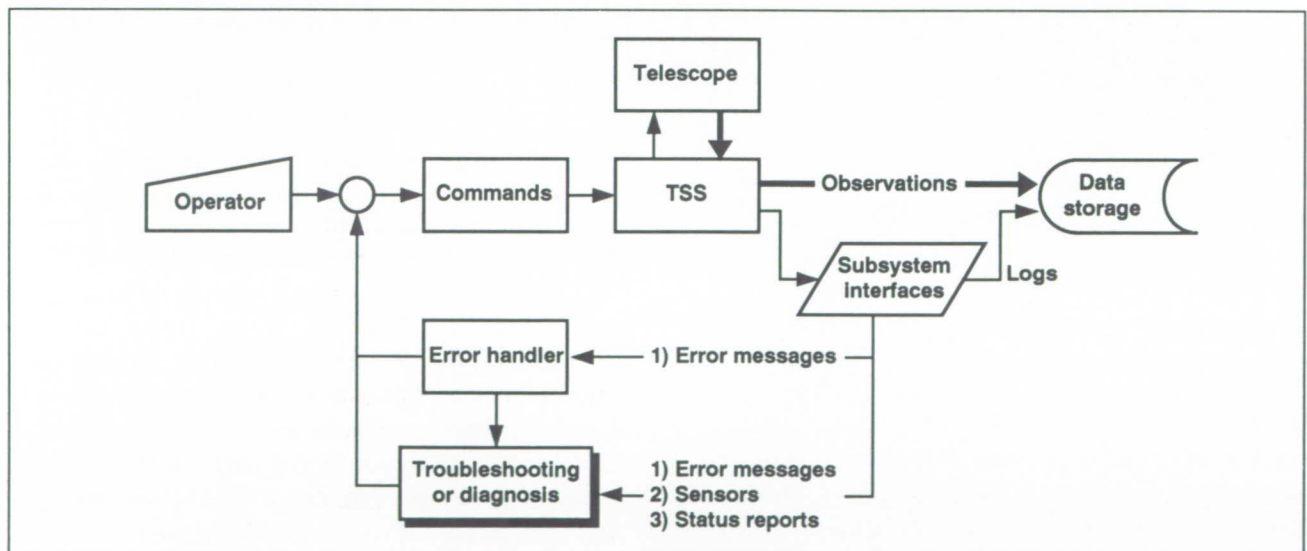


Fig. 1. Top-level diagram of SETI control-system monitoring and diagnostics.

The goal of our fault diagnosis and recovery operation is to minimize downtime for the SETI equipment caused by hardware failures, and to enable operators with a minimum of training to solve problems with the simple equipment available at telescope sites. Other desirable results should include the development of diagnostic software with a firm theoretical basis that improves understanding of the

applicability of advanced software in practical scientific applications; and the dissemination of SETI software developments to the research community.

Ames-Moffett contact: B. Glass
(415) 604-3379

Headquarters program office: OSSA

Space Station Freedom Thermal-Control-System Automation Testbed

B. J. Glass

Some complex space-based systems require constant monitoring of parameters, configuration, and component health changes. Current practice often requires human operators to scan telemetry data, watching for deviations from expected performance. In real-time, large-scale applications this monitoring by human operators often proves expensive, because many operators are required as a result of the data-processing limitations of humans. By automating some or most of the monitoring, troubleshooting, and control of these dynamic systems, the need for direct human involvement may be reduced.

The prototype thermal control system for the Space Station Freedom (SSF) program was selected as a representative system for a symbolic control application, the Thermal Expert System (TEXSYS). To automate some of the operational functions of a thermal engineer, existing artificial-intelligence techniques such as frame systems, data-driven programming, and model-based reasoning are employed to create a thermal knowledge base. Together with rules for conflict interpretation and tasks for representing procedural knowledge, this knowledge base makes up the core TEXSYS. The core TEXSYS has been added to conventional software for data acquisition and control, creating a hierarchical "expert" or "symbolic" controller.

The symbolic model-based-reasoning approach to identification and control taken here is desirable because of its ability to follow changes in both

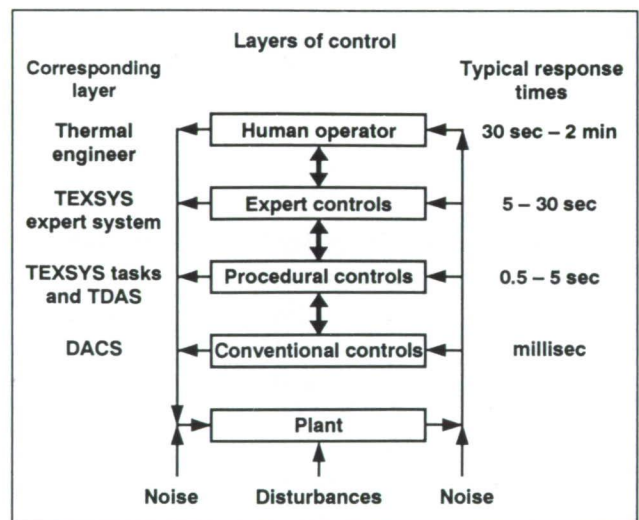


Fig. 1. An example of a hierarchical, hybrid, symbolic control architecture.

parameters and hardware configuration, and because of its ability to construct a qualitative model of the thermal testbed, even in the absence of a numerical model. A block diagram of this symbolic control approach is shown in the figure. Operational robustness is enhanced by the ability to operate with, and to reach at least partial conclusions with, incomplete data.

In tests run thus far with the thermal testbed, TEXSYS has successfully performed all real-time

nominal operations such as startup, shutdown, and setpoint changes. TEXSYS successfully identified and acted on all 17 planned system- and component-level faults, as well as identifying some unplanned faults. For example, one component fault addressed by TEXSYS was the blockage of a single evaporator by a stuck isolation valve.

The success of the hierarchical, symbolic, model-based-control approach taken here demonstrates that artificial intelligence techniques of model-based reasoning, frame-based knowledge representation, rules, and tasks can be used to successfully control complex thermal bus hardware in real time. TEXSYS is one of the first real-time expert systems to control a

large, complex physical system. The Systems Autonomy Demonstration Project's results have influenced the inclusion of expert systems into the initial design for the SSF Thermal Control System by the prime contractor. Current activity now focuses on providing consulting and software support to the SSF contractor team, and maintaining a scaled-down thermal testbed for software development at Ames.

Ames-Moffett contact: B. Glass

(415) 604-3379

Headquarters program office: OSF

Networked Processor Performance Prediction

Terry Grant

The Networked Processor Performance Prediction and Testbed Development tasks are coordinated technology-development tasks for the Data Management System (DMS) in Space Station Freedom (SSF) and similar complex on-board computing systems for future space missions. On SSF, the DMS is responsible for integrating information on board into a cooperative whole. It provides integrated data processing and communications for both the core functions and the payloads. The task goals include the capability to monitor changing user requirements, as well as other capabilities indicated by changes in the ongoing development process. The near-term objectives are to (1) evaluate design-change documentation, informal papers, and presentations on the system and payload study activities and (2) customize simulation and emulation tools for system evaluations.

This year the Data Management System Evolution Report was completed for formal publication and distribution within NASA. The report describes the DMS design at the component level, as well as the system-level architecture before restructuring. It also evaluates the weaknesses in the high-speed fiberoptic network and the local buses. Finally, the report

proposes top-level corrective measures that will extend the life of the system and reduce life-cycle costs.

While awaiting updated data-processing requirements for the restructured system, we upgraded our Distributed Processing Network Simulator, and integrated it with a commercial spreadsheet and graphics package. The package has been submitted with full documentation to COSMIC, NASA's software-dissemination center. Sample scenarios using the simulator show the blocking effects of overloaded processing or local bus activity. For example, when the local bus or data base is near capacity, data-scanning jobs can block an asynchronous sensor read, and a slight increase in the scanning load can double the time needed to complete the sensor read.

A Datagram Timing Test Report was written that describes the baseline performance for data-packet transmittal using ethernet. The baseline tests provide experimental evidence that neither high-performance central processors nor link protocol are capable of good real-time performance by themselves. They also

point to the need for both fine-granularity system clocking and special operating-system interfaces if deterministic real-time data management is required in a distributed system. Further analysis and experiments will attempt to identify robust interface mechanizations for high-performance, real-time distributed processing.

Another aspect of networked-processor performance testing is the development of tools and methods. The software code and methodology for running

repeatable network tests with multiple processing nodes were demonstrated this year to NASA Headquarters and to the Reliability and Quality Assurance support personnel at Ames, who expressed an interest in applying the approach to future project validations.

Ames-Moffett contact: T. Grant

(415) 604-4200

Headquarters program office: OSF

The Effects of Video Compression on Acceptability of Images for Monitoring Life Sciences Experiments

Richard F. Haines, Sherry L. Chuang

Future crewed space operations for Space Station Freedom (SSF) will call for a variety of carefully planned multimedia digital communications, including full-frame-rate color video, to support remote operation of scientific experiments. An investigation was done to determine if video compression is a viable solution to transmission bandwidth constraints. Three nonhuman life-sciences disciplines (plant, rodent, and primate biology) were selected for this study. A total of 33 subjects viewed experimental scenes in their own scientific disciplines. Ten plant scientists viewed still images of wheat stalks at various stages of growth. Each image was compressed to four different compression levels using the Joint Photographic Expert Group (JPEG) standard algorithm, presented in random order. Twelve and eleven staffmembers viewed 30-second videotaped motion segments showing small rodents and a small primate, respectively. Each segment was repeated at four different compression levels, in random order, using an inverse cosine transform (ICT) algorithm. Each viewer made a series of subjective image-quality ratings which were then analyzed statistically.

There was a significant difference in image ratings according to the type of scene viewed within disci-

plines; thus ratings were scene dependent. Image (still and motion) acceptability does, in fact, vary according to the compression level. The JPEG still-image compression levels, even with the large range of 5:1 to 120:1 used in this study, yielded equally high levels of acceptability. In contrast, the ICT algorithm for motion compression yielded a sharp decline in acceptability below 768 kilobits/second. Therefore, if video compression is to be used as a solution for overcoming transmission bandwidth constraints, the effective management of the ratio and compression parameters according to scientific discipline and experiment type is critical to the success of remote experiments.

The study addressed questions such as, What will happen if the video imagery that is transmitted from SSF to the ground (or vice versa) is compressed in such a manner that ultrafine spatial detail or accurate color that is important for the investigator's scientific judgment is lost? Will the remotely located investigator be able to spot incorrect procedures or specimen defects that would disqualify use of that sample? In other words, what level of video compression can be achieved before impeding the scientist's ability to

make accurate scientific judgments on his or her experiment based on transmitted images?

The JPEG standard was found to provide acceptable still-frame imagery of plants at compressions as high as 120:1, depending upon particular scene content. Resolution by itself was most important for the still-frame imagery, followed by resolution combined with color or brightness/contrast. For moving imagery using an ICT compression algorithm, a transmission bandwidth of about 768 kilobits/second was found to provide high mean acceptability for the three scenes in which camera imagery was colorful and showed high detail. The visual judgment criteria that were selected most often as being important for evaluating dynamic imagery were resolution, color, and image motion, in some combination. The present testing methodology, which involved individual subjects evaluating their own data, was effective in evaluating video compression effects.

A wide array of local (in space) and remote (on the ground) visual judgments will be made on plant

and animal specimens on board SSF in the future. Whereas this and other studies have shown that carefully selected video compression techniques provide an acceptable solution to transmission bandwidth constraints, the final quality of the remote television imagery that is achieved will depend on complex, interrelated hardware, software (video architecture), and human factors. Advanced preflight simulations using representative flight end-to-end hardware should be conducted in order to optimize this imagery and related scientific procedures; and studies should be done on the role of infrared imagery and on the effects of switching and scheduling algorithms in order to optimize the use of available transmission bandwidths.

**Ames-Moffett contact: R. Haines
(415) 604-3373**

Headquarters program office: OSSA/OSF

Robotic Vision Using an Optical Correlator

Butler P. Hine, Max B. Reid, John D. Downie

Future NASA missions will have a great need for semiautonomous and autonomous robotic systems capable of performing tasks that are either too dangerous or too expensive for humans to perform. These tasks include the construction, inspection, and maintenance of structures in space and on planetary surfaces. The robotic systems must be rugged and reliable, and must use as little volume and power as possible. Optical processing architectures, which rely on the speed and inherent parallel nature of light to perform computations, are attractive alternatives to digital electronics for performing some of the processing tasks of an autonomous robotic system in space.

Image processing is one of the most computationally intensive tasks required of an autonomous robot, and can benefit greatly from novel processing architectures designed to accelerate computationally expensive functions. Many primitive operations

required of vision feedback systems used in robotic control, such as object recognition, tracking, and orientation determination, can be performed using cross-correlation techniques. Cross correlation is well suited to analog optical implementation, using the Fourier transform ability of a lens, and can be performed at higher speeds than are possible with digital electronics at equivalent power levels. Incorporating an optical correlator as a special-purpose coprocessor in a general hybrid vision-processing system combines the speed of the optical processor with the generality of the digital one, resulting in a higher-performance system than could be obtained with either alone.

We have developed a hybrid digital-electronic/analog-optical robotic-vision-processing system to test concepts and algorithms for autonomous construction,

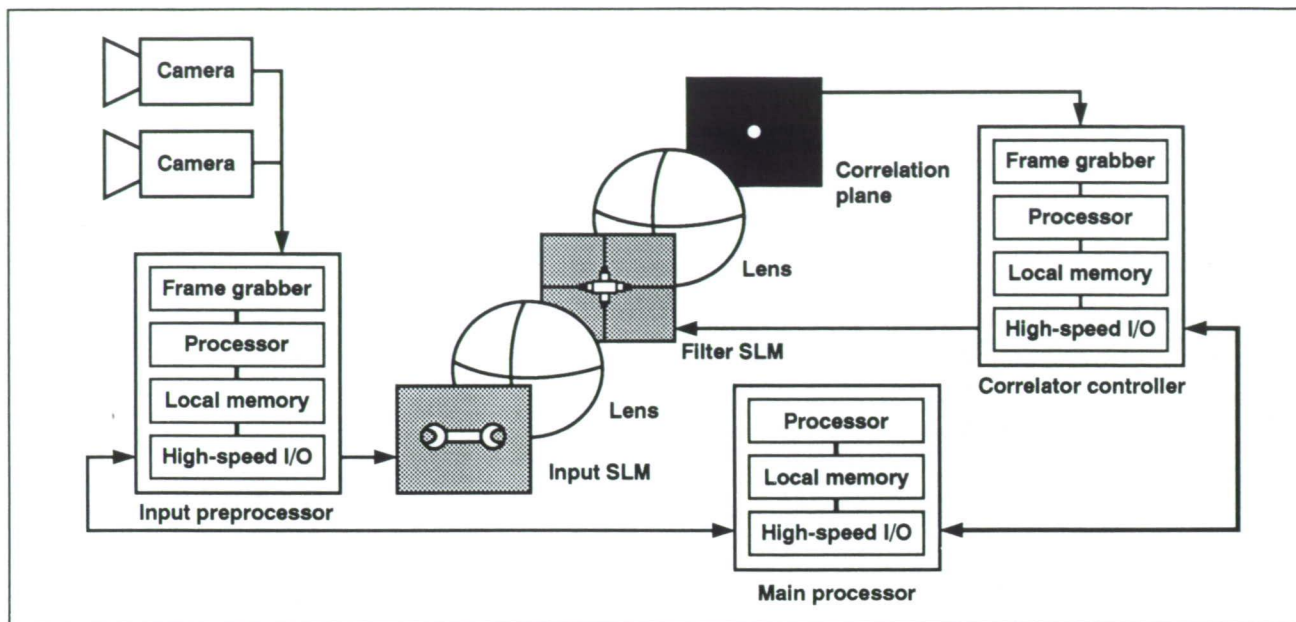


Fig. 1. The hybrid correlator vision system.

inspection, and maintenance of space-based habitats. The primary task of the system is to allow a robot arm to identify, track, and grasp a tool moving in space with all six degrees of freedom without using any kind of cooperative marking techniques for the vision system. This task is representative of one required of the Flight Telerobotic Servicer (FTS) or the Extra-Vehicular Activity (EVA) Retriever, both of which are robots designed to operate in a weightless environment. The figure is a schematic of the hybrid correlator vision system. The camera data are digitized by a frame grabber and sent through an image preprocessor before being displayed on a high-speed spatial-light modulator. The correlation filters are sequenced through the filter plane and the detected correlation plane is grasped and analyzed to provide the vision feedback information.

In our tests of the system to date, we have demonstrated tracking and grasping capabilities of one frame per second in a two-dimensional plane. The speed of the system is currently limited by the addressing time of the optical modulators and the digital image preprocessing. Both of these speed limitations can be minimized with the faster devices and processors that are currently available. In comparing the performance of the system with more conventional all-digital electronic ones developed concurrently, we have found that the hybrid system consistently performs better with regard to speed and robustness.

Ames-Moffett contact: B. Hine

(415) 604-4379

Headquarters program office: OAST

Intelligent-Knowledge-Base Refinement

Smadar Kedar

Many of NASA's tasks require complex planning, scheduling, and control. Much of the effort at the Ames Artificial Intelligence Research Branch is in developing automated systems to assist in these tasks. Often these tasks are highly integrated. To build such complex systems, multiple knowledge bases and procedures are encoded to perform multiple functions. One critical issue is how to detect and correct errors and inconsistencies in the knowledge bases. Currently, system builders refine and debug the knowledge bases manually—a time-consuming, ad hoc, error-prone approach. The intelligent-knowledge-base-refinement project at Ames develops tools to assist in systematically and automatically refining and debugging multiple knowledge bases.

Our research methodology employs as a testbed an existing integrated system for planning, scheduling, and control—the Entropy Reduction Engine (ERE). During the past year we developed a number of novel machine-learning algorithms, and implemented and tested them in ERE.

One algorithm, called “mutual theory refinement” (MTR), learns from failed predictions. The algorithm's unique contribution to machine learning is that its multiple approximate knowledge bases refine each other. Most previous algorithms required a complete and correct knowledge base in order to refine approximate knowledge bases, but this is too big a requirement for real-world domains. We also developed and implemented an extension to MTR. The extended version finds a greater variety of refinements, retracts refinements if they turn out to be inconsistent, and uses a flexible strategy. Finally, we completed preliminary experiments on the usefulness of our algorithm in making the ERE system more robust. Our results indicate that although accuracy is enhanced, efficiency is reduced. We are currently designing and implementing further extensions of the algorithm that, without degrading overall system performance below some threshold, would trade a degree of efficiency for improved accuracy.

Another algorithm, called “generalized situated control rule compilation,” reformulates the rules for controlling a plan so that they may be applicable to similar plans. Its unique contribution is the ability to compile rules for goals of prevention and maintenance. Although it provides a greater degree of generality to ERE, it also degrades its efficiency.

In ongoing work, we are investigating the contributions that machine learning can make to the area of knowledge acquisition. We developed an algorithm to assist users in modifying incorrect procedures that lead to failures. The synergy between machine learning and knowledge acquisition is new, and we expect to pursue further research in this direction.

Finally, we completed three detailed investigations into potential applications for our machine-learning algorithms. We explored an automated telescope problem, and found a niche for our research. We also explored a collaboration with the Jet Propulsion Laboratory on the application of our machine-learning algorithms to software reuse. In particular, we are considering enhancements to the Encyclopedia of Software Components, a project for browsing and reusing modules in the Deep Space Network. Finally, we contacted Johnson Space Center regarding the application of our algorithms to generating and refining flight rules for the shuttle, a problem that is difficult to solve manually.

Our plans for next year include further experimentation with these algorithms in order to empirically determine their utility. In parallel, we expect to focus on an application that will demonstrate how intelligent-knowledge-base refinement can reduce errors and increase the productivity of NASA operations.

**Ames-Moffett contact: S. Kedar/P. Friedland
(415) 604-3378/4277**

Headquarters program office: OAST

Scientists' Intelligent Graphical Modeling Assistant

Richard Keller

The Scientists' Intelligent Graphical Modeling Assistant (SIGMA) system functions, as its name implies, as an intelligent assistant to the scientist. Scientists will use SIGMA's graphical interface to "program" visually using a high-level data-flow modeling language. The terms in this modeling language involve concepts that are familiar to the scientist. SIGMA guides the scientist through the model-building process and checks the model for consistency and coherency as it is being constructed. Then SIGMA automatically translates the conceptual model into an executable program, freeing the scientist from error-prone implementation details.

During 1991, a major project accomplishment was the construction of a knowledge base of scientific concepts and equations to support scientific model-building in the planetary atmospheric sciences

domain. To construct this knowledge base, we examined existing (conventional) modeling software and isolated the basic scientific concepts and domain constructs upon which the model is based. The figure illustrates the structure of the concepts that underlie the planetary-atmospheres model we are studying. The model was developed by Christopher P. McKay in the Ames Theoretical Studies Branch to investigate the thermal and radiative structure of Titan's atmosphere. After identifying relevant scientific concepts, we translated them into machine-readable form and incorporated them into the SIGMA system. By the end of 1991, we had created a knowledge base of over 500 concepts. We also began work on a second knowledge base to support modeling activities associated with a forest ecosystem model used by researchers in the Ames Ecosystem Sciences Branch.

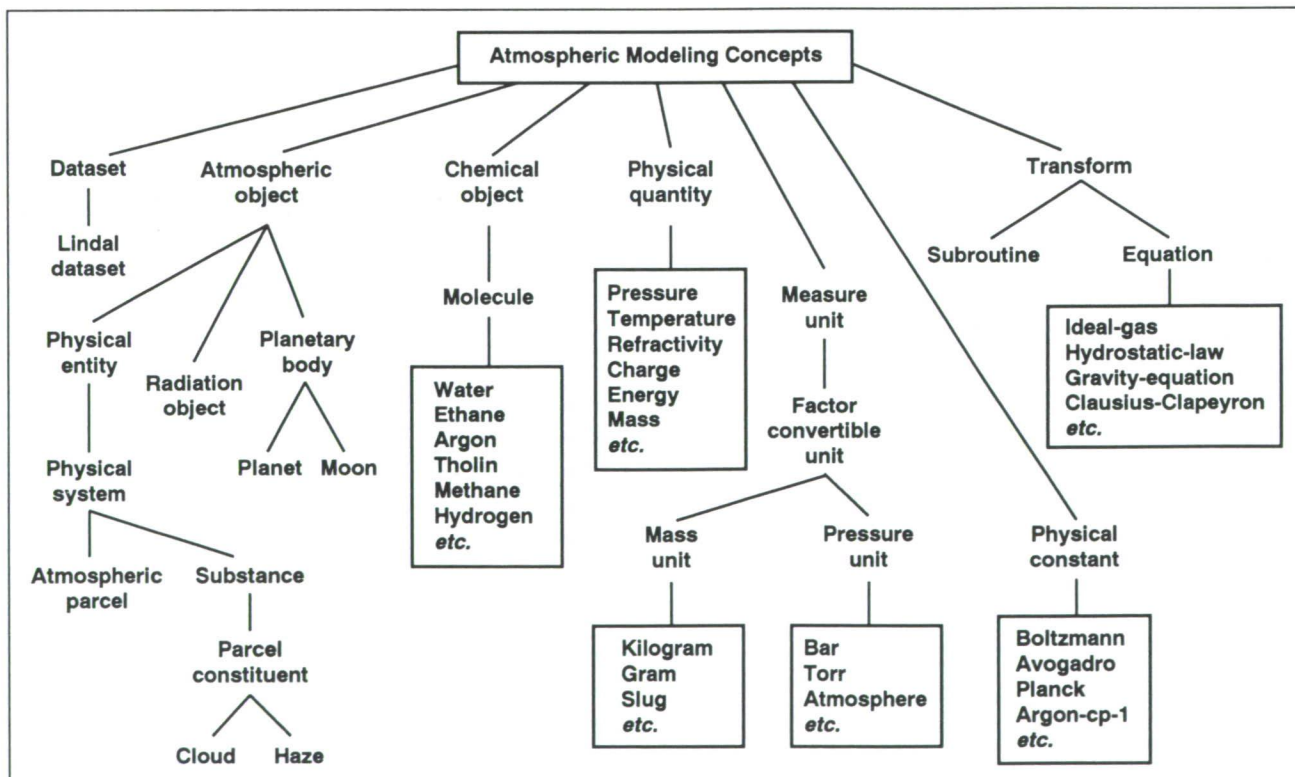


Fig. 1. Basic concepts in the atmospheric modeling domain.

A second major accomplishment for 1991 was the redesigning and reimplementation of our original system prototype, which was built during 1990. This new SIGMA system uses the same scientific knowledge base, and enables the scientist to construct simple modeling programs via an interactive dialogue. The concepts in the knowledge base form the basis for the system's intelligent interaction with planetary scientists. Through a shared understanding of the modeling problem and the relevant scientific concepts, the computer and humans work together

synergistically to create a semantically valid model. We have used the system to reconstruct a small portion of McKay's Titan model in a fraction of the time that would be needed without automated assistance.

**Ames-Moffett contact: R. Keller/P. Friedland
(415) 604-3388/4277**

Headquarters program office: OAST

Mission Controller Assistant Project

The assistant for the mission controller of the shuttle Reaction Control System (RCS) will assist in detecting faults and developing new procedures in emergency situations. Given the severe time constraints in such situations, the controllers cannot predict all possible consequences of their planned actions, thus it is useful to have a simulator that can predict these consequences.

Traditional simulators cannot use models of degraded components that are described qualitatively, e.g., a leaking pipe. During 1991, we developed a qualitative simulator of the shuttle RCS using artificial intelligence techniques. We also developed a prototype of a model-based reasoning approach to RCS fault diagnosis. The prototype system consists of three components: a hypothesis generator, a simulator, and a tracker. The hypothesis generator uses engineering models to generate all possible models that are

consistent with the sensor readings (the exhaustive model generation helps mission controllers by identifying any hypothetical faults they may have missed). The qualitative simulator predicts future behavior of the system under each hypothetical state. The tracker matches these predictions with real data and evaluates their reliability in each hypothetical situation. Thus the system can track the dynamics of the RCS and diagnose malfunctions. The mission controller assistant will also be used as part of a computer-based training system for space shuttle mission controllers.

**Ames-Moffett contact: D. Kulkarni/P. Friedland
(415) 604-4869/4277**

Headquarters program office: OAST

Deepak Kulkarni

Microprocessor for the Space Station Freedom Data Management System

Y. K. Liu

This study analyzes the feasibility of upgrading the Intel 386 microprocessor, which has been proposed as the baseline processor for the Space Station Freedom (SSF) Data Management System (DMS), to the more advanced 486 microprocessor. The study is part of an effort funded by the NASA SSF Advanced Development program.

Accomplishments in 1991 include a device driver program implemented to disable the 486 on-chip cache which has neither parity-check nor error-detection-and-correction circuitry. In space, the probability of the contents of the cache being altered is higher than on the ground because of the higher

radiation exposure. Comparisons between the 386 and 486 processors included the instruction-set architecture, power consumption, the MIL-STD-883C Class S (space) qualification schedule, and performance. The next generation of the Intel X86 family of microprocessors is currently under study for the feasibility of its use on the DMS.

Ames-Moffett contact: Y. Liu
(415) 604-4832

Headquarters program office: OSF

Real-Time Operating System for the Space Station Freedom Data Management System

Y. K. Liu, J. Gibson

An operating system is the program that acts as an interface between a computer user and the computer hardware. The primary function of an operating system is to manage computer resources such as processors, memories, input/output devices, and files. A real-time operating system is one that must respond to asynchronous, external events within a finite and specified time. The Lynx real-time operating system (LynxOS) has been selected as the operating system for the Space Station Freedom Data Management System (DMS). However, many features of LynxOS still need to be evaluated and/or fine tuned for the DMS. The LynxOS must be upgraded smoothly to minimize the impact on the DMS, which has some unique features such as remote control, a 30-year life-span, and a continuous operational environment.

In 1991, a high-speed digital timer/counter board was designed, and a device-driver program and an application program were developed to measure the

performance of the LynxOS. A benchmark program called REAL/IX, which was developed by Modular Computer Corporation to measure the performance of a UNIX-based, real-time operating system, was studied for its applicability to the LynxOS. The techniques for the DMS software upgrade were studied. That study concentrated on the techniques for upgrading the device drivers dynamically, i.e., with the system "on-the-fly." A device-driver program was successfully loaded and linked without shutting down the LynxOS. A prototype program is under development to demonstrate the feasibility and simplicity of device-driver dynamic loading for the DMS.

Ames-Moffett contact: Y. Liu
(415) 604-4832

Headquarters program office: OSF

Efficient Scheduling Algorithms

Steve Minton

The objective of this project is to develop domain-independent scheduling algorithms that can rapidly construct schedules for complex applications. In addition to being efficient, the algorithms should also be suitable for use with machine learning techniques so that their performance can be automatically adapted to their environment.

Scheduling is a difficult computational task, but it has numerous potential applications. For example, we produced an algorithm that can be used for long-term scheduling of the Hubble Space Telescope (HST). This algorithm is an improvement over the current scheduling system.

The algorithm was developed jointly with Mark Johnston of the Space Telescope Science Institute (STSCI). The prototype runs about an order of magnitude faster than the previous HST long-term-scheduling algorithm. Several years ago, Johnston and colleagues found that a neural net approach performed better than traditional scheduling programs do. By analyzing the neural net algorithm they proposed, we were able to develop an heuristic algorithm that performs even better. It is simpler than the neural net approach, and thus more efficient. We are currently working with members of STSCI to field-test the algorithm and to modify it for other applications.

Our algorithm also advances the state of the art in related constraint-satisfaction tasks. We have tested the algorithm on a standard constraint-satisfaction benchmark, the N-Queens problem, and the algorithm performs many orders of magnitude better than

traditional algorithms. We are currently analyzing the performance of the algorithm and developing machine learning methods to be used in conjunction with it.

We are working with members of the Artificial Intelligence Research Branch at Ames who are developing scheduling software for space shuttle operations at Kennedy Space Center. Although our prototype algorithm is application-independent, the results of our analysis are relevant for analyzing and improving the actual scheduling software being developed for space shuttle applications.

Finally, we are embarking on a relatively new project that will automatically discover heuristic techniques that are useful for making scheduling and constraint-satisfaction systems more efficient. Currently, developing a scheduling or constraint-satisfaction system requires significant expertise and programming ability. We have discovered, however, that many of the heuristic techniques used in such systems are generic, and therefore can be automatically adapted for specific applications. To investigate this possibility we are developing a system that will take a declarative specification of a scheduling problem and automatically compile task-specific heuristics for that problem.

**Ames-Moffett contact: S. Minton/P. Friedland
(415) 604-6522/6527**

Headquarters program office: OAST

Advanced Architectures and Software Engineering

Daniel L. Ostermiller, Andre Goforth

A requirement of the Space Station Freedom (SSF) is the accommodation of growth in data processing throughput and function, data storage capacity and performance, and network communication bandwidth by providing expandable and upgradeable system designs. The purpose of this investigation is to identify and communicate potential SSF growth options to meet future application requirements.

The SSF Data Management System (DMS) Software Assessment investigation has evaluated the software design of the Space Station's DMS from a unique perspective. Software engineering principles have been applied with the intent of not only supporting the current engineering development, but also ensuring that the delivered software can be easily adapted to the advanced architectures expected to support SSF during its anticipated 30 years of evolution. This independent assessment of the DMS design has produced several findings which were reported to NASA Headquarters throughout 1991. In 1991, we evaluated and acquired hardware and advanced software engineering tools as part of the establishment of the DMS Advanced Architecture (Ada) testbed. In 1992, Release 1 of the SSF flight software will be delivered to Ames Research Center and integrated into the testbed for analysis as described above.

Part of this activity has involved real-time scheduling research. The recently developed Rate Monotonic Scheduling (RMS) algorithm being used on SSF is attractive because its performance predictability has a sound theoretical basis. However, the algorithm is not without flaws. One of these limitations is that the algorithm can guarantee that hard deadlines will be met only when the workload is static (or bounded). Another limitation is that the algorithm is limited to single-CPU architectures. Because SSF may exceed these limitations during its evolution, these and other limitations are being investigated. Joint research has

been initiated between Ames, Johnson Space Center, and outside institutions such as the Institute for Defense Analysis, Texas A&M, and the Software Engineering Institute. Work is currently in progress to modify a single real-time scheduler to follow the rules associated with several different scheduling algorithms, including algorithms that would resolve the problems associated with the limitations of RMS mentioned above.

Advanced architecture research has been partially funded by the Defense Advanced Research Projects Agency to research multi-CPU architectures with respect to scalability, real-time response, and software-managed fault tolerance. These issues are of interest to such near-term projects as SSF and the Advanced Tactical Fighter. In order to quantify these issues, Ames has developed several parallel Ada benchmarks. In 1991, these benchmarks have been distributed to several interested parties including the Real Time Artificial Intelligence System project at Wright-Patterson Air Force Base and the Association for Computing Machinery's Performance Issues Working Group. Also in 1991, Ames co-sponsored a workshop on high-performance computing, "Ada on Supercomputers." Feedback from the conference was provided to the distinguished reviewers responsible for the design of the next revision of the Ada language (Ada 9X).

The synergistic effect of these research efforts has allowed examination of hardware and software issues that range from applied research (e.g., current SSF architecture) to basic research (e.g., future advanced architectures).

**Ames-Moffett contact: D. Ostermiller
(415) 604-4814**

Headquarters program office: OSF

Modeling Techniques for Fault-Tolerant Computing Systems

F. Ann Patterson-Hine

The complexity of computer systems currently being designed for critical applications in the scientific, commercial, and military arenas requires the development of new techniques for modeling system behavior in order to assure "ultra-dependability." The complexity of these systems, such as Space Station Freedom and the Air Traffic Control System, stems from their highly integrated designs containing both hardware and software as critical components. Current approaches to assessing the dependability of complex systems are incapable of handling the size and complexity of these highly integrated designs. Functional models can be developed for integrated systems; however, the solutions of these models cannot be obtained for general cases. Methods are needed for taking advantage of natural partitions in system models in support of incremental solution techniques. These same methods could support the analysis of systems modularized to facilitate module reuse, such as the current emphasis on software reuse in flight critical systems.

A new technique for modeling such systems has been developed which is built upon current techniques in Markov theory and combinatorial analysis. It enables the development of a hierarchical representation of system behavior that is more flexible than either technique alone. A solution strategy is taken that is based on an object-oriented approach to model

representation and evaluation. The technique is virtually transparent to the user since the fault-tree models can be built graphically and the objects are defined automatically. The tree modularization procedure allows the two model types, Markov and combinatory, to coexist, and does not require that the entire fault tree be translated to a Markov chain for evaluation. This effectively reduces the size of the Markov chain required and enables solutions with less truncation, making analysis of longer mission times possible.

Current methods of analyzing the dependability of new system designs are extremely time consuming and expensive. The techniques described above would allow libraries of system components, both hardware and software, to be constructed and used in the development of systems for particular applications. System models could be assembled from the models for individual components (stored in the library) to assess the integrated system dependability. These models would also reduce the need for approximation techniques for the solution of very large models.

**Ames-Moffett contact: F. Patterson-Hine/D. Tucker
(415) 604-4178/4668**

Headquarters program office: SSF

Superfluid Helium On-Orbit Transfer

Eric Raymond

This project focuses on the development of software tools to support the monitoring and control of a space shuttle experiment called SHOOT: Superfluid Helium On-Orbit Transfer. Ames's role in this joint effort with the Goddard Space Flight Center is to provide all software needed to control and monitor the experiment during all operational phases. Highlights of this effort include the first use of an expert system in space; an innovative use of laptop computer technology; a highly interactive, user friendly system used to teleoperate the payload from a remote ground station; and a simulation system used as both a development tool and a training tool.

The SHOOT experiment is a shuttle-payload-bay cryogenics experiment scheduled to fly on STS-54 in April 1993 on the orbiter Atlantis. The experiment uses two insulated containers (dewars) of liquid helium connected by a transfer line. The helium is normally in a state called "superfluid," in which it appears to flow without viscosity. This superfluid component of helium has, effectively, no entropy and displays quantum mechanic behavior at the bulk, macroscopic level. The main experimental objective is to demonstrate the ability to transfer this odd liquid from dewar to dewar, much as would be done during a cryogenic servicing of a helium-cooled orbiting telescope such as the planned Space Infrared Telescope Facility.

SHOOT will determine if all this is technically possible. Software being developed will provide facilities for the control and monitoring of the experiment as each hardware element and procedure are exercised. The software consists of three major components:

1. An autonomous control, monitoring, and diagnostic system (AFDeX) operated by the shuttle crew to perform transfer operations
2. An interactive, user friendly command and monitoring system (CMS) operated from the ground by a highly trained operator
3. A command and telemetry simulator (CATS) which emulates the payload for developmental testing of software and crew training

AFDeX is a rule-based expert system written in the CLIPS (a forward-chaining production-system

language developed by NASA) and C languages. The system operates on a flight-qualified GRiD 1530 80386-based laptop computer called the payload and general support computer and will be located on the shuttle's aft flight deck. The system is designed to control the experiment without any support from ground or crew; it is completely "in the loop." The system interprets telemetry from the payload with respect to its current goals and sends commands to the payload in order to achieve these goals. If a problem occurs in the payload, AFDeX will attempt to diagnose the situation via empirical associations, and recover. A user may optionally interact with the system to modify its behavior. The intent is to provide an autonomous control capability that is tolerant of a variety of failures and is able to incorporate external knowledge from a user (perhaps as the result of earlier experiments in the mission) at execution time. Additionally, this software provides the crew with real-time feedback from the payload which is used to coordinate a number of experiments that involve thrusting of reaction-control-system jets.

In contrast to AFDeX, the CMS is a ground-based system for payload operation and control that provides an expert user with a highly configurable, fine-grained interface with the experiment. Whereas AFDeX contains expert knowledge tailored for specific phases of the experiment, the CMS is a general-purpose tool which is used in all phases of operation. This system, along with the CATS simulator, represents the current state of the art in event-oriented, mouse-controlled user interfaces of the Macintosh computer. Other responsibilities of the SHOOT software staff include support of payload qualification testing, operation of the payload at Kennedy Space Center during postshipment checkout and integration, and operation of the payload from the Goddard Payload Operation and Control Center during flight.

**Ames-Moffett contact: E. Raymond
(415) 604-4744**

Headquarters program office: OSF

Photonics and Optical Processing

Max B. Reid

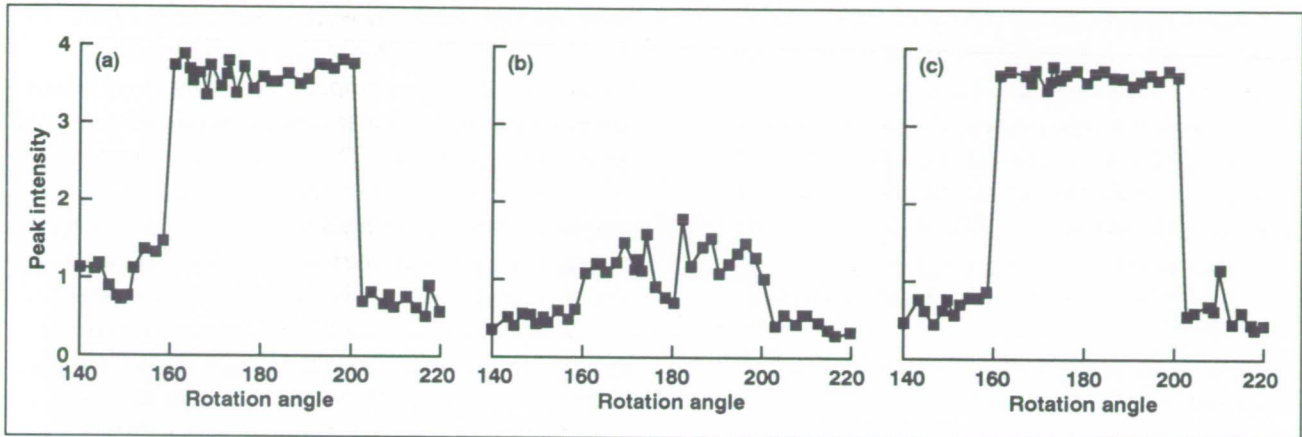


Fig. 1. Correlator response. (a) Desired response; (b) response with phase errors; (c) response with phase errors corrected.

Optical processing and advanced image processing are being applied in four research areas: Robotic Vision, Autonomous Vehicle Guidance, Autonomous Aircraft Inspection, and Optical Matrix Processing.

A practical problem that can severely limit the performance of an optical correlator is the presence of phase aberrations in the optical train, primarily those associated with the critical spatial light modulator (SLM) components. For example, consider the response functions of a binary synthetic discriminant function (SDF) optical filter designed to give equal correlation peaks over a 40-degree rotation range. The first graph in the figure shows the desired response that is achieved in an error-free optical correlator, whereas the second graph shows the actual response that is achieved when the filter is implemented in a correlator with typical aberrations in the input and filter SLMs. The performance is severely degraded by the optical aberrations, which render the filter almost useless.

To avoid these effects, research at NASA Ames has focused on modifying the filter design algorithm to include information on the phase aberrations. Experiments have shown that this improves correlator performance to the level of an aberration-free system.

The third graph illustrates the effectiveness of this technique by showing the response of a modified filter implemented in a correlator with aberrations. The performance achieved is equal to the desired result (first graph).

Besides the clear improvement in filter performance, there are two other benefits of this technique. The first is that one can significantly reduce the design time by designing all SDFs offline in a computer simulation, given accurate measurements of the component phase errors. It was previously necessary to perform the SDF design on the actual optical correlator. The second benefit is related. The technique allows SDF filters to be designed at one location in simulation, and then implemented on an optical correlator somewhere else, as long as the correlator phase-error data is provided to the filter designer.

**Ames-Moffett contact: M. Reid/D. Tucker
(415) 604-4378/4668**

Headquarters program office: OAST

Parallel Systems Research

Cathy Schulbach

Future NASA missions will increasingly use distributed and parallel computer systems. However, the difficulty in writing the software for these systems and monitoring its execution has made the development of validatable programs for such systems an intractable problem. There are three major problem areas:

1. Static and dynamic automated mapping and remapping strategies for parallel computations on multicomputers
2. Software tools and methodologies for data collection, abstraction, and visualization for multiprocessing systems; these tools will be used for performance tuning as well as debugging—to help reconstruct the schedule that caused an error after the error has occurred
3. Performance-prediction tools applicable to very large applications on multicomputers

This past year, the emphasis has been on investigating and developing new techniques for instrumenting, monitoring, and presenting the state of parallel program execution in a coherent and user-friendly manner. In addition, prototype software tools have been developed and incorporated into the run-time environments of various hardware testbeds to evaluate their impact on user productivity.

The Ames Instrumentation System (AIMS) tool set was developed, incorporating features from various

software systems such as PIE from Carnegie-Mellon University, ParaGraph from Oak Ridge National Laboratory, and Quartz from the University of Washington. With this software, the execution of FORTRAN programs can be automatically instrumented and monitored. Performance data thus collected can be displayed graphically on workstations supporting the X-Windows software package. A variety of views and statistics are possible. Two important capabilities are (1) the ability to point to certain events and navigate back to the portions of the code directly associated with that event, and (2) the ability to visualize and understand the perturbances that are due to software instrumentation.

The AIMS software has been used to compare different compiler versions as well as various parallel algorithms on an Intel iPSC/860. It will continue to be used in the performance analysis and optimization of programs for the Space Station Freedom Data Management Systems and for computational fluid dynamics codes on multiprocessors, and will also be used in other research areas.

Ames-Moffett contact: J. Yan
(415) 604-4381

Headquarters program office: OAST

Automatic Calibration for Sensor Images

Albert J. Ahumada, Jr., Jeffrey B. Mulligan

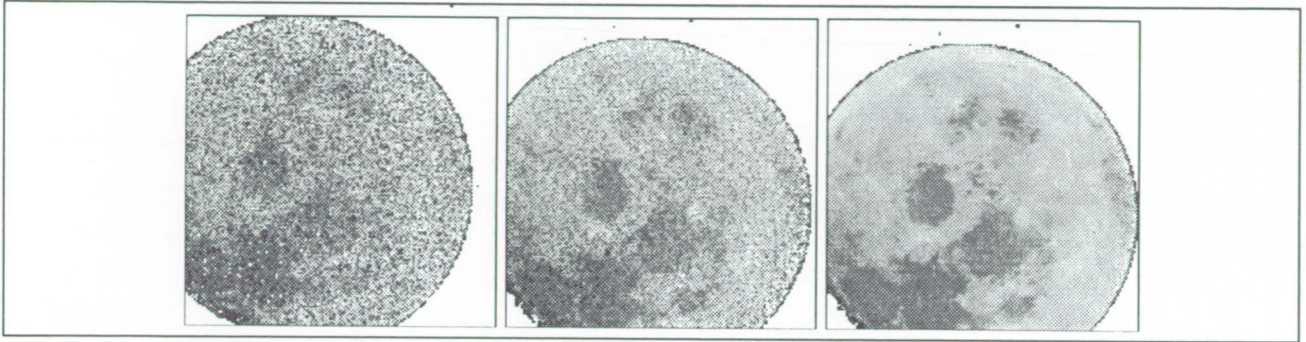


Fig. 1. Sensor image after 0, 2, and 9 calibration cycles.

Cameras used in remote sensing employ sensor arrays that must be calibrated to function properly. The spacing between sensor elements and the gain of each element must be corrected for if images are to be correctly reconstructed. Ordinarily, calibration is accomplished by using a test pattern with known geometric (spatial) and photometric (intensity) characteristics. Cameras used in space on satellites or on planetary rovers may degrade, losing sensor elements, parts of elements, or sensitivity. Methods are being developed to recalibrate degraded devices without the use of a known test pattern.

The human visual system is confronted with a similar problem: its retinal sensors are not in regular arrays, and they vary somewhat in sensitivity. The human visual system solves the problem with an adaptive neural network which maps the image from the photoreceptor mosaic to a neural representation of the image. Artificial neural networks have been developed to model the human network. Computer simulation of these networks shows that they can automatically recalibrate detector arrays whose sensor elements have been moved slightly or have lost sensitivity, as illustrated in the first figure.

The networks calibrate the mapping by comparing the estimated images for the same image moved to different positions on the sensor array, and deriving an error-correcting signal from the comparison, as illustrated in the second figure. The first algorithm to do this task was developed in collaboration with L. Maloney of New York University. This algorithm

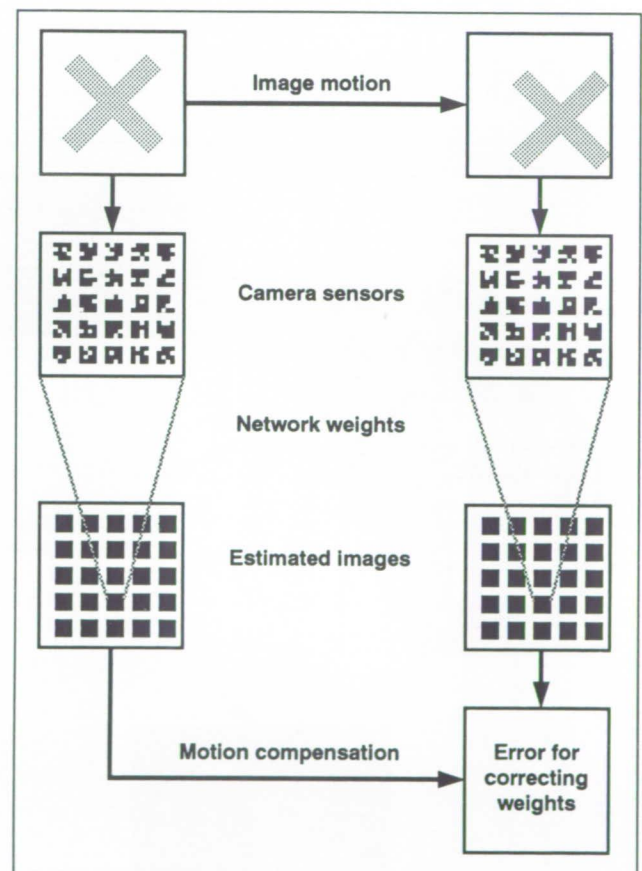


Fig. 2. Diagram of network calibration method.

calibrated correctly with known amounts of image motion. A major accomplishment has been to show that the algorithm can correctly recalibrate when the size and direction of image motion is estimated from the initially erroneous internal images. Another major accomplishment is the development of an algorithm for the case of completely missing sensor elements. This algorithm was developed in collaboration with

K. Turano of the Johns Hopkins Hospital Wilmer Eye Institute, who is trying to model visual deficits in retinitis pigmentosa, a disease of the aging retina.

**Ames-Moffett contact: A. Ahumada, Jr.
(415) 604-6257**

Headquarters program office: OAET

Electronic Chart Display Development

Vernol Battiste

Since the loss of geographical orientation remains a significant cause of civil and military aircraft incidents and accidents, the Rotorcraft Human Factors Branch has been conducting research on the cues

pilots use to maintain geographical orientation. To facilitate research in this area, a highly accurate, reconfigurable electronic chart display (ECD) system suitable for terrain navigation studies is needed.

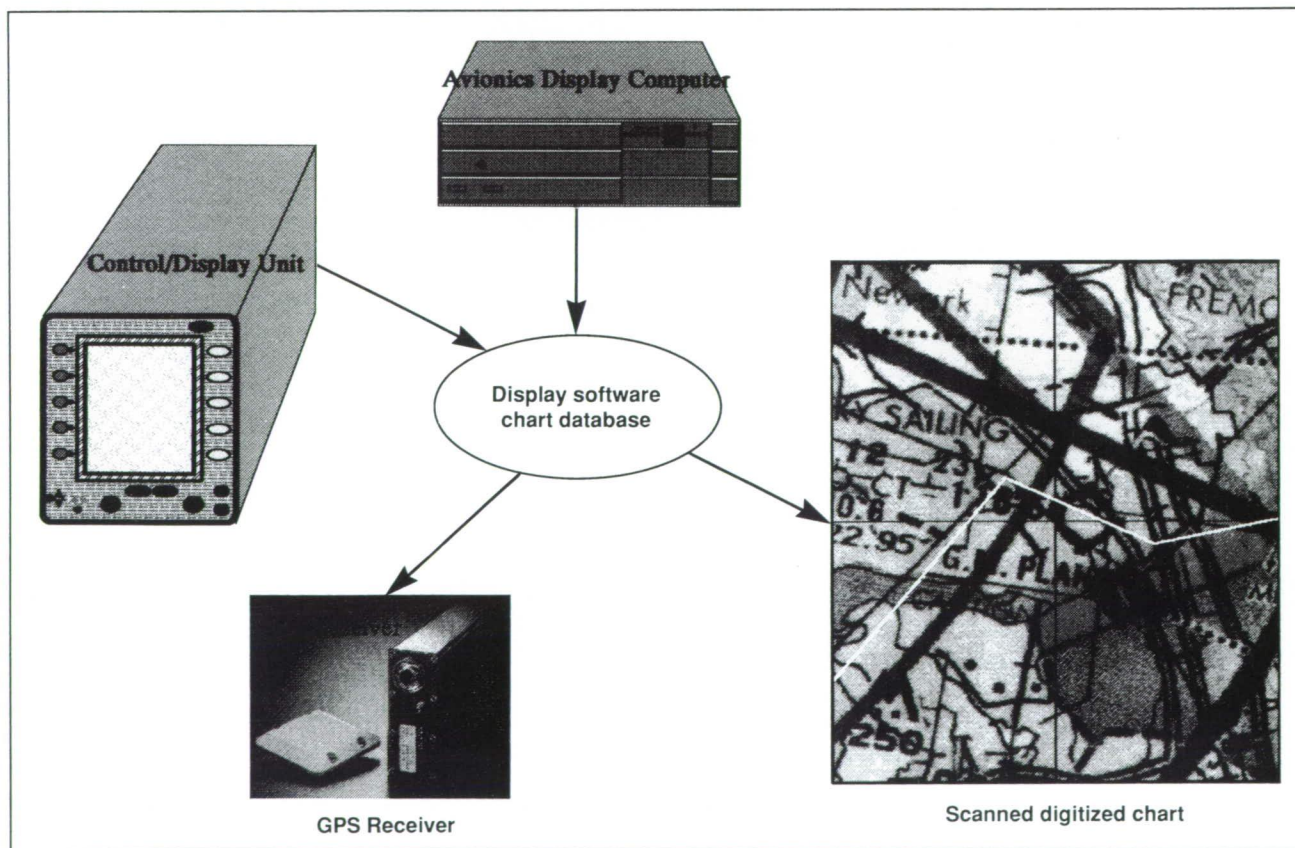


Fig. 1. Prototype electronic chart display.

The system will consist of (1) a low-cost global positioning satellite (GPS) receiver; (2) scanned, digitized charts which can be modified for each operator; (3) a high-resolution color display, suitable for day/night operations; and (4) other information required for navigation (see figure for system components and features). Preliminary flight tests conducted at Ames demonstrated the feasibility of using a low-cost GPS receiver developed by Trimbal Navigation to determine helicopter location; after minor modifications, aircraft position accuracy was within ± 25 meters. The flight data and interface software were delivered to Radar Data Systems and successfully integrated with their computer-simulated electronic chart display. In parallel, researchers at NASA, Stanford University, and the University of Illinois are conducting research to develop display formats and the pilot interface.

A prototype low-cost, dynamic electronic chart display (ECD) system coupled with GPS data was developed and ground tested in the local area around Ames Research Center. Two types of maps were installed and tested: (1) a 1:500,000 San Francisco Sectional Aeronautical Chart, and (2) several 1:100,000 USGS Metric Topographical maps of the Bay Area. Using a map-to-GPS data calibration technique, overall system accuracy is significantly greater than the accuracy of the GPS receiver (± 25 meters) alone. Using this calibration technique the ECD system's accuracy is limited only by map

pixel size: with a 1:500,000-scale map, accuracy is ± 50 meters; with a 1:100,000-scale map, accuracy is ± 10 meters. However, if GPS accuracy is degraded to the civilian level (C-code accuracy = 100 meters), overall ECD-system accuracy will be reduced. Through the visual map-to-GPS calibration technique, we can correlate the reported GPS position with a known map location, and thereby take full advantage of the increased accuracy. This final calibration is a correction to the projection of world size, and thus affords greater overall map accuracy.

Currently there is much interest in the development of ECDs for all types of vehicles, from family automobiles to aerospace planes. In all of these systems, there is a need to relate map position data with visual information to determine or confirm the driver's or the pilot's current location. The prototype system we have developed lends itself to most if not all of these applications, with some optimization for individual applications. A backup geopositioning system, such as a low-cost inertial gyro which could be used to augment the GPS system when satellite signals are blocked, should be incorporated for terrestrial applications. The prototype system will be flight tested at Ames in early 1992.

Ames-Moffett contact: V. Battiste
(415) 604-3666

Headquarters program office: OAET

3-D Auditory Displays in Aeronautical Applications

Durand R. Begault

The purpose of the research is to implement and test auditory display concepts that will allow a pilot, a crew member, or an air traffic controller to immediately, accurately, and inexpensively monitor three-dimensional (3-D) information, such as traffic location, through the use of 3-D sound. As illustrated in the figure, the overall goal is to create an integrated spatial auditory display that is both safer and easier to use than existing communications systems.

Through our basic research efforts, real-time display of acoustic spatial information, or "3-D sound," has recently become feasible. "3-D sound processing" here refers generically to any digital audio-signal-processing system that takes a single channel of audio input and produces a two-channel, binaural output. The process mimics the principal cues to normal spatial hearing, allowing the designer of such a system to place a sound anywhere in virtual space for a listener wearing headphones. This is useful for both situational awareness and improving speech intelligibility.

Hardware has been designed and implemented for experiments in the following areas: spoken audio warning-system signals, Traffic Collision Avoidance System (TCAS) advisories, and cockpit radio communications. The TCAS advisory consists of the spoken word "traffic." The actual position of the traffic is usually obtained visually, through instrument monitoring and/or out-the-window observation. In the Advanced Concepts Flight Simulator, the out-the-window position of the traffic is linked to the virtual auditory position of the word "traffic" heard through headphones. A pilot experiment was recently completed to determine if the time interval for traffic detection is reduced when binaural sound delivery is used to suggest the direction for head-up visual search of the target, compared to monotic (single-earpiece), normal practice conditions. Results showed that there was a 2.5-second improvement in detection time. An experiment currently under development pits a normal TCAS visual display against a 3-D auditory and visual head-up display. For communications, a 3-D sound hardware system can place various radio

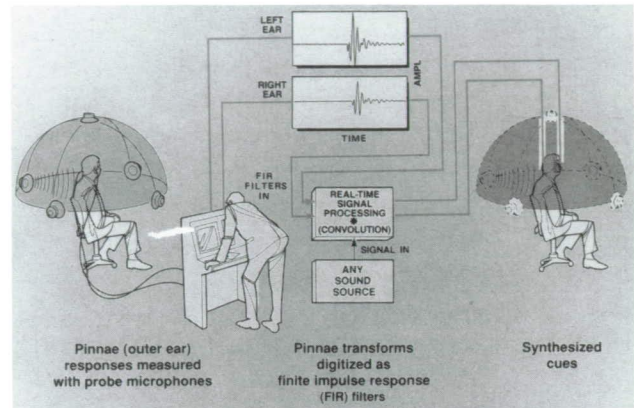


Fig. 1. Three-dimensional auditory display.

communication streams (e.g., weather, air traffic control) in separate virtual auditory positions around the pilot. The purpose of the system is to allow greater intelligibility in the presence of noise, or in situations where more than one frequency must be monitored, such as in the vicinity of an airport.

Basic research in the area of human headphone localization is also under way which supports these applied research efforts. One study compared inexperienced listeners' headphone localization of speech to the results of previous studies using noise. Another study used artificial spatial reverberation to increase the veridicality of the 3-D sound display. A third study determined that there was no perceptual degradation with a 20:1 data reduction of the filter parameters used in the 3-D sound display hardware. The results of this experiment will be important for technology transfer, since the technique can be implemented much less expensively than current methods. The results will also be applicable to important basic research questions about the fine structure of spectral cues for spatial hearing.

Ames-Moffett contact: D. Begault

(415) 604-3920

Headquarters program office: OAET

Extravehicular Activity Self-Rescue in Virtual Environments

Adam R. Brody, Stephen R. Ellis

Virtual environments promise to provide a new communications medium for a variety of uses. However, few demonstrations of their practical utility have been implemented. The Extravehicular Activity Self-Rescue in Virtual Environments project is a current example of a practical test of the utility of virtual-environment personal simulators.

While there are no flight data for separations of astronauts from spacecraft in the U.S. space program, neutral-buoyancy simulations in the weightless environment training facility (WETF) have revealed that separation incidents will occur periodically. A linear extrapolation of the simulation data yielded three incidents in seven WETF years, which corresponds to approximately one incident every 1000 extravehicular activity (EVA) hours. Crew safety is an important issue, and rescue ability is a requirement for the space station.

A rapid response is critical, and is unlikely to be achieved by a manned retrieval. This leads toward a robotic or self-rescue solution. A robotic rescue will most likely require either sophisticated ranging and sensor instrumentation that is not present in the current space-station design, or unproven visual recognition techniques. Self-rescue is conceptually simpler, in addition to being the least expensive solution to the EVA separation problem. The big questions are, What is required for this capability? Can a crewmember stop his or her own tumbling, or is an attitude-hold device required? What are the fuel requirements?

Human participation comes into play in several discrete instances. First, the crewmember will most likely be responsible for the action(s) that cause him or her to become separated from the space station. Second, upon separation, the EVA crewmember must be able to ascertain his or her location and orientation with respect to the space station. Third, the stranded crewmember must take the necessary steps to return to the station, including positioning and firing the thruster(s).

By providing a virtual-environment simulation program with the mass and moments of inertia of an EVA crewmember, and thruster characteristics for a rescue device, researchers are able to examine human performance in a rescue. Measurements such as time until response, time and fuel necessary to stop rotations, and time and fuel required to return to the station can be made for an assortment of failure scenarios. Thrusters can be altered in magnitude, capacity, moment arm, and number in order to examine the effects these parameters might have on self-rescue capability. Different control modes such as pulse, displacement proportional, force proportional, and on/off could be compared to determine which works best with regard to fuel use, time, safety, or other specified cost function.

So far, one study was performed in the virtual environment simulator of the Advanced Displays and Spatial Perception Laboratory. Simulations were conducted to assess the feasibility and to quantify the fuel and time requirements for a stranded crewmember to return to a space station after an accidental separation. A hand-held thruster similar to the Hand-Held Maneuvering Unit from the Gemini Program was used for propulsion. Virtual-environment simulators were determined to be useful for simulating accidental separations, and provided preliminary evidence that a hand-held thruster is a viable alternative for accomplishing a self-rescue. Simulation fidelity and validity remain to be established. Further work will be directed toward measuring the realism of the virtual-environment simulation and using these measures to assist in transfer of training to simulated real environments.

Ames-Moffett contact: S. Ellis

(415) 604-6147

Headquarters program office: OAET

Control Delegation in the Automated Cockpit

Stephen Casner

The increased capability for automated flightpath control in the modern cockpit has caused a similar increase in the difficulty of the crew's task of reasoning about when and how it should be used. It comes as little surprise that the increased possibility for error has led to an increase in actual error. The difficulties associated with new flight-control automation stem from the fact that there are now many novel ways to accomplish tasks that in the past were accomplished using one or two well-practiced techniques. For example, to follow a published departure route, the crew of the modern cockpit now has several options, including (1) maintain the heading, altitude, and airspeed of the aircraft manually; (2) use the autopilot to control any or all of these variables; (3) use the autopilot to control the heading, manually control the airspeed with the throttles, and ask the pilot who is not flying to monitor the altitude; (4) program and set the Flight Management Computer. With a large number of possible configurations, the crew is faced with the chore of deciding which configuration is appropriate for any given situation and also with keeping track of who or what is currently flying the aircraft, making sure that all critical flying tasks are being attended to.

A search of the Aviation Safety Reporting System (ASRS) data base revealed a substantial number of incident reports implicating crew difficulties in managing the large suite of cockpit automation resources. There is sufficient reason to suspect that the automation-resource-management task is already complex enough to warrant steps to either reduce its

complexity or to provide some form of display that assists the crew in doing the job. This problem will increase as the level of cockpit automation continues to rise.

We have studied the problem of cockpit automation resource management and have generated a computer model that specifies all of the legal transitions between system configurations. These configurations describe all of the allowable ways of assigning pieces of the flying task to the automation resources that can handle them. The computer model takes into account the work capacities of each piece of automation as well as the work capacities of the crewmembers themselves, since they, too, are available to perform flying tasks. A set of cockpit displays has been designed that continually shows what crewmember or automation resource is currently handling each flying task and which other resources are available for duty. Most important, when a resource is disengaged, the display reminds the crew of what flying tasks have now been put back in their hands and what automation resources are standing by ready to accept responsibility for them. A full-mission simulator study is being planned that will test the ability of the crew to effectively use the displays in time-critical situations that demand full exploitation of the available cockpit resources.

**Ames-Moffett contact: S. Casner
(415) 604-6908**

Headquarters program office: OAET

Design of Visual Information Displays

Stephen Casner

One feature of a good cockpit display is that it lets the pilot understand and process the displayed information with the least amount of time and effort. Studies of people using visual displays show that the ways in which different display designs achieve this goal depends on what the pilot needs the information for. Thus it is possible to design visual displays that are customized for the particular tasks that the pilot needs to perform.

To assist the designer, a computer-implemented display design tool, BOZ, accepts a description of a task that a pilot must perform and generates a visual display that arguably allows the pilot to perform the task with the least amount of effort. When designing a visual display, BOZ considers three important measures of difficulty associated with visual-display use: (1) the amount of time the pilots must spend searching for the information they need, (2) the difficulty of reasoning about the information displayed in its visual

format, and (3) the amount of information that the pilots must maintain in their memory. BOZ has been used to analyze, design, and redesign several examples of cockpit displays, especially displays that help the crew to understand the workings of the flight-control automation systems. Given that several different visual displays can always be designed for any task, BOZ also provides a means of helping to decide which displays are best. BOZ allows the designer to run simulations of any visual display in use while it keeps track of the three measures listed above. After running simulations for each of a set of alternative visual-display designs, the measures for each display can be compared to help determine which is likely to be the most effective.

Ames-Moffett contact: S. Casner

(415) 604-6908

Headquarters program office: OAET

Dynamic Anthropometric Modeling

Kevin M. Corker

One of the most fundamental requirements for model-based human engineering and analysis in a wide array of applications is a representation of human anthropometry and motion. A grant with Norman Badler, Ph.D., at the University of Pennsylvania has been established to meet this need with easily created, realistic, and physically quantifiable human figure motion via an interactive computer graphics system for human modeling in a three-dimensional (3-D) space environment. Major research areas within this project include (1) task simulation mechanisms that facilitate human task animation by developing an interface between artificial intelligence and graphical motion control; (2) reporting task-simulation results with graphical animations and various workload performance measures including reach assessments

and view assessments, collision and interference detection, strength or reaction-force assessment, and psychomotor task load; and (3) the use of human-agent models such as hand preference or fatigue within the task simulation.

The resulting computer program, JACK, allows the user to select different-size human figures or graphic mannequins that include the 5th, 50th, and 95th percentile of male and female sizes based on NASA astronaut demographics. These mannequins can then be placed within a 3-D object environment created and stored using a number of modeling packages. Articulation is achieved using a goal-solving technique based on specifying body-joint orientations or end-effector (limb) goals. Joint movement limitations

have been installed to eliminate unreasonable movements. Kinematic and inverse kinematic controls are applied so that goals and constraints may be used to position and orient the figure, with external/internal forces and torques applied to produce motion. A Fitt's-Law-based movement time concept has been incorporated based on reach-site distance and width.

Supporting graphic output in wireframe, solid-filled, or smooth-shaded modes, key poses can be stored and interpolated for animation, allowing environmental limitations to be detected as a function of human size and movement characteristics. In addition, by attaching the "view" of the environment to the mannequin's eye, JACK displays a perspective corresponding to what the mannequin would "see" while moving in the environment, thus providing the first step toward further analysis and conclusions about object visibility and occlusion.

JACK was developed in the fall of 1987, and is being further enhanced, both in house and by the

developer, as an integral part of A³I's MIDAS workstation (see Hartzell: "Army-NASA Aircrew/Aircraft Integration Program" later in this section). Enhancements include multiple articulations of the figure's spine, the inclusion of "reach-zone analysis" for varied levels of pilot restraint in the cockpit, and integration of the anthropometric mannequin into the simulated activity flow of MIDAS. As a result of this integration, designers and analysts can view the progress of a mission, the external movements of the operator performing that mission, the operator's visual activity, and, through the symbolic operator models, analysts can examine the cognitive functions of the operator.

Ames-Moffett contact: K. Corker
(415) 604-0055

Headquarters program office: OAET

Enroute Flight Planning

Kevin Corker, Everett Palmer

The objective of this work is to evaluate computer tools to assist dispatchers and flight crews in detecting the need for flight amendments in a timely fashion and developing alternative flight plans. A broader objective is to study general issues in the design of cooperative problem-solving systems. Enroute flight planning is a rich context in which to study such issues. It involves decision-making in an uncertain environment where trade-offs among different goals (e.g., safety, cost, passenger comfort) must be considered and where the amount of potentially relevant data is large. In addition, enroute flight planning is of interest because of the distributed nature of the problem solving, with dispatchers, air traffic controllers, and flight crew all playing important roles.

Based on initial studies (surveys, structured interviews with experts, and a simulator study), the project has generated a set of proposed design principles. A design for an interactive enroute replanning tool using a graphical interface was

developed and implemented. A large-scale empirical study to evaluate three alternative system designs that differ in terms of the "level" of automation or decision aiding is nearly complete.

Data have been collected from 55 of 60 subjects (30 pilots and 30 dispatchers). These subjects were first trained in the use of one version of the system and then asked to use it as a tool to complete a number of carefully constructed flight planning problems. The subjects were asked to think aloud as they completed these problems. The problems were constructed so that the effects of the designs on nonoptimum human behaviors such as fixation on a particular solution and inadequate use of available data could be determined. Preliminary results indicate that the alternative designs clearly influenced the planning behavior of the users and will provide good data for modeling the cognitive processes involved in flight planning.

Several major airlines are beginning to develop new dispatcher support systems to aid in flight planning. All are interested in the use of graphical interfaces for this purpose. The results also have important implications and uses for the training of dispatchers and pilots.

This work was accomplished through a grant with Phil Smith of the Department of Industrial and Systems Engineering at Ohio State University.

Ames-Moffett contact: K. Corker

(415) 604-0055

Headquarters program office: OAET

Flight Management System Human Factors

Kevin Corker, Everett Palmer

In cooperation with a major U.S. carrier, three studies on pilot interaction with one of the core systems of cockpit automation, the Flight Management System (FMS), were conducted. The first two studies served to identify the nature and variety of problems that pilots have with the FMS and to provide insight into pilots' mental models of the system. First, a survey of line pilots was carried out, asking them to report their experiences with the FMS on the B-737-300 aircraft. Second, observations of transition training from a conventional to a "glass-cockpit" aircraft (also a B-737-300) were made. Based on the data from these first two activities, an experimental study of pilots' mental models and awareness of the FMS was conducted using a training simulator.

All three activities yielded consistent data on the nature of problems concerning human-computer cooperation in the B-737-300 "glass cockpit." It was shown how and where automation is used in a "clumsy" way which makes it difficult for pilots to fully exploit the potential benefits of advanced cockpit systems. Major problem areas included, but were not limited to,

1. Maintaining mode awareness when switching between different levels of automation (FMS and autopilot-control-panel modes)
2. Tracking "uncommanded" mode transitions
3. Vertical awareness (e.g., tracking the aircraft status and behavior in the vertical navigation mode where it is sometimes difficult for pilots to understand underlying algorithms and to visualize the computed vertical path)

The data suggest that these problems are related to deficiencies in the design of FMS interfaces which do not clearly and coherently indicate to the user the system states and transitions, goals, and options; memory demands are increased instead of decreased by, for example, using displays as external memory. Current cockpit displays do not meet the new criteria for effective information presentation which were introduced by increasing levels of automation. This lack can affect pilots' ability to perform the supervisory tasks of adequately assessing a situation, predicting future events, and determining when it is necessary to intervene. "Clumsy" automation can actually produce a decrease in situation awareness, especially with respect to mode awareness, i.e., the knowledge of automated systems' states and behavior. This research has identified both the nature and the underlying reasons for problems in communication and cooperation between pilots and the FMS. These problems are similar to those observed in other high-technology domains.

The work was accomplished through a grant with David Woods of the Department of Industrial and Systems Engineering at Ohio State University.

Ames-Moffett contact: K. Corker

(415) 604-0055

Headquarters program office: OAET

Symbolic Operator Model

Kevin M. Corker, E. James Hartzell

The symbolic-operator-model component of the Man-Machine Integration Design and Analysis System (MIDAS) is complex and continually evolving. Nine major subcomponents and models of human performance have been integrated into the MIDAS structure: (1) attention, (2) perception, (3) task loading, (4) task prioritization, (5) strategies for scheduling, (6) contingent response generation through rule-based and (7) algorithmic-based decision making, (8) response generation, and (9) an internal world model for simulated operators in the system. During a simulation, these models translate mission goals into specific tasks; determine the load on the operator for the performance of those tasks; generate a schedule that attempts to execute assigned mission activities subject to specified constraints, state variables, and other simulation object requirements; handle contingency by applying situation-specific rules or general decision algorithms, update an internal representation of the world based on the action execution, and change the simulation world according to action specification.

These models of human performance are embedded in an agent-based, object-oriented architecture, and their function is to simulate the flow of activity through human-machine systems. The process allows attention and perception to be directed by internal-task-related requirements or to be responsive to external world/cockpit events. Data about the world are filtered through attention and perception, and are entered into the operator's internal-world representation. This representation is structured as a semantic net and supports forgetting and rehearsal effects. In addition, the semantic net allows varied relationships to be established among the information nodes in the operator's world representation. Rules of behavior and decisions based on the state of the operator's internal world as well as changing-external-world simulation cause action to be taken by the simulated operator. These actions are then scheduled and the load on the operator to perform the scheduled tasks is calculated.

The constraint-based, opportunistic model of operator scheduling behavior was developed using the blackboard architecture provided as part of the Generic Expert System Tool (GEST). (The rule-based contingent activities are also implemented using the GEST shell.) The scheduler model contains modular components or knowledge sources that represent individual stages in the scheduling process, with an extended task-based decomposition (a "divide-and-conquer" technique) used to partition the overall scheduling problem. It closely interacts with the MIDAS task-loading model for reasoning about resource interactions between plausible concurrent tasks.

The task-loading model is based on current research in multiple-resource theory, scaling, workload, and perception. Based on attributes of the mission tasks, world state, operator, and crew-station equipment, a resource classification taxonomy is used to classify individual tasks according to their demands on the visual, auditory, cognitive, and motor processing dimensions. In addition, conflict matrices are used to describe the interactions of these resource demands across different processing dimensions and tasks.

Results of simulation runs, as well as static analyses of crew stations, are provided to the designer/analyst through a screen-based interface that supports multiple types of summary statistics. Task timelines, operator loads, operational measures, and insight into the internal operation of the operator model are available through the user interface. Current efforts are being directed toward verification of model component predictions and man-in-the-loop verification of the model's operational analyses.

Ames-Moffett contact: K. Corker

(415) 604-0055

Headquarters program office: OAET

Human Performance in Virtual Environments

Stephen R. Ellis, Kenneth E. Nemire

Virtual-environment display technology can produce personalized simulators that provide, for a free-standing individual, the type of simulation illusion previously only provided to an entire aircraft crew. These new head-mounted personal simulators, however, need not simulate vehicles but may simulate environments such as remote teleoperation worksites. Just as the fidelity of the vehicle simulation used for aircraft must be measured, the realism and correctness of the virtual environments may be assessed to enhance their usefulness for mission planning, training, or scientific visualization. Assessment techniques have been developed through user testing with standardized human manual control tasks and through study of perceptual phenomena that depend on presentation of a convincing, visually enveloping spatial illusion.

The manual control task that has been studied in a virtual environment is a version of a three-dimensional (3-D) tracking task that has been used extensively in the study of human performance with panel-mounted, 3-D displays. In the current work, this task has been used to measure human manual-control plasticity as display-control misalignments were introduced between the head-mounted display and the coordinates of a hand-mounted, 6-degree-of-freedom position tracker. The subject's basic task was to move the position sensor on his or her hand to cause a virtual 3-D cursor (viewed via the stereo, head-mounted displays) to track a small target that moved irregularly in three dimensions in front of the subject. In contrast to some results in the tracking literature, subjects demonstrated a capacity to learn to perform this task with display-control misalignment ranging from 0 degrees to 180 degrees (see first

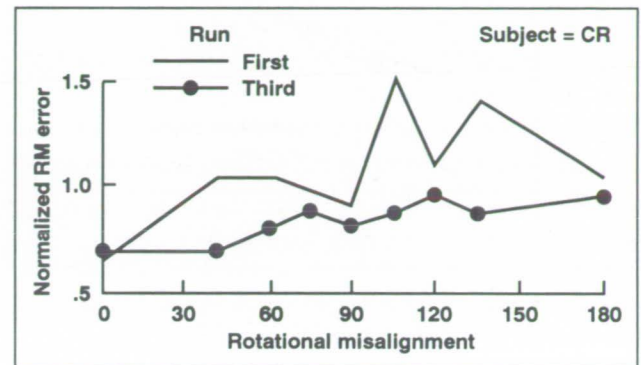


Fig. 1. Three-dimensional tracking performance in a virtual environment.

figure). With several hours' practice during one day, subjects could learn to perform the task with nine different display-control misalignments.

The perceptual phenomenon studied was the influence of visual stimuli on the perception of gravity-referenced eye level. This phenomenon has been used to measure the fidelity with which a virtual-environment system produces a simulation of 3-D space. Experiments have been performed in a virtual environment and compared with results obtained in a corresponding physical environment. A virtual pitched array was produced which was geometrically identical to corresponding physical stimuli. The virtual array had a smaller influence on perceived eye level than did the pitched physical array. The degree to which the pitched optical array influenced the subject's sense of gravitationally referenced eye level may be taken as a measure of

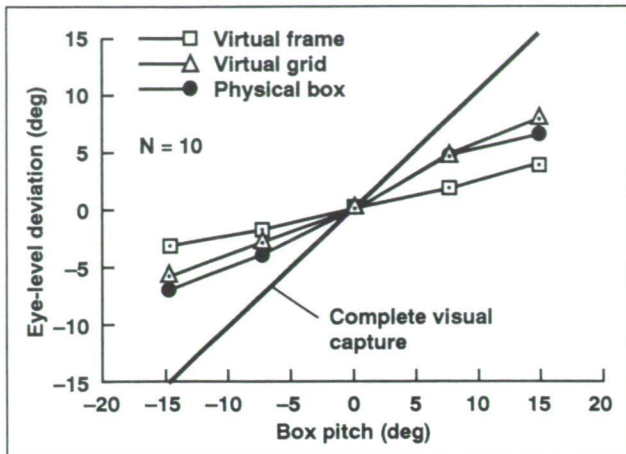


Fig. 2. Visual capture in physical and virtual environments.

the completeness of the enveloping spatial illusion. The addition of several grid patterns to the virtual pitched array increased the influence of the virtual optical array and indicates the specific type of grid that may be optimal for improving the completeness of the enveloping illusion in virtual environments (see second figure).

Ames-Moffett contact: S. Ellis
(415) 604-6147
Headquarters program office: OAET

Telerobotic Planning and Operational Interfaces

Stephen R. Ellis

The paths that robotic mechanisms trace during their missions are subject to numerous quantitative and qualitative constraints. Whereas algorithms exist to satisfy these constraints automatically, these techniques are often slow, inflexible, idealized, or incomplete. Consequently, there is a need to be able to visualize the robot's planned trajectory and to interactively edit it. The editing may be required during debugging of automatic solutions or may be used during actual collaborative mission planning when a human user interacts with an algorithm. Such interaction requires a suitable communication medium.

Virtual environments produced through head-mounted displays coordinated with simulations of robotic manipulators constitute such a medium. When

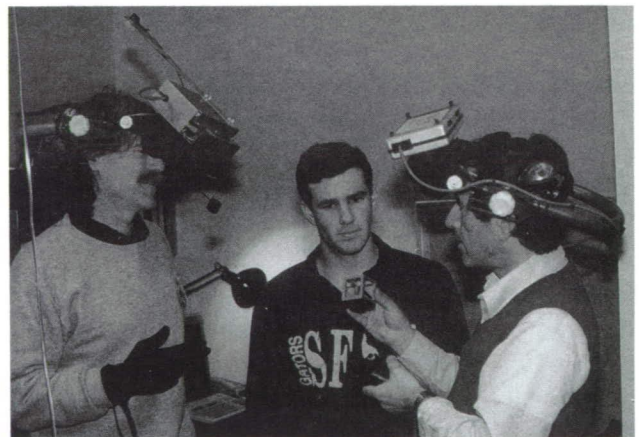


Fig. 1. Researchers wearing head-mounted displays that present virtual-environment simulation.

ORIGINAL PAGE
BLACK AND WHITE PHOTOGRAPH

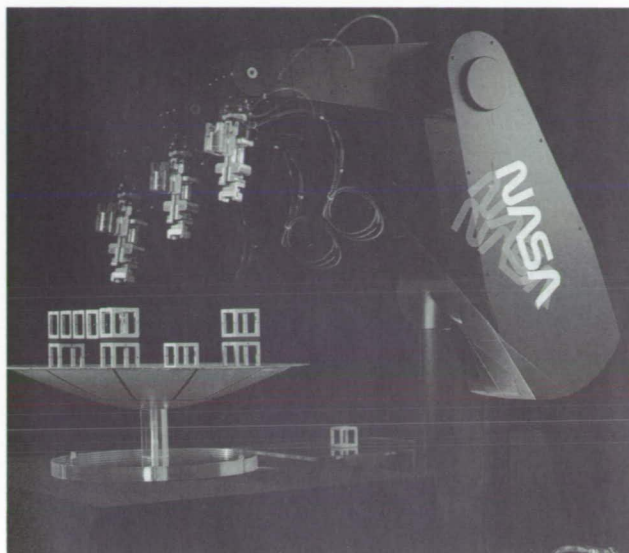


Fig. 2. The PUMA arm that will be controlled through a virtual-environment interface.

enhanced by dynamic or kinematic simulations in the form of "geometric spreadsheets," such media can extend human planning capabilities into new realms. One key benefit is that activities can be planned within the simulation and thus the difficulties presented by the long time lags associated with communication to distant robotic worksites can be avoided. They additionally promise to add flexibility and speed to the planning process.

A virtual environment created through kinematic simulation (see first figure) of a PUMA robot arm

(second figure) has been completed in the Advanced Displays Laboratory and connected through an Ethernet to a corresponding PUMA arm in a remote laboratory of the Intelligent Mechanisms Group using a specialized control protocol. Bidirectional video links have also been established. Gesture-planning software is currently being developed to plan sequences of robotic movements. An initial movement-macro definition capability has been developed and demonstrated, and icons representing potential constraints on motion, such as the forces and torques at the end effector, have been developed. Alternative menu control techniques are being developed for interacting with the macros and the virtual environment itself, and have been studied through psychophysical and biomechanical techniques.

Further development of virtual-environment interfaces for robot manipulators will generally advance the virtual-environment technology because planning of telerobotics tasks addresses issues that are functionally common to the manipulation and control of virtual objects in a large variety of application areas such as assembly training, teleoperation, or laparoscopic surgery.

Ames-Moffett contact: S. Ellis

(415) 604-6147

Headquarters program office: OAET

Distance Estimation with Night-Vision Devices

David C. Foyle, Mary K. Kaiser

Accurate distance estimation is an important task for most aircraft pilots, but it is critical for helicopter pilots. Rotorcraft can maneuver among trees and other obstacles (i.e., fly nap-of-the-Earth), land in small-clearance areas, fly at low altitudes, and maintain a hover at a fixed altitude above a certain point. All of these pilotage tasks require accurate distance estimation to implement the maneuver properly and safely. For safe operation, helicopter pilots must constantly verify that the aircraft has adequate clearance in all directions: the tail boom to the rear; the skids or wheels below; and the rotor blades above, to the sides, and in front—all must clear obstacles, sometimes by only a few feet depending on the operational requirements. Additionally, distance estimation for greater distances (up to a few hundred feet) is important to maintain altitude in those ranges, and to maintain hover in the fore/aft and lateral directions. To maintain hover, pilots typically choose objects in front of them and to the side, and then control the aircraft to maintain the distances from those objects.

Distance estimation has been identified as one of the specific problems that pilots have with existing

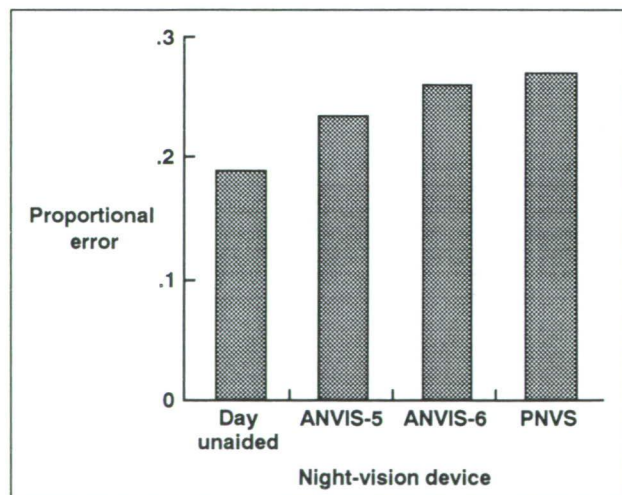


Fig. 1. Proportional distance-estimation error for daytime unaided viewing and three night-vision devices.

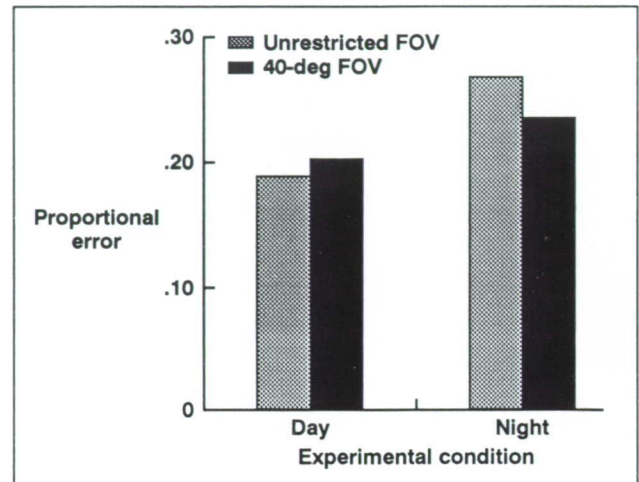


Fig. 2. Proportional distance-estimation error for unaided viewing as a function of field of view and resolution (day/night viewing).

night-vision sensors, such as night-vision goggles and infrared imaging sensors. Night-vision goggles have been reported to yield overestimations of distance. Pilots using infrared sensors have also been reported to give inaccurate object distance estimates. Some of the mechanisms that may be operating to yield inaccurate distance estimates are poor sensor resolution, misaccommodation of the pilot's eyes, and restricted field of view (FOV).

A field experiment was conducted to compare the distance-estimation accuracy of the various sensors. Seven viewing conditions were used: day unaided; day unaided, restricted FOV; night unaided; night unaided, restricted FOV; night-vision goggles (ANVIS 5); night-vision goggles (ANVIS 6); and the U.S. Army infrared Pilot Night Vision System (PNVS) sensor. Two white plywood squares (2.25 and 3.0 feet per side) placed facing the subject (upright and perpendicular to the line of sight) were used as targets. Testing was conducted at Ames in a field containing uniformly scattered small (1- to 3-inch) plants. Night

testing was restricted to periods when there was three-quarter-moon overhead illumination. Twenty target distances ranging from 20 to 200 feet were tested.

For each trial, the distance estimate was converted into proportional error (i.e., (estimated distance – actual distance)/actual distance). The first figure shows the proportional error for daytime viewing and the three night-vision devices. As one would expect, the daytime viewing conditions yielded the least error. There does not appear to be any difference among the three night-vision devices.

The second figure shows the distance errors for the four conditions with direct eye viewing. The conditions vary in FOV (unrestricted FOV; approximately 160 degrees; and in day or night viewing, yielding a resolution difference of 20/20 for daytime and 20/60 for night viewing). FOV appears not to have a systematic effect on distance estimation, but

resolution does: decreasing the resolution from 20/20 to 20/60 increases the distance error.

Potential problems with various systems have been discussed as possible factors in accidents and incidents. Detection of these problems can lead to better training and better hardware solutions. There do appear to be larger distance-estimation errors with the devices than with unaided daytime viewing. Contrary to the findings of previous studies, these errors do not appear to be in one direction (i.e., overestimation or underestimation), but are subject idiosyncratic.

Ames-Moffett contact: D. Foyle

(415) 604-3053

Headquarters program office: OAET

Flight Displays Using Superimposed Symbology

David C. Foyle, Robert S. McCann

Superimposed symbology allows the pilot to spend more time “eyes out,” retaining both aircraft and world awareness. Any high-priority information is a candidate for inclusion on such a display, such as air-traffic-control routing information, taxi information, or aircraft systems status information. The information may be superimposed on a direct-vision view of the world (via transparent electronics), on sensor information (as on the AH-64 Apache Helicopter), or on a graphics version of the world (e.g., the synthetic vision system proposed for the High-Speed Civil Transport).

The head-up display (HUD) uses the technique of placing symbology collimated at infinity in the pilot's field of view to allow pilots to see on-board aircraft displays at the same time as the out-the-window view of the world. Before the introduction of HUDs in the early 1980s, pilots had to move their eyes and refocus to view the outside world and the instruments. Pilots have found the HUD to be an extremely useful

display. Scientific studies, as well, have demonstrated that the HUD has a clear advantage over non-HUD designs.

In the early stages of HUD design, however, a human-factors design issue surfaced: it was noted that there may be a failure to attend to both the HUD information and the outside world information simultaneously. In one simulation, after some pilots had made many practice trials using the HUD for landings, an aircraft unexpectedly moved onto the runway from the taxiway. The pilots continued their landing as if the intrusive aircraft was not there, and crashed into it. Similarly, the Air Force has documented the loss of aircraft attitude awareness while pilots are engaged in dogfight exercises in spite of the fact that the HUD pitch ladders visually show them their pitch and roll angles. Likewise, the Army has noted that during initial training, helicopter pilots visually and mentally “fixate” on the superimposed symbology, and do not notice obstacles.

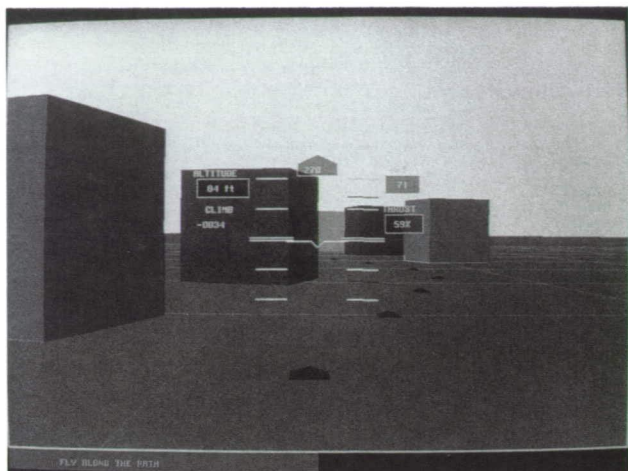


Fig. 1. Example of superimposed flight symbology on an out-the-window view from the part-task mission simulation.

The figure shows a simulation of the HUD superimposed symbology that we have used in multiple part-task mission simulations. Experimental results in our laboratory and at the University of Illinois have indicated that fixating on the HUD information does lead to an inability to process out-the-window information, but when not fixated on the HUD information, pilots can serially process both the HUD and the out-the-window information.

The cause of the inability to process both HUD and out-the-window information during fixation may be found in the many cognitive and perceptual cues that tell the pilot that the HUD, although collimated at infinity, is an instrument on the aircraft, with a different frame of reference than the world. These cues may be the physical frame of the HUD, as well as the framing caused by the displayed items; the differential motion of the world and the HUD; and the different color, texture, and form of the HUD information possibly causing a figure-ground distinction. Identified candidate design solutions to the divided-attention deficit will attempt to minimize these cues or modify the HUD designs so that these same principles operate to provide cues that the HUD information has the same frame of reference. One candidate design for displaying information is to virtually project it into the world via the HUD. That is, project the information as if it were being updated on a billboard in the distance (scene-linked HUD information). This will allow the HUD information to be referenced to the out-the-window view, and not to the aircraft frame of reference. These designs are being investigated through part-task simulation.

Ames-Moffett contact: D. Foyle
(415) 604-3053

Headquarters program office: OAET

Army-NASA Aircrew/Aircraft Integration Program

E. James Hartzell

The Army-NASA Aircrew/Aircraft Integration (A³I) Program is a joint Army and NASA development effort to advance the capabilities and use of computational representations of human performance and behavior in the design, synthesis, and analysis of manned systems. A³I is managed and executed by the Computational Human Engineering Research Office (CHERO), an organization under the U.S. Army Aeroflightdynamics Directorate and the NASA Aerospace Human Factors Research Division, both at Ames. The program's goal is to develop an engineering environment containing the tools and models needed to assist crewstation developers in the conceptual design phase. A major accomplishment is the development of a prototype Human Factors/Computer-Aided Engineering system called the Man-Machine Integration Design and Analysis System (MIDAS). This system provides design engineers and analysts with interactive symbolic, analytic, and graphical components that permit the early integration and visualization of human engineering principles. Currently hosted on a number of networked Symbolics and Silicon Graphics workstations, MIDAS serves as the framework in which research findings and models, developed by or sponsored through the CHERO, are incorporated.

Seventy to eighty percent of the life-cycle cost of an aircraft is determined in the conceptual design phase. After hardware is built, the concepts are difficult to modify. Engineers responsible for developing crew-training simulators and instructional systems currently begin work after the cockpit is built, too late to impact its design. MIDAS gives designers an opportunity to "see it before they build it," to ask "what if" questions about all aspects of crew performance, including training, and to correct problems early. The system is currently focused on helicopters, but it can be generalized for use with other vehicles.

MIDAS contains tools to describe the operating environment, equipment, and mission of manned systems with models of human cognitive and perceptual performance/behavior used in interactive and dynamic modes to evaluate aspects of the crewstation

design and operator task performance. Specifically, models of visual perception, visual attention, internal world representation, memory functions, rule-based and algorithmic decision-making, task loading, and scheduling behavior are represented. The models are encoded in an object-oriented architecture in which the individual models (as well as the system representation) are represented as interdependent agents that communicate with each other. The modular structure and strict communication protocol of this architecture allows MIDAS to support multiple representations of human performance at varied levels of detail. The testbed then serves both to support research on human performance models and to support designers of human-machine systems.

The results of MIDAS analysis are presented graphically to the research psychologists or design engineers, often as a computer simulation of crewed flight. In this sense, MIDAS is similar in concept to computational tools such as finite-element analysis and computational fluid dynamics which are used to improve designs and reduce costs. The simulation of humans interacting with equipment in a model-based gaming area provides data on operability, levels of automation, and functional allocation issues.

The program began in the fall of 1984, and four major phases of development have been completed toward a 1994 target date for a full prototype system. The most recent phase of development, demonstrated during June 1991, focused on the expansion of several elements of the system, along with the addition of a dynamic, opportunistic scheduling model, a task-loading model, and two new applied-vision models. The next phase of development will include the implementation of the full "agent-based" architecture and functionally integrated attention, perception, decision, and operator-internal-world representation models.

Ames-Moffett contact: E. Hartzell
(415) 604-5743

Headquarters program office: OAET

Context, Computation, and Complexity: Applications to Aviation Display Design

E. James Hartzell

The goal of this research with Chris Wickens of the University of Illinois is to establish how principles of display formatting and organization are modified by context effects, and how they can be provided within a computational framework in experimental scenarios that better approximate real-world complexity. Building on previous research that examined a number of specific display-design principles related to information integration, color, space, and display modalities, this research will supplement these known principles and explore their continued validity in the context of multi-element displays and in environments with increased task complexity. An objective is to establish the foundations of quantitative computational modeling that account for the higher-level cognitive processes involved in translating displayed information into task requirements, a necessary feature to allow some measure of display efficiency to be predicted in the context of the Army-NASA Aircrew/Aircraft Integration Program (A³I) Man-Machine Integration Design and Analysis System (MIDAS) workstation. The MIDAS symbolic operator model will be the vehicle by which that cognitive function is implemented.

Two general simulation environments have been used—the TASKILLAN simulation on an IRIS 2400 which provides much of the visual characterization of low-level helicopter flight with reference to HUD instruments, and a “generic display environment” created on an IBM AT to portray the graphical presen-

tation of instrument outputs. Investigations will be centered around theories of display proximity (referring to physical display variables that allow two or more channels of information to be perceived as similar) and task proximity (referring to the degree of relevance of two or more information processing channels to each other and/or to the unified goal of one task). The display quantification includes the number of display “objects,” spatial separation, consistency/compatibility in stimulus-response or stimulus-comprehension mappings, and resource competition.

The research findings and quantitative models arising from this study (which was started in 1989) are forming some of the core models used as part of the A³I program to predict operator performance and workload by simulating the complex interactions between mission demands, cockpit configuration, and pilot information-processing characteristics. An expert rule-based system, the Information Source Layout Expert, which helps a designer to evaluate displays on the basis of their consistency with cognitive function, has been implemented, and its knowledge base is being expanded to include multifunction displays.

**Ames-Moffett contact: E. Hartzell
(415) 604-5743**

Headquarters program office: OAET

Enhancing Air Traffic Control Displays

James C. Johnston, Krista Horlitz, Robert Edmiston

This aim of this project is to develop and test new display concepts that would improve the situation awareness of air traffic controllers. We believe that better use of displays will improve the safety and effectiveness with which air traffic controllers can function. The key to good human factors design is to, wherever possible, allow rapid and reliable perceptual processing of information rather than slow and unreliable cognitive processing. Present air traffic control (ATC) situation-awareness displays are outmoded; they provide visual/graphical representation of only a tiny portion of the information needed by controllers (principally X-Y map position of aircraft). Other information—especially altitude, altitude change, track vector, etc.—is not displayed graphically. It is either available only in an alphanumeric data block, where it must be fixated, identified, and then cognitively interpreted, or it is not displayed at all. It has been established that very-high-resolution color monitors will be available in future ATC equipment suites, but little is known about how best to use them to display other types of information.

The display scheme we have developed takes advantage of two important psychological principles: (1) color provides a powerful way to organize the visual field into sets of similar items—with color coding, different sets of items can be selected for attention with minimal effort; and (2) multiple items of information can be more rapidly encoded if they are

displayed as different properties of one object rather than as separate items. We have built a situation-awareness display that uses colored aircraft icons to code the track and altitude of aircraft. We are also examining schemes for visually flagging aircraft that are near boundaries between adjacent altitude layers to provide visual support for conflicts at color boundaries.

We have designed a series of laboratory experiments to determine empirically whether our new displays provide superior situation awareness. These experiments compare standard displays and our perceptually integrated displays in terms of how well viewers can locate aircraft that (1) are near a probe aircraft in altitude, (2) violate the x-y-z airspace of a probe aircraft, or (3) are on a collision course with a probe aircraft.

An extensive software package to implement these experiments has been written, and is in the final debugging phase. Data collection will begin shortly. If initial laboratory experiments on this display scheme are promising, we expect to test it further on high-fidelity ATC simulation systems available at Ames.

**Ames-Moffett contact: J. Johnston
(415) 604-5686**

Headquarters program office: OAET

Visual Cues for Temporal Range Estimation

Mary K. Kaiser, Lyn Mowafy

During rotorcraft nap-of-the-Earth (NOE) pilotage, it is desirable that the pilot be able to estimate the time it will take to reach a selected landmark in the visual scene. Mathematically, it can be shown that the time until that object passes (i.e., crosses the pilot's eye plane) is approximated by the visual angle between the object and the vehicle's heading vector divided by the rate of change of that angle. That is,

$$T_p @ f/d(f) = t_G$$

where T_p is the time to passage, f is the angle between the object and the heading vector, and $d(f)$ is this angle's temporal derivative (see first figure). This optical variable has been termed "global tau," or t_G , in the human-perception literature, since it would be gleaned from the global optical flow pattern that occurs when an observer moves in the environment. Most empirical research has focused on a related optical variable, "local tau" (t_L), which specifies when an object approaching the observer along the line of sight will reach the observer. Local tau has primarily been studied within the realm of skilled behavior (e.g., ball catching/dodging), and is of limited utility for pilotage because (a) it does not generalize to off-axis approaches, and (b) it has a limited temporal range of utility outside that required for orchestrating pilotage and strategic flight behavior.

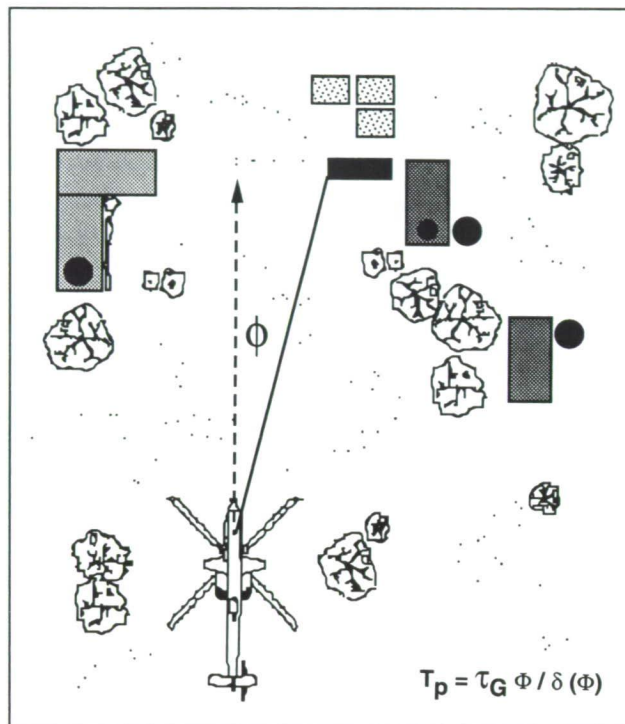


Fig. 1. Time to passage (T_p) is specified by the angular offset of an object from the heading vector (f) divided by the temporal derivative of that angle ($d(f)$).

We therefore conducted a series of studies of human observers' sensitivity to t_G . In both relative and absolute judgment tasks, observers were able to use the temporal range information provided by this optical variable. Performance was good for both relative and absolute range judgments (relative judgment data are shown in the second figure). Judgments were not affected by whether the object approached on the nasal or the temporal side of the observer (viewing was monocular) or by the object's proximity to the heading vector. This latter finding is in contrast to the performance of many passive range-estimation systems, whose performances degrade as a function of proximity to the heading vector.

Thus it appears that t_G is a source of optically specified information for perceiving time to passage that can be used adeptly by pilots for judging their spatiotemporal relationships with objects along their trajectories.

Ames-Moffett contact: M. Kaiser
(415) 604-4448

Headquarters program office: OAET

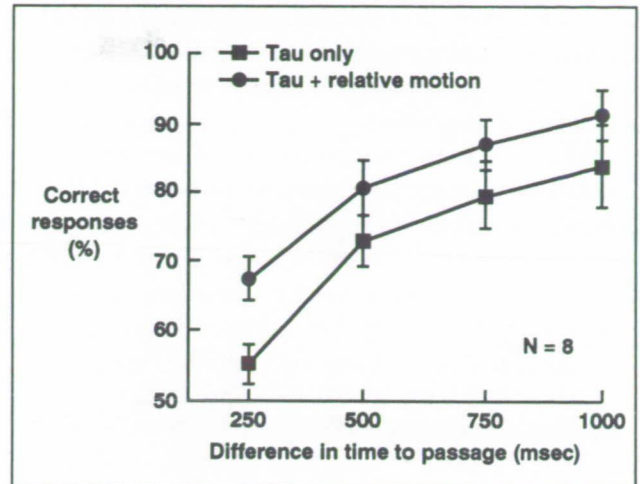


Fig. 2. Mean proportion of correct relative time-to-passage judgments as a function of temporal range separation, for eight observers.

Team Performance in Space-Analogous Environments

Barbara G. Kanki, Judith Orasanu

Crew Factors researchers have developed a program with the objective of providing guidance for the design and management of social, organizational, and task factors that are expected to affect crew productivity and well-being in long-duration space missions. Because there are limited opportunities to obtain data from actual space missions, this research concentrates on task-performing teams in operational environments that are analogous to space conditions, such as underwater research and mountain-climbing expeditions. A significant part of the research effort consists of finding appropriate space-analogous operations, gaining access to these work settings, and adapting our field methodology to fit the particular environment and mission.

In this study we have used data from the mountaineering environment. Although individual climbs can vary greatly in difficulty and duration, relevant

factors include dependency for survival on fellow crewmembers in high-stress operations, and limited access to outside support. Currently, we have data from 22 climb teams (122 individuals). We have been studying the influence of team structure and size on performance.

The 22 teams were categorized into four types: (1) teams of 2 to 4 members; or teams of greater than 4 members who (2) were military, or who (3) represented a formally or informally sponsored club or organization, or who (4) constituted a professionally guided group. Each type was also characterized according to particular social or organizational dimensions including degree of familiarity; degree of homogeneity in age, experience, and sex; and degree of formality in the authority structure, leadership, and role specialization. Team performance was defined as

a combination of task success ("summitting") and a consideration of team members' post-climb assessments of team coordination, interpersonal harmony, and effective leadership.

Teams of Type 1 and Type 4 (small groups and professionally guided groups) had the better summitting success rates and better self-assessment of team performance. In contrast, Types 2 and 3 (military and "clubs") had less success in summitting and more registered complaints in their assessments.

Although Type 1 teams achieved the best performance overall, it would be an overgeneralization to conclude that team size is the only predictor of team performance and team-member satisfaction. However, size is clearly important in determining other

team structure attributes such as management and leadership style. In this sample, smaller teams tended to be associated with different selection strategies, organizational policies, and leadership style. Thus in many cases there may be explanatory principles such as level of familiarity or homogeneity that drive the use of certain management policies and styles. Informal rather than formal differences in team structure may make the ultimate difference in team performance.

**Ames-Moffett contact: B. Kanki
(415) 604-5785**

Headquarters program office: OSSA

Social/Organizational Influences on Team Performance

Barbara G. Kanki, Judith Orasanu

This research program has been conducted through a collaborative effort including J. Richard Hackman at Harvard University, Ames researchers, and the U.S. Air Force Academy, to empirically identify major social and organizational influences on aeronautical and space crew performance. Such influences include leadership, crew formation, teambuilding, and role structure within crews, as well as the effective partitioning of authority and autonomy between flight crews and ground-based crews. Groups under investigation represent actual intact social systems performing their tasks within the normal operational context, and thus a large-scale, cross-organizational field investigation is required. The methodology for this observational study has been successfully applied in observing three U.S. air carriers, four international air carriers, and two military transport units.

Hackman's model for what makes an effective "self-correcting" crew includes four enabling conditions: (1) task design, (2) team design, (3) organizational support, and (4) team leadership. Initial results indicate that despite the fact that the organizations ranged from "struggling" to "strong" in the U.S. sample, and despite cultural differences across the international carriers, the primary differences were in

the organizational support category, which includes items such as job security, pay, and opportunity for advancement. The ways in which teams are designed and tasks are carried out seem to be standardized to a great extent. In addition to a report of the (obvious) findings (e.g., more stable economic conditions promote better team performance), each organization was provided a detailed profile of how they stood with respect to the other organizations: their strong points, average areas, and areas for improvement. This methodology or model is a useful diagnostic tool at the social/organizational level.

Many of the instruments developed and validated in this project have been adapted for use in several space-analogous environments, including the undersea and mountain-climbing environments, in order to characterize teams in terms of their organizational structure as well as their self-report assessments of team performance. Most recently, these instruments have been adapted to ground operations (specifically, launch control teams) and are being used for data collection.

**Ames-Moffett contact: B. Kanki
(415) 604-5785**

Headquarters program office: OSSA

Visibility Modeling Tool

James O. Larimer

Computer-aided engineering (CAE) has revolutionized the way engineers create designs. It is now possible to use mathematical models of objects or processes to evaluate the performance of a design before the object is actually built. Classic examples of CAE include the finite-element analysis of strength used to evaluate the forces acting on structures such as bridges, and the computational analysis of fluid dynamics used to evaluate the lift properties of wings. The visibility modeling tool is a human factors (HF) CAE tool designed to help the crewstation design engineer obtain answers to questions about the visibility of information in potential avionic displays. The primary goal of this HF/CAE visibility tool is to evaluate potential designs before they are built, thereby reducing design costs, enhancing the quality of the design engineer's product, and shortening the design time line. For this tool to be maximally useful, the evaluation that it provides to the engineer must be in an easily understood format. Thus, user friendliness through graphics is another goal of the project. The visibility modeling tool has been developed as an integrated component of the Army-NASA Aircrew/Aircraft Integration (A³I) HF/CAE system.

To model visibility it is necessary to consider (1) the three-dimensional (3-D) geometry of the crewstation or cockpit, (2) the reflective and emissive properties of surfaces and objects in that space, (3) ambient lighting, (4) the pilot's or astronaut's eye points, (5) what the pilot or astronaut is looking at, (6) how this affects convergence and accommodation,

(7) far, near, and retinal obstructions such as window posts, helmet margins, and retinal insensitivities, and (8) the current adaptation state of the pilot's visual system. All of these factors have been incorporated into the visibility modeling tool at a level of realism that is adequate to generate reasonably valid estimates of visibility.

The program is a mixture of in-house effort and grants and contracts with scientists at universities and research institutions. This mixture of effort is vertically integrated and covers a range of areas from problems of basic vision science to the application of 3-D models to problems in computer-aided design (CAD).

The basic computer system architecture (i.e., communication protocols and system integration) has been developed and tested; there is a 3-D CAD system for rapid prototyping of cockpits and cockpit avionics; and a 3-D pilot mannequin has been integrated into the system. The system also provides a computational model for the pilot's volume visual field, and a model of the legibility of letters and symbols in different presentation media and fonts has been integrated into the system. Basic developmental work is proceeding on the modeling of accommodation (i.e., human optical blur), surface quality, and ambient lighting.

**Ames-Moffett contact: J. Larimer
(415) 604-5185**

Headquarters program office: OAET

Display/Viewer System Models for Display Design

James O. Larimer

Active-matrix liquid crystal ("flat panel") displays are an attractive replacement for the traditional cathode-ray tube (CRT) avionic displays, because of their smaller space requirements. These devices, however, are complex, involving source lighting, colored filters, and light polarization. Unlike a CRT, the color, intensity, and contrast of a liquid-crystal display can change markedly when the display is viewed from different angles. The designer of such a display has a large number of choices to make. These often involve trade-offs in desired properties. For example, increasing the spatial detail by increasing the number of display dots will produce a decrease in brightness, since more of the screen will be covered with opaque drive circuitry. Computer models can allow display designers to observe the visual consequences of various design decisions before committing their designs to fabrication.

Display-configuration optimization cannot be done without knowledge of what the viewer needs to see and what he can see. Therefore, computational models for evaluating display quality must incorporate not only a model of the display, but a model of the viewer's visual system in order to evaluate the complete display/viewer system performance.

As the first step in building a workstation-based system for modeling both the physics of flat panel displays and the image processing by the human visual system, we have constructed a small prototype system. This tool allows pixel layouts and filter colors to be varied and the visual detection of display artifacts to be estimated. The tool also provides a CRT-based image of the simulated display.

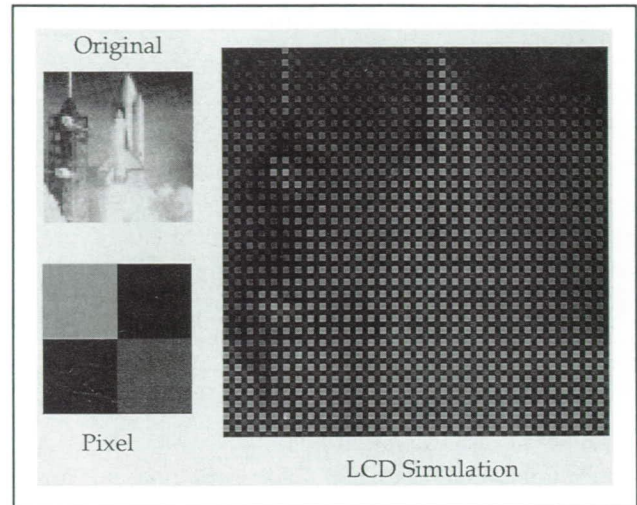


Fig. 1. Image of a rocket rendered in a low-resolution liquid crystal display. (See color plate 11 in Appendix)

The accompanying figure illustrates how an image might be visualized using a particular pixel layout. At the upper left, an original image of a shuttle launch is shown. At the lower left, a particular pixel microstructure which might be selected by the display designer is shown. The large image on the right shows the original rendered using this pixel structure. This image has been deliberately rendered at a low resolution to emphasize the appearance of the pixel mosaic.

**Ames-Moffett contact: J. Larimer
(415) 604-5185
Headquarters program office: OAET**

Data Link Human Factors Research

Sandra Lozito, Alison McGann, Kevin Corker

Digitized information transfer is a rapidly emerging and evolving communication method within the National Airspace System. The increasing focus on digitized information transfer represents an attempt to solve information transfer and management problems associated with conventional voice communications. The research at Ames Research Center focuses on the human factors issues associated with digitized information transfer and management, and includes research conducted in part-task simulation environments as well as in a full-mission environment.

In the part-task environment at Ames, we examined different formats of air traffic control (ATC) clearance information on a cathode-ray tube display. Although this study revealed no significant differences between formats, we plan to reexamine these display issues in a more context-sensitive part-task environment. The other phase of research took place in a full-mission context, using the Advanced Concept Flight Simulator at Ames. This phase allowed for the integration of other aircraft systems and procedures, as well as providing the increased fidelity of a full-mission simulation that includes real-time ATC transmissions. In the full-mission study, flight crews received ATC clearances in one of two ways: one group received clearances via voice, the other group received clearances via textual data link on a multifunction display. This study is permitting us to examine potential differences in the procedures involved in dealing with the two types of clearance transmission, and to examine alerting and message responses

specific to voice and to the data implementation used in the study. The data are currently being analyzed.

In addition to the work conducted at Ames, research on issues related to situation awareness was completed through a grant to the Massachusetts Institute of Technology (MIT). There is a concern within the aviation community that data link will result in a loss of "situation awareness" as a result of the decreased availability of voice transmissions from other aircraft. This notion of "party line" communications was explored by MIT in a survey of airline pilots and in the full-mission simulation at Ames.

The aviation community has also expressed concern about another feature of data link, the auto-load function. This function will allow a pilot to enter data from the digitized ATC clearance directly into the aircraft system (e.g., to enter an altitude change directly into the mode control panel). While this function is designed to reduce input errors and workload, the potential exists for one or all crewmembers to lose situation awareness. To research these issues in a part-task study at MIT, flight crews flew a simulation with various types of ATC clearance amendments, some that required direct (auto-load) entry into the aircraft and others that required manual entry. The data are being analyzed.

**Ames-Moffett contact: S. Lozito
(415) 604-6073**

Headquarters program office: OAET

Virtual Planetary Exploration

Michael W. McGreevy, Lewis Hitchner

The Virtual Planetary Exploration (VPE) effort is focused on developing an understanding of human spatial behaviors (locomotion, manipulation, cognition, and perception) in the context of planetary-surface exploration, with particular emphasis on visualization of, and interaction with, human-scale natural environments. This work is part of a long-term investigation of the problems of spatial information transfer in aerospace settings, and previous work with our group in that area has been widely recognized for its utility in the design and evaluation of perspective displays in aviation. The current international interest in "virtual reality" systems and applications is due in large part to pioneering efforts of the spatial information transfer team.

Virtual reality technology includes personal simulators and telepresence user interfaces. Such devices generally involve the use of body-ported displays and controls to surround the user with interactive spatial environments.

The VPE program is investigating the applications of the virtual reality paradigm to planetary-surface exploration. This is accomplished by a study of the archives of planetary exploration and by research conducted in the laboratory and in the field. Accomplishments include (1) a review of the operational experience and mission requirements regarding the role of spatial information transfer in planetary exploration; (2) field interviews with leading planetary geologists regarding geological field work and terrain data visualization; and (3) observation of exploration behaviors of geological site experts at the Amboy lava field in the Mojave Desert and at the Hualalai Volcano on the Island of Hawaii during multiday field trips.

A computer graphics tool, the Virtual Planetary Exploration User Testbed, has been developed to implement and evaluate concepts of user interactivity emerging from the reviews, interviews, and field trips. For example, a digital wrap-around display concept has been derived from the Surveyor Mosaic Spheres (Surveyor was the first U.S. uncrewed Moon lander). This same method was used to visualize images of the Viking landing sites and surrounding environments. To gain an appreciation of the user-interface issues of working with large data sets, Viking terrain data, including digital terrain models and digital image models, were obtained and explored as three-dimensional (3-D) interactive environments. As part of the review of future mission requirements, 10-centimeter-per-pixel laser rangefinder terrain data were obtained from the Planetary Rover Imaging Team, and 3-D virtual terrain environments were created and explored using the VPE system.

The VPE system has received uniformly positive comments from visiting scientists and engineers who are experienced in planetary-surface-exploration missions. A research proposal has been submitted by a NASA geologist to use the VPE system to visualize data from the Martian surface during the Mars Observer mission (to be launched in 1992). Mars Environmental Survey mission developers at Ames are collaborating on work with the VPE testbed to visualize the lander-vehicle entry trajectory, including the view from the lander as it swings and twists during its parachute descent to the surface.

**Ames-Moffett contact: McGreevy
(415) 604-5784**

Headquarters program office: OAET

Vision-Based Halftoning

Jeffrey B. Mulligan, Albert J. Ahumada

Some of the most promising technologies for large, high-resolution flat-panel displays that are being developed for aerospace applications are limited in their ability to represent shades of gray, and do better with images that are halftoned (binarized) to black and white only. The quality of such displays thus depends on the quality of the halftoning method. The commonly used halftoning methods were designed primarily for computational efficiency rather than for optimality with respect to the human visual system. To enable display designers to evaluate display quality independently of the rendering method, we are developing halftoning methods that are optimal for measures of display quality. These measures are based on computational models of human vision. These methods are expected to be slower than methods used in small printers (for example), but should have application whenever quality of the halftoned image is the paramount objective.

We have proceeded by optimizing a display-quality metric that measures the visibility of display artifacts. For this metric, the visual system is modeled as a linear filter that loses sensitivity at high spatial frequencies. We use the method of "simulated annealing" as our optimization procedure. In this method, the picture elements are considered one by one for a possible white/black reversal. An element is more likely to be changed if the change improves the overall quality, but it can also be changed to decrease the quality if the "temperature" of the process is high enough. If the temperature parameter is decreased at a very slow rate, the optimal halftone can be found, although this may require an inordinate amount of computer time. If the temperature is simply set to zero, the procedure converges rapidly to a situation where any single change makes the quality worse.

We have found that setting the temperature to zero produces images that are superior to those of the

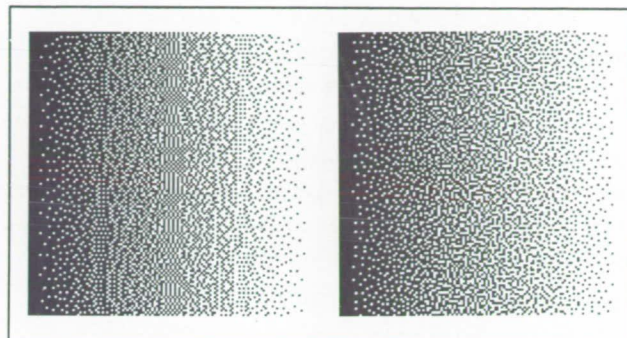


Fig. 1. Optimal image halftoning based on human vision models.

best competing method with respect to both the error metric and the subjective visual quality, as illustrated by the figure. For the visibility metric, computational methods were developed that run quickly on our engineering workstations. Even better images can be obtained with annealing schedules, whose properties we are studying to provide time-quality trade-off curves.

Unlike the methods commonly used for halftoning, our approach is tightly coupled to a model of the visual system; this will enable future advances in visual-system modeling to be applied directly to this problem. It also provides a general method for finding optimal halftones for more complex inputs, such as color images and image sequences. Furthermore, optimally halftoned images, for which the visible error is minimized, are useful benchmarks against which images halftoned by other methods may be compared.

**Ames-Moffett contact: J. Mulligan
(415) 604-3745**

Headquarters program office: OAET

Automation and Crew Coordination

Judith Orasanu, Barbara G. Kanki, Everett Palmer

The purpose of this simulator study was to examine the effect of cockpit automation on crew performance and crew coordination. Automation was varied by the choice of two radically different versions of the DC-9-series aircraft, the traditional DC-9-30 and the glass-cockpit derivative, the MD-88. Volunteer airline crews who were qualified in one of the two aircraft flew a predetermined scenario designed in the same manner as line-oriented flight training scenarios employed for training purposes by the airline.

The goals of the study were achieved primarily by comparing various performance measures of the crews in dealing with the situations introduced in the scenario, and particularly by examining the effect of the automation (two models of the same aircraft) on crew performance, coordination, and communication. The simulator runs were videotaped and examined in detail. In addition, two experts, the instructor, and a line-qualified pilot observer rated crew performance, and the crew rated their own performance and perception of workload. Errors in procedures were recorded, analyzed, and classified as to severity. Attitude questionnaires were administered to all members of the volunteer group, those who flew the scenario as well as those who did not.

The performance differences between the crews of the two aircraft were small, but the DC-9 crews generally showed better performance. There were no criteria on which the MD-88 crews performed better than the DC-9 crews. Furthermore, DC-9 crews rated their own workload as being lower than did the MD-88 pilots. It should be noted that whereas the groups were about equal in total flying experience, the DC-9 pilots were more experienced in flying DC-9s, and it is difficult to separate the effects of this factor. There were no significant differences between the two aircraft types with respect to the severity of errors committed during the simulated flight. The attitude questionnaires provided some interesting insights, but failed to distinguish between DC-9 and MD-88 pilots. Further analyses will focus on (1) more refined analyses of crew errors and associated behaviors and (2) detailed analyses of communication patterns that distinctively characterize crew coordination strategies associated with each aircraft type.

Ames-Moffett contact: J. Orasanu

(415) 604-3403

Headquarters program office: OSSA

Crew Factors in Aircrew Performance

Judith Orasanu, Barbara G. Kanki

Fundamental interactive and sequentially organized communication processes are critical to crew performance. They are the mechanisms by which crewmembers coordinate their activities, transmit and receive information, create a social climate, and solve problems. The Ames Crew Factors program has developed new techniques for analyzing group processes in both natural and high-fidelity simulated environments. We maintain a growing library of full-mission-simulation videotapes that includes 68 crews and over 100 hours of data.

Certain communication patterns (interactive speech act sequences) have been linked to crew performance differences (e.g., crew errors and coordination), as well as to other crew factors such as leader personality and levels of automation. Our communication-based program for analyzing group processes includes diverse perspectives representing different levels and types of analysis. The following analyses were all based on the transcribed and coded videotape data from a single full-mission flight simulation.

One analysis examined the language used for problem solving and decision making as crews coped more or less effectively with in-flight emergencies (in the simulator). Low-error crews engaged in more contingency planning, managed time and crew resources better, collected more relevant information before making a decision, and showed greater constraint sensitivity in making decisions. A second analysis of specific language functions suggested that more effective captains use communication to build common situation models with their crews, which assure coordinated, effective efforts. Analysis of interaction patterns has shown that high-performing captains, who are also highly task- and interpersonal-communication-oriented, appear to encourage two-way communication with their crews, while lower-performing captains, who are more authoritarian, create a generally authoritarian cockpit atmosphere. How these various communication patterns influence crew performance is the subject of ongoing analyses.

Ames-Moffett contact: J. Orasanu
(415) 604-3403
Headquarters program office: OSSA

Distributed Cognition

Everett Palmer

The introduction of industrial automation is often driven by noncognitive considerations, but automation inevitably has powerful effects on cognition. Automation on the flight decks of commercial jet transports is rapidly changing both the cognitive tasks that are faced by individual crewmembers and the cognitive properties of the flight deck itself as a system. Although a great deal is known about the abstract properties of individual cognition, much less is known about the properties of cognitive systems such as the flight deck, where the information-processing capabilities of the system result from a complex set of interactions among pilots and representational media.

The objective of this work is to develop a comprehensive framework for understanding cognition in real-world technical settings, where task-relevant information processes occur simultaneously in the automated system and in the individual operators. We have coined the term "distributed cognition" to refer to this approach. Cognitive science attempts to explain the behaviors of cognitive systems by reference to the representations they process. Many of the task-relevant representations processed by a cognitive system composed of people and technology in interaction are directly observable. A cognitive analysis of such a distributed system seeks to show how the properties of the system emerge from the interactions among the representations and representational media that constitute the system.

Three analyses of particular flight functions were based on simulator video data. They describe (1) the cognitive properties of the flight deck with respect to clearance handling, (2) the use of the B-727 second-officer's panel as a communicative resource in non-normal procedures, and (3) the use of approach plates and navigation displays in the B-747-400. The same theoretical framework was applied to jumpseat observations and aircraft documentation to produce an analysis of the use of speed bugs and flight-deck system memory for speeds at which configuration changes are required. An analysis of Air Safety Reporting System report narratives concerning altitude deviations demonstrates the role of redundant pathways for task-relevant information in error detection and correction.

It is hoped that the theory and methods developed in this project will improve the ability to anticipate the cognitive consequences of changes to flight-deck instrumentation and procedures.

This work was accomplished through a grant with Dr. Edwin Hutchins in the Cognitive Science Department of the University of California, San Diego.

**Ames-Moffett contact: E. Palmer
(415) 604-6073**

Headquarters program office: OAET

Electronic Checklists

Everett Palmer, Asaf Degani

Research in the area of cockpit procedures has shown that one of the disadvantages of a paper checklist is the lack of an explicit display of pending and completed procedural steps, as well as the inability to switch reliably between multiple active procedures. Electronic checklists can provide an external memory of pending, completed, and skipped steps. A touch-operated checklist can also use direct-manipulation graphic techniques to aid the pilot in switching from one procedure to another without losing track of partially completed checklists or getting lost in a bulky paper procedures manual.

Two electronic checklist designs, a manually sensed checklist and an automatically sensed checklist, were implemented and tested in a line-oriented flight simulation on the Advanced Concepts Flight Simulator. A paper checklist was used as a control. The crews were instructed and trained in the two electronic checklist versions. They were instructed to manually verify the paper checklist information, and to use the electronic checklists as a memory aid.

With both types of electronic checklist, all configuration tasks and actions on the secondary flight displays and overhead panel are still to be performed by the flight crew. With the manually sensed checklist, the pilot needs to manually acknowledge each item. The checklist automatically checks the condition of each item and displays the configuration, but it will not move to the next sequential item until the pilot has acknowledged the current item. With the automatically sensed checklist, the pilot does not have to manually acknowledge every item—the

checklist only requires acknowledgment of items that are sensed in the incorrect position. In broad terms, the manually sensed checklist provides a higher level of involvement and a lower level of automation than the automatically sensed checklist.

To verify whether the pilots were actually monitoring the state of the aircraft, they were observed after (1) a deliberate failure was caused in a system, and (2) the checklist was caused to provide a false indication that the system was correctly configured. In all cases the pilots were able to determine the true status of the system from the secondary displays or overhead panel, and had been instructed to do so for every checklist condition. In this experiment, the anti-skid system and the spoiler status were put in the incorrect configuration, and then the checklist (sensing incorrectly) indicated that the system was in the correct condition.

With both the manual and the automatic electronic checklists, the crews detected fewer of the configuration problems than with paper checklists. This is an example of "primary-secondary task inversion"—when a system intended as a backup becomes the primary indicator. In this case, the pilot started using the electronic checklist as a primary indicator, as opposed to the backup system it was designed to be.

**Ames-Moffett contact: E. Palmer
(415) 604-6073**

Headquarters program office: OAET

Human Self-Motion Perception

John Perrone, Leland S. Stone

Humans generally use a combination of visual and vestibular motion information to determine their direction of motion (heading) within their local three-dimensional (3-D) environment. They can also use visual motion to recover information about the 3-D structure of their environment (e.g., object distances and shapes). Visual self-motion information is important in any activity that involves movement of oneself or a craft through the environment and hence is an integral part of flight control and simulation. In the microgravity environment of space, the vestibular system does not function normally, and humans must therefore rely more heavily on vision when performing tasks during self-motion. Thus, understanding how humans use visual-motion cues for self-motion and structure estimation is critical for anticipating the deleterious effects of microgravity on performance and for designing either visual displays or training paradigms to counteract such effects.

We have a research program under way that combines human psychophysical experiments and computational modeling to gain insight into the self-motion-estimation problem. Some of the experiments have dealt with the processing of two-dimensional retinal image motion which represents the first stage of self-motion estimation. These experiments have revealed that speed and direction can be greatly misperceived under certain contrast conditions. These

results have led us to examine the possibility that certain natural viewing conditions (e.g., fog) could result in misperceptions of heading or approach angles. Such experiments have also enabled us to validate or rule out certain models of biological visual processing.

A second class of experiments has tested human performance in heading-estimation tasks. Our data are consistent with our own biologically based model of self-motion estimation which is able to recover observer heading, rotation, and depth information using networks of direction and speed-tuned motion sensors similar to those found in the motion-processing areas of the primate brain. The rationale for using a biologically based system is two-fold. First, it is likely to allow extrapolation to a wider range of performance predictions and second, such "reverse engineering" will, it is hoped, eventually lead to the design of artificial vision systems that are as robust and as fast as the human brain. By using computational modeling plus performance testing, we hope to bridge the gap between physiology and human performance.

**Ames-Moffett contact: L. Stone
(415) 604-3240**

Headquarters program office: OAET

Intelligent Integrated Displays for Launch-Control Operators

Roger Remington

Before the launch of a space shuttle, thousands of operations and tests are performed to ensure that all orbiter and support facility systems are operational and ready for launch. These steps, which range from activating the orbiter's flight computers to removing the launch pad from the itinerary of the visitor center's tour buses, are carried out at diverse locations by a team of launch personnel with highly specialized fields of expertise. The responsibility for coordinating this team rests with the NASA Test Director (NTD). We are studying the behavior of the NTD with the goal of building a detailed computational model of that behavior. We describe, in detail, the NTD's performance as a team member who must coordinate a complex task through efficient audio communication, note taking, and manual consultation. A model of the routine cognitive skills employed by the NTD to follow the launch countdown procedure manual has been implemented using the Soar cognitive architecture. The value of such a model is its ability to evaluate the cognitive demands of the current task, including the procedures and the suite of displays and controls available to accomplish the procedures. By modeling the NTD it will be possible to identify critical display needs and to evaluate, in a similar fashion, alternative interfaces to ensure that proposed solutions adequately enhance NTD capability.

The modeling effort is a central component of a larger program undertaken by the Human Interface Research Branch of the Aerospace Human Factors Research Division at Ames, whose goal is to develop specifications for advanced, integrated displays for launch-control personnel. In addition to modeling NTD behavior, we are developing prototype displays that address information presentation and control problems already apparent as a result of the modeling to date. In both the modeling and the display prototyping, the operational personnel in the NTD office are collaborative partners, whose role is to

inform and educate the research and development team, and to evaluate the resulting displays. The process of iterative evaluation will culminate in a set of specifications that describe the suite of interface tools required by the NTDs and how these tools will be integrated to ensure easy access to needed information. The program schedule is timed to coincide with the introduction of new hardware and software in the launch-control room that will significantly enhance the computational capability available to each team member.

The modeling and display prototyping are now proceeding in parallel. Modeling was begun in February 1990 with the initial information-gathering trip to Kennedy Space Center. Several subsequent observational trips have been made. In addition, we were able to analyze audio tapes of launch-control communications during several launch attempts. At present, we have a running computational model that simulates NTD communication during the last 20 minutes of launch countdown, assuming normal functioning. The model is currently being upgraded to account for interactions other than oral communications, and to deal with problem situations.

Display prototyping began in June 1991. At present we have an interactive electronic version of portions of the large operations manual which specifies all the tests that must be completed prior to launch. This electronic manual has been enthusiastically received by the NTDs themselves. We are currently extending its capability and developing a companion schedule display. The electronic manual and schedule will be integrated and tested during 1993.

**Ames-Moffett contact: R. Remington
(415) 604-6243**

Headquarters program office: OAET

Crew Fatigue Factors in Flight Operations

Mark R. Rosekind, Philippa Gander

The Ames Fatigue Countermeasures Program investigates the extent of fatigue, sleep loss, and disruption of circadian rhythms in different flight environments, and the impact of these factors on pilot performance. Field studies done in actual flight conditions are an important tool in this investigation. Previous field research has resulted in the world's largest data base on fatigue and circadian factors in flight crews. The data have been extensively analyzed to better understand the relationship between sleep and circadian rhythms in pilots. The results of two field studies designed to measure individual crew fatigue factors in flight operations are described below.

Commercial long-haul operations—A study was completed that investigated the factors influencing sleep timing and sleep quality during commercial long-haul flight operations. Twenty-nine flight crews were monitored before, during, and after a scheduled line of flying (up to nine days). Pilots were assessed with physiological and self-report measures, and a NASA cockpit observer detailed operational events during flights.

There were several important findings. The typical duty-layover cycle for these long-haul pilots consisted of 10 hours of duty and 25 hours of layover (off-duty period). During the layover, flightcrew members typically had two distinct sleep periods. The timing and duration of the sleep obtained during layover was greatly influenced by the circadian timing system and cumulative sleep loss. Generally, pilots preferred to sleep during local night. These results have significant implications for long-haul commercial flying. The circadian system can greatly affect sleep quality and duration in this complex operational setting. Also, the actual time available for sleep is less than the scheduled off-duty time. Finally, the duration of a layover

should take into account the local time of arrival, as well as the preceding sequence of trips. A NASA Technical Memorandum, TM-103852, on the results of this study has been published.

Commercial short-haul operations—Flight crews were studied before, during, and after a scheduled line of flying (3–4 days). Pilots were assessed with physiological and self-report measures, and a NASA cockpit observer detailed operational events during flights. Significant findings emerged in several areas. Overall, pilots lost about an hour of sleep each trip night and reported sleeping poorly compared to how they slept at home. The daily duty hours averaged more than twice the daily flight hours, so other activities besides flying composed a duty day. The pilot flying the aircraft had a significant increase in heart rate during descent and landing, showing a physiological response to the flight activity. More caffeine, alcohol, and snack foods were consumed during trips than at home.

These results provide important information on short-haul air transport operations. The current flight and duty time regulations should perhaps be evaluated based on duty hours rather than flight hours (which are currently used). The number of flight segments per day should continue to be regulated. Finally, methods to relax after duty would be helpful for short-haul pilots coming off their duty period. A NASA Technical Memorandum, TM-88321, on the results of this study has been published.

**Ames-Moffett contact: M. Rosekind
(415) 604-3921**

Headquarters program office: OAET

Fatigue Countermeasures in Flight Operations

Mark R. Rosekind, Philippa Gander

An active program is under way to identify, develop, and evaluate countermeasures to mitigate the effects of fatigue, sleep loss, and circadian rhythm disruption. These countermeasures can involve personal strategies, operational guidelines, and other approaches (e.g., education and training) to help pilots maintain their alertness and performance during flight operations. Field studies are an important way to obtain information and test countermeasures in actual flight conditions. Laboratory studies are also used to help distinguish the possible effectiveness of fatigue countermeasures before implementation on the flight deck. The results of both a field study and a laboratory study on possible fatigue countermeasures are described below.

Inflight sleep— Previous NASA research has documented the cumulative sleep loss and circadian changes that can create decreased alertness and fatigue in long-haul flying. A recent field study examined the effectiveness of a preplanned cockpit rest period in improving performance and alertness on the flightdeck during long-haul flights. The study was conducted with three-person nonaugmented B-747 crews flying trans-Pacific routes. One group of pilots was given a 40-minute rest period during the low-workload, cruise portion of flight. One pilot rested at a time, on a prearranged rotation. A comparison group of pilots did not have a rest period and continued their regular activities throughout the flight. A variety of physiological, performance, and self-report measures were used to determine whether the preplanned rest subsequently improved alertness and performance. The results showed that the pilots in the rest group were able to fall asleep quickly (in about 6 minutes) and sleep efficiently (for about 26 minutes) during the rest period. The brief nap helped pilots to perform better during later portions of a flight, on night flights, and after multiple flight legs, than pilots who did not get a rest period. Physiological measures of sleepiness suggested that pilots who had rested were subsequently more alert.

A brief preplanned rest period can act as a "safety valve" for some of the fatigue associated with long-haul flying. Based on the positive results of this study,

the Federal Aviation Administration has asked a NASA/Industry group to draft an Advisory Circular that will sanction preplanned cockpit rest in specific types of flight operations.

Bright light— The use of timed exposure to bright light has been suggested as a chronobiologic countermeasure for long-duration space operations. A laboratory study was conducted to test the effectiveness of bright light in accelerating the adaptation of sleep and circadian rhythms to schedule changes during simulated weightlessness (6-degree head-down tilt). Subjects were exposed to five hours of bright light daily for three consecutive days during and after a schedule change. The experimental treatment consisted of light pulses ending at the time of the daily temperature minimum, and was predicted to accelerate adaptation to the new schedule. The control treatment consisted of light pulses centered on the time of the daily temperature peak, which was predicted to have no effect. A variety of physiological and performance measures were taken.

The findings suggested that timing of the light exposure made little or no difference in the rates of circadian rhythm adaptation. The different circadian rhythms adapted at different rates, comparable to the rates recorded after time zone crossings in ambulatory subjects. These data suggest that bright light may not be a robust countermeasure to aid resynchronization after schedule shifts in simulated weightlessness. Another significant finding was that the polygraphic recording of sleep in simulated weightlessness showed shorter sleep periods, similar to findings in actual space flight. This indicates that simulated weightlessness in laboratory conditions is a promising analog to long-duration space flight for testing fatigue countermeasures. A NASA Technical Memorandum, TM-103874, on the results of this study has been published.

Ames-Moffett contact: M. Rosekind
(415) 604-3921

Headquarters program office: OAET

The Astronaut Science Advisor

Irving C. Statler

The objective of the Astronaut Science Advisor (ASA) (also called PI-in-a-box) is to provide on-line support to astronauts performing a scientific experiment when the principal investigator (PI) on the ground may not be available for consultation. The mechanism uses an "expert system" concept to enable an astronaut, who may be only minimally trained in the science, to adapt the experiment to changes in available time, equipment troubles, and data that do not fit expectations, and thereby enhance the on-board science.

The effectiveness of such an advisory system depends to a large extent on its acceptability to the operator. Consequently, a considerable effort is being made to ensure good astronaut-ASA interaction through an understanding of the expected interactions and an appropriate user-friendly design of the interface. The purposes of the Aerospace Human Factors Research Division's participation in this project team are to develop anecdotal scenarios of interactions, particularly in unexpected situations, to stimulate discussions among members of the team about these scenarios, and to establish consensus on expected interactions. After interactions are agreed upon, it is possible to decide what data must be displayed and in what format for the interface design.

The experiment selected for the first application of the ASA is a test of the effects of microgravity on the human oculovestibular system. This experiment has flown on two Skylabs, and recently flew on SLS-1 (June 1991). It is scheduled to fly on SLS-2 in May 1993. It is also a likely experiment for Space Station Freedom.

An early version of the ASA was used during the baseline data collection in preparation for the SLS-1 mission. During the SLS-1 mission, this ASA was

situated in a conference room next to the science monitoring area in a preliminary experiment to see how it might support the PI on the ground while a basic experiment was being conducted on the Spacelab. Because of a variety of circumstances not related to its normal operation, the ASA proved to be of only limited value to the PI during the flight. However, it was demonstrated that the ASA might have been very useful aboard the Spacelab, had it been designed and used properly. There were several unplanned situations in which the ASA (even in its current form) could have saved the astronauts much time and stress. The SLS-1 experience brought certain human factors issues to the attention of the project team. A paper on the lessons learned from SLS-1 relative to human factors was presented at a meeting of NASA researchers in July 1991. These issues have relevance to the design of most advisory systems.

The ASA is expected to fly for the first time with the experiment on visually induced perception of self motion on SLS-2. We expect to introduce many modifications to it before then. We are continuing to develop the task analyses for the operator's interactions with the ASA. Many of the scenarios will be modified as a result of SLS-1. Using these task analyses, we will assist the Information Sciences Division in designing the interfaces. These will eventually be evaluated by the astronauts. Our division will participate in the interface evaluation, training, and the evaluation of the ASA by the astronauts during SLS-2.

**Ames-Moffett contact: I. Statler
(415) 604-6938**

Headquarters program office: OAET

Perceptual Compression of Digital Video

Andrew B. Watson

The next era of space exploration, especially the "Mission to Planet Earth," will generate immense volumes of scientific and operational data. For example, the Earth Observing System (EOS) is expected to generate more than one terabyte per day. Much of this information will be imagery, broadly defined as measurements distributed over space and time. We confront a major technical challenge in managing this great flow of imagery: in collection, preprocessing, transmission to Earth, archiving, and distribution to scientists at remote locations. Expected requirements

in most of these areas clearly exceed current technology. Part of the solution to this problem lies in methods of coding digital imagery that are more efficient and flexible than existing techniques.

We are exploring image codes that are designed to match the capability of the human eye, in the form of what we call a perceptual components architecture (PCA). This is a scheme for decomposing the video signal into the elementary signals to which the human eye is tuned. In theory, this should produce highly efficient codes.

The figure shows the fundamental PCA decomposition of the video signal. It depicts regions in three-dimensional (two space and one time) frequency that are partitioned from one another and separately sampled, quantized, and coded. The regions are localized in spatial frequency and orientation, and in temporal frequency.

We have implemented two prototypes of PCA, one in the high-level language Mathematica, the other in the programming language C. The former is useful for algorithm design and testing, the latter for evaluating code performance. Initial tests on full-color, motion-video image sequences are promising. Current work is devoted to optimizing quantization parameters for PCA.

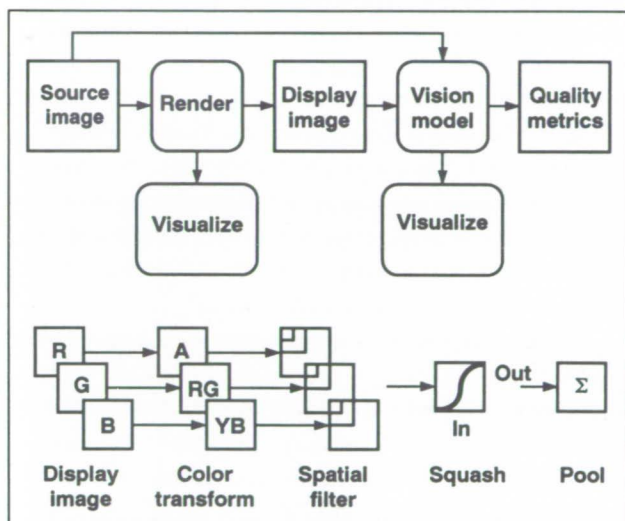


Fig. 1. Three-dimensional frequency partition of the video signal implemented by the perceptual components architecture.

Ames-Moffett contact: A. Watson
(415) 604-5419

Headquarters program office: OAET

Listening with Someone Else's Ears

Elizabeth M. Wenzel

A recent development in advanced interfaces is the virtual acoustic display, a system that enhances situational awareness by presenting three-dimensional auditory information over headphones. Primary advantages include the ability to monitor and identify sources of information from all possible locations, improved intelligibility in sources of noise, enhanced segregation of multiple sound sources, and, in conjunction with the other senses, reinforcement of information combined with a greater sense of presence or realism. Such features could be especially critical for applications that are inherently spatial, such as air traffic control, aviation collision-avoidance warning systems, extravehicular activity in space, and telerobotic control.

Synthesis of virtual sources involves the digital filtering of sounds using filters based on acoustic head-related transfer functions (HRTFs) measured in human ear canals. In practice, measurement of the HRTFs of each potential user may not be feasible. Thus a critical research question is whether inexperienced listeners can obtain useful directional information in a virtual acoustic display without the cues being individualized for each user. Early experience has suggested that using nonindividualized HRTFs is possible, as long as the filters that are used were originally measured for someone with accurate localization in both real-world and synthesized conditions. This study represents a more formal test of this hypothesis. Sixteen blindfolded listeners judged the apparent spatial location (azimuth (left/right) and elevation (up/down)) of stationary sounds presented either through loudspeakers in the free field (a non-

reverberant environment) or through headphones. The headphone sounds were synthesized using HRTFs from a "good localizer" in a previous study.

Localization of both free-field and virtual sources was accurate for 12 of the subjects; two showed poor elevation accuracy in both free-field and headphone conditions, and two showed degraded elevation accuracy only with virtual sources (first figure). High rates of confusion errors (reversals in judgments of azimuth and elevation) were also observed for about half of the subjects, and tended to increase for the virtual sources. As in previous studies using individualized HRTFs, individual differences occur primarily for elevation. Azimuth judgments, on the other hand, appeared to be accurate overall. Azimuth confusions (largely reversals to the rear) approximately tripled when nonindividualized filters were used. No previous studies have analyzed confusions in elevation. Although the average rates are lower, confusions in elevation are also a potential source of increased error in the simulation of localized sources.

In general, the data suggest that most listeners can obtain useful directional information from a spatial auditory display without individually tailored HRTFs, particularly for the dimension of azimuth. However, the high rates of reversals for some people remain problematic. Comparison to a study using subjects' own HRTFs suggests that "listening through someone else's ears" primarily results in an increase in front-to-back reversals. Note, however, that the existence of free-field confusions shows that these reversals occur

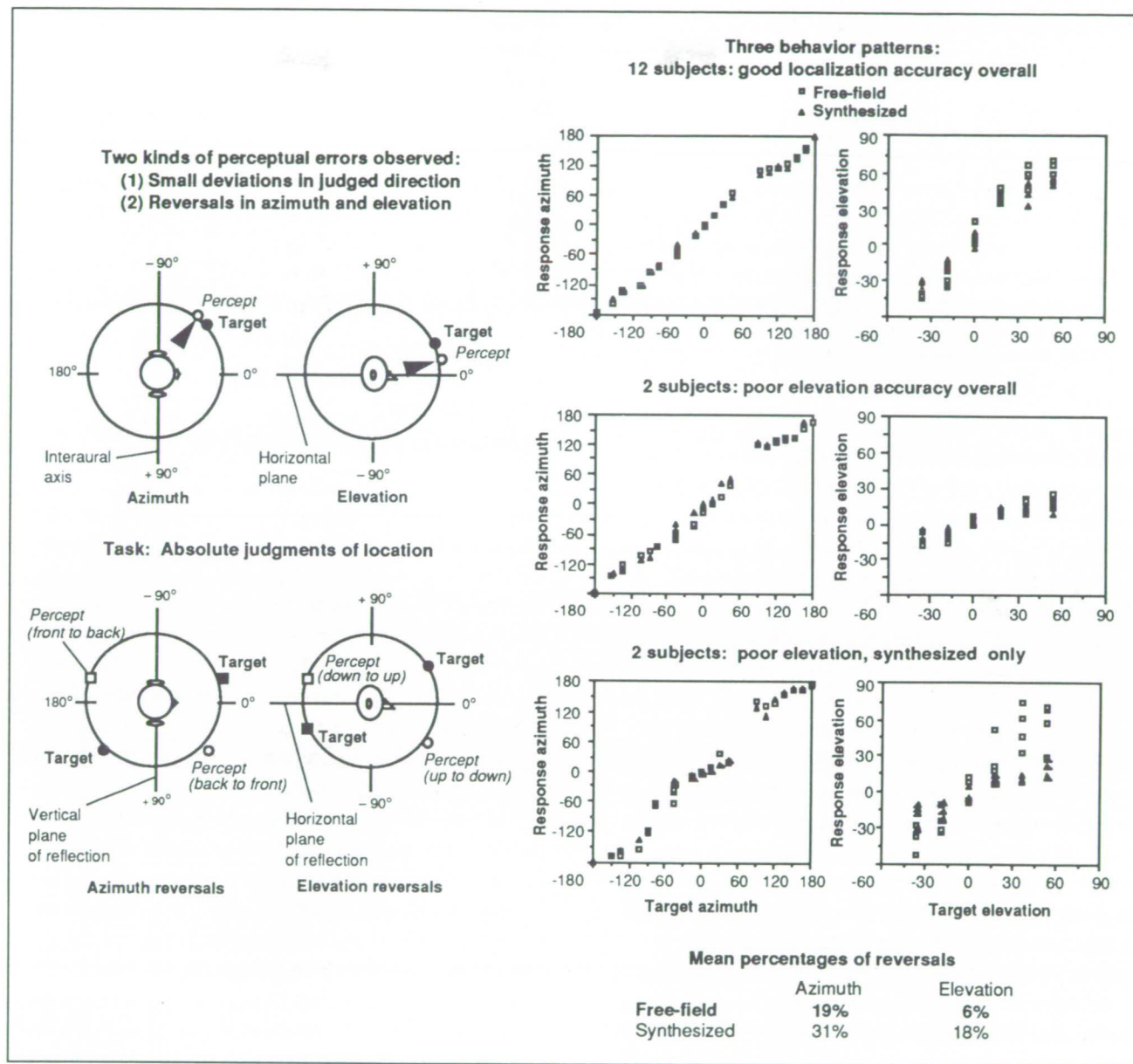


Fig. 1. Listening with someone else's ears.

in the real world and so are not strictly the result of the simulation.

The reversals are probably due in large part to the fact that the sounds used here were stationary as well as to the predicted ambiguity resulting from the so-called cone of confusion. Assuming a stationary,

spherical model of the head, a given interaural time or intensity difference (two critical localization cues) correlates ambiguously with the direction of a sound source, with a conical shell describing the locations of all possible sources (second figure). Thus, in the

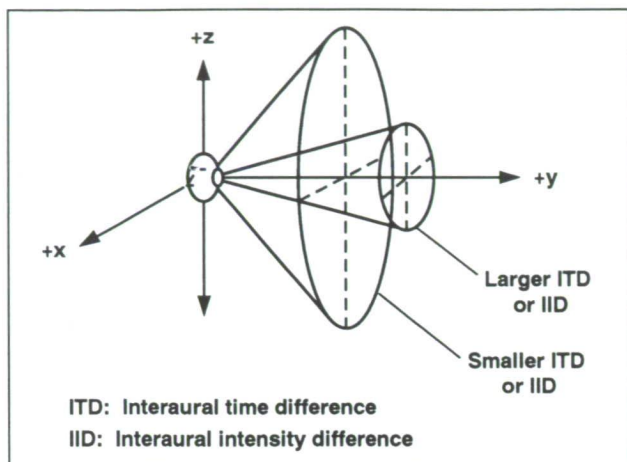


Fig. 2. Cones of confusion.

absence of other distinguishing features, any position along that cone could be confused with any other. Several stimulus characteristics may help to minimize these errors and are being examined in current and future studies. For example, the addition of dynamic cues that are correlated with head motion, well controlled environmental cues that are generated from models of room acoustics, and correlated visual cues should improve the ability to resolve these ambiguities and substantially enhance the efficacy of any virtual acoustic display.

Ames-Moffett contact: E. Wenzel
(415) 604-6290

Headquarters program office: OAET

Simulating Complex Virtual Acoustic Environments

Elizabeth M. Wenzel

Spatial auditory displays require the ability to generate localized sound cues in a flexible and dynamic manner. Researchers at Ames are currently investigating the underlying perceptual principles of auditory displays and are also developing an advanced signal processor (a "convolvotron") based on these principles. Rather than using a spherical array of speakers, the processor maximizes portability by synthetically generating three-dimensional sound cues in real time for delivery through earphones. Unlike conventional stereo, sources are perceived outside the head at discrete distances and directions from the listener. This is made possible by numerically modeling the effects of the outer ears (the pinnae) on the sounds perceived at various spatial locations. These "head-related transfer functions" (HRTFs) can then be applied to arbitrary sounds (voices, for example) in order to cause them to seem spatially located. The convolvotron is a set of two printed-circuit boards hosted by an 80386 personal computer which is capable of synthesizing up to four independent and simultaneous localized sources and implementing smooth-motion trajectories in a head-stable environment. It is currently being used in a variety of government, academic, and industrial

laboratories as well as in the Ames Spatial Auditory Displays Lab.

Whereas the initial implementation simulates only the direct paths of up to four virtual sources to the listener, it possesses a high degree of interactivity. That is, in a simple anechoic space, it is possible to freely manipulate source position, listener position, and listener orientation in a dynamic, real-time display. For a variety of reasons, it is desirable to be able to achieve the same level of interactivity in more complex acoustic environments. One important reason is that psychoacoustical research suggests that synthesis of purely anechoic signals can result in perceptual errors, in particular front-back reversals and failure of externalization. There is reason to believe that such errors can be alleviated by providing more complex cues resulting from reverberant environments.

Of particular interest here is the work on "image models" for simulating room characteristics with synthetic early reflections using a kind of "ray-tracing" approach. Following such models, we simulate the presence of a reflecting surface (e.g., a wall) in the environment by placing a delayed "image" source

behind the reflector to account for the reflection of the source signal, as if a virtual loudspeaker were mounted behind the wall (see figure). Thus what the listener hears is the superposition of the direct path from the source on the image sources coming from all the reflectors in the environment. Currently, the filtering effect of the reflecting surface is modeled with a finite impulse response filter that is changed in real time. The output from this filter is passed into a long delay line with variable tap points for each of the image sources to be simulated. Thus, whereas reflecting properties such as high-frequency absorption can be changed overall, all surfaces behave in a similar fashion in this simulation. The tap points are adjusted to correspond to the propagation delay from each image source being modeled. Finally, the delayed signal for each image source is processed with the appropriate HRTF filters to create one component of the binaural output. The superposition of these components on the original HRTF-filtered source (the direct path from source to listener) is then presented over headphones. Arbitrary source, reflector, and listener positions with variable listener orientation are possible.

This kind of dynamic modeling requires enormous computational resources for real-time implementation in a truly interactive display. Even with a convolver it is not practical to render more than first- or second-order reflections from a very small number of reflecting surfaces. However, recent research and our own early experience indicates that much of the useful information is present in these

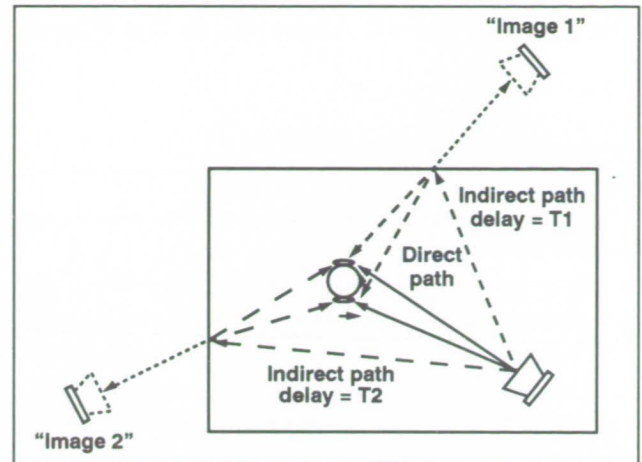


Fig. 1. Image model of a reverberant environment. Two early reflections added.

early reflections, particularly lateral reflections. In future work, we plan to extend this simulation to more realistic models of acoustic environments. Some of the issues that need to be addressed are diffuse reflections, scattering reflectors, diffraction and partial obscuration by walls or other objects, atmospheric absorption, near-field effects (e.g., head-shadowing), and perceptually viable methods of simplifying the synthesis technique.

Ames-Moffett contact: E. Wenzel

(415) 604-6290

Headquarters program office: OAET

Neural Network Algorithms for Passive Ranging

Yair Barniv

Helicopters in covert nap-of-the-Earth operations require passive ranging for obstacle avoidance. A single or a stereo pair of forward-looking cameras can be used to produce a stream of images (per camera). The velocity vectors of all points in the image plane, as obtained from the imagery stream, constitute the Optical Flow (OF) which can directly yield ranges to these points. Two main approaches have been considered: feature-based, which requires the identification of objects in successive frames, and field-based, which operates on all pixels. Both approaches require massive information storage and processing capabilities.

Neural Networks (NNets), consisting of highly parallel, multiply connected processing units, are potentially suitable for such tasks. NASA has demonstrated the applicability of NNets as associative memories, binary encoders, and obstacle detectors in navigation systems. Our goal is to investigate the applicability of NNets for the problem of passive ranging.

There are several ways to derive range from OF. One way, which is independent of image-plane location and the vehicle's maneuvers, is based on calculating the (local) divergence which measures the local expansion at any desired point. Divergence is reliable in areas of appreciable texture. Global divergence, defined as the average divergence over the area of an object, is more robust for objects that exhibit distinct edges. Such objects, e.g., man-made ones, tend to have uniform texture, and thus local divergence is not reliable. The two divergence methods therefore appear to be complementary.

We are currently working on combining the above two methods. The (local) divergence, which is a field-based method, is to be calculated by an NNet trained to derive divergence by examples. The global divergence (a feature- or object-based method) is

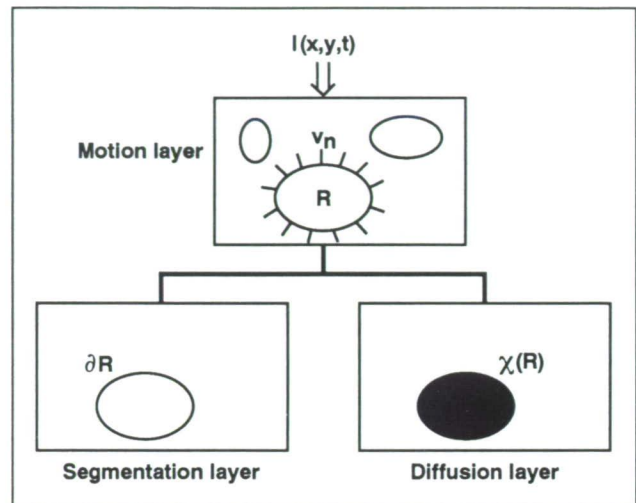


Fig. 1. Estimating range using a neural network.

derived by another NNet which emulates a biological model of cells found in the vision system of monkeys. This work was originally performed with our support at the Technion, Israel, and is currently undergoing performance evaluation and modifications here at Ames.

A block diagram of the global divergence method is shown in the figure. The stream of images $I(x,y,t)$ enters the first layer of neurons which calculate the motion-vector component normal to the local edge for all points in the scene. The segmentation layer delineates objects based on their moving edges while the diffusion layer performs the averaging operation on the (local) divergence over the area of every object. The details of the field-based algorithm were described last year.

Ames-Moffett contact: Y. Barniv

(415) 604-5451

Headquarters program office: OAST

Automated Nap-of-the-Earth Guidance and Control

V. H. L. Cheng

The automated nap-of-the-Earth (NOE) guidance and control development effort involves conceptualization, development, and evaluation of candidate guidance and control laws with obstacle-avoidance capabilities in the ground-hugging flight regime. The effort will provide technologies needed to realize pilot-directed flight with automatic obstacle-avoidance safeguard, or completely hands-off flight.

To demonstrate the feasibility of an automatic system, the initial effort has focused on the development of a basic but functionally complete set of guidance and control capabilities that observes the capabilities and limitations of obstacle-detection sensor systems being developed. A workstation-based,

real-time graphical helicopter simulation (HELsim) has been developed to provide the readily available means for rapid evaluation of conceived guidance and control laws.

The first version of a full three-dimensional obstacle-avoidance guidance and control system has been developed and implemented on the in-house graphical simulation. The obstacle-detection sensor function is simulated in real time using the depth buffer hardware in the graphics workstation to provide range measurements. These range measurements are converted to altitude data stored in an inertial data base for use by the guidance system. The first figure shows the components of the guidance and autopilot

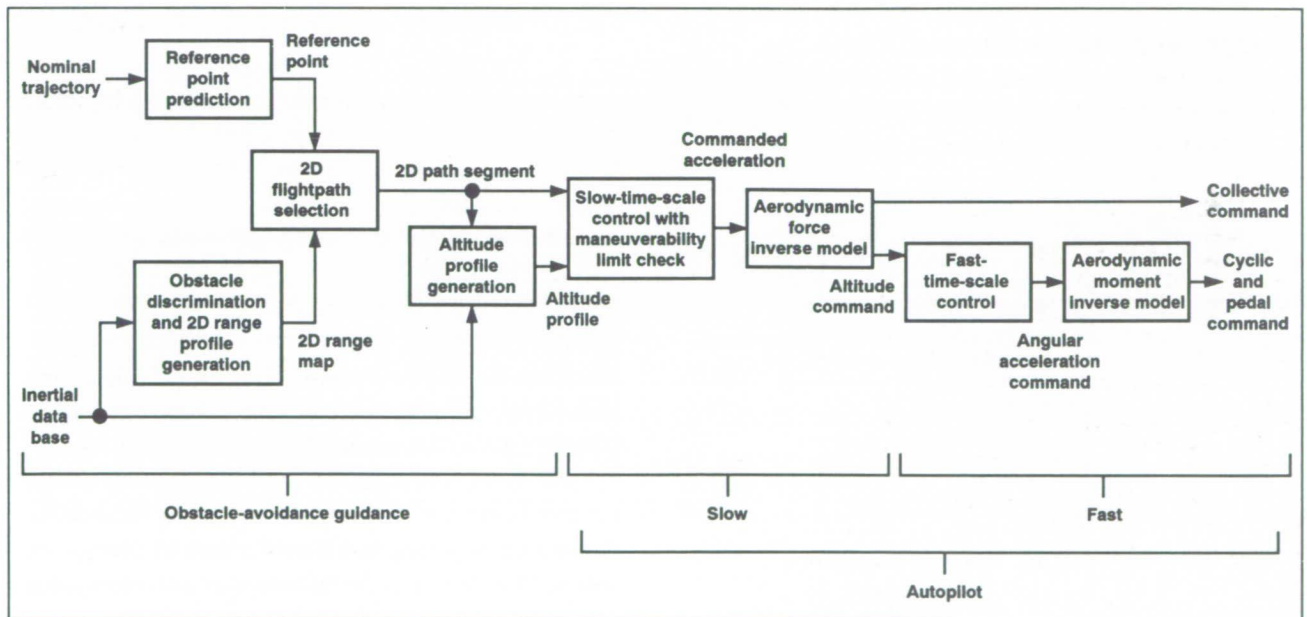


Fig. 1. Automated nap-of-the-Earth guidance and control systems.

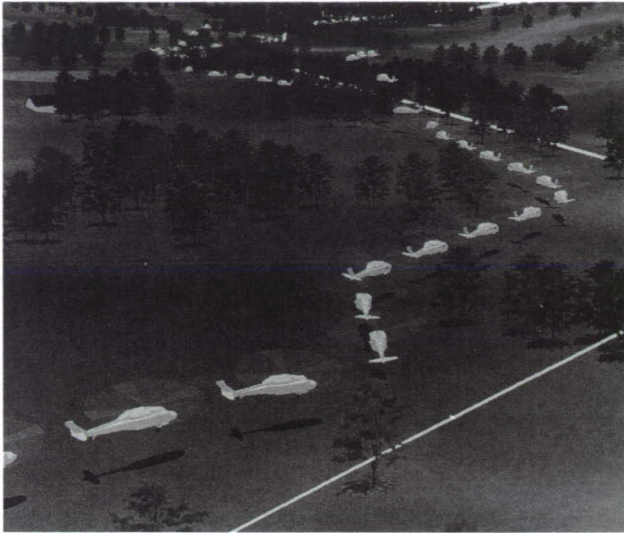


Fig. 2. Sample obstacle-avoidance trajectory flown with automatic guidance and control.

systems. The autopilot design is based on time-scale separation and nonlinear aerodynamics inverse, and it generates the necessary vehicle control commands. Special logic has been defined to safely couple to the autopilot the trajectory commanded by the guidance, within the tight margins in the NOE regime.

The second figure shows a sample trajectory flown by the fully automatic guidance and control systems. The guidance system is trying to follow a nominal trajectory indicated by the white line, with deviations resulting from obstacle-avoidance maneuvers.

Ames-Moffett contact: V. Cheng
(415) 604-5424

Headquarters program office: OAST

Helicopter Flight Simulation

V. H. L. Cheng, T. Lam

The helicopter flight simulation HELSIM was originally developed by the Automated Nap-of-the-Earth Program as an in-house research tool for evaluating automatic helicopter guidance techniques in nap-of-the-Earth flight. It is an interactive helicopter flight simulation program that runs on Silicon Graphics, Inc., 4D computer graphics workstations.

In addition to the capability of simulating automatic flight, HELSIM has the provision for manual control inputs: the current implementation allows for pitch and roll cyclic inputs through a joystick, and for collective and directional (pedal) inputs through the mouse. The helicopter aerodynamics model is generic, although the graphics model shows a UH-60 helicopter. HELSIM permits multiple viewing perspectives, including a cockpit view, a God's eye view, and a wingman's view. The graphical display in the figure illustrates these views, along with other commonly

used window displays including a digital terrain map, a simple instrument display, and HELSIM's control panel. HELSIM's other features include adjustable lighting conditions, flight history recording/playback, and a retrace capability that allows a stored trajectory to be displayed statically showing the helicopter's position and attitude at different instants of time.

A limited "object editor" has been developed in conjunction with HELSIM, allowing easy definition of data bases involving objects such as trees, buildings, and telephone poles. The objects are placed automatically on the terrain surface. Random generation of many objects simultaneously over user-defined areas is possible, facilitating quick definition of natural-looking scenarios.

Because of the modularity and flexibility of the simulation, HELSIM can be easily adapted to other

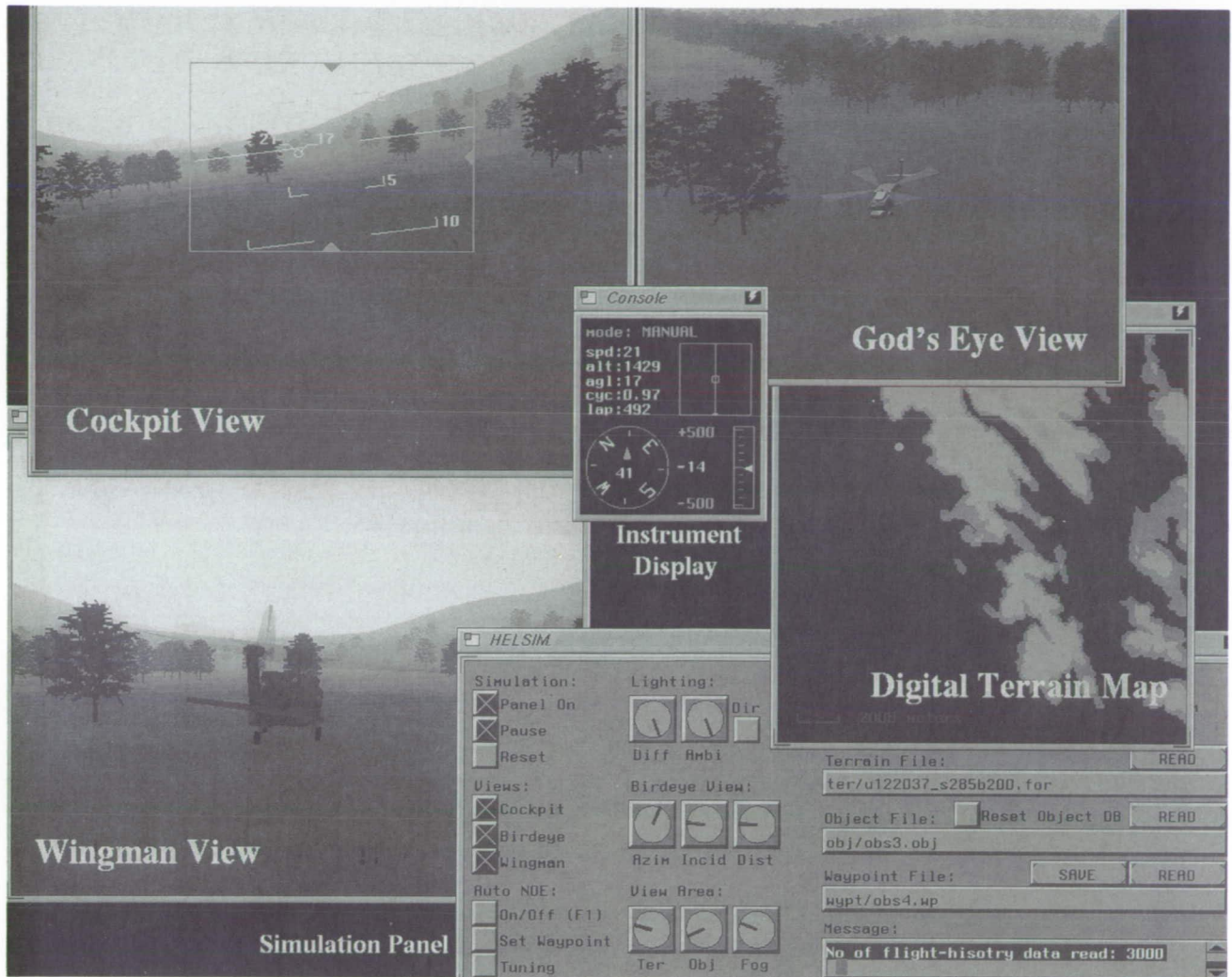


Fig. 1. Example of HELSIM graphical display.

applications: human factors research, pilot interface and display development, controller design, etc. It has been disseminated to various organizations within NASA, other government agencies, industry, and academia.

Ames-Moffett contact: V. Cheng

(415) 604-5424

Headquarters program office: OAST

ORIGINAL PAGE
BLACK AND WHITE PHOTOGRAPH

Evaluation of Automated Nap-of-the-Earth Guidance

R. Coppenbarger, V. H. L. Cheng

Extensive evaluation via computer simulations has been carried out to identify the capabilities and limitations of two separate guidance laws developed for rotorcraft automated nap-of-the-Earth flight: one developed by a contractor and the other developed by the Aircraft Guidance and Navigation Branch at Ames. In spite of the automation, the application involves human-occupied vehicles, and thus ride comfort remains an issue.

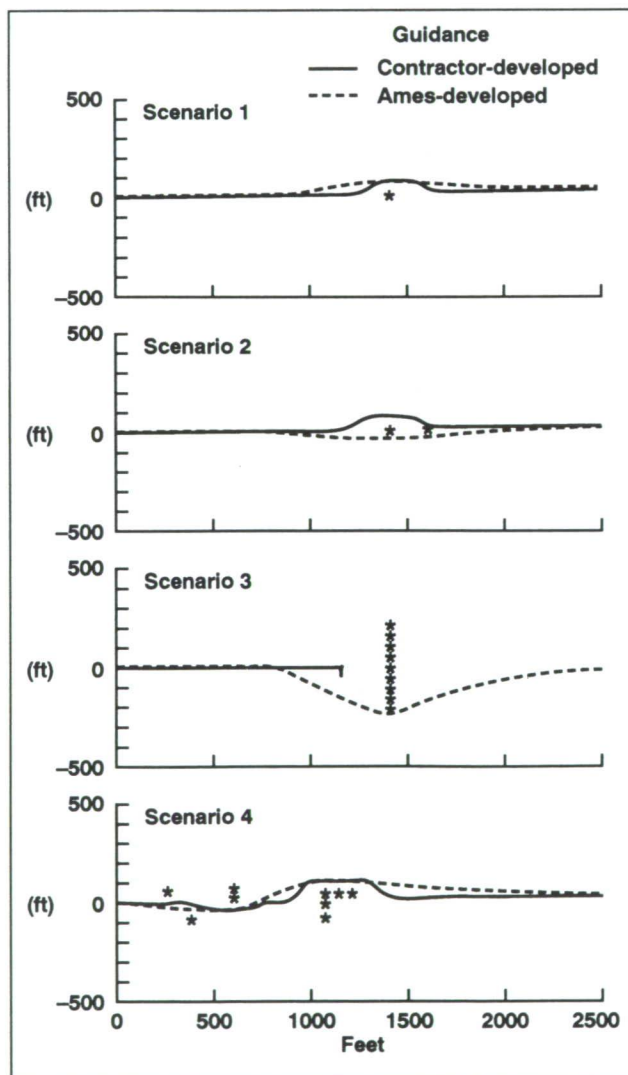


Fig. 1. Example of obstacle-avoidance guidance trajectories.

The contract effort addressed this issue directly via piloted simulation on the Vertical Motion Simulator at Ames. Initial findings based on pilot opinion generally concluded that the maneuvers to avoid the obstacles modeled in the simulation were acceptable. Subsequently, the guidance was transferred to an in-house computer for closer examination of its obstacle-avoidance capabilities. This follow-on evaluation revealed that the automatic guidance scheme is limited in its ability to negotiate obstacle scenarios more general than the one used in the piloted simulation. Furthermore, it requires idealized obstacle information, which is unrealistic for sensors that cannot see through objects.

The Ames guidance, on the other hand, has not yet been tested under piloted conditions. However, its development has emphasized the limitations of the sensors. In addition, it is designed to make full use of the sensor's field of view for obstacle-avoidance flightpath selection, in contrast to the contractor-developed guidance's search of an unnecessarily narrow corridor.

The figure illustrates the trajectories generated by the two different guidance schemes under four simple scenarios. The third scenario shows a situation in which the contractor-developed guidance fails to recognize the possibility of going around the row of objects. However, despite the superior performance of the Ames guidance in flightpath selection, it is less mature in addressing the issue of pilot-acceptable maneuver limits. This is where the findings from the contract effort will be beneficial for future refinement of the automatic guidance law.

Ames-Moffett contact: R. Coppenbarger
(415) 604-5433
Headquarters program office: OAST

RASCAL Flight Facility

Michelle M. Eshow

The Rotorcraft Aircrew Systems Concepts Airborne Laboratory (RASCAL) is being built up from a UH-60A Black Hawk helicopter at Ames Research Center. RASCAL will support several national research programs for Ames and the U.S. Army Aeroflightdynamics Directorate, including Super-augmented Concepts for Agile Maneuvering Performance (SCAMP) and the Automated Nap-of-the-Earth Program (ANOE). Other programs are the Army's Rotorcraft Pilot's Associate and Covert Day/Night Operations for Rotorcraft programs, as well as FAA research interests in helicopter terminal-area operations.

The RASCAL facility will be built up incrementally to support the progressive phases of the research programs. The first facility-development phase is to install complete instrumentation of the vehicle controls and states to support SCAMP-related work in model verification and baseline agility measures. This capability is nearly complete; a first flight of the vehicle with the data-collection system operating was conducted, on schedule, in December 1991. Early in 1992, a stereo video imaging system will be added to support the ANOE obstacle-detection research. Subsequent phases include installation of rotor-state sensors in 1993; a color, wide-field-of-view helmet-mounted display in early 1994; passive ranging sensors in early 1995; and a full-authority, programmable, fly-by-wire flight control system by late 1995. A paper describing the research programs and the plans for development of RASCAL was presented at

the International Symposium on In-Flight Simulation for the 1990s in Braunschweig, Germany, in July 1991.

Aircraft development this year included installation of a baseline set of motion sensors and a data-acquisition system, as noted above. In addition, major progress was made in designing the research systems required to achieve all of the capabilities required through 1995. The design team considered many interrelated attributes of the system, including safety, achievable research flight envelope, and research productivity, flexibility, cost, and schedule. The resulting system design provided a major step toward the detailed specification of components such as the helmet-mounted display, video image generation, guidance and display computers, rigid-body and rotor-state sensors, flight control computers, fly-by-wire actuators, safety-monitoring features, and the supporting ground development facility. A phased-development approach was proposed that is consistent with funding plans and research program requirements over the next four years.

More detailed specification of the RASCAL components and initiation of contracts to provide them is planned for 1992.

**Ames-Moffett contact: M. Eshow
(415) 604-5272**

Headquarters program office: OAST

Four-Dimensional Aircraft/Air Traffic Control Integration Study

Steven Green, Wim den Braven

A real-time air traffic control (ATC) simulation was conducted to investigate issues regarding the integration of an aircraft equipped with the four-dimensional (4-D) Flight Management System (FMS) into an advanced ATC environment. The ATC environment, simulated at Ames, was based on the Center/TRACON Automation System (CTAS). The 4-D-FMS-equipped aircraft was simulated by the Langley Transport Systems Research Vehicle (TSRV) cockpit simulator which was linked to the Ames ATC simulation in real time. This experiment, completed in May 1991, was the second joint ATC simulation involving both Ames and Langley.

The previous study (July 1989) indicated that 4-D aircraft operations, under moderate traffic conditions, were not feasible if the pilot flew a vertical profile (i.e., top of descent, and speed in cruise and descent) that was substantially different from the controller's plan. "Differing profiles" often resulted in a traffic conflict, the resolution of which would result in an overall reduction in traffic fuel efficiency (compared to the case where no 4-D clearance was issued). In addition, the study found that 4-D operations were too complex and difficult under voice communications; digital datalink may be required.

The focus of this simulation was to develop and evaluate the Profile Negotiation Process (PNP) to allow an FMS-equipped aircraft to negotiate with ATC for the most efficient trajectory subject to ATC constraints (e.g., separation, routing, scheduling, or metering). The PNP requires the exchange of trajectory data between the air and the ground, and the capability of ATC to analyze profile proposals. The ground-based part of an air/ground datalink system was developed at Ames and integrated with CTAS to assist the controller with the monitoring of traffic and the creation of datalink messages. Conflict probing and resolution functions were also developed for CTAS to allow the controller to evaluate the traffic situation and determine conflict-free trajectories.

The figure illustrates the controller's display during one of the traffic scenarios. The display shows the TSRV (NASA 515) on a delay vector as well as CTAS's analysis of the TSRV's preferred trajectory

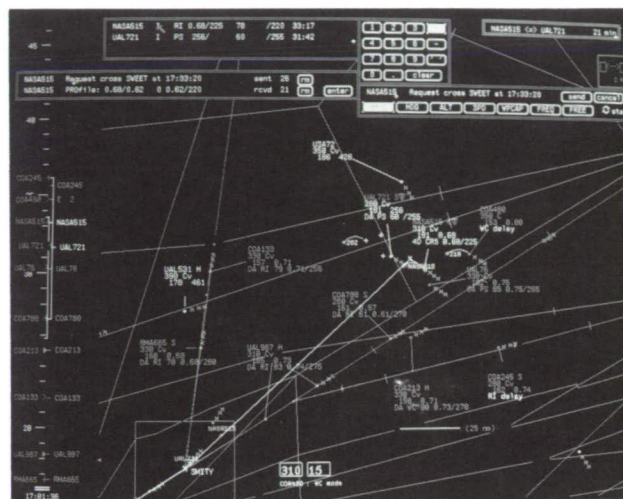


Fig. 1. Integration of advanced cockpit and ATC automation via datalink.

(note the conflict predicted in 21 minutes). The controller would solve this problem by using CTAS to determine a modified vertical profile or horizontal path that would resolve the conflict and meet the schedule. The display also shows the datalink control panel (right) and the datalink message status panel (left), as well as other CTAS features.

Simulation results showed that the PNP successfully produced conflict-free trajectories while improving fuel efficiency (on the order of 8% for a 200-nautical-mile flight with a descent from FL310 to FL110 and a delay of 8 minutes) under moderate traffic conditions. However, the controllers did indicate the need for the PNP to be more transparent, with the automation making more of the decisions regarding conflict resolution and fuel burn minimization. The datalink was well received by the controllers, and much was learned regarding the ground-based issues of air/ground datalink operations, particularly the synergism gained by integrating datalink with CTAS.

**Ames-Moffett contact: S. Green
(415) 604-5431**

Headquarters program office: OAST

Field Evaluation of CTAS

A. David Jones

Simulation studies of the Center/TRACON Automation System (CTAS), a set of automation aids to assist controllers in decision-making, have demonstrated a strong potential for air traffic control (ATC) system-wide benefits including fuel savings, reduced delays, and increased controller productivity. However, before a decision is made to implement these tools nationwide, another step is required: field evaluations at selected centers and Terminal Radar Approach Control Facilities (TRACONs). This step is required because the tools are sufficiently complex that simulations alone cannot validate the use of the tools; rather, live traffic evaluations by the controller staff at selected sites are required to verify the utility and reliability of the tools under all runway configurations and in 24-hour operations. The Federal Aviation Administration (FAA) has agreed to conduct these evaluations jointly with NASA and has recently designated two centers (Denver and Dallas/Fort Worth) and two TRACONs (Denver and Dallas/Fort Worth) for initial field testing. NASA participation in the CTAS evaluations is critical for two reasons. First, if the evaluations are successful, a decision will be made to implement these Ames-developed tools system-wide. Second, the knowledge obtained in transitioning from the present system to a more automated one that incorporates CTAS is critical to NASA's advanced ATC automation program, which will consider the potential of new technology coupled with increased automation for the ATC system.

For each of the FAA designated sites, the following will take place:

1. Real-time simulation evaluations at Ames conducted by an FAA-designated team of controllers with

broad experiences, as well as evaluations with controllers from the designated site

2. Safety/system validation at the FAA Technical Center
3. Initial site visit/coordination
4. Informal training/evaluations by two or three selected controllers using the CTAS tools in a nonoperational area
5. Training of the controller staff and informal evaluations in the operational area
6. Formal evaluation/analysis of automation system benefits

In order to meet its responsibilities in the joint NASA-FAA evaluation program for CTAS, Ames has created an ATC Field Systems Office within the Flight Systems and Simulation Research Division. This new office, working closely with the ATC research staff in the Aircraft Guidance and Navigation Branch, is responsible for ensuring that Ames successfully meets its commitments to the FAA during the evaluation phase. The office will (1) clearly define Ames' responsibilities in the context of the total NASA/FAA program, (2) manage hardware and software interfaces with FAA facilities, (3) conduct validation testing of transferred hardware and software, (4) provide necessary documentation, (5) support FAA safety and operational validation testing, and (6) support the field operational testing at up to three FAA-designated sites.

Ames-Moffett contact: D. Jones

(415) 604-5928

Headquarters program office: OAST

The Traffic Management Advisory Station

Frank Neuman

The Federal Aviation Administration (FAA) has designated the Denver and Dallas/Fort Worth Terminal Radar Approach Control Facilities (TRACONs) and the associated enroute centers as the initial evaluation sites for the Center/TRACON Automation System (CTAS), an integrated set of automation aids developed at Ames. Based on these evaluations, a national implementation decision will be made which will lead to a nationwide implementation of CTAS in the current air traffic control system as well as the future Advanced Automation System.

The initial installation of CTAS consists of the set of tools known as the Traffic Management Advisor (TMA) which is concerned with sequencing and scheduling; the initial site is the Denver Air Route Traffic Control Center (ARTCC) in Longmont, Colorado. The hardware associated with the TMA is located in the traffic management area of the ARTCC operation. Initial evaluation will begin in 1992.

The TMA station (see figure) consists of two physical displays (19-inch color monitors), each with a keyboard and associated processors, that communicate with each other and receive traffic data from the host computer and weather data from the National Meteorological Center. Each of the monitors can perform several functions. One function is the TMA, which presents the traffic on time lines in a mixed graphic and alphanumeric format. Alternatively, the same monitor can display atmospheric data via a graphical user interface. The second monitor can be configured as a horizontal situation display, which displays radar positions of aircraft in a plan view format. In addition, a laser printer, located outside the operations area, provides hard copies of traffic data, such as trajectory and traffic statistics plots.

The primary display to be evaluated is the TMA. The TMA assists the traffic management coordinator in four ways:

1. It generates and displays in a graphical form the sequential order and landing-time schedule for arrival aircraft.
2. It allows the traffic management coordinator to override the automatic schedule—for example, to manually insert additional aircraft.

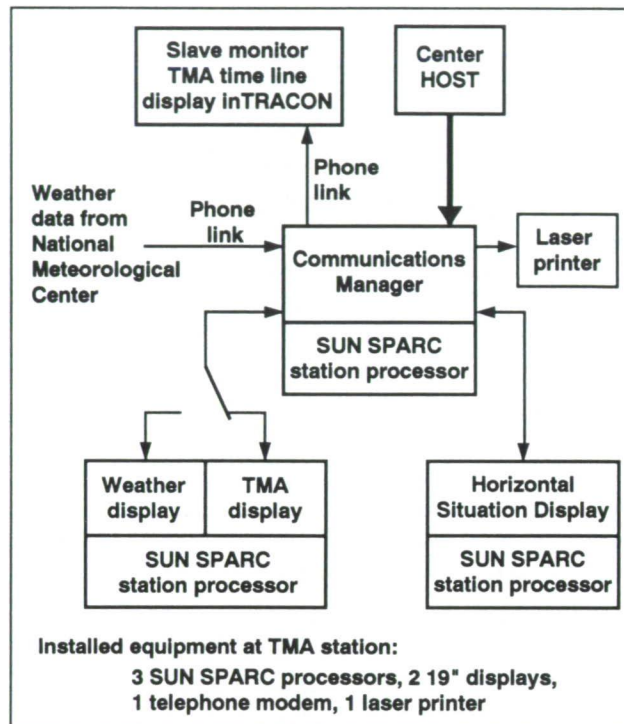


Fig. 1. Field installation of TMA station.

3. It provides several traffic-prediction displays to aid in decision-making.
4. It provides historical 24-hour traffic-analysis data on the screen and as hard copy.

The expected outputs from the field evaluations of the TMA are as follows:

1. An improved TMA capability based on traffic-management-coordinator recommendations.
2. A determination of whether the aid provides a potential benefit to Denver in the form of more effective data collection.
3. Identification of how the TMA can be used to assess the effect of potential operational changes, such as runway change or closure, or modified aircraft arrival rate for the center as a whole and for specific arrival gates.

Ames-Moffett contact: F. Neuman
(415) 604-5437

Headquarters program office: OAST

Attitude Control with Linear Error Dynamics

Previous attitude control theory can be divided into two major approaches, which will be referred to as the state linearization approach and the Lyapunov approach. This work introduces a third approach, the error linearization approach, which incorporates features of the other two but avoids their main problems.

In the state linearization approach, nonlinear transformations are used to realize an exact linear model for the rotational dynamics, and linear control theory is applied. A serious problem with this approach is that it is based on an improper definition of attitude error. Another serious problem is that the attitude control law is singular at certain attitudes, even with no attitude error.

In the Lyapunov approach, a control law is postulated by intuition. It is based on a proper definition of attitude error in terms of rotation group algebra. However, since the resulting error dynamics are nonlinear, the stability analysis requires the discovery of Lyapunov functions by intuition. Moreover, important concepts such as damping and loop bandwidth are not well defined as in linear control theory.

In the new error linearization approach, an attitude control law is derived to realize linear

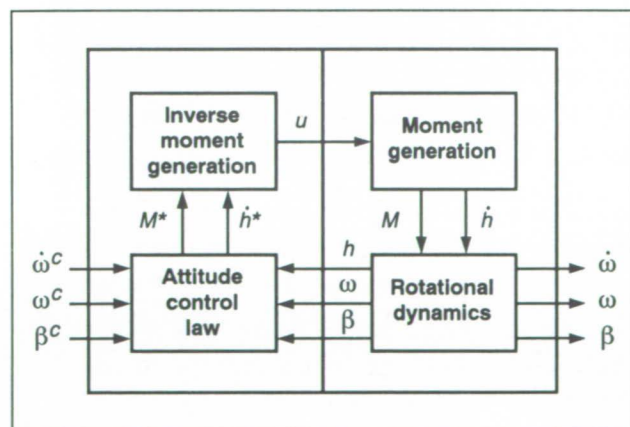


Fig. 1. Simplified attitude controller and vehicle.

Russell Paielli, Ralph Bach

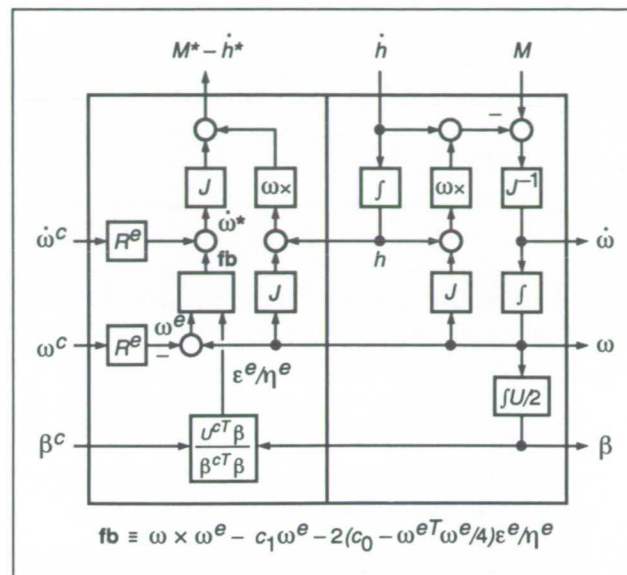


Fig. 2. Attitude control law and vehicle rotational dynamics.

unforced error dynamics as in the state linearization approach but, as in the Lyapunov approach, the control law is based on a proper definition of attitude error in terms of rotation group algebra. The non-minimal (four-parameter) Euler parameter form is used for attitude in the rotational dynamics model because it is globally nonsingular, but the minimal (three-parameter) Euler parameter form is used for attitude error in the error dynamics model because it has no nonlinear mathematical constraints to prevent realization of linear error dynamics. The control law is singular only when the attitude error angle about any eigenaxis is exactly π radians. A simple heuristic fix around the singularity allows the control law to be used globally.

A simplified diagram of the attitude controller is shown in the first figure, and a detailed diagram of the attitude control law is shown, along with the rotational dynamics, in the second figure. The

symbols are defined as follows: β represents the four Euler parameters corresponding to the attitude of the body frame relative to the inertial frame, ϵ represents the first three Euler parameters, and η represents the fourth; ω represents the body coordinates of the inertial angular rate; M represents the body coordinates of the applied moment; h represents the body coordinates of the internal angular momentum (stored in reaction wheels or control moment gyros); U represents a column-orthogonal transformation

matrix that is a function of the Euler parameters; J represents the inertia tensor; and R represents a rotation matrix. Superscripts are defined as follows: c indicates an open-loop feedforward command; e indicates a rotational error; and $*$ indicates a closed-loop feedforward/feedback command.

Ames-Moffett contact: R. Paielli

(415) 604-5454

Headquarters program office: OAST

Passive Range Map Refinement Using Texture and Segmentation

Banavar Sridhar

The design of intelligent guidance and control for aerospace systems requires information about the location of objects in the nominal path of the vehicle. Electro-optical sensors provide a covert way of computing range during helicopter flight. The optical-flow-based computation of range provides range information only in certain distinguishable parts of the image. Object location information over the field of view (FOV) is referred to as a range map. The objective of this program is to increase the regions where range information is available by performing texture analysis and object segmentation in the image.

Gray-scale images are characterized by pixels of varying intensity. Any image can be described by the texture or the nature of the distribution of the gray levels across the image. Research on the use of texture for image segmentation is motivated by the classification problems associated with target detection and remote sensing. This usually involves a single object against a background and orthographic imaging conditions. In the helicopter range refinement problem, we have several objects at various ranges and nonorthographic imaging conditions.

We approach this problem in a hierarchical manner: (1) perform an initial segmentation based on

co-occurrence matrix or relative contrast algorithm, (2) remove the effects of average tone by tone-normalizing the image, and (3) use a homogeneity measure such as intensity variance to further segment the tone-normalized image. The figure shows the original image and a segmented image produced by the segmentation algorithm. In addition, because of the non-crisp nature of object boundaries in an image, the advantages of using fuzzy segmentation is under evaluation.

Significant accomplishments during this year include (1) development of the three-step segmentation algorithm, (2) application of the algorithm to a real-world image consisting of vertical objects on the ground at various distances, and (3) development of a segmentation based on fuzzy clustering. The results of this research were presented at the 1991 AIAA Conference on Aerospace Sensors.

Our results indicate that it will be necessary to combine several different texture measures and methods in a hierarchical way in order to achieve an object segmentation that is useful in enhancing range information. We plan to report on the application of

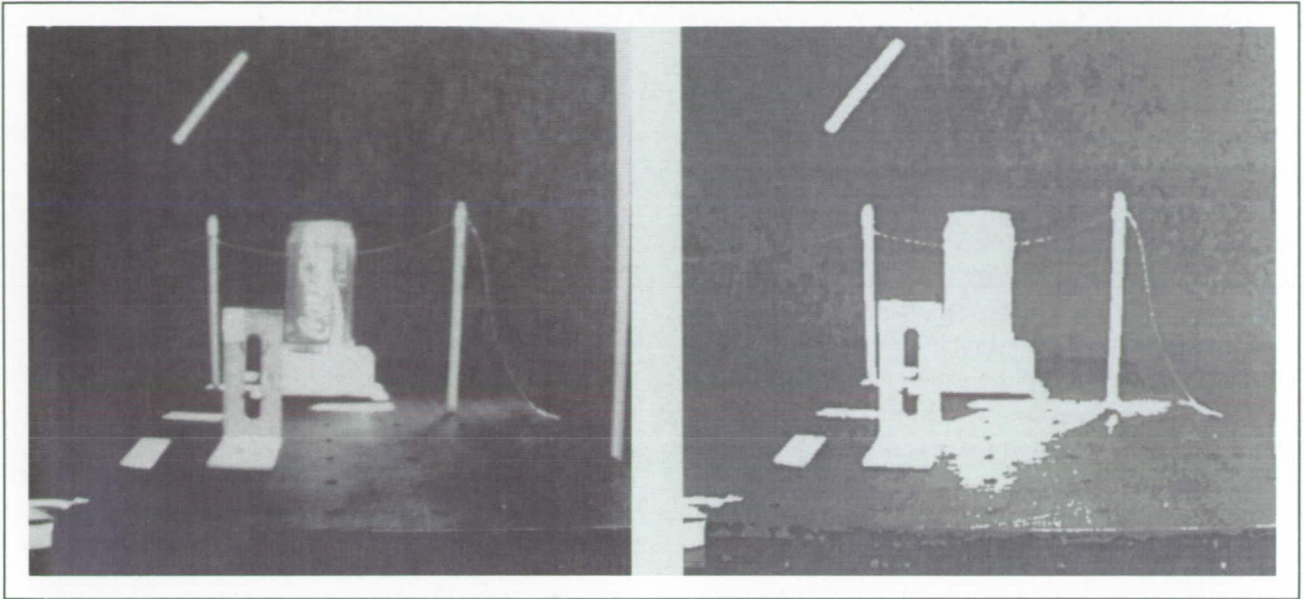


Fig. 1. Image segmentation.

this method to outdoor scenes collected from a helicopter. The object segmentation together with the range map from the integrated motion and stereo algorithms will provide an enhanced range map for use by rotorcraft obstacle-avoidance algorithms.

Ames-Moffett contact: B. Sridhar

(415) 604-5450

Headquarters program office: OAST

ORIGINAL PAGE
BLACK AND WHITE PHOTOGRAPH

Vision-Based Techniques for Rotorcraft Low-Altitude Flight

Banavar Sridhar, Raymond Suorsa

The development of a methodology for detecting the distances to obstacles based on the maximum utilization of passive sensors presents challenging problems in computer vision and image understanding. Our research is focused on identifying and developing the key components of vision-based obstacle-detection capability for rotorcraft nap-of-the-Earth flight. Because vision alone is not adequate for detecting small obstacles such as wires, it is expected that the system will include an active sensor whose search area can be directed to complement the vision system. The research effort is composed of vision algorithm development, evaluation, and real-time processing.

The block diagram shows the configuration of an integrated vision/active range sensor system. We have

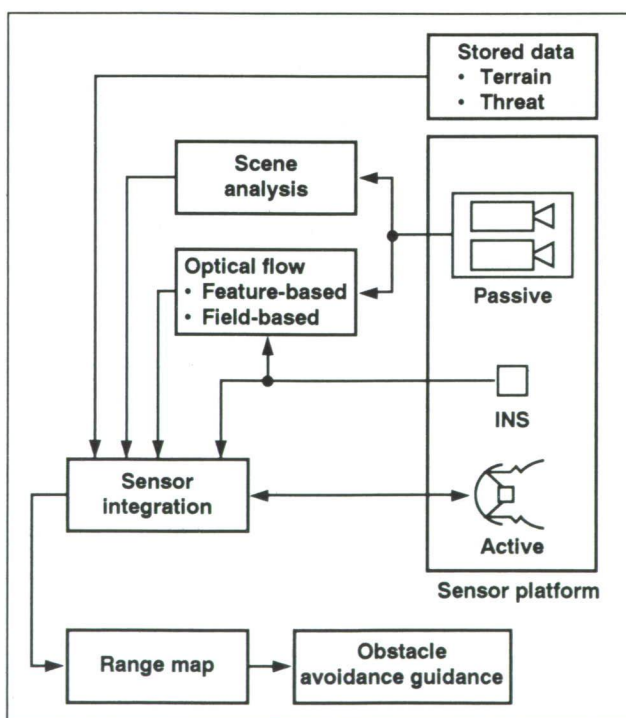


Fig. 1. Obstacle detection system.

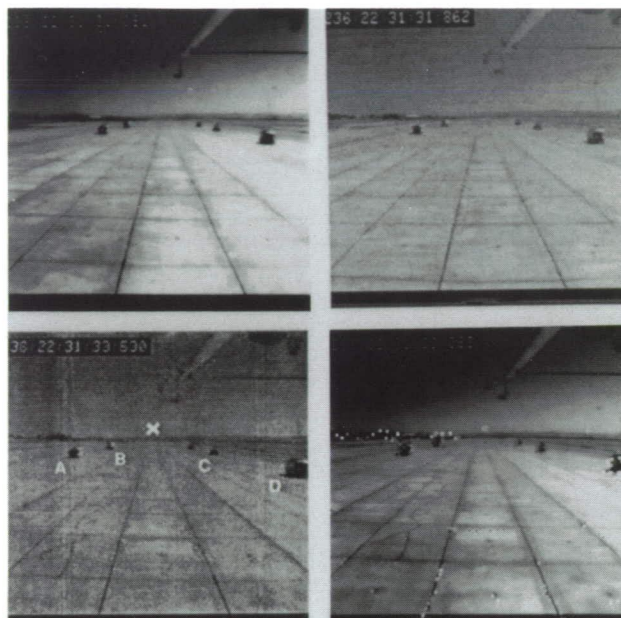


Fig. 2. Flight sequence.

developed algorithms for passive ranging using both feature-based and field-based techniques. Scene analysis methods, e.g., texture and segmentation, will be used to enhance the sparse range map resulting from the passive ranging algorithms.

We have evaluated the feature-based passive ranging algorithms using image sequences acquired in flight. The data base was developed using the NASA CH-47 helicopter. The second figure shows four images in a sequence of 76 images. The helicopter was flying above the runway at an altitude of about 13 feet and a speed of 20 knots. The helicopter covers a distance of about 1 foot between images. A laser tracker was used to measure the distances to the trucks A, B, C, and D parked along the runway. This information provides the truth data shown in the table. The images were processed using an extended

Kalman filter (EKF). The table shows the range estimates based on this algorithm. The range estimates agree well with the true range for trucks A, C, and D. The range estimate for truck B is less accurate and can be reduced by the use of stereo (two or more cameras).

We have presented, for the first time, results of using vision-based algorithms for acquiring range information using images acquired from helicopter flight. Our contributions are twofold: (1) development of flight data for verification of vision-based algorithms, and (2) a passive ranging methodology tailored to the needs of helicopter flight. Our preliminary results indicate that it is possible to get adequate range estimates except at regions close to the focus of expansion (FOE). As we get closer to the FOE, the error in range increases because the magnitude of the disparity gets smaller, resulting in a low signal-to-noise ratio. The performance of the motion-based passive ranging method can be improved near the FOE by using stereo. We have developed an integrated stereo and motion algorithm using the EKF. The use of stereo has additional benefits. Stereo provides range information when the helicopter is stationary and, furthermore, the stereo range can be used to initialize the EKF.

We plan to continue the evaluation of the method using other flight scenarios obtained with the CH-47. The image data base will be further augmented by

Table 1. Range estimates

Truck	Range (ft)		Standard deviation (ft)	% Error
	True	Estimated		
A	325	324	25	0.3
B	576	499	77	13.3
C	451	452	50	0.2
D	205	215	10	4.8

flight tests to be conducted by mounting stereo cameras, including a forward-looking infrared camera, on the NASA RASCAL UH-60 helicopter.

A major issue in the implementation of vision algorithms is the trade-off between computational speed and the denseness of the range map. Currently, we are looking at different hardware with the objective of developing a laboratory-based, real-time vision system. A modified subset of the laboratory system will be flight tested in future years.

The obstacle-detection algorithms are quite general, and have potential for use in the autonomous guidance of mobile robots and in the hazard-detection phase of the autonomous lander on Mars.

**Ames-Moffett contact: B. Sridhar
(415) 604-5450**

Headquarters program office: OAST

Flow Through Boundary-Layer Bleed Holes

Wei J. Chyu

Numerical techniques have been developed to compute the supersonic/transonic flow through boundary-layer bleed holes typically found in supersonic inlet systems. The external flow field, along with flow through the bleed holes and the flow in the plenum chamber, was simulated. A fully implicit, flux-split, three-dimensional (3-D) Navier-Stokes code was used along with a multizonal (two) grid approach and a Chimera grid-embedding technique. Two-dimensional flow solutions were computed using the Baldwin-Lomax algebraic turbulence model. The effects of the following parameters on the flow fields were studied: (1) location of the bleed holes relative to an incident shock wave (i.e., before, at, or after the shock wave); (2) the size of the bleed holes relative to the boundary layer thickness; (3) the number of bleed holes; (4) the spacing between bleed holes; and (5) the free-stream Mach number. The first figure illustrates the overall problem and computational

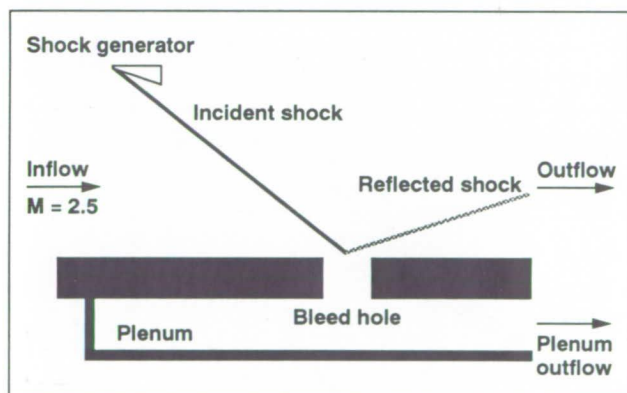


Fig. 1. Computational domain.

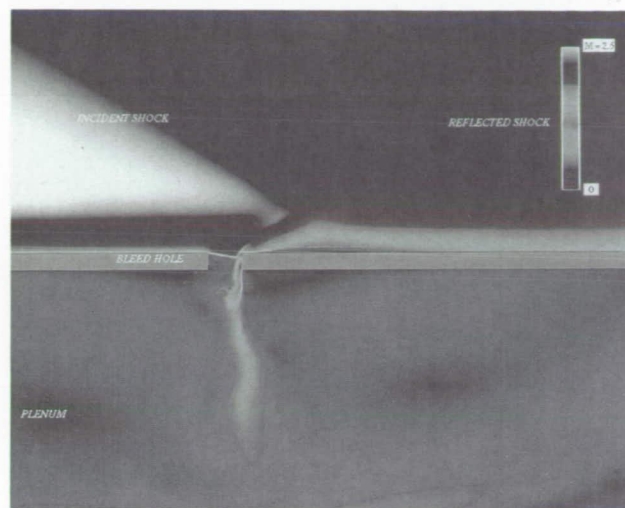


Fig. 2. Overall flow field Mach contours, $M_\infty = 2.5$, $\delta_{shock} = 30^\circ$. (See color plate 12 in Appendix)

domain. The second figure presents the overall flow field for a free-stream Mach number of 2.5 with a 30-degree deflection-angle shock impinging just downstream of the bleed hole. The details of the flow through the bleed hole are shown in the third figure.

The results presented represent a significant advance in extending computational-fluid-dynamics capability to inlet-boundary-layer bleed flow simulation, and permits the investigation of a broader spectrum of design variables associated with high-performance inlet operation. To date, the design of

PRECEDING PAGE BLANK NOT FILMED

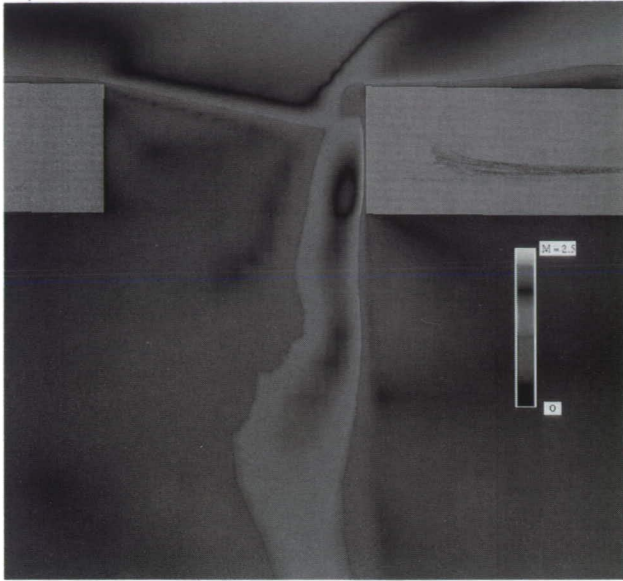


Fig. 3. Mach contours through bleed hole region.
(See color plate 13 in Appendix)

boundary-layer bleed mechanisms is based solely on empirical techniques with minimal understanding of the physics involved. These computational procedures will allow a wide variety of parameters to be investigated and more effective and efficient boundary-layer control techniques to be developed. Computations are being extended to 3-D bleed simulation using the F3D Navier-Stokes code combined with Chimera grid techniques.

Ames-Moffett contact: W. Chyu
(415) 604-6208
Headquarters program office: OAST

High-Speed Civil Transport Design and Analysis

Susan E. Cliff-Hovey, Michael D. Madson

The objective of this work was to apply computational fluid dynamics (CFD) codes to a candidate High-Speed Civil Transport configuration. This work is in support of a design effort to determine the maximum lift/drag ratio for the next generation of supersonic commercial transports.

Two Euler codes, TEAM and AIRPLANE, and a full-potential code, TRANAIR, were used to obtain aerodynamic quantities on a modern supersonic transport. Different flow-field grids were used for the three codes: a structured quadrilateral grid was used with TEAM, an unstructured tetrahedral grid with AIRPLANE, and a solution-adaptive unstructured Cartesian grid with TRANAIR. AIRPLANE was used to provide the aerodynamic effect of the nacelles on the baseline configuration.

Force coefficients predicted by AIRPLANE and TRANAIR (the unstructured-grid codes) were in excellent agreement. Results from TEAM (the structured-grid code) differed significantly, since unstructured-grid codes more accurately model the actual surface

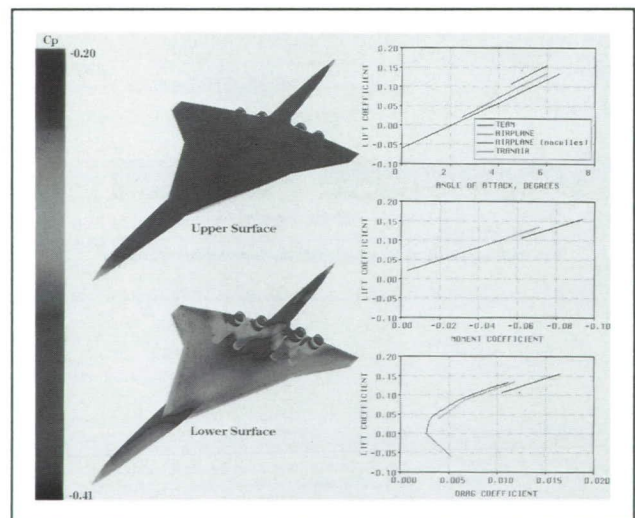


Fig. 1. Surface pressure contours for a modern supersonic transport, $M = 2.01$, $\alpha = 6.0^\circ$, as computed by the AIRPLANE code, and force and moment coefficients from three CFD codes. (See color plate 14 in Appendix)

geometry. The effects of the nacelles were computed by AIRPLANE, and changes in the lift and drag coefficients were added to the baseline computational results during the design process. The figure shows the lift, drag, and moment coefficients predicted by the three CFD codes and the increments in the force coefficients due to the nacelles. It also shows the pressure coefficient contours computed by AIRPLANE for the complete configuration.

In the design process, it is important to be able to calculate the effects of nacelles on the baseline configuration. The ability to determine these effects computationally improves the accuracy of the design process, as well as reducing the design time. The

aerodynamic effects of the nacelles on the configuration were significant, and changed the angle of attack at which the maximum lift/drag ratio occurred.

As a first-order approximation to optimization with the presence of the nacelles, the lower-surface pressure coefficients obtained with AIRPLANE on the full configuration will be interpolated onto the baseline configuration (no nacelles) during the design optimization process.

**Ames-Moffett contact: S. Cliff-Hovey
(415) 604-5656**

Headquarters program office: OAST

Aircraft Optimization

John W. Gallman

An aircraft optimization program was developed for design studies of subsonic transports. This computer program enables detailed studies of the interactions between disciplines, the sensitivities of mission constraints, and the influence of new technologies on aircraft performance. An aircraft design is almost always a compromise between the objectives of different engineering disciplines. For example, a very long wingspan would reduce aerodynamic drag, but would create an aircraft that was too heavy to be practical. The best design compromise is often counterintuitive, particularly for a novel aircraft configuration like the joined wing. Using numerical optimization enables the designer to study the influence of mission constraints on overall performance by comparing candidate configurations that represent the best compromise between critical disciplines. A study of constraint sensitivity aids in the identification of the key design issues. The designer is then able to focus his efforts in areas that have the most potential to improve aircraft performance.

The aircraft optimization code focuses on the design trade-offs between aerodynamics and structures. The code also considers all the flight conditions required for a particular mission and estimates overall performance in terms of direct operating cost. The

vortex-lattice method is used to calculate aerodynamic forces for the complete aircraft, and the finite-element model is used to analyze the wing and tail structures. Weight estimation depends on a full-stressed design algorithm that includes a constraint on buckling and a correlation with a statistically based method for total lifting-surface weight. NPSOL, a numerical optimizer developed at Stanford University, is used to integrate the analysis methods and to design aircraft with minimum direct operating cost. The first figure shows a typical aerodynamic model, the structural box model used for wing and tail structures, and some design optimization results.

Optimization problems with 17 variables, 9 mission constraints, and bound constraints on each variable were solved to design aircraft with minimum direct operating cost. The design variables included geometric quantities that describe the area, span, thickness, twist, and longitudinal position of the lifting surfaces. Also included are mission dependent quantities such as engine thrust, cruise altitude, and take-off flap deflection. The mission requirements are to transport 115 coach passengers 2,000 nautical miles at a cruise Mach number of 0.78. All designs have a stick-fixed static margin of 0.2 based on a

reference chord of 13.69 feet. A balanced runway length of 7,800 feet at sea level is used for the take-off- and landing-field length constraints. Other constraints include an engine-out climb gradient greater than 2.4%, a cruise thrust greater than cruise drag, and cruise trim at cruise lift coefficient. The trim constraint is enforced at an average cruise weight. Trimming moments required for other weights or flight conditions are generated by deflecting the elevator. Sufficient pitch control for take-off rotation is also required. The evaluation of direct operating cost includes estimates of crew, maintenance, depreciation, fuel, and insurance costs.

A group of conventional and joined-wing transports were designed using the aircraft optimization program, and were compared on the basis of direct operating cost, gross weight, and cruise drag. As part of this design study the relative importance of individual mission constraints was studied by consecutively adding constraints to the design problem. The second figure illustrates five different design problems, all of which include constraints on range, cruise thrust, trim, and stability. Landing-field length is an inactive constraint with no noticeable effect on the optimum design. The first set of bars in the figure (Problem 1) presents a comparison of joined wings

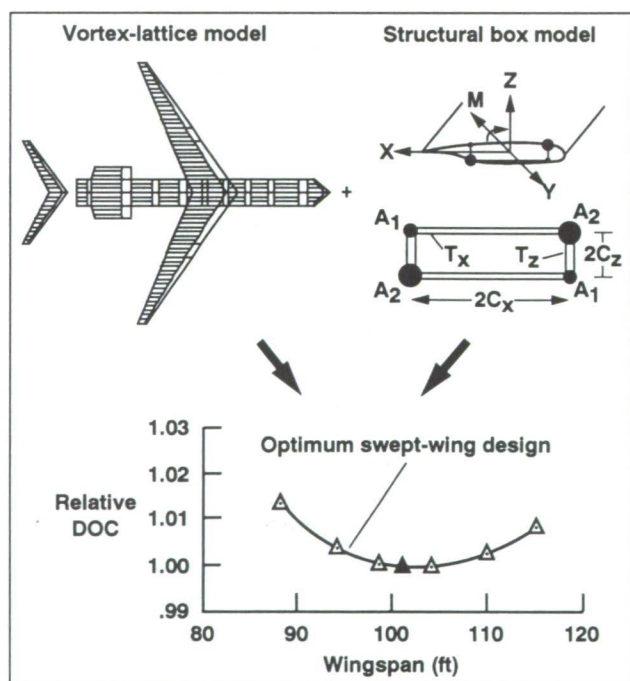


Fig. 1. Typical aerodynamic and structural models used in the aircraft optimization code to design for minimum direct operating cost (DOC).

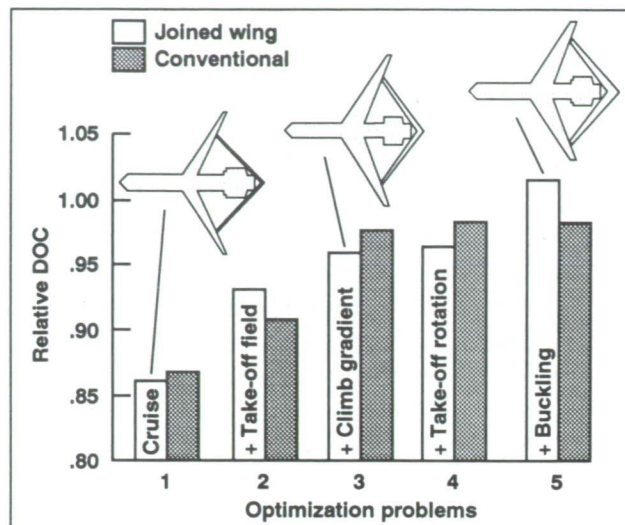


Fig. 2. Effect of constraints on joined-wing and conventional transports. All problems include constraints on range, trim, stability, cruise thrust, and landing-field length.

with conventional aircraft designed for a cruise condition only. Problem 2 adds a take-off-field-length constraint to this basic design problem, and Problems 3 through 5 each include the effects of an additional constraint. The top views shown for the joined-wing designs show how drastically the optimum design can change as constraints are added to the design problem.

A new design problem was formulated to improve the joined wing's performance with respect to the take-off-field-length constraint. The joined wing suffers a substantial penalty in maximum lift because of a short tail moment arm and the corresponding large tail download required to trim in take-off configuration. This issue was addressed by increasing the flap span, decreasing the elevator span, and adding a fuel tank in the tail for center-of-gravity management. All of the results shown in the second figure include these modifications. A similar figure for the original problem showed a much more pronounced penalty for take-off field length and conventional designs, with superior performance for all problems except cruise. Problem 4 shows that the joined wing saves 2% in direct operating cost before the buckling constraint is considered. Addressing this constraint in more detail has the potential to reverse the final comparison between conventional and joined-wing aircraft. The second figure shows that the current joined-wing design, labeled Problem 5, costs

approximately 3.2% more to operate than a conventional aircraft designed for the same medium-range transport mission.

These results demonstrate the usefulness of the aircraft optimization code and indicate that joined wings have overall performance characteristics similar to conventional transports. Key design issues for joined wings were identified as maximum lift and tail buckling by solving optimization problems with different sets of constraints. Increasing the joined wing's ability to generate maximum lift by redefining the design problem improved performance and suggested that reducing the effect of the buckling

constraint might give the joined wing an advantage over the conventional configuration. Currently the joined wing costs approximately 3.2% more to operate than a conventional aircraft designed for the same 2,000-nautical-mile mission. The aircraft optimization code can be used to study the buckling constraint for joined wings or the effect of new technologies such as composite structures or hybrid laminar flow on conventional aircraft performance.

Ames-Moffett contact: J. Gallman

(415) 604-6266

Headquarters program office: OAST

Supersonic Transport Wing Design

Raymond M. Hicks, James J. Reuther

The objective of this work is to apply computational fluid dynamics (CFD) codes to the design of supersonic transport wings. A quasi-Newton numerical optimization algorithm coupled with Euler CFD codes will be used as the primary design method for developing advanced wings for the next-generation supersonic transport. Validation of the new designs will be accomplished by wind tunnel testing.

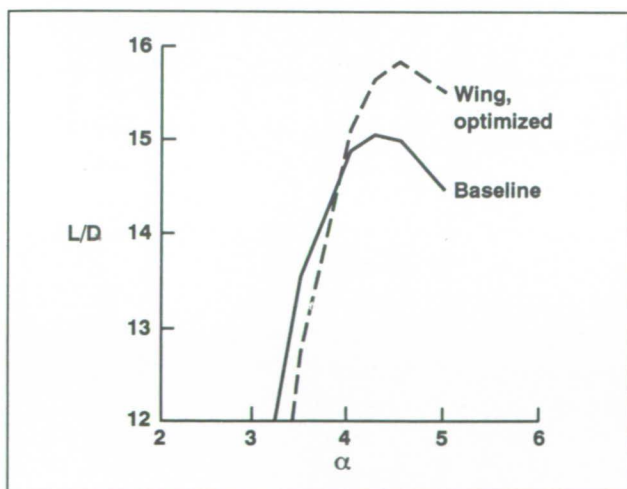


Fig. 1. Supersonic transport wing optimization.

A new wing for a state-of-the-art supersonic transport configuration has been designed. The lift/drag ratios of the baseline and redesigned wings are shown in the figure. Note that the maximum lift/drag ratio of the optimized wing is substantially higher than that of the baseline wing. This is a significant improvement since the baseline wing was carefully designed by personnel of a major airframe manufacturer with many years of experience in aircraft design.

The next-generation supersonic transport must meet stringent economic and environmental constraints. Such requirements make conventional cut-and-try design techniques obsolete. An automated design method with realistic physical modeling was needed to meet this new challenge. The numerical optimization design code developed during this study meets those needs.

Ames-Moffett contact: R. Hicks

(415) 604-5656

Headquarters program office: OAST

Supersonic Aerodynamics of a Highly Swept Oblique Wing

Robert A. Kennelly, Jr., Stephen C. Smith, James M. Strong

The objective of this work is to extend the experimental data base for oblique-wing configurations to higher sweep angles and Mach numbers, and to obtain both surface-pressure data appropriate for validation of computational-fluid-dynamics design tools, and flow-visualization photographs that illustrate separation and shock waves.

Pressure orifices and internally mounted transducers were retrofitted to an existing Ames-designed oblique-wing model (see figure). The fuselage was modified to reduce aerodynamic and geometric interference with the wing at high sweep angles (up to 72 degrees). The test was conducted in the Ames 9- by 7-Foot Supersonic Wind Tunnel, which was operated over nearly its entire Mach range, from 1.6 to 2.4.

A unique set of experimental data on a very highly swept oblique wing has been obtained at low cost and on a time-available basis in the Unitary Plan Wind Tunnel complex. In addition, a new test technique was tried in collaboration with researchers Blair McLachlan and James Bell in the Ames Fluid Dynamics Research Branch, where surface-pressure data were obtained using barometric paint.

Oblique-wing aircraft may prove to be attractive for high-speed civil transport if more conventional design approaches encounter difficulties with, for example, sonic boom, community noise, or subsonic performance. The test results suggest that the achievable lift-to-drag ratios do not fall too rapidly with Mach number if the sweep angle is sufficiently high. It may thus be reasonable to consider oblique wings for

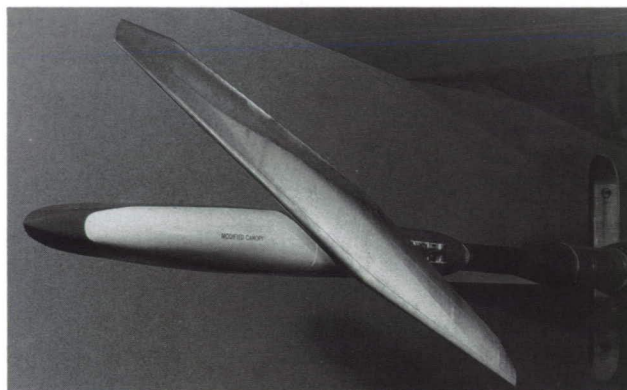


Fig. 1. Highly-swept-oblique-wing model in Ames 9- by 7-Foot Supersonic Wind Tunnel.

higher-speed applications than previously. In this role, the oblique wing would be exploited for its mission flexibility and structural efficiency rather than for its superiority to slender (symmetric) configurations, which vanishes at Mach numbers above about 2.0.

Minor stream-angle corrections are being applied to the data, and the pressure-tube routing has been revised prior to a tentatively scheduled test in the 11-Foot Transonic Wind Tunnel. A paper on oblique-wing performance is being prepared.

**Ames-Moffett contact: R. Kennelly, Jr.
(415) 604-5860**

Headquarters program office: OAST

Business Jet Design Modifications Using TRANAIR

Michael D. Madson, Robert A. Kennelly, Jr.

The objective of this research was to compute the aerodynamic characteristics of a modern business jet using a full-potential computational fluid dynamics (CFD) code called TRANAIR, and to recommend design modifications based on the CFD results.

The TRANAIR code, developed by Boeing under contract to NASA, was used to compute the aerodynamics of the Learjet Model 60. Results identified several areas where design modifications were necessary. With advice from NASA, Learjet personnel developed and analyzed a number of proposed configuration changes until the desired aerodynamic characteristics were achieved. A parallel effort using a wing-alone code, R22OPT, also produced a design with reduced shock strength in the wing root region, but was unable to account fully for fuselage effects.

Three key areas of the Model 60 configuration that were modified based on TRANAIR calculations are indicated in the figure. High Mach numbers near the leading edge of the pylon were significantly reduced by redesigning the pylon airfoil section. A wing root "glove" was designed to reduce the high Mach numbers found near the leading edge of the wing root. Also, undesirable buffeting characteristics at the base of the winglet were reduced by lengthening the chord of the wing at the winglet intersection. These modifications significantly reduced the drag of the model, and increased the overall aerodynamic efficiency.

TRANAIR has the ability to quickly and routinely obtain the flow characteristics about arbitrary and complex aerodynamic configurations in the transonic flow regime. A series of cases were run which led to the redesign of an otherwise complete business jet concept. The modifications suggested by TRANAIR

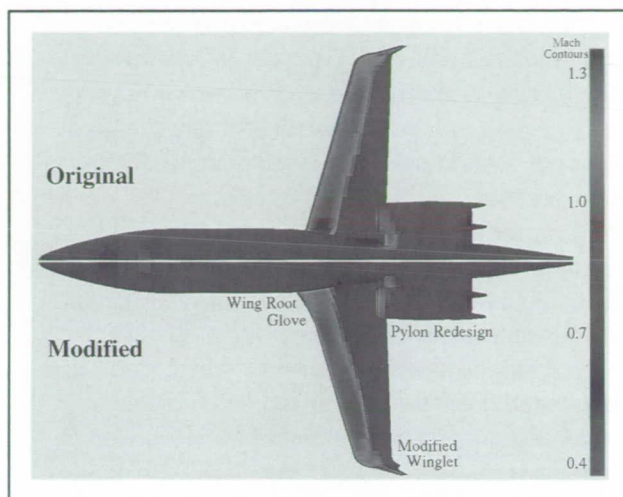


Fig. 1. TRANAIR Mach contour predictions for Learjet Model 60 original geometry (upper half of figure) and modified geometry (lower half of figure), $M_\infty = 0.75$, $\alpha = 4^\circ$. (See color plate 15 in Appendix)

computations were implemented into the design specifications for the model.

Wind tunnel and flight testing of the Model 60 will be used to validate the TRANAIR data. A grid study will be undertaken to determine how sensitive various aerodynamic quantities are to the density of the flow-field grid. TRANAIR is being used by Learjet in the design of their newest business jet model.

Ames-Moffett contact: M. Madson

(415) 604-3621

Headquarters program office: OAST

Design and Analysis of Low-Sonic-Boom Configurations

Michael D. Madson, Susan E. Cliff-Hovey

The objective of this research is to use computational fluid dynamics (CFD) codes to analyze the sonic boom characteristics of a supersonic configuration designed to have a low-sonic-boom pressure signature. Wind tunnel data is difficult to obtain at many locations away from the body, but CFD codes allow for the evaluation of the entire flow field.

Two Euler codes (AIRPLANE and TEAM) and a full-potential code (TRANAIR) were used to obtain pressure signatures below the body of the Langley Mach 2 model. The signatures are taken less than a body length from the model and extrapolated to desired distances from the model for prediction of ground overpressures and comparison with experimental data.

Near-field pressure signature predictions have been evaluated by comparing CFD results with experimental data on the low-sonic-boom wind tunnel model. Data from the initial wind tunnel test measured pressure signatures beneath the centerline of the model (on ground track). Results from CFD indicated that peak pressures were actually occurring away from the model centerline (off ground track) as indicated in the figure, where magenta and red signify high pressure and blue indicates low pressure. This phenomenon had not previously been observed. A subsequent wind tunnel test was conducted that verified the presence of the maximum off-ground-track peak pressure location for the low-boom model. Modifications to the planform have led to significantly reduced off-ground-track pressure peaks, and demonstrated the value of CFD in both supersonic design and analysis.

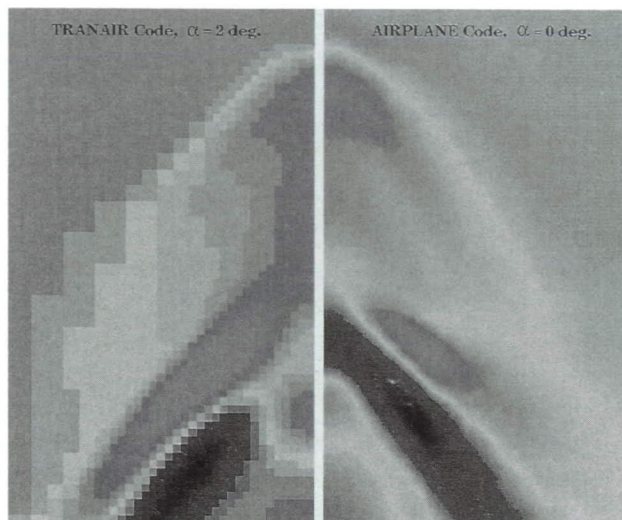


Fig. 1. Pressure coefficient contours at 0.25 body length below the low-sonic-boom model. (See color plate 16 in Appendix)

Design modifications and CFD analysis will continue in an effort to reduce the off-ground-track pressure peaks, and to increase the range to meet design specifications. The resulting design will be tested in the Ames 9- by 7-Foot Supersonic Wind Tunnel.

**Ames-Moffett contact: M. Madson
(415) 604-3621**

Headquarters program office: OAST

Unstructured Cartesian-Grid-Based Euler Solutions

John E. Melton

A structured Euler code was used as the basis for the development of a topologically independent, unstructured, Cartesian-grid Euler code (TIGER). The use of a Cartesian, refinable grid allows computationally efficient grids to be generated with an automated procedure, eliminating the time-consuming task of generating a body-fitted, multiple-block grid. Cells may be repeatedly split into eight smaller cells in order to provide increased resolution in areas where large flow-field variations exist. Because this refinement is done locally, specific regions of the flow field can be analyzed with higher grid resolution, thereby avoiding unnecessary refinement in other regions of the flow field. An efficient program structure was critical in order to avoid large penalties in computational time and memory. The resulting code runs at a rate equivalent to conventional structured computational fluid dynamics (CFD) codes, and uses simple, straightforward programming techniques to take advantage of the vector processing capabilities of the CRAY Y-MP. The interactive graphical program (GIRAFFE) is capable of displaying data by means of color mapping and contour lines on user-specified, unstructured flow-field planes. A typical example of the results generated using the TIGER code is presented in the figure, which shows the pressure distribution predicted by TIGER for a high-speed transport configuration with a deflected leading-edge flap. The overall configuration is shown in the insert. Portions of four of the computational grid planes are shown, with each grid cell color coded according to the local pressure coefficient.

The computational analysis of aerospace vehicles requires the ability to capture fine details of the flow field surrounding arbitrarily shaped configurations. An

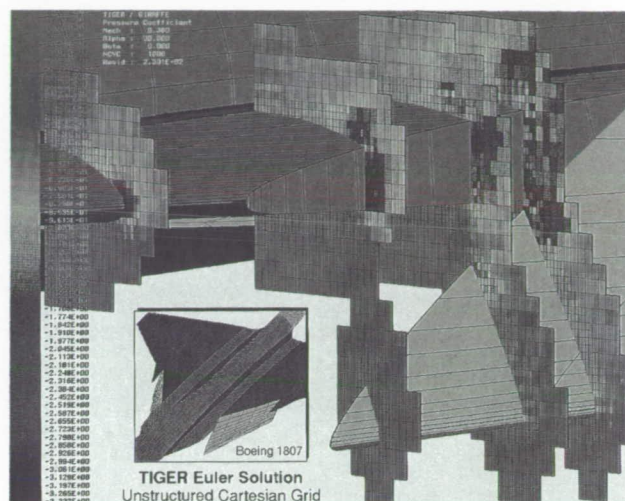


Fig. 1. Computations about a high-speed transport with a deflected leading edge, $M_\infty = 0.3$, $\alpha = 30^\circ$. (See color plate 17 in Appendix)

unstructured methodology allows for localized grid refinement appropriate for each free-stream condition. This localized grid refinement increases computational efficiency, because the refinement is not required to extend throughout the entire flow field. The use of a Cartesian-based grid allows for an automated grid-generation procedure applicable to arbitrary, three-dimensional configurations, dramatically reducing the time required to produce CFD simulations about complicated vehicles.

Ames-Moffett contact: J. Melton
(415) 604-1461

Headquarters program office: OAST

Experimental Sonic Boom

Joel P. Mendoza

Theoretical and experimental investigations are currently under way to determine if candidate high-speed civil transport (HSCT) configurations can satisfy acceptable standards of sonic boom overpressure levels. Computational fluid dynamics (CFD) methods, including linear theory, are being used to design the candidate low-boom configurations. The objective of this work is to experimentally verify the sonic boom overpressure characteristics predicted by the CFD computations. Two HSCT models were constructed complete with empennage and flow-through nacelles. One is an airplane designed to cruise at a Mach number of 2.0; the other is an airplane designed to cruise at a Mach number of 3.0. Both models were constructed integrally with a sting instrumented with strain gages to measure normal force and pitching moment, as shown in the figure. The models were tested in the Ames 9- by 7-Foot Supersonic Wind Tunnel at Mach numbers of 2.0 to 2.5. Although it would be of some interest to measure the sonic boom characteristics of the Mach 3.0 airplane, ongoing studies have been concentrating on Mach numbers a little greater than Mach 2.0.

The theoretically determined sonic boom overpressure characteristics were experimentally verified. Linear theory, however, which was used in the design, did not accurately predict the overpressure characteristics associated with nacelles, since the nacelles were choking. A shock/boundary layer interaction has been suggested as a possible cause for the nacelle choking. Isolated nacelles



Fig. 1. Mach 2 high-speed civil transport model mounted in the Ames 9- by 7-Foot Supersonic Wind Tunnel.

have been tested by Wichita State University (WSU) to investigate the performance of the nacelles. Additional tests at WSU with the nacelle mounted close to a flat surface are being considered. CFD calculations have indicated that off-ground-track overpressure levels may be greater than the on-ground-track sonic boom level. Additional wind tunnel tests at Ames are in progress to study this phenomenon.

Ames-Moffett contact: J. Mendoza

(415) 604-3067

Headquarters program office: OAST

Cruise Missile Turboprop Installation Interactions Test

Ronald C. Smith

A cooperative Navy/NASA wind tunnel test program was conducted in the Ames 14-Foot Transonic Wind Tunnel. The objective of the program was to explore the nature and extent of the interactions between a counterrotating propfan propulsion system and a typical cruise-missile airframe. The emphasis was on assessing the mutual interactions between the propfan and the missile control surfaces. To achieve these objectives, a new powered model was designed and fabricated. The model, shown in the figure, consisted of a missile wing/body combination, control surfaces, and an air-turbine-powered, counterrotating turboprop simulator. The model was designed to allow the control surfaces to be mounted either forward or aft of the propfan propulsion system. The entire model was mounted on a flow-through, six-component internal balance supplied by NASA Ames. Each of the counterrotating hubs was mounted on a separate rotating balance designed to measure the thrust and torque of each propeller. In addition, the propeller blades and control surfaces were instrumented with strain gages to measure dynamic and static loads, respectively. Two propeller blade systems, designed and fabricated by NASA Lewis, were tested. The first propeller design simulated a large-diameter, low-tip-speed concept typical of a geared turboprop; the second design simulated a small-diameter, high-tip-speed concept typical of a gearless turboprop.

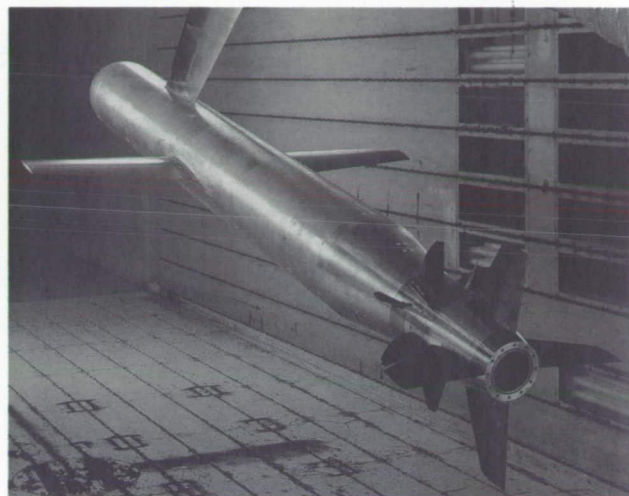


Fig. 1. Cruise missile model installed in the Ames 14-Foot Transonic Wind Tunnel.

The overall test was successful, achieving practically all of the test objectives. The interactions of the propeller blades and the control surface were found to be well within acceptable limits, and the efficiency of the propfan itself was not compromised significantly because of the presence of the control surfaces.

Ames-Moffett contact: R. Smith
(415) 604-6272

Headquarters program office: OAST

Simulation of the SOFIA Flow Field

Christopher A. Atwood, William R. Van Dalsem

The Stratospheric Observatory For Infrared Astronomy (SOFIA) will be a 3-meter-class Cassegrain telescope that uses a Boeing 747SP as an observation platform. An artist's concept of the observatory is shown in the first figure. This project is currently a cooperative effort between NASA and Germany's space agency (DARA). Airborne astronomy systems of this type offer capabilities that augment land- and space-based options, including inexpensive maintenance and upgrade potential.

The use of an aircraft-based observatory presents some challenges. The use of a solid window is precluded by the limited transmission by solids of infrared spectra of interest. Therefore the telescope cavity must remain open to the free stream. Wind tunnel tests have shown that violent shear-layer oscillations with concomitantly dangerous levels of acoustic loading occur for untreated open-cavity configurations. There is, therefore, a need to develop cavity flow-control treatments to suppress the flow unsteadiness. To reduce the risk of injury to the crew or damage to the platform, both experimental and computational fluid dynamics (CFD) analyses will be used in the design cycle. The purpose of this work is to develop the CFD tools for use in the SOFIA design.

An implicit Navier-Stokes model was used with overlapping zones to allow refinement of the solution

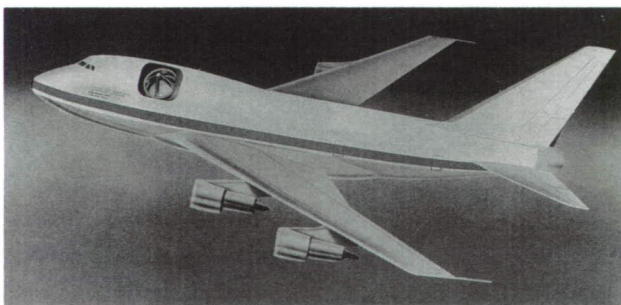


Fig. 1. Artist's concept of SOFIA.

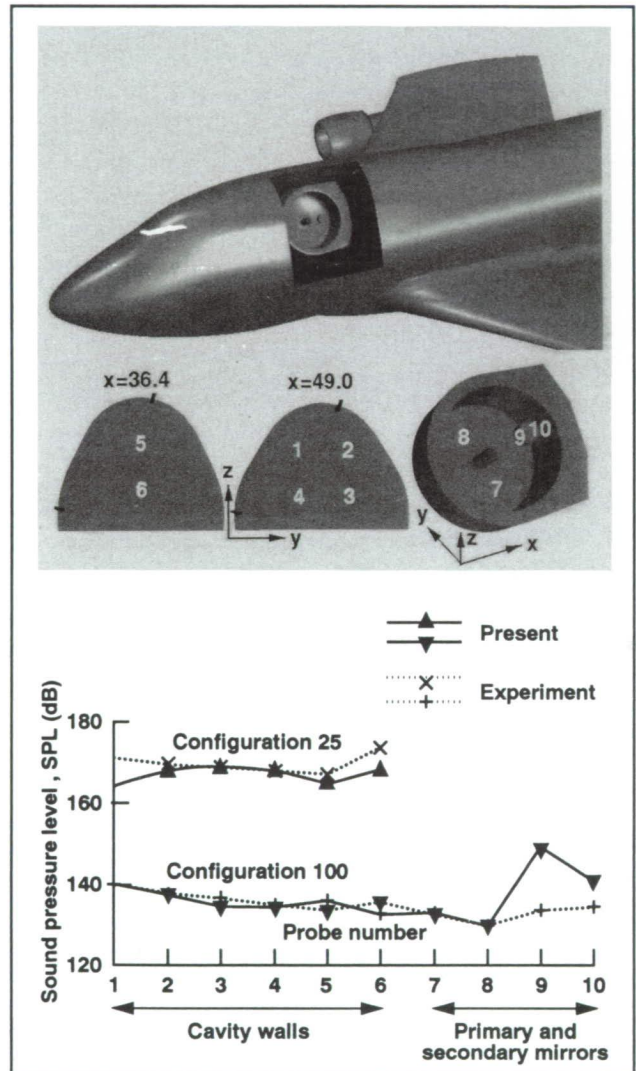


Fig. 2. Experimental and numerical sound levels for the noisy and quiet configurations.

while preserving the fidelity of the geometry. The computations used the same simplified geometry as modeled in the wind tunnel: a shortened wing and no tail surfaces. The effect of these modifications is small near the cavity region, which is of primary interest. Results of the simulations of the noisy untreated geometry (Configuration 25) and the quiet treated ramp (Configuration 100) are summarized in the second figure. The third figure shows instantaneous pressure levels and streamlines on the quiet configuration.

Ames-Moffett contact: C. Atwood
(415) 604-3974
Headquarters program office: OSSA

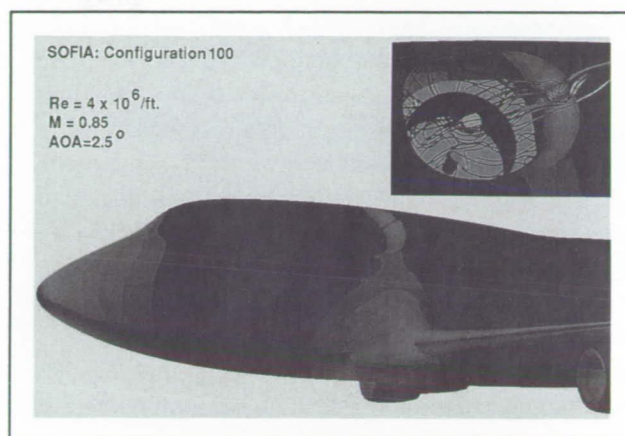


Fig. 3. Surface pressures and streamlines for the quiet configuration. (See color plate 18 in Appendix)

Simulation of High-Speed Impulsive Rotor Noise

James Douglas Baeder

The reduction of noise generated by helicopters and tiltrotors is essential for the long-term survivability of rotorcraft in both civilian and military operations. Impulsive noise is unquestionably the most annoying kind of noise. It is annoying because the ear is particularly sensitive to pressure changes over a very short period of time. The prediction of high-speed impulsive (HSI) noise, one of two types of impulsive noise from rotors, is difficult. HSI noise is caused by compressibility effects. As the rotational speed of the rotor increases, the aerodynamics become nonlinear, and shocks form with supersonic pockets. If the rotor tip velocity is large enough, a phenomenon known as delocalization occurs. In this case, the supersonic pocket connects to the region away from the rotor in which the flow is supersonic relative to the blade. When this happens, the pressure fluctuation in the far field is large and rapid, hence the term high-speed impulsive noise. The first figure highlights the large changes that occur at delocalization.

In this work, the three-dimensional (3-D) compressible Euler and Navier-Stokes equations are solved to simulate the initial formation and then the

propagation of the acoustic wave to an observer located a considerable distance from the rotor blade. The computer code used for this simulation, the Transonic Unsteady Rotor Navier-Stokes code (TURNS), was originally developed for looking at rotor-blade aerodynamics in hover and forward flight. This code was chosen for the investigation because it is accurate yet also maintains computational efficiency. Computational grids for calculating aerodynamics tend to be highly clustered in the vicinity of the rotor blade and extend only a short distance from the rotor. Thus, to simultaneously calculate the acoustics, the grid must be extended to large distances from the rotor and clustered along the region of acoustic propagation.

Results in hover show excellent agreement with those from experiment. The second figure shows pressure time histories for an observer in the plane of the rotor over three rotor diameters from the center of rotation. The phenomenon of delocalization is well shown. Below delocalization the pressure time history is smooth and symmetrical. Above delocalization the

noise is impulsive, with a much greater amplitude. Simpler methods are unable to predict this sharp rise in amplitude or the change in wave shape. Similar agreement with experiment is obtained with other rotor blade shapes as well as in forward flight when the flow is not delocalized. The agreement deteriorates somewhat in forward flight when the flow is delocalized. However, there is similar disagreement in such cases between measurements in a wind tunnel and those obtained in forward flight. Overall, the feasibility of using a unified computational-fluid-dynamics approach to examining the nonlinear acoustics of rotors is clearly demonstrated.

The visualization of these data on graphics workstations is providing new insight into the initial formation and propagation of nonlinear acoustic waves. The simulations provide greater detail and precision than is available experimentally. The density, velocity components, and pressure are computed for several hundred thousand grid points

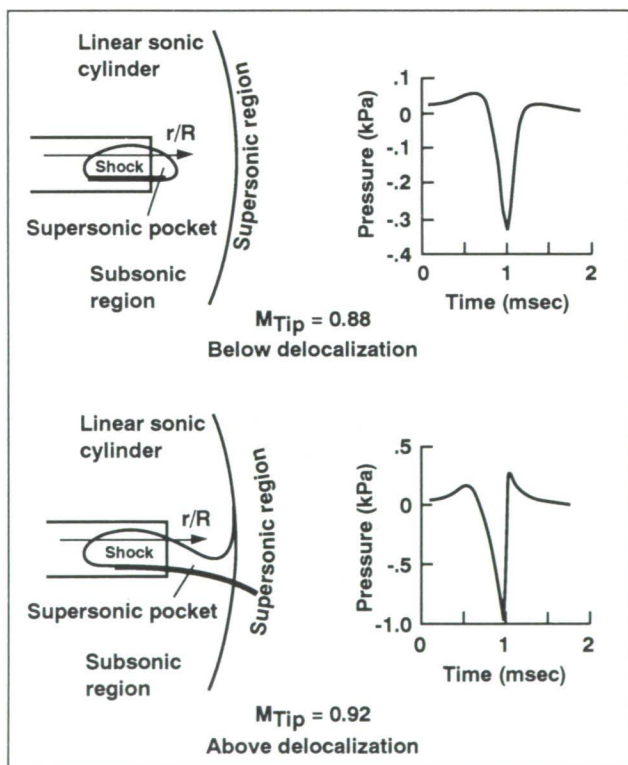


Fig. 1. Changes in HSI noise at delocalization.

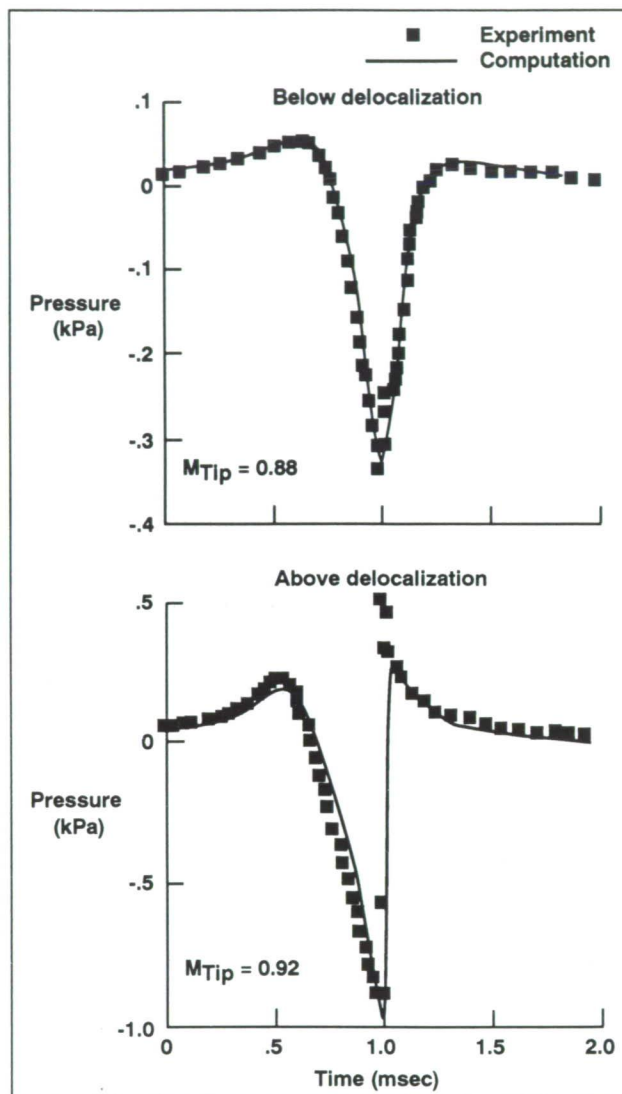


Fig. 2. Comparison of pressure time histories.

for each case. Furthermore, the results may be further manipulated on the computer to highlight particular features. The results are now available as a computational data base for use by acousticians developing simpler, more approximate theories and models.

Ames-Moffett contact: J. Baeder/J. McCroskey
(415) 604-4473/6428
Headquarters program office: OAST

A New Wing-Design Code for High-Speed Civil Transports

I. Chang, F. Torres

A new wing-design code, based on the three-dimensional (3-D) Euler equations and a constrained numerical optimization technique, has been developed. It consists of three major modules: (1) a flow solver, (2) a numerical optimizer, and (3) a geometry modifier. The three components were combined to interface with each other as a single design tool.

The first module of the wing-design code is the flow solver. The flow solver solves the Euler equations by a Runge-Kutta multistage, finite-volume method. Convergence to steady-state solutions is accelerated by several techniques, such as local time steps, implicit residual smoothing, and enthalpy damping. The current version of the flow solver is further accelerated by a fast multigrid algorithm. It is capable of calculating both transonic and supersonic wing flows.

The second module consists of the numerical optimizer. The optimizer solves a general problem that involves minimizing an objective function subject to a given set of constraints. The optimizer is based on a feasible direction method for constrained minimization. A one-dimensional search method that locates the minimum of a constrained function with polynomial interpolation without first finding bounds on the solution is used. The method is relatively simple but it works well for design purposes.

The third module of the wing-design code is the geometry modifier. It consists of two basic elements: a basic field-grid generator and a set of shape functions for perturbing wing sections. In the design optimization process, there are hundreds of variations of a given geometry to be evaluated. Therefore it is essential to have a fast field-grid generator for the success of the design method. The entire 3-D grid system for the wing can be generated by a combination of stretching and conformal mappings. Hence it is much less expensive to generate a new grid system for each perturbation of the wing geometry during the design process than it is to calculate a new flow solution for it. The grid topology is of the H-H type. It provides an appropriate grid feature for sharp leading-edge airfoil geometries which are common for

supersonic wings. The geometry of the wing can be quite general. The usual defining parameters such as sweep, dihedral, local twist, and planform shape are taken into account.

During the optimization procedure, selected airfoil sections of a wing are perturbed by linear combinations of shape functions to render an optimal wing that satisfies certain mission requirements. The shape functions can be described by mathematical expressions involving trigonometric and exponential functions. They can be applied to perturb either upper surfaces or lower surfaces of airfoil sections at specified spanwise locations.

An application of the present code is to improve the cruise efficiency of a supersonic model wing. The planform of this model wing is a double-delta. A crank of the wing that occurs at 60% of the span divides the entire wing geometry into two portions. The root portion of the wing is defined by blunted leading-edge airfoil sections and the tip portion is defined by sharp leading-edge airfoil sections. The design objectives were

1. A Mach number of 2.1
2. Maximum lift-to-drag (L/D) ratio
3. Leading-edge radius of each defining wing section held constant
4. Horizontal thickness distribution of each defining wing section held constant, and hence the volume of the wing held constant

The first figure shows the comparison of pressure on the suction side and the pressure side of the baseline and optimized wings. The dark blue indicates a region of lower pressure, whereas bright red indicates high pressure. The blue region on the upper surface expands into the tip portion of the wing and the red region on the lower surface is clearly swelled toward the trailing edge of the wing. This means that pressure on the upper surface is reduced whereas pressure on the lower surface is increased. The result is an improvement in cruise efficiency (L/D) of 5.3% at a Mach number of 2.1 and an angle of attack of 5 degrees. An aerodynamic

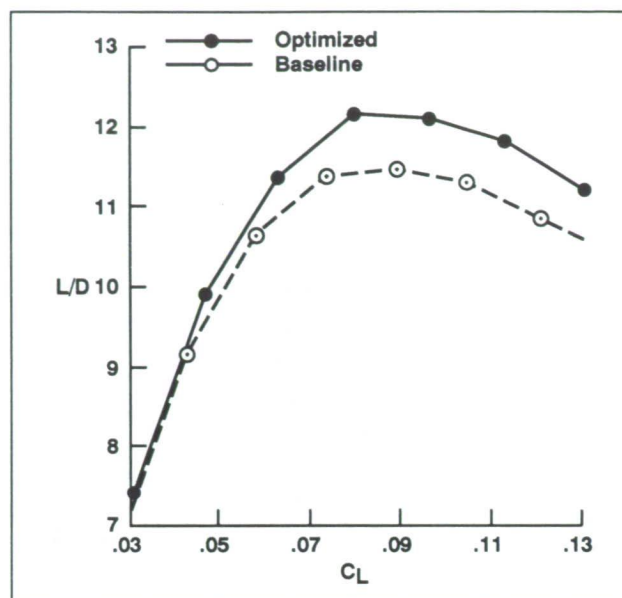
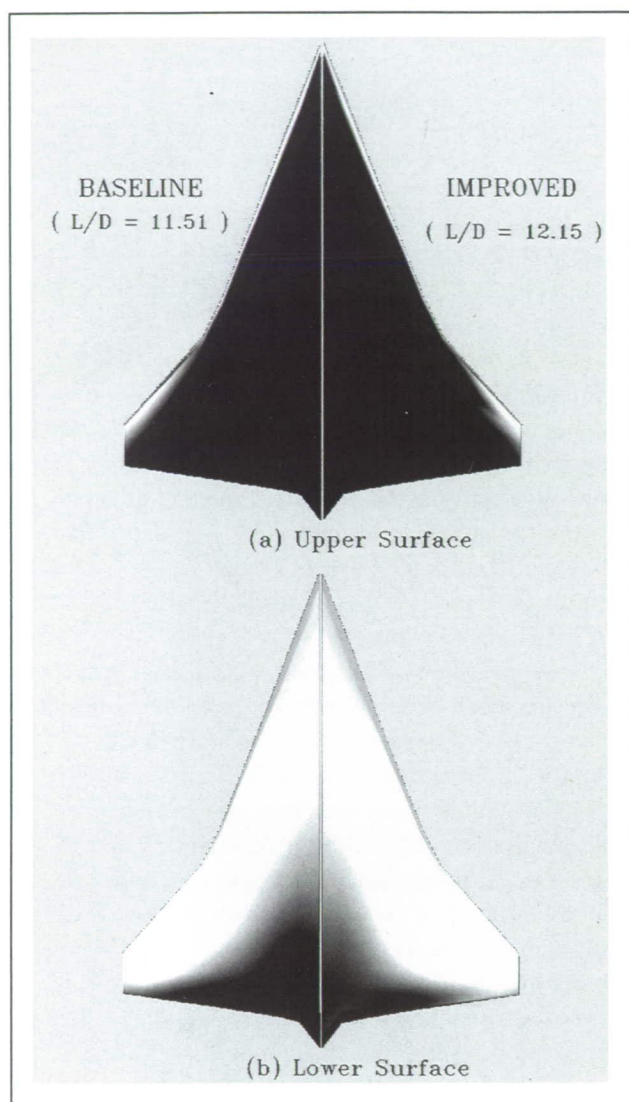


Fig. 2. Aerodynamic analysis of baseline and optimized wings at supersonic speed.

analysis was performed for the model wing and the improved optimized wing at Mach 2.1. The L/D versus centerline (C_L) curves are plotted in the second figure. It can be seen that there was indeed an improvement in the new wing, which demonstrates the usefulness of the wing-design code.

Ames-Moffett contact: I. Chang

(415) 604-6396

Headquarters program office: OAST

Fig. 1. Comparison of pressure on suction side and pressure side of baseline and optimized wings. (See color plate 19 in Appendix)

Direct Numerical Simulation of Turbulent Flow over Riblets

Haechon Choi, Parviz Moin, John Kim

Surface-mounted longitudinal grooves in turbulent boundary layers lead to a net drag reduction in spite of a substantial increase in the surface area. It has been shown experimentally that v-groove riblet surfaces can produce consistent net drag reduction (as large as 8%) provided that the height and spacing of riblets are less than 25 wall units. However, the mechanism of drag reduction by riblets in turbulent boundary layers is not known. The objective of this work is to understand the mechanics of turbulent drag reduction by riblets.

Direct numerical simulation is used to simulate turbulent flows over longitudinal riblets. A second-order-accurate, finite-difference method is used to solve unsteady, incompressible Navier–Stokes equations in a generalized coordinate system. We have computed the fully developed flow in a channel with riblets on one wall, and have considered two cases with $S^+ = 20$ and 40, where S^+ is the spanwise spacing of the riblets, in wall units. The computations revealed a drag increase of about 10% with $S^+ = 40$, whereas there was apparent drag reduction with $S^+ = 20$. This is in agreement with the experimental findings.

Instantaneous flow fields indicate that small-scale structures are created near the wall by riblets, and it appears that the drag-reduction mechanism by riblets is a result of alteration of the location of the streamwise vortices with respect to the wetted surface. Instantaneous velocity vectors superimposed on contours of streamwise vorticity in a cross-stream plane are shown in the figure for the cases of $S^+ = 40$ and 20. For flat-plate boundary layers, it is known that regions of high skin friction are closely related to the location and strength of streamwise vortices near the wall. The downward motion caused by strong

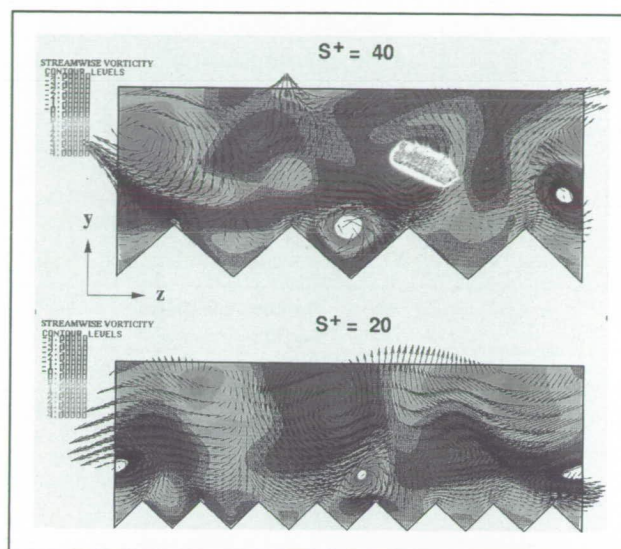


Fig. 1. Velocity vector and contours of streamwise vorticity in a (z,y) plane. Contour levels are from -4 to 4 by increments of 0.5 . (See color plate 20 in Appendix)

streamwise vortices is what creates these high-skin-friction regions on the wall. From the figure, one can see that a strong streamwise vortex is located between two riblets for the case of $S^+ = 40$, so that more surface area is exposed, leading to higher skin friction. For the case of $S^+ = 20$, however, streamwise vortices are located farther away from the wetted surface than in flat-plate boundary layers, resulting in lower skin friction.

Ames-Moffett contact: P. Moin/J. Kim
(415) 604-5127/5867

Headquarters program office: OAST

Modeling Compressed Turbulence

Gary N. Coleman, Nagi N. Mansour

There are many important applications in which models of the turbulence in compressible fluids must be used. Some examples are the prediction of astrophysical phenomena and the design of internal combustion engines, hypersonic flight vehicles, and supersonic combustors. Unfortunately, the accuracy of the turbulence models is at times less than accept-

able. In this project, we attempt to improve the accuracy of these models by comparing them to numerical simulations of homogeneous turbulence that is subjected to a three-dimensional mean compression.

Shown in the figure are time histories of the rate of dissipation of turbulent kinetic energy during the compression. For this case, the compression speed is very rapid (compared to the timescale of the turbulence) and the turbulent velocities are much less than the mean speed of sound. Over the time period shown, the flow volume decreases to one-eighth of its initial value.

Using the simulation results (the symbols and the dotted curve) and rapid-distortion theory, adjustments were made to the previous model (the dashed curve) so that the correct behavior is now produced (solid curve). We find that changes in the fluid viscosity caused by the temperature increase induced by the compression must be included in the turbulence model equations.

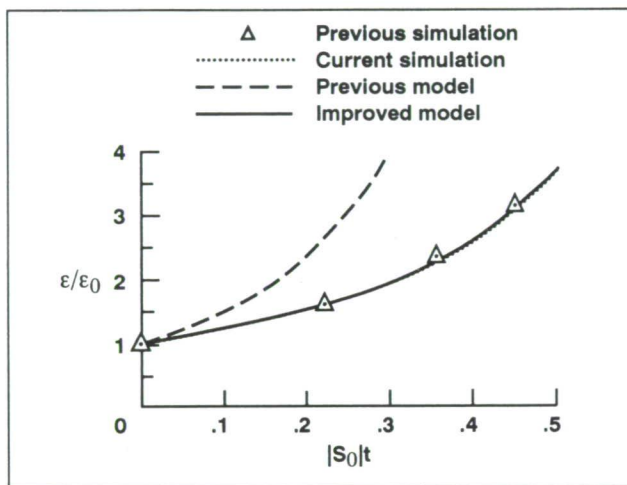


Fig. 1. Time history of the rate of turbulent kinetic energy dissipation, ϵ , during a three-dimensional compression; Nondimensional compression rate = -47 , turbulent Mach number ≈ 0 .

Ames-Moffett contact: G. Coleman
(415) 604-4727

Headquarters program office: OAST

Supersonic Laminar Flow Control

Jolen Flores, Eugene Tu, Lyndell King

Modern aircraft have turbulent airflow over a large part of their wings. Aerodynamic drag from this turbulence lowers aircraft flight performance and fuel efficiency. Reducing the turbulent layers of air produces laminar flow that aircraft designers say would yield considerable fuel savings in a commercial-size transport. One way of reducing this drag is by the use of suction systems on the wing, designed to maintain laminar flow over the wing. This technique, known as laminar flow control (LFC), has been successfully applied to subsonic aircraft for commercial use.

NASA has initiated the High-Speed Research Program (HSRP) to develop technology for the next generation of high-speed civil transports. One element of this program is to determine the feasibility of supersonic laminar flow control on a highly swept wing planform. The centerpiece of this program element is the F-16XL Supersonic Laminar Flow Control (SLFC) Experiment. The main objectives of the SLFC are (1) achieve 50–60% laminar flow on a highly swept wing at supersonic speeds, (2) deliver validated computational-fluid-dynamics codes and design methodology to industry for designing supersonic laminar flow wings, and (3) establish initial LFC suction-system design criteria that allow industry to more accurately integrate the concept into the design of a high-speed civil transport and determine the benefits.

The work highlighted here is the validation of a mean flow code and the successful coupling of the code to a stability-analysis code. The conditions for the computations were chosen to match those of the flight experiments, that is, Mach number = 1.6, angle of attack = 2 degrees, and altitude = 44,000 feet. Shown in the figure is the geometry of the F-16XL, which is a modified F-16A with the original wing replaced with a double-delta wing with a sweep angle of 70 degrees before the wing break. The computational model includes the fuselage, canopy, inlet, and wing portions of the geometry back to the first wing break. The white region on the wing indicates the area

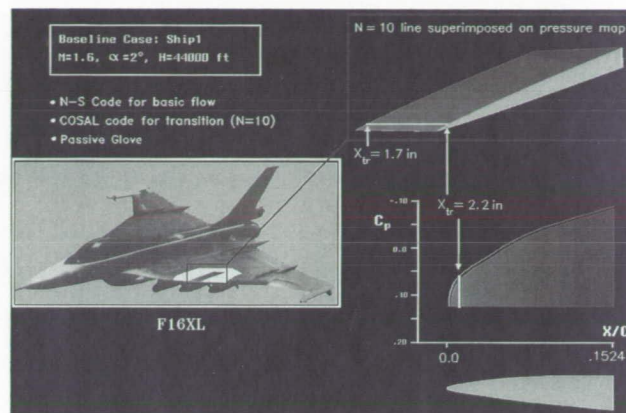


Fig. 1. Composite figure of F-16XL geometry, pressure map on wing glove, and predicted transition location. (See color plate 21 in Appendix)

(the glove region) to which suction will be applied. The validation results shown here are for the no-suction case.

The solution methodology is as follows. First, a mean-flow solution is conducted by solving the Navier–Stokes equations for the above-mentioned flight conditions. This requires about 13 hours of CPU time for a million-grid-point system. The computed pressure distribution is then compared with experimental flight data at the span stations just inboard and outboard of the glove region. Once the solution accuracy is verified, the solution in the form of pressure distributions on the wing is read into a compressible stability analysis (COSAL) code. This code solves a linearized set of stability equations using the pressure distributions provided by the mean-flow code as a boundary condition. This code then indicates where transition to turbulence occurs for each span station.

As indicated in the figure, the pressure map for a small portion of the wing, highlighted in green, was used as input to the COSAL code. The COSAL code predicted that transition to turbulence would occur about 1.7 inches from the leading edge of the wing for

the span station just inboard of the pressure field. Transition to turbulence for the outboard section was predicted to occur at about 2.2 inches from the leading edge. This was close to the measured transition location in the flight experiment. The figure also contains a plot of the pressure coefficient as a function of the wing chord. The procedure needs to be streamlined and further confidence gained in the mean-flow solutions and transition predictions. This

will be accomplished by further validation with flight experiments. Future work will then be conducted to determine the influence of different flight conditions and suction distributions on transition to turbulence.

Ames-Moffett contact: J. Flores

(415) 604-4005

Headquarters program office: OAST

Three-Dimensional Simulations of Multistage Compressor Flows

Flows within turbomachines are extremely complex because of their highly three-dimensional (3-D) nature and because of aerodynamic interactions between rotor blades and stator vanes. The weight and size of turbomachines need to be minimized to improve overall aircraft efficiency. These design constraints force the designer to place blade and vane rows close to each other, thus causing significant potential and viscous interactions between rotor and stator airfoils. A computational tool that can analyze these interactions can be very useful in understanding these effects and will aid in the design of more efficient and reliable turbomachines.

A 3-D, unsteady, thin-layer Euler/Navier-Stokes zonal code (STAGE-3) has been developed to analyze flows in multistage turbomachines. The code is based on a third-order-accurate, upwind, implicit scheme. Body-conforming "O" grids are used to accurately resolve the viscous effects associated with each airfoil. The "O" grids are overlaid on sheared Cartesian "H" grids that resolve the inviscid flow field between airfoils. These Cartesian grids are allowed to slip past each other, simulating the relative motion between rotor blades and stator vanes. STAGE-3 is designed to simulate turbomachines with arbitrary numbers of stages, and it also allows for different numbers of airfoils in each row.

STAGE-3 has been used to model the flow in a 2.5-stage compressor for which a large body of experimental data exists. The Mach number is 0.07 and the Reynolds number is 100,000 per inch at the

Karen L. Gundy-Burlet, Man Mohan Rai

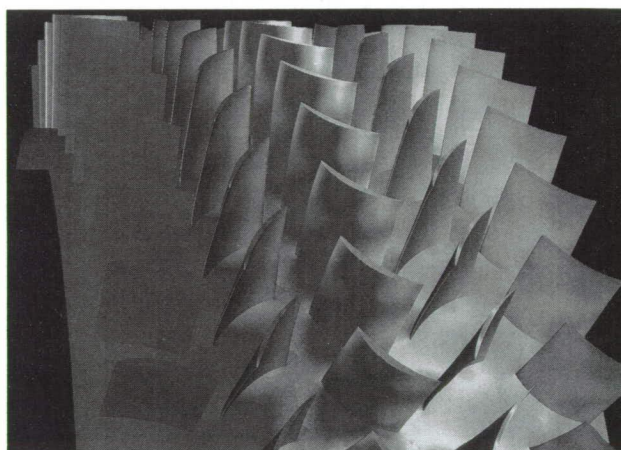


Fig. 1. Instantaneous surface pressures in a 2.5-stage compressor.

inlet of the compressor. For the purposes of the calculation, the flow was assumed to be fully turbulent. The figure shows the instantaneous pressure distribution on the hub, blade, and vane surfaces for a preliminary calculation of the flow within the compressor. Note the significant pressure variations in the radial direction, indicating the three-dimensionality of the flow. Time-averaged pressures on the blades compare well with experimental data.

Ames-Moffett contact: K. Gundy-Burlet

(415) 604-4475

Headquarters program office: OAST

Hypersonic Shock-Wave/Boundary-Layer Interaction Flows

C. C. Horstman, M. I. Kussoy

A series of shock-wave/turbulent-boundary-layer interaction experiments has been completed in the Ames 3.5-Foot Hypersonic Wind Tunnel.

The test model, shown in the figure, is sufficiently large to generate fully developed turbulent boundary layers ahead of the interaction at Mach numbers up to 8. The interactions studied included both single- and double-fin flows. These flow fields approximate several salient features of a hypersonic airbreathing inlet.

The measurements include surface oil flow, pressure, skin friction and heat transfer. Also, detailed mean-flow surveys through the flow field are obtained with probes attached to a traverse mechanism located within the model. The results will be used for code validation and compressible turbulence modeling studies.

In addition to the experimental work, a companion compressible-turbulence-model development program is under way. Initial computed results show that standard algebraic models are inadequate for predicting these complex flows at hypersonic speeds.



Fig. 1. Hypersonic crossing shock-wave/turbulent boundary layer interaction, as in $M_\infty = 8.2$, $Re_x = 9 \times 10^6$, shock generator angles $10^\circ \times 10^\circ$, $15^\circ \times 15^\circ$.

Ames-Moffett contact: C. Horstman
(415) 604-6255
Headquarters program office: OAST

Hypersonic Forebody Analysis

Scott L. Lawrence

As a single-stage-to-orbit demonstrator, the National Aerospace Plane (NASP) will be required to perform under a wide range of flight environments ranging from low subsonic through supersonic to hypersonic continuum flow, and ultimately to transitional and noncontinuum flow. In the hypersonic continuum regime, the air surrounding the forebody is heated to levels sufficient to cause dissociation and ionization. In addition, flight velocities are such that fluid mechanical time scales are of the same order as the time scales associated with the chemical reactions, so the flow is not in chemical equilibrium. Because present ground facilities are unable to produce the combined effects of Mach number and

total energy associated with hypersonic flight, prediction of chemistry effects depends largely on computational fluid dynamics (CFD).

In the present study, a space-marching flow solver is applied to a generic hypersonic forebody flow field. This configuration was developed under the NASP program for the purpose of CFD code validation, and experimental data exists for this model at high-Mach-number conditions. The model is 36 inches long and has a spherical nose with a radius of 0.35 inch. The lower surface is composed of three conic sections which provide two compression surfaces downstream of the nose.

Real-gas effects are investigated at realistic flight conditions for their impact on surface pressure and heat transfer as well as on integrated inlet data such as mass capture and kinetic-energy efficiency. The conditions were chosen to roughly correspond to Mach 15 flight at an altitude of 36 kilometers. Because the space-marching code requires a supersonic initial condition, the blunt nose region of the flow field is computed with a time-dependent Navier-Stokes solver, and data at the outflow provides the starting plane for the marching code. The space-marching solutions were computed on a grid containing 130 circumferential points and 65 radial points in each flow-field cross section. Solutions were obtained using three different gas models: (1) perfect gas; (2) equilibrium air; and (3) nonequilibrium air (finite-rate air chemistry). Identical models are used in the space-marching and time-dependent flow solvers.

Temperature contours in the last computed cross section (at 75% of the total body length) of the flow field are shown in the first figure. Clearly evident in this cross section are the outer (bow) shock wave and the wall boundary layer. Because the axes of the

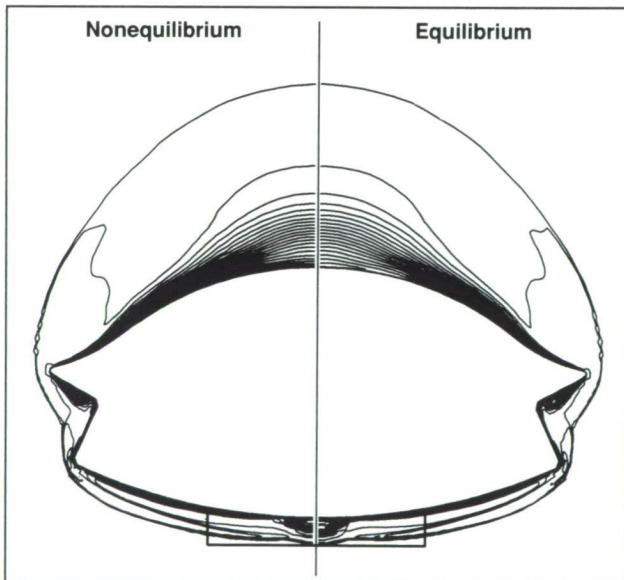


Fig. 1. Temperature contours at the inlet face station ($x/L = 0.75$).

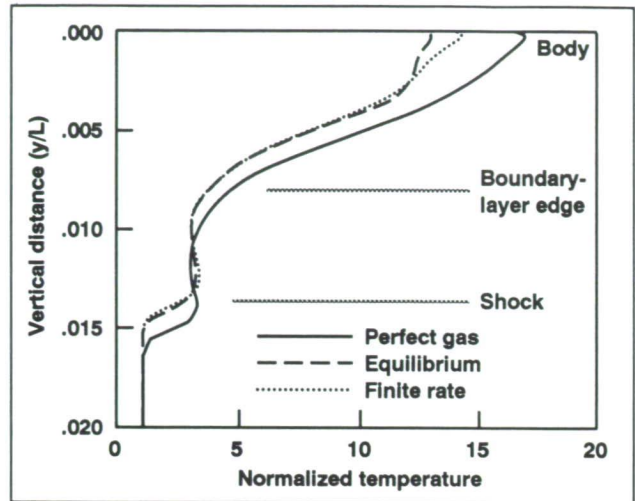


Fig. 2. Lower centerline temperature profiles at $x/L = 0.75$.

conic sections that make up the lower surfaces are canted upward relative to the vehicle axis, the lower-surface flow field behaves like the flow field on the lee side of a cone. Thus the viscous boundary layer tends to flow inboard, creating the high-temperature core at the centerline. It is in this core region that the real-gas effects are most pronounced. The lower centerline temperature profiles shown in the second figure indicate plausible trends. The perfect-gas case yields the highest peak temperatures because energy is not absorbed through molecular vibration and dissociation. The infinite chemical reaction rates assumed in the equilibrium case produce the highest levels of dissociation and, consequently, the lowest peak temperatures within the boundary layer. Effects of the gas model on surface heating and on the useful energy of the flow entering an inlet, such as the one superimposed on the first figure, can be significant.

Ames-Moffett contact: S. Lawrence
(415) 604-4050
Headquarters program office: OAST

S3D—An Interactive Surface-Grid-Generation Tool

Raymond C. Luh, Larry Pierce, David Yip

Advances in computer technology and computational fluid dynamics (CFD) in recent years have made possible the computation of flow fields around realistic three-dimensional geometries. One problem with realistic geometries is that they tend to be complex. No longer are these geometries defined by simple, analytic forms as was the rule in the past. As a result, the task of generating a computational grid, which is the first step in any CFD analysis, has become increasingly labor intensive and time consuming.

A computational grid is the collection of a large number of points about or within an object. Of particular importance are those points that lie directly on the surface of the object to help define its shape. Not only is the generation of a surface grid a prerequisite to that of a volume grid, but it is seen to have a dominant effect on the quality of the volume grid and to be very time consuming.

S3D is a new and evolving surface-grid-generation tool that promises to significantly reduce the time required to generate a grid. The program is implemented in the dynamic color-graphics environment of a workstation to take advantage of the latest in interactive technology.

An example of S3D's capability is shown in the first set of figures. One can change quickly from a set of discretized cross-section data, with each cross section containing a different number of points, to an ordered rectangular array of points as shown. In the process, prominent geometric features such as high curvatures and slope discontinuities which directly impact the physics of the problem can be preserved.

The second set of figures illustrates S3D's capability to perform surface-surface intersection, which is another frequently encountered problem in surface

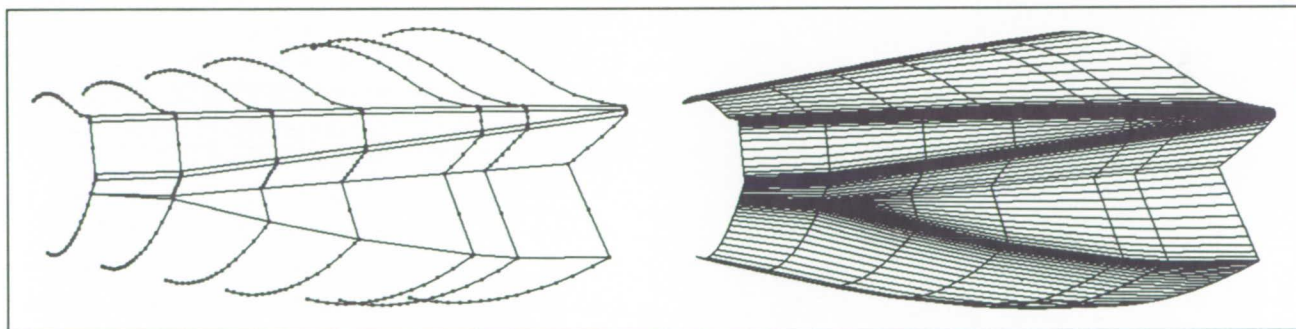


Fig. 1. An example of S3D's capability. (a) Initial geometry defined by a set of discretized cross-section data; (b) prominent geometric features are preserved in transitioning to an ordered rectangular array of points.

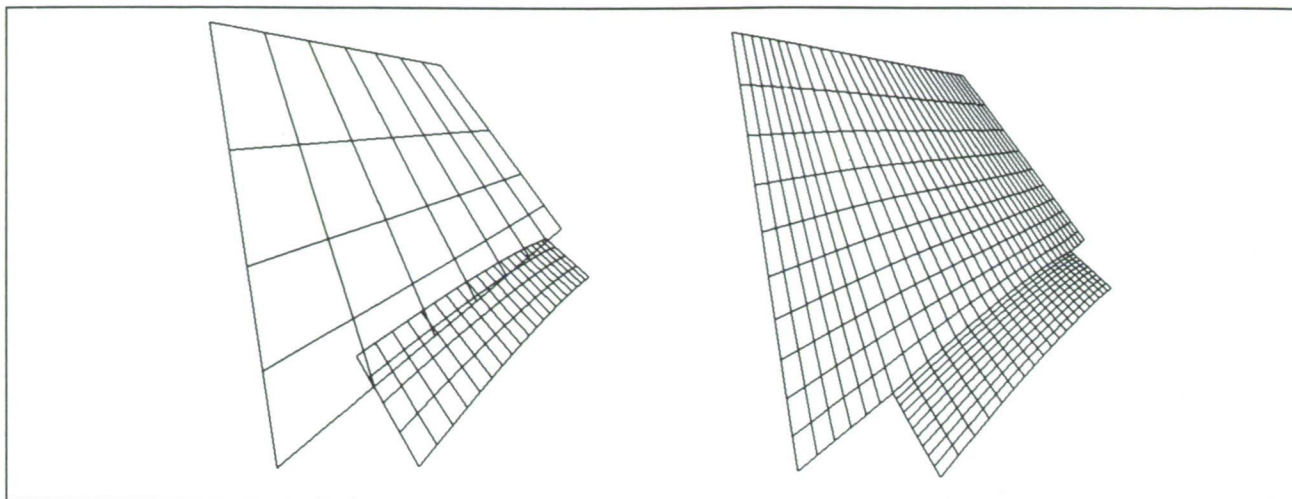


Fig. 2. An illustration of S3D's capability to perform surface-surface intersection. (a) Before: two surfaces passing through each other; (b) after: the intersection curve is defined and the desired surface grid is obtained.

grid generation. Starting with two surfaces that pass through each other as shown, S3D can be used to quickly define the intersection curves and make the necessary cuts, and to generate a surface grid as desired.

Ames-Moffett contact: R. Luh
(415) 604-4494

Headquarters program office: OAST

Pressure-Sensitive Paint in the Supersonic High-Sweep Oblique Wing Test

B. G. McLachlan, J. H. Bell, R. A. Kennelly

The use of pressure-sensitive paint was tested as part of the supersonic high-sweep oblique wing test that was conducted in the Ames 9- by 7-Foot Supersonic Wind Tunnel. The paint use was piggybacked on the larger experiment, the objective of which was to evaluate the performance and surface flow characteristics of a generic oblique-wing model for Mach numbers ranging from 1.6 to 2.5. The lower surface of the wing was coated with the pressure-sensitive paint. Because of the extreme test conditions—a low test-section static pressure and a high total temperature—it was not possible to determine the absolute pressure level by using the paint. Relative pressure changes, however, could be seen. A representative example of the data acquired is shown in the first figure. Displayed is a map of the lower-surface pressure field over the forward-swept portion of the oblique wing. Conditions are noted in the figure. Color denotes pressure level: red is low pressure, blue is high pressure. The unique field-measurement capability of the paint method is evident; the paint captures the passage of the fuselage bow shock over the outboard portion of the wing, and the passage over the wing inboard portion of a shock arising from reflection of the wingtip shock off the fuselage. More subtle features such as the formation of streamwise vortices over the wing surface caused by cross-flow-induced separation can also be seen.

The oblique-wing test represents the first use of the initial pressure-paint formulation under supersonic flow conditions. From this experience we now have

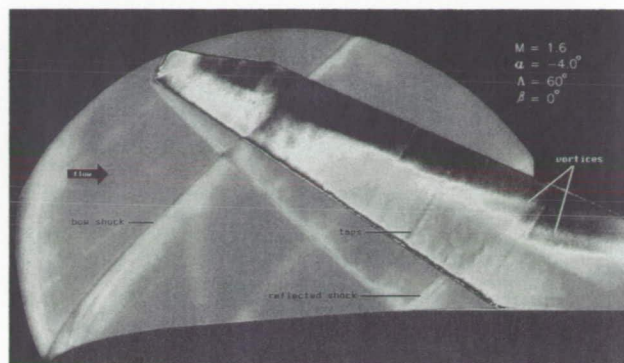


Fig. 1. False-color map of pressure field over forward-swept portion of wing lower surface. Color denotes pressure level: red is low pressure, blue is high pressure. (See color plate 22 in Appendix)

more information on the practical operating range of the pressure paint and the experimental methodology associated with its use in a large-scale supersonic facility. It must be noted that this test represents one part of a larger luminescent-sensor-development effort being carried out in a cooperative research program between the Fluid Mechanics Laboratory at Ames and the Chemistry Department at the University of Washington.

Ames-Moffett contact: B. McLachlan
(415) 604-4142

Headquarters program office: OAST

Surface Representation with a Scanning 3-D Laser Digitizer

Marshal L. Merriam, Timothy J. Barth

Computational fluid dynamics relies on an accurate computer representation of the aircraft surface. When this is not provided, acquiring it may be the most expensive part of the computation. If the surface is available as a model, it can be automatically described using a three-dimensional (3-D) laser digitizer.

The laser digitizer is a noncontact measuring device that performs the same function as a coordinate measuring machine (CMM), but with much greater speed. The laser digitizer can produce surface measurements at a rate of about 14,500 per second.

The special circumstance of having a model of a surface but no computer description of it comes up regularly. For example, the surface may be (1) found in nature (airfoils with accumulated ice); (2) manufactured inaccurately (castings); or (3) made by hand (experimental optimizations). As an example of the latter, consider the work done at Ames on the SOFIA (Stratospheric Observatory for Infrared Astronomy) project, in which an infrared telescope is flown in a Boeing 747 to get above most of the atmosphere. Since glass is nearly opaque in the infrared spectrum, it is necessary to create a hole in the fuselage. It is

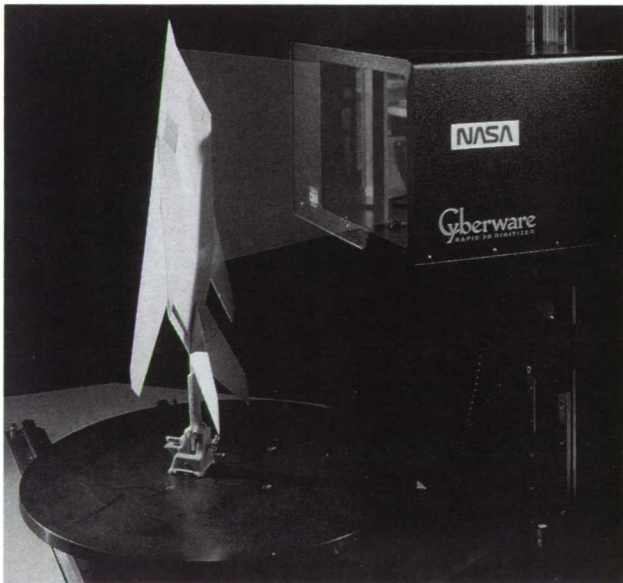


Fig. 1. Laser digitizer setup showing traversal mechanism and laser sheet used for model measurement. (See color plate 23 in Appendix)

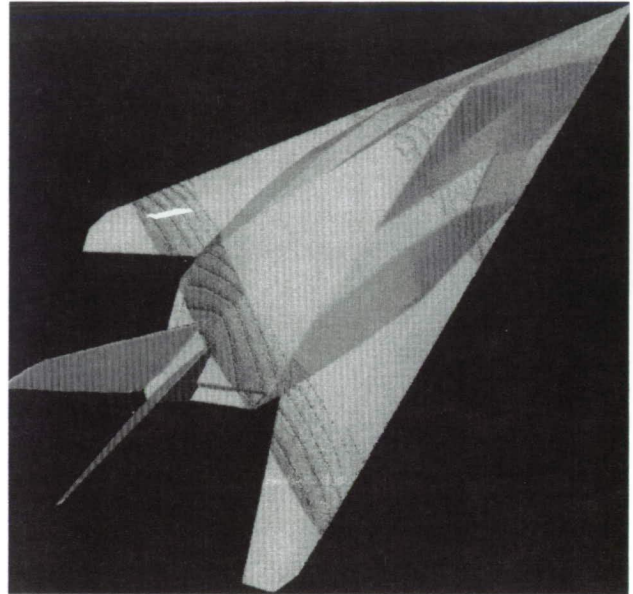


Fig. 2. Computer-readable surface representation of F117A.

possible to sculpt the edge of the hole in such a way that the boundary layer does not enter the fuselage. The flow affects both the noise inside the airplane and the optical quality of the telescope. The shape was obtained experimentally in a wind tunnel by successive modifications to a 1/8-scale model.

A computer description of the surface was required for simulation, verification, optimization, and full-scale fabrication. The CMM was too slow to provide the required resolution. The laser digitizer took all of the required measurements in a few minutes. The process of converting the measurements to a usable surface representation was done by hand, and took several weeks.

We have now automated the process of converting the measurements into a surface, through a process analogous to milling. The first figure shows a model of an F117A being scanned. The second figure shows the computer representation of this same model as a triangular-faceted polyhedron.

Ames-Moffett contact: M. Merriam
(415) 604-4737

Headquarters program office: OAST

Dynamic Subgrid Scale Model for Large-Eddy Simulation of Turbulence

Parviz Moin

The hierarchy of methods for turbulence computation, in order of decreasing computational effort, consists of (1) direct numerical simulation (DNS), in which all of the essential turbulence scales of motion are computed and no modeling approximations are made; (2) large-eddy simulation (LES), in which the effects of the smallest eddies upon the large-scale motions are modeled; and (3) the widely used Reynolds-averaged modeling which can be viewed as the limit of large-eddy simulation, in which the computational grid is too coarse to resolve any of the details of turbulence motions.

The basic philosophy of LES is to explicitly compute only the large-scale motions that are directly affected by the boundary conditions, and to model the small-scale motion (subgrid scale model). The premise of LES is that the small-scale motion is more universal and therefore its statistical effect on the large-scale motion can be modeled more easily. LES has always been purported to be attractive for engineering calculations because it is significantly less computer intensive than DNS yet it promised to be more accurate and robust than Reynolds-averaged models. Unfortunately, subgrid scale models have faced some of the same problems as Reynolds-averaged models, including improper asymptotic behavior near walls, variation of the optimal "coefficient" in different flows, and the necessity for ad hoc "intermittency" functions for the computation of transition from laminar to turbulent flow.

A recent major advance in subgrid scale modeling for LES is to parameterize the subgrid scale stresses using data from the computed large-scale field at several scales; that is, the subgrid scale stresses are extrapolated from the numerical solution during the computation. A particular mathematical formulation of this process leads to an eddy viscosity model with a coefficient that depends on space and time. In retrospect, the notion of an eddy viscosity coefficient that adjusts to the instantaneous local state of the flow

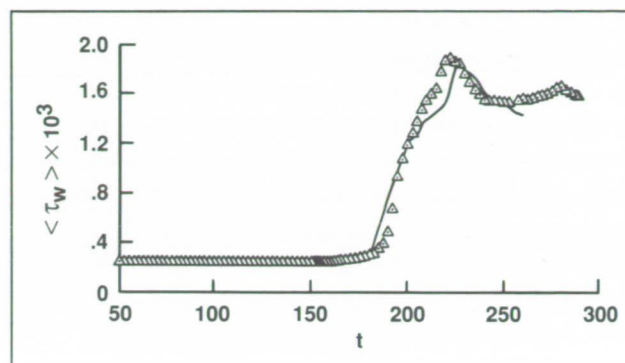


Fig. 1. Development of the wall shear stress in turbulent channel flow. Symbols are "exact" data from DNS; the line is from LES using the dynamic model. The sudden rise of the wall shear stress is a hallmark of transition.

is intuitively appealing. The resulting dynamic model has overcome the above-mentioned deficiencies of previous subgrid scale models and has performed remarkably well in several transitional and turbulent flows without requiring any ad hoc adjustments (see figure). The concept has been extended to compressible flows where it has led to a dynamic model for the turbulent Prandtl number.

The procedure leading to the dynamic model may be viewed as an altogether new approach to modeling, and its applications to date have shown it to be promising. Its inherent robustness should facilitate the use of LES in engineering computations, particularly in turbomachinery where the Reynolds numbers are relatively low.

Ames-Moffett contact: P. Moin

(415) 604-5127

Headquarters program office: OAST

Low-Aspect-Ratio Wing Experiment

M. Olsen, H. L. Seegmiller

The first phase of a code-validation experiment was completed in the Ames High Reynolds Number Channel II facility. The test is providing data on the flow around a low-aspect-ratio wing at transonic speed. During this phase of the project, surface pressure measurements were obtained on the wing-alone and wing/body configurations, along with boundary-condition measurements designed to provide the information necessary to model the flow fields numerically. The experimental conditions include a wide range of Mach numbers and angles of attack. Data at two Reynolds numbers were obtained, including one (14×10^6 based on root chord) which is representative of cruise conditions at 20 kilometers altitude. One of the unique aspects of this test is a flow feature peculiar to low-aspect-ratio wings at high angles of attack, the detached leading-edge vortex. This physical phenomenon allows aircraft to attain extremely high angles of attack without stalling. In contrast to a stalled wing, a wing with a detached

leading-edge vortex actually produces more lift than the classical linear theory predicts.

The experiment was conducted with careful attention to measurement accuracy and uncertainties; the results should guide the future development of computational models. Some of the flow fields attained in the test were extremely sensitive to small changes in the test conditions, and these were identified. This information was obtained by monitoring statistical uncertainties and comparing these with actual experimental repeatability obtained during the course of the test. For the flow conditions of this test (transonic Mach number and high angle of attack) this attention to detail was critical to provide a set of measurements that can be reliably used to test aerodynamic codes and the turbulence models used in them.

The experimental measurements obtained to date are mean surface pressures (see first figure),

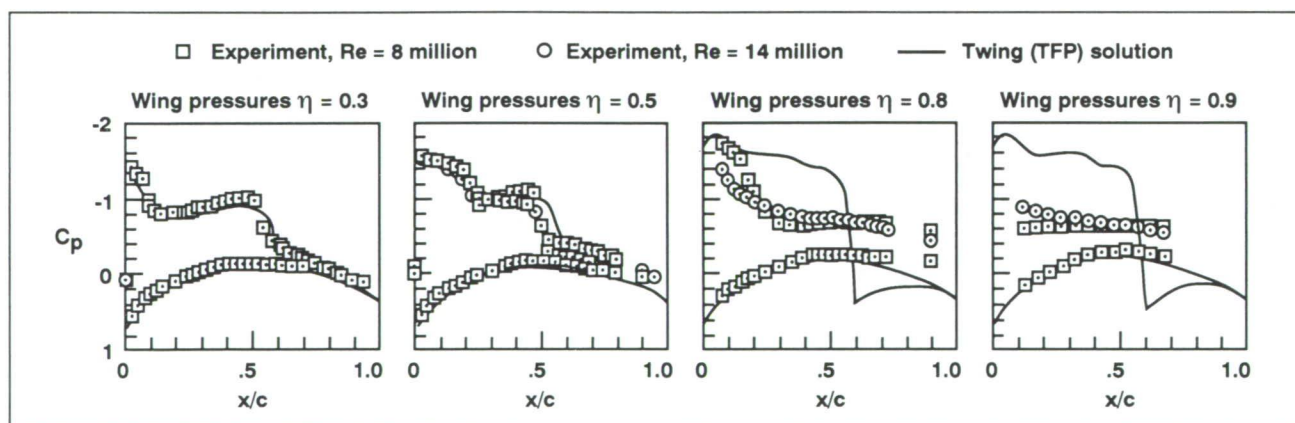


Fig. 1. Transonic full potential code predictions compared with experiment, Mach 0.8, $\alpha = 7.92^\circ$.

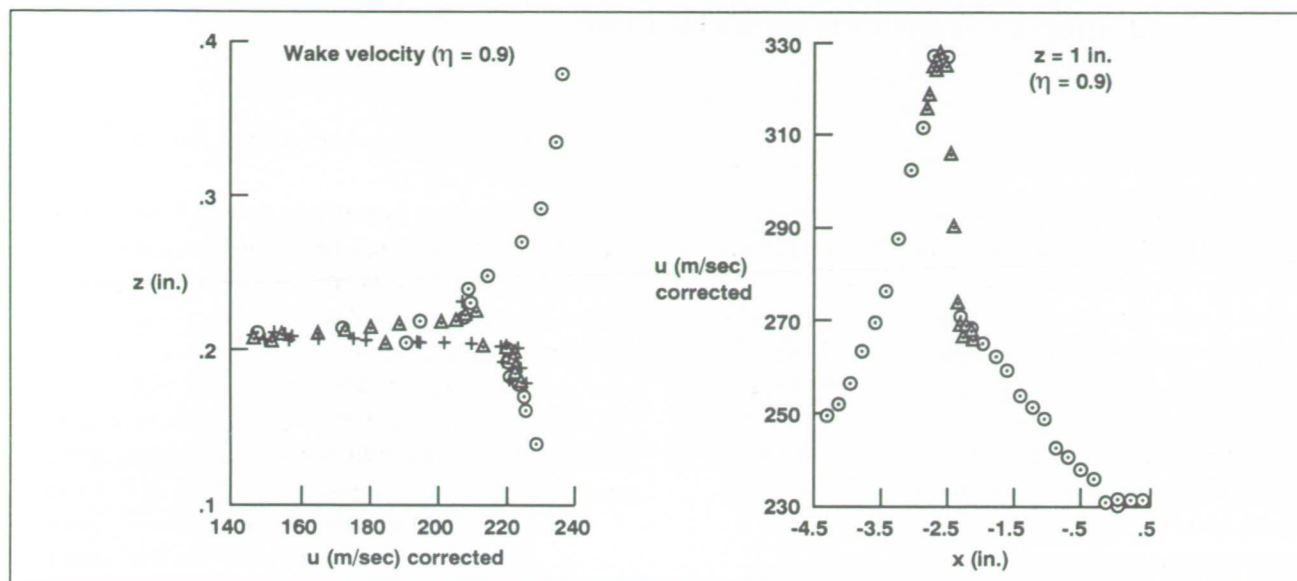


Fig. 2. Laser-Doppler-velocimeter measurements at 90% span, Mach 0.775, $\alpha = 5^\circ$.

tunnel-wall surface pressures, tunnel-wall boundary layer profiles (via pitot probes), and inflow-plane velocity measurement (via laser Doppler velocimeter (LDV)). Currently, the LDV is being used to measure two components of the velocities over the wing and to make wake-velocity measurements at the trailing edge (second figure). The two-dimensional measurements will provide an overall check for the turbulence models in computational fluid dynamics codes.

In the next phase of the experiment, an attempt will be made to measure the third component of

velocity with a modified LDV system. Surface oil-flow measurements (which show the direction of the airflow at the surface of the wing) will be performed. An attempt to measure the wing-surface boundary layers with three-hole and five-hole pressure probes is also planned.

Ames-Moffett contact: M. Olsen
(415) 604-6200

Headquarters program office: OAST

Direct Simulation of Transition on a Flat Plate

Man Mohan Rai, Parviz Moin

In recent years, computational fluid dynamics techniques have been used successfully to compute flows in geometrically complex configurations. However, success with regard to accuracy and reliability has been limited to cases in which the effects of turbulence and transition could be modeled in a straightforward manner. Even in simple flows, the accurate computation of skin friction and heat transfer using existing turbulence models has proved to be a difficult task, one that requires extensive fine tuning of the constants in these models. In complex flows (for example, in turbomachinery flows in which wakes impinge on airfoil surfaces causing periodic transition from laminar to turbulent flow), the development of a model that accounts for all scales of turbulence and predicts the onset of transition in a geometrically complex region may be impractical. Fortunately, the computing speeds and storage capability that are available today, along with current trends in computing, suggest that it may be possible in some cases to perform direct simulations of turbulence and transition at moderate Reynolds numbers in the near future.

Here we report on a direct simulation of transition and turbulence in a spatially evolving boundary layer on a flat plate. This flow contains laminar, transitional, and turbulent flow regions, and hence is a test case that has many of the characteristics found in more complex flows. A high-order-accurate, finite-difference approach to direct simulations of transition and turbulence in compressible flows was developed to compute this flow. The technique involves using upwind-biased differences for the convective terms, central differences for the viscous terms, and an iterative-implicit, time-integration scheme. This finite-difference method can, in a straightforward manner, be used for complex geometries.

The main objective of the study was to determine the computability of such a flow with currently

available computer speeds and storage. The purpose was to estimate the scope of the problems that can be solved in the near future (assuming certain trends in computing capability), and in this process to also address some algorithmic issues such as accuracy, inlet and exit boundary conditions, and grid-point requirements. A study of the flow physics involved and the creation of a data base for turbulence and transition modeling were an integral part of this effort.

The numerical results are in qualitative agreement with experimental data and indicate that the essential features of the transition process have been computed. The first figure shows the computed skin friction along the flat plate (both a fine-grid (Grid B) and an earlier coarse-grid (Grid A) computation) and

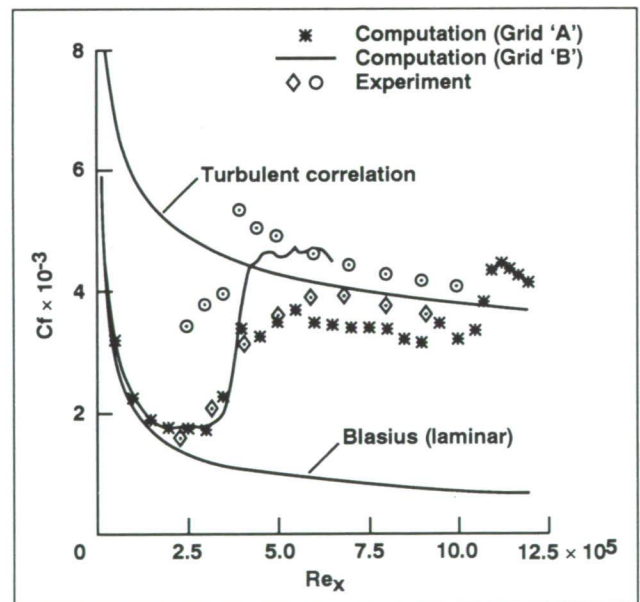


Fig. 1. Computed and experimental skin friction along the flat plate.

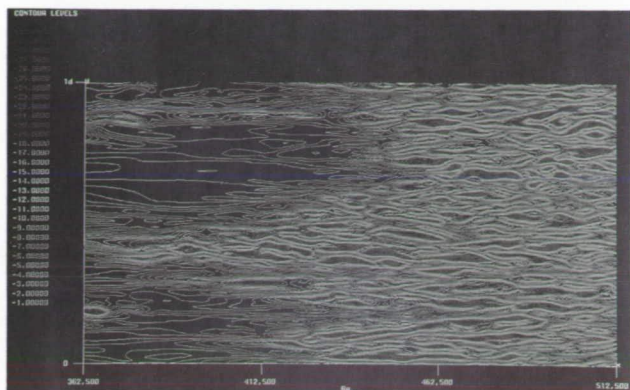


Fig. 2. Spanwise vorticity contours close to the surface of the flat plate. (See color plate 24 in Appendix)

experimental data from two different experiments. The computed transition region is seen to fall within the range of experimental data. The second figure shows instantaneous spanwise vorticity contours just above the plate. Of interest is the abrupt appearance of the vortical structures. The region shown in this figure includes the late stages of transition and early turbulence.

Ames-Moffett contact: M. Rai

(415) 604-4499

Headquarters program office: OAST

An Experimental/Computational Study of Heat Transfer in Sharp-Fin-Induced Turbulent Interactions

P. E. Rodi

A combined experimental and computational study has been performed of sharp-fin-induced shock wave/turbulent boundary layer interactions at Mach numbers of 5, 6, and 11. New experimental data were obtained at Mach 5 and include mean surface heat-transfer and pressure distributions and surface flow visualization for a range of fin angles of attack. Additional measurements were also taken to study the apparent conical nature of such interactions. This data set can also be used for code-validation and compressible-turbulence-modeling studies.

Conical Navier-Stokes calculations have been performed to take advantage of the apparent conical symmetry. Computations were made for two angles of attack at each of the three Mach numbers. Careful evaluation of the performance of this numerical approach has been carried out with an emphasis on the surface-heat-transfer predictions (see figure).

The results indicate that although the viscous portion of the flow field prevents the interaction from being purely conical, the conical Navier-Stokes approach (using a Baldwin-Lomax model) does appear useful as an alternative to a fully three-dimensional calculation for determining a quick

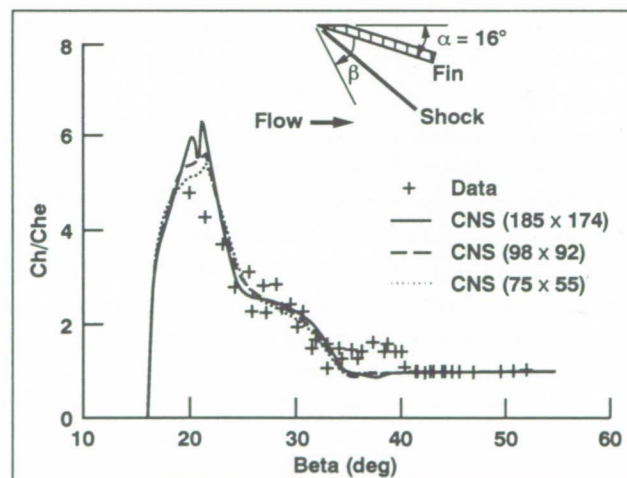


Fig. 1. Heat transfer comparison, Mach 5, $\alpha = 16^\circ$.

estimate of the extent and severity of sharp-fin-induced shock wave/turbulent boundary layer interactions.

Ames-Moffett contact: P. Rodi

(415) 604-6211

Headquarters program office: OAST

The Evolution of a Turbulent Mixing Layer

Michael M. Rogers, Robert D. Moser

In previous work we have extensively studied the evolution of plane mixing layers begun from simple low-wavenumber disturbances to a laminar mean profile by using direct numerical simulations of the incompressible Navier–Stokes equations. These simulations have shown how three-dimensionality grows in such mixing layers, and have led to the identification of several vortex structures associated with this growth, several of which have been observed experimentally. In these “clean” flows, the layer rolls up into Kelvin–Helmholtz “rollers,” which are separated by “braid” regions that are largely depleted of spanwise vorticity. Predominantly streamwise “rib” vortices form in these braid regions early in the three-dimensional evolution. Also associated with the growing three-dimensionality, the spanwise rollers contain concentrated regions of spanwise vorticity that are a result of vortex stretching.

A transition to turbulence may occur in cases that undergo a pairing of the spanwise vortices if the level of three-dimensionality prior to the pairing is high enough. The turbulence in such flows is characterized by the breakdown of the organized large-scale structures and is associated with strong vortex stretching, which produces strong positive and negative regions of all vorticity components. However, this turbulence still retains symmetries present in the initial condition and has none of the random “jitter” present in real flows.

Here we have simulated a turbulent mixing layer that begins from turbulent splitter-plate boundary layers (which were also generated by direct numerical simulation), each with a momentum-thickness Reynolds number of 300. The resulting flow has no symmetries and provides a large sample of turbulent eddies, producing good turbulent statistics and linear layer growth. The mixing-layer Reynolds number based on the velocity difference and the visual layer thickness exceeds 12,000 in the developed flow. We seek to determine the extent to which an understanding of the pretransition organized structures can aid in interpreting the flow structure in this fully turbulent field.

Experimental turbulent mixing layers contain large, roughly two-dimensional rollers. The simulated layer described here has similar structures early in its development (see first figure). However, these roller vortices are much more complex than their clean-flow counterparts, containing many small-scale vortical structures. Later, the spanwise coherence of the rollers is reduced, indicating that experimental mixing layers may be subject to additional disturbances besides the turbulence in the splitter-plate boundary layers.

The turbulent rollers described above are separated by braid regions that are largely devoid of vorticity (an especially good example can be seen at the right edge of the second figure). Within these



Fig. 1. Spanwise vorticity contours (red = positive, blue = negative) at a time when most of the layer vorticity has “rolled up” into eddies with significant spanwise coherence. (See color plate 25 in Appendix)

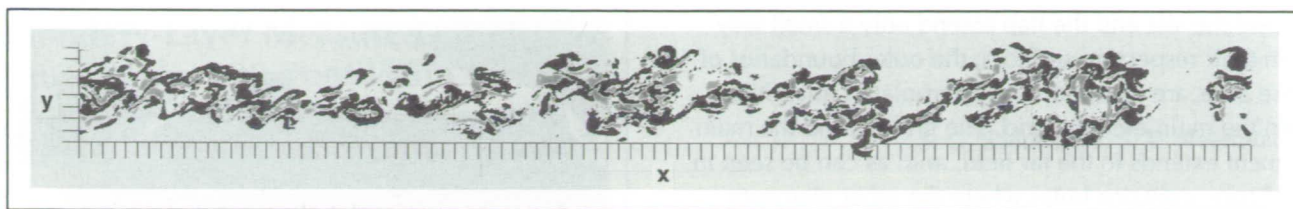


Fig. 2. Spanwise vorticity contours (red = positive, blue = negative) at a time later than that shown in the first figure. (See color plate 26 in Appendix)

braid regions compact, roughly axisymmetric rib vortices are typically present. Their evolution and structure is very similar to that of their clean-flow counterparts, including their entry into neighboring braid regions at late time.

The large-scale rollers undergo a pairing process that is more complex than that in pretransitional mixing layers. Pairing is initiated by the co-rotation of the rollers, but the individual rollers soon lose their identity as their small-scale core structures intermingle. Several "tearing" amalgamations, involving the splitting of one roller between its stronger neigh-

bors, have also been observed. Such behavior has been documented in experimental mixing layers.

In conclusion, knowledge of laminar mixing layer evolution has aided in understanding dynamically significant events in the turbulent mixing layer examined here. Equally apparent, however, is the greatly increased complexity of the small-scale vorticity field in the turbulent case.

Ames-Moffett contact: M. Rogers

(415) 604-4732

Headquarters program office: OAST

Flow over Multielement Airfoils

The incompressible, viscous, turbulent flow over single- and multielement airfoils is numerically simulated in an efficient manner by solving the incompressible Navier-Stokes equations. The solution algorithm uses the method of pseudocompressibility with an upwind-differencing scheme for the convective fluxes, and an implicit line-relaxation scheme. The motivation for this work includes interest in studying high-lift takeoff and landing configurations of various aircraft. In particular, accurate computation of lift and drag at various angles of attack up to stall is desired.

The geometry is discretized using a grid around each element of the airfoil configuration. Each grid consists of an ordered sequence of points; the equations governing the fluid physics are solved for the flow quantities at each grid point. Each of these individual grids overlaps the other in a random

Stuart E. Rogers, N. Lyn Wiltberger, Dochan Kwak

fashion. In order to propagate information between the grids and update the solution at the grid boundaries, the flow quantities are interpolated from the interior regions of neighboring grids and passed to the computational boundaries. This passing of information between grids is done in an implicit manner in the flow code, which adds to the stability and robustness of the computations. A typical flow case in this study converges to a steady-state solution in less than 200 iterations. This requires only 2-4 minutes of computer time on a CRAY YMP, depending on the number of elements used in the airfoil configuration. An example of the type of geometry in this work is shown in the first figure. This configuration consists of a leading-edge slat, a main element, and a single slotted flap. Also shown in this figure are the different grids used around each of the elements. The grids

YAV-8B V/STOL Research Aircraft Flow Simulation

Merritt H. Smith, Kalpana Chawla, William R. Van Dalsem

The aerodynamic environment encountered by powered-lift aircraft operating in ground effect is unique among flight vehicles. It is characterized by low forward speed with embedded regions of high subsonic or supersonic jet flows. During ground-effect operations, complex recirculating flows generated by the jets produce large changes in the aerodynamic loads on the flight vehicle. Analytic prediction and small-scale experimental methods have produced mixed results in this flight regime, with the result that costly full-scale powered tests are required to evaluate the performance of candidate designs. The ability to accurately predict vehicle performance without resorting to full-scale tests will be critical to future powered-lift aircraft projects. The goal of this project is to predict the flow field about a powered-lift aircraft, the YAV-8B Harrier, in low-level jet-borne flight by solution of the Reynolds-averaged Navier-Stokes equations and to validate this computational fluid dynamics (CFD) solution by comparing results to infrared images of the NASA YAV-8B Harrier V/STOL Systems Research Aircraft (VSRA) under similar flight conditions.

The flow about the YAV-8B Harrier was simulated at an altitude of 30 feet above ground level and at a speed of 30 knots with nozzles vectored 81 degrees from the aircraft centerline. A component performance model of the Pegasus engine was used to specify the mass flow through the engine inlet and nozzles and to set the nozzle exit temperatures. Propulsion-induced lift loss known as the "suckdown" effect was predicted, although the magnitude of the effect was greater than expected. Discrepancies are due most likely to an undeflected flap which was modeled in the up position for geometric simplicity. Flap deflection is responsible for supercirculation about the wing-flap combination on the flight vehicle; a correct modeling of the geometry should improve the prediction. All expected large-scale flow features were predicted, including fountain flows and the ground vortex (see photo).

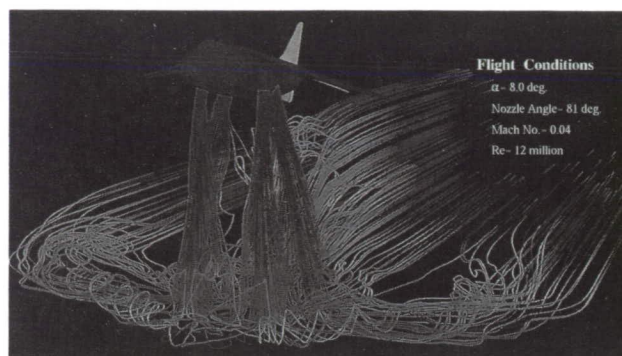


Fig. 1. Flow about the YAV-8B Harrier (particle traces colored by time since release). (See color plate 27 in Appendix)

A preferred unsteady mode was identified in the time history of the lift. This frequency (382 hertz, Strouhal number = 0.46, based on rear jet conditions) is centered in the range of expected oscillations due to jet shear-layer instabilities. Time-accurate analysis shows that the source of the oscillation is near the exit of the rear jet, which suggests that the generation of ring vortices on the jet shear layer may be the cause.

Infrared images of the flow field about the YAV-8B Harrier VSRA flight vehicle were collected using an AGEMA infrared imaging system. Comparisons of these images with the computations are ongoing, but preliminary indications show that the flow solver is accurately modeling the general behavior of the complex multiple-jet flow field. Work is under way to develop a numerical infrared signature-prediction technique which will render simulated infrared images from CFD results. This technique will allow a quantitative comparison between the CFD results and the flight flow field, as well as provide a predictive capability for new designs.

**Ames-Moffett contact: W. Van Dalsem/K. Chawla
(415) 604-4469/4981**

Headquarters program office: OAST

Canard–Wing Aerodynamic Interaction

Eugene L. Tu

Many modern aircraft, both operational and experimental, use canards for improved aerodynamic performance. The use of canards can often result in increased maximum lift and decreased trim drag for faster, more efficient aircraft. In addition, canard configurations have significantly different stability and trim characteristics from conventional aft-stabilizer configurations. For example, with the capability of present-day automatic control systems, an inherently unstable canard configuration can lead to improved aircraft maneuverability and agility. For closely coupled canards, aerodynamic performance is a direct function of the aerodynamic interaction between the canard and wing. However, depending on the geometry and the flow parameters, this interaction can be either favorable or unfavorable. Proper use of canards in future aircraft designs requires an accurate understanding of their influence on the flow about the wing.

Using computational fluid dynamics to solve the Navier–Stokes equations, the flow about a canard–wing–body configuration is computed and analyzed in detail. The effects of the canard on wing surface pressures, canard–wing–vortex interaction, and wing–vortex breakdown are studied. The first figure illustrates a side-by-side comparison of surface pressure and canard/wing leading-edge vortices for the configuration with and without the canard (canard-on and canard-off) at a Mach number of 0.90 and an angle of attack of 12 degrees. In the absence of the canard, the wing leading-edge vortex bursts, which reduces the positive influence of the vortex on the wing surface pressures. For the configuration with the canard, the wing vortex remains stable, thereby demonstrating

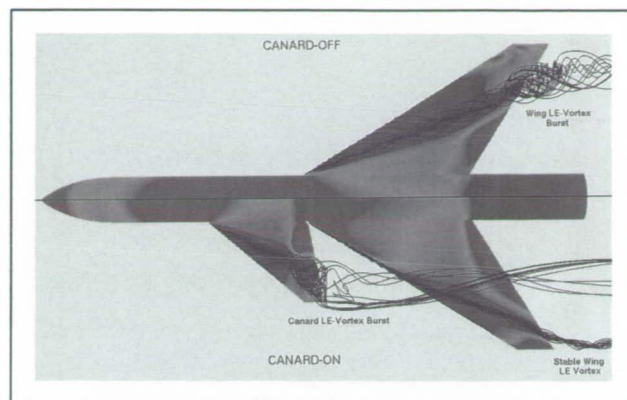


Fig. 1. Comparison between canard-on and canard-off surface pressure and off-surface particle traces at Mach 0.90 and an angle of attack of 12 degrees. (See color plate 28 in Appendix)

the potential of the canard to delay wing-vortex breakdown.

The second figure shows a comparison of computed results with wind-tunnel data. The lift- and moment-coefficient curves are separated into different regions of the geometry in order to better understand the influence of the canard. Because of the downwash generated in the canard's wake, the canard-on wing-portion lift is significantly lower than the canard-off wing-portion lift. However, the canard-on total lift is supplemented by the canard-portion lift and is higher than the canard-off total lift. The moment curves show that the canard does not significantly alter the wing's contribution to the total pitching moment. The nose-up pitching moment for the canard-on configuration

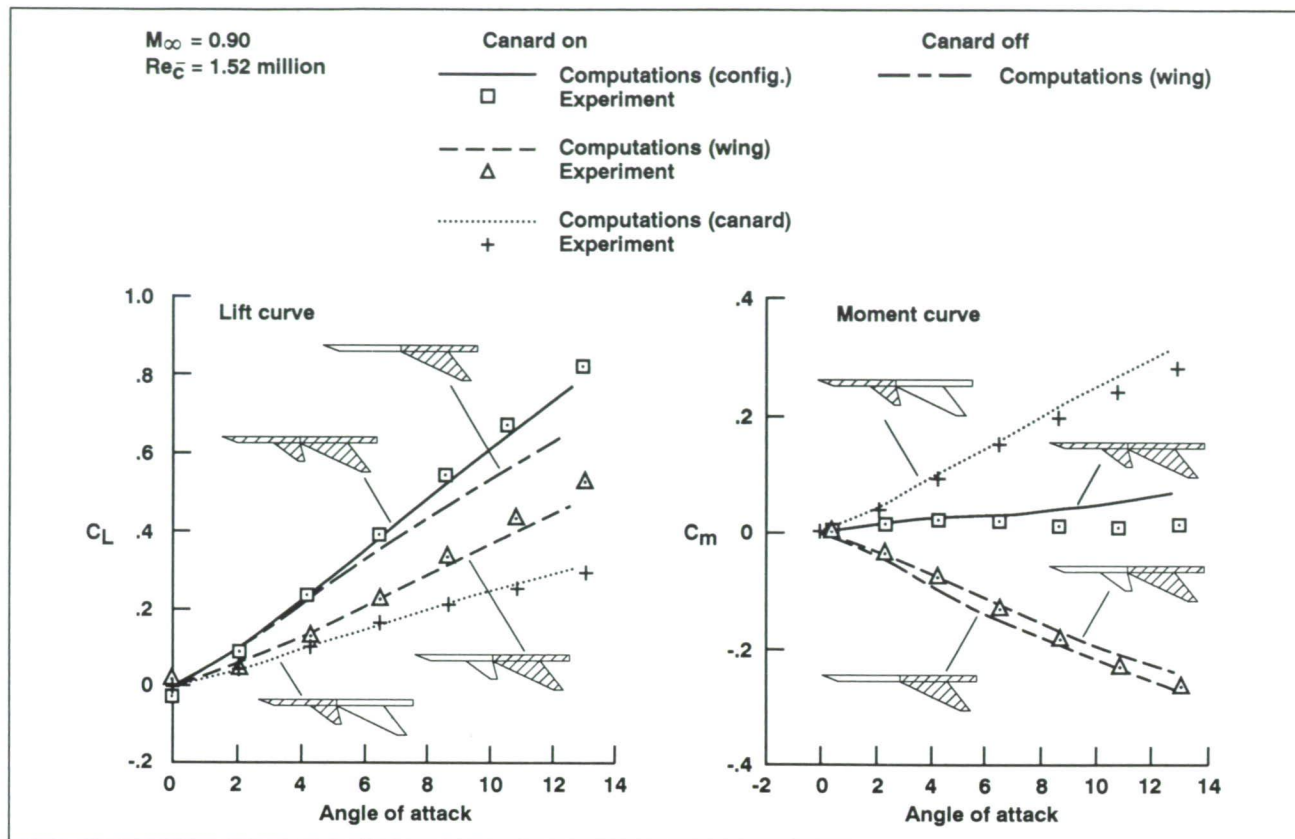


Fig. 2. Comparisons between computation and experiment of component lift and moment coefficients for the canard-on and canard-off configurations at Mach 0.90.

is mostly due to the canard's contribution to the moment. The comparison with experimental measurements also illustrates that the distribution of lift and moment between the canard and wing regions is captured well in the computations.

The computational tools and techniques demonstrated in this study serve to further the understanding

of canard-wing aerodynamic interaction and could be used to optimize the use of canards in future aircraft designs.

Ames-Moffett contact: E. Tu

(415) 604-4486

Headquarters program office: OAST

Comparison of Compressibility Corrections for Turbulence Models Applied to High-Speed Shear Layers

J. Viegas

Since 1972, it has been known that application of the classical k - ϵ turbulence model in computations of the flow in single-stream free-shear layers shows more spreading than actually occurs. Compressibility corrections have been developed that should reduce the mixing in shear layers by lowering the eddy viscosity through a reduction in the turbulence energy.

Two compressibility corrections to the k - ϵ model were studied and each was found to reduce the spread rate of free-shear layers for increasing convective Mach numbers over a wide range of conditions. This finding led to a significant improvement in the prediction of mixing of high-speed shear layers over the standard k - ϵ model. However, neither model agreed well with experiment over the entire range of convective Mach numbers studied, although the Zeman model was found to give the best overall spread-rate predictions. It was also found that spread rate based on vorticity thickness compared better with the data than did the spread rate based on impact pressure thickness and was less sensitive to the Mach numbers of the individual streams. Thus vorticity thickness may be the better variable to correlate compressible-shear-layer spread-rate data.

The figure shows the spreading rate (C_w) of the free-shear layer based on vorticity thickness normalized by the spreading rate at $M_c = 0$ for both experiment and the computations versus the convective Mach number (M_c). The convective Mach number is defined as the velocity difference between the two streams divided by the sum of their sound speeds. The Mach numbers of the two calculated streams are

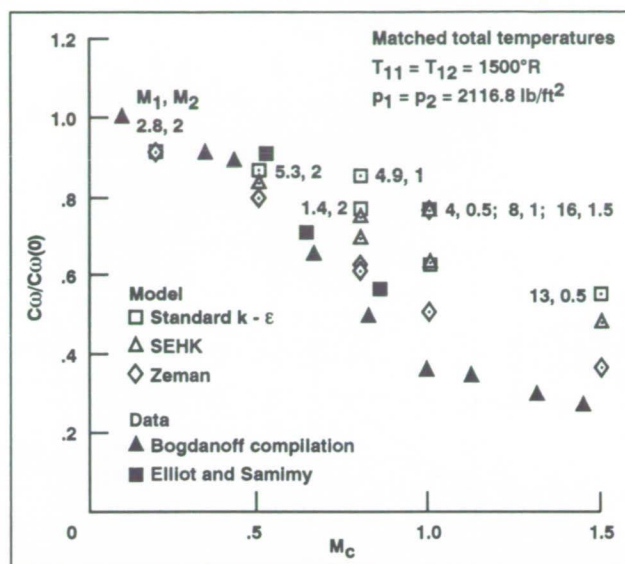


Fig. 1. Effect of compressibility on normalized vorticity thickness growth rate.

shown in the figure. The experimental data show the decrease in spread rate with increased M_c whereas the computations using the standard k - ϵ model do not adequately predict this reduction. Each compressibility correction reduces the spread rate as desired, with the Zeman model giving the largest reduction and the best agreement with the data.

Ames-Moffett contact: J. Viegas
 (415) 604-5950

Headquarters program office: OAST

Simulation of Turbulent Flow on a Highly Parallel Computer

Alan A. Wray

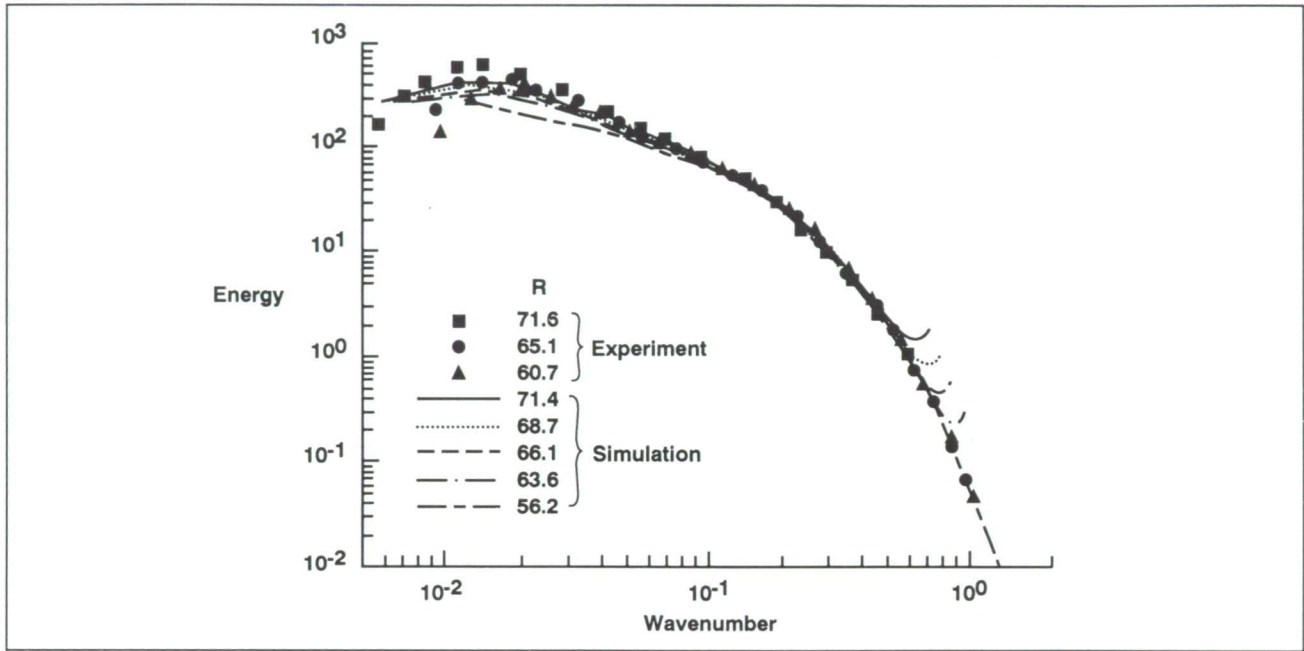


Fig. 1. Energy spectra from a simulation done on the Ames Intel supercomputer.

The computation of turbulent fluid flow requires the most advanced supercomputers available. Such machines in the future will have hundreds or thousands of processors, each with its own dedicated memory. These machines differ from most existing supercomputers, such as the Cray Y-MP, which have a small number of processors sharing a large common memory. It is therefore crucial to begin learning how to implement our computationally intensive fluid-flow simulations on this new type of machine. This project has shown that a typical turbulent-flow program can run on such a machine at a very high performance level—in the case of the 128-processor Intel Gamma computer, at a speed exceeding that of 11 Cray Y-MP processors.

This performance level was achieved by first constructing a highly optimizing compiler for the individual processors, then implementing an efficient interprocessor communication procedure, and finally applying these to program and compile an existing turbulent-flow program. This program has typically

been run on a Cray Y-MP at a speed of approximately 160 million floating-point operations per second (Mflops). On the 128-processor Intel machine, speeds as high as 1770 Mflops have been achieved. Using 512 processors on an Intel Delta computer at the California Institute of Technology in Pasadena, a speed of 5,450 Mflops has been attained. The greatly enhanced speed of these new machines will allow simulations of turbulent flow of significantly greater accuracy and scientific interest than current computers can produce.

The figure shows velocity power spectra curves at various Reynolds numbers (R) from a simulation done on the Ames Intel machine. The symbols represent experimental turbulence data measured in a wind tunnel.

Ames-Moffett contact: A. Wray
(415) 604-6066

Headquarters program office: OAST

Initial Rollup of a Wingtip Vortex

Greg G. Zilliac, Jim S. Chow, Peter Bradshaw

The wingtip vortex flow is of great importance because of its effect on practical problems such as landing separation distances for aircraft, blade–vortex interactions on helicopter blades, and propeller cavitation on ships. It also continues to be a perplexing problem for the computational scientist because of the presence of large gradients of velocity and pressure in all three dimensions, especially in the near field at high Reynolds numbers. In the case of wings with nearly elliptic loading, a discrete vortex forms at the tip, fed by vorticity from the tip boundary layer. As the vortex moves downstream, it rolls up more and more of the wing wake until its circulation is nominally equal to that of the wing. The rollup distance is small compared to the separation of aircraft on the approach path, but not necessarily small compared to the distance between the interacting lifting surfaces, such as the main wing and the tail on aircraft. The flow in the near-field rollup region is therefore important in its own right as well as in providing a possible means of control of the far-field vortex.

In our experiment, surface oil-flow visualization, laser-illuminated smoke visualization, surface pressure measurements, and velocity-field measurements by use of a 7-hole pressure probe have been completed for the flow over a rectangular wing with rounded tip. The Reynolds number based on chord was 4.6 million and the angle of attack was 10 degrees. Given the trade-off between taking extensive measurements at one flow condition and taking fewer measurements at several flow conditions, the former option was chosen, because measurements at closely spaced points are needed to resolve the large spatial gradients in the thin tip boundary layer and the rollup region, and because it would give the computational scientist a solid test case to compare his or her results with.

From the results acquired to date, we have been able to build a detailed qualitative and quantitative picture of the process by which the tip boundary layer separates and rolls up into a vortex. The highly three-dimensional nature of the flow near the tip region is



Fig. 1. Measured surface-pressure-coefficient contours. (See color plate 29 in Appendix)

reflected in the surface-pressure-coefficient contours shown in the first figure. Highlighted is the suction peak due the main tip vortex where a minimum pressure coefficient of -1.30 was measured. A numerical integration of this surface pressure distribution gives a lift coefficient of 0.51 , which is consistent with Prandtl's results for a rectangular wing with low aspect ratio. The second figure shows normalized

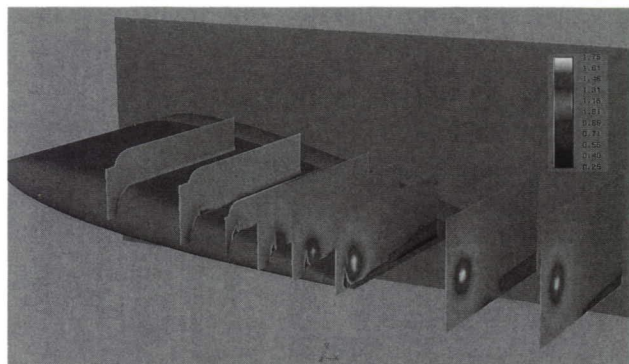


Fig. 2. Measured normalized velocity magnitude.
(See color plate 30 in Appendix)

velocity magnitude at several streamwise-data-plane locations as measured by seven-hole pressure probe. The velocity magnitude in the core of the vortex increases as one progresses down the chord of the wing. A maximum velocity of 1.77 times the free-stream velocity was obtained just downstream of the trailing edge. This level of vortex-core velocity is higher than what was previously thought to exist.

In the near future, all six components of the Reynolds stresses will be measured at the same data locations as the seven-hole pressure probe, by use of cross-wire probes, and laser Doppler velocimeter equipment will be used to survey the core of the tip vortex. In combination with the mean flow data, this data base will be used to validate a three-dimensional Navier-Stokes computation of the identical configuration (including wind tunnel walls).

Ames-Moffett contact: G. Zilliac
(415) 604-3904

Headquarters program office: OAST

The NAS Parallel Benchmarks

D. H. Bailey, H. D. Simon, T. A. Lasinski, J. T. Barton

Defining meaningful benchmarks and obtaining accurate benchmark results for new supercomputers is essential not only for the procurement of supercomputers by NASA and other organizations, but also for the analysis of architectures and compiler technology.

Highly parallel systems with peak computing power roughly equivalent to conventional vector supercomputers exist today. Unfortunately, evaluating the performance of these parallel systems in a meaningful way is difficult. Data regarding the sustained performance of these systems on problems of interest to the computational aerophysics community are particularly scarce.

In light of these challenges, the authors, together with other researchers at Ames, have developed a new approach to benchmarking. The concept is to define benchmark problems only by "pencil and paper" definitions. The problems to be solved are completely defined in a technical paper, which includes a precise definition of the input data and an excerpt of correct output results. While some algorithmic approaches are suggested or required, researchers

are free to explore a wide variety of algorithms and implementation techniques to select the most effective solution for a given computer system. The benchmarks require that the problems be implemented in some parallel extension of FORTRAN or C, but considerable flexibility is allowed.

The authors' technical paper "The NAS Parallel Benchmarks" defines eight problems to be solved. These range from fairly simple "kernels" to three rather sophisticated "simulated computational fluid dynamics (CFD) applications" that represent the basic data movement and computational requirements of a modern CFD computation. Sample FORTRAN codes are available to researchers on request, but these codes are simple one-processor implementations intended as merely a starting point for programmers and are not intended to represent a good approach for a parallel system.

These benchmark problems have now been implemented on a number of parallel computer systems, and some performance results are shown in the table. Figures are included for three systems:

Table 1. NAS parallel benchmark results (MFLOPS)

Benchmark	Problem size	Y-MP 8	CM-2 32K	iPSC/860 128
Embarrassingly parallel	2^{28}	1399	659	362
Multigrid	256^3	2706	308	824
Conjugate gradient	2×10^6	631	104	70
3-D FFT PDE	$256^2 \times 128$	1795	414	696
LU solver	64^3	1705	186	224
Scalar penta. solver	64^3	1822	109	122*
Block tridiagonal solver	64^3	1554	94	199*

*Runs with 64 processors rather than 128.

the Cray Y-MP (eight processors), the CM-2 from Thinking Machines (32,768 bit-wise processors or 2,048 floating-point processors), and the iPSC/860 from Intel (128 processors). Intel results noted with an asterisk indicate runs with 64 processors rather than 128.

These results show that whereas the current generation of highly parallel computers shows great promise, the computers do not yet deliver sustained performance on aerophysics problems equivalent to the best conventional supercomputers (comparing full

systems to full systems). It is hoped, however, that the next generation of highly parallel systems will deliver sustained performance at or above that of conventional supercomputers. In any event, the NAS parallel benchmarks will help in measuring the progress of this technology.

Ames-Moffett contact: D. Bailey
(415) 604-4410

Headquarters program office: OAST

Modeling of the Fabrication of Ceramic Coatings and Composites

Domenick E. Cagliostro

Ceramic coatings and composites retain their properties at high temperatures in an oxidizing environment. This characteristic makes them suitable candidates for use as thermal protection and hot structural elements in advanced aerospace vehicles. Ceramic coatings and composites can be made by pyrolysis of a gaseous reactant, depositing a solid matrix that surrounds a solid or a high-strength fiber. Interactions between the chemistry and the physical processes that occur during deposition determine the time necessary to fabricate the coating or composite and also determine its final chemical and mechanical properties.

Mathematical models have been developed at Ames to describe the deposition process. These models can be used to guide the design of reactor hardware, determine operating conditions, and establish preferred characteristics of the substrate. The models have been used to investigate the effects of fabric lay-up and operating conditions for a composite made of a woven carbon fabric and a silicon-carbide matrix formed from the pyrolysis of dichlorodimethylsilane in hydrogen. The figure shows the predicted and experimental deposit thickness vs. time. The final porosity of the composite at 145 hours is predicted to be 20.0% compared to 18.8% found experimentally. Both predicted results compare favorably with experiment. The models have also been used to make an analytical study of the response of a well characterized reactor, the stirred tank—a design that can be scaled and is suited to make multiple parts simultaneously.

One model has been modified to include the case of deposition of multiphase materials. Predictions are

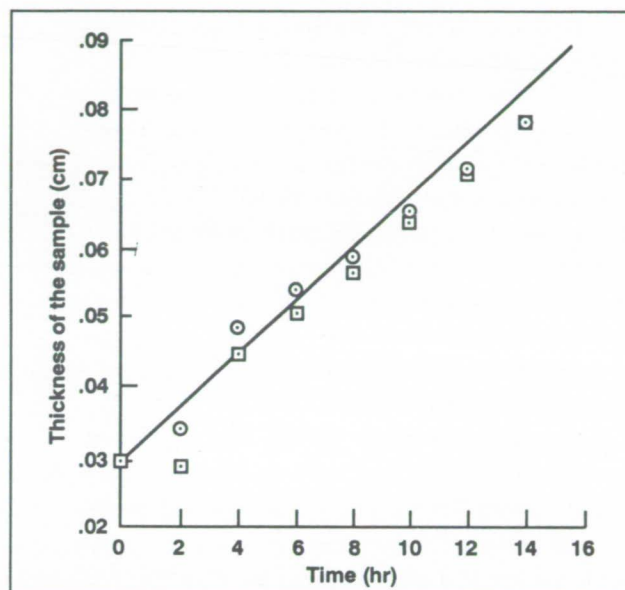


Fig. 1. Thickness of the sample vs. time. The different symbols represent experimental data from two runs under identical conditions; the solid line is the model prediction.

extended to the case of a graded coating of silicon carbide and titanium diboride. Experimental work is in progress to make silicon-carbide and titanium-diboride coatings on carbon honeycomb fabrics to test the properties of this coating and to validate the model.

Ames-Moffett contact: D. Cagliostro
(415) 604-6109

Headquarters program office: OAST

MESUR Heat Shield Computations

William D. Henline

NASA is currently studying a Mars planetary probe mission, MESUR (Mars Environment Survey), which is designed to "hard-land" several surface diagnostic probes on the Martian surface. These probes will perform various seismic, geophysical, and atmospheric survey measurements. The probes are launched from Earth and directly enter the Mars atmosphere in a ballistic manner. During entry, the probes experience significant aerodynamic heating and must be provided with a thermal protection system (TPS) or heat shield. The design and specification of such a heat shield is critical in this case, since net payload of the probe will be a strong inverse function of the aeroshell mass fraction. The MESUR probe aeroshell is a blunt, 70-degree half-angle conical body; determination of the surface heating on such a shape is a difficult process. Significant progress in this area has been made in the last year at Ames.

A vehicle entering the Mars atmosphere experiences surface heating from an atmosphere of predominantly carbon dioxide (approximately 95% CO₂, 5% nitrogen). Accurate determination of this aerothermodynamic heating can only be obtained from a definitive calculation of the hypersonic, real-gas flow field that surrounds the entry body as it flies through the atmosphere. Results from this calculation will include the various heat fluxes such as conduction and exothermic energy released to the surface. Until the present calculations were performed, a complete analysis of these effects on blunt body shapes of the MESUR type have not been available, especially for a CO₂-dominated atmosphere. Knowledge of transport properties, gas-reaction-rate kinetics and, especially, surface-catalytic-rate coefficients is very sparse for the CO₂ system. In order to ascertain the range of MESUR heat-shield mass fractions possible with the current level of knowledge, a systematic study of the parameters was performed; a recently enhanced Navier-Stokes shock-capturing code (NSCAND) was used for this study. This program is configured with a variety of transport and gas-

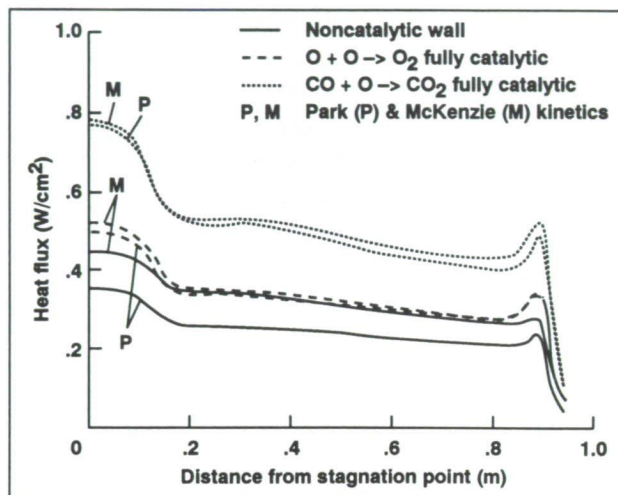


Fig. 1. Effect of surface catalysis and gas kinetics.

reaction models for the Mars atmosphere and has a complete set of boundary conditions to model a finite-rate, catalytic heat-shield surface.

Variation of the gas-phase reaction rates and transport coefficients for the nominal peak heating point for the MESUR flight body showed that surface heating is a strong function of these values. Surface heating is most strongly affected by gas reaction rates if the material is noncatalytic, while heating is most sensitive to transport coefficients if the surface is fully catalytic. The effect of surface catalysis itself for a nonablating surface (which is the case here) is profound. The figure shows the range of heating values obtained for MESUR in this study. There is a factor-of-two difference between the lowest noncatalytic values and the highest fully catalytic values. The present study has thus shown that accurate information on surface catalysis is imperative for the design of the heat shields for CO₂ planetary atmospheres.

Ames-Moffett contact: W. Henline
(415) 604-6623

Headquarters program office: OAST

Composite Flexible Blanket Insulation

Demetrius A. Kourtides

Recent tests have shown that a composite flexible blanket insulation (CFBI) fabricated with a specially woven interlock fabric is capable of providing thermal protection to structures exposed to very high heat-flux rates and temperatures. The insulation system is composed of (1) an outer layer of silicon carbide fabric that has been woven in a special interlock design, (2) a layer of alumina insulation, (3) alternating layers of aluminoborosilicate and aluminized polyimide, and (4) aluminoborosilicate fabric on the back surface. The insulation system is sewn using a silicon carbide thread with a locking-type stitch. Applications being studied for these insulations include thermal protection systems for aeroassist space transfer vehicles (ASTV) and insulation for the cryogenic tank of the National Aerospace Plane (NASP). The materials were fabricated by ILC Space Systems Division using NASA Ames specifications.

An example of results obtained from arc-jet testing is shown in the figures. The first figure shows the surface and back-face temperature of the insulation when exposed to a front-face heat flux of 34.3 Btu per

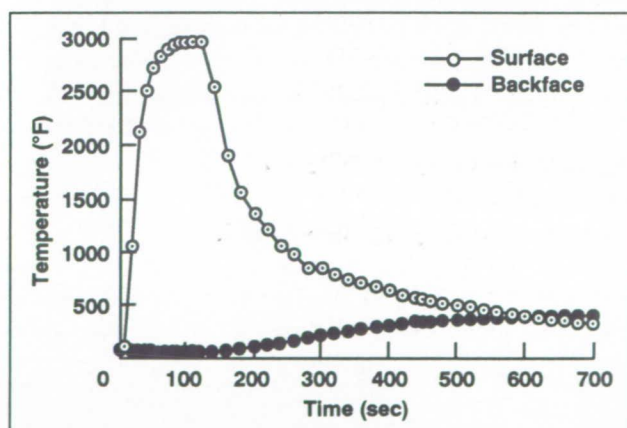


Fig. 1. Thermal response of composite flexible blanket insulation at 34.3 Btu/ft²·sec.



Fig. 2. Composite flexible blanket insulation after exposure to 34.3 Btu/ft²·sec for 120 seconds.

square foot·seconds for 120 seconds. As seen in the figure, the front-face surface temperature reaches approximately 2950 °F with the back face reaching a maximum of 500 °F. The insulation was 1 inch thick with a density of 10 pounds per cubic foot. Previous insulations using a conventional silicon carbide fabric, such as 5 harness satin weave or plain weave, were able to withstand only 2700 °F. The second figure shows the blanket after exposure to the arc-jet tests. As seen in the photograph, the fabric is intact with no holes on the surface. The results obtained from these tests clearly demonstrate the capability of this flexible insulation to withstand high heat-flux rates and temperatures.

Ames-Moffett contact: D. Kourtides
(415) 604-4784

Headquarters program office: OAST

Advanced Toughened Uni-Piece Fibrous Insulation (TUFİ-MT)

Daniel B. Leiser

Arc-jet testing of an advanced toughened-uni-piece-fibrous-insulation (TUFİ) thermal protection material to determine the improvement in the composite's original temperature capability (2500 °F) has successfully demonstrated a higher temperature capability (2900 °F) for this family of low-density composite insulations. This novel composite has graded density, tensile strength, and thermal conductivity. It has a high-emissivity, intermediate-density surface treatment and improved impact resistance. The material has demonstrated reusability (five cycles of 10 minutes to 2900 °F) while not losing its optical properties at high temperature. In addition, no thermal stress problems were observed in the severe thermal gradient that is characteristic of an arc-jet test.

The advanced version, designated TUFİ-MT, uses a high-temperature-capability substrate, the Alumina-Enhanced Thermal Barrier (AETB-40), which contains 40% by weight alumina fiber. The surface recession of the TUFİ-MT with the AETB-40 substrate was limited to a nominal 0.04 inch after 50 minutes at 2900 °F. Previous attempts to apply a high-emissivity coating to the AETB-40 substrate, or to others containing more than 40% refractory fiber by weight, have been unsuccessful because of thermal-stress cracking and/or thermal-expansion mismatch between the insulation substrate and the coating. TUFİ with its original emissivity agent and AETB-20 substrate was the first graded-property, reusable surface insulation to be produced and tested successfully for future use on the Space Shuttle. It has shown very good performance in

flight rain-erosion tests and in acoustic vibration testing. TUFİ demonstrates a one- to three-order-of-magnitude improvement in impact resistance over the standard fully dense Reaction Cured Glass (RCG) coating used now on the Shuttle tiles. In addition, damage resistance of the TUFİ can be varied during processing to match durability requirements for different applications.

The TUFİ system has demonstrated its capability to be used on refractory substrates because of its lower modulus and higher effective thermal-expansion coefficient than those of the baseline RCG coating. The TUFİ system is simple, and it can be easily modified and applied to different heat-shield materials with complex shapes. Because of its open porosity it also allows easy rewaterproofing without the use of a hypodermic-needle injection which is used for the current Shuttle tile system.

Further improvements in TUFİ materials are currently being pursued through (1) the use of surface overlays, (2) the development of more stable emittance agents, and (3) modifying the amount and composition of the matrix glass. These TUFİ systems will continue to be evaluated for their reusability in high-temperature convective heating environments (arc-jet) and for their relative impact resistance.

**Ames-Moffett contact: D. Leiser
(415) 604-6076**

Headquarters program office: OAST

TOPHAT Thermal Protection System Performance

Salvatore R. Riccitiello

Initial tests in the mid-1980s showed that the TOPHAT thermal protection system would provide for a toughened high-temperature system capable of withstanding temperatures up to 2700 °F, while maintaining a system density equivalent to that of the state-of-the-art black tiles used on the Space Shuttle. An advantage of incorporating a tough ceramic-matrix composite outer shell is that the system can withstand small-particle impacts that are orders of magnitude higher than the Shuttle tile system can withstand.

An aeroconvective heating test has shown that the advanced TOPHAT system can withstand 3000–3100 °F without any surface recession and minimum loss of mass. The objective of this latest test

series was to establish the upper reuse surface temperature for the three-ply, carbon/silicon-carbide ceramic matrix composite (CMC), and the thermal response of the interior insulating components. An example of the aeroconvective test model and results from exposure to a heat flux of approximately 100 Btu per square foot-seconds is shown in the first two figures. It should be noted that the interior thermal response is higher than expected. This can be easily explained by the side-wall heating during the test which amounts to approximately 30% of the stagnation heat flux.

In-house research has also focused on the methods of attachment of the TOPHAT to rigid insulation

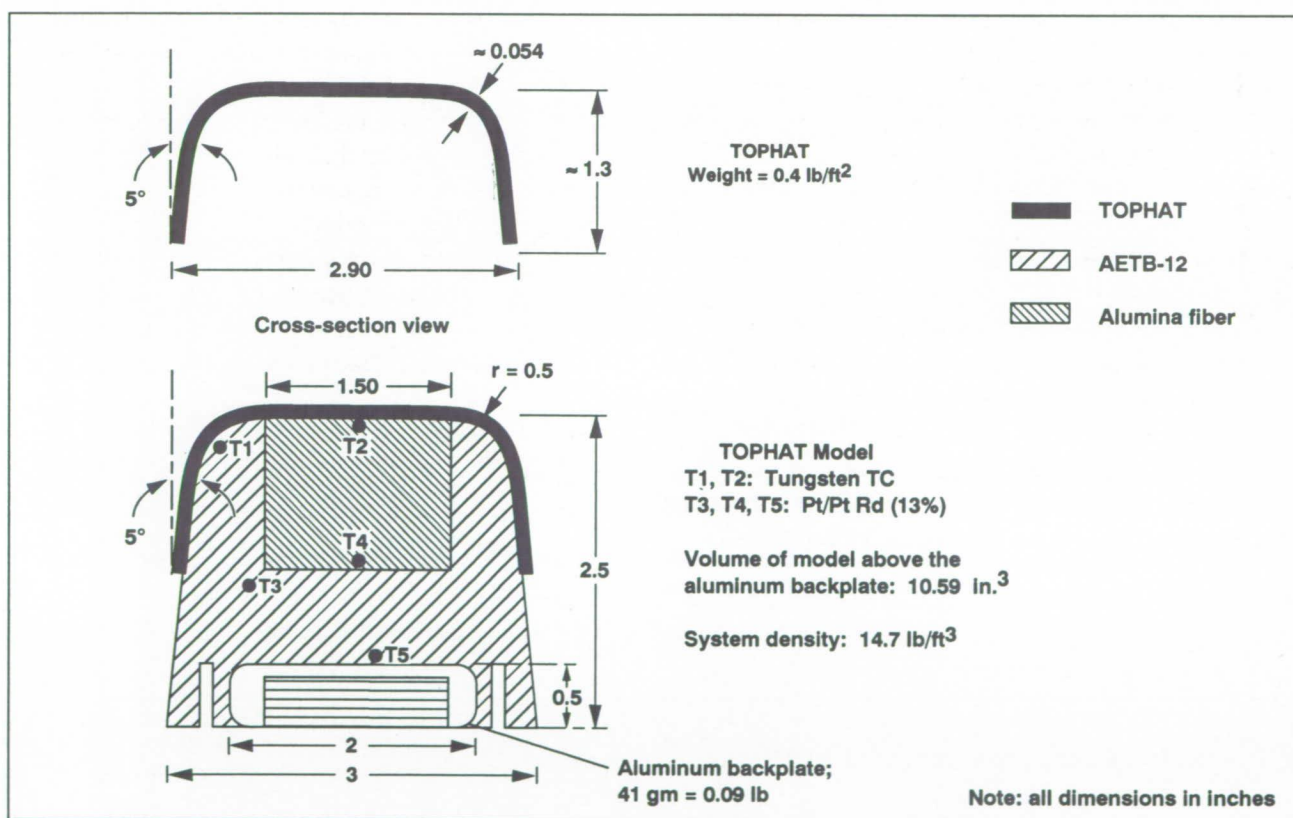


Fig. 1. Arc-jet model design.

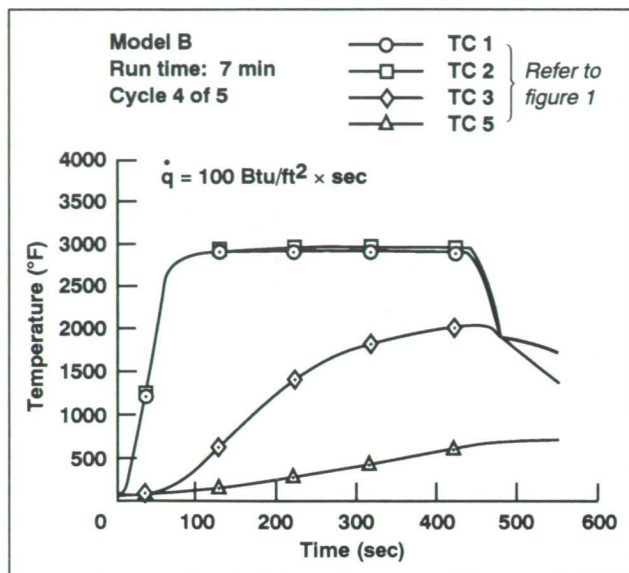


Fig. 2. Thermal response of TOPHAT model.

materials. Previous methods involved clips or pins through CMC tabs that extended down from the TOPHAT surface. A recent method uses a breechlock design. This allows for the locking of the CMC directly to the rigid insulation as shown in the third figure.

These recent results show that the TOPHAT thermal protection system is a viable candidate for advanced spacecraft heat shields in conditions where temperatures from 3000 °F to 3100 °F are expected and where durability with regard to particle impact and handling is important.

Ames-Moffett contact: S. Riccitiello
(415) 604-6080
Headquarters program office: OAST

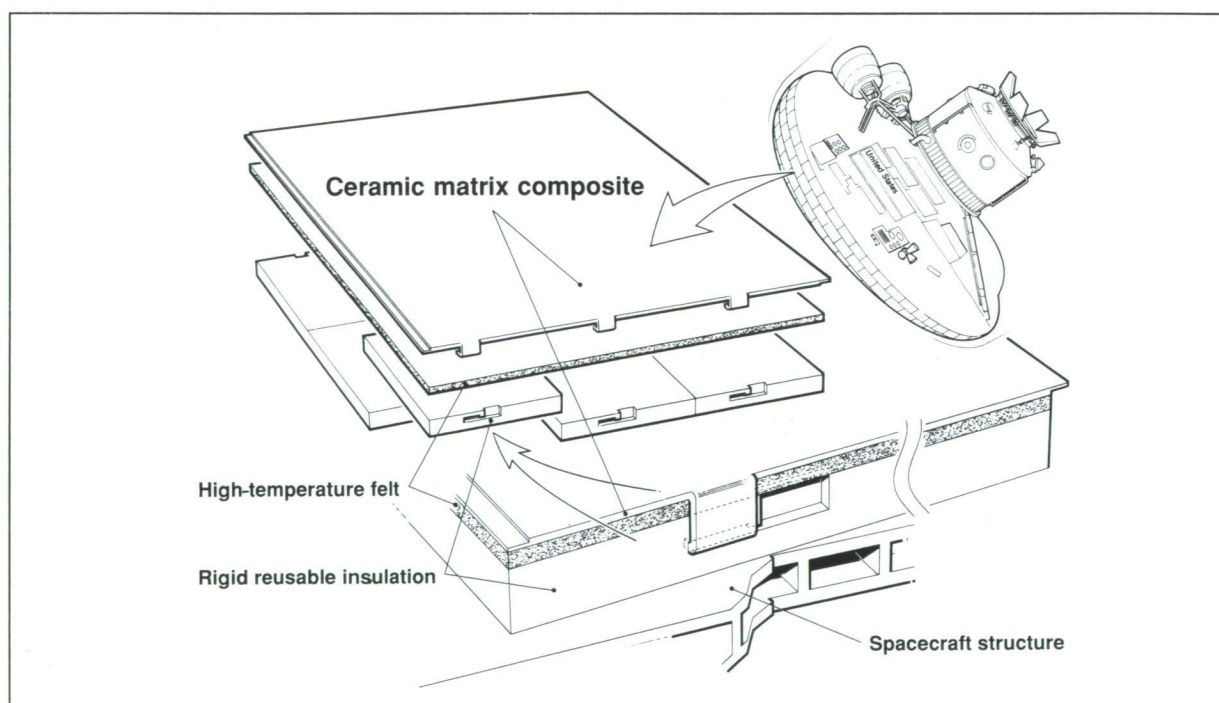


Fig. 3. Breechlock attachment method of TOPHAT to rigid insulation.

TABI Aeroacoustic Performance

Paul M. Sawko

The use of flexible ceramic blankets as an external thermal protection system (TPS) for advanced space vehicles will require the TPS to not only survive extreme aerothermal environments, but to have a resistance to high aeroacoustic noise levels that can involve fluctuating airloads on the blanket surface. Ceramic blankets flying on the Shuttle Orbiters are sewn quilted blankets that can function continuously at temperatures up to 1200 °F. These are called advanced flexible reusable surface insulation (AFRSI) blankets. During launch, aeroacoustic noise levels seldom exceed 156 decibels, but some advanced vehicles must withstand noise levels in the range of 170 decibels at higher temperatures (over 2000 °F).

Threadless ceramic blankets have been developed by weaving 1800-denier silicon carbide yarn into single-ply, integrally woven core structures filled with alumina or aluminoborosilicate filler. These blankets are called tailorable advanced blanket insulation (TABI). Although TABI provides a TPS with a temperature capability up to 2500 °F, it does not increase survivability of high aeroacoustic noise, in the 170-decibel range.

An advanced version of this integrally woven core structure has been developed that has a woven fabric surface toughened to resist high aeroacoustic noise without the application of a ceramic overcoat. The improved version, designated TABI-AI, is fabricated from 600-denier silicon carbide yarn and uses an angle-interlock weave architecture as a fabric surface. This design provides a more durable surface which is resistant to high aeroacoustic noise. TABI-AI has shown no change after exposure for 600 seconds to a 170-decibel noise level in a mini-wind-tunnel test facility with a fluctuating pressure environment of 2.7 pounds per square inch and a dynamic pressure of 510 pounds per square foot. The figure shows a comparison of the aeroacoustic survivability of the

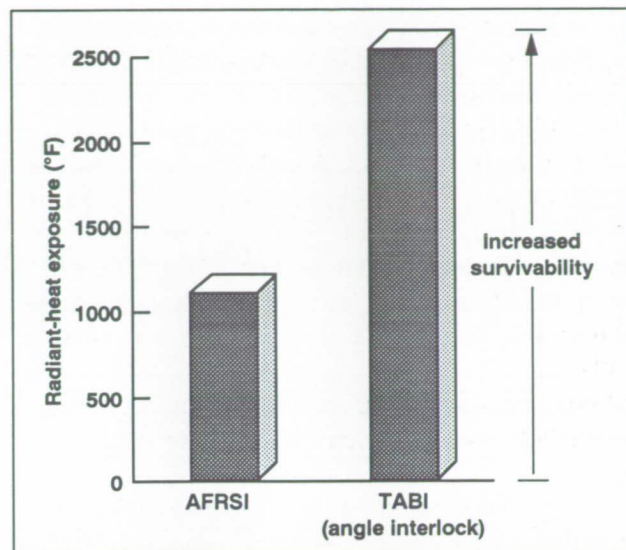


Fig. 1. Aeroacoustic survival of flexible TPS after 600 seconds at 170 decibels.

TABI-AI with that of the AFRSI blankets. The TABI-AI surface had first been exposed to a 2500 °F radiant heat cycle for 2 minutes, and the AFRSI was exposed to only a 1200 °F cycle for 10 minutes.

TABI-AI has shown remarkable improvement in durability with regard to aeroacoustic noise (170 decibels) when compared to contemporary sewn-blanket systems such as the AFRSI used on the Shuttle Orbiters. This angle-interlock version of TABI should be considered for future space vehicles or other applications where resistance to high aeroacoustic noise is important.

Ames-Moffett contact: P. Sawko
(415) 604-6079

Headquarters program office: OAST

Computerized Film Reading

Leslie A. Yates

In aeroballistic-range experiments, aerodynamic coefficients are obtained by fitting calculated trajectories to measurements of the position and orientation of a model. These experimental measurements are obtained by "reading" a series of orthogonal shadowgraphs taken at known times as the model flies down the range. In the past, these readings have been manual; measurements were subject to both human interpretation and error, and the time requirements for film reading were excessive. In addition, only points and edges of the model image were used to define its position and orientation, and the vast majority of information recorded in the shadowgraphs was ignored.

To improve the quality of the measurements and to reduce the time requirements, a computerized film-reading system has been developed for axially symmetric models. In this system, the shadowgraphs are first digitized using a scanner. Software then identifies the pixels in the digitized image that are associated with the fiducial lines and the model image. Methods to eliminate "noisy" data have been developed for the line-identification procedures. A weighted least squares method is used to find the center of the fiducial lines, and the centroid method (a variation of weighted least squares methods) is used to find the axis of symmetry and the center of the model image. The weighting is a function of the grey scale

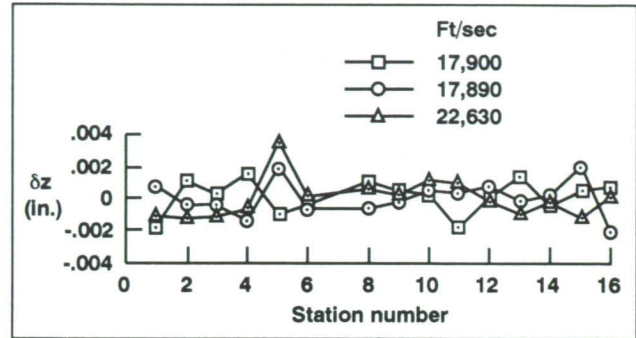


Fig. 2. Computer and manual position measurements for three sphere shots.

and is proportional to the area of the pixel covered by the fiducial line or model image. From these readings, the model position and orientation in the aeroballistic range can be determined.

This system has been used to read the shadowgraphs for calibration-sphere and blunt-cone tests, and the time requirements for film reading have been greatly reduced. The accuracy of the computerized readings was found to be the same as or better than that of the manual readings. In the first figure, measurements of the angle of attack obtained from the computerized and manual methods are shown. The angles of attack were fitted using a five-degree-of-freedom parametric identification procedure; the residual errors for the computerized readings were slightly better than the residual errors for the manual readings. The deviation of the experimental position measurements from the calculated trajectory are shown in the second figure for three spheres tested in the aeroballistic range. The average velocities of the spheres were 17,890, 17,900, and 22,630 feet per second. The accuracy of the aeroballistic-range position measurements is better than 0.002 inch. Because of magnification between film and range measurements, this translates to 0.001 inch for the shadowgraph readings. The pixel size is 0.003 inch; hence, using all the available information to define the fiducial lines and model image locations improves the reading to better than the pixel resolution. Other

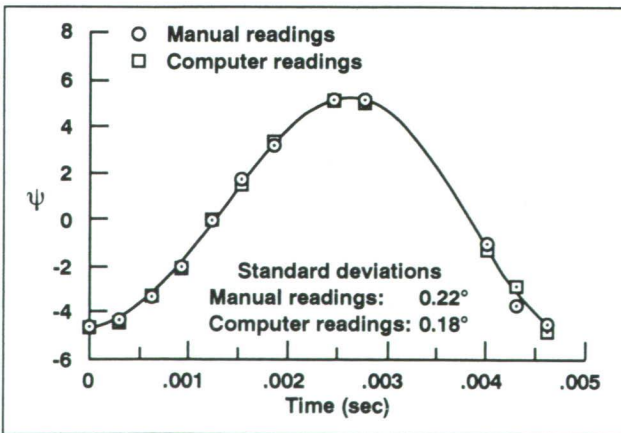


Fig. 1. Computer and manual orientation measurements for a blunt cone.

studies indicate that the accuracy of the readings is presently limited by the quality of the shadowgraphs and not the resolution of the scanner.

Ames-Moffett contact: L. Yates

(415) 604-3436

Headquarters program office: OAST

Constructed Images from Computed Flow Fields

Leslie A. Yates

Experimental interferograms, schlieren, and shadowgraphs contain invaluable information for validation of ideal- and real-gas computational fluid dynamics (CFD) codes. The intensity patterns in infinite- and finite-fringe interferograms are proportional to integrated functions of the refractive index

(density for ideal-gas flows). Flow features such as shocks, shear layers, and expansion fans are recorded in schlieren and shadowgraphs. When flow-field simulations have been compared to these images, contour plots for planes of data have been used. For three-dimensional flows or for models that are free to roll, no single computational plane provides all the information necessary for realistic comparisons to these experimental images.

Software has been developed that constructs these images from ideal- and real-gas, two- and three-dimensional, and axially symmetric computed flow-field solutions. The computational grids can be structured or unstructured, and multiple grids are an option. Interferograms are constructed from line integrals of the refractive index. The intensity variations in schlieren are proportional to the angular deflection of the light. Shadowgraphs are obtained by adding contributions of the deflected light beams at each point on the image plane; the thickness of the dark and bright regions is partially controlled by the position of the image plane. The dependency of the thickness of these regions on the image plane's position is also observed in experimental shadowgraphs. An example of a constructed shadowgraph is shown in the figure.

The constructed images are similar to the experimental images: flow features in both the constructed and the experimental images are represented by the same variations in the grey scale, and the constructed images include all three-dimensional effects observed in the experimental images. These similarities facilitate the comparison of computation and experiment.

Ames-Moffett contact: L. Yates

(415) 604-3436

Headquarters program office: OAST

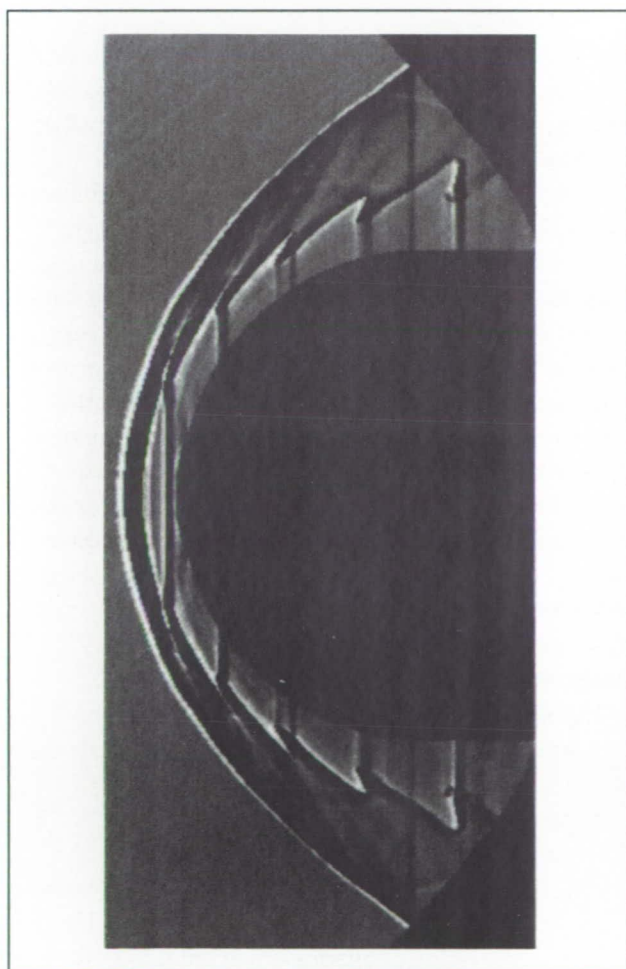


Fig. 1. Constructed and experimental shadowgraphs for a hemisphere-cylinder in a combustible mixture.

Trim-Angle Measurements

Leslie A. Yates, Ethiraj Venkatapathy

Aerodynamic coefficients and trim angles for the Aeroassist Flight Experiment were predicted from computed flow-field simulations and from free-flight tests conducted in the aeroballistic range at Ames Research Center. An ideal-gas, three-dimensional flow solver, FL3D, was used for the computations. An effective specific heat ratio (γ) was used to model the real-gas effects; an appropriate γ was chosen from shock shape comparisons.

A six-degree-of-freedom, weighted least squares parameter-identification code that calculates aerodynamic coefficients and trim angles from free-flight data was developed. In this parameter-identification code, differential corrections are made to the nonlinear aerodynamic coefficients until the best fit of the calculated trajectory to the experimental position and orientation measurements is obtained. Since the experimental data was limited, higher-order terms in the series expansions of the aerodynamic coefficients were fixed by the flow-field computations. The experimental zero- and first-order terms in the series expansions and the trim angle were found using the parameter-identification procedure. The experimental

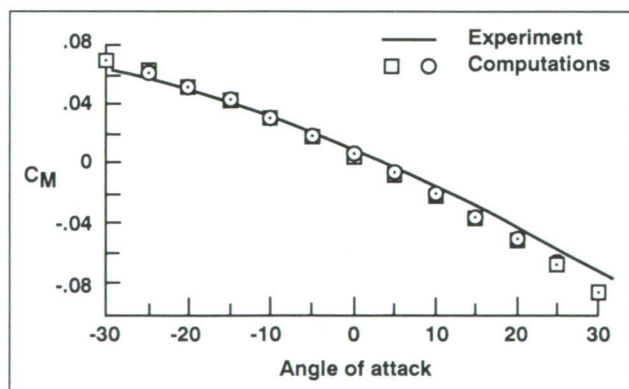


Fig. 1. Moment coefficient at design center of gravity.

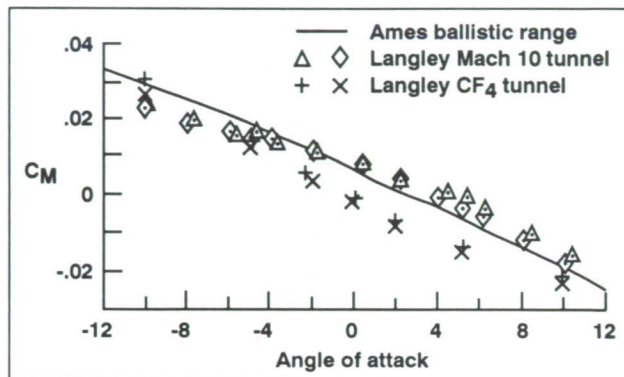


Fig. 2. Comparison of moment coefficients for three facilities.

and computed moment coefficients are shown in the first figure. The zero- and first-order terms as well as the trim angle are in good agreement.

The second figure shows the moment coefficients for three different facilities: the Ames aeroballistic range and NASA Langley's 31-Inch Mach 10 and Hypersonic CF₄ Tunnels. The trim angle for the range tests is 14.5 degrees as opposed to the design trim angle of 17 degrees. The effective γ for the range tests and FL3D simulations was 1.20. The Langley trim angle results are 12 degrees for the Mach 10 tunnel tests ($\gamma = 1.34$) and 17 degrees for the Hypersonic CF₄ Tunnel tests ($\gamma = 1.11$). The differences in trim angle are attributable to differences in γ . Accurate predictions of the trim angle require proper modeling of the real-gas effects at flight conditions.

Ames-Moffett contact: L. Yates
(415) 604-3436

Headquarters program office: OAST

Lunar Outpost Life-Support-System Analysis

Mark G. Ballin, William C. Likens, Vincent J. Bilardo, Jr.

A conceptual design of a life-support system (LSS) has been developed as part of an ongoing comprehensive study of advance-processor technologies and system architectures for an initial lunar outpost (ILO). The design is based on a mission scenario requiring intermittent occupation of a lunar-surface habitat by a crew of four. It incorporates physiochemical-process technologies that were considered for Space Station Freedom (SSF). A system-level simulation model of the design was developed to obtain steady-state material balances for each LSS processor. The mass-flow-rate predictions were used to obtain estimates of the LSS mass, volume, and power consumption by means of processor sizing correlations that were extrapolated from SSF processor designs. The results were used to analyze the impacts of varying crew size, mission duration, processor operation strategy, and crew

cabin loads on the LSS mass, average power consumption, volume, periodic resupply mass, and waste accumulation rate. The merits of the design were quantified relative to an open-loop LSS, and the implications of this assessment for future LSS research and technology development were identified.

The first figure illustrates the flows of material within the design. The design makes use of high-readiness SSF-era process technologies that enable regeneration of air and water, thus minimizing the need to resupply these consumables. Carbon dioxide is removed from the crew cabin and oxygen is recovered in the atmosphere revitalization subsystem. Two grades of water quality are provided by the water reclamation subsystem: a potable grade for crew consumption, and a hygiene grade for showers, laundry, dishwashing, and other facilities requirements.

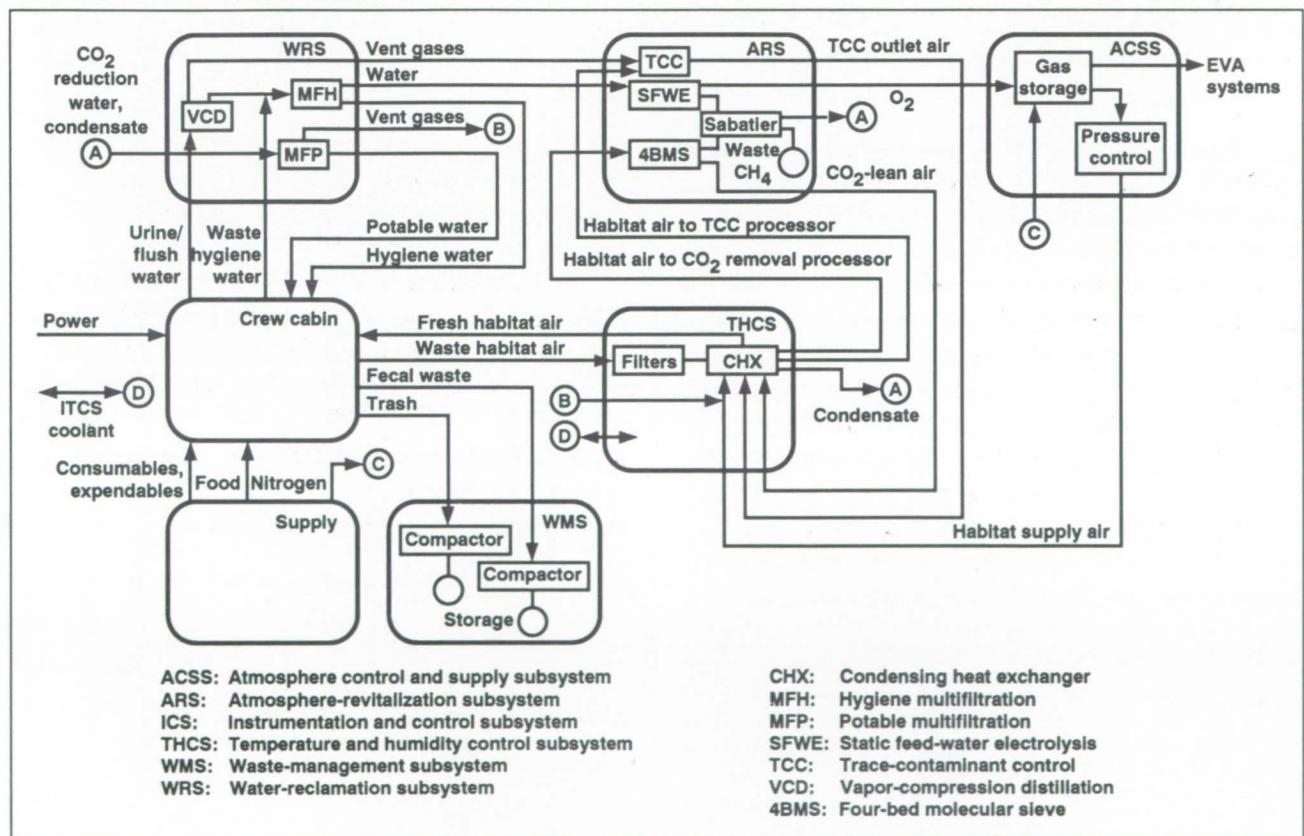


Fig. 1. Life-support-system design for an initial lunar outpost.

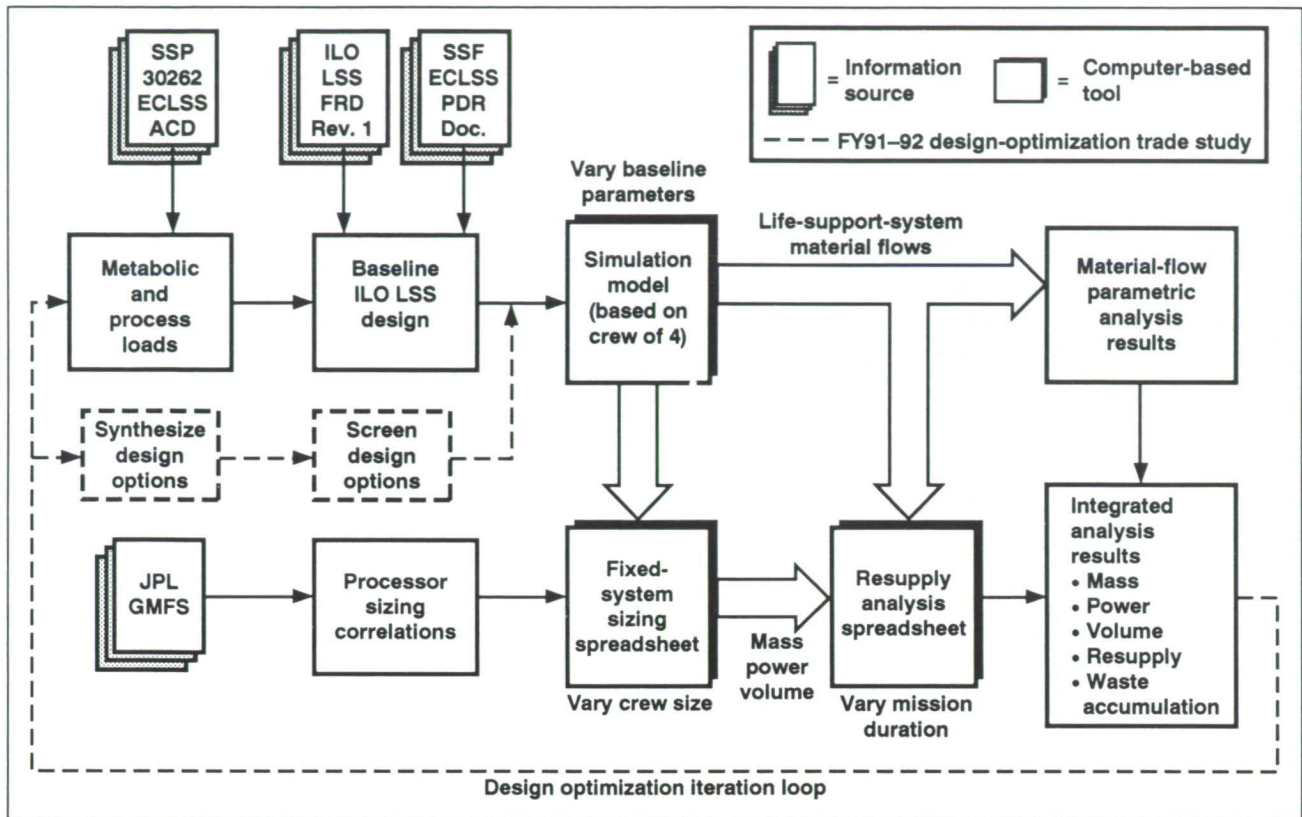


Fig. 2. Analysis methodology for an initial lunar outpost.

The methodology used in system-level analysis of an ILO life-support system is shown in the second figure. Reference values of parameters that impact operational loads were first established for the design. These and other sources of information, such as an Ames-developed functional-requirements document and SSF preliminary-design-review documentation, were used to develop a baseline design. A simulation model was then developed to generate steady-state mass balances throughout the system. A spreadsheet analysis was used to size the emplaced system and to estimate resupply and waste accumulation as functions of design and operation, crew size, and mission duration. The system sizing information was deter-

mined from processor sizing correlations, which estimate mass, average power consumption, and volume as functions of mass flow rate and other operational parameters.

Initial assessments of the LSS design indicate that life-support-resupply mass requirements can be reduced by a factor of 10 over conventional non-regenerative systems for mission durations of 30 days.

Ames-Moffett contact: M. Ballin/V. Bilardo, Jr.

(415) 604-5771/5752

Headquarters program office: OSSA

Adsorption Research for Life-Support Systems

John E. Finn, Sanford S. Davis

NASA's plans for crewed exploration of space in the next century require that nearly all air and water (and, ultimately, solids) be recycled in closed-loop life-support systems, because of the high cost of storage and the logistical difficulties of resupply. One problem associated with such closed systems is the increase in levels of unwanted compounds in the air and water streams. These substances result mainly from human metabolism and equipment off-gassing. Some of them are dangerous at very low or trace concentrations. These contaminants must therefore be concentrated and then eliminated via trace-contaminant removal devices.

Adsorption (e.g., by activated carbon) is a particularly attractive candidate for a means of trace contaminant control on space missions, and it has been used throughout the history of piloted space flight. However, the long-duration missions of the future require better methods of designing adsorption columns and predicting their behavior than the methods that are now used. This year, we initiated a research program aimed at understanding this application of adsorption. The areas of importance are improved prediction of trace-level adsorption equilibria and dynamics, and numerical algorithms for

solving the mathematical models. The research includes both theoretical and experimental efforts.

A rigorous mathematical model for a sorption bed (such as an activated-carbon bed or an ion-exchange column) can be expressed as a set of coupled partial differential equations that must be solved on a computer. A highly accurate and computationally efficient, finite-difference technique, developed by Sanford Davis of Ames' Fluid Dynamics Research Branch, has been applied to this set of equations. The figure shows an example solution of the equations obtained by this method for a simple mixture consisting of a single type of contaminant in a carrier fluid. Each curve represents concentration in the fluid phase at one point in time. The figure shows that, for each particular time, the level of contaminant in the fluid drops from its entrance value as the fluid passes through the bed and adsorption occurs. As time progresses, the region of the bed near the entrance becomes saturated with contaminant, and the result is a saturation wave that moves down the bed. Ultimately, the contaminant concentration at the exit of the bed rises above zero, and "breakthrough" occurs. In a real adsorption bed, the sorbent must be replaced or regenerated before this happens.

Our experimental work on this project consists of testing new theories for predicting the multicomponent adsorption equilibria of trace compounds, determining the physical parameters that describe the physics of the adsorption bed, and checking the accuracy of the mathematical model. We have designed and constructed an apparatus for precisely measuring the adsorption equilibria of multiple contaminants on various sorbents at very low concentrations and pressures. In addition, we have designed an apparatus for studying adsorption-bed dynamics.

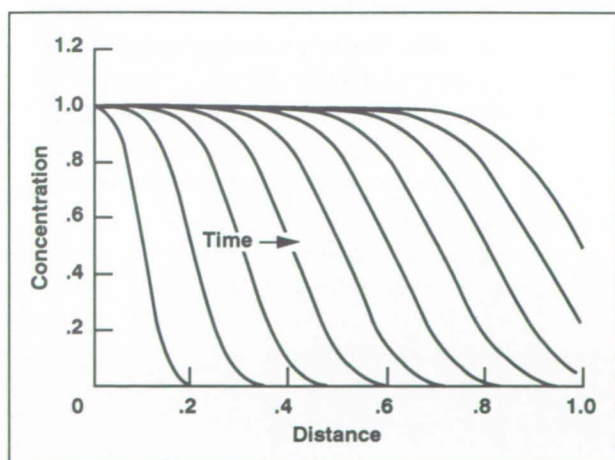


Fig. 1. Concentration of a single contaminant species in the fluid phase as a function of distance down the adsorption bed and time. All quantities are normalized.

Ames-Moffett contact: J. Finn

(415) 604-1028

Headquarters program office: OAST

The CELSS Test Facility: A Foundation for Crop Research in Space

C. L. Straight, R. D. MacElroy

Bioregenerative life-support systems of various configurations are appropriate for a number of space-exploration scenarios, e.g., lunar and Mars bases, or Mars transit. The Controlled Ecological Life Support System (CELSS) is such a system, and depends heavily on the growth, development, and productivity of higher plant crops. There are, however, significant questions about the behavior of crops in space that must be answered before a design for a bioregenerative life-support system can be completed. In general, these questions are concerned with comparisons between crop growth on Earth and in space, and require investigations of crop growth from seed to maturity in the space environment. Data must be gathered for a variety of potential food crops on such issues as maturation time, transpiration rate, harvest index (the ratio of total biomass to edible biomass) and gas exchange rate (oxygen and carbon dioxide). These questions can only be addressed by an appropriate combination of ground and spaceflight experimentation.

The CELSS Test Facility (CTF) is a crop-research chamber that will be flown on Space Station Freedom (SSF). The facility will occupy two standard SSF racks; the plant growth volume and various support subsystems will occupy one and a half racks, and a support module will take up the balance of the total volume. The CTF will be used to study the productivity of typical CELSS higher plant crops under microgravity conditions (see figure).

The CTF consists of a number of subsystems. The demarcations between them are somewhat arbitrary, but, in general, each subsystem supports a major system function: plant life support, monitoring, control, recycling, operations, sample collection, germination, or data acquisition. Some technologies have been identified as critical, requiring early test flights in Space Shuttle middeck locker configurations. These are hardware designs that provide nutrient delivery, water condensation and recovery, gas/liquid

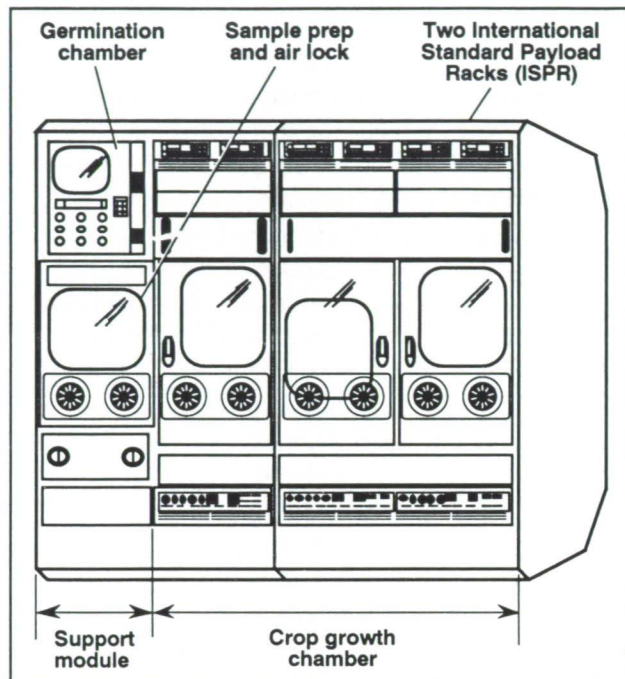


Fig. 1. CELSS test facility concept.

mixing and separation, and plant germination. The systems or responses represented are those that are ordinarily gravity dependent in normal operation. Support hardware, after being tested in microgravity flight, will provide designs that will reduce the overall technical risk of the project.

The CTF will provide the first long-term microgravity crop-research capability for investigating full cycles of crop growth in the space environment. The facility will permit the collection of data needed to plan concepts for bioregenerative life-support systems for use on space-exploration missions.

**Ames-Moffett contact: J. Bosco
(415) 604-6486**

Headquarters program office: OSSA

Advanced Life-Support System Design

ORIGINAL PAGE
BLACK AND WHITE PHOTOGRAPH

Rebecca C. Williamson, Peter J. Sharer, Bruce W. Webbon

As the U.S. space program plans for a return to the lunar surface and ultimately for a mission to Mars, space suits and portable life-support systems will have to be developed to meet the mission requirements. One question that needs to be addressed with regard to an advanced-concept portable life-support system is how to effectively and efficiently maintain thermal comfort throughout an extended period of orbital extravehicular activity (EVA). Operational experience with the current EVA system shows that the astronaut's heat balance is poorly controlled, which results in the body being simultaneously warm in some areas and cold in others. It is hypothesized that an advanced heat-balance system could "read" an astronaut's metabolic rate by means of some noninvasive sensor and then automatically change its heating or cooling function. This not only could lead to greater overall thermal comfort and a more stable heat balance, but would also allow longer EVA sessions with less chance of astronaut fatigue.

A set of experiments was designed to simulate orbital EVA and to quantify the physiological cost of the activity. Three male subjects performed upper-body exercises using a unique arm-crank device. The first figure shows the device outside of its enclosed chamber; the second figure shows the device housed within its chamber in the actual research situation. The device allows motion in four directions: roll, pitch, yaw, and a linear motion aligned with the spine. The bench on which the subject lies is supported by a gimballed shaft which can be locked in place. The subject's body weight is counterbalanced by weights at the opposite end of the shaft. Thus, when the shaft is in the unlocked position (the actual EVA simulation situation), the subject stabilizes the body against all upper-body movement at the feet, which are secured in foot restraints that do not move relative to the ground.

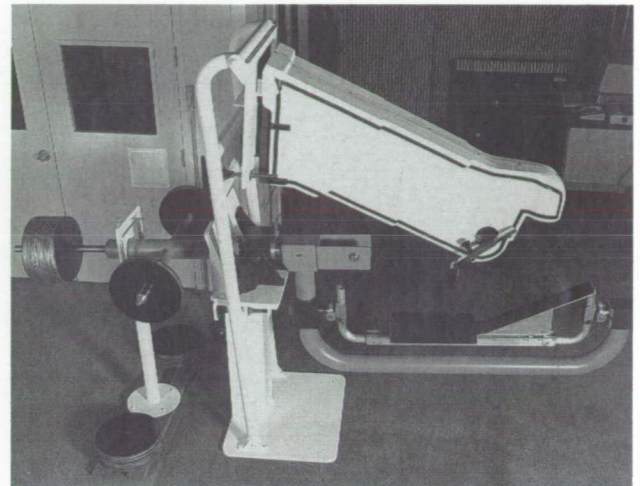


Fig. 1. The extravehicular-activity simulation device.

The first series of experiments was designed to demonstrate the utility of this new exercise technique as a 0-g EVA work simulation device. For these initial tests, subjects were dressed in exercise shorts with no cooling system. First, as a control, the subjects sat upright in front of the ergometer and performed the various protocols to compare this exercise device with other upright-arm-crank research devices. The subjects were then put on the device in the supine position, and they performed all protocols at least three times. Subjects performed identical work protocols with the device in both the locked and the unlocked position so that the investigators could observe the metabolic rate and other physiological parameters when isometric lower-body stabilization was performed by the subject.

Results of these experiments are currently being analyzed, but preliminary findings suggest that the average metabolic rate reached in three of the

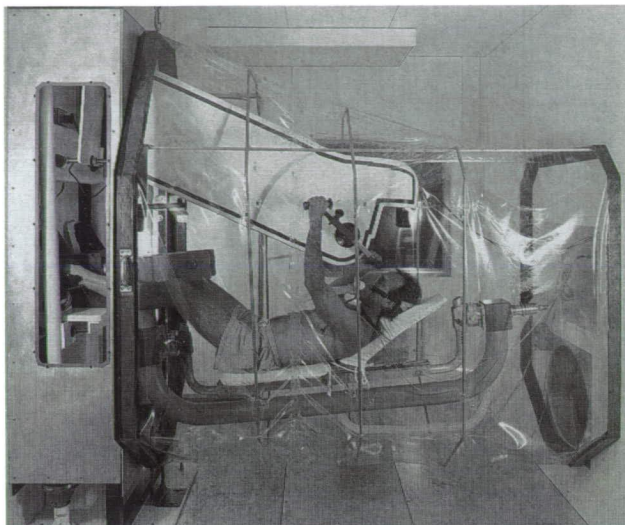


Fig. 2. The extravehicular-activity simulation device housed in its environmental chamber.

protocols—the low constant workload, the moderate constant workload, and the transient workload—most closely mirror the average metabolic load of actual EVAs. This suggests not only that the exercise protocols may replicate the generic muscular movements of an average EVA (i.e., dynamic upper-body work combined with isometric lower-body work), but that

the metabolic loads on the subject may be similar to those on EVA astronauts. Although the higher-constant-workload protocol elicited higher average metabolic costs than those thought to occur during orbital EVA, these data will indicate the upper limits that must be understood in order to build a thermal controller capable of keeping an astronaut comfortable during short periods of hard work.

Next year, a similar set of exercise experiments with a larger subject pool will be conducted to confirm the data. After analyzing the data from these follow-on experiments, a prototype thermal controller will be developed. Exercise experiments with subjects wearing this prototype controller will be conducted to provide more information on how heat balance and thermal comfort during an EVA can be manipulated by a thermal control system. It is hoped that these experiments will provide enough information to develop an advanced-design portable life-support system that will keep astronauts comfortable and safe for advanced exploration missions on the Moon and on Mars.

**Ames-Moffett contact: R. Williamson/B. Webbon
(415) 604-3685/6646**

Headquarters program office: OAST

Resonant Infrared Photoconductor

Jam Farhoomand, Robert E. McMurray

Quantum efficiency is perhaps the single most important parameter of an infrared photoconductor. This parameter is the measure of the fraction of incident photons that are absorbed and converted into free charge carriers by the photoconductor. An ideal photoconductor has a quantum efficiency of exactly unity. We have been investigating the feasibility of a novel method to achieve unity quantum efficiency by establishing a resonant absorption cavity inside the detector element and tuning the front-surface reflectivity and the dopant concentration of the detector. This approach offers many other advantages, such as enhanced photoconductive gain, improved noise performance, and better immunity against ionizing radiation.

Consider a detector element of thickness d and index of refraction n : the faces of this detector, made parallel to within a tight tolerance, constitute the end reflectors of an internal Fabry-Perot etalon. If d is selected so that $d = m\lambda_0/2n$, where m is an integer and λ_0 is a desired vacuum wavelength within the spectral response of the detector, the detector will be resonantly absorptive. The figure shows the cross-sectional diagram of a resonant photoconductor.

Theoretical formulation indicates that one can achieve unity quantum efficiency at selected wavelengths if the back surface of the detector is 100% reflective and the relation $R = A^2$, where R is the reflectivity of the front surface of the detector and $(1-A)$ is the absorptivity per single pass, is satisfied. Under these conditions, the incident radiation is totally absorbed and converted into an electrical signal by the detector at its resonant wavelengths and is 100% reflected elsewhere in the spectral range of the detector. Both R and A can be controlled— R by partially metalizing the front surface, and A by changing the dopant concentration.

We are currently in the process of fabricating a gallium-doped-germanium far-infrared detector. An initial cut is made of a wafer of germanium semiconductor that has the proper doping characteristics to a

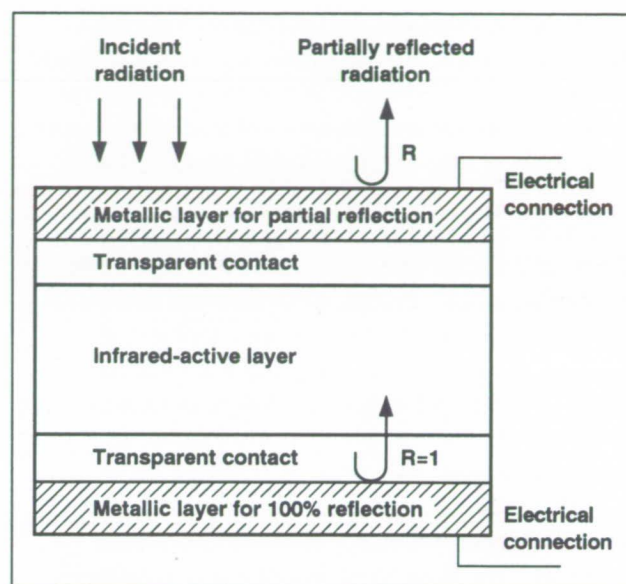


Fig. 1. Typical cross-sectional diagram of a resonant photoconductor.

thickness of about 100 micrometers. This wafer is then chemimechanically polished on both sides until it is reduced to a thickness of 50 ± 5 micrometers and a surface parallelism of better than 2.5 micrometers/centimeter. Both surfaces of the thinned germanium wafer are then ion-implanted with boron to form the transparent contacts (see figure). One side of the wafer is metalized with a thick layer of gold, both as a 100% reflecting back surface and as the back electrical contact. The opposite side is metalized, preferably with gold, to a specific thickness so that its reflectivity is tuned to the single-pass absorptivity of the detector. A comprehensive characterization of the detector performance under various conditions is under way.

Ames-Moffett contact: J. Farhoomand/R. McMurray
(415) 604-3412/3179

Headquarters program office: OAST

Mars Environmental Survey (MESUR)— Feasibility of a Low-Cost Global Approach

G. Scott Hubbard, Paul F. Wercinski,
George L. Sarver, Robert P. Hanel, Ruben Ramos

In situ observations and measurements of the Mars environment are objectives of a feasibility study initiated at Ames Research Center for a mission called the Mars Environmental Survey (MESUR). The purpose of the MESUR is to emplace a pole-to-pole global distribution of landers on the martian surface to make both short- and long-term observations of the atmosphere and the surface. The basic concept is to deploy probes that would directly enter the Mars atmosphere, provide measurements of the upper atmospheric structure, take electronic images of the local terrain before landing, and survive landing to perform surface imaging and meteorological, seismological, and soil-chemistry measurements.

MESUR is a relatively low-cost mission to advance both Mars science and human-presence objectives. The mission philosophy is to (1) develop a network over a period of years using a series of

launch opportunities, thereby minimizing the annual cost; (2) develop a level of effort that is flexible and responsive to a broad set of objectives; (3) focus on scientific study while providing a solid basis for human exploration; and (4) minimize project cost and complexity wherever possible.

The MESUR baseline mission scenario assumes that each of the probes is flown to Mars independently, as shown in the figure. The probes are enclosed in individual bioshields at launch. Shortly after launch, the bioshields are opened and the spin-stabilized probes are released. The probes fly to Mars in an Earth-oriented attitude and arrive at Mars staggered in time to achieve longitudinal coverage of the surface. Atmospheric entry begins at an altitude of 125 kilometers; the entry vehicle decelerates to subsonic velocities at 10 kilometers altitude. At this altitude, a parachute is deployed and the lander

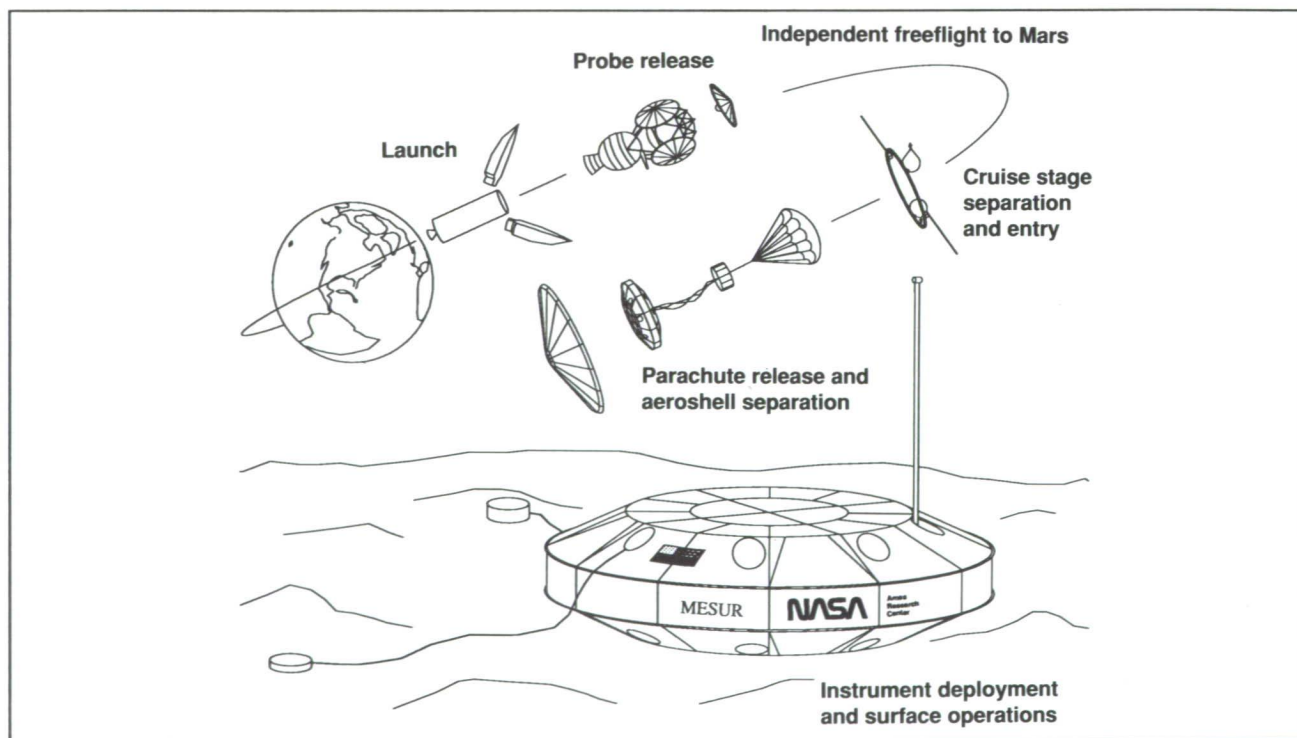


Fig. 1. MESUR mission scenario.

descends to the surface with final impact cushioned on an air bag. After landing, scientific instruments are deployed and the lander begins operations.

Building up the MESUR global network would take place over three launch opportunities using a total of five Delta II launch vehicles. The current MESUR baseline mission profile consists of a single launch of four probes in the 2001 opportunity, a dual launch of four probes and a communications orbiter in the 2003 opportunity, and a dual launch of eight probes (four on each expendable launch vehicle) in 2005. The lander network thus would grow from four to eight to sixteen stations. The completed network is designed to be operational for at least one Mars year, with planned operations ending in 2007.

In order to meet the diverse scientific objectives, each MESUR lander would carry the following instrument payload: (1) an atmospheric structure experiment, (2) descent and surface imagers, (3) a meteorology package, (4) an elemental-composition

instrument, (5) a three-axis seismometer, and (6) a thermal analyzer/evolved gas analyzer.

Engineering features would include (1) long life to support the flow of scientific data from the completed network, (2) simple entry aeroshells with decelerator parachutes and landing air bags, (3) low-average-rate data storage and high-rate transmission when interrogated, and (4) a small radioisotope thermoelectric generator consisting of a repackaged single General Purpose Heat Source brick.

This feasibility study is intended primarily to show a practical way to design a capability for characterizing the surface and atmospheric environment of Mars on a global scale. The goals are to increase our scientific knowledge of Mars, and to allow planning for the eventual exploration of the planet by robots and humans.

**Ames-Moffett contact: P. Wercinski
(415) 604-3157**

Headquarters program office: OAST

An Si(Li) Gamma-Ray Detector Stack for Future Mars Missions

**G. Scott Hubbard, Robert E. McMurray, Jr.,
Robert G. Keller, Paul F. Wercinski, John T. Walton, Kari Vierinen**

Gamma-ray (γ -ray) spectroscopy instruments have been developed for orbiting planetary missions such as the Mars Observer. They have been proposed for payloads of several potential Mars-surface robotic missions, as well as an orbiting Lunar mission and the Near Earth Asteroid Rendezvous mission. Gamma-ray spectroscopy is used to determine the elemental composition of materials. The two detectors of choice for γ -ray spectroscopy are a scintillator such as sodium iodide (NaI(Tl)) or a high-purity germanium (HPGe) semiconductor detector. The performance of scintillators is relatively poor for high-resolution spectroscopy (60 thousand electron volts (keV)) at energies of 1.33 million electron volts (MeV), although they operate without cooling. An HPGe detector has excellent energy resolution (<2 keV at 1.33 MeV), but must be cooled to approximately -175°C , and therefore requires either a stored cryogen (liquid nitrogen) or a mechanical cryogenic

cooler (e.g., a closed-cycle Stirling engine) for use in space missions. Both cooling methods have inherent drawbacks for planetary missions: stored cryogens are short-lived, and mechanical coolers add substantial mass, volume, and power requirements to spaceflight instrumentation. Thus any detector that is capable of operation at higher temperatures would be a desirable alternative. We present experimental data for a lithium-drifted silicon (Si(Li)) detector stack that will provide suitable resolution at the energies of interest (~ 10 keV at 1 MeV), and which will operate over much of the Mars-surface ambient temperature range (-140°C at the poles to -60°C at mid-latitudes). For this initial investigation we set operation at -100°C as a goal. This temperature was the approximate minimum daily temperature at the Viking Lander 1 site.

Throughout the development of the Si(Li) stack concept, Monte Carlo analysis has been used as a

predictive tool to evaluate various experimental approaches. A Monte Carlo program was modified to evaluate our idea through numerical simulation of γ -rays being collected by a suitable volume of Si(Li) devices. The Monte Carlo simulation uses random number generation to model the nonrandom, probabilistic interaction of γ -rays in a detector. Initial simulation results have provided a clear theoretical prediction and the impetus to proceed with actual measurements.

In order to collect experimental data, we fabricated a unique stack of Si(Li) devices in a specially constructed vacuum chamber. To reduce unwanted γ -ray scattering, we employed low-atomic-number materials in the construction of the cryostat, the device used to contain the detector and the γ -ray source. To create the detector stack, we simply placed the Si(Li) detector devices on top of each other. The Si(Li) detectors are each approximately 5 millimeters thick, with an active area about 2 centimeters in diameter and an overall diameter of 2.5 centimeters (first figure). To avoid scattering materials and to approach experimentally as closely as possible the boundary conditions used for the Monte Carlo simulations, which assume a continuous volume of silicon, we devised bias and signal contacts from thin aluminum foils which are threaded in an "S" pattern between the detectors. To provide a demanding test of our concept and the Monte Carlo simulation, we selected the isotope Cesium-137 (^{137}Cs), which has one principal γ -ray peak at 662 keV where Compton scattering clearly dominates photoelectric absorption by several orders of magnitude.

Inherent to γ -ray interactions in Si(Li) detectors is a low-energy background which makes determining the characteristic γ -ray more difficult. The background was significantly reduced by using the technique wherein the first detector(s), nearest the source, acts as an anticoincidence detector that can be used to reject backscattered Compton events. These are the events that cause a continuum tail of less than full energy collection, which becomes a background to full

energy lines at other photon energies. Single-channel analyzers were used, with the lower level discriminators set at 100 keV, to ensure that events were detected in both the "front" (nearest the source) and "back" sections of the stack simultaneously, using a coincidence gate. The two main parameters that were varied were the position of the split in the stack (i.e., ratio of thickness of front and back segments) and the setting of the lower level discriminator applied to each of the two segments. The parameters for the best computed results were then used in experimental tests to confirm the calculations. A 1:3 ratio of front-to-back thickness was determined from Monte Carlo analysis as the most effective in rejecting Compton scattered events.

Strong correlation was obtained between theory (Monte Carlo model predictions) and experimental data obtained from a stack of four Si(Li) devices, using a ^{137}Cs source (662 keV). All the principal spectroscopic features predicted by the theoretical simulation are substantiated by the experimental data: the ^{137}Cs photopeak, the Compton background, and a "shoulder" between the Compton peak and the ^{137}Cs peak.

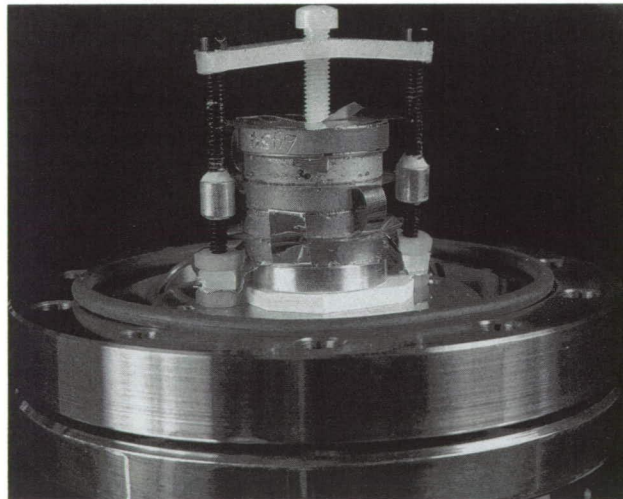


Fig. 1. Si(Li) gamma-ray detector.

As yet we have not identified the source of this shoulder, although it may be another background peak also resulting from scattering of the ^{137}Cs photons in the Si(Li).

In order to make an initial assessment of the feasibility of employing the Si(Li) stack as a spectrometer, we collected data using two γ -ray sources, sodium-22 (^{22}Na) and ^{137}Cs . The second figure displays the stack resolution for the two nearby peaks: 511 keV and 662 keV. As can be seen from the comparison with data from a NaI radiation detector and an HPGe device, the Si(Li) stack provides resolution intermediate between the other two types of detectors, at temperatures which are experienced on the surface of Mars.

We have demonstrated the initial feasibility of using the Si(Li) stack approach to provide intermediate resolution at temperatures experienced on the surface of Mars. Further improvements and optimization in Compton suppression methods will undoubtedly reduce the observed background. We intend to continue tests of resolution as a function of temperature. From unpublished results at Lawrence Berkeley Laboratory, it appears that some crystals and certain processing treatments perform better at elevated temperatures than others do. With our tests we plan to assess the extent of this variation in detector performance with temperature. Further tests will be carried out with multiple line sources, and additional optimization of current background suppression techniques will be conducted.

Ames-Moffett contact: P. Wercinski/G. Sarver
(415) 604-3157/3172
Headquarters program office: OSSA

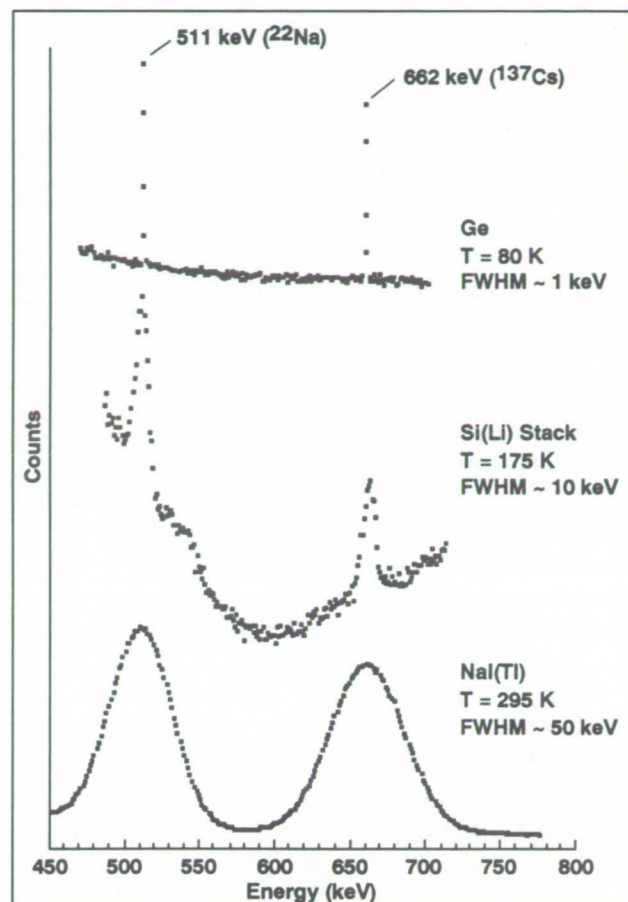


Fig. 2. Resolution comparison for HPGe, Si(Li), and NaI detectors for 511- and 662-keV energies.

Superfluid-Helium-Gap Heat Switch

Ali Kashani, Ben Helvensteijn, Randall Wilcox

Several NASA astrophysics missions, such as the Large Deployable Reflector (LDR), require refrigeration systems that would cool some of their components to a temperature of 2 kelvin. A magnetic refrigerator is one system that has this capability. Magnetic refrigeration is achieved by magnetic cycling of a paramagnetic refrigerant. During part of the refrigeration cycle, thermal contact must be made between the refrigerant and the 2-kelvin heat source. A superfluid-helium-gap (He II gap) heat switch has been developed to accomplish this task. In the on mode the gap is filled with He II, allowing heat conduction. In the off mode the gap is emptied, isolating the 2-kelvin heat source from the refrigerant.

The 2-kelvin heat source is thermally anchored to a tube that contains He II at 2 kelvin throughout the refrigeration cycle (see figure). The He II tube is inserted inside a blind hole in the refrigerant and forms an annular gap with the refrigerant. At the open end of the gap, a thin-walled stainless steel tube is used to hermetically seal the gap and maintain a low-thermal-conduction path in the off mode. The He II in the heat switch is divided into two volumes, i.e., the He II tube and the He II gap, to improve the thermal efficiency of the heat switch. The He II cross section must be sufficiently large to minimize temperature gradients, while the amount of helium cycled should be kept to a minimum.

The supply and removal of helium to and from the gap are accomplished by an activated-carbon pump (ACP). The ACP consists of an enclosed volume that contains activated carbon. Activated carbon adsorbs helium when it is cooled and desorbs helium when it is heated.

A prototype of the 2-kelvin heat switch with a gap size of 0.018 centimeter has been tested. The ratio of the thermal conductance of the heat switch in the on

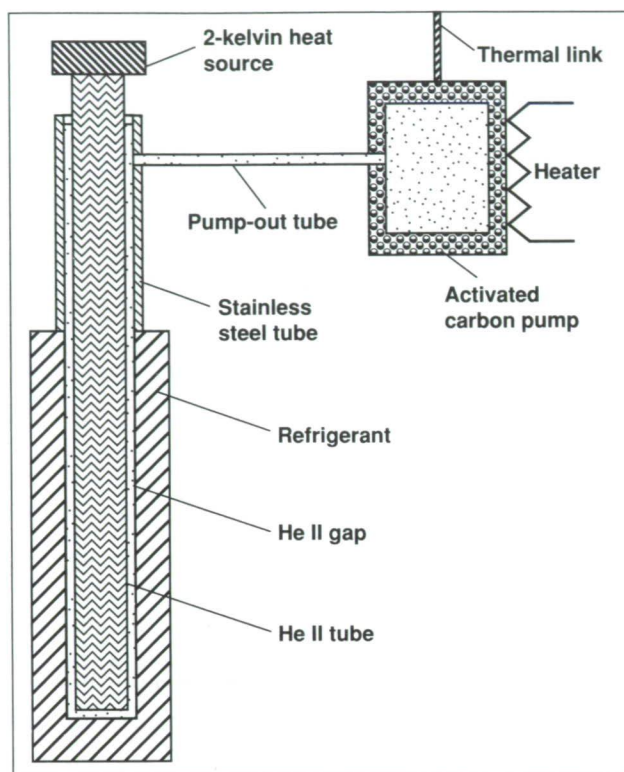


Fig. 1. He II-gap heat switch.

mode to that in the off mode has been measured. This ratio varies from about 1000 to about 3000 as the power from the heat source is reduced from 0.6 milliwatt to 0.07 milliwatt. The time it takes for the heat switch to fully close is nearly three minutes. Its opening time is about six minutes.

**Ames-Moffett contact: A. Kashani/B. Helvensteijn
(415) 604-6534**

Headquarters program office: OAST

Advanced Low-Temperature Readouts

Robert E. McMurray, Jr., Mark E. McKelvey, Craig R. McCreight

It has become clear that in many applications, the limitation on sensitivity in an integrated infrared (IR) focal plane array comes from the cryogenic readout electronics rather than the detector elements. In hybrid IR arrays, these electronics must operate at the detector temperature, which can be 2 kelvin or lower, in low-background far-IR applications. We have undertaken a project to develop improved low-temperature readout electronics, using state-of-the-art design techniques and fabrication facilities. The objective is to focus the design on optimized low-temperature (<10-kelvin) performance, in contrast to previous efforts which have concentrated on higher-temperature (e.g., >60-kelvin) operation. These new devices have the potential of dramatically improving the overall IR focal plane performance in parts of all of the instruments on missions such as the Space Infrared Telescope Facility (SIRTF).

Valley Oak Semiconductor completed the designs and layouts for this project. The basic approach is to produce n- and p-type metal-oxide semiconductor field-effect transistors on a thin (2-micrometer), lightly doped epitaxial layer. This approach was chosen to reduce the excess low-frequency noise, anomalous current-voltage characteristics, and hysteresis seen in earlier devices operated at <10 kelvin. In addition to the individual test transistors and unit cell structures, arrays of up to 256 by 256 elements were included, to determine the yield of large integrated readouts. The devices were fabricated at the TRW Microelectronics Center foundry, and delivered in March 1991.

Test devices have been probed and packaged at Cincinnati Electronics Corporation, where three 256-by-256 indium antimonide hybrid arrays are being produced for NASA evaluation. A test team consisting of investigators at the University of Arizona (UA), Goddard Space Flight Center, the Jet Propulsion Laboratory, and Ames has been studying these devices, and have already found a number of significant improvements. At the individual-transistor level, the lowest noise ever achieved by a true cryogenic

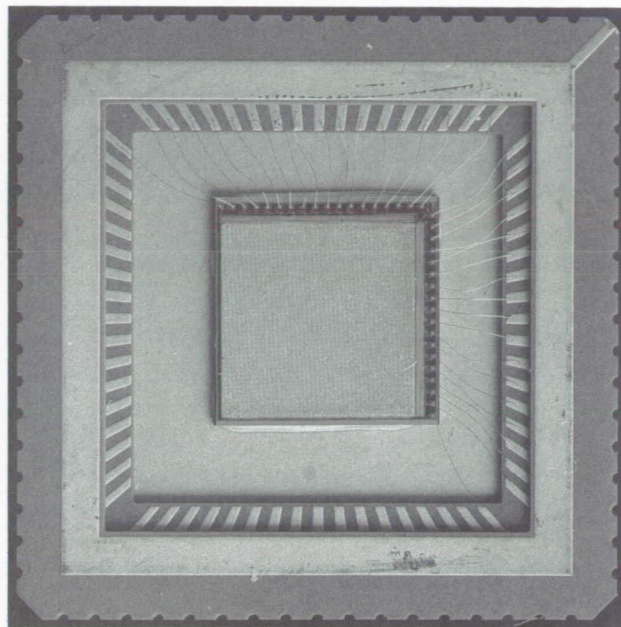


Fig. 1. Photograph of Valley Oak Semiconductor 256-by-256-element cryogenic readout. The pixel size is 30 μm , and the array is fully multiplexed through one output lead.

field effect transistor (equivalent to approximately 30 electrons root-mean-square) has been measured at 2.1 kelvin at UA. Additionally, cryogenic data on the 256-by-256 readouts (see figure) obtained at Ames verify that the large structures are fully functional, and their noise level is from about 30 to about 100 electrons as required for the SIRTF camera and spectrograph instruments. These experiments will continue, and additional development phases for SIRTF applications are anticipated.

**Ames-Moffett contact: R. McMurray, Jr./
M. McKelvey
(415) 604-3179/6643
Headquarters program office: OAST**

He-3–He-4 Dilution Refrigerator

Pat Roach, Ben Helvensteijn

A refrigerator for satellite applications that will cool to 0.1 kelvin or lower is being developed at Ames. The intended use is for cooling infrared and x-ray detectors used for astronomical telescopes. Such detectors have much higher sensitivity and much lower noise at very low temperatures; this improvement is vital for observations of faint signals against the cold background of deep space.

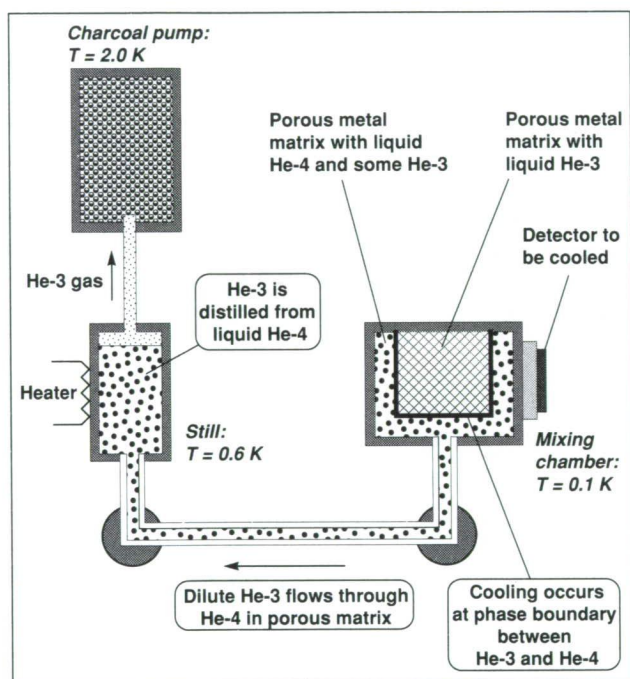


Fig. 1. Operation of dilution refrigerator with the porous metal matrix to confine liquids in zero gravity.

The dilution refrigerator is widely used on the ground for achieving temperatures as low as 0.01 kelvin. A commercial version of the refrigerator that is particularly suitable for space applications has recently been developed. It is compact and reliable, has no moving parts, and is completely controlled by computer-actuated heaters. It uses charcoal adsorption pumps for all its pumping requirements.

A dilution refrigerator uses isotopes of liquid helium (He-3 and He-4) as working fluids; it would not normally function in the zero gravity of space because the liquids would float out of their proper locations. The refrigerator is being modified by adding a matrix of porous, sintered metal to the liquid chambers. This will control the location of the liquids in zero gravity by confining them within the matrix pores by surface tension forces.

The first figure shows how such a refrigerator operates. The lowest temperatures occur in the mixing chamber where there is a phase boundary between liquid He-3 and liquid He-4 . Cooling is produced when He-3 crosses this boundary into the He-4 . From the mixing chamber the He-3 flows through the He-4 to a higher-temperature chamber where it is fractionally distilled from the He-4 . The resulting He-3 gas is collected by the charcoal pump.

Initial testing of the commercial refrigerator with the porous matrix added to the main liquid chambers has been successfully completed. The second figure

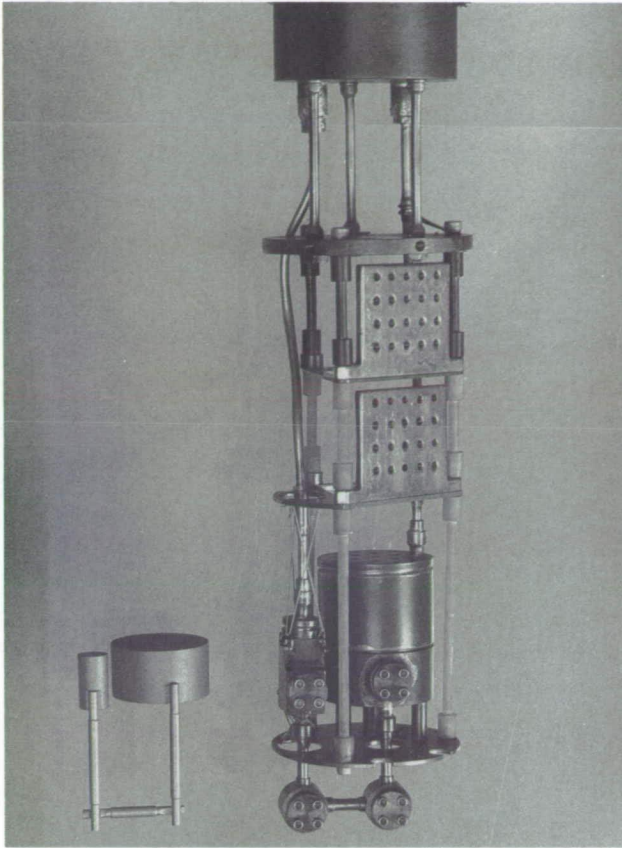


Fig. 2. Low-temperature section of dilution refrigerator. On the right are the chambers that hold the liquid helium; on the left is the porous metal that is put in the chambers to retain the liquid in zero gravity.

shows a new design to accommodate a connecting line with the porous matrix, and it also shows the porous matrix that will be put in the chambers. Preliminary tests without the porous matrix have been carried out and the new design works well. The entire system with the porous matrix will be tested soon.

When the porous matrix is installed in all chambers and in the connecting line, the effect of gravity on the design will be tested by operating the refrigerator (1) with one chamber below the other, (2) with one chamber above the other, and (3) with both chambers inverted. These tests will provide assurance that the operation of the refrigerator is gravity-independent and that it will operate in zero gravity.

**Ames-Moffett contact: P. Roach/B. Helvensteijn
(415) 604-3191/6534**

Headquarters program office: OAST

ORIGINAL PAGE
BLACK AND WHITE PHOTOGRAPH

Oakland Hills Fire Storm: Remote Sensing and Emergency Management

James A. Brass

On October 20, 1991, a small brush fire started in the hills above Oakland, California. Fanned by high winds, unseasonably high temperatures, and low humidity, the fire spread rapidly, burning nearly three square miles of affluent neighborhoods on the wooded hillsides. When it was over, the Oakland Hills Fire was called the worst urban disaster in U.S. history.

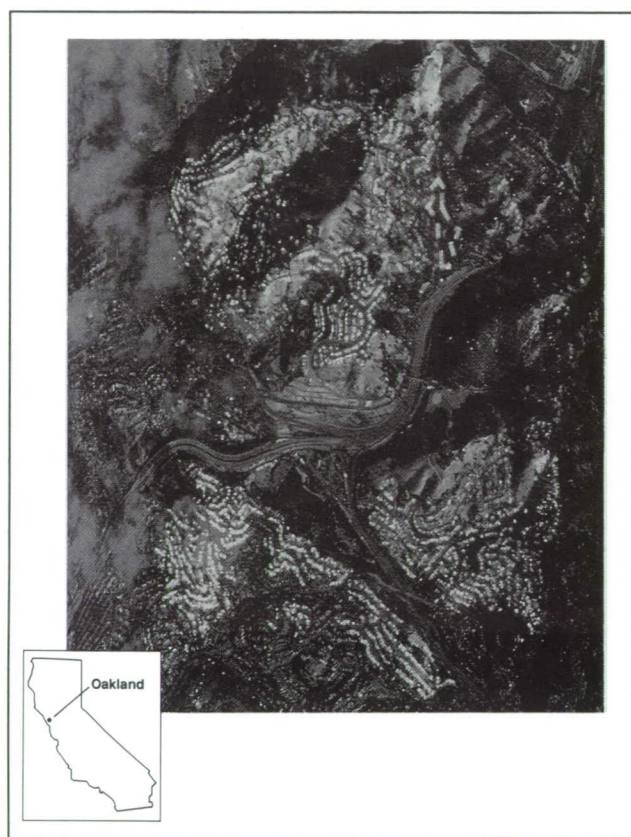


Fig. 1. Airborne Thematic Mapper image of the Oakland Hills Fire. (See color plate 31 in Appendix)

The conflagration caused an estimated \$2 billion in damage, including the loss of homes, businesses, and lives.

As the fire progressed, numerous agencies were summoned. An immediate problem was fire reconnaissance. Dense black smoke covered much of the area, masking fire lines and spot fires. Because of the fire's intensity and the uneven terrain, the construction of a control line was difficult. With expertise in ecosystem research, flight operations, and engineering, the Ames Research Center has had extensive experience in using aircraft data to map fires, most notably the Yellowstone Fires of 1988. At the request of other federal, state, and local agencies, Ames deployed the C-130 and ER-2 aircraft with a full complement of remote sensing equipment to detect and monitor the fire.

Ames' multidisciplinary team gathered sufficient information to enable fire managers at the incident command center to see the extent of the fire, where the fire was moving, and the locations of hot-spot development. The figure is one of the thermal infrared images used to map existing fires (red) and hot spots (yellow and white). The real-time scanner data and the aerial photographs collected after the fire provided the only synoptic look at the fire for damage assessment and documentation of fire behavior.

Ames-Moffett contact: J. Brass

(415) 604-3329

Headquarters program office: not applicable

Ozone-Depletion Research

Guy V. Ferry

Laser-based particle spectrometers and Ames particle samplers are flown on the ER-2 and DC-8 to measure concentration and size distribution of aerosols in situ, and to sample particles for subsequent analyses of size and chemical composition. Thus the total population, the ice particle content, and the nitric, hydrochloric, and sulfuric acid contents of stratospheric aerosol particles are being determined. Sampling conducted during the Airborne Arctic Stratospheric Experiment in late 1991 verifies that the stratospheric aerosol layer was enhanced as a result of the eruption of Mt. Pinatubo in the Philippines in June 1991. This eruption has resulted in the addition to the background particle concentration of an enhancement concentration. The similarity in shape, phase, and elemental composition of the enhancement particles to the background aerosols, known to consist predominantly of dilute hydrogen sulfate droplets,

permits computations of optical properties via a Mie-scattering algorithm. It thus can be shown that the light extinction in the near-ultraviolet is enhanced five-fold, and in the near infrared greater than 10-fold—in agreement with sun-photometer measurements at Mauna Loa, Hawaii, and aboard a DC-8 aircraft. A comparison with the aerosol enhancement that followed the 1982 El Chichon eruption permits estimates of a high single-scattering albedo, and predictions of stratospheric residence times and transport into the upper troposphere of the Pinatubo volcanic aerosol.

Jindra Goodman of San Jose State University is a co-investigator on this project.

Ames-Moffett contact: G. Ferry

(415) 604-5497

Headquarters program office: OSSA

Detection of Changes in Migratory Waterfowl Habitats in California

Liane S. Guild, Laurence L. Strong

The Central Valley of California provides winter habitats critical to the survival of migratory birds—an international resource. The tremendous diversity of these habitats and the large area over which they are distributed makes it difficult to assess their value to migratory birds without innovative remote sensing techniques. The goal of this study, a cooperative effort between the U.S. Fish and Wildlife Service (FWS) and NASA, was to help the FWS to develop its use of satellite remote sensing data and technology to understand the diversity, spatial distribution, and temporal dynamics of winter habitats of migratory waterfowl in the Central Valley.

The four specific objectives of the study were to (1) inventory and map wetland and upland migratory waterfowl habitats in the Central Valley and Klamath Basin of California using Landsat Thematic Mapper (TM) data; (2) detect and identify annual and seasonal

changes in winter habitats of migratory waterfowl using TM data; (3) detect changes in surface water availability with a weekly frequency using Advanced Very-High-Resolution Radiometer (AVHRR) data in a mixture model; and (4) evaluate remotely sensed predictions of migratory waterfowl winter habitats.

The data from four study areas were acquired from September to March in 1988–89 and 1989–90. The TM data—33 full images and 17 quarter scenes—provided observations from four to seven dates in each winter for each of four study areas: (1) the Sacramento Valley and the Sacramento–San Joaquin Delta, (2) the Tulare Basin, (3) the grasslands in the San Joaquin Valley, and (4) the grasslands in the Klamath Basin. The 162 AVHRR images provided coverage of all study areas. These data were georeferenced, and a classification system and

sampling scheme for estimating spectral reflectance statistics for waterfowl habitats was developed. Ancillary satellite data included color infrared aerial photography acquired from a NASA ER2 aircraft in the fall in 1988 and 1989; National Wetlands Inventory data; and data on survival, movements, and habitat use by radio-tagged waterfowl.

TM data from the winter of 1988–89 for the Sacramento Valley, the San Joaquin grasslands, and the Tulare Basin were analyzed for mapping the dynamics of water availability which was spatially and temporally dynamic. In the Sacramento Valley, water availability varied from 18,002 hectares in early September to 83,656 hectares after a 7.6-centimeter rain in mid-March. Water availability in the Tulare Basin was greatest (6,837 hectares) in late October, when the area of pre-irrigated agricultural fields was large, and least in late March (2,423 hectares). Water availability in the grasslands increased from 1,932 hectares in late September to 7,906 hectares

by mid-November, and appeared to be relatively stable for the remainder of the winter compared to that in other study areas.

We compared AVHRR and TM estimates of water availability for the Sacramento Valley on five dates in the winter of 1988–89 for which data were available for both sensors. AVHRR estimates of water availability were larger than TM estimates for all dates. The correlation between the two methods was strong. Selection of samples for estimating the spectral reflectance of the mixture-model components was critical to the model's success in estimating water availability. Spectral contrast among the three mixture-model components (i.e., water, green vegetation, all other habitats) was greatest in the near infrared.

Ames-Moffett contact: L. Guild

(415) 604-3325

Headquarters program office: OSSA

Meteorological Satellite Downlink and Display System

Steve Hipkind

A Meteorological Satellite Downlink and Display System (MSDDS) was acquired in 1991 by the Earth Systems Projects and Planning Office. Access to the satellite cloud imagery available from both the geostationary and polar orbiting meteorological satellites is a key requirement in making meteorological forecasts for the large aircraft field missions managed by the project office. The meteorological forecasts are essential for making flight planning decisions during the missions.

The MSDDS is a transportable system that can be set up at virtually any deployment location. It is capable of receiving the direct, digital data from both the geostationary meteorological satellites and the National Oceanic and Atmospheric Administration (NOAA) polar orbiter satellites. Its processing software allows the user to automatically schedule the acquisition of selected data, and provides for user selection of the geographical sector and resolution to display. The imagery data can be Earth located and transformed into user-defined projections, so that other

latitude/longitude data, such as aircraft flight tracks, can be overlaid directly onto the satellite images.

The first deployment of this new facility was the 1991–92 Airborne Arctic Stratospheric Expedition II. The system was shipped and installed in September 1991 at the base of operations, a refurbished hangar at the Bangor International Airport in Bangor, Maine. The 3-meter geostationary antenna was set up on the ground just outside of the hangar, and the 1.4-meter tracking antenna for the polar orbiting satellites was installed on the roof of the hangar, providing a clear line of sight in the north and south directions. As of this writing in mid-December 1991, the system has been operating continuously since its installation in September, and has performed well through conditions that have included snow, ice, and temperatures below 0 °F.

Ames-Moffett contact: S. Hipkind

(415) 604-5076

Headquarters program office: OSSA

ERS-1 Investigations of High-Latitude Wetlands

Leslie A. Morrissey

The predominance of methane-producing wetlands in the tundra and taiga (boreal forest) makes these ecosystems important contributors to the global methane budget. The synthetic aperture radar (SAR) of the European Remote Sensing Satellite (ERS-1), launched in July 1991, provides the first spaceborne SAR system for multiyear, multitemporal assessment of high-latitude ecosystems. Analysis of ERS-1 C-band SAR data is under way to determine the type and extent of wetlands (methane source areas), the extent and timing of inundation (anaerobic substrates for methane production), and leaf area (methane transport pathway). This research is being conducted in collaboration with the Jet Propulsion Laboratory and the Ames methane project with funding from NASA's Polar Oceans Program.

Initiated in April 1991, the ERS-1 project has focused on the acquisition of ERS-1 data for Barrow, Alaska, during the first summer of operations; acquisition and initial processing of DC-8 AIRSAR data over Alaska wetlands and California rice fields and wetlands; and field data collection concurrent with the

SAR overflights. ERS-1 SAR is being acquired and processed through the Alaska SAR Facility at the University of Alaska, Fairbanks.

Preliminary examination of AIRSAR data over Alaskan wetlands suggests better discrimination of northern wetland bogs with SAR than with optical satellite sensors. Morrissey was selected to be a member of the Polar Data Advisory Group which has been tasked to review and advise the polar Earth Observing System Distributed Active Archive Centers, the Alaskan SAR Facility, and the National Snow and Ice Center on future directions and data requirements, and was invited to chair a session on ecosystem dynamics for the American Association for the Advancement of Science Arctic Science Conference to be held in Valdez, Alaska, in September 1992.

**Ames-Moffett contact: L. Morrissey, G. Livingston
(415) 604-3617/3232**

Headquarters program office: OSSA

Terrestrial Ecosystem Trace-Gas Fluxes: Application of a Global Model

Christopher S. Potter, Pamela A. Matson, Steven A. Klooster

The magnitude and geographic distribution of terrestrial sources and sinks of radiatively important trace gases, and the degree to which the fluxes of these gases might be altered by a changing climate, are important unresolved issues of global change. The trace gases carbon dioxide, methane, and nitrous oxide significantly influence the energy balance of the Earth. Moreover, these gases can directly affect plants, animals, and microorganisms, and play important roles in the chemistry of the troposphere and the stratosphere. In an effort to improve our knowledge of planetary trace-gas dynamics, research is under way at Ames to develop simulation models that are driven by global-scale climate and remote-sensing data bases and that incorporate knowledge of ecosystem processes that regulate trace-gas emissions.

The model currently under development traces the flow of carbon and nitrogen among vegetation, soils, microorganisms, and the atmosphere. Multi-temporal satellite observations from the Advanced Very High Resolution Radiometer (AVHRR) are used to estimate absorbed photosynthetically active radiation and, ultimately, net primary productivity (NPP, an estimate of the total amount of carbon entering the terrestrial system each year). Within the terrestrial ecosystem, carbon and nitrogen are transformed from organic to inorganic forms, with release of trace gases mediated by such soil characteristics as moisture, texture, and water-filled pore space as well as characteristics of organic matter and microbial activity.

Implementation of the model requires monthly updates of climate, solar radiation, and AVHRR data acquired at a 1-degree latitude/longitude grid-cell resolution for the entire globe. Other input variables include vegetation class, physical and chemical characteristics of soils, and inundation percentages in wetlands. All variables are entered as raster arrays in a geographic information system, and are available simultaneously for input to the model.

Simulation results indicate that undisturbed tropical forests are significant global sources of trace



Fig. 1. Global carbon dioxide emissions from soil. (See cover photo)

gases. We estimate that forest soils account for more than 40% of carbon dioxide emissions (see figure) and more than 50% of nitrous oxide emissions. Spatial patterns of NPP, surface temperature, and soil-nutrient status account for a significant proportion of the geographic variability in trace-gas fluxes.

Future research will include evaluation of the effects of tropical deforestation and land-use change on global trace-gas fluxes; therefore, we expect that there will be an increasing need for fine-resolution satellite data. To accommodate these data, model performance is being tested on parallel computers through Ames' Numerical Aerodynamic Simulation program. Access to high-performance computers will aid in the development and incorporation of thematic data from a variety of sources.

Expected contributions of this research include improved understanding of the factors that control trace-gas fluxes between terrestrial ecosystems and the atmosphere, more accurate assessments of gas fluxes on a regional and a global scale, and a better understanding of the role of forests and land-use change in global biogeochemical cycles and global change.

**Ames-Moffett contact: C. Potter
(415) 604-6164**

Headquarters program office: OSSA

Measurement of Graphitic Carbon (Soot) in the Stratosphere

Rudolf F. Pueschel

In connection with the High-Speed Research Program, Ames particle samplers are being modified to analyze samples for graphitic carbon (soot). The task is to establish "baseline" values for soot in the stratosphere by piggybacking on routine ER-2 flights, to be followed by sampling during dedicated research flights. Samples analyzed to date indicate an average total black-carbon mass concentration in the stratosphere of 1.8 ± 1.1 nanograms per cubic meter, of which about 10% appears to be externally mixed soot. Using a soot absorption cross section of 10 square meters per gram for the externally mixed fraction, the corresponding aerosol absorption coefficient is approximately 2×10^{-9} per meter. Using values for total stratospheric light extinction

of approximately 10^{-6} per meter, as measured by the SAGE II satellite sunphotometer and/or computed from particle size distributions measured aboard the ER-2, the present-day single-scattering albedo is in excess of 0.99. Future perturbations of the background graphitic carbon resulting from high-speed commercial transport will be estimated by expected fleet size and fuel consumption with a black-carbon emission factor from jet fuel which is yet to be determined.

Ames-Moffett contact: R. Pueschel

(415) 604-5254

Headquarters program office: OAST

Evolution of Carbon Fixation

Lynn J. Rothschild

Biological carbon fixation (primary production) was crucial in early evolution because it liberated life from dependence on abiotically produced organic carbon. Biological carbon fixation permitted the development of the biogeochemical carbon cycle, the evolution of a complex community structure among living organisms, and, indirectly, the formation of an aerobic environment on Earth through oxygenic photosynthesis. Photosynthetic carbon fixation, the subject of this research, may have evolved very early, 2.9 to (possibly) 3.5 billion years ago.

The goal of this research is to determine experimentally the impact of increased levels of carbon dioxide (CO_2) on photosynthetic carbon fixation, with an emphasis on microbial communities. The results are used to model biogeochemical carbon cycling in an evolutionary context, that is, in ancient communities when levels of CO_2 were probably substantially higher. These evolutionary studies could provide information with which to predict the future ecologi-

cal impact of the increasing levels of atmospheric CO_2 .

Several microbial-mat communities (thought to be analogs for ancient ecosystems) are currently under study. These include mats composed primarily of bacteria (e.g., *Lyngbya* mats from the intertidal of Laguna Ojo de Liebre, Baja California), and mats composed primarily of eukaryotes (e.g., *Cyanidium* mats from Yellowstone National Park). For each community we determine (1) the changes in carbon fixation rate during a diurnal cycle under ambient (i.e., modern) conditions, (2) the impact of light and CO_2 on the rate of carbon fixation during a diurnal cycle, and (3) the fate of the fixed carbon under different conditions by determining how much fixed carbon goes into DNA synthesis (i.e., reproduction) under different levels of CO_2 .

During fiscal year 1991, in collaboration with Lori Giver (a Ph.D. student at Indiana University,

Bloomington) we performed measurements in the field to determine the impact of ambient vs. altered levels of CO₂ on carbon fixation in the *Lyngbya* and *Cyanidium* mats. We also measured the impact of adding other nutrients, including organics (i.e., acetate, glucose, phosphate, nitrate, and ammonia), on carbon fixation during a diurnal cycle. From these measurements, we calculated the total fixation per diurnal cycle under ambient and altered levels of CO₂. Preliminary measurements of carbon fixation were made in another eukaryotic mat (*Zygogonium*, Yellowstone) in order to add to the sample size. All communities showed an immediate and dramatic response to elevated levels of inorganic carbon (≥ 2 times ambient) for all daylight hours except immediately after sunrise or immediately before sunset. Similar changes were rarely seen with the addition of the other nutrients. When there was an impact, there was either an enhancement or a depression of carbon fixation, and the effect depended on the nutrient added, the time of day it was added, and the type of mat community.

The *Lyngbya* and *Cyanidium* mats were also analyzed for the partitioning of fixed carbon into

nucleic acids as a substitute for cellular reproduction. A first attempt at measuring gross nucleic acid synthesis was performed immediately outside the laboratory building, under ambient conditions (*Lyngbya* and *Cyanidium*) and under increased levels of CO₂ (*Lyngbya*). Simultaneous measurements were made of carbon fixation. This experiment allowed correlation with the field data, as well as the gross estimation of nucleic acid synthesis, the amount of carbon fixed, and the total fixed carbon partitioned into nucleic acids. The *Cyanidium* experiments, like those with *Lyngbya*, showed two daily peaks in DNA synthesis—late morning and afternoon. Preliminary data on carbon fixation and DNA synthesis in *Lyngbya* exposed to high levels of inorganic carbon for several days suggest that the immediate response to high levels of inorganic carbon may not translate into increased reproductive rates in this community when the mat has been exposed to high levels of CO₂ for several days.

Ames-Moffett contact: L. Rothschild
(415) 604-6525

Headquarters program office: OSSA

Earth Science Advanced Aircraft

Philip B. Russell, Jennifer Baer-Riedhart, Steven S. Wegener

Research-platform aircraft, including the ER-2, the C-130, and the DC-8, have made major contributions to our current understanding of Earth science. Aircraft measurements have proved to be an indispensable complement to measurements from space, ground, and balloons. Many of the measurements made from aircraft cannot be made by other techniques, and these measurements are especially powerful in revealing the processes by which natural and manmade global change occurs.

In spite of the marked success of the current Earth science aircraft fleet (at NASA and other agencies), many groups in the Earth science community have cited the need for aircraft with still greater capabilities: higher ceiling, longer range and/or duration, heavier payloads, and the ability to follow the terrain. In response to this need, Ames established an Earth

Science Advanced Aircraft (ESAA) team in September 1990. The objectives of the team were to (1) identify the best ways of applying NASA's aeronautical capabilities to the advanced-aircraft needs of the broad Earth science community, (2) to foster NASA's continuing leadership role in multi-investigator Earth science aircraft missions, (3) to interact with ESAA activities at other agencies and institutions, and (4) to develop funded projects to achieve the above goals.

The first project to result from ESAA team activities is the Small High-Altitude Science Aircraft (SHASA) Project to develop and test-fly the Perseus-A unpiloted scientific-research aircraft. The goal for Perseus A is to advance stratospheric research by carrying scientific payloads of at least 50 kilograms to altitudes of at least 25 kilometers. SHASA is managed

by the Ames Dryden Flight Research Facility, which will host the Perseus A high-altitude test flights in 1993. A Perseus proof-of-concept aircraft completed successful low-altitude test flights in November 1991.

Other accomplishments of the ESAA team include hosting several workshops to define the Earth science community's aircraft needs; conducting performance simulations of the broad range of existing and conceptual aircraft candidates; establishing a university course to design a terrain-following Earth science aircraft; giving presentations to the Department of Energy and other groups concerned with climate and remote-sensing research; and stimulating and coordinating the development and integration of scientific

and engineering instruments and a common data system for Perseus A.

Future activities include continuing the above efforts, developing telemetry and telescience techniques that will best utilize Perseus A and other aircraft, and using the pioneering aeronautical achievements of Perseus as a stepping-stone to the development of more capable Earth science advanced aircraft (e.g., with greater payload, range, duration, and altitude).

**Ames-Moffett contact: P. Russell
(415) 604-5404**

Headquarters program office: OSSA/OAST

Biospheric Monitoring and Disease Prediction

**Michael Spanner, Byron Wood, Louisa Beck,
Sheri Whitney, Rick Rossi, Liane Guild**

The World Health Organization (WHO) estimated that in 1982 there were 250 million malaria cases globally. Nearly half of the world's population lives in areas where ongoing antimalaria activities are currently being carried out. According to WHO, global malaria has increased significantly over the past 15 years. Factors that have influenced this increase include reduced funding and manpower, increased resistance of the mosquito vector to insecticides, and the appearance of drug-resistant forms of malaria. Near-real-time data on the temporal and spatial dynamics of the vector populations are required for effective disease control. A phased multiyear research program has been initiated by NASA to develop predictive models of vector population dynamics and malaria transmission using remotely sensed data and geographic information systems.

Research is under way on the second phase of the Biospheric Monitoring and Disease Prediction (Di-Mod) Project, which focuses on malaria transmission in southwestern Mexico. Remotely sensed data were used to determine the six major vegetation types associated with the malaria vector. These vegetation types were identified during field research, and their spatial extent was determined using Landsat Thematic

Mapper (TM) data. TM data were also used to distinguish between grasslands and pastures. This distinction is important because cattle grazing on the pastures provide a blood meal for mosquitoes.

Research has been completed on the development of a technique to determine land-cover categories when the land is obscured by clouds. Clouds are a severe problem in the remote sensing of tropical areas. The sampling technique used to determine the proportion of land cover that is under clouds is termed kriging. Kriging is an interpolation procedure that provides estimates for unsampled locations by taking a weighted average of surrounding known values. Using kriging, estimations of the probability of the land cover under a cloud being pasture had an average error of less than one percent. Geographic information systems techniques have been used to develop a data base on the proportions of various land-cover types surrounding villages. The type of land cover surrounding a village determines the risk for malaria transmission.

Another activity of the Di-Mod project in 1991 was a three-week workshop entitled "Remote Sensing, Environmental Change, and Human Health,"

sponsored by the Aspen Global Change Institute in Aspen, Colorado. The workshop was organized by Byron Wood of Ames Research Center and Robert Washino of the University of California at Davis. Thirty researchers in the natural sciences, social sciences, and engineering, from universities and government agencies in the United States and abroad, participated in the meeting. The session focused on the relationships between human health and environmental changes such as deforestation and develop-

ment of water and agricultural resources that can be monitored and/or predicted using remote sensing. This workshop was important in bringing together investigators attempting to solve public health issues related to vector-borne diseases.

**Ames-Moffett contact: M. Spanner/B. Wood
(415) 604-3620/4187**

Headquarters program office: OSSA

Radiative Effects of Aerosols and Clouds

Francisco P. J. Valero

The Radiation Group in the Atmospheric Physics Research Branch at Ames has as its primary goal the study of the interactions between atmospheric aerosols and solar and terrestrial (infrared) radiation. The aerosols of interest vary from Arctic haze, oil-fire smoke particles, and volcanic clouds, to liquid water and ice clouds. We are working to determine the manner in which clouds absorb and scatter radiative energy, so that we can predict their effects on climate and devise new techniques for remotely sensing cloud physical parameters. In 1991, our group participated in three field projects: the Kuwait Oil Fire Experiment, the Pinatubo Airborne Measurements Experiment, and the First International Satellite Cloud Climatology Project Regional Experiment, Phase II (FIRE II).

The radiative effects of the smoke from the Kuwait oil fires were assessed by measuring upwelling and downwelling and solar flux, as well as spectral solar extinction below, above, and within the smoke plume. Radiative flux divergence measurements were made to determine smoke-induced heating and cooling rates. We concentrated our measurements in homogeneous, well mixed regions of the smoke approximately 100 kilometers downstream of the fires. In some of the thickest parts of the smoke, we found that the transmission of solar radiation to the surface was only 8%; 78% of the solar radiation was absorbed by the smoke particles. The calculated

instantaneous heating rate inside the plume reached 24 kelvin every day. Whereas these effects are probably typical of those regions in the Persian Gulf area directly covered by the smoke, we concluded from our measurements that there is no evidence to suggest significant climatic effects in other regions.

Our group participated in NASA's Caribbean mission in July 1991 to characterize the cloud produced by the eruption of Mt. Pinatubo. We measured the extinction of solar radiation, upwelling and downwelling radiative flux, and scattered flux with instrumentation carried onboard the NASA Wallops Electra. Our results, which showed the latitudinal and spectral dependence of reduced transmission of solar energy caused by the volcanic cloud, were some of the first to show the progression of the high-altitude (approximately 25 kilometers) cloud as it traversed the globe; they indicate that this eruption created one of the thickest volcanic clouds ever observed. We found that the effective size of the particles composing the cloud, which consisted of both ash and sulfuric acid droplets, was between 0.18 and 0.35 micrometers; this corresponds to a columnar mass loading between 35 and 80 mg/m².

The significance of these results is increased by the fact that our measurements were made within one month after the eruption, well before the cloud would reach its maximum optical thickness and spatial

coverage. We continued to track the progression of the Pinatubo cloud with measurements in September 1991 at Mauna Loa, Hawaii; in November 1991 at Coffeyville, Kansas; and in November 1991 from the Ames ER-2 research aircraft, which flew out of Houston, Texas. From our results, with extrapolations based on the effects of the El Chichon eruption in 1982, one would expect a slight drop in average global temperature at the surface of perhaps 0.5 °C to 0.7 °C, and a warming in the upper atmosphere, where the cloud resides, of approximately 4 °C.

During the FIRE II cirrus cloud experiment in November and December 1991, we deployed several radiometers on the ER-2 research aircraft and on the ground in Coffeyville. Cirrus clouds are critical to the energy transport system of our planet. Composed of ice crystals and usually optically thin, they allow a fair amount of solar radiation to penetrate to the surface while simultaneously allowing a smaller amount of

infrared energy to be radiated to space than would occur in their absence. The goal of FIRE is to characterize the morphology, microphysics, evolution, and destruction of cirrus clouds with specific emphasis on improving climate modeling and satellite retrieval algorithms. Our instrumentation was uniquely suited to support this endeavor: we determined cloud temperature, optical thickness, water phase, and particle size, all from remote platforms. We also measured scattered upwelling and downwelling spectral fluxes which will be useful to characterize the cirrus radiation budget and its effect on the global energy balance.

Ames-Moffett contact: F. Valero
(415) 604-5510

Headquarters program office: OSSA

Studies of Stratospheric Trace Gases

James F. Vedder

Minor constituents play an important role in upper atmospheric photochemistry and serve as tracers in transport and mixing studies of tropospheric-stratospheric exchange processes. Measurements of trace gases are essential to an understanding of the mechanisms by which these minor constituents, both naturally occurring and anthropogenic, that originate in the troposphere reach the stratosphere. Most of these gases are sources of constituents directly involved in the chemistry of ozone depletion. Some contribute to the warming of the atmosphere. Data on tracer distributions are important in the development of models for predicting photochemical effects in the stratosphere.

The work reported here is a joint effort of Ames Research Center and the National Center for Atmospheric Research (NCAR). NCAR is funded separately by NASA Headquarters. Since its participation in the Airborne Arctic Stratospheric Expedition in 1989, the Whole-Air Sampler for the ER-2 research aircraft has been modified to carry 29 sampling canisters (the

original instrument carried 14 canisters). In addition, the original electronic controller for the system has been replaced by a more versatile unit. In May 1991, the electrical and mechanical integration of the modified Whole-Air Sampler in the ER-2 was completed. In August, three test flights were accomplished for the Whole-Air Sampler along with the other instruments to be used in the Airborne Arctic Stratospheric Expedition II. Canisters with air samples from the last two of the three flights were shipped to NCAR for analysis by gas chromatography of about 30 trace gases. In September, samples from two ER-2 flights were collected and shipped to NCAR for analysis. All of the preparations for the deployments to Eielson Air Force Base, Alaska, and to Bangor, Maine, for the missions were completed.

Ames-Moffett contact: S. Wegener
(415) 604-6278

Headquarters program office: OSSA

Cloud and Radiation Parameterizations for Use in Weather and Climate Models

Douglas L. Westphal

The cloud and radiation parameterizations used in today's climate models are generally considered inadequate, and they prevent complete acceptance by the scientific community of predictions of phenomena such as global warming. These models are being improved, and some now incorporate simplified versions of the Sundqvist moisture treatment wherein separate continuity equations are solved for cloud water and rain, in addition to water vapor. Evaluation of model improvements is difficult using conventional methods such as comparison to monthly mean outgoing longwave radiation (OLR). Even when inaccuracies are detected, their cause is difficult to pinpoint because of the complicated interactions between the cloud parameterization, dynamics, prescribed cloud optical properties, and the radiative transfer model. This difficulty is particularly true for derived quantities such as OLR.

We suggest that weather prediction models be used to evaluate the parameterizations against actual observed weather events for which ground-based, satellite, and aircraft observations of moisture and radiative fields are available. These types of data were

collected during NASA's First International Satellite Cloud Climatology Project Regional Experiment (FIRE) Cirrus Field Program which took place in Coffeyville, Kansas, in late 1991. During the field experiment, we made 12- to 24-hour forecasts using the Ames version of the Pennsylvania State University/National Center for Atmospheric Research dynamical model with a variety of moisture parameterizations including a cumulus parameterization, a large-scale saturation scheme, Sundqvist's method, and a detailed microphysical treatment developed at Ames. Comparisons with the quick-look field data reveal large differences in the model simulations that use the different schemes. As the processed field data are made available, we will use them to quantify the performance of the different parameterizations.

**Ames-Moffett contact: D. Westphal
(415) 604-3522**

Headquarters program office: (Funded through DOE)

Airborne Tracking Sun Photometer

Robert C. Wrigley

The NASA Ames Airborne Tracking Sun Photometer (ATSP) collected data that are the basis of atmospheric correction of remotely sensed imagery obtained as part of the First International Satellite Land Surface Climatology Project Field Experiment (FIFE). FIFE is funded by the Ecosystem Dynamics and Biogeochemical Cycles Branch of NASA's Earth Sciences and Applications Division. This experiment was conceived as a vehicle for developing and validating methods to convert satellite-observed radiances into climatological variables that will be used to analyze biosphere-atmosphere interactions. A significant problem in using satellite radiances to quantitatively derive surface properties is determining the effect of the intervening atmosphere which reduces the transmission of incoming and emitted radiation and contributes its own scattered and emitted radiation.

To provide quantitative corrections for the atmospheric effects in remotely sensed data acquired from aircraft and satellite-borne platforms, a physical approach was used. In the summers of 1987 and 1989, over the Konza Prairie in Kansas, atmospheric measurements were made with the ATSP at the same time that remotely sensed data were acquired. The ATSP, mounted on Ames' C-130 aircraft, measured solar extinction in six wavelengths during five 2-week periods in Kansas. These data have been used to obtain aerosol optical depths, water vapor absorption, aerosol size distribution, aerosol phase functions, and aerosol single-scattering albedos. Radiative-transfer models were applied to remove atmospheric effects from the remotely sensed data. Data that may be corrected for atmospheric effects include those acquired by the NS001 Thematic Mapper Simulator (TMS), the Advanced Very High Resolution Radiometer, the Landsat Thematic Mapper (TM), and the satellites SPOT and GOES. Because the major objec-

tive of FIFE is the conversion of satellite-observed radiances into climatological variables dealing with albedos, surface energy fluxes, and energy balances, determination of the differences between satellite and surface radiances caused by the intervening atmosphere is critical.

A simple radiative-transfer model based on a single-scattering approach was programmed in Pascal. This model used the derived aerosol properties (spectral optical depth, phase function, and single-scattering albedos) and the known Rayleigh scattering properties to correct two flightlines of TMS and TM data for atmospheric effects. Both qualitative and quantitative comparisons of results from the model show that it provides good to excellent correction for atmospheric effects in TMS and TM data. We have applied the simplified atmospheric correction model to entire images of TMS and TM instead of individual points within images to yield surface radiances within a few percent. This computationally efficient approach clearly reduces or nearly eliminates the limb brightening effects so prominent in airborne data.

The ATSP has been selected for inclusion in the HAPEX/Sahel mission in Africa in August and September, 1992. This mission shares many of the same objectives as FIFE for understanding the interaction of the land surface with climate. The atmospheric correction methodology developed for the remote-sensing data of FIFE will be a significant contribution to the HAPEX/Sahel mission. The methods have also been applied to similar data from the Oregon Transect Ecosystem Project using both airborne and ground sun-photometer data.

Ames-Moffett contact: R. Wrigley

(415) 604-6060

Headquarters program office: OSSA

The Search for Extraterrestrial Intelligence (SETI)

Peter R. Backus

The Search for Extraterrestrial Intelligence (SETI) Microwave Observing Project (MOP) group is finishing work on powerful systems that will search for signals produced by technological civilizations that may exist on distant planets. The MOP will outperform the combined efforts of all previous searches by a factor of nearly a billion. Columbus Day, 1992, "inauguration day" for the MOP, will be the beginning of a new era in the attempt to answer the question, Are we alone?

In the Targeted Search mode, SETI scientists will examine about 1000 nearby Sun-like stars for pulsed or continuous signals that may drift in frequency. The search will span frequencies from 1 to 3 gigahertz (GHz) and be conducted over a five- to seven-year period using the largest radio telescopes for about 5% of available time. The 140-foot telescope at the National Radio Astronomy Observatory in West Virginia will be a dedicated site. To use these telescopes efficiently, advanced electronics and computers are being designed, developed, and integrated into a transportable targeted-search system (TSS) composed of a radio-frequency subsystem (RFS), a multichannel spectrum analyzer (MCSA), a signal-detection subsystem (SDS), a system-control subsystem (SCS), and a data-collection-and-archive subsystem (DCAS).

The RFS amplifies the radio waves at the observing frequency and converts them to a lower frequency for further processing. Preliminary design of the RFS is proceeding in cooperation with researchers at the Jet Propulsion Laboratory. The requirements challenge the state of the art with wide instantaneous bandwidth (320 Megahertz (MHz)) and continuous coverage from 1 to 3 GHz. A portion of the RFS has been developed to interface with the Arecibo Observatory in Puerto Rico in 1992.

The MCSA divides a dual-polarization, 10-MHz segment of the data from the RFS into 14.3 million channels at a resolution of 1 Hz. Simultaneous resolutions of 1, 2, 4, 7, 14, and 28 Hz provide sensitivity to pulse durations of 0.025 to 1.5 seconds. The MCSA relies on a new custom integrated circuit that was designed and fabricated during the past year. The new chip has improved signal-processing fidelity over that of an earlier chip developed by students at

Stanford University. Other work focused on completing the MCSA circuit boards, particularly the board that outputs the data to the SDS. Every 1.4 seconds for each resolution and polarization, approximately 1000 channels with power higher than a threshold value are sent to the pulse detector for analysis. At the same time, the measured power in all channels at one resolution for both polarizations, about 28.6 million numbers, are sent to the continuous-wave detector.

The SDS pulse detector searches the MCSA's thresholded data for groups of three pulses with a common spacing that may be part of a regularly spaced pulse train. Improvements in the efficiency of the software have cut the hardware required from four to two processor boards. The pulse detector has been interfaced to the SCS, and initial tests of data transfer from the MCSA have been successful. The SDS continuous-wave detector is also being assembled. Data are stored on arrays of disks with a capacity of 20 billion bytes of information. A custom circuit board using commercially available parts is being developed for an efficient detection algorithm that sums the energy along a representative set of potential signals within the range of possible frequency drift rates. A sensitivity within 1 decibel of optimum is achieved.

The SCS schedules observations, configures the TSS, points the telescope, and evaluates potential signals reported by the SDS. Powerful HP9000-series workstations have been acquired and code has been developed to implement the basic functions required for observations scheduled for Columbus Day. The DCAS is a high-capacity magneto-optical disk and data-base software program within the SCS.

SETI is being used as the central theme for science curriculum materials for grades five through eight. A summer workshop was held to develop prototype teaching guides that are now being tested in local schools. Continued development is being funded by the National Science Foundation.

**Ames-Moffett contact: D. Broucker/L. Webster
(415) 604-3650/6726**

Headquarters program office: OSSA

Biochemistry of Bone Mineral Deficits in Space

Sara B. Arnaud

The biochemical basis for (1) the deficit in the accumulation of mineral in bone in growing animals and (2) the loss of minerals from the lower extremities of mature skeletons during spaceflight is an area of active research in musculoskeletal physiology. Scientists from the Institute of Biomedical Problems in Moscow, the University of North Carolina, the University of California at Santa Cruz, Hunter College, and Ames Research Center have collaborated in analyses of the rat femur, a major weight-bearing bone. The objective was to identify the precise anatomic location in the shaft of the femur where the interface between mineral and matrix, at the molecular level, was most affected by spaceflight. As illustrated in the figure, made from scanning the surface of the bone by electron microscopy, active areas of formation and resorption during normal growth are located at different sites.

Similar analyses were carried out on bone of animals from two biosatellite missions. The first spaceflight, Cosmos 1887, landed after 12.5 days at a location where another 2 days were required for the scientists who would process the specimens to arrive. The second flight, Cosmos 2044, lasted 16 days, and the animals were on the ground less than 11 hours before specimens could be obtained. The upper and lower halves of the diaphyses from the first flight and four sections from the second flight (as illustrated in the figure) were analyzed for the concentrations of minerals, collagen, cross-links (see below), and osteocalcin, a noncollagenous protein. The primary minerals in bone are calcium and phosphorus. The major protein is type I collagen, made up of polypeptide chains arranged in helical strands that aggregate to form fibrils. Fibrils are stabilized and strengthened by the action of an enzyme (lysyl oxidase) that reacts with end groups of specific amino acids in collagen to form molecular bridges, or cross-links. Four cross-links found in the bone specimens were assayed. Osteocalcin is synthesized by the osteoblast or bone-forming cell, and has an affinity for the crystals of mineral in bone.

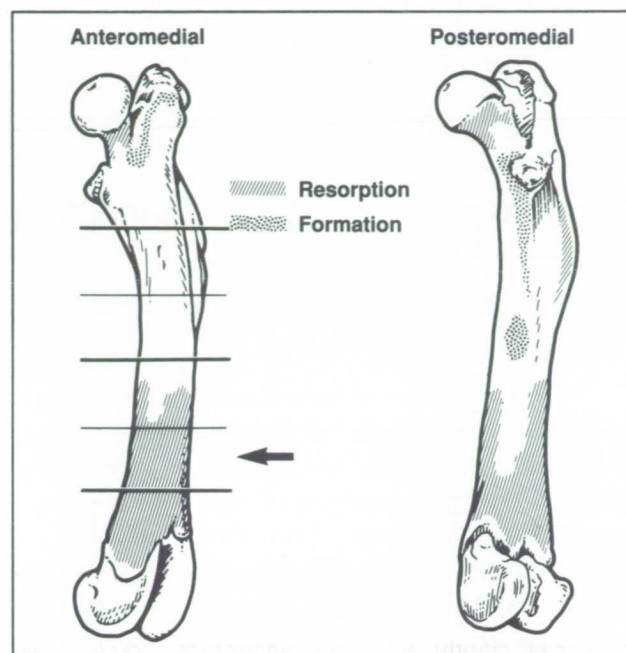


Fig. 1. Whole-bone map of areas of resorption and formation, observed by scanning electron microscopy, in the femur of a 14-week-old rat during normal growth. The site where biochemical analyses revealed maximum deficits in mineral and matrix is designated by the arrow.

Concentrations of minerals, collagen, and osteocalcin in the lower half of femur were lower in flight animals than in controls after the first mission. After the second mission, the most distal section of the femur in flight animals showed the mineral deficit associated with reduced levels of one of the cross-links measured. Of importance were similar findings in the ground-based control group that was subjected to the same diet and environment as the flight animals. Curiously, the most depressed levels of the reduced cross-link were found in the bones of rats from a flight simulation model, in the absence of a mineral deficit. Except for this case, the ratios of two cross-links and

osteocalcin were found to be related to the mineral levels in bone segments. It appears that exposure to microgravity is only one stimulus that induces the alterations in the molecular structure of matrix and mineral found in a localized area of the distal shaft of the growing rat femur after spaceflight. In both ground-based and flight experiments, the deficits in mineral and

matrix in bone in young rats were localized to the most distal section of the shaft of the femur.

Ames-Moffett contact: S. Arnaud
(415) 604-6561

Headquarters program office: OSSA

Intramuscular Pressure to Optimize Space Exercise

Richard E. Ballard, Michael Aratow, Donald E. Watenpugh

A serious problem experienced by astronauts during long-duration spaceflight is muscle atrophy. In order to develop countermeasures for this problem, a simple method for monitoring in vivo function of specific muscles is needed. Previous studies document that both intramuscular pressure (IMP)—the fluid pressure created by a muscle as it contracts within its fascial compartment—and electromyography (EMG) provide quantitative indices of muscle contraction force during isometric exercise. EMG is conventionally used to monitor isometric muscle contractions. However, there are no data available concerning the usefulness of IMP versus EMG during dynamic exercise.

IMP and surface EMG activity were measured continuously and simultaneously in the tibialis anterior (TA) and soleus (SOL) muscles of nine normal male human volunteers (28–54 years). These parameters were recorded during both concentric and eccentric exercises which consisted of plantar flexion and dorsiflexion of the ankle joint. Concentric exercise occurs when the muscle fibers are shortening during activation; eccentric exercise occurs when the muscle fibers are lengthening during activation. Concentric exercise is analogous to walking up stairs; eccentric is analogous to walking down. Eccentric muscle activation is common in the Earth's gravity. The lack of such exercise during spaceflight is thought to cause preferential atrophy of antigravity muscles, particularly of the soleus.

During our experiments, a Lido Active isokinetic dynamometer continuously recorded ankle-joint torque and position. IMP, measured by a small

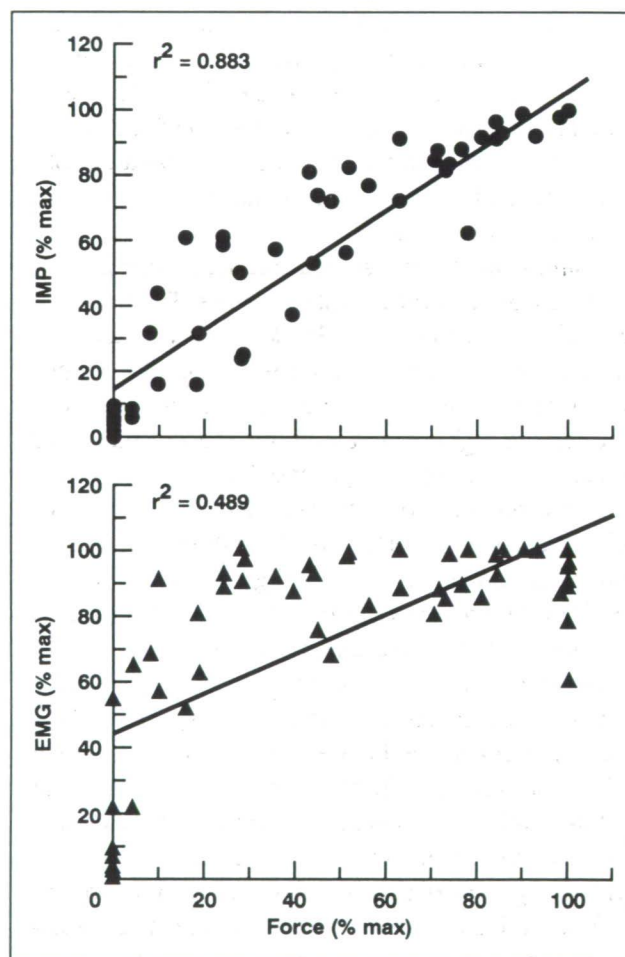


Fig. 1. Soleus IMP (circles) and EMG (triangles) during eccentric plantar flexion. Coefficients of determination (r^2) show IMP to correlate better than EMG with contraction force.

catheter emplaced under local anesthesia, correlated linearly with contraction force for both SOL ($r^2 = 0.937$) and TA ($r^2 = 0.948$) during concentric exercise. SOL and TA EMG did not correlate as well with force during concentric exercise ($r^2 = 0.716$ and 0.802 , respectively). During eccentric exercise, SOL and TA IMP also correlated linearly with contraction force ($r^2 = 0.883$ and 0.904), but SOL and TA EMG correlated poorly with force ($r^2 = 0.489$ and 0.702). The figure shows the linear correlations of soleus IMP and EMG with contraction force during eccentric plantar flexion.

IMP measurement thus provides a better index of muscle contraction force than EMG during dynamic

(concentric and eccentric) exercise. IMP reflects intrinsic mechanical properties of individual muscles, such as length-tension relationships, whereas EMG reflects only the electrical initiation and maintenance of a contraction. IMP is invasive, but it provides a more powerful tool than EMG for developing exercise hardware and protocols for astronauts exposed to long-duration flight.

Ames-Moffett contact: R. Ballard/A. Hargens
(415) 604-5747/5746

Headquarters program office: OSSA

Acute Blood-Volume Redistribution with Posture

Gregory A. Breit, Donald E. Watenpugh, Alan R. Hargens

In microgravity, astronauts frequently complain of facial swelling, headaches, and nasal congestion, which are attributed to a redistribution of body fluids toward the head. A major research effort within the Ames Life Science Division is to understand the mechanisms of these fluid shifts. Experiments were conducted to determine the distribution of local volume changes that occur during the transition from Earth to microgravity and back. This transition was simulated by placing eight human subjects on an electric tilt table and rotating them from upright standing (90-degree head-up tilt) to 54, 30, 12, 0 (supine), -6 (head-down tilt), -12, -6, 0 (supine), 12, 30, and 54 degrees, then back to standing, for 30-second periods with 10-second transitions between angles. Head-down tilt (6 degrees) is considered the best posture for simulation of microgravity in humans. Vascular-volume changes in the neck and calf were measured by two techniques: (1) strain-gauge plethysmography, to quantify relative volume changes in the whole neck and calf; and (2) photoplethysmography, which measures relative skin microvascular blood-volume changes only.

The first figure shows the average percent changes in calf and neck volumes in response to tilt. Going from head-up to head-down, neck volume

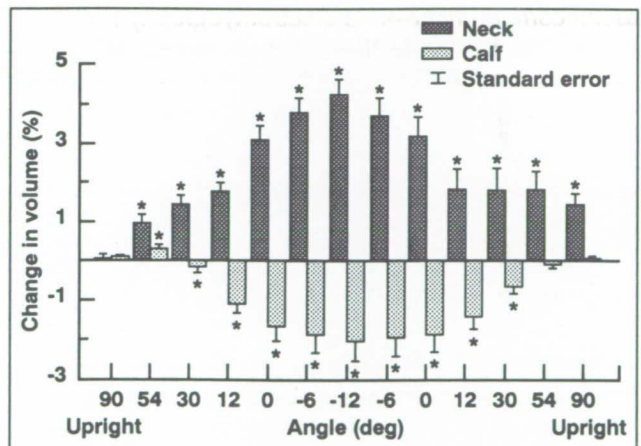


Fig. 1. Percent changes in neck and calf volume during tilting from upright standing posture to 12 degrees head down, and back to standing, as measured by strain-gauge plethysmography.

increased and calf volume decreased progressively, returning to near baseline upon resumption of standing posture. Percent microvascular volume changes in the skin (second figure) were much larger than those observed in the whole neck and calf. In contrast to the whole-area measurements, skin blood volumes at

both the calf and the neck increased significantly from standing to 0 degrees horizontal. From 0 to -12 degrees tilt, skin blood volumes at both sites decreased, the volume at the neck decreasing to near baseline. On the return to upright posture, microvascular volumes followed a similar pattern, first reaching a peak, and then decreasing to near baseline.

Whereas the changes in whole-area volume are probably due to a shift of venous blood from the lower body to the upper body during head-down tilt, the observed changes in cutaneous microvascular volume are attributed principally to active microcirculatory flow regulation. The initial increase in cutaneous blood volume at both sites (with the change from upright to horizontal posture) is believed to be a result of increased loading of the cardiovascular pressure sensors, or baroreceptors. In the neck, the added direct effect of increased blood pressure in the neck may contribute to increased flow. Although microvascular volumes subsequently decrease during the transition from 0 to -12 degrees at both the neck and the calf, these two similar reactions probably have different mechanisms: decreased arterial pressure in the calf versus autoregulation in the neck in response to the local increase in arteriolar pressure. These results demonstrate that whereas macroscopic blood-volume responses to gravitational stress are mainly a

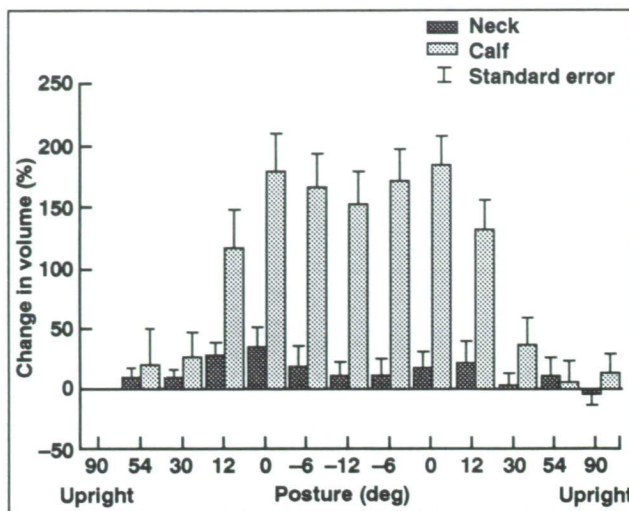


Fig. 2. Percent changes in skin microvascular blood volume at the neck and calf during tilting, as measured by photoplethysmography.

result of bulk fluid shifts, microvascular responses are generally independent of direct inertial effects, relying more on central and local flow regulation.

Ames-Moffett contact: G. Breit/A. Hargens

(415) 604-0073/5746

Headquarters program office: OSSA

Behavioral and Neural Adaptation to Altered Gravity

Nancy G. Daunton, Merylee Cocoran, Muriel Ross

In studies of rats chronically exposed to hypergravity (2 G), we have recently found that different behavioral functions readapt to normal G at different rates. For example, after approximately two weeks of exposure to 2 G, animals lost the ability to perform the righting reflex. The ability to right did not return within two days of exposure to normal G, although after eight days in normal G, the animals were able to right normally (see first figure). However, in another test of vestibular function, which measured orientation with respect to gravity, recovery occurred within the first 48 hours of exposure to normal G.

Evaluation of the neural structure of the gravity-sensing receptors in the vestibular end organs showed a decrease of approximately 30% in the number of synapses in type II hair cells in animals exposed to 2 G for two weeks. This change in neural structure may be associated with a decreased sensitivity to linear acceleration and gravity after removal from the centrifuge, which leads to the disorientation with respect to gravity and to the poor performance of the righting reflex after hyper-G exposure. Further studies must be performed to determine the time course of changes in the number of synapses in the

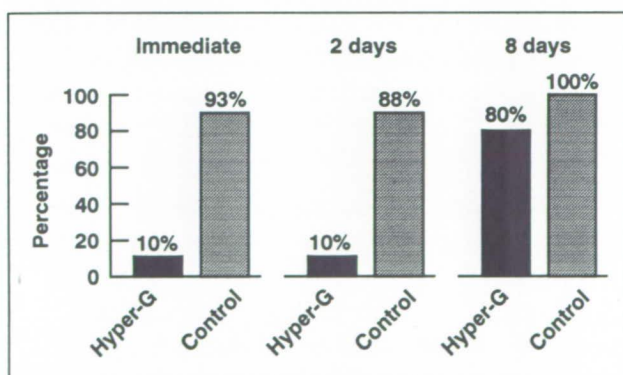


Fig. 1. Percentage of animals that righted during a test of the righting reflex conducted immediately after, two days after, and eight days after removal from a 2-G environment. Control animals experienced only the normal G environment.

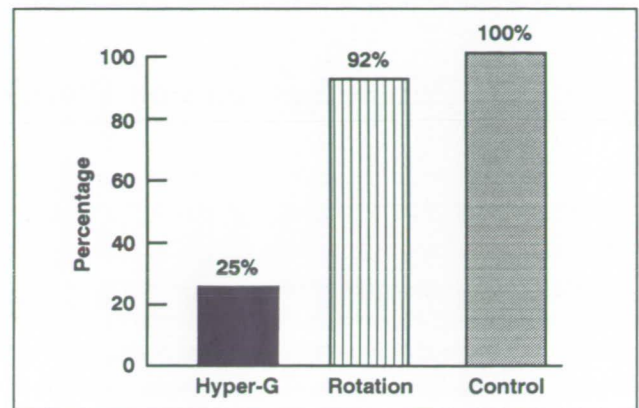


Fig. 2. Percentage of animals that righted successfully immediately after removal from the centrifuge. Hyper-G animals experienced 2 G, plus rotation at 20.5 RPM, rotation animals experienced only rotation, and control animals experienced only normal G without rotation.

gravity-sensing end organs as the animals readapt to normal G.

We have shown that the effects seen on vestibular and neuromuscular function and on vestibular end-organ morphology after centrifugation were due to the hypergravity component rather than the rotational (angular velocity) component of centrifugation. Thus, these functions do allow us to monitor actual behavior adaptation to altered gravity. Animals that were exposed only to the rotational (angular velocity) component of centrifugation did not show changes in any of our tests of locomotion or vestibular function (see second figure), nor did they show changes in morphology of the gravity-sensing vestibular end organs.

The next series of studies will investigate the effects of both shorter (1–4 days) and longer (several months) periods of exposure to hyper-G on the time course of adaptation to hyper-G and readaptation to normal G. In addition to behavioral studies of vestibular and neuromuscular function and studies of the

peripheral vestibular system, changes in the peripheral and central portions of the neuromuscular system related to limb coordination during locomotion will be investigated.

Ames-Moffett contact: N. Daunton
(415) 604-4818
Headquarters program office: OSSA

Effects of Glucose Solutions on Thermoregulation

A physical exercise load above 50% of the maximal working capacity during extravehicular activity (EVA) would increase body heat production beyond the steady-state heat removal capacity of the thermal system in the current EVA suit. The result would be an increase in body temperature in proportion to work intensity which would cause heat exhaustion and incapacitation if it continued unabated. Results from microgravity simulation (bed-rest) deconditioning studies indicate that there is an excessive increase in body core temperature during exercise after bed rest. The cause of this "excessive hyperthermia" appears to be reduced heat transfer from the core (working muscles) to the skin as a result of excessive vasoconstriction of skin blood vessels. Thus, in space, heat cannot reach the skin for dissipation from the skin by the astronauts' thermal-underwear cooling system or by evaporation of sweat. The well-documented reduction of total body water in astronauts in microgravity probably also contributes to decreases in exercise-induced sweating and evaporative heat loss.

The mechanism of this excessive hyperthermic response and methods for attenuating it are being investigated in the Laboratory for Human Gravitational Physiology at Ames. In a recent study, six men (35 ± 7 years of age) were dehydrated (i.e., deconditioned) by four hours of thermoneutral water immersion. They then consumed about 460 milliliters of a 34% glucose/water solution. Fifteen minutes later, they performed 70 minutes of lower-extremity (cycling) exercise in the supine position. The rectal temperature during exercise without prior fluid intake was $38.6 \pm 0.1^\circ\text{C}$, but was only $38.2 \pm 0.2^\circ\text{C}$, a statistically significant difference, when the glucose solution had been ingested (see figure). Fluid ingestion may also have reduced the resting rectal temperature.

John E. Greenleaf, Alan S. Dearborn, Andrew C. Ertl

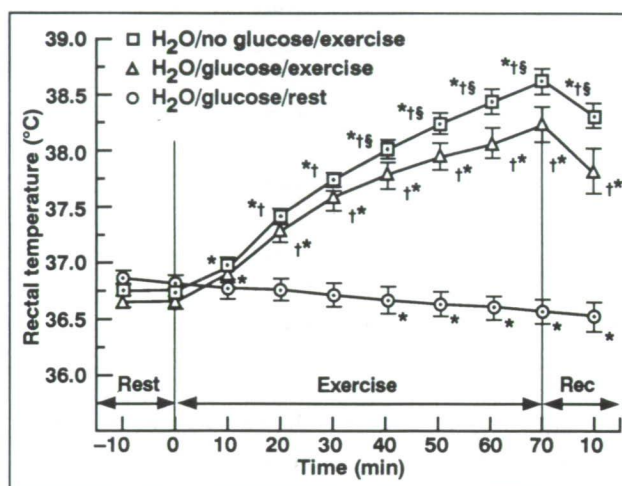


Fig. 1. Mean (\pm SE) rectal temperature during rest and exercise at 60% of maximal working capacity without and with glucose ingestion after 4 hours of water immersion (H_2O). * $P < 0.05$ compared to -10 minutes value; † $P < 0.05$ compared to corresponding rest value and to corresponding $\text{H}_2\text{O}/\text{Glucose}/\text{Exercise}$ value.

These results indicate that prehydrating astronauts before EVA with a glucose/water beverage could be helpful in reducing potential exercise hyperthermia. Consumption of glucose during EVA would also provide an energy source for alleviating fatigue associated with increased metabolism. Better formulated rehydration drinks will enhance performance and well-being of astronauts during EVA.

Ames-Moffett contact: J. Greenleaf
(415) 604-6604
Headquarters program office: OSSA

Role of Muscle Function and Growth Hormones in the Prevention of Muscle Atrophy

Richard E. Grindeland

A variety of studies conducted on animals in our laboratory after spaceflight or exposure to simulated microgravity (suspension by the hind legs), and in vitro studies done by H. Vandenburg at Brown University, have shown that muscle-wasting in space is due to decreased exertion of force by the muscles (not bearing weight) and to deficient growth-hormone (GH) secretion and/or decreased tissue sensitivity to the hormone. We have also repeatedly demonstrated that GH secretion, as measured by bioassay, is dramatically decreased in rats during spaceflight (space-flight rats) and in suspended rats. During the current year we have investigated the effects of two protein-anabolic hormones with or without exercise on the atrophy of suspended rat muscles and the effects of horizontal or head-down suspension of rats on GH secretion, and we have further developed the procedure for measurement of skeletal muscle hormone receptors.

Effects of GH and exercise on muscle atrophy in suspended rats. Studies in our laboratory and others have shown that various exercise countermeasures were able to deter muscle atrophy in suspended rats by 50% at most. GH given to suspended rats had only minimal benefits. When GH was given to hypophysectomized suspended rats it was only about half as effective as it was in hypophysectomized ambulatory rats. Whereas the GH did stimulate growth of the atrophic muscles, it also stimulated general body growth so that atrophic muscles gained nothing relative to body weight.

Hypophysectomized rats were suspended and exercised (three bouts of five climbs up a 1-meter ladder while carrying 20% of their body weight), given GH (1 milligram per kilogram body weight; Genentech recombinant human GH), or given both treatments. Neither exercise nor GH alone had much effect, but the combined treatment completely prevented atrophy in five of the seven muscles studied. The GH-exercise regimen promoted body growth but the exercised muscles grew twice as much as the total body, indicating a preferential targeting of the hormone action. The quality of the muscle (i.e., maintenance of slow fiber type) was also affected by

the countermeasure; both fast and slow fiber types were beneficially affected.

Effects of insulin-like growth factor-I and exercise on muscle atrophy in suspended rats. Insulin-like growth factor-I (IGF-I) is a peptide hormone which, on the basis of in vitro studies, is thought to be the primary hormonal regulator of protein synthesis in skeletal muscle. GH stimulates tissue production of this hormone, believed to take place primarily in the liver, which gives rise to the plasma IGF-I. GH also stimulates the production of IGF-I messenger RNA in muscle cells; it is presently unclear if the latter IGF-I is of physiological importance except in tissue repair after injury or denervation of the muscle. IGF-I has been tested only once in animals in significant doses; because the hormone used in that study was isolated from plasma there is some question about its purity. The IGF-I used in the present study was a genetically engineered hormone provided by Genentech, Inc. In an experiment using the same protocol as that used in the study described above, rats were given IGF-I rather than GH in an effort to forestall muscle atrophy; we expected that IGF-I would be more effective than GH. The IGF-I stimulated growth of the heart, spleen, liver, and testes significantly, but had only a slight effect on skeletal muscle, and only on certain muscles. There was no interaction between exercise and IGF-I as there had been for GH. On a molar basis, about four times as much IGF-I was given as GH. Thus, GH appears to be a much more effective hormone. It is also of interest that body weights of animals treated with IGF-I grew more than muscle weights.

Effect of horizontal or head-down suspension and recovery from suspension on secretion of GH under basal and stimulated conditions. Space-flight and suspended rats show a 50% to 70% decrease of secretion of bioassayable GH, which may contribute to muscle and bone losses in these animals. The reduced GH secretion is due in part to a decrease in synthesis and secretion of the hypothalamic factors that regulate secretion of GH and in part to decreased basal secretion of GH by pituitary cells and decreased

responsiveness to the regulatory factors (previous observations from our laboratory). In one earlier study the effect of horizontal versus head-down suspension of rats on GH secretion was investigated: horizontal suspension suppressed GH secretion significantly, and head-down suspension suppressed it even further. In the present study we have repeated that experiment and have also investigated the effects of one week of recovery from head-down and horizontal suspension. We have largely verified the results of the previous study and have shown that pituitary function is still affected one week after the animals are allowed to ambulate again after a two-week suspension.

Pituitary cells from suspended, recovery, and control rats were removed and then cultured for four hours in the absence or presence of growth hormone releasing factor (GRF). Doses of GRF were either 0.2 or 0.8 nanomole. Media and cells were removed and assayed by radioimmunoassay or biological assay.

Suspended rats show markedly higher basal secretion of GH after recovery from suspension, regardless of suspension position. However, horizontally suspended rats also show exaggerated responses to the GRF, whereas those rats recovering from head-down suspension return to essentially ambulatory control levels after stimulation by GRF. The differences between the values for horizontally suspended rats and those for ambulatory controls are much less

	Soleus muscle weight (mg), mean \pm standard error
Ambulatory	
saline	97 \pm 5
IGF-1	102 \pm 4
Suspended	
saline	88 \pm 3
IGF-1	93 \pm 4
exercise	93 \pm 3
exercise + IGF-1	96 \pm 3

Doses of GRF (nM)	Media growth hormone concentration (ug/ml)		
	0	0.2	0.8
Donar rat			
Ambulatory	1.4	4.5	4.4
Suspended-horizontal	1.3	1.5	3.9
Suspended-head down	0.1	0.1	0.5
Recovery from horizontal suspension	3.8	11.0	17.0
Recovery from head-down suspension	3.8	3.0	5.4

than those seen in the first experiment of this type; the reason for the differences between the experiments is unknown.

Muscle hormone receptors. We have been able to measure IGF-I receptors readily in skeletal muscles of suspended rats but have had difficulty reproducing measurements of muscle GH receptors; this difficulty does not hold for GH receptors in liver. The procedure we used entailed purification of the receptors on a wheat-germ agglutinin column and subsequent precipitation with polyethylene glycol. This procedure can be capricious for GH (but not necessarily for other hormones). We have now markedly simplified the homogenization of muscle tissue without loss of receptors, and we have simplified the centrifugation procedure. Most important, we have been able to use fractions from differential centrifugation directly, thereby obviating the need to purify the receptors and to precipitate with polyethylene glycol. The newly developed procedure will be used to measure receptors in muscles of suspended and space-flight rats.

Ames-Moffett contact: R. Grindeland
(415) 604-5756
Headquarters program office: OSSA

Cellular Growth and Aging Phenomena

Rosalind A. Grymes, Joan Vernikos

Observation of mammalian cells in orbit has revealed changes in metabolism, proliferative cycling, and growth-factor responsiveness similar to those characteristic of senescent (aged) cells at 1 G. Werner's syndrome (WS) is an inherited premature aging disorder. Many of its clinical symptoms involve the skin and connective tissue. In culture, skin cells from WS patients overexpress the enzyme collagenase I. They also fail to respond to growth factors, such as platelet-derived growth factor (PDGF), that normally induce the enzyme. Collagenase I is crucial in collagen remodeling and removal. Collagen is the most important connective tissue molecule; it is 90% of the dry weight of the skin. The model of WS is used to understand the causes of senescence. Similarities between senescent cells and those exposed to microgravity may allow results obtained with this model system to predict the responses of cells and (potentially) humans to microgravity.

Last year, we explored the hypothesis that the failure of WS cells to respond to PDGF is a result of a defect in the hereditary material (DNA). Normal DNA sequences were supplied to WS and control cells by recombinant DNA methods. The WS defect was not affected by this treatment. We then studied the regulatory proteins FOS and JUN that interact with DNA recognition sequences. The FOS and JUN proteins transfer growth factor signals to target genes, such as that for collagenase I. We discovered abnormal levels of these proteins in WS cells.

In 1991, we extended our studies to a different pathway regulating collagenase I expression. Collagenase I can be suppressed by hydrocortisone (HC) treatment. This effect, in addition to the induction of enzyme by PDGF, results from interactions between FOS/JUN and DNA. The suppressive pathway approximates normality in WS cells. While these cells synthesize up to 10 times the normal amount of collagenase I, they are more sensitive than control cells to HC shut-down. Collagenase I was reduced 79–92% in HC-treated WS cells, versus 56–58% in aged normal controls. Interestingly, while WS cells are unresponsive to PDGF, pretreatment with HC

followed by combined exposure to HC and PDGF showed additive suppression (18–52%).

WS also involves chromosome breakage. Many breakage events have been observed near the collagenase I gene (on the long arm of chromosome 11). DNA is normally condensed and protected, but it is unwrapped piecemeal during replication and transcription. Local breakage of DNA near the control sequences of the collagenase I gene might cause a disruption of normal regulatory patterns, as observed in WS. All the previously mentioned observations—constitutive overexpression, insensitivity to normally inductive stimuli, and hypersensitivity to suppression—could result from physical interruption of the local milieu. This type of change would also be consistent with the recessive inheritance of the syndrome. A recently published paper reported that binding of FOS:JUN heterodimeric protein aggregates bends the DNA in a different fashion than does binding by JUN:JUN homodimers. The FOS:JUN configuration is favored, but high protein concentrations of JUN result in the production of the homodimer moiety. We found aberrant regulation of the quantities of the messenger RNAs that direct production of FOS and JUN, which could lead to unusually high levels of JUN, in the WS cells.

Similarities between WS cells and microgravity-exposed mammalian cells, chronologically aged cells, and cultured senescent cells suggest the value of this model system. In completely separate research, two other groups have investigated abnormalities of cellular signal processing involving FOS/JUN transcriptional control. Limouse and coworkers (a collaboration between INSERM in Toulouse, France and the Institute of Biomedical Problems in Moscow) have studied the activation of cells by phorbol-esters in microgravity. They found that cells carried aboard Cosmos 2044 were deficient in their responses to phorbol-ester stimulation. Similarly, de Groot and coworkers (Netherlands Institute for Developmental Biology and the University of Utrecht, The Netherlands) showed that both epidermal growth factor and

phorbol-ester-stimulated expression of *c-fos* and *c-jun* was depressed in microgravity. Our studies of senescent cells parallel this work.

The accessibility of skin tissue enhances the attraction of dermal cell systems for study. In cultured WS cells, we find several defined anomalies and a single underlying genetic defect. Current techniques allow in-depth study of both the expressed abnormalities and the DNA defect. Results indicate the general

utility of this model for studying hypotheses related to spaceflight effects on mammalian systems. In addition, our results have added significantly to an understanding of the relationship between gene expression and both aging and genetic disease.

**Ames-Moffett contact: R. Grymes
(415) 604-3239**

Headquarters program office: OSSA

Circulatory Changes during Simulated Microgravity

Yasuaki Kawai, M. Shannon Stout, Gita Murthy

Facial edema, nasal congestion, headache, space motion sickness, and reduced performance are commonly observed in astronauts during spaceflight and in subjects exposed to simulated microgravity. These symptoms may result from alterations of blood circulation in the head. It is known that microgravity causes a shift of blood and tissue fluids from the lower body toward the upper body. However, there is little knowledge of cerebral and cutaneous blood flow in the head during microgravity. This study was undertaken to compare cerebral blood flow (CBF) and cheek-skin bloodflow (SkBF) in humans before, during, and after exposure to 24 hours of microgravity as simulated by 6-degree head-down tilt (HDT). In eight healthy males, CBF velocity and SkBF were measured by the transcranial Doppler ultrasonic technique and laser Doppler flowmetry, respectively. As shown in the first figure, CBF velocity increased significantly from a baseline value (pre-HDT upright sitting posture) of 55.5 ± 3.7 to 63.2 ± 4.1 centimeters per second at 3 hours of HDT ($p < 0.05$). This increase was sustained throughout 24 hours of HDT. After 1 hour of post-HDT seated recovery, the velocity

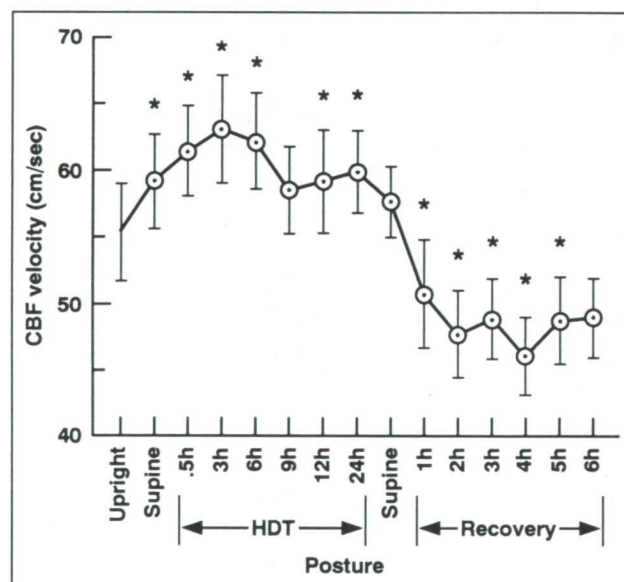


Fig. 1. Effects of HDT on cerebral blood flow velocity (mean \pm SE, $n = 8$). Asterisks indicate significant difference from the baseline value at pre-HDT upright posture ($p < 0.05$).

decreased significantly to 50.8 ± 4.0 centimeters per second ($p < 0.01$). These results suggest that elevation of arterial pressure in the head as a result of the hydrostatic effect of HDT increases cerebral blood flow. Decreased CBF velocity during recovery may explain, in part, the orthostatic intolerance observed in astronauts returning to Earth.

The second figure shows that SkBF in the cheek, expressed in millivolts (mV), also increased significantly from 112 ± 26 mV (baseline) to 185 ± 41 mV at 12 hours of HDT ($p < 0.05$), and then returned to near-baseline values by the end of HDT. It is suggested that the cutaneous circulation in the cheek lacks regulation during the first 12 hours of HDT because of increased local blood pressure. These measurements should be extended to actual microgravity, possibly on a Space Shuttle mission.

Ames-Moffett contact: A. Hargens

(415) 604-5746

Headquarters program office: OSSA

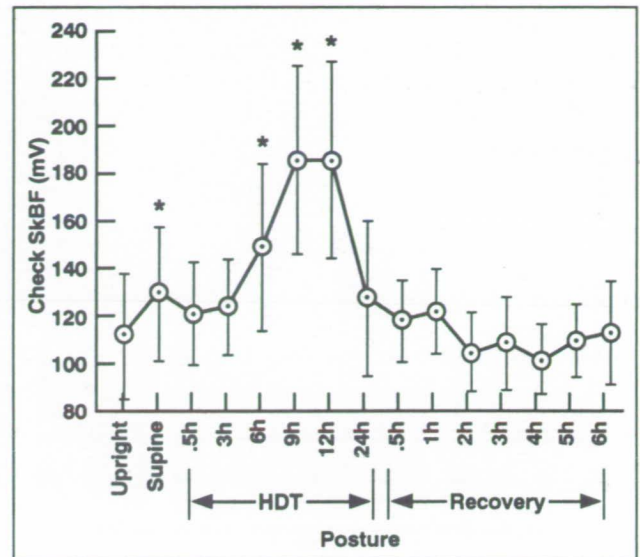


Fig. 2. Effects of HDT on skin blood flow in the cheek (mean \pm SE, $n = 8$). Asterisks indicate significant difference from the baseline value at pre-HDT upright posture ($p < 0.05$).

Increased Intracranial Pressure during Simulated Microgravity

The headaches and space motion sickness commonly reported during exposure to microgravity may be a consequence of or be exacerbated by increased intracranial pressure (ICP). ICP may be elevated by increased capillary blood pressure and flow in vessels above the heart during microgravity. In our study of ICP during simulated microgravity (6-degree head-down tilt (HDT)), alterations of ICP were examined by using a noninvasive tympanic membrane displacement (TMD) technique.

The TMD technique is based on the principle that movement of the ear drum or tympanic membrane, induced by the stapedial muscle reflex, produces slight but significant ear-canal volume displacements that can be measured with a special computer-based instrument. The tympanic membrane is attached to

Gita Murthy, Donald E. Watenpaugh, Alan R. Hargens

the first of three connected bones of the middle ear; the third bone, the stapes, is attached to the oval window of the inner ear. The pressure of the fluid in the inner ear is essentially equal to ICP because of a direct connection by a duct to the ventricular system of the brain. Alterations in ICP (and inner ear pressure) cause inward or outward displacements of the tympanic membrane, during stapedial reflex stimulation, when the ICP increases or decreases, respectively. Tympanic membrane displacements are measured by a volume displacement transducer probe attached to a headset. The probe is tightly sealed (like an earplug) into the ear canal.

In six male subjects (ages 22 to 46) movements of the tympanic membrane, and hence changes in ICP,

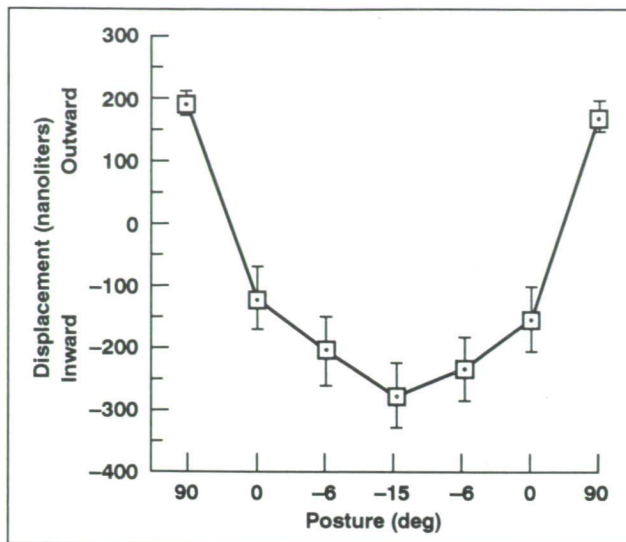


Fig. 1. Tympanic membrane displacement response with stepwise postural changes from 90 degrees upright sitting to 15 degrees HDT and return to 90 degrees upright sitting.

were compared in various postures for each subject (see figure). The subjects spent 10 minutes in each posture. Significant displacements of the tympanic membrane occurred upon each transition to a new posture. Based on a sigmoidal relationship that exists between TMD and ICP, our results indicate that ICP increased from about 2 millimeters of mercury to 17 millimeters of mercury when posture changed from upright sitting to 6 degrees HDT. Because increased ICP may adversely affect crew performance during spaceflight, ICP should be measured during actual microgravity.

**Ames-Moffett contact: A. Hargens/D. Watenpaugh
(415) 604-5746/5747**

Headquarters program office: OSSA

Macular Bioaccelerometer Plasticity in Novel Gravitational Environments

Muriel D. Ross

A question to be answered by gravitational research on living systems is whether gravity as a force vector exerts a continuum of effects on the system under study. That is, are the effects of microgravity opposite but equal to the effects of hypergravity? The answer to this question is being sought for the gravity-sensing end organs of the mammalian inner ear through a combination of investigations carried out on centrifuged animals and on animals exposed to microgravity on the recent Space Life Sciences-1 (SLS-1) shuttle mission.

The mammal used in our studies is the Sprague-Dawley rat. The inner-ear gravity receptors of any mammal could be used as model systems because the basic organization of the receptors is the same in all mammals, including humans. The gravity receptors, or maculas, are biological accelerometers. They consist of a test mass of tiny crystallites called otoconia ("ear dust") and an underlying detecting unit, the neuroepithelium. The test mass is only

loosely attached to the neuroepithelium, whereas the latter is anchored to the skull. Differences in motion of the test otoconial mass with respect to the underlying neuroepithelium, which moves with the skull during linear acceleration of the head, are thought to provide the necessary signals to the receptor cells, called hair cells. Thus, the maculas are sensitive to both gravitational and translational linear accelerations.

This report deals almost entirely with findings in the neuroepithelium. Study of the otoconial mass under various G forces is incomplete. The neuroepithelium is of more immediate interest because of its organization as a parallel distributed information processing system. It is also highly miniaturized, with each macula consisting of only about 1 to 1.5 cubic millimeters of neural tissue. The fundamental organization and adaptive capabilities of the maculas thus have technological as well as biological relevance. Better parallel processing computers or linear

accelerometers can result from this and similar research on neural networks.

Two chief findings have emerged over the past year of study. The first of these pertains to the fundamental organization of a gravity receptor and the possibility that this architecture reflects a basic property of all neural tissue. Maculas are organized into two main circuits: (1) highly channeled and (2) distributed modifying. A stimulus to the highly channeled circuit is immediately processed (by the type I hair cell receptor) for output; the distributed modifying circuit utilizes feedforward-feedback loops and inserted type II hair cells to distribute information over small parts of the network and to modify final network output. It is postulated that, in more complex areas of the nervous system such as the retina and the brain cortex, more such loops and interneurons are added to achieve more advanced information processing and, ultimately, cognitive functioning. It is further predicted that it is the distributed modifying circuit that should be most adaptive to new environmental conditions.

To test this hypothesis, six rats were exposed to 2 G for 14 days on a centrifuge while another six rats served as ground controls and a third group of six rats were placed at the center of the centrifuge and served as on-centrifuge controls. All rats were killed at the end of 14 days. In a microgravity experiment in which rats were flown on SLS-1, ten rats were killed on the day the shuttle landed (SLS-1 recovery day zero, R + 0) and another nine rats were killed nine days postflight (R + 9). After preparation of the macular tissue for viewing in a transmission electron microscope, 50 serial sections per rat were cut from samples of all but the R + 9 group. All synapses of the hair cells were photographed and identified as to type of hair cell, and the results were tabulated. In addi-

tion, more than 800 synapses from maculas of the centrifuged animals were measured. The synapses from flight animals have not yet been measured.

Preliminary findings from the hypergravity study are that the number of synapses decreased by about 30% in type II hair cells of animals exposed to hypergravity compared to those in both groups of controls, but there were similar numbers of synapses in type I hair cells of centrifuged animals, on-centrifuge controls, and ground controls. Early findings in maculas of rats obtained on R + 0 are that the number of synapses in type II hair cells increased by about 25% compared to all controls. A slight increase in synapses in type I cells also may have occurred. No statistically significant differences in length or diameter of synapses was detected in the centrifuged material.

These results are intriguing because they are the first evidence that synapses do change in maculas as a result of alteration of gravitational force. While much more data are needed, the early interpretation is that macular connectivities are under the influence of gravity and retain plasticity. This second chief finding, that plasticity is retained, also supports the hypothesis that the distributed modifying type of circuit is the most adaptable to changed environmental forces and may thus be the type of circuit most involved in memory and learning. Computer simulations of this kind of circuitry may be most helpful in developing new neural network architectures for implementation in robotic devices and in parallel-processing computers.

Ames-Moffett contact: M. Ross
(415) 604-5757

Headquarters program office: OSSA

Dynamic Inter-Limb Resistance Exercise Device

Douglas F. Schwandt, Alan R. Hargens, Scott E. Parazynski

Essential for fitness on Earth, resistive exercise is even more important for astronauts endeavoring to maintain muscle and bone strength in the absence of gravity. We have developed a dynamic inter-limb resistance exercise device (see first figure). It features a rope, an instrumented pulley, and a modular harness system. Energy is delivered from one limb to another limb, obviating the need for external energy storage or supply. Sensors in the pulley (see second figure) measure force and motion for performance feedback display and data acquisition. Exercise protocols may be presented to the subject through the compact display, permitting isotonic, isokinetic, and isometric contractions for a variety of exercises. Free-floating exercise using this hardware prevents vibration in

sensitive experiments on board spacecraft. Compact, with low mass (less than 10 pounds) and volume, the inter-limb resistance exercise device is also well suited for a "safe haven" compartment of the Space Station Freedom or another long-duration crewed facility.

In cooperation with the Exercise Countermeasure Project at Johnson Space Center, the inter-limb resistance exercise device was successfully tested and documented on videotape during a KC-135 parabolic flight to simulate microgravity. With each of four subjects exercising during one of four sets of ten parabolas, a variety of arm and leg exercises were performed during the simulated microgravity. These included leg press, running in place, calf press (ankle

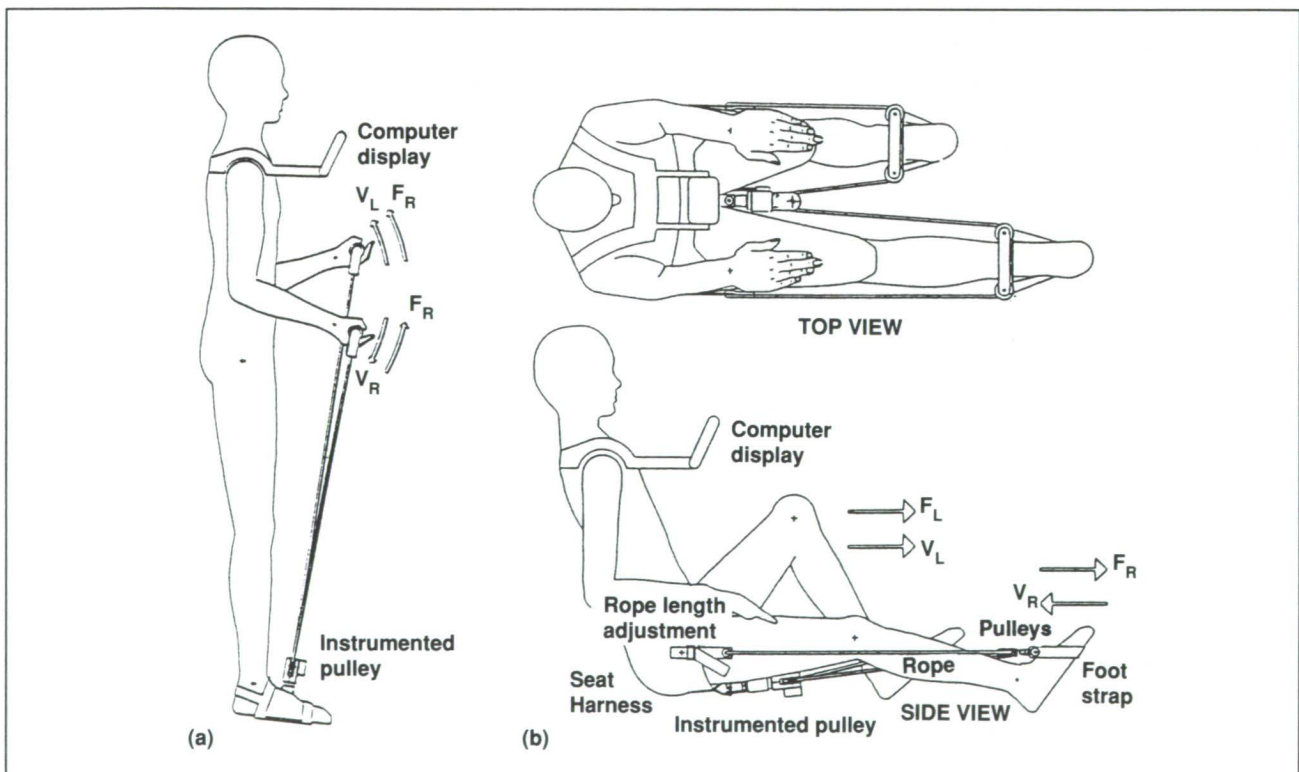


Fig. 1. Human subject using inter-limb resistance exercise device.

extension), leg abduction, biceps curl, triceps press, arm rowing, and military press. Arm exercises and leg exercises in which a shoulder harness was used for resistance recruited back muscle groups for spinal loading. Such exercise may be important for reducing back pain associated with exposure to microgravity. All exercises were performed at submaximal effort.

The exercise device performed well in this preliminary, short-duration microgravity study. Three subjects performed the leg press, and generated peak forces ranging from 640 to 1156 Newtons (144 to 260 pounds) (sum of force from both legs). Two subjects performed the calf press and generated peak forces of 702 to 782 Newtons (158 to 176 pounds). The biceps curl exercise produced up to 623 Newtons (140 pounds) for one subject. Forces approaching peak values were sustained throughout the range of motion for all exercises. Subjects successfully donned, reconfigured, and removed the inter-limb resistance exercise device during the tests.

The inter-limb resistance exercise device could potentially be used by sports fitness centers and for personal training at home. Its usefulness in rehabilitation is being explored in collaboration with the

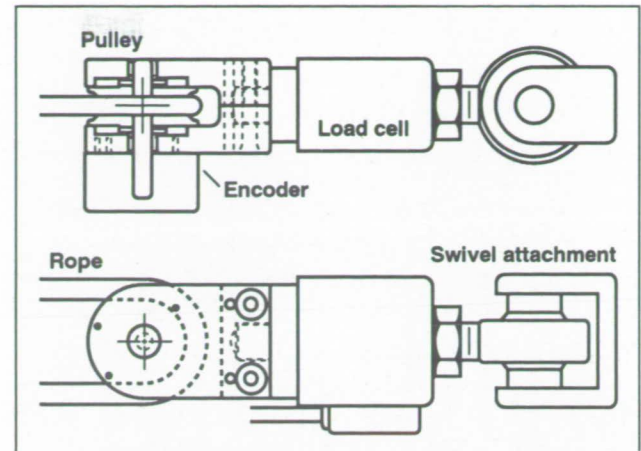


Fig. 2. Schematic drawing of the instrumented pulley.

Palo Alto VA Rehabilitation Research and Development Center.

Ames-Moffett contact: D. Schwandt/A. Hargens
(415) 604-5747/5746

Headquarters program office: DDF

A 4-Day Head-Down Bed-Rest Analog for Quick Screening of 0-G Countermeasure Effectiveness

Joan Vernikos

A variety of procedures have been proposed, tested, and used to counteract or prevent the physiological effects of spaceflight. Although validation of their effectiveness in flight is essential, the various countermeasures cannot be adequately screened by in-flight testing alone because of infrequent opportunities.

Head-down (−6-degree) bed rest (HDBR) has proved to be an acceptable analog for the study of most of the effects of spaceflight on the body. Bed-rest studies of 7-day to 17-week duration have generally been used for the assessment of countermeasure effectiveness. As part of a program to delineate artificial-gravity requirements for humans, we developed a two-step approach that allows rapid screening

of a large variety of countermeasures using, first, a 4-day, −6-degree HDBR model, and then subsequent validation in a 60-day HDBR model focusing on those countermeasures that appear most promising.

Our initial evaluation of this approach shows that only four days of HDBR are required to produce significant changes in many physiological systems known to be affected by spaceflight. The following changes take place: (1) orthostatic tolerance (30 minutes at 60° head-up tilt, as shown in the photograph) is decreased; (2) circulating blood volume is decreased; (3) physical performance/peak oxygen consumption (measured by horizontal bicycle ergometer) is decreased; and (4) sodium excretion

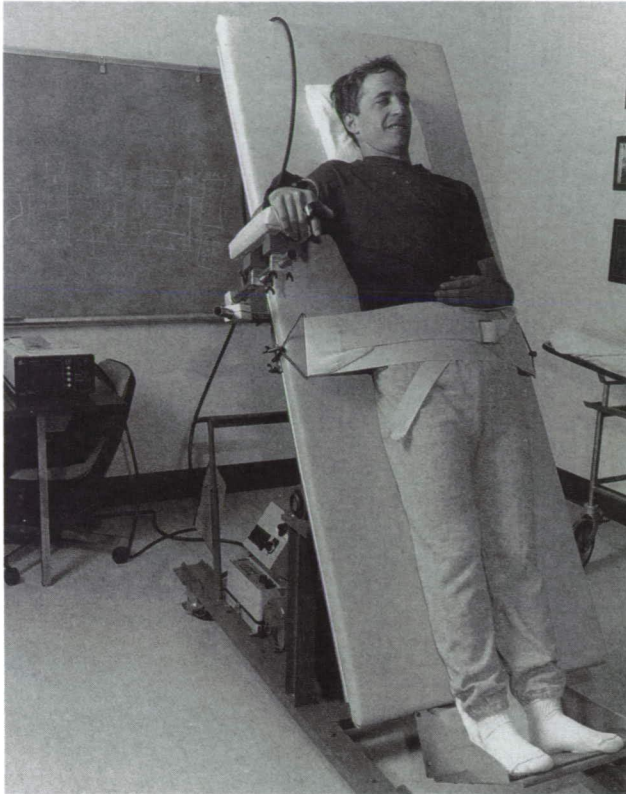


Fig. 1. Sixty-degree head-up tilt test used to determine level of orthostatic tolerance. Blood pressure and heart rate are monitored throughout the test.

on the first day of HDBR is increased. Fluid-and-electrolyte-regulating hormones are inhibited after four hours of HDBR. It is possible that other parameters, such as blood and urinary markers of calcium and bone metabolism, may also show early changes that could be useful in predicting the effects of more prolonged HDBR exposures.

The 4-day HDBR model consists of one control ambulatory day, when pre-bedrest orthostatic tolerance and plasma volume are measured. Orthostatic tolerance and plasma volume are again tested on day 4 of HDBR, after which subjects are returned to HDBR. Peak oxygen consumption in a horizontal bicycle ergometer is tested on the following morning. This approach provides a convenient, fast, and relatively inexpensive means of screening a broad range of countermeasures and their permutations in a large number of subjects—before expensive bed-rest studies or flight experiments are undertaken.

Ames-Moffett contact: J. Vernikos

(415) 604-3736

Headquarters program office: OSSA

ORIGINAL PAGE
BLACK AND WHITE PHOTOGRAPH

Atrial Natriuretic Peptide Reduces Leg Capillary Filtration

Donald E. Watenpaugh, Alan R. Hargens

Atrial natriuretic peptide (ANP) is produced by the atria of the heart and secreted by them when they are distended. Because spaceflight may involve conditions that distend the atria, ANP could participate in human adaptation to microgravity. ANP may reduce blood volume, as hemoconcentration is commonly associated with ANP administration. In a study at the University of Texas Southwestern Medical Center in Dallas (in collaboration with researchers there), we investigated whether ANP increases fluid movement out of the circulation in the legs of human subjects (leg capillary filtration). We also attempted to relate effects on leg filtration to two systemic indicators of hemoconcentration, hematocrit and plasma oncotic pressure.

In 10 normal, healthy male subjects, leg capillary filtration was measured as the increase in leg volume produced by impeding the venous drainage from the leg. This method emphasizes the effect of vascular permeability changes on capillary fluid movement.

ANP significantly increased the hematocrit and the plasma oncotic pressure relative to baseline control values (see first table). Mean filtration rate in the calf, however, was decreased 47% during ANP

Influence of placebo infusion on capillary filtration

$\bar{X} \pm SE$, $n = 7$, $\alpha = 0.05$.

	Pre-infusion control	Placebo
ANP (pmol/l)	21 + 2	22 + 2
Heart rate (beats/min)	66 + 4	68 + 4
Hematocrit (%)	44 + 1	44 + 1
Leg filtration (vol%/min)	0.11 + 0.02	0.09 + 0.01

infusion. Heart rate was elevated during ANP infusion. Infusion of ANP elevated plasma ANP concentrations well above levels normally found in humans. Placebo infusion had no effect (second table).

The hematocrit and plasma oncotic pressure increases confirm that a pharmacologic ANP stimulus produces hemoconcentration. Although we expected ANP to increase leg filtration in accordance with the systemic hemoconcentration, it actually reduced leg filtration. Increased plasma oncotic pressure reduces capillary filtration. The plasma oncotic pressure increase with ANP, however, only partially explains the decrease in filtration. The results suggest that ANP may reduce capillary permeability in the legs, while increasing it elsewhere. Thus the effects of this peptide on body fluid movements are site specific—an observation that should be considered in investigations of ANP's potential role in human adaptation to microgravity.

This work was supported by a NASA Graduate Student Research Fellowship to Donald Watenpaugh.

Influence of ANP infusion on plasma oncotic pressure and capillary filtration

$\bar{X} \pm SE$, $n = 6$, * different from control, $p < 0.05$.

	Pre-infusion control	ANP
ANP (pmol/l)	30 ± 4	2568 ± 595*
Heart rate (beats/min)	61 ± 5	73 ± 6*
Hematocrit (%)	43 ± 1	45 ± 1.0*
Plasma oncotic pressure (mm Hg)	21.7 ± 0.6	24.9 ± 1.0*
Leg filtration (vol%/min)	0.15 ± 0.03	0.08 ± 0.02*

Ames-Moffett contact: D. Watenpaugh
(415) 604-5747

Headquarters program office: OSSA

Influence of Loading History on Muscle Fiber Cross-Sectional Area

Robert T. Whalen

Rapid metabolic, compositional, and microstructural adaptations occur in muscle fibers subjected to a change in their habitual activity pattern. Although muscle fibers are known to functionally adapt to specific types of activity, little work has been done to model fiber properties as functions of the loading environment. The objective in this study is to formulate a mathematical model that relates muscle fiber cross-sectional area to the daily fiber stress history.

During muscle excitation, the forces and stresses imposed on the contractile elements of fibers act principally along the fiber (see first figure). The model assumes that each muscle contraction imparts a mechanical stimulus to muscle which is proportional (possibly nonlinearly) to the magnitude of the peak cyclic fiber force. The model derivation further assumes that as muscle tissue approaches homeostasis,

the daily cumulative stimulus, S , approaches a constant, tissue-regulated level of stimulus. The cumulative stimulus over the course of a day can be expressed as a sum of the contributions from all the daily loading cycles.

The expression for cross-sectional area is

$$a_x \propto [\sum f_i^\kappa]^{1/\kappa}$$

where a_x is the cross-sectional area, the term inside the brackets is the total daily stimulus from all load cycles, f_i is the peak cyclic force, and κ is an empirical exponent parameter. High values of κ imply that muscle is very sensitive to the level of muscle-fiber mechanical stress.

The following two examples illustrate the characteristics of the model when muscle is exposed to ideal

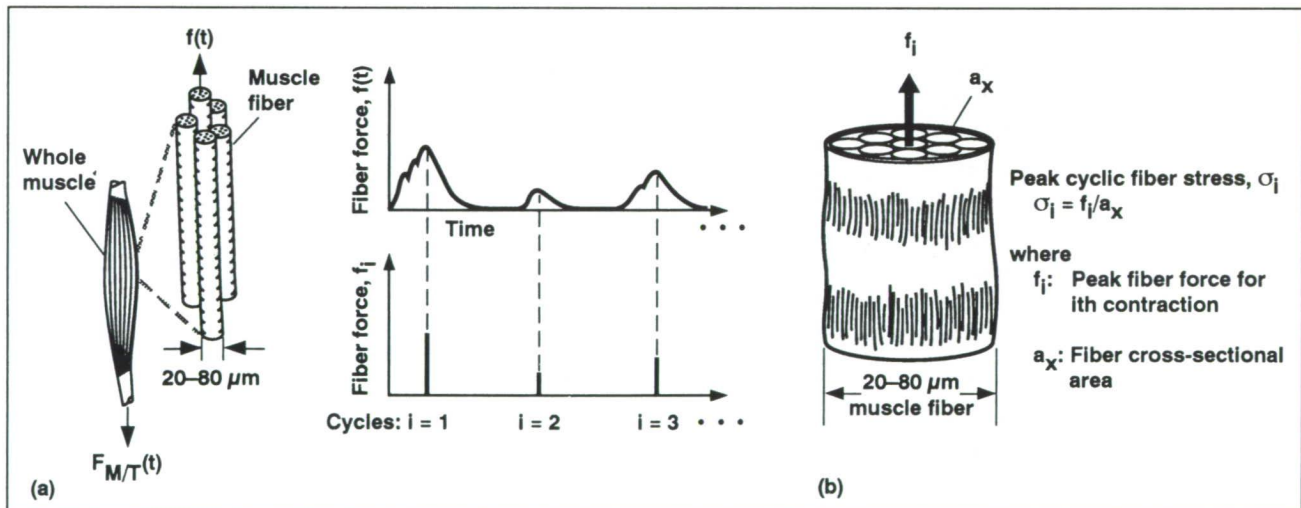


Fig. 1. (a) A typical fiber loading history showing three loading cycles. The model assumes that the peak cyclic force regulates cross-sectional area and therefore muscle mass. (b) The peak cyclic normal component of the muscle fiber stress, σ_i , for the i th cycle is defined as the peak fiber force, f_i , divided by the fiber cross-sectional area, a_x .

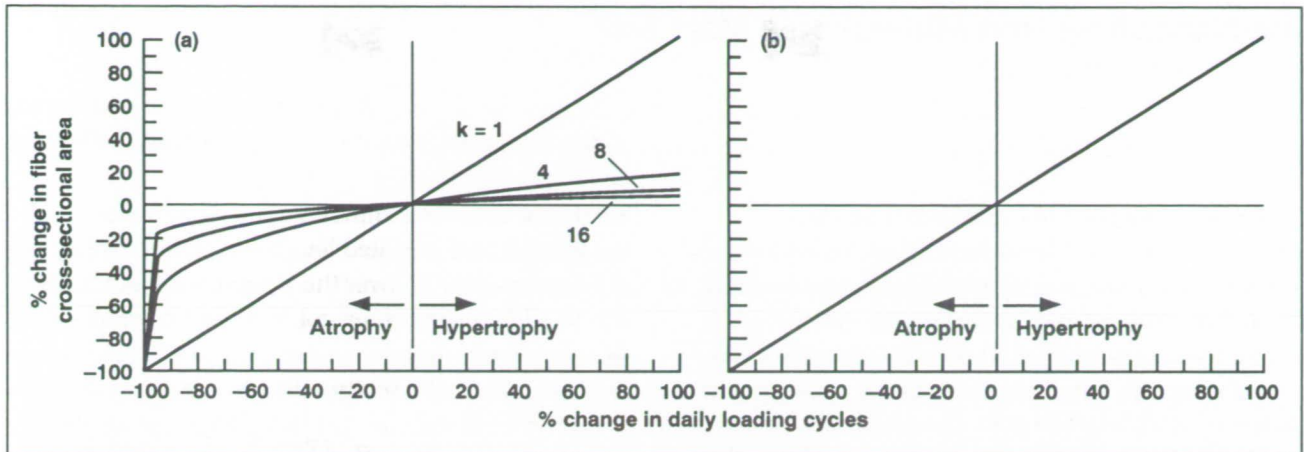


Fig. 2. (a) Predicted changes in fiber cross-sectional area with changes in number of daily loading cycles (fiber force held constant). Curves represent different values of the exponent parameter, κ . (b) Predicted change in fiber cross-sectional area with a change in fiber force (number of daily loading cycles held constant). Note that predicted changes are independent of κ .

loading states. In the first graph in the second figure, the peak cyclic force is held constant and the number of daily loading cycles is allowed to vary. For high values of κ , fiber area is relatively insensitive to the duration of cyclic loading (i.e., number of daily loading cycles) until severe disuse is reached. On the other hand, if the number of loading cycles is held constant, the change in fiber area is independent of κ and directly proportional to the peak cyclic fiber force (second graph).

The model postulates that muscle fibers maintain a tissue-level stimulus by increasing fiber cross-sectional area, which decreases fiber stress, when exposed to increased daily cumulative mechanical stimuli. Conversely, a decrease in fiber area during disuse, e.g., during spaceflight, tends to maintain a tissue-level stimulus by increasing the cyclic fiber

stress. The value of κ determines the characteristics of the model, with higher values of κ consistent with observations of muscle adaptation to various exercise regimens.

We believe that, in order to maintain muscle and bone mass, normal earthbound activity must be replaced with an equivalent form of activity in microgravity. The modeling of musculoskeletal functional adaptation and the quantification of daily physical activity therefore have particular relevance to long-term spaceflight.

Ames-Moffett contact: R. Whalen

(415) 604-3280

Headquarters program office: OSSA

The Nanophase Iron Mineral(s) in Mars Soil

**Amos Banin, Talia Ben-Shlomo,
Leon Margulies, David F. Blake, Andreas U. Gehring**

Evidence suggests that iron-enriched clays, containing nanophase lepidocrocite which crystallizes from more amorphous ferrous and ferric iron hydroxides and double hydroxy phases on the extensive microscopic surfaces of phyllosilicate (smectite clay) minerals, strongly resemble many of the known properties of the Martian soil. These analogs are produced under conditions that may be geologically and chemically realistic on Mars. While much of the oxidized iron in the system remains amorphous, part of it crystallizes as lepidocrocite, an oxyhydroxy iron mineral typically formed on Earth as the result of reoxidation of ferrous iron. Although iron in lepidocrocite is fully oxidized, the formation of this oxyhydroxy mineral is preferred where conditions of limited aeration (low redox) prevail and where ferrous iron is slowly undergoing oxidation, as may well be the case for certain environments on Mars. The reflectance spectra and chemical reactivity of the iron-enriched clays mimic those of the Martian soil.

Mild heat treatment converts the lepidocrocite to maghemite and imparts enough magnetism to cause adherence of the powders to a weak magnet, as was observed for the Martian soil. It should be emphasized that we do not suggest, on the basis of the existing set of observations and measurements, a definite identification of lepidocrocite on Mars. Other iron oxide minerals, particularly nanophase hematite, have been shown to have a similar assemblage of properties, although hematite is not as complete in its compliance with the observed properties of soils on Mars. More detailed data on the mineral nature of the Mars soil are necessary, therefore, to establish unambiguously the identity of the iron oxide mineral(s) present in it. Such data may be forthcoming in the near future from Mars Observer and other missions to Mars.

**Ames-Moffett contact: A. Banin
(415) 604-6631
Headquarters program office: OSSA**

The Satellites of Mars

Jeffrey F. Bell, Fraser Fanale, Dale P. Cruikshank

In a study of the potentials of natural resources in near-Earth space, data on the composition of Mars' two satellites, Phobos and Deimos, have been examined. These bodies are of interest in the context of space resources as possible repositories of naturally occurring water (in the form of subsurface ice) and other materials that may be of use in the crewed exploration of Mars and other planetary bodies in the vicinity of Earth. Infrared spectroscopy indicates that neither satellite has significant amounts of water bound in the minerals of the surface rocks. However, magnetospheric data from the Soviet Phobos-2 spacecraft suggests that the satellites are venting water vapor to space. Theoretical models indicate that an initially icy Phobos could retain ice at depths of 100–1000 meters over the age of the Solar System.

A significant ice component is also suggested by the very low density of Phobos as measured by the Phobos-2 spacecraft. The most likely composition for the satellites is a carbonaceous-chondrite-like assemblage of anhydrous silicates, carbon, organic solids, and ice. This composition suggests that the satellites of Mars were originally formed in the outer asteroid belt and later captured by Mars. Our knowledge of Phobos and Deimos is still inadequate to permit an unambiguous evaluation of their utility as resources.

**Ames-Moffett contact: D. Cruikshank
(415) 604-4244
Headquarters program office: OSSA**

Low-Temperature Phase Changes in Cometary Ice Analogs

David Blake, Lou Allamandola

Comets are thought to be the most primitive objects in the solar system; they contain pristine remnants of the solar nebula and perhaps of the interstellar molecular cloud that preceded it. From remote observations, it is known that cometary bodies contain mostly water ice with varying amounts of other volatiles, rocky materials, and prebiotic organic matter. A knowledge of the phases and components contained within cometary ice will provide insight into extraterrestrial prebiotic organic chemistry, as well as provide ground truth for proposed cometary missions (e.g., the Comet Rendezvous and Asteroid Flyby (CRAF)).

We have been studying ices made from water and small amounts of methanol (CH_3OH) as laboratory analogs of cometary ice. Methanol has been identified in the comae of several comets, and is also thought to be a major component of interstellar ice. When a 2:1 $\text{H}_2\text{O}:\text{CH}_3\text{OH}$ mixture is vapor-deposited onto a thin carbon substrate held at 85 kelvin (K) (-188°C) inside the microscope, an amorphous solid is formed. As the ice is warmed, a phase separation occurs at about 120 K (-153°C) (see first figure). Two components can be identified by electron diffraction. One is a type II clathrate hydrate compound, which consists of crystalline cages of water ice containing methanol as a guest in the structure. The second component is amorphous material, probably excess methanol that would not fit into the clathrate cage structure. As this

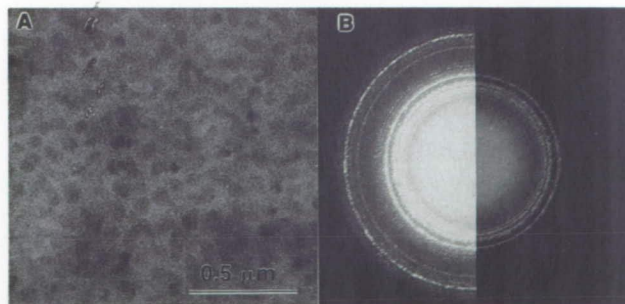


Fig. 1. (a) TEM micrograph of 2:1 $\text{H}_2\text{O}:\text{CH}_3\text{OH}$ ice after phase separation and crystallization of the clathrate hydrate at 120 K. (b) Electron diffraction pattern of the clathrate II hydrate of methanol, obtained from a region similar to that shown in (a).

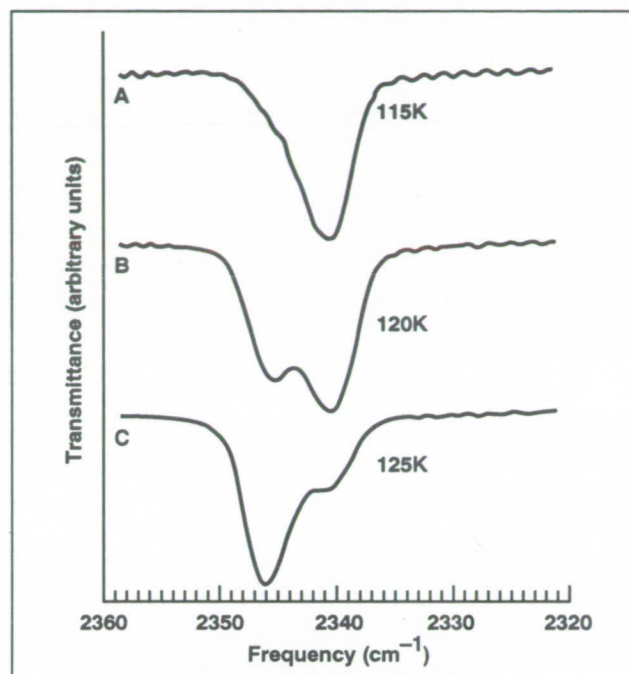


Fig. 2. Infrared vibrational spectrum of CO_2 within a 2:1 water:methanol ice, obtained at (a) 115 K, (b) 120 K, and (c) 125 K.

two-component system is warmed further, the amorphous material sublimates at 145 K (-128°C) and the clathrate II hydrate releases its methanol at about 150 K (-123°C).

These observations of cometary ice analogs may lend insight into the physical and gas-release properties of comets. The initial temperature at which clathrate is formed is lower than that for any previously reported phase transitions for cometary ice analogs. This crystallization event could cause anomalous release of volatiles from the comet nucleus and could also entrap a variety of small molecules. The enclathrated molecules would be retained until the disintegration of the clathrate at temperatures higher than those necessary to maintain the volatiles as pure solid phases.

Infrared (IR) studies of these same ice mixtures show that small shifts in the positions of peaks in the spectra can be used to identify the presence of gas

molecules trapped within clathrate. The second figure shows the shift in the IR spectrum of CO₂ trapped within a water:methanol ice, recorded at temperatures below, at, and above the clathrate crystallization temperature. This discovery opens the possibility that the presence of clathrate hydrates within solar-system

and interstellar ices can be deduced by remote astronomical measurements.

Ames-Moffett contact: D. Blake
(415) 604-4816

Headquarters program office: OSSA

Planetary Lightning

Spacecraft observations of Venus using electric-field detectors have shown the presence of frequent lightning discharges. However, such observations cannot determine the spatial location of the discharges because radio waves can propagate many thousands of kilometers before they are detected. To determine whether volcanism or cloud processes produce the lightning, a two-year search for optical pulses from lightning activity on Venus was conducted using the star sensor on the Pioneer Venus Orbiter. Although a substantial fraction of the night hemisphere was searched, no lightning was detected. After this search was completed, the Galileo spacecraft encountered Venus, and its instruments searched for lightning. Again, the radio-wave instrument found lightning pulses, but no optical pulses from lightning were found. These results imply that the lightning activity is occurring only on the day side where sunlight is available to drive rising plumes of air.

Images from the Voyager 2 spacecraft have been used to map the lightning activity on Jupiter. These images show the presence of 12 intense storms, mostly confined to a narrow latitude band at 49 degrees north. In the figure, bright storms can be seen at 25, 57, 87, and 110 degrees east longitude. However, two storms occur at 13.5 degrees north latitude and in the longitude range of the "disturbed" region. This region is the only one on Jupiter that has strong north/south winds. One of the two storms here appears to be associated with a wave in the wind flow that forces the wind 4400 kilometers to the south. Similar, but much smaller, disturbances occur on Earth when the west-to-east temperate-zone winds

**William J. Borucki, John W. Dyer, Julio A. Magalhaes,
H. Sarma Lakkaraju, Chris P. McKay**

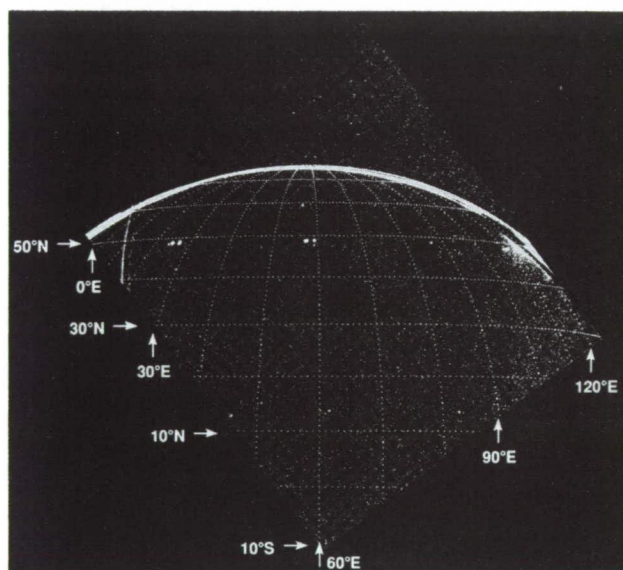


Fig. 1. Lightning storms on Jupiter.

rise over the Rocky Mountains. The implication is that the lightning storms at 13.5 degrees north latitude and the wave on Jupiter indicate the presence of a large obstruction to the flow. Since Jupiter is a fluid planet, the obstruction cannot be solid, but might be a bubble of heated air rising from the hot core of the planet. The heat from the core of Jupiter is generally expected to flow to the polar regions, where the majority of the lightning activity is observed. This distribution of lightning activity is quite different from that on Earth, where most of the activity is in tropical and temperate latitudes. It is hypothesized that the difference is caused by the different sources of energy that power

the thunderstorms on the two planets. On Earth the energy comes from absorbed sunlight in the equatorial regions, whereas on Jupiter the energy comes from the hot core of a fluid planet.

Laboratory simulations of lightning on other planets are needed to determine how to relate the observed optical energy from spacecraft observations of planetary lightning to the total energy released by lightning activity. To attempt to measure the fraction of the total energy that appears as radiation is very dangerous if large electric sparks are produced in atmospheres of hydrogen and methane. Consequently such laboratory work at Ames is conducted by firing laser discharges into small containers of these gases. During the past year, work was carried out to compare the state properties of these laser-induced

plasmas with those of actual lightning discharges. Laboratory measurements showed that temperatures exceeded 17,000 kelvin and the electron concentration reached 7×10^{17} per cubic centimeter, which is similar to, but somewhat lower than, the values reached in a lightning discharge column. However, these values are adequate for making measurements of the optical energy radiated and measuring the amounts of various gases produced in the atmosphere by lightning activity.

Papers discussing these results have been accepted for publication in scientific journals.

Ames-Moffett contact: W. Borucki
(415) 604-6492
Headquarters program office: OSSA (SLC)

Search for Lightning on Neptune

William J. Borucki, Phan Pham

During the Voyager 2 spacecraft encounter with Neptune, the radio-wave instrument detected the presence of "whistlers," which are low-frequency radio waves that sound like the whistle of a descending projectile. Such waves are caused by a strong pulse of lightning-generated radio waves that are propagating along magnetic-field lines many tens of thousands of kilometers above the planet's atmosphere. Because lightning was predicted to occur on Neptune, approximately 400 images of the night side were taken by the imager to determine the optical energy, spatial distribution, and frequency of lightning flashes. Since the images were obtained at a large distance from Neptune, and since the lightning is expected to occur beneath the upper layer of clouds, it is expected that the images of the lightning discharges will be dim. Furthermore, galactic cosmic rays, sunlight scattered from the atmosphere, and other processes cause spurious signals in the images. During the last year, computer programs have been written that search each of the images for the presence of lightning events; spurious events are recog-

nized and rejected. A substantial portion of the southern hemisphere has now been searched without any events being found.

Day-side images of Neptune showed an almost featureless uniform cloud layer; however, both a large, dark oval with bright clouds occurring along its perimeter and a small, bright, rapidly moving cloud at high southern latitudes were observed. Because cloud features cannot be seen on the night side, it is not yet known whether any of these features were present in the field of view when the images were obtained. Further work must be done to locate these features at the appropriate times. Preliminary results are expected to be ready for presentation at the Neptune-Triton Conference in January 1992. A final report with data from more of the surface of Neptune should be completed later in the year.

Ames-Moffett contact: W. Borucki
(415) 604-6492
Headquarters program office: OSSA (SLC)

Two-Dimensional Infrared Array Cameras

Jesse D. Bregman, David M. Rank

Recent advances in infrared-detector technology have resulted in the availability of large-format two-dimensional arrays. In particular, Amber Engineering in Goleta, California, has developed 128- × 128- and 256- × 256-pixel multiplexers, with each pixel capable of storing a relatively large amount of charge (a few tens of millions of electrons). The multiplexers were able to bond detector materials responsive in the 1–5.5-micrometer (indium antimonide, InSb) and 3–18-micrometer (gallium-doped silicon, Si:Ga) spectral regions, and these are potentially powerful devices for ground-based astronomy. As a first step in evaluating and exploiting these arrays, we constructed and operated two cameras, both of which use 128- × 128-pixel arrays. One camera had an InSb array and the other an Si:Ga array. This arrangement has enabled us to optimize the two cameras for use in their respective wavelength ranges (1–5.5 micrometers for the InSb array and 8–14 micrometers for the Si:Ga array).

The InSb camera was first used in January, 1991, only five months after delivery of the array. The initial

tests showed some promise, so development of the camera was pursued. In addition, an Si:Ga array was borrowed from Amber Engineering in May, 1991, and a camera using that array was constructed. By the summer, both cameras were operating as well as any in existence and the first scientific results were delivered by the InSb camera when we measured extended molecular emission from a source known as IRAS 21282+5050, a young planetary nebula.

Narrow-band infrared filters have been added to both cameras to allow us to isolate specific emission bands. We expect to image many objects in both the 3–4- and 8–14-micrometer regions to study the relative distributions of molecular emissions. A polarimeter was added in the summer, and test observations were made of the Orion nebula region.

Ames-Moffett contact: J. Bregman

(415) 604-6136

Headquarters program office: OSSA

Research on the Origins of Chondrule Dust Rims

Ted Bunch

Fine-grained, dusty rims on chondrules are post-chondrule-formation structures that have been linked by some researchers to dust accretion in the nebula. Other investigators favor a planetary origin (transient atm ablation/regolith penetration). Little work has been done toward gaining clearer insight into rim origin. A multidisciplinary team (University of Tel Aviv: M. Podolak, D. Prialnik; Brown University: P. Schultz) was formed in order to apply observational, experimental, and theoretical techniques to the problem.

To gain a clearer perspective on the origin(s) of rims, a number of first-order questions are being systematically addressed: (1) What are the plausible processes responsible for isotopic differences between rims and host chondrule? (2) What is the source of iron (Fe)-enrichment and other compositional differences of rims? (3) What is the significance of rim thickness to chondrule size, and the occurrence of coarse-grained rims to the formational mechanism? (4) What was the degree of rim heating? (5) What role did pro- and/or retrograde metamorphism play in the observed characteristics? (6) If rims formed by nebular processes alone, were modifications made by parent body processing (ablation, regolith impact)? (7) What is the relationship between opaque matrix and opaque rims?

Some of our observations on chondritic meteorites are consistent with a heating/melting origin event for rim formation. Textures of opaque matrix and rims are similar to each other: porous to compact, fine-grained (<0.002 millimeter) assemblages of anhedral grains that have diffuse grain contacts suggestive of similar thermal/mechanical histories. Terrestrial ablation rinds on two of the chondrites are also similar in some textures, phase contents, and compositions compared to opaque matrices and rims. In addition, very Fe-rich olivine, present as crystals in the ablation rinds, contains large amounts of chromium, sodium, aluminum, titanium, phosphorus,

sulfur, nickel, and calcium, similar to Fe-olivine found in Allende rim and matrix olivine and in chondritic meteorite rim olivine. Textures in some rims appear to show sintering or melt/reaction relationships with the host chondrule. Fe, silicon (Si), and magnesium (Mg) contents of opaque matrices and rims when projected onto the Fe-Si-Mg ternary diagram are confined within the field predicted for the crystallization of a rock melt. A computer code is being used to model the thermal histories of chondrules as they pass through a gas/dust medium. Results show that chondrules with a radius of greater than 0.2 centimeter (cm) and a thermal conductivity of 2×10^4 ergs/kelvin cm, passing through a transient atm (scale height = 37 kilometers (km) and surface pressure = 1.53×10^3 dynes/cm²) will begin to melt at velocities (v) greater than 3 km/second (km/s) and will not reach total melting before they are stopped. Chondrules smaller than 0.05 cm will not melt at v less than 3 km/s, but will totally melt at v greater than 4 km/s which indicates a narrow survival window for smaller particles under these parameters. Finally, vertical gun experimental testing is being conducted by launching olivine/enstatite projectiles (at v = 2–6 km/s) into dusty atmospheres (to test ablation melting) and into low density targets (to test regolith penetration processing). Whether or not rims are formed by parent body processes, the possibility remains for thermal and/or mechanical processing of objects with accretion velocities of 1–4 km/s.

Three publications have resulted from these team efforts in the last two years and three more are in preparation.

Ames-Moffett contact: T. Bunch

(415) 604-5909

Headquarters program office: OSSA

Molecule Formation in Star-Forming Regions

Steven B. Charnley, Alexander G. G. M. Tielens

Hot molecular cores are high-temperature (150–300 kelvin), dense clumps of gas and dust that may represent a state of the interstellar medium that is common to regions of massive star formation. Observations of several star-forming regions (e.g., Sgr B2, W51, and OMC-1) demonstrate that hot-core chemistry is extremely rich and also that strong chemical differentiation can exist between individual cores. Two well-studied sources are the Hot Core and Compact Ridge components of Orion (Orion A); it is believed that in these regions, molecular ice mantles have recently been evaporated from warm dust grains. The molecular composition of the Hot Core is typified by large quantities of fully saturated molecules such as water, ammonia, methane, and hydrogen sulfide; deuterated species; and large quantities of acetylene (C_2H_2), hydrogen cyanide (HCN), isocyanic acid (HNCO), methyl cyanide (CH_3CN), vinyl cyanide (CH_2CHCN), and ethyl cyanide (CH_3CH_2CN). The chemistry of the Hot Core is markedly different from that found in cold molecular clouds, and also from that observed in nearby sources within Orion A. The Compact Ridge, by contrast, appears to be typified by large quantities of methanol and other large oxygen-bearing molecules such as methyl formate ($HCOOCH_3$), dimethyl ether (CH_3OCH_3), ketene (CH_2CO), formic acid ($HCOOH$), acetaldehyde (CH_3CHO), formaldehyde, and ethanol, as well as some of the simpler species that are also found in the Hot Core.

Many of the above compounds are observed to be present in large quantities only in hot cores; the reason for these remarkable differences in chemical composition is an outstanding problem in theoretical

astrochemistry. Its resolution would lead to a better understanding of dust-grain surface chemistry and of molecule formation in star-forming regions.

Infrared observations and theoretical calculations indicate that interstellar ices appear to consist mainly of simple molecules. Therefore, we have modeled the chemistry that results after the evaporation of ice mantles that contain various proportions of the composition $H_2O/NH_3/CH_4/CO/HCN/HNC/C_2H_2/CH_3OH/H_2CO/C_2H_4/C_2H_6/O_2/N_2$ into gas with physical characteristics similar to those found in the Orion cores. The figure shows the evolution of molecular abundances in models of the Hot Core and the Compact Ridge.

Employing plausible mantle compositions which are constrained by observations, we have been able to account for the differentiation observed between the Orion hot cores: ice mantles with large amounts of ammonia and little methanol can explain the Hot Core composition, whereas methanol-rich mantles must account for that of the Compact Ridge. Ammonia can drive a reaction sequence that can plausibly reproduce the observed abundances of nitrogen-bearing molecules such as the simple nitriles. Methanol is essential for the formation of $HCOOCH_3$ and CH_3OCH_3 , whereas ethene and ethane are necessary mantle precursors for CH_2CO and CH_3CHO .

Abundances of compounds in the Hot Core are determined by an active gas phase chemistry that is driven by the evaporation of the products of dust-grain surface chemistry. We have been able, for the first time, to account for the large abundances of complex oxygen-bearing organic molecules observed

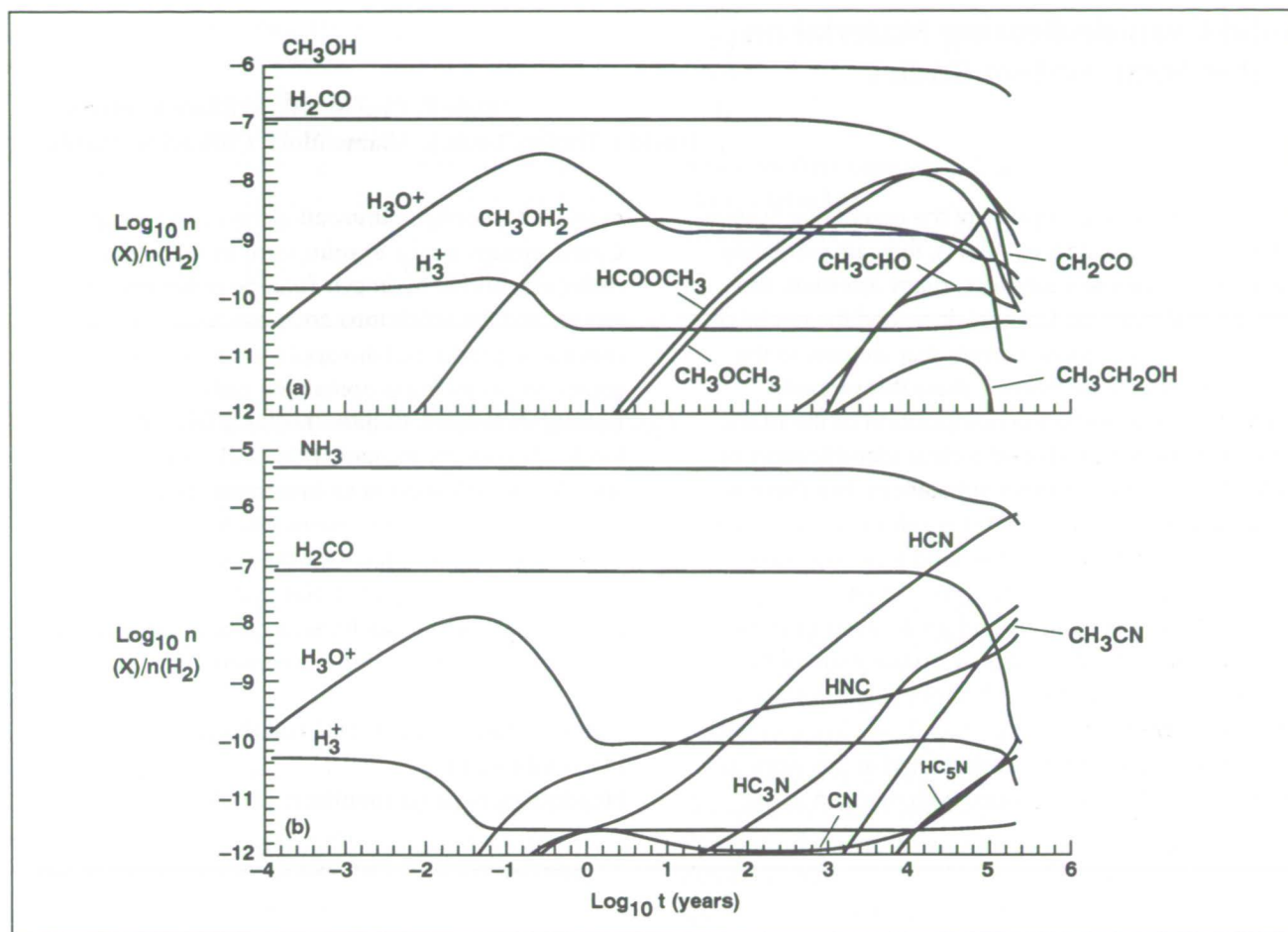


Fig. 1. Molecular abundances as a function of time after the evaporation of (a) methanol-rich ice mantles and (b) ammonia-rich ice mantles.

in the Compact Ridge. Contrary to previous speculations, these species do not appear to require formation on grain surfaces. This work suggests that gas-phase observations of hot cores may be used to infer the original composition of ice mantles and the molecular chemistry that occurs in them.

Ames-Moffett contact: S. Charnley

(415) 604-5910

Headquarters program office: OSSA

Hydrocarbons Produced in the Hydrothermal Aquifers of Yellowstone National Park

David J. Des Marais

Hydrothermal systems are receiving attention from exobiologists because of their possible role in the origin and early evolution of life and also because they may have harbored life on Mars. The capacity of hydrothermal systems to produce organic matter is an important aspect of this role. Yellowstone National Park contains an extensive, well documented hydrothermal system which emanates light hydrocarbon gases from its numerous springs and fumaroles. Accordingly, an attempt was made to understand the origin of these gases.

The abundances of the higher hydrocarbons relative to methane are far in excess of those expected for a mixture at thermodynamic equilibrium (see first figure). At equilibrium, $\log([\text{ethane}]/[\text{methane}])$ is

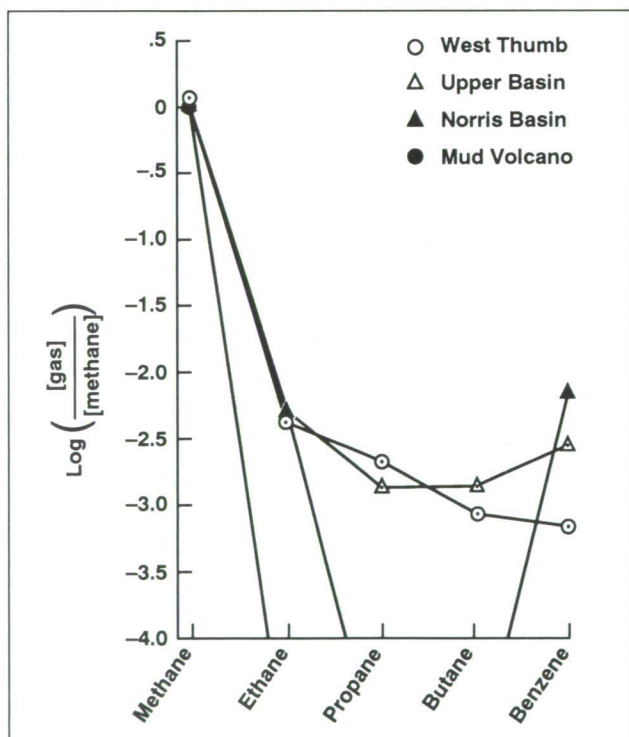


Fig. 1. Abundances of various hydrocarbons relative to methane. Maximum approximate subsurface temperatures for these sites are as follows: West Thumb 210 °C, Upper Basin 250 °C, Norris Basin 270 °C, and Mud Volcano > 300 °C. Note that higher hydrocarbons generally become less abundant at higher temperatures.

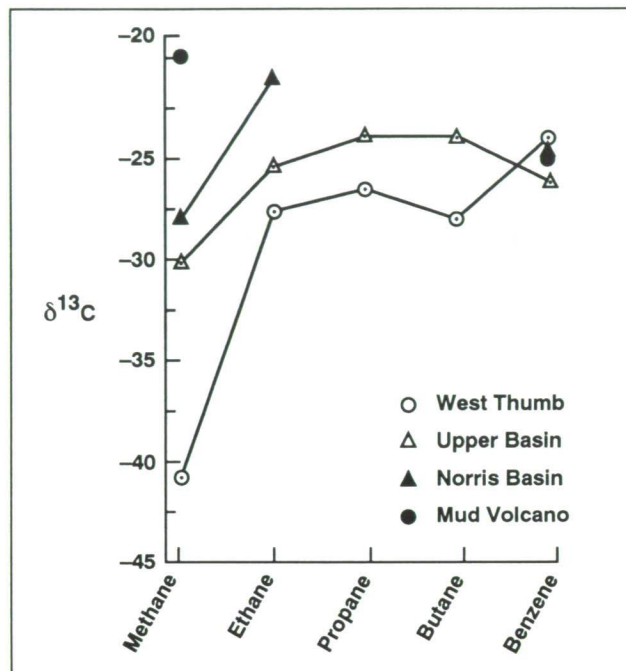


Fig. 2. Carbon isotopic composition of various hydrocarbons. Note that hydrocarbons have greater $\delta^{13}\text{C}$ values (see text footnote for definition of $\delta^{13}\text{C}$) at greater subsurface temperatures, because of the selective thermal decomposition of ^{12}C -enriched molecules.

about -6; larger hydrocarbons are much less abundant than ethane. Therefore, the patterns of abundance and the carbon isotopic composition of these gases (second figure) reflect the kinetic characteristics of the processes by which the compounds are synthesized and destroyed. The $^{13}\text{C}/^{12}\text{C}$ values (measured as $\delta^{13}\text{C}$)* of the hydrocarbons generally increase with increasing molecular weight. This trend shows that these gases are produced by the thermocatalytic decomposition of larger organic compounds, including insoluble organic residues. Hydrocarbon mixtures produced from hotter environments typically have higher $^{13}\text{C}/^{12}\text{C}$ values as well as simpler suites of compounds, whose abundances reflect the relative thermal stabilities of the molecules. The hydrocarbons

* $\delta^{13}\text{C} = (((^{13}\text{C}/^{12}\text{C}) \text{ sample} / (^{13}\text{C}/^{12}\text{C}) \text{ standard}) - 1)1000$

apparently are mixtures of gases produced from a variety of depths and temperatures. At very high temperatures, at which the organic matter of sedimentary origin is highly degraded, a likely gas mixture would include carbon dioxide, nitrogen, ^{13}C -enriched methane, and hydrogen.

Most of the hydrocarbons observed in Yellowstone springs and fumaroles are derived from preexisting sedimentary organic matter of biological origin which has been thermally degraded. Some methane might have a truly abiotic source through reactions involving carbon dioxide, hydrogen, and

water. Hydrothermal systems in continental environments apparently cannot escape the ubiquity of biological organic matter, which has found its way into the Earth's crustal sediments over billions of years. The potential for hydrothermal systems to create organic matter abiotically must be assessed at least in part by carefully controlled laboratory studies.

**Ames-Moffett contact: D. Des Marais
(415) 604-3220**

Headquarters program office: OSSA

Planetary Protection and the Mars Environmental Survey Mission

Donald L. DeVincenzi

The search for evidence of extant or extinct life on Mars, or for evidence of organic chemical evolution, remains a scientific objective for future Mars exploration missions. In order to preserve the scientific integrity of experiments addressing this objective, Mars lander spacecraft will have to be designed to comply with planetary protection provisions as specified in existing international policy. Planetary protection (PP) refers to the prevention of biological cross-contamination of planets by spacecraft-borne microbes during planetary exploration missions. Because such provisions could affect mission design, cost, and complexity, it was important to assess the impact of possible PP controls on the Mars Environmental Survey (MESUR) mission being developed at Ames Research Center.

Three PP implementation scenarios for the MESUR mission were examined in collaboration with Robert Howell of the Bionetics Corporation:

1. If current policy is strictly interpreted, it is likely that active bioload reduction of hardware by heat treatment would be required to meet existing specifications. Previous experience with such procedures on Mars landers (e. g., Viking) was reviewed and documented. In spite of differences in the missions and spacecraft, it was determined that many of the same procedures employed on earlier missions would be

required for MESUR, including contamination control of spacecraft parts, lander bioload reduction by heat, encapsulation in a bioshield, trajectory biasing, and limits on orbiter lifetime.

2. Bioload-reduction methods that use techniques other than heat were reviewed and analyzed for their effectiveness for the MESUR spacecraft. It was concluded that if the PP requirements are not relaxed, then heat treatment, with its known negative effects on spacecraft components, is probably the only technique capable of achieving the necessary bioload reductions specified by the existing policy.

3. Analyses were also conducted to determine how the requirement for active bioload reduction varied with variations in the input parameters and factors.

PP implementations that involve careful cleaning and maintenance of cleanliness, but not heat treatment, were developed for MESUR, and implications for the mission design were analyzed. Parallel analyses of key parameters in light of new data from Mars and new data on terrestrial microbes were also conducted. The net result of these studies suggests that less severe cleaning techniques could be effective. Additional analyses conducted in collaboration with Harold P. Klein suggested that there were, in fact, sound arguments for such a relaxation in

Solving a Coupled Schrödinger Equation for the $X^2\Pi$ State of OH

David Goorvitch, David C. Galant

We have applied extrapolation to the limit in a finite-difference method to solve a system of coupled Schrödinger equations. This combination results in a method that requires knowledge only of the potential energy functions for the system. This numerical procedure has several distinct advantages over the more conventional methods, such as Numerov's method or the method of finite differences without extrapolation. These advantages are (1) initial guesses for the term values are not needed; (2) no assumptions need be made about the behavior of the wavefunctions such as the slope or magnitude in the nonclassical region; (3) the algorithm is easy to implement, has a firm mathematical foundation, and provides error estimates; (4) the method is less sensitive to round-off error than other methods because a small number of mesh points is used; and (5) it can be implemented on small computers.

Coupled differential equations arising in bound-state problems in quantum mechanics have been solved by using three general schemes. The schemes are (1) the construction of piecewise continuous wavefunctions, (2) the use of an appropriate set of complete basis functions, and (3) the use of a finite-difference method. The first scheme involves subdivision of the radial axis into a number of subintervals, and construction of piecewise continuous wavefunctions. The wavefunctions at the extreme points of the interval are of the Wentzel–Kramers–Brillouin form. The amplitude and slope of the wavefunction is matched at the left and right boundaries of each subinterval. A renormalized Numerov method is used to keep the wavefunctions from overflowing. In the second method, use is made of a solution of the uncoupled problem for the complete basis functions of the coupled problem. The number of basis functions needed to describe the coupled wavefunctions depends upon the magnitude of the coupling interaction. The problem is then reduced to that of solving a large number of algebraic equations.

The third method requires the solution of the coupled case as a finite-difference problem. This third method is very easy to set up and the only information needed is the form of the potential function. The third method is tempting to use, because we do not have to make any assumptions about the a priori form of the wavefunction at the end points of integration, nor do we have to match the amplitude and slope at a large number of subintervals. However, the finite-difference method leads to a rather large $2L + 1$ banded matrix of order $2N$, where N is the number of mesh points and L is the number of coupled equations. This matrix is very sparse, having a band width of L . Solving a $2L + 1$ banded matrix does not present any real problem because of available matrix routines that rotate a symmetric banded matrix to tridiagonal form and then solve it using well known standard techniques.

The $X^2\Pi$ ground state of OH is well known to exhibit large rotational–vibrational coupling, with the result that the transition intensities are highly irregular. This effect on the transition intensities, first applied to HCl, used perturbation theory. Unfortunately, the rotational–vibrational coupling in OH is too large to be well described by the perturbation approach.

We have solved the coupled Schrödinger equation for the $X^2\Pi$ state of OH. Our algorithm results in term values that agree with experimentally derived values within 6 parts in 10^4 . The calculated wavefunctions are compared indirectly through experimentally derived rotational constants and are found to be accurate to better than 3 parts in 10^3 . A comparison of our method with another numerical method shows results that agree within one part in 10^4 .

Ames-Moffett contact: D. Goorvitch
(415) 604-5502
Headquarters program office: OSSA

Water on Mars

Robert M. Haberle

The spacecraft missions of the 1960s and 70s revealed the presence of water in the Martian atmosphere. On the average, the Martian atmosphere holds the equivalent of about 1 cubic kilometer of ice. However, this amount varies with season by about a factor of two. This seasonal fluctuation indicates that there are surface sources and sinks for atmospheric water, and that Mars has a hydrologic cycle. The central issue concerning this hydrologic cycle is the nature and distribution of the surface reservoirs. For example, is the observed variability of atmospheric water due to exchange with surface ice deposits in the polar regions? Or is it the result of water being driven into and out of the soil? Or, perhaps, are there subsurface deposits of ice—such as permafrost—that participate?

The answers to these questions have profound implications for the current climate of Mars. This is because water is a volatile substance and is therefore sensitive to temperature and wind. Unfortunately, direct measurements at the surface of Mars will not be made for many years. Therefore, we must rely on models. Hydrologic-cycle models must faithfully represent those processes that are crucial to the behavior of water. At the surface, these are the sublimation and condensation of ice, the diffusion of water vapor into and out of the soil, and the adsorption and desorption of water onto soil particles and grains. In the atmosphere, the processes are mixing by turbulence within the boundary layer, horizontal and vertical transport by winds, and cloud formation and precipitation. During 1991, we have built two models that address, in isolation, some of these processes.

The first model focuses on the vertical exchange of water between the surface and the atmosphere. It includes the processes important for simulating the behavior of water at and within the surface, as well its mixing within the boundary layer. The model has been used to study the importance of the large variation in daily temperatures on Mars and how that variation affects the movement of water between the atmosphere and the soil. It was found that in spite of

the large daily temperature variation, there is only a small daily variation in the amount of water exchanged between the atmosphere and the regolith. There are several reasons for this. First, for typical Mars soils, the effect of the large daily surface-temperature variations penetrates only a few centimeters. This limits the amount of water available for exchange. Second, the surface and the atmosphere equilibrate rapidly, and the presence of water in the atmosphere limits the surface flux proportionately.

The second model focuses on the horizontal and vertical transport of water by winds. The model simulates the global wind system by solving conservation equations. However, before carrying out full-scale transport calculations, we have tested the model's performance against available data to be sure its results can be trusted. In this respect we have emphasized the two most important components of the circulation: the low-latitude, zonally symmetric "Hadley" circulation, and the mid-latitude "weather" systems of migrating high- and low-pressure systems. To the extent that these components are known on Mars, the model seems to be performing well. The strength and latitudinal extent of the Hadley circulation simulated by the model correlates well with data and with other models, and the number and speed of the traveling weather systems it simulates is in good agreement with those inferred from measurements made by the Viking landers. The most remarkable aspect of these simulations, however, is that they are performed with an extremely simplified representation of heating and friction. This minimizes computer time and facilitates long-term (yearly) simulations. Next year, we plan to carry out annual simulations to determine if there are any net annual sources or sinks for atmospheric water. This will help to identify interesting regions on Mars for future study.

**Ames-Moffett contact: R. Haberle
(415) 604-5491**

Headquarters program office: OSSA

On the Origin of the Nitrate Reductase from *Halobacterium Denitrificans*

Lawrence I. Hochstein, Frank Lang

We previously proposed that the reduction of nitrate to dinitrogen (denitrification) is an energy-yielding respiratory process that preceded oxygen respiration. We hypothesized that if denitrification were primitive, the denitrification enzymes in Archaeobacteria should be more primitive than in the Eubacteria. Earlier, we demonstrated denitrification in the Archaeobacterium *Halobacterium denitrificans*, an organism we isolated from a local saltern. We have isolated and characterized the first enzyme in the process, the nitrate reductase, from this organism. The enzyme is identical to eubacterial nitrate reductases and, even more remarkable, it exhibits the property

that is most characteristic of halobacterial enzymes: it exhibits no salt-dependent properties. In fact, it is inhibited by salt. These results suggest that this enzyme arose via a lateral gene transfer from a non-archaeobacterial organism, and imply that nitrate respiration may not be a primitive process. The assumption that Archaeobacteria can be relied on as reservoirs of primitive information may be questionable.

Ames-Moffett contact: L. Hochstein
(415) 604-5938
Headquarters program office: OSSA

The Relationship of Halobacterial ATPases to ATP Synthases and Vacuolar ATPases

Lawrence I. Hochstein, Helga Stan-Lotter

The ATPase from *Halobacterium saccharovorum* is inhibited by nitrate and N-ethylmaleimide, both specific inhibitors of vacuolar ATPases. The presence of ATP or ADP reduces N-ethylmaleimide inhibition, which suggests that the inhibitor acts at or near the active site. When the enzyme is incubated with [¹⁴C]-N-ethylmaleimide, the bulk of radioactivity is associated with subunit I, and ATP or ADP also reduce incorporation of the inhibitor. No charge shift of subunit I was detected after labeling with N-ethylmaleimide, indicating an electroneutral reaction; this is consistent with the selective modification of sulfhydryl groups in subunit I at or near the

catalytic site. Antiserum against subunit A, which is the catalytic subunit of the *Neurospora* vacuolar ATPase, reacts with subunit I from the ATPase of *Halobacterium saccharovorum*. This confirms our previous assertions that the enzyme from *Halobacterium saccharovorum* is a vacuolar type of enzyme.

Ames-Moffett contact: L. Hochstein
(415) 604-5938
Headquarters program office: OSSA

Center for Star Formation

David Hollenbach, Patrick Cassen

The Center for Star Formation Studies, a consortium of scientists from the Space Science Division at Ames and the Astronomy Departments of the University of California at Berkeley and Santa Cruz, conducts a coordinated program of theoretical research on star and planet formation. The Center, under the directorship of D. Hollenbach, supports postdoctoral fellows, senior visitors, and students; meets regularly at Ames to exchange ideas and to present informal seminars on current research; hosts visits by outside scientists; and conducts a week-long workshop on selected aspects of star formation each summer.

The Star Formation Summer Workshop of 1991 was held at the University of California at Santa Cruz; it included, in addition to the Center scientists, about 50 astrophysicists from all over the world. The topics discussed included protostars and disks, disks and low-mass companions, flows near young stellar objects, high-mass star formation, and the interaction of massive protostars with their environment.

In 1991, research in the Center included studies of both low- and high-mass star formation, as well as studies of the interaction of high-mass stars with the protostellar environment. In this context, low-mass stars are those whose mass is less than about 10 times that of the sun. The distinguishing feature between low- and high-mass star formation is that high-mass stars are much more luminous, and the radiation pressure and ionizing flux of photons from high-mass stars have significant dynamical effects on the collapsing clouds and the protoplanetary disks orbiting the stars.

Work on low-mass star formation centered on (1) the evolution of the protoplanetary disk, which forms and evolves as the gravitationally collapsing interstellar cloud spirals into the protostar, and (2) the origin and consequences of the energetic protostellar winds, which have been a major observational discovery of the past decade. We have modeled the passage of the infalling gas and dust through the shock wave that marks the boundary between the infalling material and the protoplanetary disk. The processing of dust through the accretion shock plays an important role in the final composition of the

planets and the comets that form in the disk. We have also studied the dynamics of the material in the disk, and have determined how turbulent viscosity may arise which leads to the spiraling of the disk material onto the protostar and the transport of angular momentum outward.

Not all of the disk material, however, spirals onto the protostar. Some is dispersed back into the interstellar medium, some is incorporated into planets or companion stars (binary systems), and some is accelerated by magnetic fields near the protostar to form a massive protostellar wind. We have shown that roughly half of the spiraling material near the protostar is incorporated into the protostellar wind, which is largely neutral and emerges perpendicular to the disk at speeds of about 100 kilometers per second. Up to a solar mass of material can be expelled into the star-forming cloud by this mechanism, and the momentum input may help to support clouds from rapid collapse into stars.

Work on high-mass star formation has focused in the past year on the dispersal of the protoplanetary disks around these stars by the effect of the strong ultraviolet radiation field produced by the stars. This radiation field ionizes and heats the surfaces of these orbiting disks to temperatures of about 10,000 kelvin. The outer parts of the disks then evaporate to the interstellar medium, producing ionized outflows with speeds of 10–50 kilometers per second. We have proposed that these outflows may be observed at radio and infrared wavelengths, and may explain the frequency with which dense, compact, ionized regions are observed around massive stars. The interaction of these and higher-velocity outflows from massive stars have a profound effect on their environment. We have shown that the shock waves produced in the flows naturally produce water masers, a phenomenon long observed to be correlated with massive star formation.

**Ames-Moffett contact: D. Hollenbach
(415) 604-4164**

Headquarters program office: OSSA

Prokaryotic Membrane Evolution

Linda L. Jahnke, Helga Stan-Lotter, Lawrence I. Hochstein

Methane-oxidizing bacteria (methanotrophs) are known to synthesize two types of cyclic triterpenes—hopanoids and sterols—in relatively large amounts. Both compounds are synthesized by the same biochemical pathway; however, sterols are thought to be more highly evolved because their synthesis requires additional steps involving enzymes that need oxygen. Hopanoids are normally found only in prokaryotes, whereas sterols are normally found only in eukaryotes. Although both molecules have been proposed as membrane stabilizers, their true function and the nature of this evolutionary transition is not clearly understood. As a first attempt to understand the function of these lipid molecules in bacterial membranes, we have isolated and characterized two membrane types from a methanotrophic bacterium, *Methylococcus capsulatus*.

The structure of a gram-negative bacterial cell consists of a cytoplasmic membrane surrounded by a rigid cell wall (murein layer) and an outer membrane. Electron micrographs reveal that *M. capsulatus* has such a cell structure. In addition, however, this bacterium has a complex internal membrane system thought to be involved in energy production. There was the possibility that the sterols and/or the

hopanoids would be specifically associated with one or another of these membrane types. After rupturing the cells, we were able to separate the cell membranes by using sucrose density gradients. This technique takes advantage of differences in membrane density to essentially float the membranes apart.

Chemical characterization of the isolated membranes demonstrated that both the hopanoids and the sterols are associated with the outer membrane in this bacterium. Our analyses also demonstrated that methanotrophs contain small amounts of another membrane lipid, lipopolysaccharide, which in most bacteria composes the entire outer leaflet of the outer membrane bilayer. The presence of lipopolysaccharide in the outer cell envelope is thought to provide the cell with a hydrophobic barrier. Our findings suggest that the hopanoids and sterols may have evolved to serve a similar function in the methanotrophic bacteria.

Ames-Moffett contact: L. Jahnke
(415) 604-3221

Headquarters program office: OSSA

Modulated-Voltage Microvolume Metastable Ionization Detector for Gas Chromatography

Daniel R. Kojiro, Norishige Takeuchi, Donald E. Humphry

Flight experiments on board the Viking mission to Mars and Pioneer Venus conducted successful analyses using gas chromatographs (GC) with thermal conductivity detectors (TCD). Future missions require analytical instrumentation with more sensitivity and greater sample identification capabilities that can operate with extremely limited resources. The detection and identification of a multitude of chemical species over several concentration ranges is often a primary requirement. The Cometary Ice and Dust Experiment (CIDEX), set to fly on the Comet Rendezvous and Asteroid Flyby Mission, employs metastable ionization detectors (MID) an order of magnitude smaller, yet with three orders of magnitude greater sensitivity, than the earlier flight TCDs. The CIDEX MIDs have an internal volume of 180 microliters (μl) and use a voltage modulator which expands the MID response range from three orders of magnitude to over six orders of magnitude. The CIDEX MID can detect and measure sample component concentrations ranging from a few parts per billion (ppb) to over 1000 parts per million (ppm) in one analysis.

In order to further conserve resources, a microvolume version of the MID (μMID), with an internal volume of 15 μl , is now under development. The small internal volume allows the μMID to operate at very low carrier-gas flow rates, thus minimizing the amount of carrier gas that must be provided for any given analysis or mission. This aspect of the μMID makes it particularly attractive for use with carrier-gas flow rates of below a few milliliters per minute (ml/min), which are commonly used with capillary columns. Often, conventional GC detectors must employ a make-up gas flow to obtain optimal operation with capillary columns.

This μMID has already demonstrated capabilities similar to the CIDEX MIDs at carrier flow rates below 2 ml/min. To demonstrate the sensitivity of the μMID and its compatibility with the voltage modulator, a gas mixture containing air, methane (CH_4), and carbon dioxide (CO_2) was analyzed using a voltage-modulated μMID and a newly developed in situ polymerized capillary column with a carrier-gas flow rate of 1.9 ml/min. The concentration of CH_4 is 60 ppb and

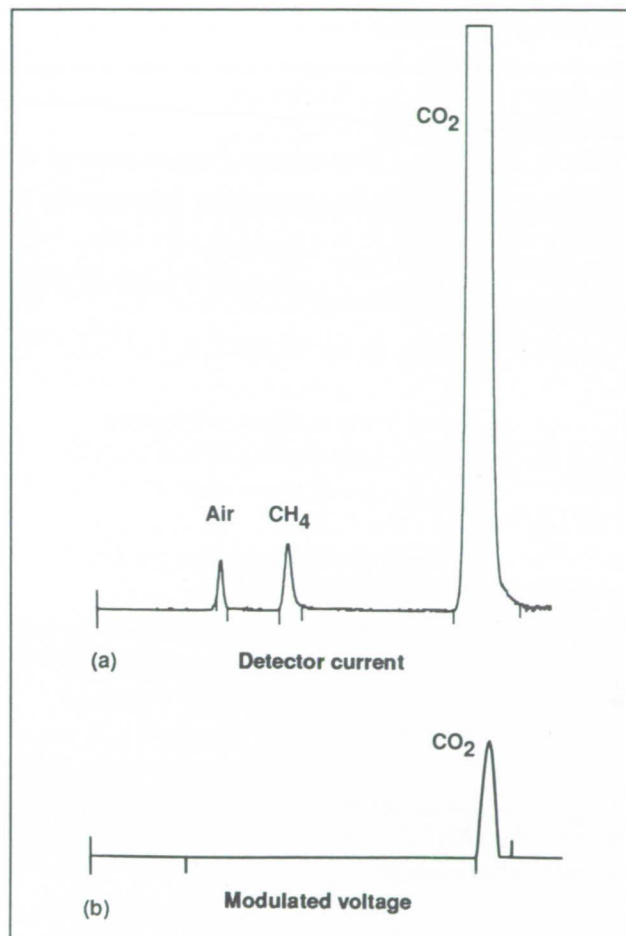


Fig. 1. Modulated-voltage μMID analysis of CH_4 and CO_2 in helium. Concentrations are given in text.

that of air is approximately 80 ppb. The figure shows the resultant detector current and modulated-voltage chromatograms which demonstrate the sensitivity of the μMID under these conditions and its compatibility with the experimental column. The CO_2 concentration is 267 ppm and produces a saturated peak in the current chromatogram (first graph). However, the modulated-voltage chromatogram (second graph) produces an easily measured peak, thus demonstrating the compatibility of the μMID with the voltage modulator.

Combining the μ MID with the voltage modulator and in situ polymerized columns produces a GC capable of analyzing gas mixtures with sample component concentrations ranging from a few ppb to over 1000 ppm, using carrier-gas flow rates below 2 ml/min.

Ames-Moffett contact: D. Kojiro
(415) 604-5364
Headquarters program office: OSSA

Space Shuttle Glovebox Experiment for Testing Particle-Dispersion Methods

J. R. Marshall

In mid-1992, the Space Shuttle Columbia will carry the first U.S. Microgravity Laboratory, USML-1, into Earth orbit. The many facilities within this laboratory include a glovebox experiment module which will serve 16 individual experiments. In one of these experiments—the Particle Dispersion Experiment (PDE)—methods of dispersing fine sand-size particles in microgravity will be investigated in preparation for experiments planned for Space Station Freedom in the Gas Grain Simulation Facility (GGSF). The interaction (e.g., aggregation) of the dispersed particles will also be investigated so insight may be gained into the causes of atmospheric cleansing after geological and anthropological events such as volcanic eruptions, nuclear explosions, dust storms, and meteorite impacts.

The PDE uses a small, manually operated pump that pressurizes a 100-cubic-centimeter air reservoir to about 15 pounds per square inch gauge. This reservoir of compressed air is released as a pneumatic pulse for dispersing sand particles in eight separate experiment modules. Each of the eight modules constitutes a separate experiment; each module contains its own capsule of particles, but the size, shape, quantity, and composition of the sand varies from module to module. After a module is plugged into the pump unit and the reservoir is pressurized, the sand is fired as a pneumatically impelled jet of material into the 2-inch cubic chamber of each module. The behavior of the sand in the chamber will be recorded on video through either of two windows in each module. The choice of eight separate modules rather than eight experiments in one module was

made because of material-containment concerns in a microgravity environment.

The objective of the experiment is two-fold. First, the experiment will act as a “testbed” for the GGSF with regard to particle-dispersion techniques. It will determine the efficacy of pneumatic dispersion and reagitation, the “wall effects” of the various module materials, and the role of variables such as particle size and particle composition. Second, the experiment will allow scientific observations of particle aggregation over protracted periods of suspension in microgravity. The rate of particle aggregation, the shapes of the aggregates, the resistance offered by aggregates to redispersion, and the influence of particle size and shape on the aggregation process will provide valuable information on the behavior of particles injected into planetary atmospheres. When particles are thrown into the atmosphere by volcanic eruptions, meteorite impacts, or other means, their influence on climate and various other planetary phenomena depends largely on their residence time aloft. This is a function of the rate at which materials coalesce or aggregate into larger, more rapidly falling clusters. These aggregates are not readily preserved in nature because of their fragile character. The microgravity environment of the Space Shuttle will permit the simulation of long-term atmospheric suspension of natural materials, which is impossible to achieve in an ordinary laboratory.

Ames-Moffett contact: J. Marshall
(415) 604-4983
Headquarters program office: OSSA

Object 2201 Oljato: Asteroid or Comet?

**L. A. McFadden, A. L. Cochran, E. S. Barker,
D. P. Cruikshank, W. K. Hartmann, S. J. Ostro**

2201 Oljato is an object that has generally been regarded as an asteroid. It was first discovered in 1947 but was later lost, only to be rediscovered in 1979. Its orbital behavior has been noted for its association with meteor showers, and its modeled orbital evolution is chaotic—a property that might indicate a history more similar to comets than to asteroids. Other investigators found that perturbations in the interplanetary magnetic field that were measured at the orbit of Venus (with the Pioneer spacecraft) were correlated with the crossing of Venus' orbit by 2201 Oljato. This led to the suspicion that the asteroid was emitting material much as a comet would be expected to do, although at a very reduced level of emission. Telescopic observations of 2201 Oljato's visible and near-

infrared spectral properties, radar reflectivity, infrared radiometric properties, and other characteristics were made in 1979 and 1983. A review of these data shows that 2201 Oljato has a high surface reflectance, a property not commonly associated with comets. The data leave more questions than they answer, but they do corroborate the peculiar nature of this object. A more concentrated observational effort will be made in December 1992, when the asteroid can be easily observed from Earth.

**Ames-Moffett contact: D. Cruikshank
(415) 604-4244
Headquarters program office: OSSA**

History of Water on Mars: A Biological Perspective

**Christopher P. McKay, E. Imre Friedmann,
Robert A. Wharton, Wanda L. Davis**

Current biological interest in Mars focuses on the prospect that early in Martian history, conditions may have been suitable for the origin of life. We have attempted to roughly characterize the history of environmental conditions on Mars by dividing the time since the planet's formation into four epochs based on biological considerations. In Epoch I, during which a primordial carbon-dioxide (CO_2) atmosphere was actively maintained by impact and volcanic recycling, we presume that the mean annual temperature was above freezing, the pressure exceeded one atmosphere, and liquid water was widespread. Under such conditions, similar to those early in the Earth's history, life could have arisen and become abundant. After the initial period of recycling, atmospheric CO_2 was irreversibly lost as a result of carbonate formation, and the pressure and temperature declined.

In Epoch II, the mean annual temperature fell below freezing, but peak temperatures still rose above freezing at some time during the year. Hence ice-covered lakes, similar to those in the McMurdo Dry

Valleys of Antarctica, could have provided a habitat for life.

In Epoch III, the mean and peak temperatures were below freezing and there would have been only transient liquid water. A similar climatic situation occurs in the mountainous (higher than 1000 meters) Ross Desert of the McMurdo Dry Valleys. Here, high above the ice-covered lakes, air temperatures, even in the summer, virtually never exceed freezing. Microbial ecosystems living in endolithic rock "greenhouses" similar to those we have been studying in the Antarctic could have continued to survive.

Finally, in Epoch IV, the pressure dropped to near the triple point pressure of water; liquid water could no longer have existed on the surface, and life on the surface would have become extinct.

**Ames-Moffett contact: W. Davis
(415) 604-3186
Headquarters program office: OSSA**

Titan's Greenhouse and Anti-Greenhouse Effects

Christopher P. McKay, James B. Pollack, Regis Courtin

Titan is the largest natural satellite of the planet Saturn and is the only moon in the solar system that has an atmosphere. The surface temperature of Titan is 94 kelvin (-288°F) and has an atmosphere with a surface pressure of 1.5 atmosphere composed primarily of nitrogen (N_2) with several percent methane (CH_4), and about 0.3% hydrogen (H_2). The Voyager 1 flyby of Titan revealed that there is an optically thick organic haze in the upper atmosphere. The N_2 and CH_4 in the atmosphere of Titan react under the influence of sunlight to form complex hydrocarbons leading ultimately to solid organic material that condenses to form a high-altitude haze layer that obscures the surface of Titan from view. Without a direct view of the surface we can only speculate as to its nature. Because the surface temperature on Titan is so cold compared to that of Earth, CH_4 and other light organic molecules (primarily ethane (C_2H_6)) exist at the surface as liquids. The amounts of these hydrocarbons required to supply the atmosphere over the lifetime of the solar system, and the accumulation of organic molecules produced in the atmosphere, suggest that the surface may have very deep deposits of organics. However, at these cold temperatures water is frozen hard, and the Titan oceans and lakes would have no water activity.

Titan's thick atmosphere results in a strong greenhouse effect. The greenhouse gases (H_2O and CO_2 on Earth, Venus, and Mars, and CH_4 , N_2 , and H_2 on Titan) allow solar energy to reach the planet's surface but block the infrared energy as it flows away from that surface. The atmospheric gases then radiate some of this energy back to the surface, thereby warming it. The magnitude of this greenhouse warming compared to the direct solar warming is an indication of the strength of the greenhouse effect. By this measure, Titan has the second strongest greenhouse effect in the solar system—after Venus.

The situation is more complicated on Titan where, in addition to a greenhouse effect, there is an anti-greenhouse effect. The upper atmospheric haze layer has radiative properties that are exactly the opposite of the greenhouse gases mentioned above. The haze on Titan blocks the solar energy but allows

the surface radiation to escape freely. Hence we call this layer an anti-greenhouse layer. The anti-greenhouse properties of Titan's haze are the result of its composition. The organic substances that compose the haze are dark brown and orange and are opaque to visible light (solar energy). But these same organic substances are virtually transparent to the long-wavelength infrared radiation (wavelengths about 50 micrometers, or about five hundredths of an inch) that comes from the surface of Titan. The anti-greenhouse layer prevents solar energy from reaching the surface and readily allows the thermal energy to leave. In contrast to the greenhouse effect which warms a planet's surface, the anti-greenhouse effect cools a planet's surface.

We have used a computer model of Titan's atmosphere to investigate the relative roles of the greenhouse effect and the anti-greenhouse effect on Titan. If Titan had no atmosphere, its surface temperature would be 82 kelvin (-312°F); this temperature is called the effective temperature. Our calculations show that the greenhouse effect on Titan warms the surface above this effective temperature by 21 kelvin (38°F), but the anti-greenhouse layer cools the surface by 9 kelvin (16°F). The net effect, since the greenhouse effect is stronger than the anti-greenhouse effect, is that the surface is currently 12 kelvin (22°F) warmer than the effective temperature. If the organic haze layer responsible for the anti-greenhouse layer on Titan were somehow completely removed, then the surface temperature would be 23 kelvin (41°F) warmer than the effective temperature.

There are plans for a joint NASA/European Space Agency mission to Titan that will include sending an entry probe through the atmosphere of Titan to the surface. Known as the Cassini Orbiter and Huygens Probe Mission, this project should help us unlock more of the secrets of a world that is in many ways similar to our own.

Ames-Moffett contact: C. McKay
(415) 604-6864

Headquarters program office: OSSA

The Diffuse Interstellar Dust Absorption Feature Near 3.4 Micrometers in the Near Infrared

Yvonne J. Pendleton, Lou Allamandola,
Farid Salama, Scott Sandford, Xander Tielens

The hydrocarbon component of the diffuse interstellar medium which produces an absorption feature near 3.4 micrometers in the near infrared has been investigated by Ames scientists in a way that combines observational, theoretical, and laboratory expertise. The research group has obtained data from the NASA Infrared Telescope Facility (IRTF) using the 32-channel linear array cooled grating spectrometer. The data are from various lines of sight and have shown convincing evidence that the 3.4-micrometer absorption feature arises from material that is distributed throughout the diffuse interstellar medium (ISM). This work follows a recent publication by our group in which we suggested that the origin of the feature was the diffuse dust. The present study has expanded the sample of objects (number and type) observed, and the data have allowed more detailed analyses of the 2.7–3.8-micrometer region. The hydroxyl (O-H) feature near 3.0 micrometers that appears in the spectra of galactic-center objects (among others) appears not to be correlated with the 3.4-micrometer hydrocarbon (C-H) stretch feature which is thought to be caused by saturated aliphatic hydrocarbons. The lack of correlation suggests that the features arise from different carriers.

The relative strength of C-H features seen near 3.4 micrometers (due to CH₂ and CH₃ subgroups) indicates the presence of fairly complex organic compounds such as hexane. Comparison to labora-

tory spectra obtained at Ames has shown that the interstellar features are better fit by compounds that contain electronegative groups such as O-H (i.e., butanol). There is some indication that the electronegative groups could be polycyclic aromatic hydrocarbon (PAH) molecules, which could possibly be responsible for the absorption feature seen at 3.4 micrometers. Comparison to the residue that remains after ultraviolet irradiation of mixtures of ices typically found in dense interstellar clouds shows that the observational spectra can be fit fairly well by the analogous laboratory astrophysical spectra. Comparison to the Murchison meteorite data shows that the 3.4-micrometer feature seen in the diffuse ISM is not inconsistent with the meteoritic data, which suggests that the saturated aliphatic hydrocarbon component in the meteorite has remained unaltered from its origin in the ISM. Further observations are scheduled for June 1992 on the IRTF to follow up the preliminary detection of the PAH molecules in absorption, and to further investigate the nature of the C-H and O-H features in the diffuse dust. Collaborators from outside institutions include Kris Sellgren at Ohio State University and Mauricio Tapia at the University of Mexico.

**Ames-Moffett contact: Y. Pendleton
(415) 604-4391**

Headquarters program office: OSSA

Simulation of Titan's Aerosols

Shelly K. Pope

The aerosols that make up the global haze layer on Saturn's moon Titan play a major role in determining fundamental properties of the atmosphere. Though they are very small and occur at a density of only a few particles per cubic centimeter, the aerosols extend through a large vertical range. The result is an optically thick haze layer by which the surface of Titan is obscured from view, at least in visible wavelengths. Thus the aerosols are important in controlling the amount of sunlight that reaches the surface of Titan. This, in turn, affects Titan's thermal emission and its atmospheric heat budget. The aerosols also figure into the chemical budget; their formation in the upper atmosphere and subsequent sedimentation onto the surface constitute a removal mechanism for the chemicals of which they are composed.

In order to understand the chemistry and radiation budget of Titan's atmosphere, the composition and distribution of the aerosols must be known. To determine the aerosol distribution, researchers have used spacecraft observations of the brightness and polarization of Titan as a function of phase angle (spacecraft/Titan/sun angle). Models of the atmosphere using these observations have yielded information on the limits on the unknowns: the aerosol distribution and the particles' scattering properties. More information on the aerosol distribution can be

extracted if the particles' scattering properties can be described and input into the model as a known parameter. The scattering properties depend entirely on the wavelength of the incident light and on the particle size, shape, and refractive index.

Work done by Tom Scattergood (at State University of New York at Stony Brook and Ames Research Center) and others has addressed the question of what size and shape of particles are formed in a simulated Titan atmosphere. Various gas mixtures relevant to Titan's atmosphere have been exposed to ultraviolet light, resulting in the production of aerosol particles. The particles are collected and then examined with a scanning electron microscope. In a related study, Shelly Pope has designed and built a chamber in which aerosols are produced in a similar way, but this chamber has the capability to cool the simulated atmosphere to temperatures similar to those of Titan. The goal of this work is to explore the effect of temperature on the size and shape of particles produced in a simulated Titan atmosphere.

**Ames-Moffett contact: S. Pope
(415) 604-6538**

Headquarters program office: OSSA

An Infrared Camera for Operation at 10 and 20 Micrometers

Thomas L. Roellig, Mark E. McKelvey, Lynne K. Deutsch, Yvonne J. Pendleton, Fred C. Witteborn, Craig R. McCreight

During fiscal year 1991, development was started on a new infrared camera system to be used for astronomical observations from a variety of ground-based observatories. By using state-of-the-art infrared detector array technologies, it will be possible to use the new camera to observe objects through both the 10- and 20-micrometer atmospheric windows. The new camera will have a circular variable filter that will allow low-resolution spectrophotometric images to be taken at 8 to 14 micrometers and will also incorporate three band-pass filters at 18, 20, and 22 micrometers to take images through the 20-micrometer atmospheric window. In addition to the normal mode of operation, a polarimeter is being constructed to be used in conjunction with the camera. This will allow polarimetric studies to be made in all the camera's operating wavelengths.

The area of sky that is a single-camera image depends on the telescope being used. For a telescope such as the Infrared Telescope Facility on Mauna Kea, an image size of 14 × 14 inches will be obtained. With the expected very high sensitivity of the camera, this image size will allow a number of interesting astronomical studies to be made of objects that are too faint to be imaged by previous infrared cameras.

These include a wide variety of extragalactic objects as well as the fainter star-formation regions and planetary nebulae in our own galaxy. By using the polarimetric capability, the magnetic field strength and direction can be determined for objects as diverse as the galactic center and other active galactic nuclei.

During fiscal year 1991 the major components of the camera were ordered, and assembly has started. The detector array, cryostat assembly, and optical train have been assembled. We are awaiting delivery of the array drive electronics, which are expected to arrive in early 1992. The first engineering runs on a telescope are expected to take place in late summer, 1992. The camera is being developed by a joint team with members from both the Space Sciences Division and the Space Projects Division. Additional collaborators are M. W. Werner of the Jet Propulsion Laboratory, T. McMahon of Sterling Software, T. Gustavson of the California Institute of Technology, and N. Jennerjohn of San Francisco State University.

Ames-Moffett contact: T. Roellig
(415) 604-6426

Headquarters program office: OSSA

Oxygen Evolution and Life on Mars

Lynn J. Rothschild

One of NASA's goals is to look for evidence of life elsewhere in the Solar System; Mars is considered the most promising planet. Because of the hypothesized similarities in the environments of Earth and Mars in their early development, it is thought that a Martian biota probably would be based on organic carbon. As a result of this, and because of the great abundance of inorganic carbon relative to organic carbon on Mars, this Martian biota would have been under selective pressure to evolve a means to assimilate (fix) inorganic carbon, as have organisms on the Earth.

The major by-product of most types of carbon fixation on Earth is oxygen. It is as a result of photosynthesis, the most widespread type of biological carbon fixation, that Earth became aerobic. The ultimate goal of this project is to map the concentration of oxygen over the surface of Mars in order to understand the subsurface. We expect that such an experiment will generate data that will be useful for Mars exploration in several respects. Relatively high levels of oxygen in some locations may be indicative of biological activity. Oxygen is a vital resource for human exploration; thus, the oxygen survey proposed here for Mars would yield results that would be useful in site selection for human exploration. The Viking Gas Exchange Experiment showed that humidifying the Martian regolith at the Viking lander sites released oxygen, so in an indirect way, local concentrations of near-surface oxygen could be indicative of increased humidity. Water is also of interest for exobiological and human explorations of Mars. Finally, data on carbon fixation under Martian conditions, especially concentrations of carbon dioxide, will be of importance in food and oxygen production on Mars in conjunction with human exploration.

The possibility of extant life on Mars is exciting, but also remote. Especially problematic are the lack of

water, the extremely cold temperatures, the ultraviolet and ionizing radiation, and the soil oxidants. There are several terrestrial ecosystems that have evolved partial defenses against Martian environmental conditions, including antarctic and endoevaporitic microorganisms. This year we identified and studied another potential model system, a "cryptic" microbial mat. The microbial mat is a Mars analog community because it lives under a protective layer of sand, apparently lives on low amounts of water, and produces its own organic material from inorganic precursors, in this case by photosynthesis. The mat is found in the inter- to supertidal zones in Laguna Ojo de Liebre, Baja California. A transect was taken from the road to the edge of the lagoon, approximately 100 meters. The mat was sampled every meter, and was mapped. At four different types of sites, carbon fixation rates were determined every 2 hours. Total carbon fixed per square meter per day was determined for each site. Sites along the transect similar to the four study sites were assigned to the related study site, and from this assignment total carbon fixation along the transect at a width of 1 meter was estimated to be 4.05 grams \pm 5% per day. This corresponds to 0.337 moles of carbon, and therefore probably 5.39 grams of oxygen were evolved in conjunction with the carbon fixation. While this amount is substantially below what would be expected from a highly productive ecosystem such as an equivalent area of grass, it was easily detected with the methodology used.

**Ames-Moffett contact: L. Rothschild
(415) 604-6525**

Headquarters program office: OSSA

Carbonates on Mars? Some Old Information

Ted L. Roush, John P. Monteverdi,
Glenn C. Carle, James B. Pollack

An enigma is presented by the presence of some Martian surface features that are indicative of the work of liquid water, together with the current instability of liquid water on Mars. One suggested explanation is that Mars once had a denser atmosphere (2–5 bars), composed chiefly of carbon dioxide (CO_2), which resulted in warmer surface temperatures and hence the presence of liquid water. Because of the current tenuous atmosphere on Mars (0.01 bars) a question arises. Where is the rest of the CO_2 ? As observed on the Earth, chemical weathering of silicates by slightly acidic groundwater results in the precipitation of carbonate rocks, and it has been suggested that a similar mechanism operated during an early clement period on Mars. Because of the smaller mass of Mars, the recycling of the carbonates to the interior (as a result of plate tectonics), where they would decompose and release the CO_2 via volcanic activity, eventually halted, and the CO_2 became permanently trapped. Thus the identification of carbonates on the Martian surface provides information regarding the early atmospheric evolution on Mars. Additionally, carbonate deposits on Earth commonly contain fossils of extinct organisms; hence

the identification of such deposits on Mars are of extreme interest with regard to the question of the evolution of life during the early history of Mars.

Vibrational motions of the atoms that compose molecules, e.g., carbonates, give rise to the absorptions of infrared energy. The specific energy corresponding to these spectral absorptions provides direct compositional information regarding the surface and/or atmospheric materials. Recently, Earth-based spectral observations of Mars have provided some evidence of the presence of carbonates on Mars. One inherent limitation of these observations is the spatial resolution on the surface, often tens of thousands to millions of square kilometers.

Our research focuses on infrared spectral data returned by the Mariner 6 and 7 spacecraft as they passed by Mars in 1969. We have been working closely with Terry Martin of the Jet Propulsion Laboratory who has restored these data to digital format. The data have been calibrated for both wavelength position and absolute intensity; they exhibit many absorption features, some of which are also present in the more recent Earth-based observations (see figure). Some of these features are consistent with the

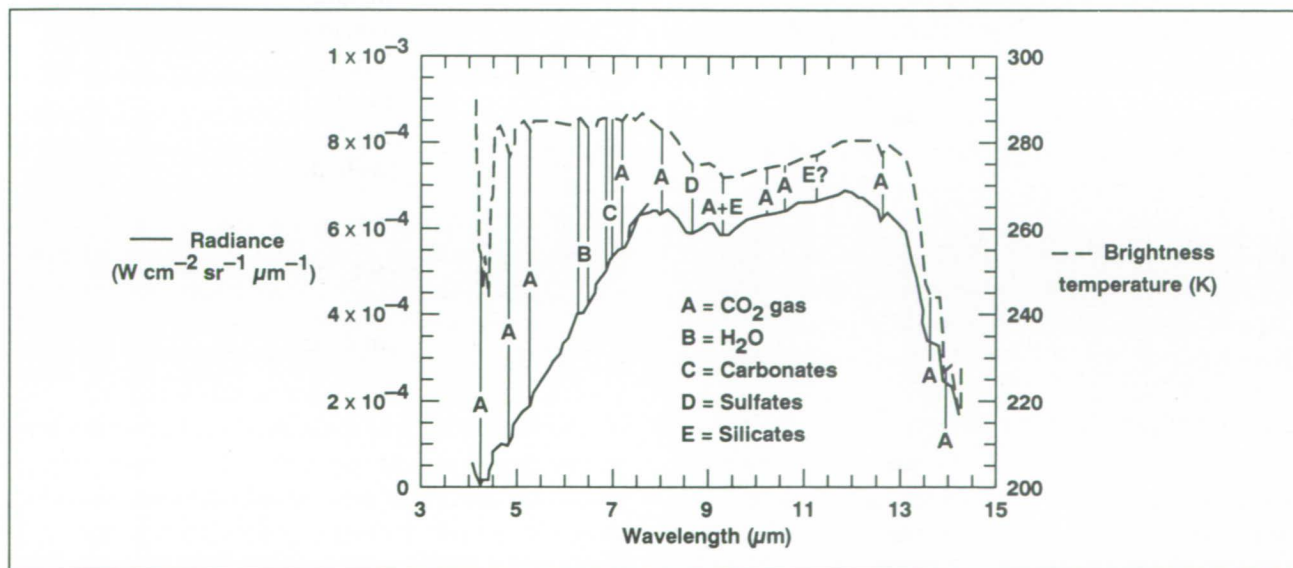


Fig. 1. Radiance (solid curve) and brightness temperature (the temperature of the black body which yields the radiance; dashed curve) of Mariner 7 spectrum #98. Several absorption features due to atmospheric (e.g., CO_2 , silicates) and surface (e.g., carbonates, sulfates, silicates) constituents are indicated.

presence of carbonate-bearing phases present on the Martian surface. Because the distribution of these features can be mapped on Mars and the spectra can also be theoretically modeled, the composition, abundance, and variation of these materials across the Martian surface can be assessed. Specific sites on the

surface that have high carbonate content can be identified.

**Ames-Moffett contact: T. Roush/J. Pollack
(415) 604-3526/5530
Headquarters program office: OSSA**

Diode Laser Spectroscopy of Stable Isotopes

T. B. Sauke, J. F. Becker

Variations in the stable isotopic ratios of carbon and oxygen in Martian rock and soil samples can be caused by several factors, such as the fractionation that occurs as a result of past or present volcanism, the incorporation of carbon dioxide from the atmosphere to Mars' surface, or the existence of other reservoirs of carbon or oxygen—for example, water or possibly organic carbon that has been formed by either biological or nonbiological processes. Measurement of the isotopic variations can provide much important information about, and insight into, the planet's physical and chemical evolution, including its possible past inhabitants. We are developing a stable isotope laser spectrometer (SILS) which uses high-resolution tunable diode lasers to measure ratios of stable isotopes of carbon and oxygen in carbon dioxide obtained from soil and rock samples. Modern high-temperature diode laser systems are reliable, lightweight, and rugged, and therefore well suited for flight hardware applications. Because of these attributes, the SILS instrument will be proposed for performing isotopic analysis of planetary soils on planned near-term Mars missions such as the Mars Environmental Survey and Mars Rover Sample Return.

Laser spectroscopy offers several important advantages over the conventional mass spectrometer for measurements on a planet's surface. For example, the complex and detailed sample preparation and purification necessary for reliable mass spectrometer measurements are unnecessary when a laser spectrometer is used, because contaminant gases typically do not interfere with the measurement.

One project goal is to improve the accuracies of isotopic ratio measurements that can be made with

the SILS. We have implemented high-speed assembly language data-acquisition software that signal averages successive spectral scans, improving our signal-to-noise ratio. The software incorporates a routine for automatically compensating for the inevitable spectral drifts that occur during signal averaging. Other instrumental artifacts that result in artificial broadening of measured spectral lines present a challenge to accurate measurements. We have developed methods to determine the amounts of excess broadening caused by various instrumental imperfections, and to incorporate these effects into the data-fitting model. When fully implemented, these developments should result in measurement accuracies of better than 99.9%.

In an application of tunable diode laser spectroscopy to the measurement of stable isotopic ratios of carbon, isotopic ratio measurements were made on the carbon dioxide generated from magnesium oxide (a model mineral) crystals at elevated temperatures, in an attempt to determine whether soluble trace carbon was diffusing from the bulk material. Using the SILS, the time dependence of the $^{12}\text{C}/^{13}\text{C}$ isotopic ratio of the CO_2 gas liberated from magnesium oxide crystals after suddenly increasing the temperature from 296 °C to 390 °C was measured. The SILS presently has an accuracy of better than 99.6% which makes it suitable for this type of measurement. During the first 90 minutes, an oscillation in the $^{12}\text{C}/^{13}\text{C}$ ratio with an amplitude of 0.8% of the original ratio was observed, in agreement with a computer simulation of one-dimensional diffusion. These initial results suggest that significant amounts of carbon can exist dissolved in a

mineral structure. Moreover, the results indicate that the SILS, even in its present state of development, is capable of measuring isotopic ratios with sufficient accuracy to provide information of importance to planetary scientists.

**Ames-Moffett contact: T. Sauke
(415) 604-3213**

Headquarters program office: OSSA

Experiments to Identify Mineral Biomarkers

Biomarkers can be used to determine if past (or present) biological activity has occurred on a planet's surface. Minerals produced under biologic control have distinctive characteristics (including morphologies, structures, and microchemistries) that are unique to the host organism that produced them, and that are distinguishable from abiotically produced minerals that have the same chemical composition. As a result, minerals formed by biologically controlled mineralization processes have been proposed as biomarkers.

The objective of our study is to determine what experiments, or series of experiments, can identify mineral biomarkers by distinguishing between biologically and abiotically produced minerals that have the same chemical composition. We have begun with the mineral magnetite because it is readily produced both abiotically and biologically. Magnetite is a late magmatic mineral that forms as a consequence of the cooling of a magma that is rich in iron. Magnetite is produced by several organisms, includ-

ing magnetotactic bacteria, and serves several biological functions. It is an electron carrier in the cytochrome system; and it is used to harden outer surfaces for scraping, and to detect the Earth's magnetic field for navigation. Employing the techniques of scanning electron microscopy, X-ray diffraction, and differential thermal analysis, we have begun to identify characteristics of biologically produced magnetite (extracted from *Aquaspirillum magnetotacticum*) and characteristics of known abiotically produced magnetite. Features specific to or related to each type have been observed. Additionally, information on particle size distribution, phase changes, and microchemistries has been inferred from the data collected thus far.

**Ames-Moffett contact: D. Schwartz
(415) 604-3668**

Headquarters program office: OSSA

A Novel Method for Preparing PLOT Columns

Thomas C. Shen

We have developed a novel method for preparing porous-layer open tubular (PLOT) columns. This method involves a straightforward in situ polymerization of a monomer. The product is directly coated on the metal tube. The method is simple, reproducible, and provides high separation efficiency. It eliminates many of the steps needed for conventional PLOT column preparation.

PLOT columns offer many advantages over packed or wall-coated gas chromatography columns. Currently, all PLOT columns are made either by static coating procedures, dynamic coating procedures, or a combination of static and dynamic coating procedures. In general, existing methods require that polymerization of monomers take place in the first step. Polymers are then sieved to recover the size required for packing in the columns. These methods are complicated and require special expertise and

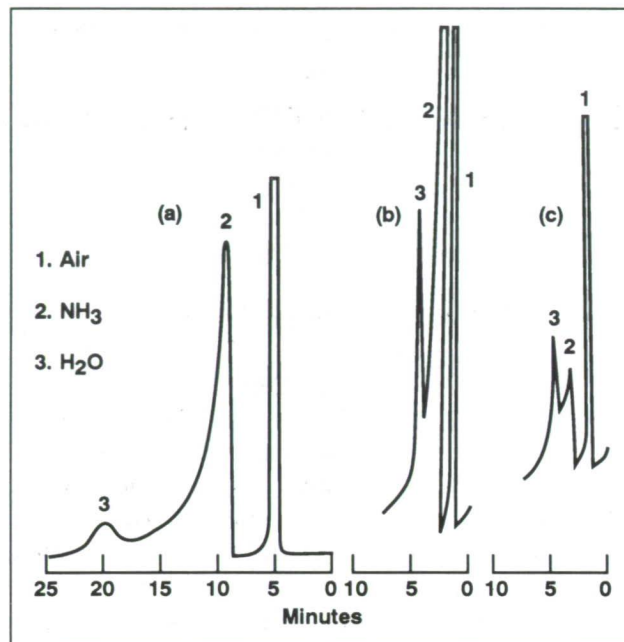


Fig. 2. Water and ammonia separation by DVB/EGDM columns. (a) 56 molar % EDGM at 109 °C, 2.0 ml/min He, (b) 21 molar % EDGM at 105 °C, 4.0 ml/min He, (c) 10 molar % EDGM at 105 °C, 4.2 ml/min He.

facilities. These difficulties and the resulting high cost have limited the applications of PLOT columns. Our method accomplishes the polymerization and the coating of the column surface in the same step. The in situ polymerization procedure allows for straightforward preparation of a PLOT column in metal tubing. The important requirement in this technique is finding a suitable solvent system that provides suspension polymerization of the monomers and does not swell the polymers to any extent.

Two types of PLOT columns have been prepared.

1. Divinyl benzene (DVB) PLOT columns prepared from in situ polymerization give very good separation of light gases, as demonstrated in the first figure. As the DVB concentration increases, the separation efficiency also increases. At a DVB concentration of 25%, the separation efficiency of the PLOT column is

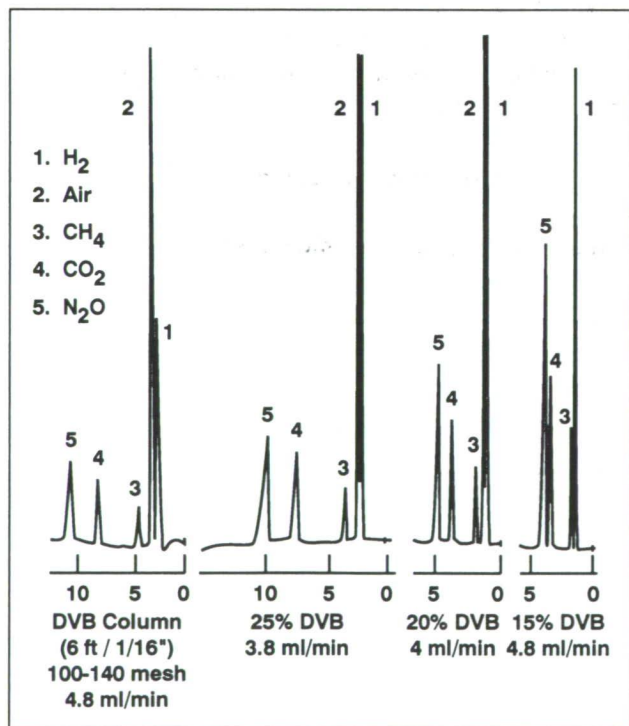


Fig. 1. Separation of some light gases using various DVB PLOT columns and a packed column.

almost as good as the packed column. The advantage of the PLOT column is that a lower concentration and a smaller sample can be detected using highly sensitive detectors than with a packed column. This advantage is very important in a space mission.

2. PLOT columns using copolymers of DVB and ethylene glycol dimethylacrylate (EGDM) for separation of water and ammonia were also developed. The chromatograms for these columns are shown in the second figure. Their relative retentions increase with increasing EGDM or styrene concentration (i.e., increased pore size) (see table 1). These results are consistent with our earlier findings.

Ames-Moffett contact: T. Shen

(415) 604-5769

Headquarters program office: OSSA

Table 1. Effect of molar percent of comonomers in DVB columns in water and ammonia separation

Comonomer mole %	Relative retentions
EGDM	
0	1.0
10	1.7
21	2.3
56	3.5
Styrene	
0	1.0
10	2.5
20	3.3
45	3.8

Telepresence for Planetary Exploration

Carol R. Stoker, Owen Gwynne

The focus of this project is to develop telepresence operation of remote vehicles—a key technology that will be necessary for future robotic and human exploration of the Moon and Mars. This exploration effort will require the synergistic efforts of humans and machines. Teleoperated robotic vehicles will, in all likelihood, fulfill much of this need; however, this capability has yet to be demonstrated in a realistic setting. Thus we are developing telepresence systems to support scientific field work in the marine environment. Telepresence is a high-fidelity form of remote control in which the natural sensory capabilities of the human operator (e.g., vision, touch) are projected into a robot at a distant worksite. Telepresence systems are being integrated with underwater remotely operated vehicles that are commercially available today. The union of “off-the-shelf” technology with state-of-the-art telepresence systems will enhance the capabilities of these underwater vehicles for exploratory work and subsequent data analysis.

The main goal of this year's work was to develop a telepresence-controlled remotely operated under-

water vehicle (TROV) and to conduct a pilot study to demonstrate the potential of using such vehicles to conduct the scientific reconnaissance of a coral-reef ecosystem.

The TROV uses an S2 Phantom (TM Deep Ocean Engineering) remotely operated underwater vehicle controlled by a “telepresent” operator. The fundamental difference between using telepresence to control an underwater vehicle and using more traditional methods is that, with telepresence, the user has the sense of being present in the remote environment. Ideally, the operator can see what the TROV “sees” and feel what the TROV “feels.” A sketch of the TROV concept is presented in the figure. The operator wears an imaging system consisting of two high-resolution video displays, placed in close proximity to the eyes, which are fed by articulated stereo cameras on the underwater rover. This configuration provides the operator with images of the surrounding environment. Because the operator's head movements servo-control the robotic rover's stereo cameras, the operator is immersed in the scene as if he or she were actually

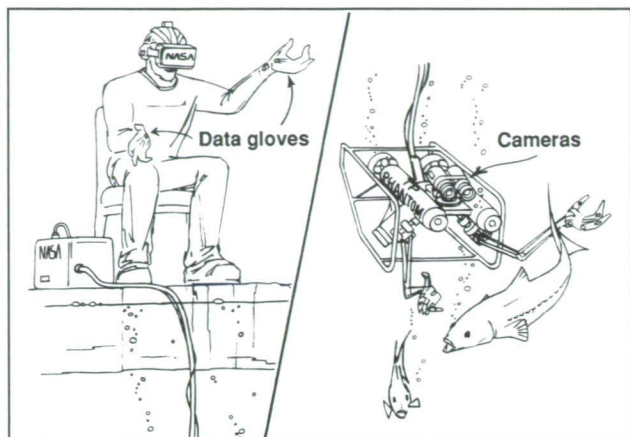


Fig. 1. Telepresence is used to operate a TROV. Position of camera platform on the vehicle is articulated by head motions of an operator wearing a visual system that receives images from the underwater cameras. The manipulators on the vehicle are servo-controlled by the operator's hand motions using "data gloves."

present at the remote site. The robotic rover "senses" the surrounding environment and transmits this information to the human operator. The telepresence aspect of the TROV operation was implemented this year. Our future plans call for developing servo-controlled manipulators for the vehicle which will be operated with "data gloves."

The first field test of the TROV was performed in December 1991 in the National Marine Sanctuary near Key Largo, Florida. The field phase of this program was jointly sponsored by the National Oceanographic and Atmospheric Administration, and was supported by the National Undersea Research Center. The TROV was used to perform the reconnaissance of a deep coral-reef ecosystem. This field trip provided scientists and engineers with the opportunity to work with the telepresence system for the first time in an environment other than the laboratory. The

TROV was used to inspect corals for evidence of disease and to map the coral distribution in an area that will be the future location of the Aquarius Habitat, a permanent underwater habitat. In addition to providing a scientific tool for the investigation, this in situ demonstration brought this new technology to the attention of a much broader scientific community. The experience and insight gained from the pilot study will be used to develop a more refined TROV system for use in future investigations of the marine environment.

The telepresence project, and the TROV capability, has been selected as the first pilot demonstration project for the new National Science Foundation/NASA Antarctic Space Analog Program. The goal of this project, scheduled for the 1992 austral summer, is to perform an integrated demonstration of telepresence, advanced power systems, and satellite communications/data link in Antarctica. The TROV will be used to perform the detailed reconnaissance of a permanently ice-covered lake in Antarctica. The environments of these lakes are thought to be similar to those of lakes that existed on Mars in the ancient past. The use of the TROV will allow the lakes to be explored in considerably more detail than has previously been possible. The TROV will be operated with power provided by solar cells built by Lewis Research Center. In a later phase of the project, it will be possible to control the TROV in Antarctica from a remote location, using satellite telecommunications.

The telepresence project could lead to a revolutionary way of conducting science in hostile or remote environments on Earth, and will provide a positive near-term beginning for the Space Exploration Initiative in the exploration of other planetary bodies.

Ames-Moffett contact: C. Stoker

(415) 604-6490

Headquarters program office: OSSA

New 120-Detector Infrared Spectrometer

Fred C. Witteborn, Jesse D. Bregman, Thomas P. Greene

Low- and intermediate-resolution spectroscopy in the thermal infrared has proved to be a valuable tool for Kuiper Airborne Observatory (KAO) studies of astronomical phenomena ranging from comets to supernovae. The faint object grating spectrometer (FOGS) has served this purpose since 1984 in the 5- to 10-micrometer range for KAO studies and in the 7.5- to 13-micrometer range for ground-based studies. It has provided essential data for identifying spectral features in SN1987a, comets Halley and Wilson, Mars, T-Tauri stars, carbon stars, numerous planetary nebulae, H II regions, and even some galaxies. The experience gained in the operation and maintenance of FOGS, coupled with improved detector fabrication techniques, has made possible an improved spectrometer which is now operational in the 3- to 17-micrometer range.

The development of an upgraded successor to the FOGS is driven by both scientific and practical goals. The scientific requirements are the need for resolving powers up to 1000 to study spectra of interstellar ices and ice impurities (5–9 micrometers); the need to obtain 2% absolute spectral accuracy over the 3- to 13-micrometer range for mineralogical studies of the moon, planets, and asteroids in the thermal IR; and the need for improved celestial standards throughout the 3- to 30-micrometer spectral range. The practical goals are to improve the efficiency of observing by simultaneous coverage over a wider spectral range and by introducing additional external controls to permit a wide range of investigations to be performed

without opening the vacuum system. Because of its higher spectral resolving power and the higher efficiency resulting from its large detector complement, the new system is called HIFOGS (high-resolution faint object grating spectrometer).

During 1991, detailed design, fabrication, assembly, and testing of HIFOGS were completed. Bismuth-doped silicon detectors and their cryogenic electronics were purchased from Aerojet ElectroSystems. Optical components were built (some were purchased from Infrared Labs). Software for operating HIFOGS and reducing data was developed. The optics and detectors must operate inside a liquid helium Dewar. This assembly was completed, aligned, and tested. Initial tests on the 1-meter telescope at Lick Observatory and on the KAO verified that HIFOGS works well.

While HIFOGS is now operational, further extensions of its capabilities are under way. Detectors for extending the wavelength coverage to 30 micrometers have been received (cost free) from the European Space Agency because of their strong interest in our establishment of 3–30 micrometer spectral standards. This development will continue in parallel with an active observation schedule in 1992.

**Ames-Moffett contact: F. Witteborn
(415) 604-5520**

Headquarters program office: OSSA

Gravity Waves in the Atmosphere of Venus

Richard E. Young, Howard Houben

Several studies have indicated that internal gravity waves of synoptic scale or smaller could be a significant presence in the atmosphere of Venus. In addition, there are convincing observations from the Soviet VEGA Venus Balloon Mission that gravity waves generated by surface topography reach cloud level with significant amplitude, and that gravity waves generated by other means are ubiquitous as well. Gravity waves are thought to play a critical role in the maintenance of the observed atmospheric superrotation.

During the last year, a two-dimensional gravity-wave-simulation computer code was modified to simulate gravity waves in the atmosphere of Venus. The code accounts for all nonlinear interactions in the equations of motion, and can therefore examine the effects that gravity waves have on the atmosphere. Several numerical problems were overcome, and an entirely new computational algorithm was incorporated into the code. This new numerical procedure solved the difficulties initially encountered, and, in addition, increased the speed of the existing code by a factor of 20.

Numerical simulations were undertaken to study the behavior of gravity waves generated near the

surface of Venus as they propagated up through the atmosphere. Initially, only waves that had no phase speed with respect to the ground were considered. It was found that the vertical variation of the atmospheric westward winds, together with the changes in temperature with height, acted to filter upward-propagating waves. Waves that have horizontal wavelengths of less than about 100 kilometers do not reach cloud levels (about 50 kilometers altitude) with significant amplitude, whereas waves that have horizontal wavelengths longer than 100 kilometers propagate freely to cloud level and above. Cloud-level wave amplitudes are comparable to those observed by the VEGA balloons, with a vertical wind amplitude of the order of 1 meter per second. As the waves evolve, they act to induce low-level mean winds in the opposite direction to the background winds. Eventually the wave-induced winds become comparable to the background wind, and the waves break down into turbulence.

**Ames-Moffett contact: R. Young
(415) 604-5521**

Headquarters program office: OSSA

Airbursts and Craters on Venus

Kevin Zahnle

Comet and asteroid impacts, although infrequent, are a hazard of living on the surface of a planet. To some extent the sea of atmosphere surrounding the Earth protects us against small, relatively frequent events, but it can do little to protect us from the larger, more dangerous events. The extent to which the atmosphere protects us is difficult to gauge on Earth, since impact craters, particularly the smaller ones that are of most interest to us in this context, are quickly obliterated by erosion. But conditions are different on Venus.

NASA's recent Magellan spacecraft mission to Venus—an orbiting radar imaging system (12.6-centimeter wavelength) that penetrated the planet's clouds—revealed another planet of impact craters, volcanoes, and lava flows. Perhaps the biggest surprise was that, in general, erosion is not an important process on Venus. All impact craters on Venus look fresh, although some are probably more than a billion years old. An absence of small craters was not surprising, because the thick atmosphere was expected to filter out the smaller impactors. Instead—unexpectedly—the Venusian surface is randomly marked with roughly circular radar-dark splotches that on the radar images look suggestively like shadows cast by falling bodies. The splotches apparently record near-surface shocks or “airbursts” of impacting objects that were catastrophically disrupted by aerodynamic forces. Because the Venusian atmosphere is so dense (unshocked density 0.066 grams per cubic centimeter, shocked density approximately 0.5 grams per cubic centimeter), the airshock can shatter standing stones, reducing the surface to radar-dark gravel.

We have devised a simple three-part model for (1) the flight of an impactor through a thick atmosphere, (2) its catastrophic disruption, and (3) the interaction of the resulting shock wave with the ground, to compare with the Venusian data. The aerobraking model (the first part) can be independently tested against the Venusian cratering record itself. This is done by Monte Carlo simulation, using reasonable approximations to the modern populations of potential impactors extrapolated from the observed populations of asteroids and comets in Venus-crossing

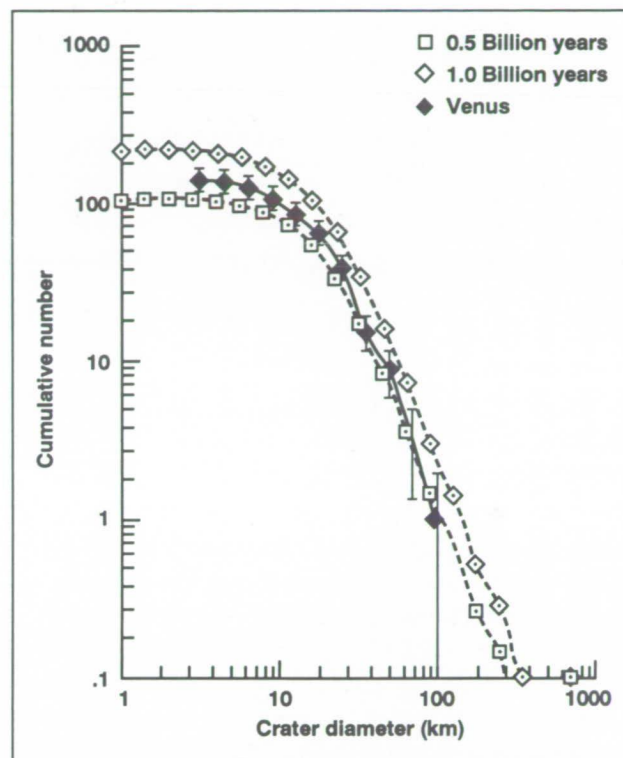


Fig. 1. The cumulative number of craters larger than a given diameter observed on Venus and compared to Monte Carlo simulations with surface exposure ages of 0.5 and 1.0 billion years.

orbits. Objects large enough to reach the surface with a fair part of their original velocity form craters. In the simulations, crater diameters are estimated using conventional crater-scaling relations. The crater simulations closely reproduce the observed Venusian crater statistics (see figure).

The airburst model (the second part) is based on approximate models for strong explosions developed by Soviet researchers. The explosion is modeled as a hot isobaric interior cavity surrounded by a massive thin shell. Movement of individual mass elements of the shell is governed by Newton's law, accounting for the mass of air swept up and the pressure of the cavity. The cavity pressure is determined by conservation of energy, accounting for the volume of the cavity

and the kinetic energy of the shell. Typical Venusian airbursts are produced by kilometer-sized bodies with net energy yields of order 10^5 to 10^6 megatons of TNT. For comparison, the largest thermonuclear device ever exploded had an energy yield of 60 megatons, and the Tunguska event in 1908, an airbursting asteroid or comet, had an energy yield of 10–30 megatons.

The interaction of the shock wave with the ground (the third part of the model) is modeled by the impact of parallel plates: one plate is the thin shell of shocked air, and the other is the surface itself. The

model yields peak shock pressures experienced by surface rock as a function of depth and distance from ground zero. Surface shocks large enough to reduce rocks to rubble are felt within 20–30 kilometers of the impact site, which is consistent with the size of the observed features.

**Ames-Moffett contact: K. Zahnle
(415) 604-3148**

Headquarters program office: OSSA

X-29 High-Angle-of-Attack Control Improvements

Jeffrey E. Bauer, Robert Clarke

The objective of this research was to flight-validate improvements in the control system of the X-29 aircraft under high-angle-of-attack flight conditions. The improvements were made in the course of high-angle-of-attack (α) envelope expansion and military utility flight testing; they included reducing the roll damper gain and increasing the command authority levels in pitch and roll.

During the envelope expansion, wing rock was an area of primary concern because of the large instability in roll damping that was predicted from wind-tunnel tests. As the envelope was cleared to an α of 50 degrees, this instability was much less than predicted, and roll control power was higher than expected. Through the use of an in-flight gain selection or the Dial-A-Gain feature of the flight-control system, 20-percent reductions of the roll damper gain were flight tested and later implemented in the flight control software with no significant increases in wing rock.

Load-factor envelope expansion showed that the α authority was reached earlier than expected. Pilots found that full-aft stick inputs were required at 200 knots calibrated airspeed (KCAS) and a 25-degree α (see figure), whereas the prediction was that the airplane could be flown to an α of 35 degrees at this airspeed. Subsequently, the pitch stick authority was increased by 30 percent at high-speed conditions and 100 percent at low-speed conditions. This change allowed the elevated load-factor envelope to be opened with no apparent problems.

Pilot comments had indicated that there was excellent roll coordination but slow stability axis roll rates during envelope expansion. The initial flight-control-system gains had been designed to ensure that large sideslip angles and inertial-kinematic coupling into the pitch axis would not occur. Flight tests showed a decreased tendency to develop sideslip, and no problems with coupling were found; Dial-A-Gain

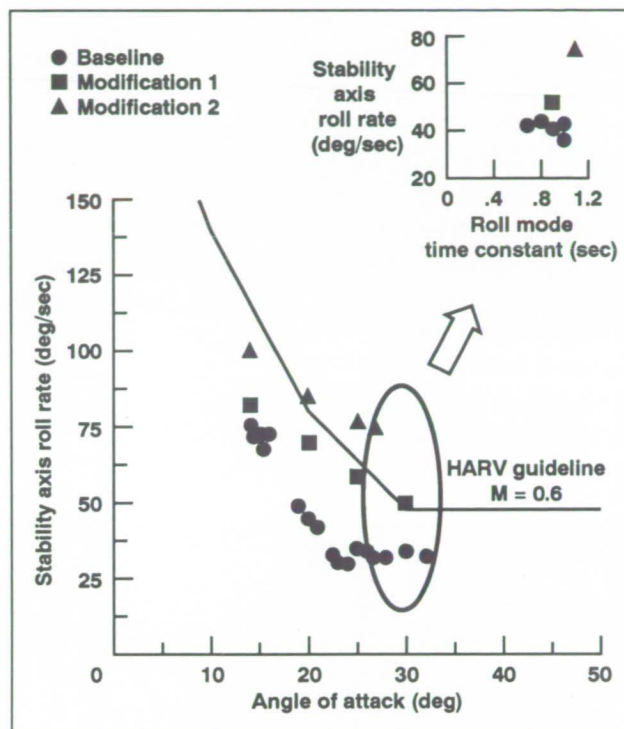


Fig. 1. X-29 high-angle-of-attack control improvements.

increases of as much as 100 percent in the lateral stick authority were therefore allowed (with appropriate changes in the aileron-to-rudder interconnect gain). The figure shows increases in the stability-axis roll rate and the predicted change in airplane handling-qualities parameters. These increases in torsional agility have been shown in flight tests to translate directly into increases in high- α combat effectiveness against a single F-18 adversary.

Ames-Dryden contact: J. Bauer

(805)258-2240

Headquarters program office: OAST

A Real-Time Flight-Control Clearance Test Technique for Hypersonic Vehicles

John T. Bosworth

Collecting and displaying critical information is the key to enhancing the safety and efficiency of the envelope-expansion, flight-test phase of a new research vehicle. With real-time information, a pilot or the ground monitoring station is in a much better position to adjust the flight plan to avoid unsafe conditions or to ensure that quality data is obtained. Previous experience has shown that real-time monitoring capabilities produced significant improvements in safety and efficiency. Real-time monitoring for the National Aerospace Plane (NASP), however, is more difficult than it is for conventional research aircraft.

The NASP vehicle presents a highly integrated system with interactions between the propulsion,

airframe, cooling, and flight-control functions. The stability of the overall system depends on a complex relationship between many individual systems on board the aircraft. This relationship is most often nonlinear and has multi-input, multi-output (MIMO) characteristics.

The NASP is designed as an accelerator vehicle. The increased complexity and, consequently, increased weight of a throttle-able engine may or may not be included in the initial research vehicle. The heating constraints associated with much of the flight envelope preclude long periods of steady-state flight. The vehicle would burn fuel at an extremely high rate,

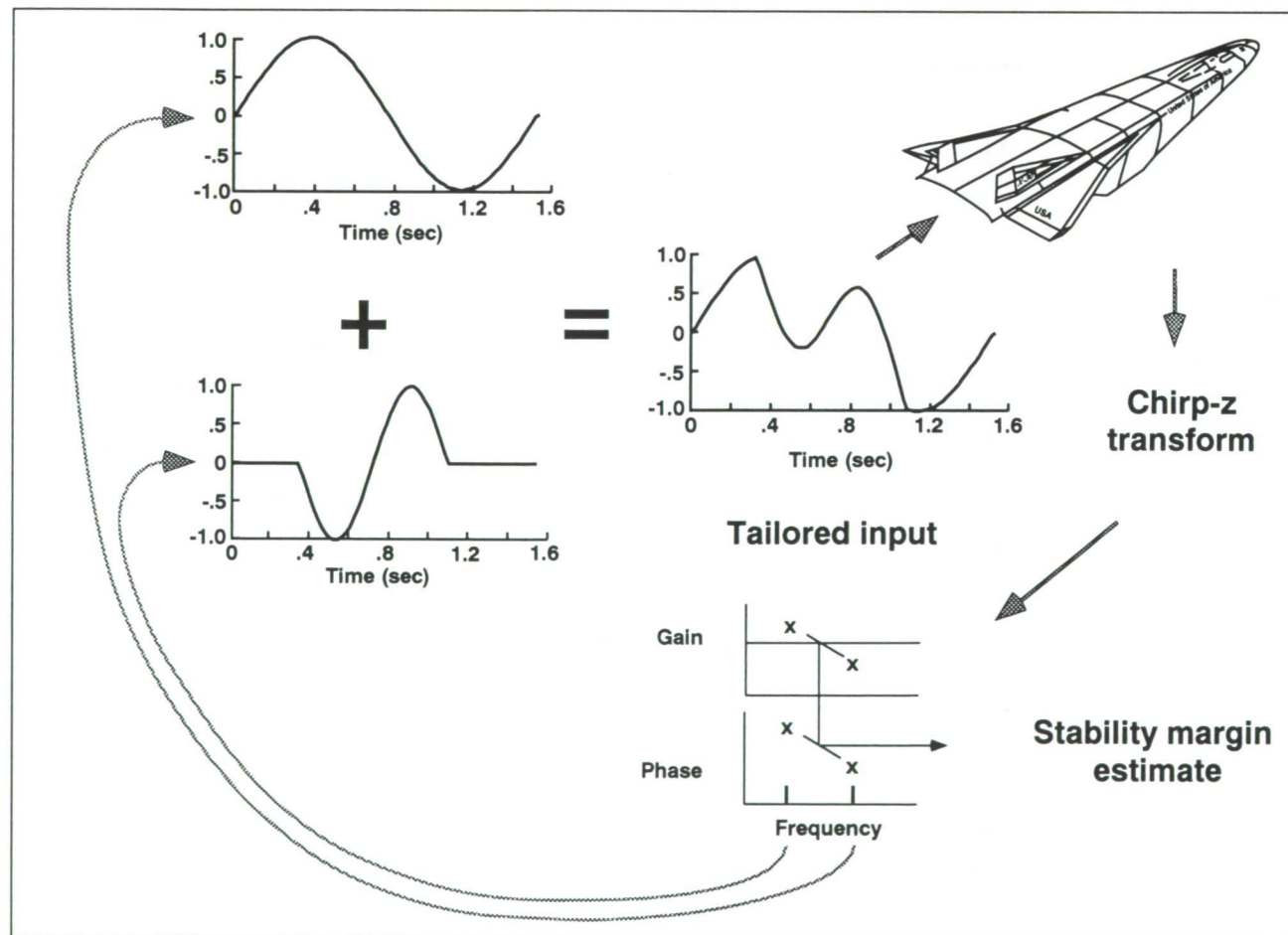


Fig. 1. Adaptive algorithm for estimation of stability margin.

which would cause quick changes in vehicle weight and inertias.

Previous real-time flight-control clearance techniques relied heavily on frequency domain techniques which required a frequency sweep input of greater than 50-second duration. This longer input provided gain and phase information over a large range of rigid-body frequencies. From this data, gain and phase margins were calculated. The fast Fourier transform (FFT) technique was used to process the data. The FFT calculations and display of information were accomplished in seconds. The time required for the frequency sweep input is what makes this technique impractical for the NASP. MIMO systems require multiple inputs and therefore more time, which is already a problem because of the non-steady-state nature of the vehicle.

The effort to reduce the required input time resulted in a tailored input (see figure), which contains only frequencies critical for calculating the system stability. These inputs were about 1.5 seconds in

duration. For a single-input, single-output system, the signal would contain two frequencies on either side of the expected crossover frequency. Linear interpolation could be used to obtain an estimation of the stability margin. For MIMO systems, three points would be used to obtain an estimation of the minimum singular value. A chirp-z transform can be used to evaluate only the desired frequencies, thereby reducing the computation time required. If the crossover (or minimum) does not occur within the expected frequency range, then the input can be adjusted to obtain a better estimate of the stability margin. With the short-duration input, it is also possible to make measurements of the nonlinear effects using varying amplitudes. This new system could provide a flight-control clearance technique for the NASP.

Ames-Dryden contact: J. Bosworth

(805)258-3792

Headquarters program office: OAST

Determination of Thrust-Vectoring Effectiveness on Jet Aircraft by Infrared Photography

Albion H. Bowers, Larry D. Birkelbaw

Maneuverability of current- and future-generation fighter-type aircraft has increased greatly in recent years. Many future fighter designs are taking advantage of thrust vectoring for maneuverability in the high-angle-of-attack regime and for maneuver enhancement at low angles of attack. The NASA F-18 high alpha research vehicle (HARV), thrust-vectoring control system (TVCS) aircraft is being used to evaluate the capabilities of this technique.

A highly detailed model of the thrust-vectoring effectiveness was required for the control-law design and simulation work. The simulation model data were developed from wind-tunnel tests by using scale models. A ground test of the full-scale aircraft was conducted to quantify the differences between the aircraft installation and the wind-tunnel models. A new infrared imaging technique was used to evaluate the vectoring effectiveness.

The aircraft was tied down on a thrust stand during the tests. Digitized infrared photographs were taken during the test in the tailpipe exit plane, approximately 30 to 50 feet from the aircraft centerline. This system captured images, stored the infrared intensities (in the 3- to 5- and 8- to 12-micrometer wavelength regions), and stored the data digitally. The data was then transferred to a workstation and analyzed. This technique worked most effectively for the 8- to 12-micron wavelength region, although results were nearly as satisfactory with the 3- to 5-micrometer wavelength data. All images were 70 pixels by 140 pixels. The data were stored at 12.5 frames per second. The images were later viewed for undeflected- and vectored-thrust conditions. The frames that showed that steady conditions had been reached were then averaged for a composite frame of the infrared intensity. A cutoff intensity was

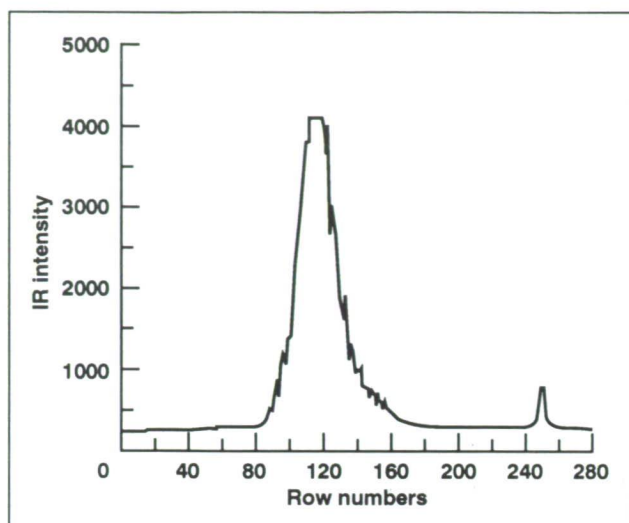


Fig. 1. Column-weighted-average plume path for infrared image.

set to provide a threshold for removing the ambient infrared.

Another routine was used to produce weighted averages along the vertical rows of pixels from the images. In the figure, the plume is centered about row 120; the threshold value used was approximately 300. Once the weighted average of the vertical rows of pixels was determined, the points were plotted to

reveal the path of the exhaust plume. Two images were needed for each point: a control image with no vectoring, and a vectored image. The vectoring effectiveness for the particular test point is determined as the difference between the two. Initial evaluations showed good correlation with wind-tunnel results.

Full-scale aircraft results differed from the wind-tunnel results by approximately 15 percent at large deflections. These variations may be explained by the differences between cold wind-tunnel and hot aircraft gas flows, geometry differences between the model and the aircraft, or scaling differences.

The F-18 HARV TVCS used post-exit vanes to deflect the exhaust stream after it emerged from the tailpipes of the engines. This ground-test technique will also work on more sophisticated designs such as gimballed nozzles. Proposed follow-on work is being evaluated for imaging of the exhaust plumes during vectored maneuvers in flight and in cold jet studies on the ground for a thorough evaluation in more diverse environments.

Ames-Dryden contact: A. Bowers
(805)258-3716

Headquarters program office: OAST

Flight-Determined Stability Margins for Multiloop Control Systems

John J. Burken

Advanced, statically unstable aircraft are being designed with a high degree of stability augmentation to ensure enhanced flight-control performance. The computation of stability margins during flight became a necessity during the envelope expansion of the X-29A aircraft, and a real-time stability assessment technique was developed for the longitudinal control axis.

Stability margins for the traditional single-input, single-output control systems have been used routinely since the 1940s. However, the method to evaluate a quantitative measure of robustness of modern multiple-input, multiple-output control systems became available only recently. A measure

of stability is determined by using scaled or structured singular-value analysis. The approach computes the transfer function for each loop in the return difference matrix. Computing the singular values at many frequencies measures the robustness of the control system.

Flight data were collected for the X-29A lateral-directional multiloop control system at various flight conditions. A series of fast Fourier transforms was then performed to generate the transfer functions needed for the analysis, and the structured singular values were computed (see figure). Similar analyses were performed using the X-29A simulation models to

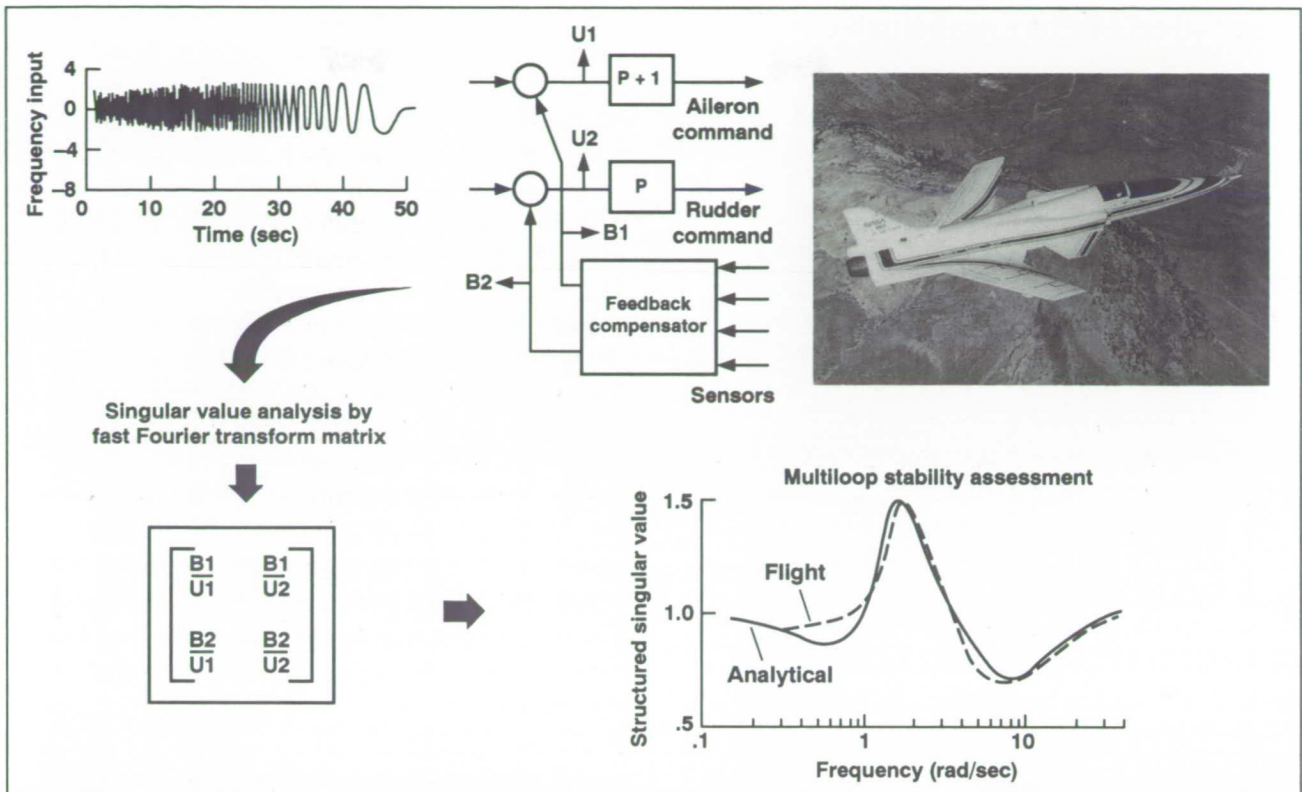


Fig. 1. Flight-determined multivariable stability analysis.

predict stability margins. Data analyses comparing predictions with actual measured data showed good correlation.

Extracting multiloop singular values from flight data and using the data as a measure of robustness validates the application of this technique. This validation extends the single-loop gain and phase margin concepts for stability assessments to multiloop control systems. These multiloop stability assessment techniques will be used to display the analytical and

flight-measured results in a control room during flight. This on-line stability assessment technique will greatly reduce the time required to expand the flight envelope of advanced aircraft.

Ames-Dryden contact: J. Burken
(805)258-3726

Headquarters program office: OAST

Automated Flight Qualification

Vince Chacon

Researchers at the Ames-Dryden Flight Research Facility are studying the application of automated flight-qualification techniques for performing closed-loop validation of human-rated flight-control systems. Flight-test experiences from the first digital fly-by-wire aircraft (through the X-29A forward-swept-wing aircraft) have repeatedly demonstrated the need for an integrated design, development, and test environment for highly integrated flight-control systems. Automated testing techniques are being developed to reduce the time and cost of flight-qualifying complex, embedded digital flight systems on aircraft.

New levels of automation were used to flight-qualify the F-18 high alpha research vehicle (HARV) flight-control systems (see figure). Computer-aided

systems testing techniques were used to efficiently link the systems test engineer with the simulation and cockpit displays and controls, the iron-bird test hardware, and the actual vehicle systems. The development of (1) a test scripting language, (2) closed-loop control of the testing environment, (3) graphical user interfaces, and (4) quick-look monitoring displays were emphasized to add automation to the tester's decision-making capabilities.

These features have enabled the F-18 HARV project to test the new and modified on-board systems more efficiently by reducing human error and increasing the accuracy and repeatability of test results. Tests that previously had taken weeks to accomplish can now be done in a few hours.

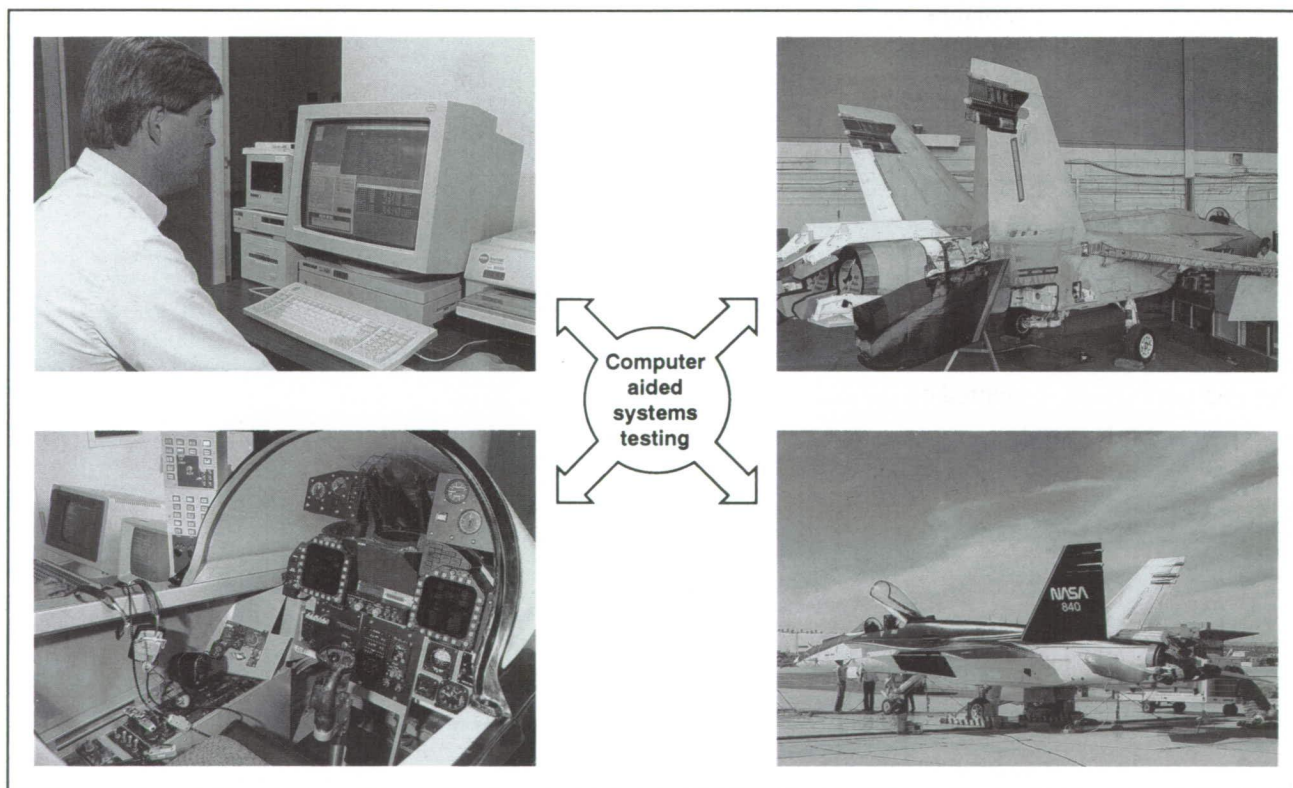


Fig. 1. Automation used to flight-qualify the F-18 high alpha research vehicle.

ORIGINAL PAGE
BLACK AND WHITE PHOTOGRAPH

Operational experiences in developing and using these automated testing techniques have highlighted the need for incorporating certain testability features into newly developed flight systems. Research is continuing on methods of further integrating the simulation, and on on-board and test systems to

further improve automated flight-qualification technologies.

Ames-Dryden contact: V. Chacon

(805)258-3791

Headquarters program office: OAST

X-29 Aerodynamic Characterization

David F. Fisher, John H. Del Frate

In September 1991, the X-29 forward-swept-wing airplane finished a series of high-angle-of-attack aerodynamic characterization flights that focused on the vortical flows on the forebody and on the separated flow on the wing and the vertical tail. The purpose of these flights was to determine if the forebody vortical flow could explain some differences between the predicted high-angle-of-attack flying qualities and the flight results. For example, at an angle of attack (α) of 45 degrees, the airplane has a nose-right yaw asymmetry that switches to nose left at $\alpha = 50$ degrees. Both flow-visualization and pressure measurements were used to define the forebody vortical flows. Smoke emitted from ports near the nose apex was used to visualize and track the vortices shed by the forebody—in particular by the forebody strake. The flow visualization was documented with video and still cameras mounted on the right wingtip



Fig. 1. Example of smoke entrained in forebody vortices as viewed from wingtip camera.

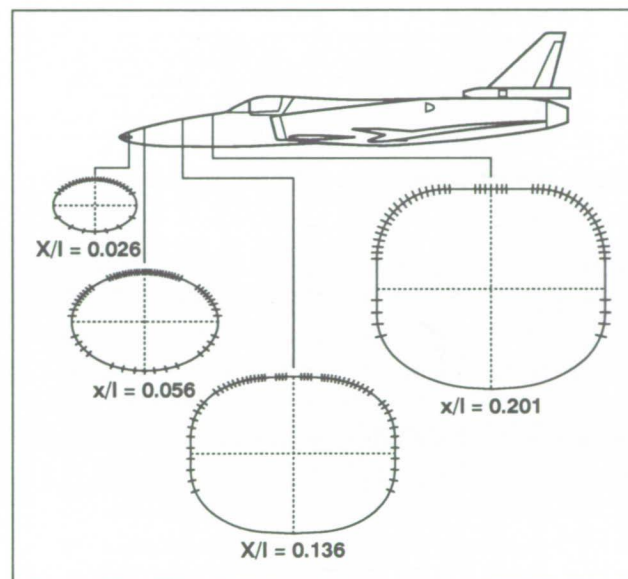


Fig. 2. Locations of pressure orifices on the X-29 forebody.

and at the base of the vertical tail. For selected flights and test conditions, a photo chase plane was also used.

An example of the forebody smoke-flow visualization is shown in the first figure for $\alpha = 48$ degrees and sideslip angle (β) = -6 degrees. The vortical flows on the X-29 were not as tight and coherent as those seen previously on the F-18 high-alpha-research-vehicle leading-edge extensions. This result is probably due to the effect of the noseboom and the interaction of the strake and forebody flows. As can be seen in this case, the vortices are asymmetric—the

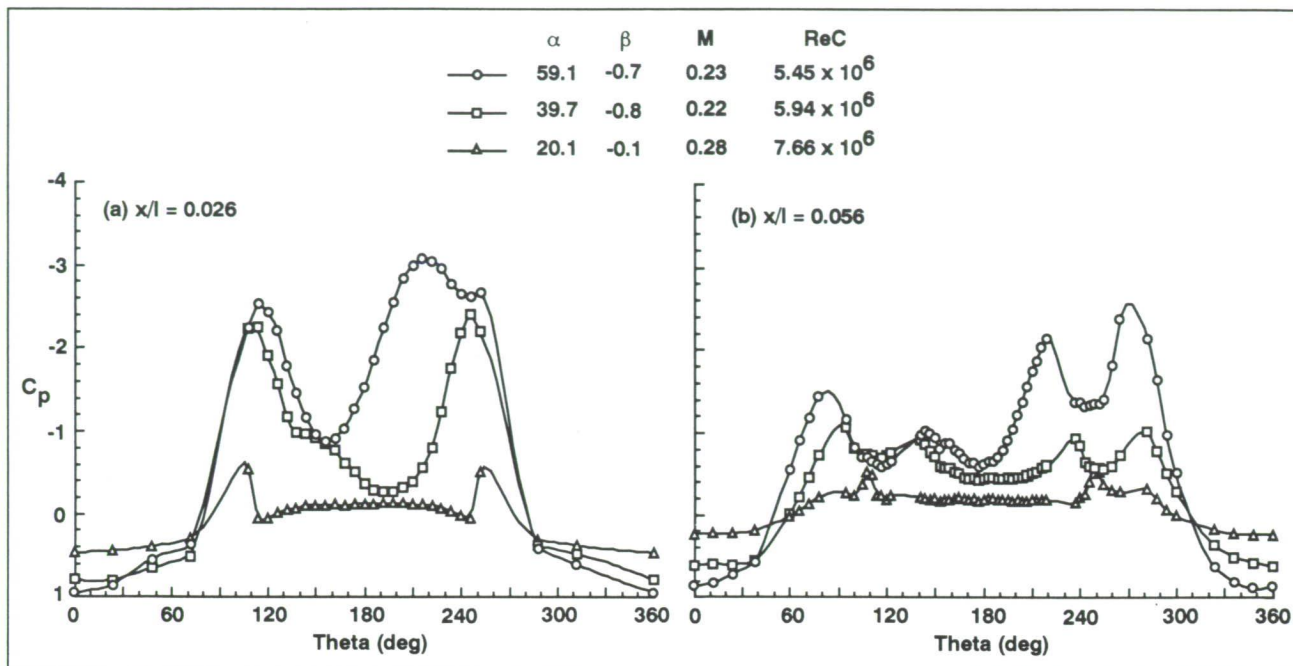


Fig. 3. Forebody pressure distribution as a function of circumferential angle, θ .

right vortex is higher than the left, as a result of sideslip.

The fuselage forward of the cockpit was extensively instrumented with surface-pressure measurements, as shown in the second figure. Four circumferential rows of static pressure orifices were installed at $x/l = 0.026, 0.056, 0.136$, and 0.201 . Pressure distributions on the forebody were obtained at $\alpha = 15$ – 67 degrees during “1-g” quasi-steady-state

flight conditions. Data were also obtained in wind-up turns at $\alpha = 15$ – 40 degrees for Mach numbers up to 0.6 .

Sample pressure-coefficient data from the forebody are plotted as a function of radial location, θ , in the third figure. At $\alpha = 20$ degrees and above, the effect of a pair of forebody-strake vortices was indicated by a sharp suction peak in the pressure distributions at $x/l = 0.026$. These suction peaks generally increase in magnitude with angle of attack. Typical asymmetries in the pressure distributions can be seen at $\alpha = 39.7$ degrees and above at $x/l = 0.026$ and at $\alpha = 59.1$ degrees for $x/l = 0.056$.

The forebody pressure coefficients were integrated over the projected side area, and the forebody yawing-moment coefficients were determined. The forebody and total-aircraft yawing-moment coefficients at zero sideslip are presented as a function of α in the fourth figure. As shown, the right yawing moment at $\alpha = 45$ degrees is not due to the forebody side forces; however, at $\alpha \geq 50$ degrees, a significant portion of the left yawing moment is due to the forebody side forces.

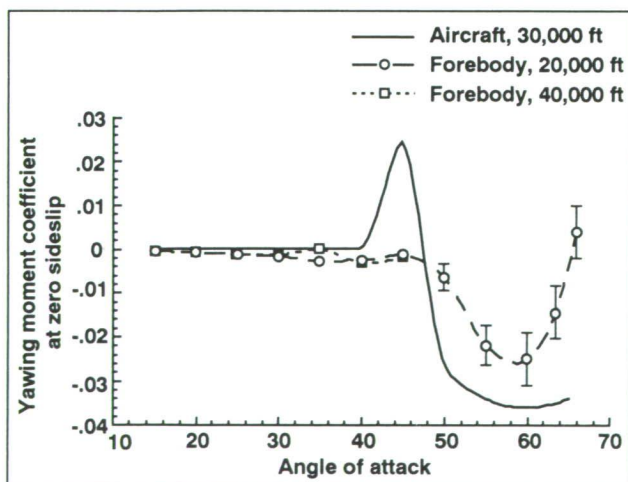


Fig. 4. Comparison of X-29 aircraft and forebody yawing moment coefficients at zero sideslip.

Ames-Dryden contact: D. Fisher

(805)258-3705

Headquarters program office: OAST

Supersonic Flight-Test Verification of Phase Reversal

Robert J. Geenen, Bianca T. Anderson

The F-16XL supersonic laminar flow experiment recently documented successful active laminar flow control at supersonic speeds. The aircraft is equipped with a special fluted-wing-glove test section with a perforated titanium surface (first figure). The surface of the test section has millions of tiny laser-drilled holes which make it porous. A turbocompressor draws air through the porous surface to reduce the boundary-layer thickness and promote extended laminar flow. Hot-film anemometers are used to determine the state of the boundary layer. Hot films measure high-frequency velocity fluctuations on the surface of the test section. Small-amplitude fluctuations in velocity indicate laminar flow, whereas large fluctuations indicate turbulent flow.

The F-16XL project has been using commercially available hot-film sensors that consist of a thin nickel element deposited on a thin capton (plastic) patch. Each 0.5- by 0.6-inch patch contains one sensor and is glued to the surface at the desired measurement point. Adjacent to the hot film is a temperature-compensating resistor that allows the anemometer driving the hot film to adjust to large ambient temperature changes. Recently, the Langley Research Center (LaRC) developed their own custom hot-film sensors. The LaRC sensors are produced with multiple

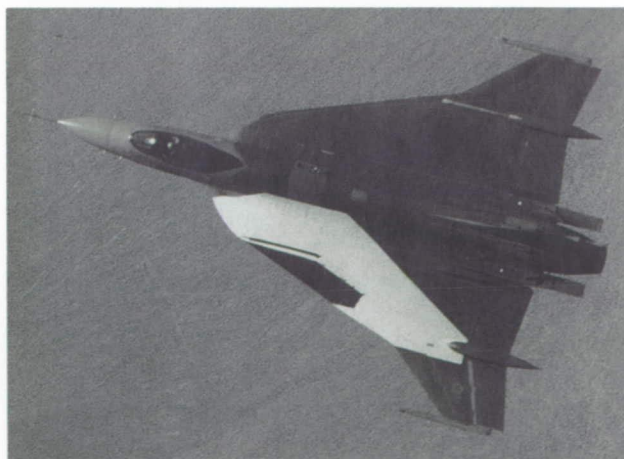


Fig. 1. F-16XL with wing glove.

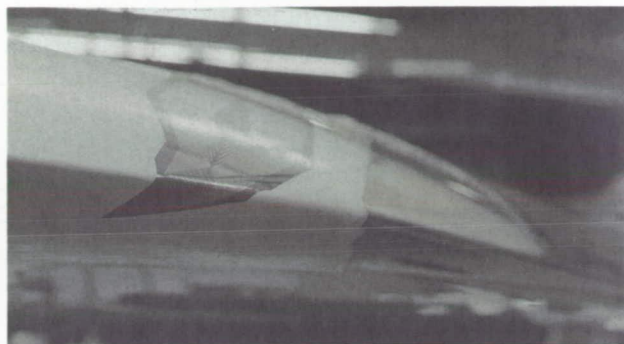


Fig. 2. Langley Research Center hot-film sheet.

closely spaced hot films on a single capton sheet. These sheets include built-in temperature compensating resistors. The advantage of the LaRC sheets is that they allow as many as 20 point measurements within 1 inch.

Wind-tunnel tests using closely spaced hot-film sensors were conducted to find the exact location of the stagnation point on a cylinder. When the stagnation point lies between two sensors on the sheet, the time histories of those sensors are 180 degrees out of phase. To see the phase shift, a disturbance must be present in the signals. This disturbance must appear in the spectrum of both signals at a fixed frequency for an extended period of time. If the time history is low-pass filtered below the disturbance frequency, the phase reversal does not appear. If the data is filtered above the disturbance frequency, the phase reversal is clearly evident. In the case of the wind tunnel test, the disturbance was most likely caused by the tunnel itself. The question was whether there would be a disturbance in flight sufficient to allow phase reversal to be detected.

An experiment was conducted as a follow-on to primary testing on the F-16XL ship 1. This test used an LaRC hot-film sheet containing 20 sensors mounted on the leading edge of the wing (second figure). A

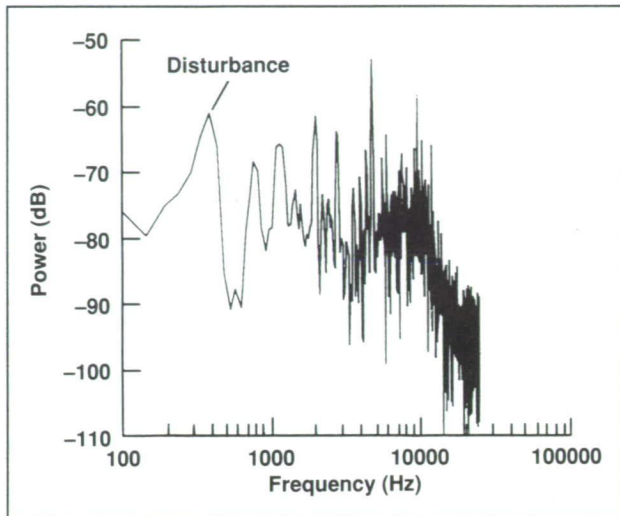


Fig. 3. Spectrum of hot-film signal.

phase reversal would indicate the location of the stagnation point at that span station. The spectrum from one of the test points is shown in the third figure. This plot shows a disturbance at 390 hertz. The fourth figure shows the time histories filtered with a cutoff frequency above and below the disturbance frequency. The phase reversal is evident when the time history is properly filtered.

The phase reversal was not consistent for varying flight conditions. A disturbance must be present to detect phase reversal, which is not always the case during a flight experiment. However, once refined, this technique could have many applications. Aside from being used to map the attachment-line movement on a wing leading edge, phase reversal could be used to map vortex-impingement footprints on forebodies or vortex flaps. Vortex-impingement

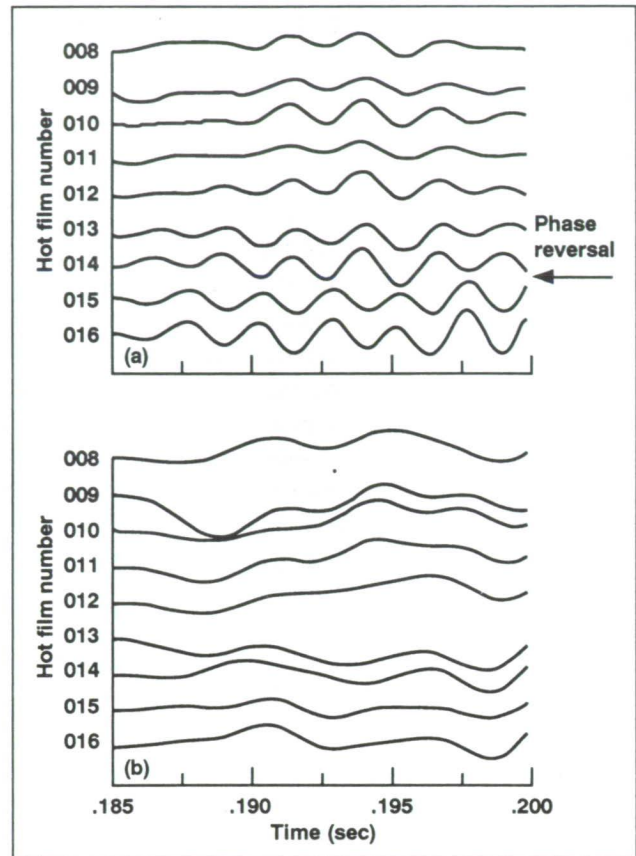


Fig. 4. Time history with low-pass filter, (a) at 450 hertz, (b) at 300 hertz.

mapping is currently the subject of a Director's Discretionary Fund study.

Ames-Dryden contact: R. Geenen
(805)258-2265

Headquarters program office: OAST

Performance-Seeking Control Flight Results

Glenn Gilyard

Improvements in propulsion-system performance can be achieved by the use of sophisticated control algorithms designed to extract the full performance potential of the propulsion system. The Dryden Flight Research Facility has developed, flight tested, and evaluated a performance-seeking control (PSC) algorithm that optimizes the propulsion performance during quasi-steady-state maneuvers by applying trims to the propulsion system. The engine trim values are determined from an on-board, adaptive, real-time optimization process. The PSC methodology, illustrated in the first figure, consists of estimation, modeling, and optimization processes. The estimation

process uses a Kalman filter to estimate five component deviation parameters. These parameters are designed to account for the off-nominal behavior of the engine during flight. The second step formulates and uses the compact propulsion-system model to estimate unmeasured engine outputs required to obtain an optimal solution. The third step uses linear programming to obtain the optimal solution based on the estimates of the unmeasured variables and constraints. Flight testing on the Dryden F-15 Highly Integrated Digital Electronic Control airplane to date has covered the subsonic flight envelope and has included the full throttle range.

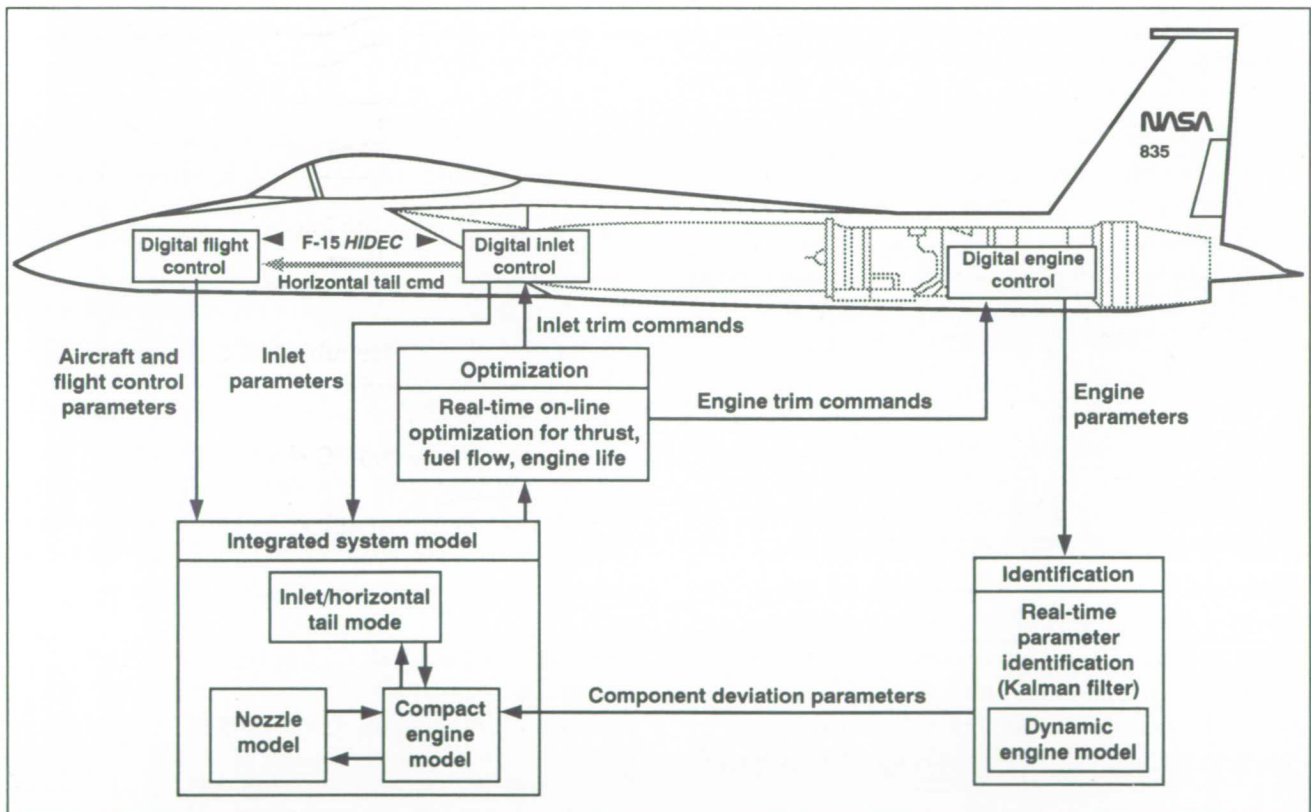


Fig. 1. Simplified block diagram of the performance-seeking control system on the F-15 airplane.

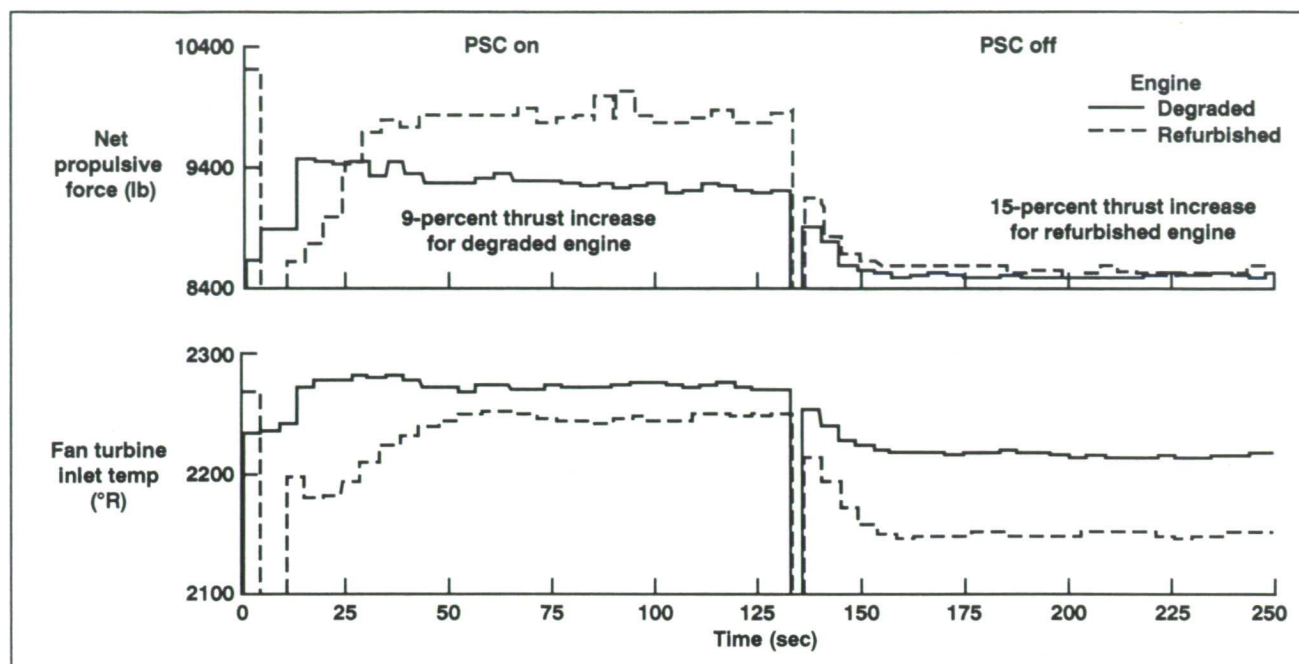


Fig. 2. Adaptive benefits of the PSC algorithm for a degraded and a refurbished engine (military power cruise at Mach 0.90 and 15,000 feet).

The maximum-thrust mode is designed to maximize net propulsive force (FNP) at military or maximum afterburner power settings. The maneuver flown consisted of stabilizing the aircraft at the desired flight condition (the throttle of the nontest engine was varied as required). The flight data in the second figure were obtained first with PSC on, then with PSC off. This maneuver was conducted separately for a degraded engine (left side) and a refurbished engine (right side). For the degraded engine, PSC improved the maximum thrust obtainable by 9 percent. PSC increased the thrust of the refurbished engine by 15 percent. In addition to these significant thrust increases, the PSC algorithm adapted the different engine health conditions to maximize thrust. The degraded engine operates hotter to obtain a given level of thrust with PSC off. In the degraded-engine case, with PSC on, the engine has reached a maximum

temperature limit (≈ 2270 degrees Rankine) which in turn limits the thrust increase available. The thrust increases demonstrated would be advantageous in situations such as combat or an engine failure.

A qualitative evaluation of the major modes of operation indicate that the algorithm performed as designed. The system dynamics of the closed-loop algorithm appear to be good. The subsonic flight phase has provided a general validation of the PSC technology objectives. It is clear that PSC technology can provide significant benefits to the next generation of fighter and transport aircraft. Upcoming flight phases will evaluate supersonic PSC operation.

**Ames-Dryden contact: G. Gilyard/B. Burcham
(805)258-3724/3126**

Headquarters program office: OAST

Airborne Instrumentation Computer System

Paul Harney

The Dryden Flight Research Facility has developed a flexible airborne instrumentation computer system (AICS) that incorporates a unique type of microprocessor called a transputer for enhanced measurement and data-handling capabilities on board research aircraft. While it relies on standard-instrumentation recording techniques for most data, the AICS provides additional monitoring and computational features that greatly increase overall data system effectiveness. Through the parallel-processing features of transputer architecture, the AICS provides a rapid and extensive capacity for solving varied types of instrumentation problems with software control and a minimum of hardware modification.

One successful use of the AICS has been to interface avionics data-bus formats to the aircraft pulse-code-modulation (PCM) data system by the AICS acting as the bus controller. In this manner, the two sources of information can be merged and transmitted as one data stream. This method has been used on F-15 and F-16XL engine test programs and most notably for the F-104 Optical Airdata System demonstration of laser-sheet-pair-derived airspeed. Another important use of AICS was in a project to

investigate the feasibility of using high-performance jet aircraft to obtain high-altitude wind data in support of space shuttle launches. As part of the experiment, real-time on-board calculations of air data parameters were required for comparison to ground-based postflight computations. The AICS was able to perform these calculations easily by taking raw air-pressure data from the existing PCM system and, in the merging process described, making the necessary calculations and inserting the results into the transmitted data stream.

The AICS is considered to be an interim system to meet rapidly expanding flight-research instrumentation and data requirements, and, in fact, is considered to be "phase one" of an airborne information management system which will feature extremely high-speed computations such as digital filtering, data compression, and time-domain-to-frequency-domain conversion.

**Ames-Dryden contact: P. Harney
(805)258-3803**

Headquarters program office: OAST

Systems-Research Testbed Aircraft

Dave McBride

The Dryden Flight Research Facility is developing a modern systems-research testbed aircraft to permit rapid response to flight-research experiments and new-technology test needs. This testbed aircraft will be capable of supporting component disciplinary experiments in a timely and cost-effective way. It will provide flight-test capabilities to support NASA-developed flight-systems research experiments as well as other government-agency- or industry-developed advanced concepts.

Multiple experiments are being integrated on a two-seat F-18 aircraft configured for systems research and support. Advanced actuator technology is being developed in a joint NASA/Air Force/Navy activity, and evaluation criteria for validation of new actuators are being established. Planned activities include a composite actuator and the electrically powered actuator design program, which includes smart-actuator, electromechanical-actuator, and electrohydrostatic-actuator development programs. A fiber-optic-control-system-integration experiment is also in development jointly with Lewis Research Center and industry. Advanced fiber-optic engine and aircraft sensors will be flight tested. The integration of

a flush air data system is also planned for the vehicle to investigate miniaturized sensor technology and advanced real-time compensation algorithms.

This testbed aircraft will provide the platform for advanced systems-research experiments to exploit "open-systems" architectures that incorporate advanced memory-reflecting concepts for on-board applications. These applications are currently being developed under the Small Business Innovative Research program. The Airborne Research Transputer System is an innovative airborne avionics concept that brings advanced technology to flight applications. This activity will provide an economical, flightworthy chassis that will allow rapid integration of new open-systems concepts. Other potential experiments include the development of advanced flutter-excitation systems and flight research that involves advanced displays.

**Ames-Dryden contact: D. McBride
(805)258-3681**

Headquarters program office: OAST

Thrust-Vectoring Research

Joseph W. Pahle

The objective of this research is to develop effective methods for integrating thrust-vectoring control with aerodynamic surfaces to aid in control-system design and optimal use of integrated propulsion-aero control power. Flight tests using thrust-vectoring control have recently begun on the F-18 high-angle-of-attack research vehicle.

First-generation thrust-vectoring control systems commonly use paddles or vanes located around the engine nozzle to deflect the thrust exhaust plume. The performance of the thrust vanes is a complex relationship that is dependent on gross thrust, nozzle exit

radius, nozzle pressure ratio, and on the other vanes that surround the engine. A mathematical model of the vane performance was developed from a single-engine cold-jet test conducted at Langley Research Center. Static ground tests were performed on a thrust stand to verify design load limits and to compare thrust-vectoring performance to the cold-jet results for fixed vane positions. Axial thrust loss caused by vectoring was measured directly from the thrust stand. Since normal and side force were not available from the thrust stand, infrared video was used to indicate the amount of thrust deflection achieved (see figure).

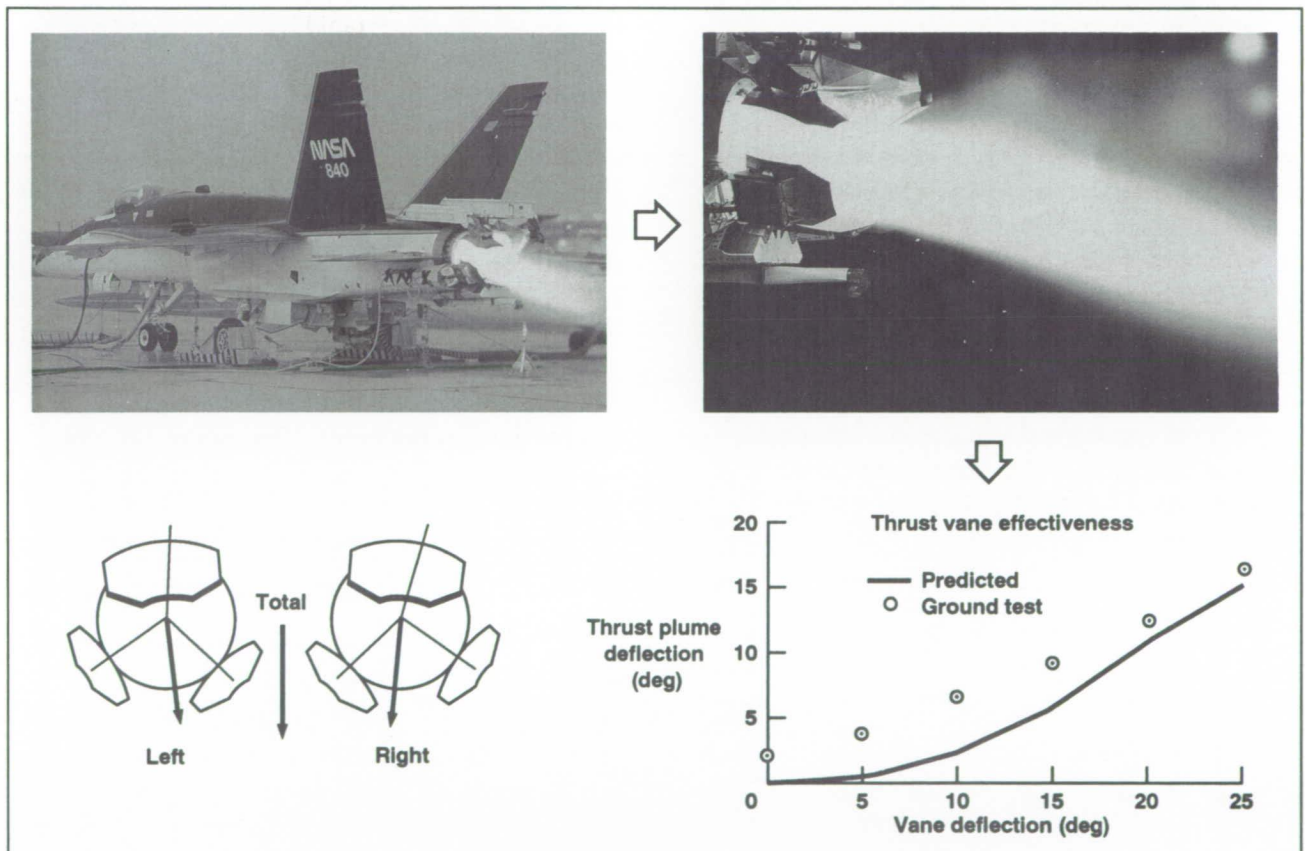


Fig. 1. Thrust-vectoring research.

ORIGINAL PAGE
BLACK AND WHITE PHOTOGRAPH

Preliminary analysis indicates that throughout the vectoring range actual thrust vectoring is greater than that predicted.

To coordinate the six vanes in flight, a vane mixer was developed from the cold-jet model. The mixer uses pitch and yaw vectoring commands from the control laws, as well as gross thrust and nozzle exit radius from the engine, to determine the vane deflec-

tions required. The mixer is currently in flight-test evaluation. Flight data will be used to refine the thrust-vectoring system model and to update the mixer.

**Ames-Dryden contact: J. Pahle
(805)258-3185**

Headquarters program office: OAST

In-Flight Structural Excitation

Lura E. Vernon

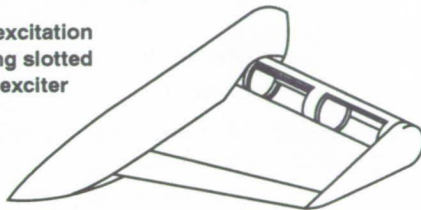
To verify that the desired flight envelope of new and modified research aircraft is free of aeroelastic instabilities, flight flutter testing is usually done. Flight flutter testing consists of determining the aircraft's dynamic stability by evaluating the structural dynamic/aeroelastic response caused by some form of structural excitation. The success and efficiency of this process depends on many interrelated factors, but the most important factor is the achievement of consistently adequate structural excitation. The objectives of this research are to develop a self-contained, strap-on exciter that is independent of other aircraft systems and requires low electrical power for operation, and to provide structural-response data of sufficient quality that stability

analysis can be accomplished with more confidence and fewer errors.

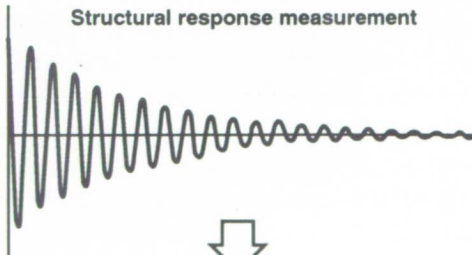
An experimental exciter has been designed and built by Dynamic Engineering, Inc. This exciter is an airfoil with a rotating slotted cylinder attached to the trailing edge (see figure). A series of flight-test experiments have been defined for the F-16XL airplane to acquire data on the response to structural excitation in the subsonic, transonic, and supersonic flight regimes. The F-16XL airplane has been instrumented with accelerometers to measure the structural response of the wings, vertical stabilizer, and fuselage to excitation provided by the exciter. The exciter has been



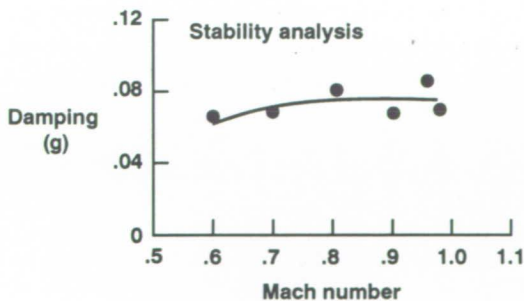
Structural excitation
Vane/rotating slotted
cylinder exciter



Structural response measurement



Stability analysis



flight qualified through environmental testing and has been installed on the airplane.

This research will greatly advance the safety in flight flutter testing and significantly reduce flight-test time. Successful development of the exciter will mean the realization of a complete strap-on structural excitation system that would be used regularly on research aircraft. The exciter will be flight-tested in the subsonic, transonic, and supersonic flight regimes.

Ames-Dryden contact: L. Vernon

(805)258-2337

Headquarters program office: OAST

Fig. 1. In-flight structural excitation.

Flight-Simulator Electric Control Stick

Charles A. Wagner, Michael D. Najera

An electrically powered, two-axis flight-simulator control stick and a complementary rudder pedal set have been developed at the Dryden Flight Research Facility. This stick-pedal system is a major upgrade of an older version that has been operational at Dryden for 20 years. Each axis of this new system uses a commercially available, rare-earth-magnet torque motor for force generation, and a potentiometer, a tachometer, and a torque transducer for feedback. The mechanical designs of the stick and pedal units were developed at Dryden for straightforward fabrication using common machine-shop techniques. The figures are photographs of the two-axis stick and the rudder pedals, respectively. With minor mechanical modifications, the two-axis stick can be converted into a wheel-column configuration, and toe brakes can be added to the rudder pedals. The stick shaft will accept a variety of aircraft hand grips.

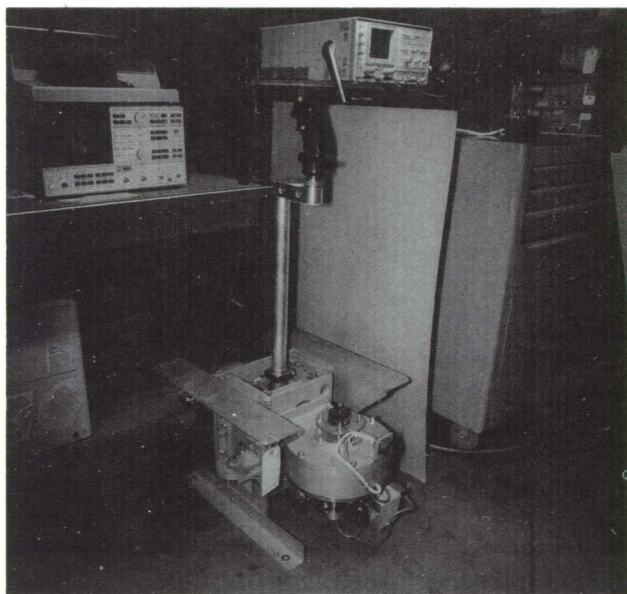


Fig. 1. Two-axis stick.

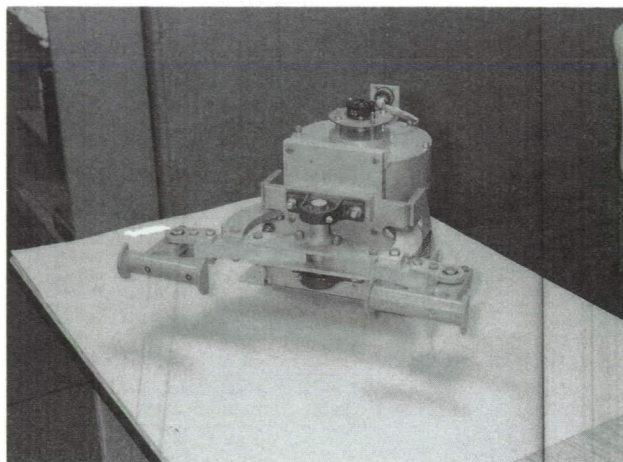


Fig. 2. Rudder pedals.

The accompanying electronics enclosure (one standard 19-inch rack) incorporates a processor system that provides real-time, digital input-output (I/O) communications with a host simulation computer, a readout of setup parameters or I/O parameters in engineering units on a terminal, and complete control over all force functions. For best performance, the internal servo loop uses analog circuitry. Analog I/O is available. The enclosure also contains all power supplies and power amplifiers required to operate the stick and pedals; the system is powered by 115 volts AC, 60 hertz at 30 amps maximum standard wall power.

The following functions have been implemented thus far: linear force gradient, breakout, damping, friction, travel limits, trim initial condition, trim rate, trim limits, rigid stick mode, and moving-nonmoving

trim. In addition, each axis will accept digital and analog force inputs from external sources. The magnitudes of the above functions can be scaled to use the full force, gradient, and travel limits of each axis. These limits are shown in the table.

Numerous safety features are incorporated to protect the system and the user. A soft-start feature applies force at a controlled rate when the system is first engaged. Each axis will shut itself down when any of the following occurs: failure of any power supply, motor overheating, potentiometer or tachometer failure, or any unsafe motion. To reduce the likelihood of a motor overheating, a circuit limits motor current to a progressively lower level as the motor approaches maximum temperature. When any shutdown occurs, the motor is shorted, providing an effective brake. An electronic latch shows the cause of any shutdown on a front-panel indicator.

Although it has not yet been implemented, there is software that can be used to generate nonlinear force gradients, change setup parameters in real time under host-computer control, and implement low-

Stick performance limits

Parameter	Pitch	Roll	Yaw
Minimum friction force, lb	0.14	0.17	0.7
Maximum force, lb	87	74	260
Maximum force gradient, lb/in. ^a	100	50	500
Maximum travel limits, in.	±8	±6.7	±4

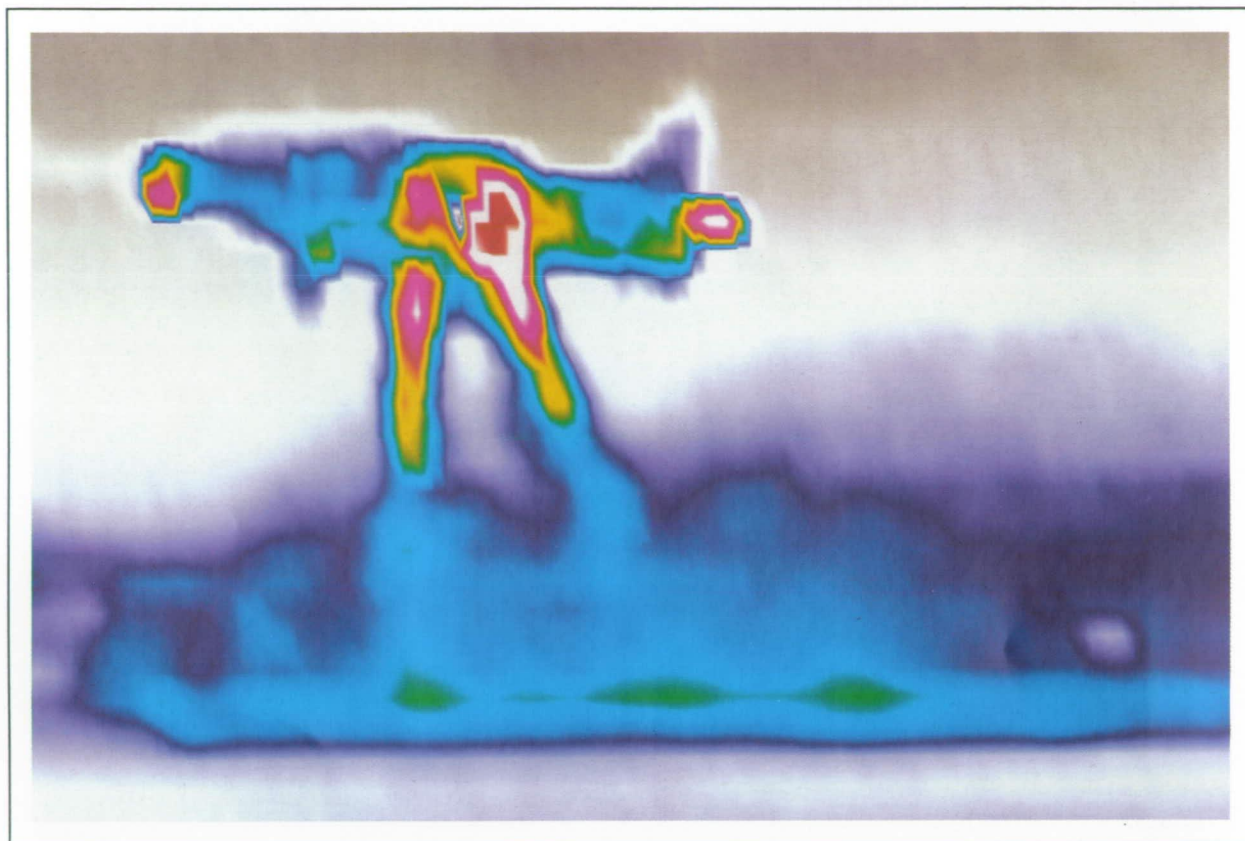
^aIncludes effects of mechanical deflections combined with the electrically-controlled gradient. Mechanical deflections dominate the deflections.

bandwidth servo-loop functions such as trim. These enhancements are planned as follow-on developments.

**Ames-Dryden contact: C. Wagner
(805)258-3781**

Headquarters program office: OAST

The color plates in this appendix correspond to black and white photographs in the text. Each caption provides the location of the corresponding photograph.

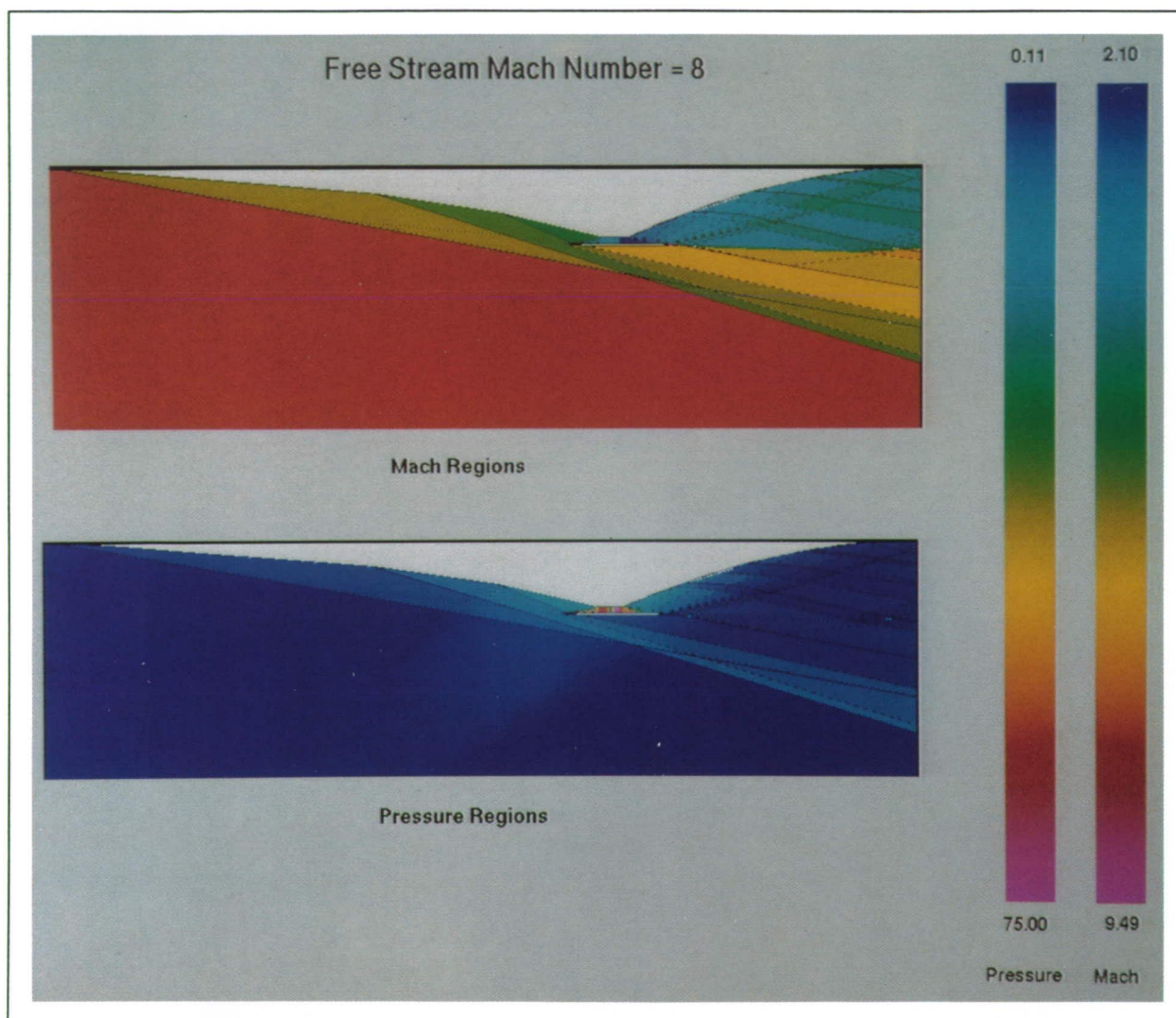


Color plate 1. Infrared flow visualization of YAV-8B Harrier aircraft. (fig. 1, page 1)

ORIGINAL PAGE
COLOR PHOTOGRAPH

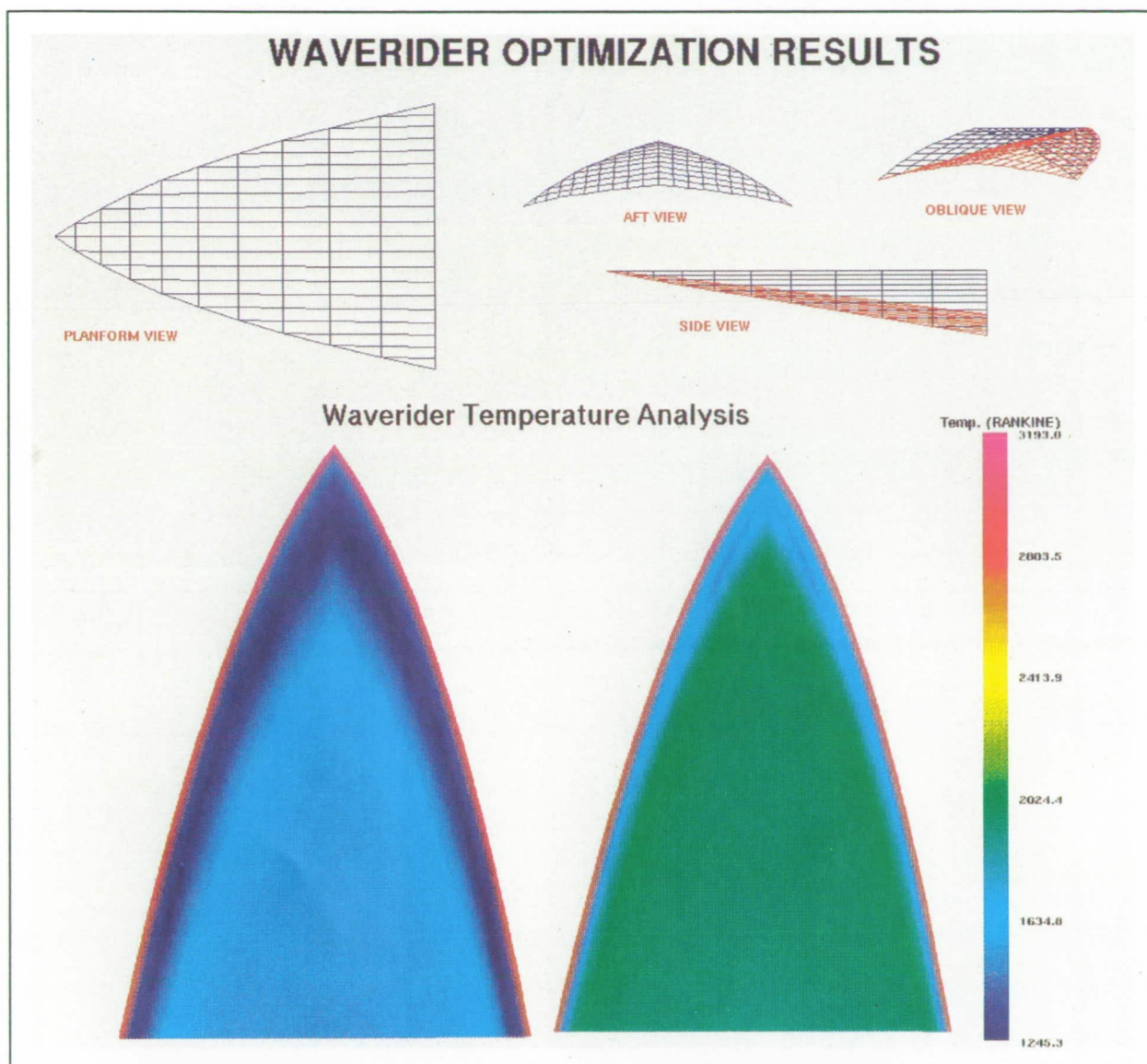
PRECEDING PAGE BLANK NOT FILMED

PAGE 304 INTENTIONALLY BLANK



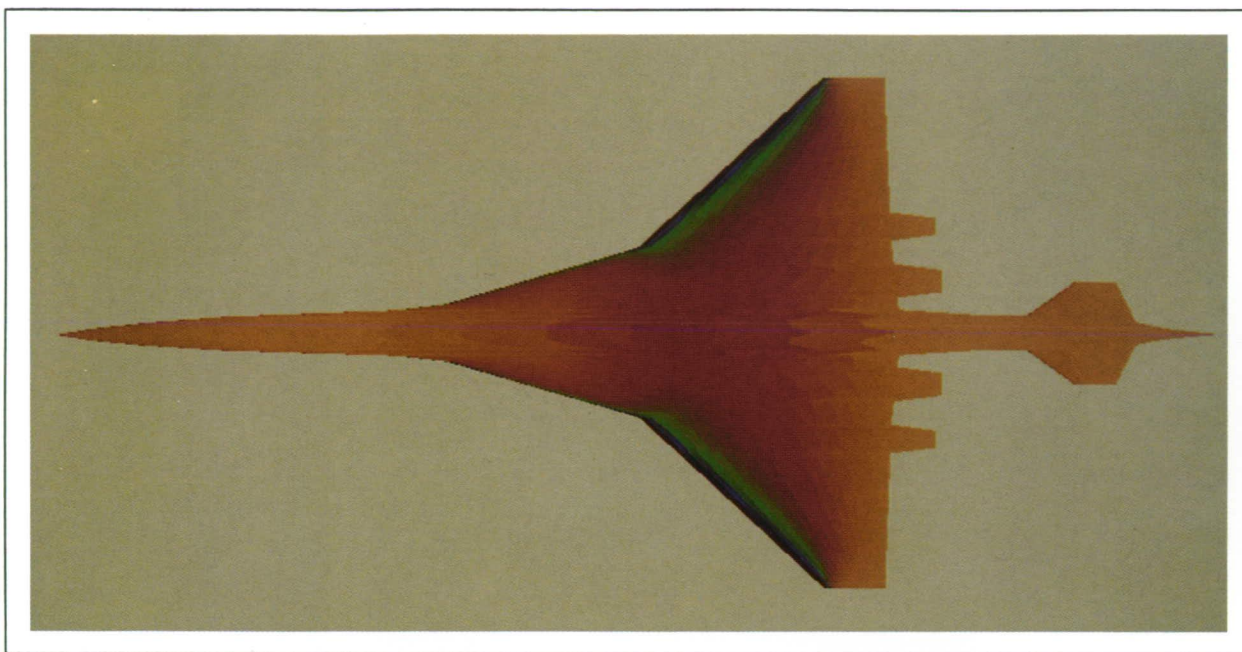
Color plate 2. Mach and pressure flow field nose to tail. (fig. 1, page 2)

ORIGINAL PAGE
COLOR PHOTOGRAPH



Color plate 3. Optimized Mach 8 Waverider general configuration and surface temperature distribution. (fig. 1, page 4)

ORIGINAL PAGE
COLOR PHOTOGRAPH

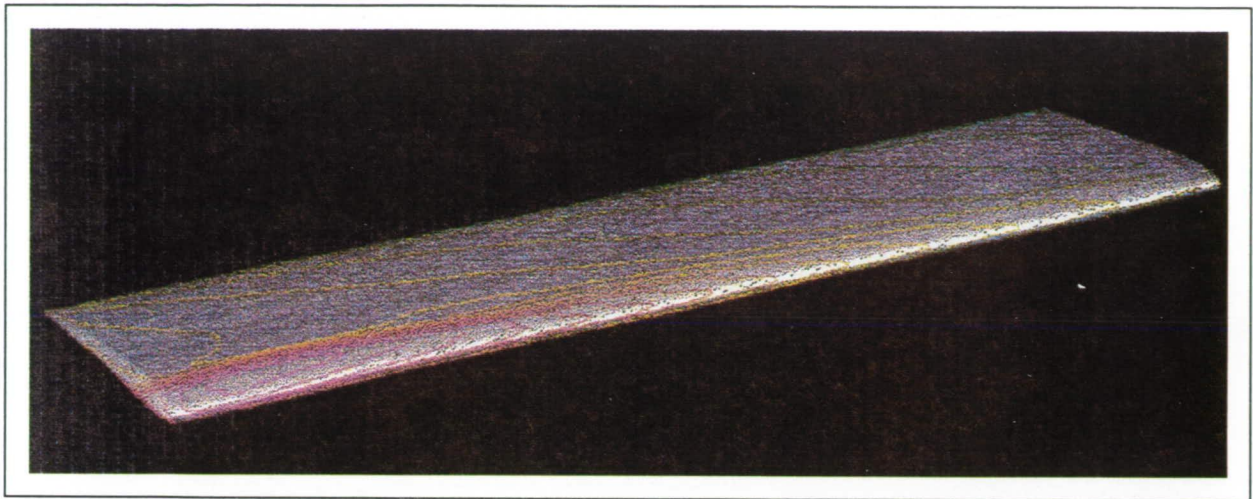


Color plate 4. Pressure distribution predicted using VORLAX. (fig. 2, page 12)

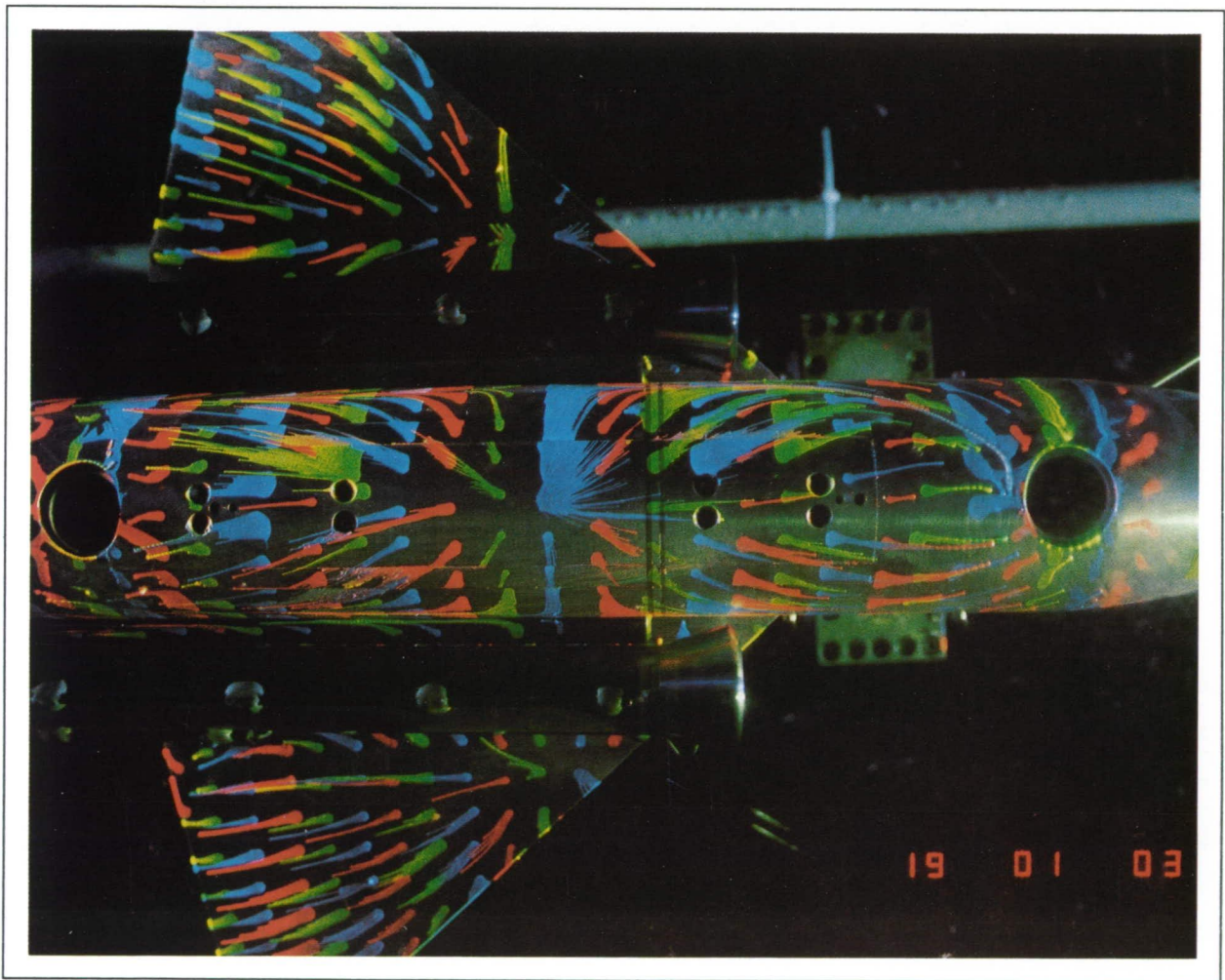
ORIGINAL PAGE
COLOR PHOTOGRAPH



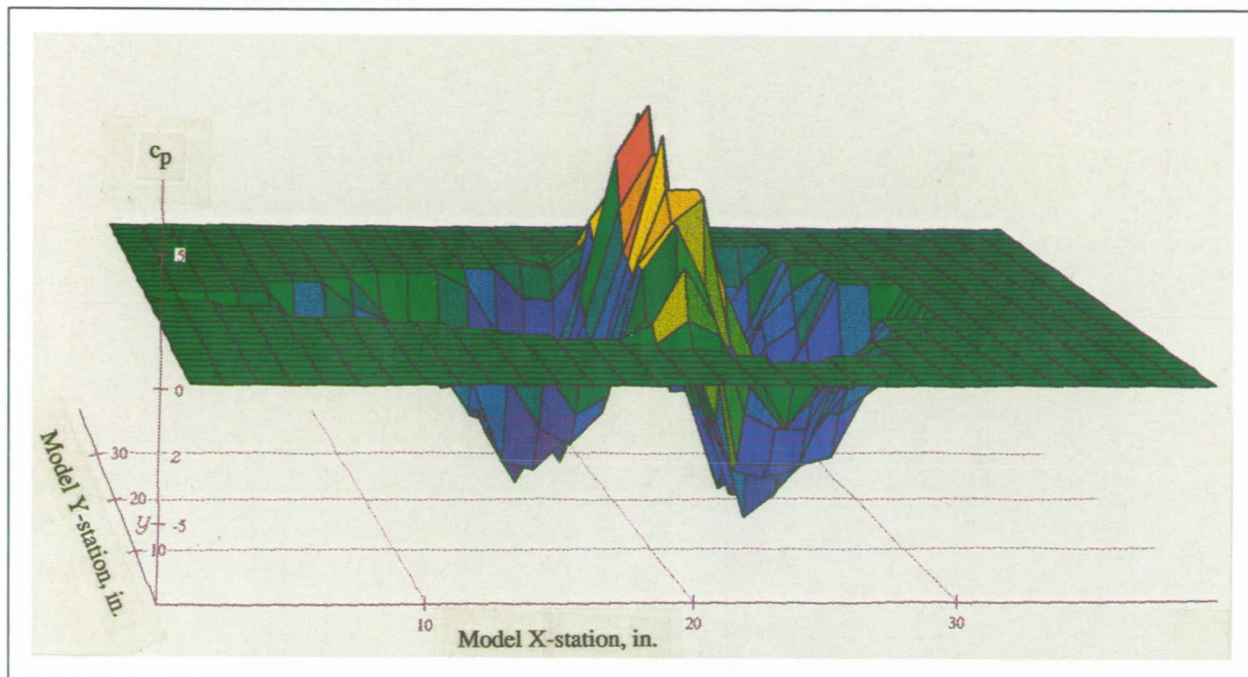
Color plate 5. Viewing foliage through the unassisted human eye (top) fails to reveal areas of plant stress that are highlighted (in red) when the passive chlorophyll detector is used. (fig. 2, page 16)



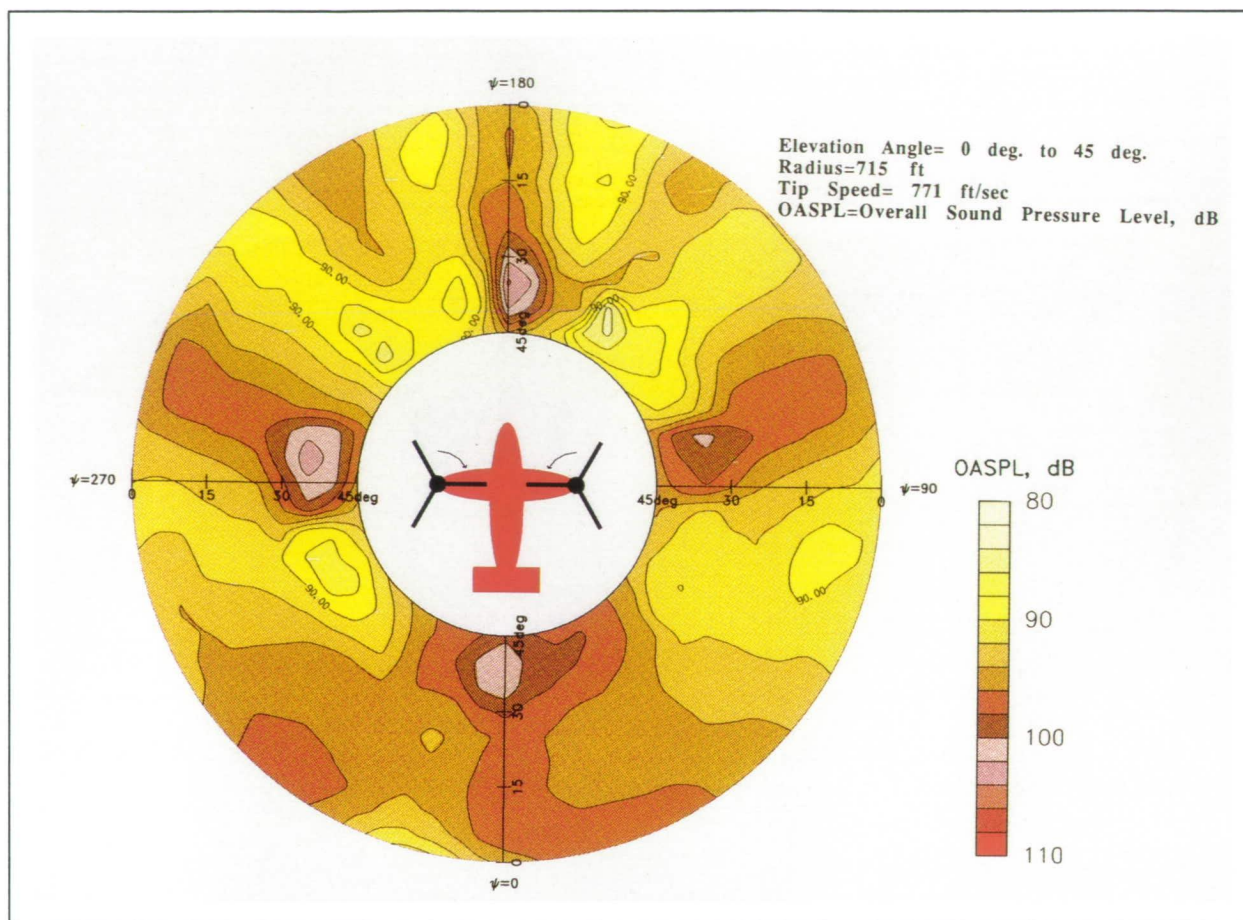
Color plate 6. Calculated Mach contours for AH-1G blade for high-speed flight conditions where compressibility is encountered. (fig. 2, page 17)



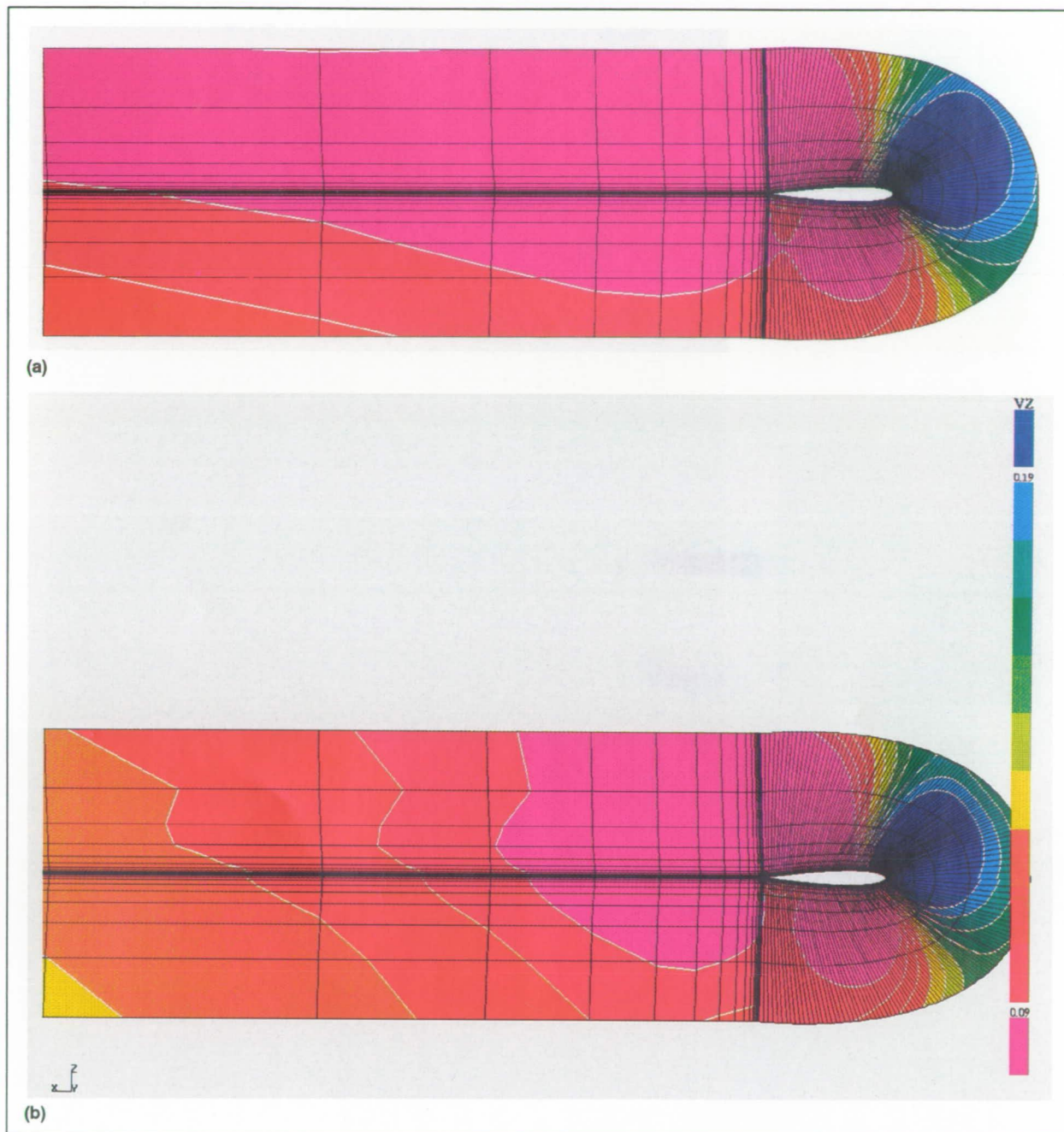
Color plate 7. San Jose State University model showing an oil flow pattern for a high-wing configuration with $NPR = 3.48$, $h = 4.5$ inches. (fig. 2, page 29)



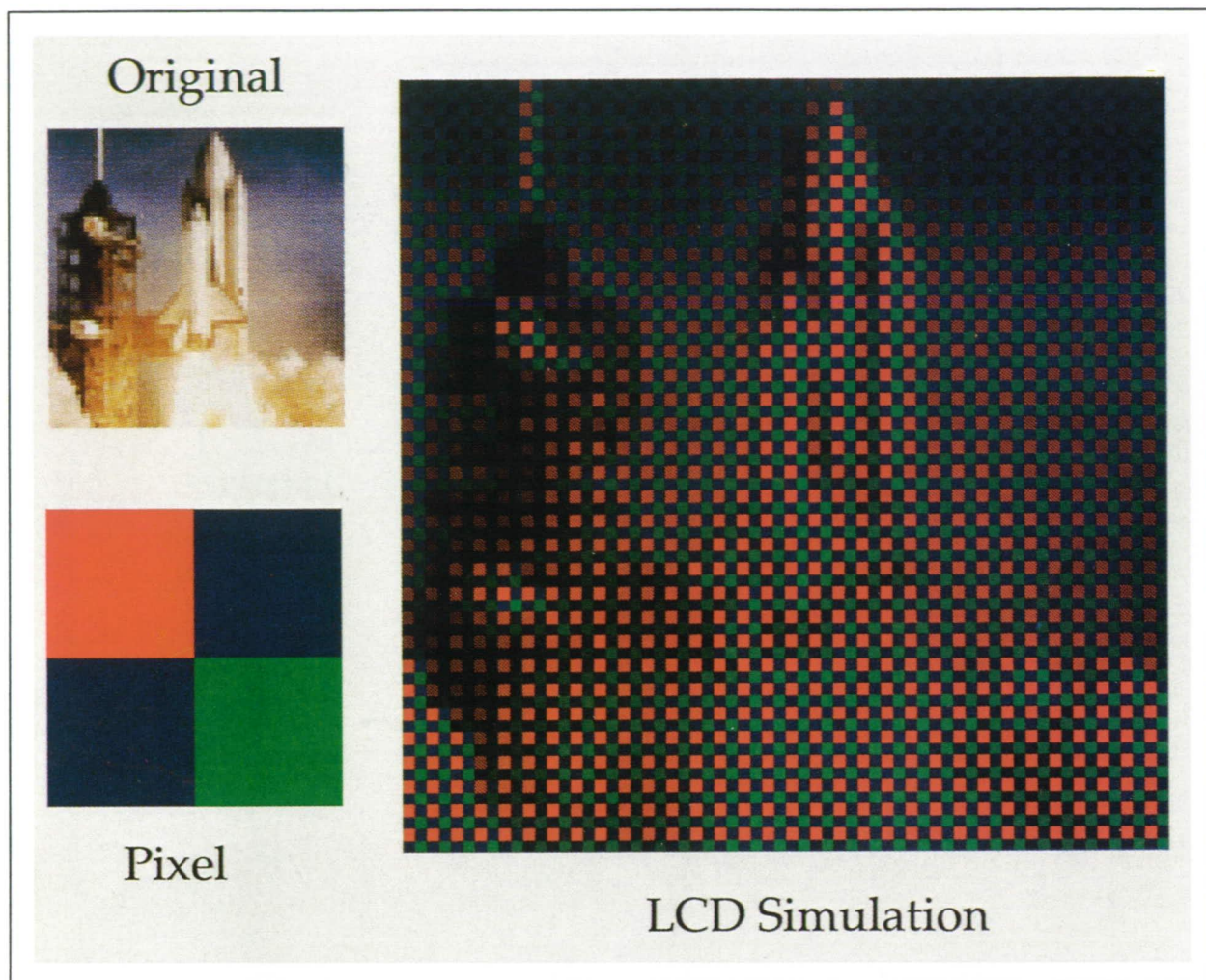
Color plate 8. Plot of pressure top location versus C_p for a two-post delta-wing configuration with NPR of 4.0, a height of 6 inches, and a jet spacing of 16 inches. (fig. 4, page 29)



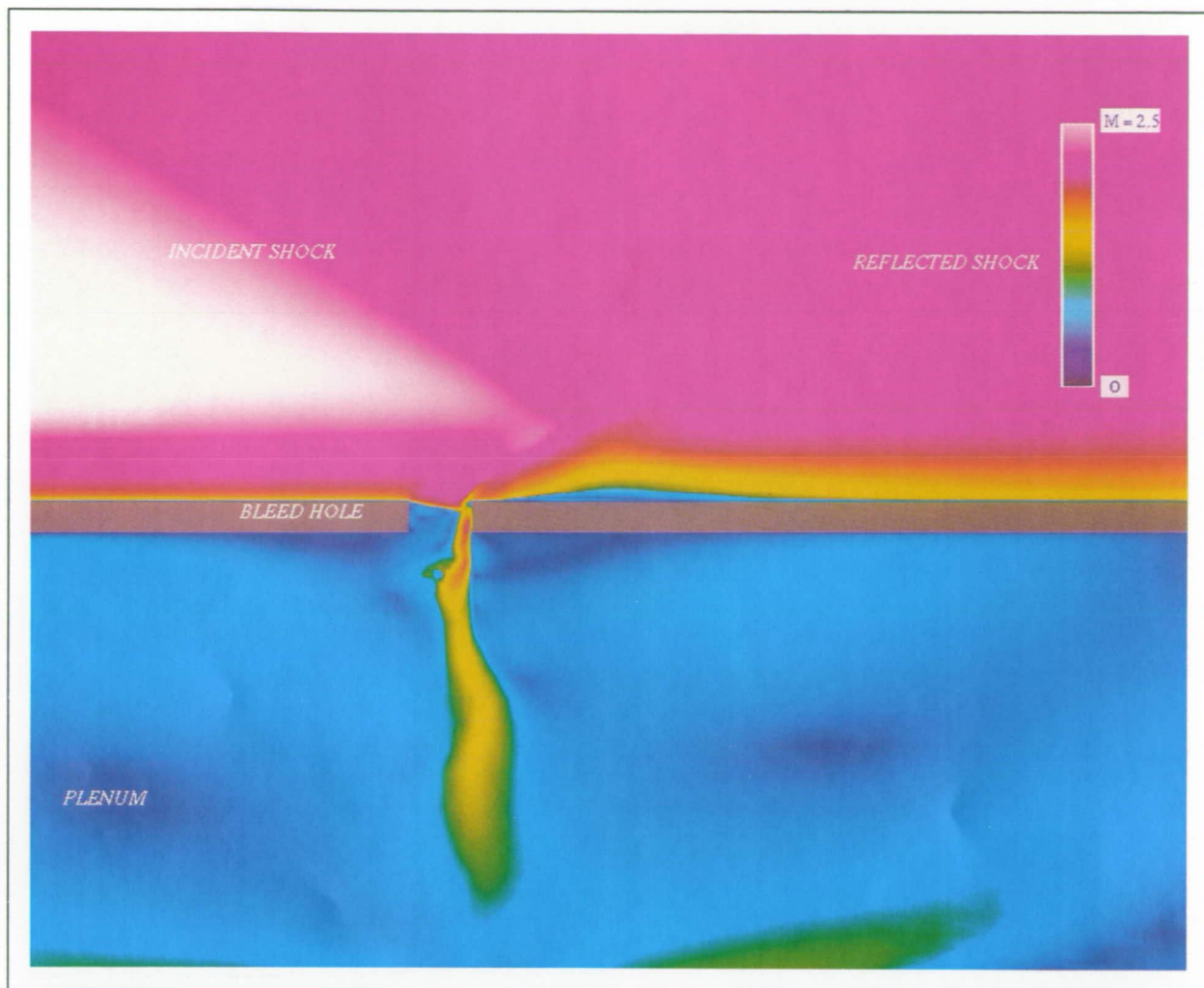
Color plate 9. Acoustic intensity over the surface of a hemisphere centered on the XV-15 aircraft.
 (fig. 1, page 33)



Color plate 10. Comparison of computed vertical velocity contours at wing plane of symmetry. (a) ARC3D, far-field boundary at 17 airfoil chords, (b) ZAP3D, far-field boundary at 1.2 airfoil chords. (fig. 1, page 55)

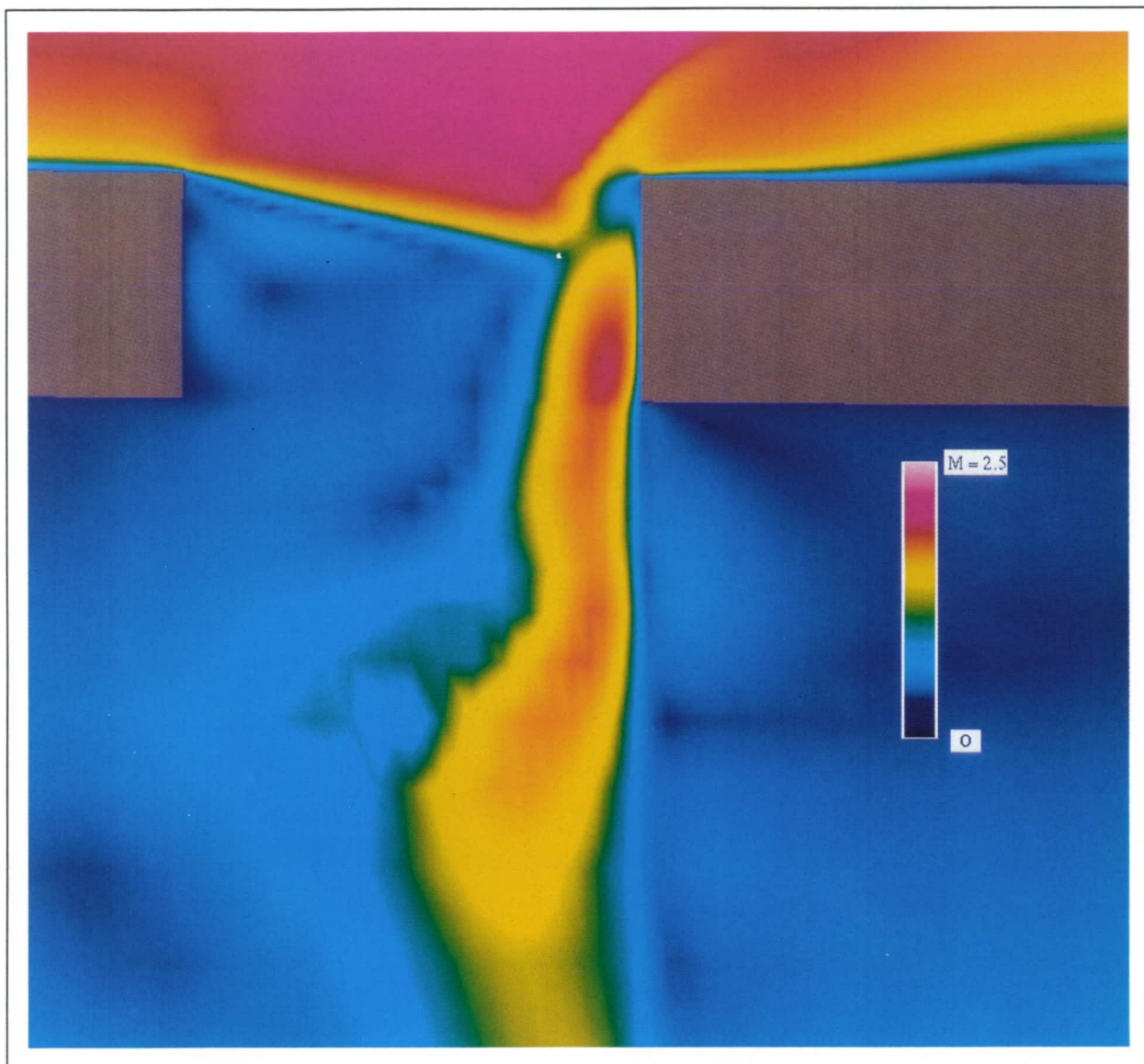


Color plate 11. Image of a rocket rendered in a low-resolution liquid crystal display. (fig. 1, page 114)

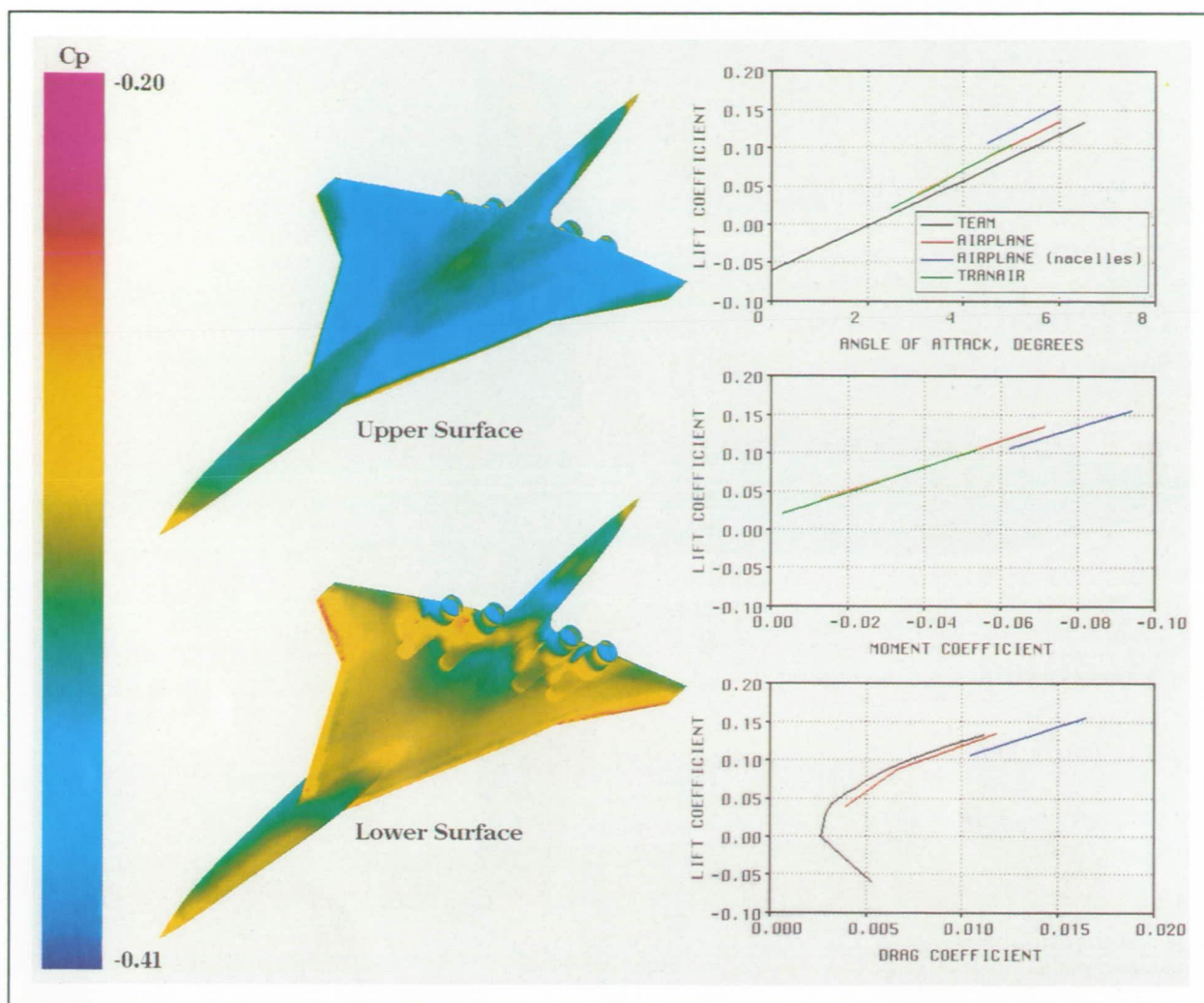


Color plate 12. Overall flow field Mach contours, $M_\infty = 2.5$, $d_{shock} = 30^\circ$. (fig. 2, page 147)

ORIGINAL PAGE
COLOR PHOTOGRAPH

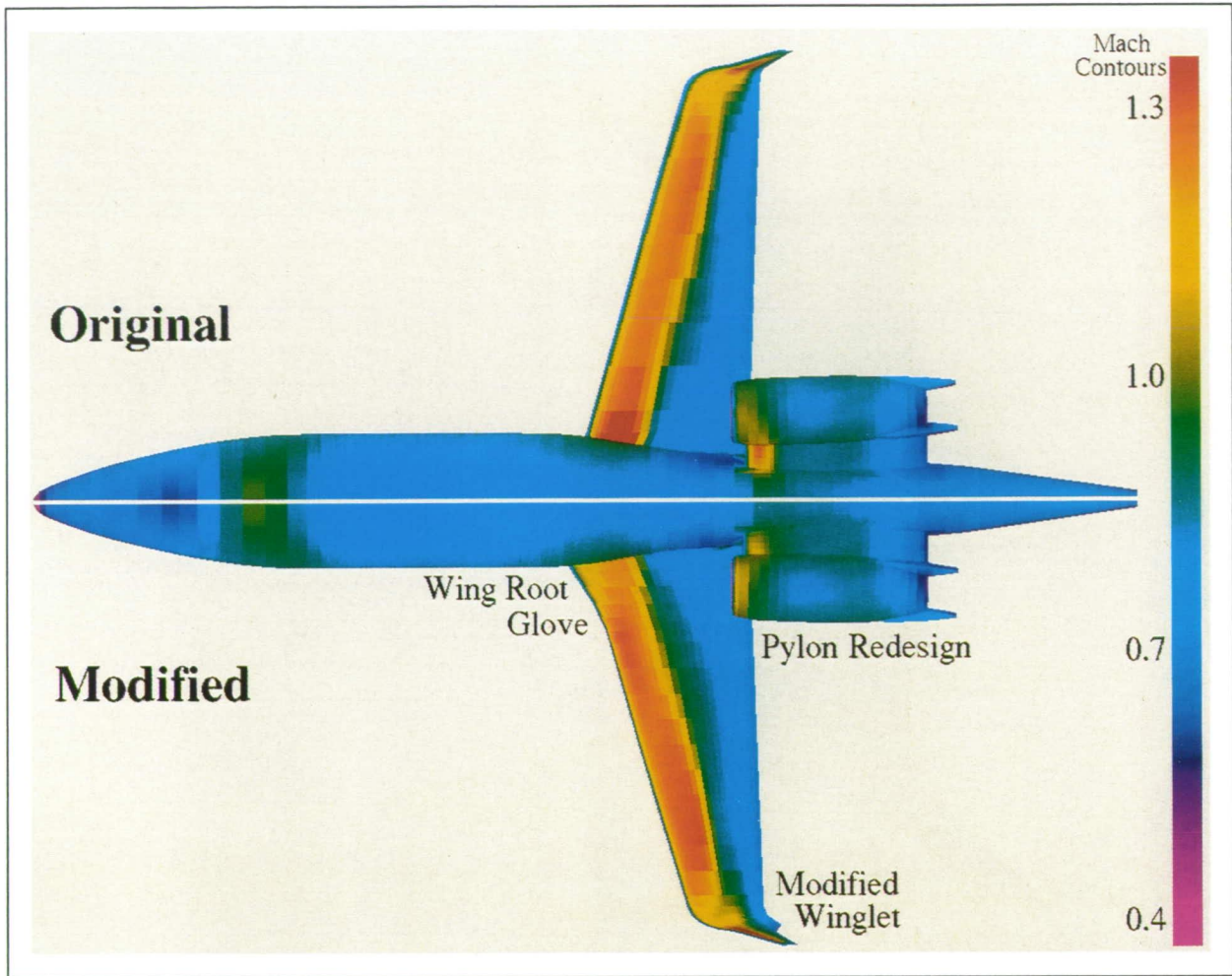


Color plate 13. Mach number distribution through bleed hole region. (fig. 3, page 148)



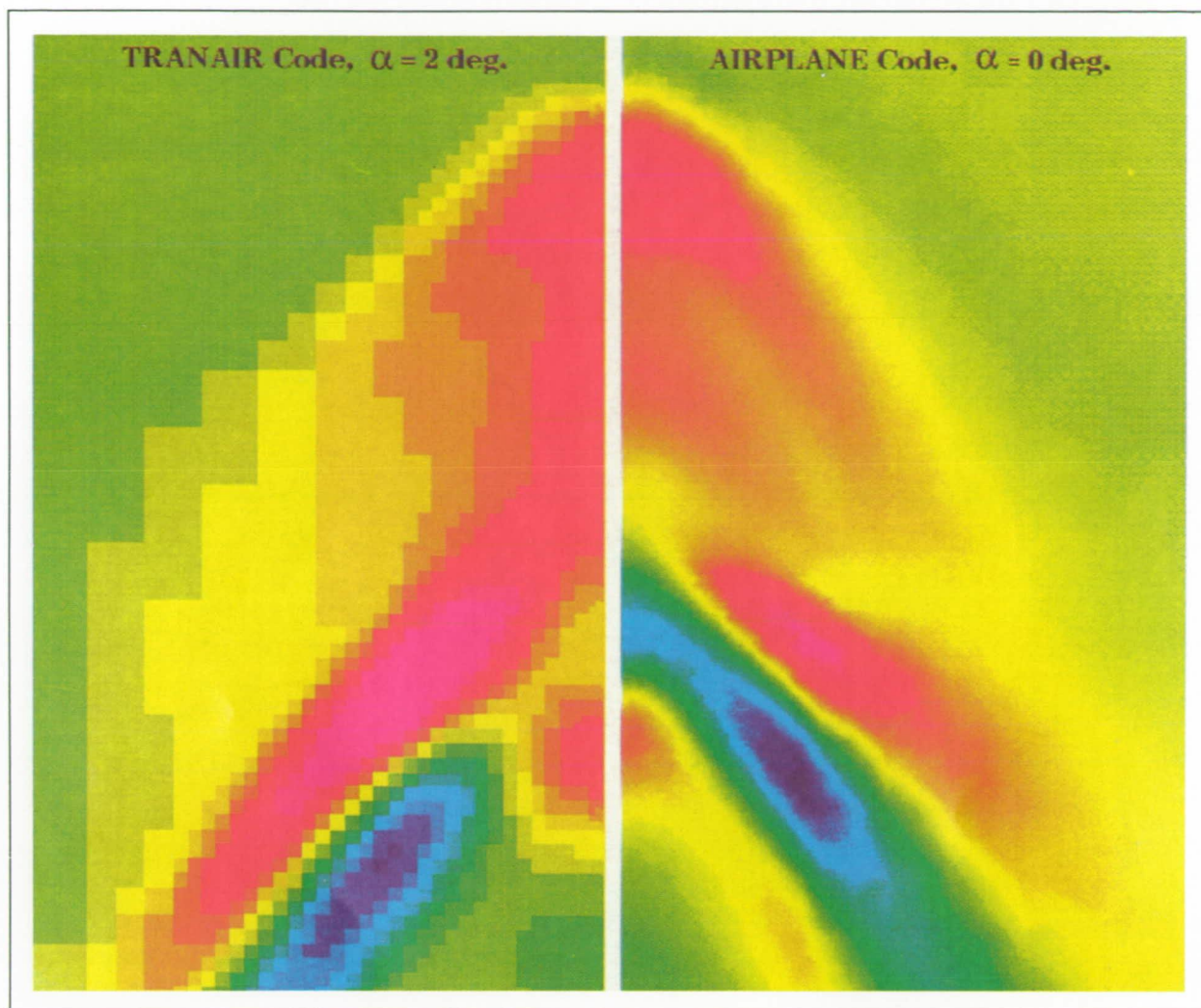
Color plate 14. Surface pressure contours for a modern supersonic transport, $M = 2.01$, $\alpha = 6.0^\circ$, as computed by the AIRPLANE code, and force and moment coefficients from three CFD codes. (fig. 1, page 148)

ORIGINAL PAGE
COLOR PHOTOGRAPH



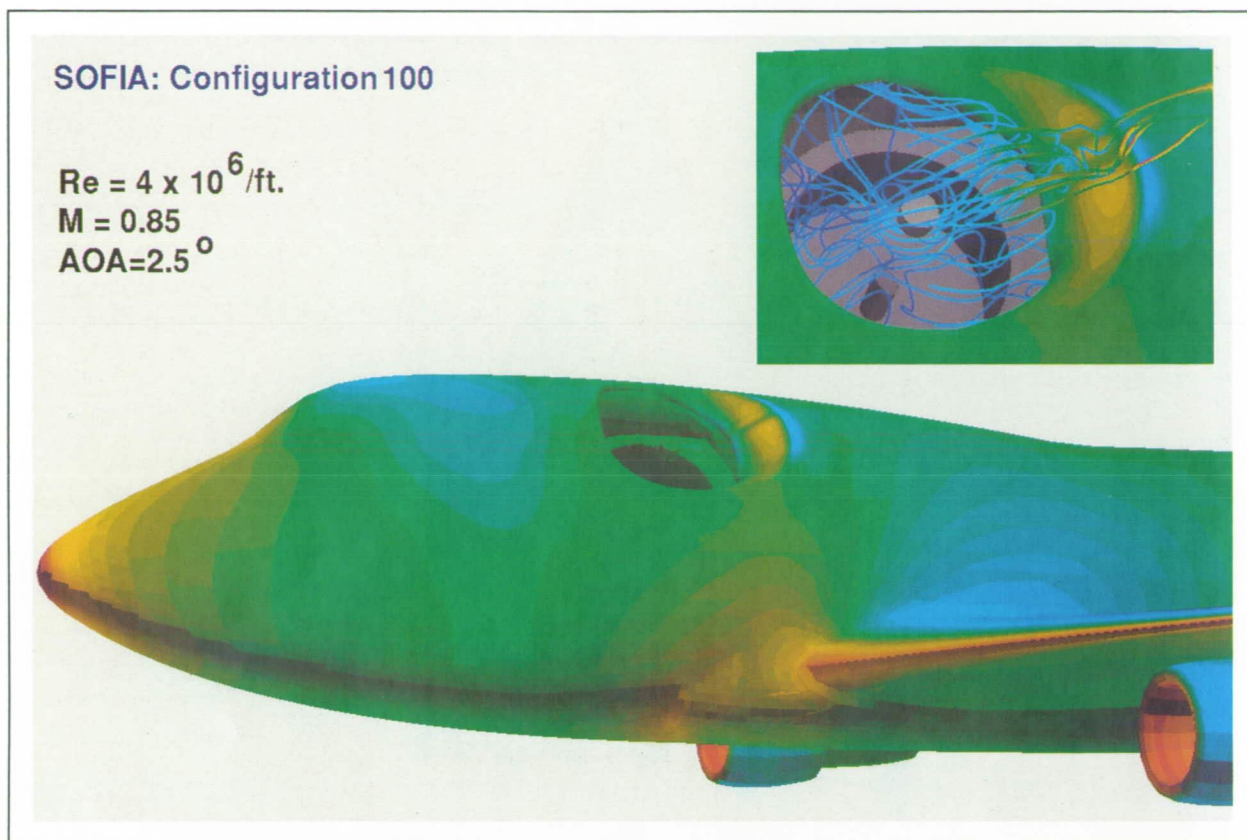
Color plate 15. TRANAIR Mach contour predictions for Learjet Model 60 original geometry (upper half of figure) and modified geometry (lower half of figure), $M_\infty = 0.75$, $\alpha = 4^\circ$. (fig. 1, page 153)

ORIGINAL PAGE
COLOR PHOTOGRAPH



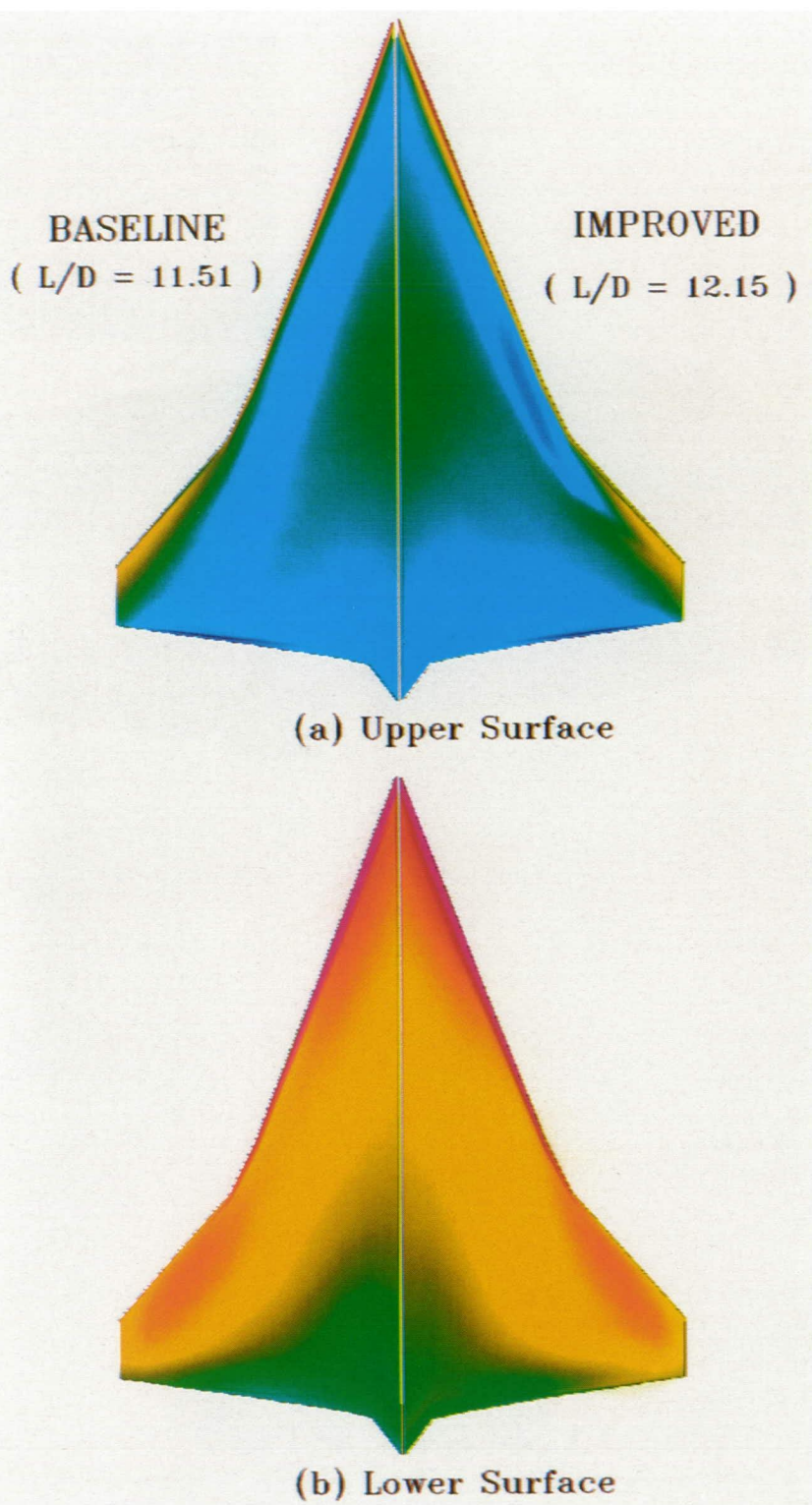
Color plate 16. Pressure coefficient contours at 0.25 body length below the low-sonic-boom model. (fig. 1, page 154)

ORIGINAL PAGE
COLOR PHOTOGRAPH

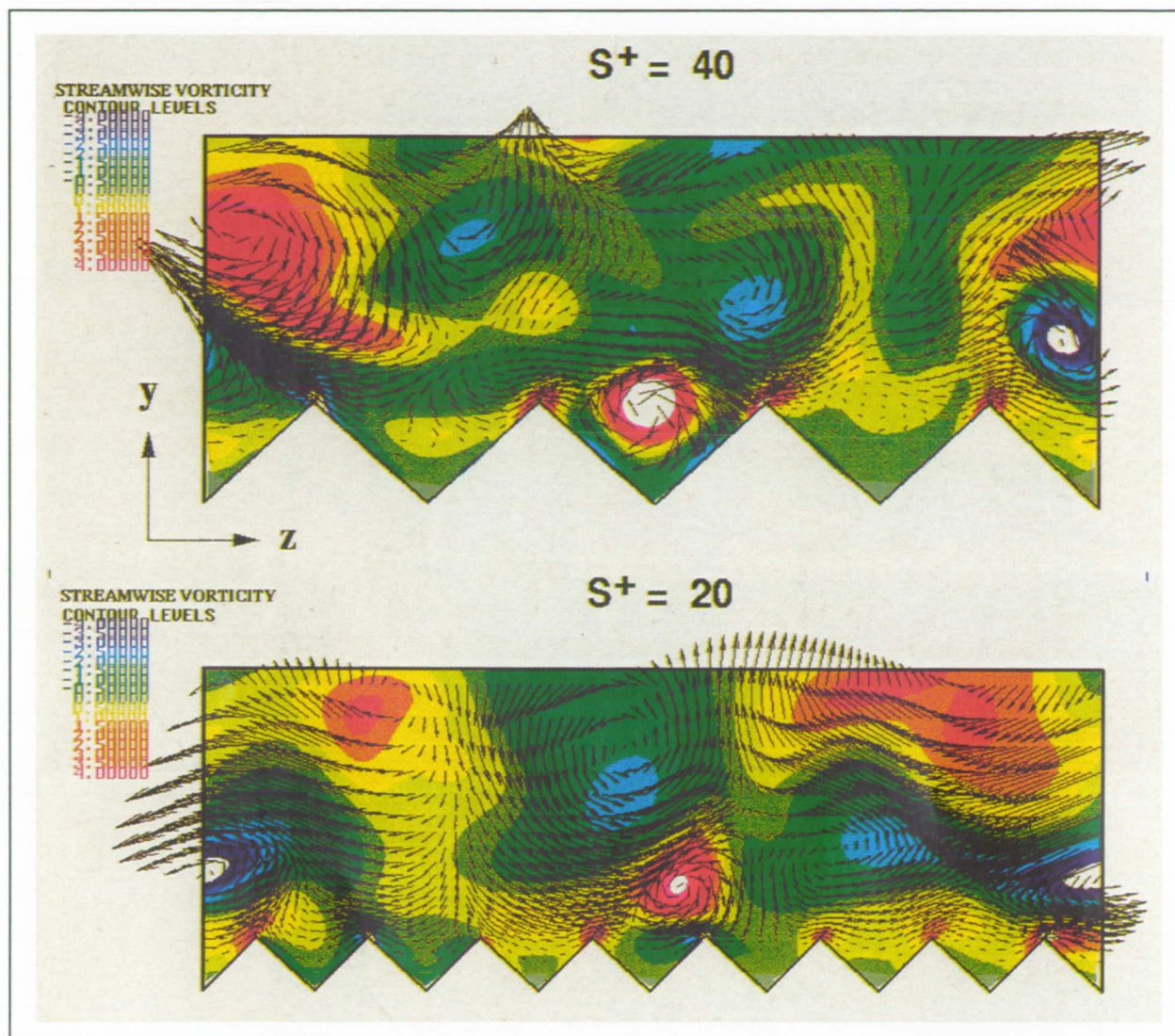


Color plate 18. Surface pressures and streamlines for the quiet configuration. (fig. 3, page 159)

ORIGINAL PAGE
COLOR PHOTOGRAPH

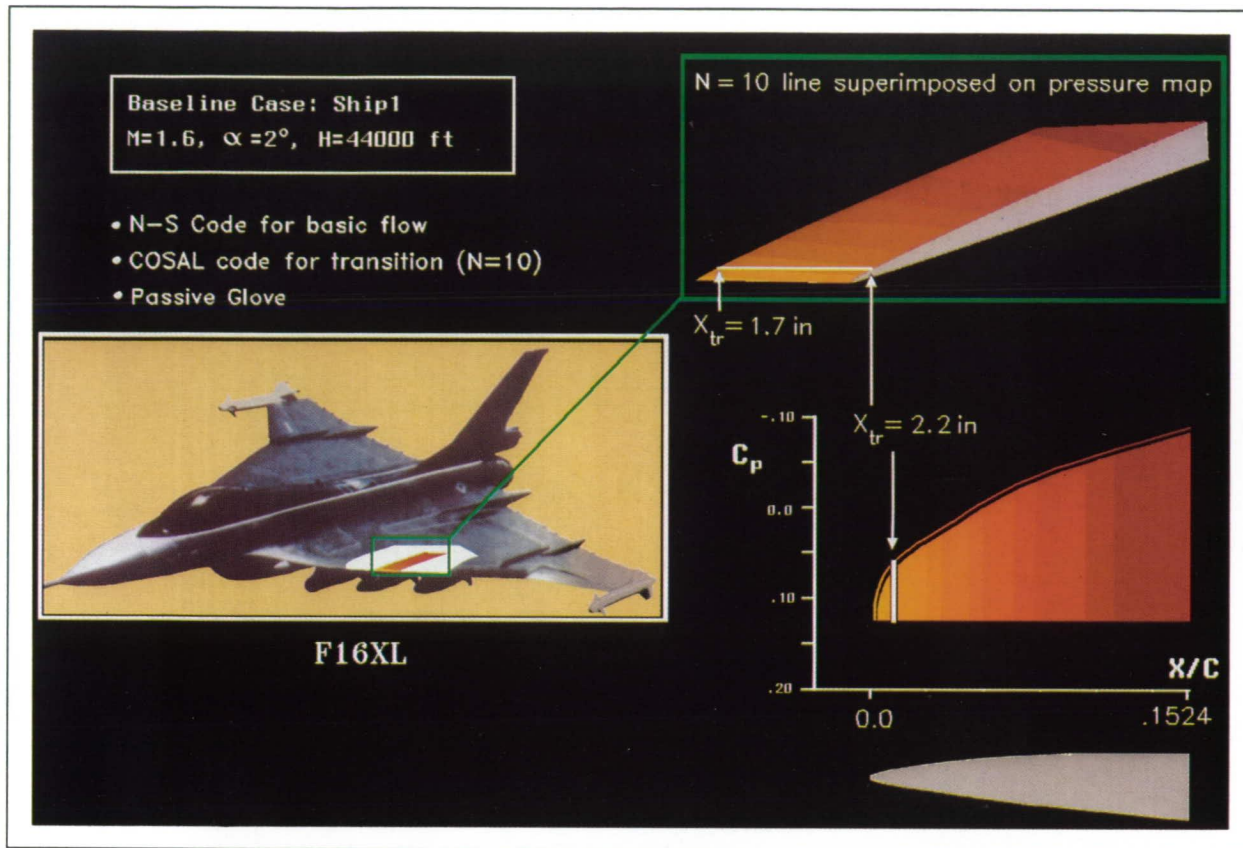


Color plate 19. Comparison of pressure on suction side and pressure side of baseline and optimized wings. (fig. 1, page 162)



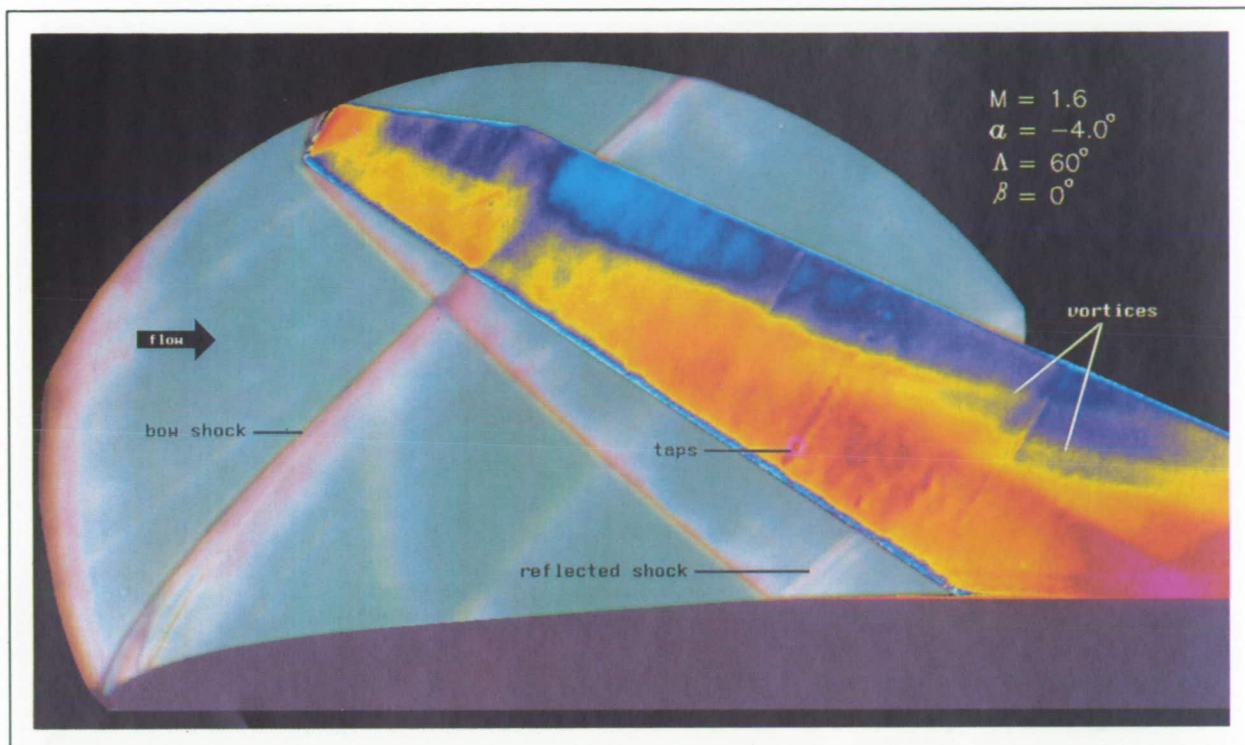
Color plate 20. Velocity vector and contours of streamwise vorticity in a (z, y) plane. Contour levels are from -4 to 4 by increments of 0.5. (fig. 1, page 163)

ORIGINAL PAGE
COLOR PHOTOGRAPH



Color plate 21. Composite figure of F-16XL geometry, pressure map on wing glove, and predicted transition location. (fig. 1, page 165)

ORIGINAL PAGE
 COLOR PHOTOGRAPH



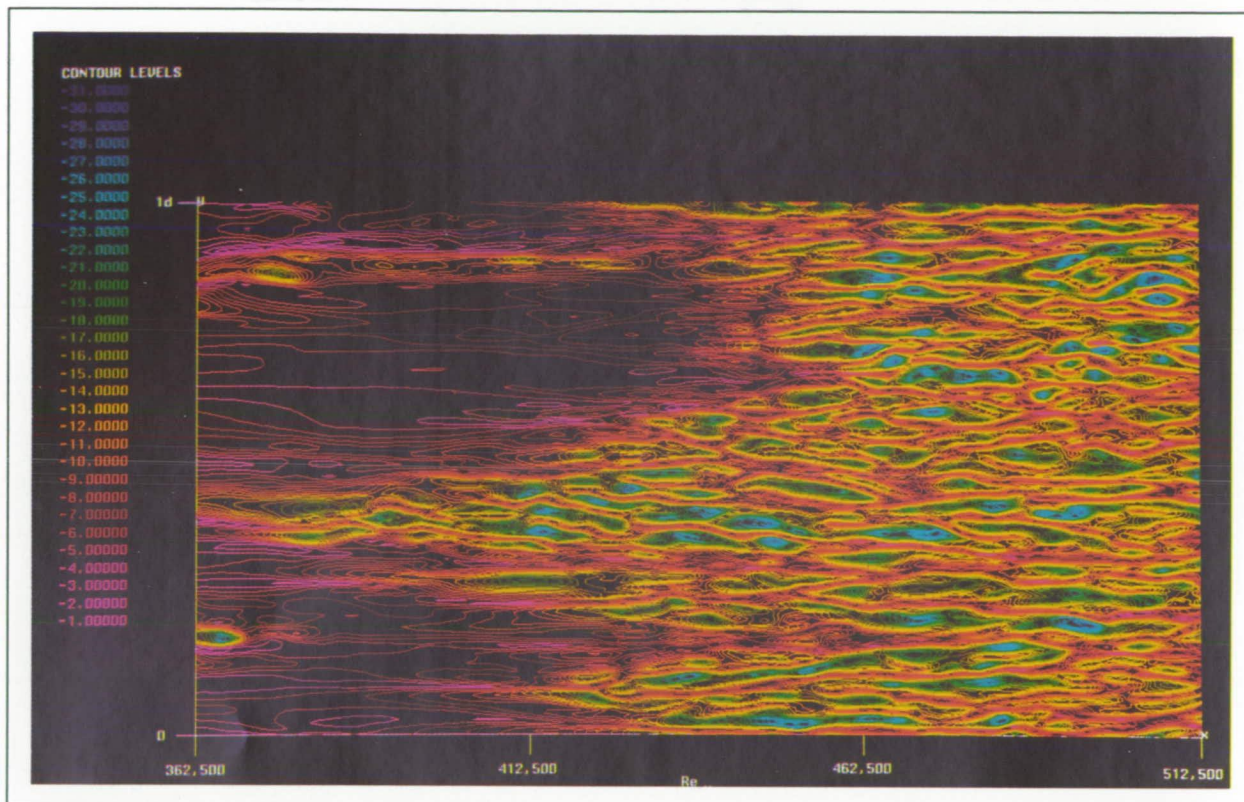
Color plate 22. False-color map of pressure field over forward-swept portion of wing lower surface. Color denotes pressure level: red is low pressure, blue is high pressure. (fig. 1, page 171)

ORIGINAL PAGE
COLOR PHOTOGRAPH

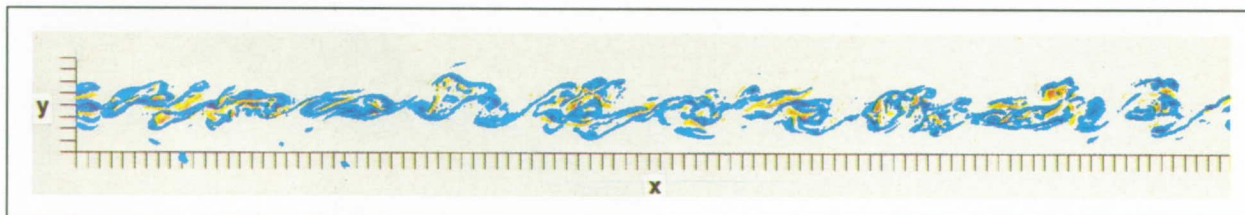


*Color plate 23. Laser digitizer setup showing traversal mechanism and laser sheet used for model measurement.
(fig. 1, page 172)*

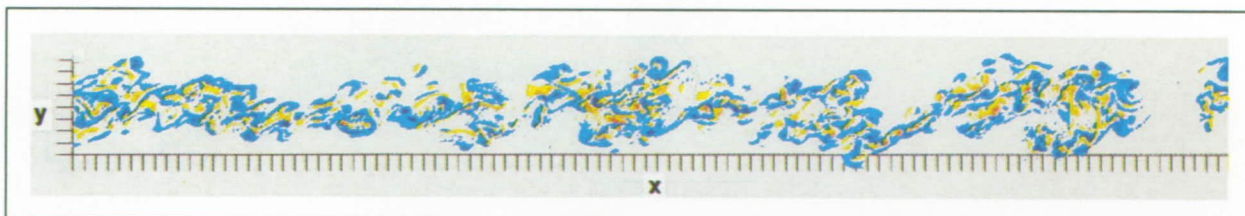
ORIGINAL PAGE
COLOR PHOTOGRAPH



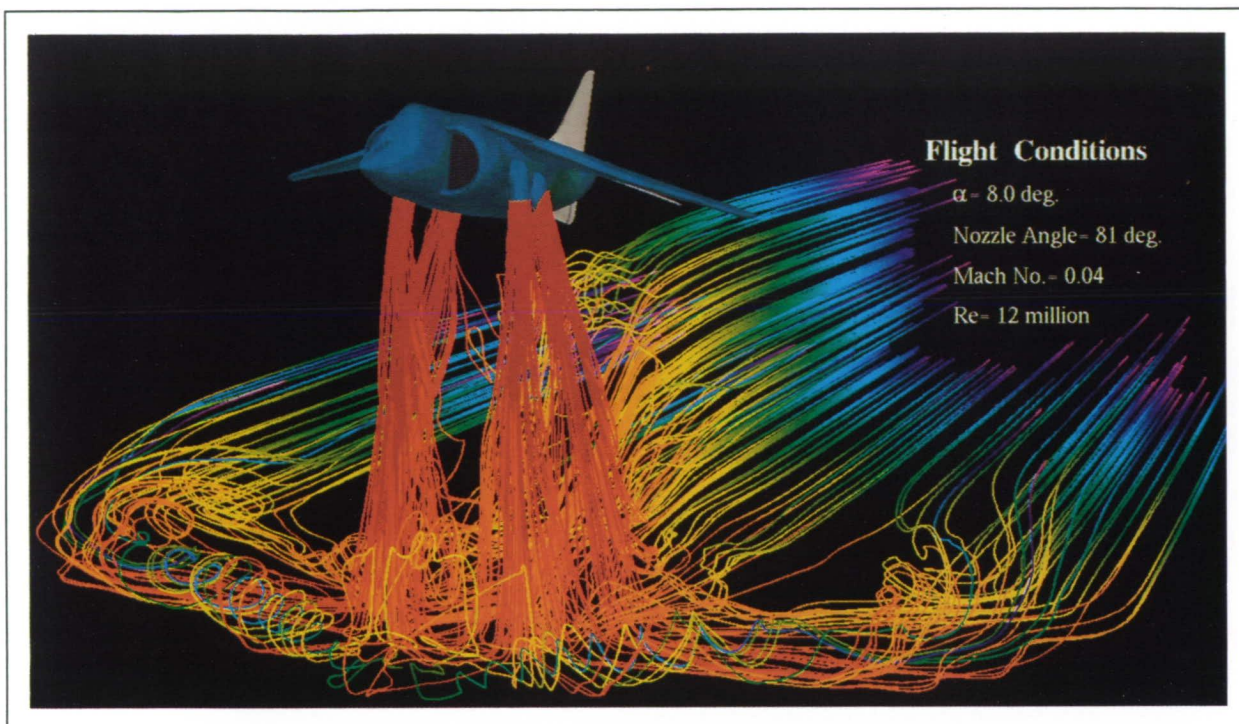
Color plate 24. Spanwise vorticity contours close to the surface of the flat plate. (fig. 2, page 177)



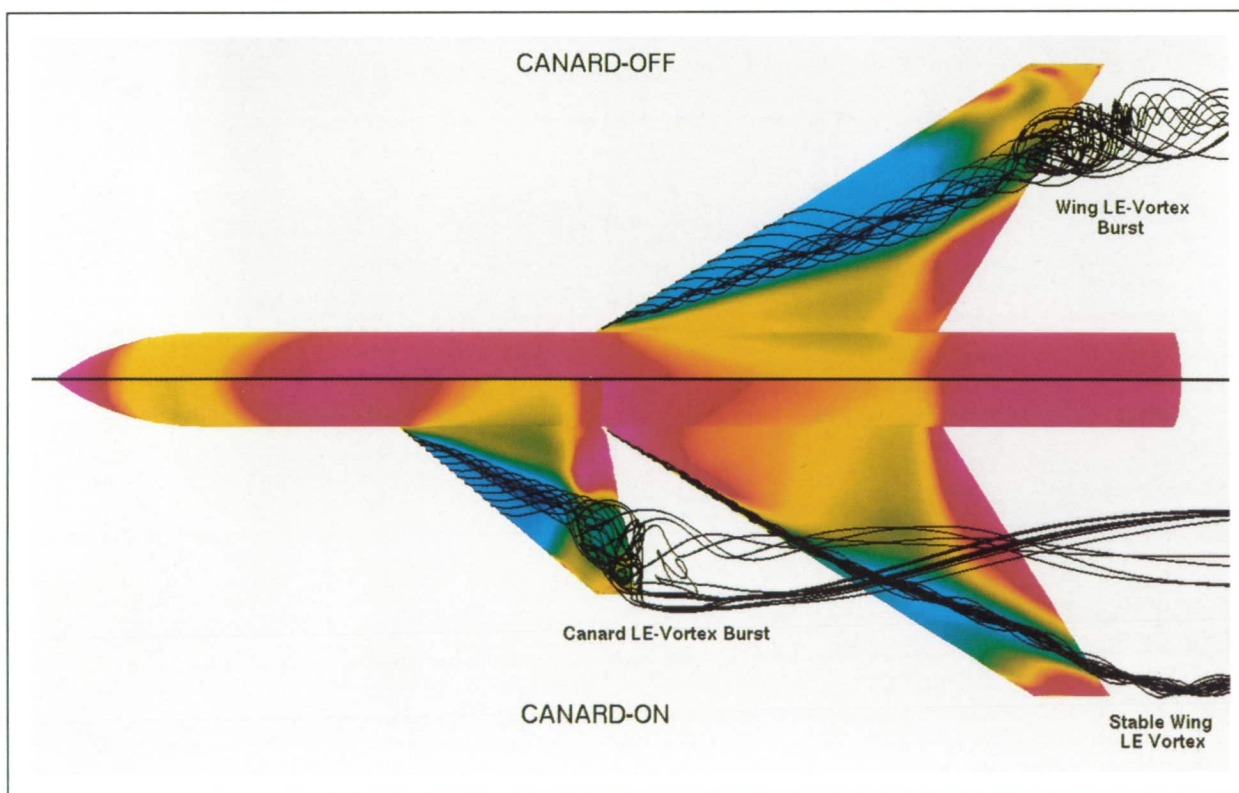
Color plate 25. Spanwise vorticity contours (red = positive, blue = negative) at a time when most of the layer vorticity has "rolled up" into eddies with significant spanwise coherence. (fig. 1, page 178)



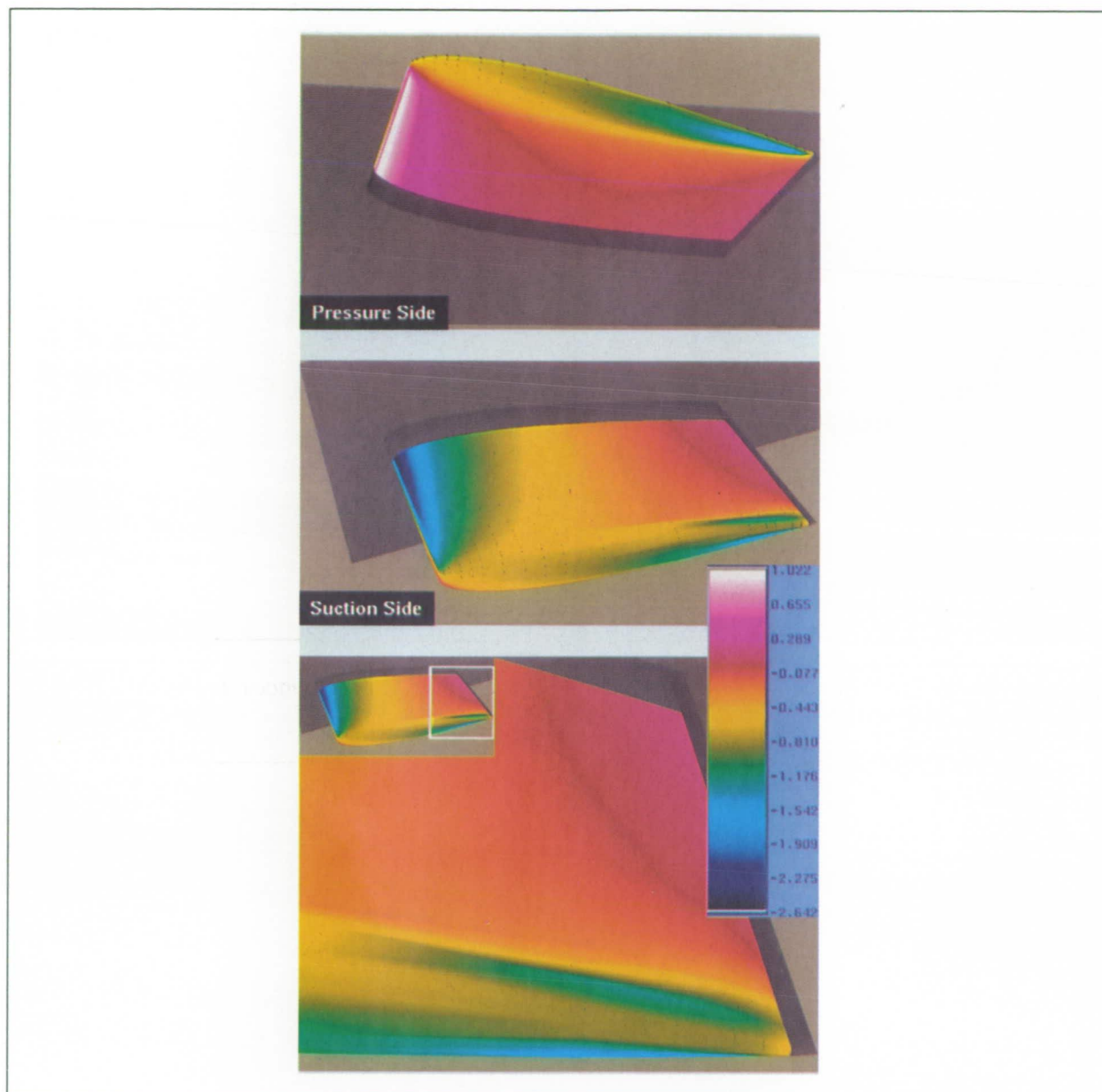
Color plate 26. Spanwise vorticity contours (red = positive, blue = negative) at a time later than that shown in the first figure. (fig. 2, page 179)



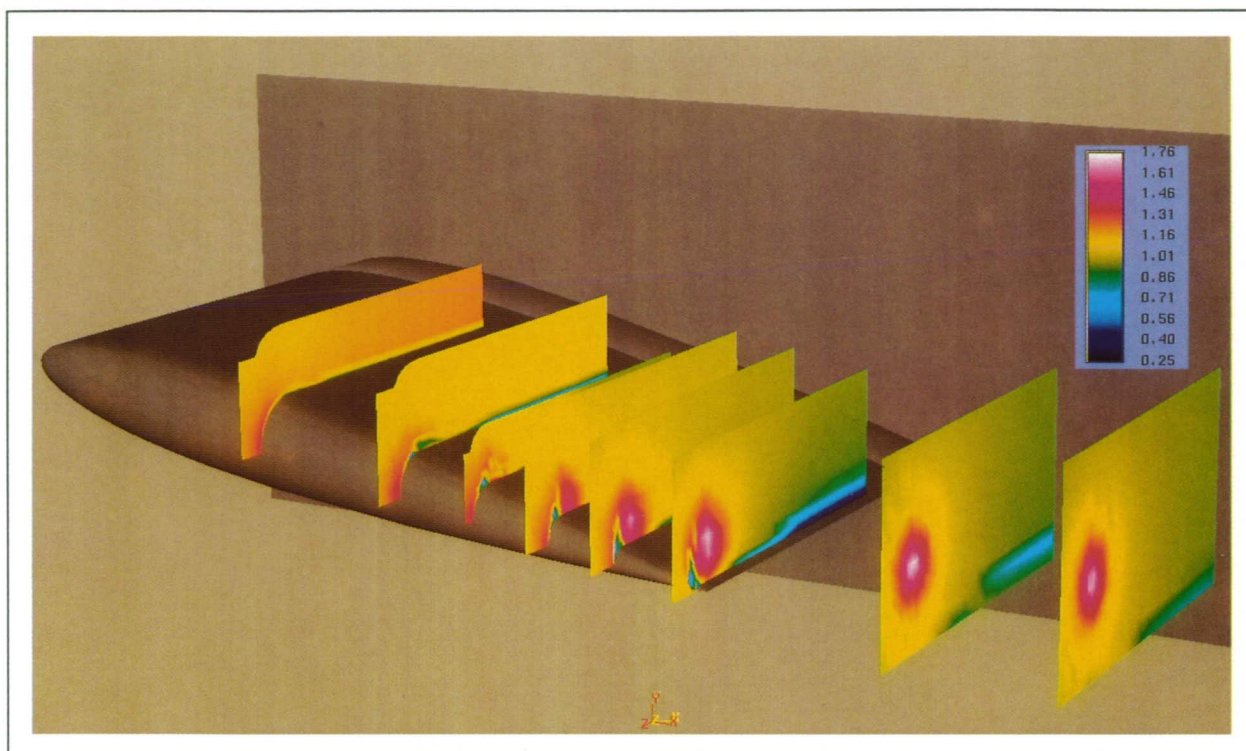
Color plate 27. Flow about the YAV-8B Harrier (particle traces colored by time since release). (fig. 1, page 182)



Color plate 28. Comparison between canard-on and canard-off surface pressure and off-surface particle traces at Mach 0.90 and an angle of attack of 12 degrees. (fig. 1, page 183)

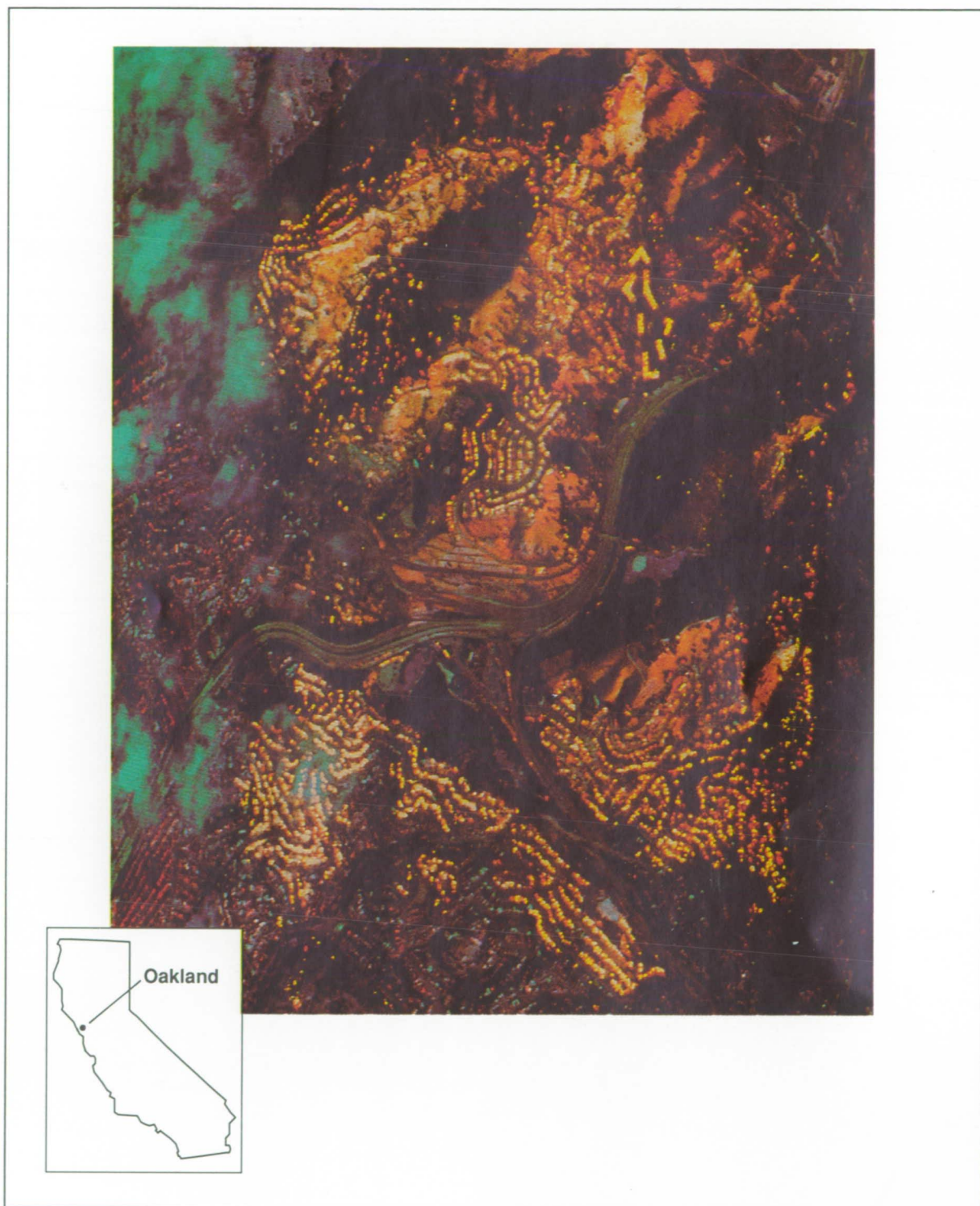


Color plate 29. Measured surface-pressure-coefficient contours. (fig. 1, page 187)



Color plate 30. Measured normalized velocity magnitude. (fig. 2, page 188)

ORIGINAL PAGE
COLOR PHOTOGRAPH



Color plate 31. Airborne Thematic Mapper image of the Oakland Hills Fire. (fig. 1, page 216)

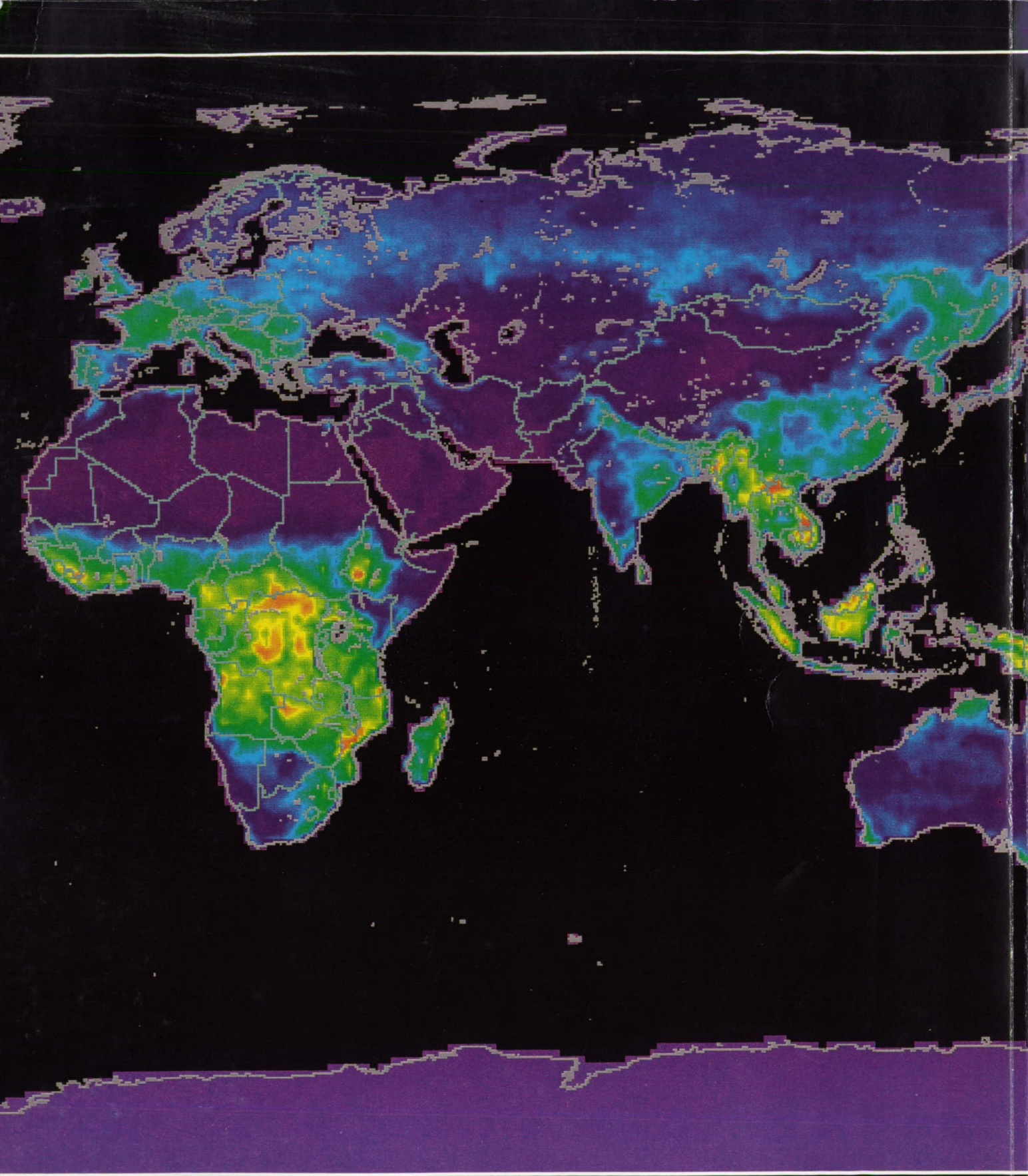
ORIGINAL PAGE
COLOR PHOTOGRAPH

REPORT DOCUMENTATION PAGE

Form Approved
OMB No. 0704-0188

Public reporting burden for this collection of information is estimated to average 1 hour per response, including the time for reviewing instructions, searching existing data sources, gathering and maintaining the data needed, and completing and reviewing the collection of information. Send comments regarding this burden estimate or any other aspect of this collection of information, including suggestions for reducing this burden, to Washington Headquarters Services, Directorate for Information Operations and Reports, 1215 Jefferson Davis Highway, Suite 1204, Arlington, VA 22202-4302, and to the Office of Management and Budget, Paperwork Reduction Project (0704-0188), Washington, DC 20503.

1. AGENCY USE ONLY (Leave blank)		2. REPORT DATE October 1992	3. REPORT TYPE AND DATES COVERED Technical Memorandum – Fiscal Year 1991	
4. TITLE AND SUBTITLE Research and Technology 1991			5. FUNDING NUMBERS	
6. AUTHOR(S) Ames-Moffett and Ames-Dryden investigators				
7. PERFORMING ORGANIZATION NAME(S) AND ADDRESS(ES) Ames Research Center Moffett Field, CA 94035-1000			8. PERFORMING ORGANIZATION REPORT NUMBER A-92063	
9. SPONSORING/MONITORING AGENCY NAME(S) AND ADDRESS(ES) National Aeronautics and Space Administration Washington, DC 20546-0001			10. SPONSORING/MONITORING AGENCY REPORT NUMBER NASA TM-103924	
11. SUPPLEMENTARY NOTES Point of Contact: John T. Howe, Chief Scientist, Ames Research Center, MS 200-1B, Moffett Field, CA 94035-1000; (415) 604-5500 or the contact person(s) at the end of each article				
12a. DISTRIBUTION/AVAILABILITY STATEMENT Unclassified — Unlimited Subject Category 99			12b. DISTRIBUTION CODE	
13. ABSTRACT (Maximum 200 words) Selected research and technology activities at Ames Research Center, including the Moffett Field site and the Dryden Flight Research Facility, are summarized. These activities exemplify the Center's varied and productive research efforts for 1991.				
14. SUBJECT TERMS Aeronautics, Space technology, Space sciences, Earth sciences, Life sciences, Computer science, Research and technology			15. NUMBER OF PAGES 352	
			16. PRICE CODE A16	
17. SECURITY CLASSIFICATION OF REPORT Unclassified	18. SECURITY CLASSIFICATION OF THIS PAGE Unclassified	19. SECURITY CLASSIFICATION OF ABSTRACT	20. LIMITATION OF ABSTRACT	



National Aeronautics and Space Administration
Ames Research Center
Moffett Field, CA 94035-1000

TM 103924